FLOW AND TRANSFORMATIONS IN POROUS MEDIA

EDITED BY: Renaud Toussaint, Bjørnar Sandnes, Daniel Koehn, Piotr Szymczak and Einat Aharonov

PUBLISHED IN: Frontiers in Physics

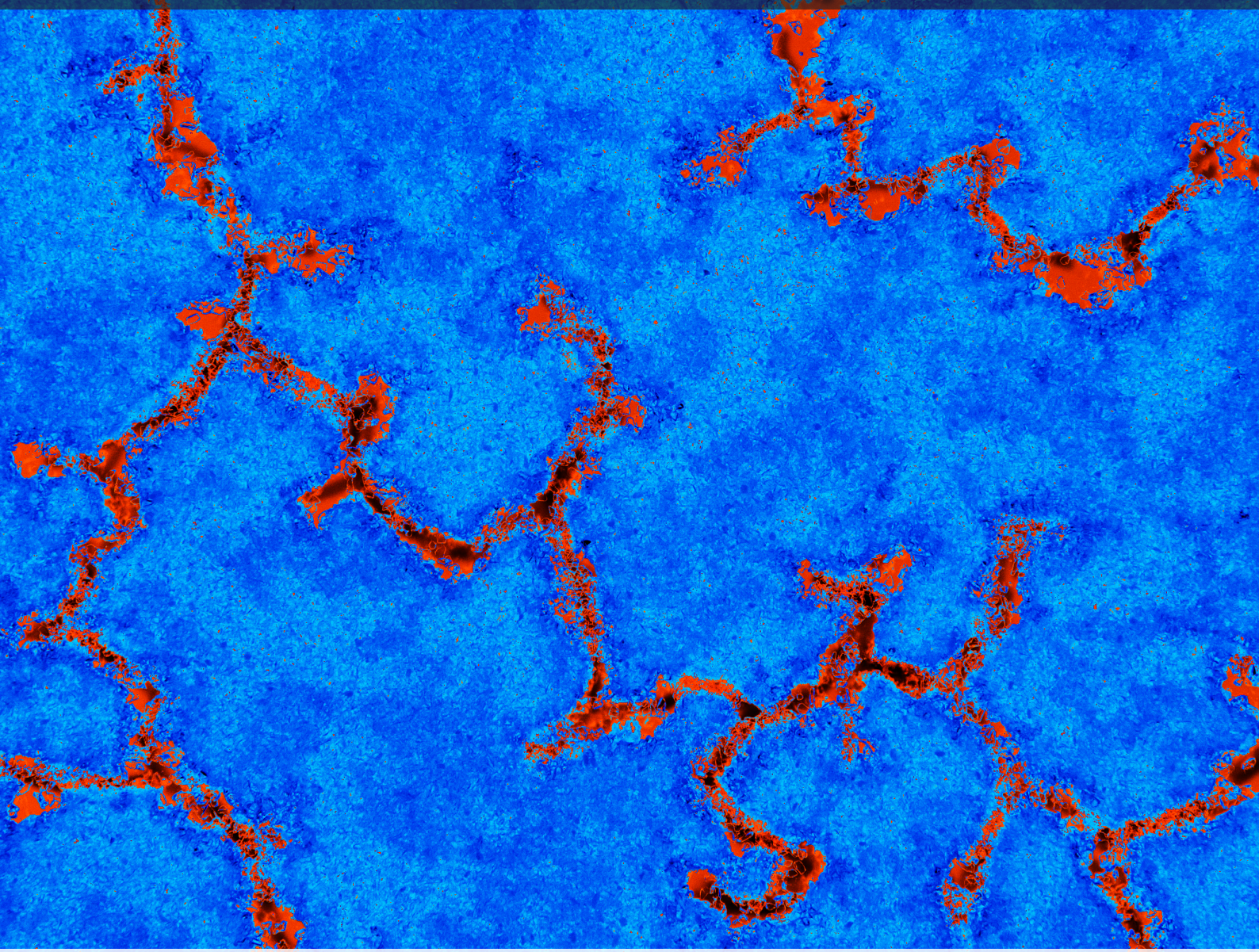

frontiers Research Topics

frontiers

ISSN 1664-8714
ISBN 978-2-88945-077-0
DOI 10.3389/978-2-88945-077-0

About Frontiers

Frontiers is more than just an open-access publisher of scholarly articles: it is a pioneering approach to the world of academia, radically improving the way scholarly research is managed. The grand vision of Frontiers is a world where all people have an equal opportunity to seek, share and generate knowledge. Frontiers provides immediate and permanent online open access to all its publications, but this alone is not enough to realize our grand goals.

Frontiers Journal Series

The Frontiers Journal Series is a multi-tier and interdisciplinary set of open-access, online journals, promising a paradigm shift from the current review, selection and dissemination processes in academic publishing. All Frontiers journals are driven by researchers for researchers; therefore, they constitute a service to the scholarly community. At the same time, the Frontiers Journal Series operates on a revolutionary invention, the tiered publishing system, initially addressing specific communities of scholars, and gradually climbing up to broader public understanding, thus serving the interests of the lay society, too.

Dedication to Quality

Each Frontiers article is a landmark of the highest quality, thanks to genuinely collaborative interactions between authors and review editors, who include some of the world's best academicians. Research must be certified by peers before entering a stream of knowledge that may eventually reach the public - and shape society; therefore, Frontiers only applies the most rigorous and unbiased reviews.

Frontiers revolutionizes research publishing by freely delivering the most outstanding research, evaluated with no bias from both the academic and social point of view.

By applying the most advanced information technologies, Frontiers is catapulting scholarly publishing into a new generation.

What are Frontiers Research Topics?

Frontiers Research Topics are very popular trademarks of the Frontiers Journals Series: they are collections of at least ten articles, all centered on a particular subject. With their unique mix of varied contributions from Original Research to Review Articles, Frontiers Research Topics unify the most influential researchers, the latest key findings and historical advances in a hot research area! Find out more on how to host your own Frontiers Research Topic or contribute to one as an author by contacting the Frontiers Editorial Office: **researchtopics@frontiersin.org**

FLOW AND TRANSFORMATIONS IN POROUS MEDIA

Topic Editors:
Renaud Toussaint, IPGS, Centre National de la Recherche Scientifique, University of Strasbourg/EOST, France
Bjørnar Sandnes, Swansea University, UK
Daniel Koehn, University of Glasgow, UK
Piotr Szymczak, University of Warsaw, Poland
Einat Aharonov, Hebrew University of Jerusalem, Israel

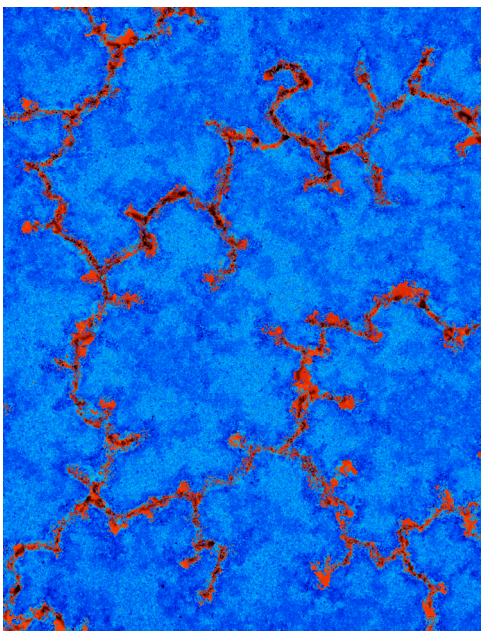

Deformable porous medium fractured by pressurized air. The injected air penetrates the loose packing of wet granular material in rapid bursts, creating a branching, fracture-like pattern. (False color image).
Image by Bjørnar Sandnes.

Fluid flow in transforming porous rocks, fracture networks, and granular media is a very active interdisciplinary research subject in Physics, Earth Sciences, and Engineering.

Examples of natural and engineered processes include hydrocarbon recovery, carbon dioxide geo-sequestration, soil drying and wetting, pollution remediation, soil liquefaction, landslides, dynamics of wet or dry granular media, dynamics of faulting or friction, volcanic eruptions, gas venting in sediments, karst development and speleogenesis, ore deposit development, and radioactive waste disposal.

Hydrodynamic flow instabilities and pore scale disorder typically result in complex flow patterning. In transforming media, additional mechanisms come into play: compaction, de-compaction, erosion, segregation, and fracturing lead to changes in permeability over time.

Dissolution, precipitation, and chemical reactions between solutes and solids may gradually alter the composition and structure of the solid matrix, either creating or destroying permeable paths for fluid flow. A complex, dynamic feedback thus arises where, on the one hand, the fluid flow affects the characteristics of the porous medium, and on the other hand the changing medium influences the fluid flow.

This Research Topic Ebook presents current research illustrating the depth and breadth of ongoing work in the field of flow and transformation in porous media through 15 papers by 72 authors from around the world. The body of work highlights the challenges posed by the vast range of length- and time-scales over which subsurface flow processes occur. Importantly, phenomena from each scale contribute to the larger-scale behavior. The flow of oil and gas in reservoirs, and the flow of groundwater on catchment scale is sensitively linked to pore scale processes and material heterogeneity down to the micrometer scale. The geological features of the same reservoirs and catchments evolved over millions of years, sometimes as a consequence of cracking and fracture growth occurring on the time scale of microseconds. The research presented by the authors of this Research Topic represents a step toward bridging the separation of scales as well as the separation of scientific disciplines so that a more unified picture of flow and transformation in porous media can start to emerge.

Citation: Toussaint, R., Sandnes, B., Koehn, D., Szymczak, P., Aharonov, E., eds. (2017). Flow and Transformations in Porous Media. Lausanne: Frontiers Media. doi: 10.3389/978-2-88945-077-0

Table of Contents

frontiers in Physics

EDITORIAL
published: 28 October 2016
doi: 10.3389/fphy.2016.00042

Editorial: Flow and Transformation in Porous Media

Bjørnar Sandnes[1]*, *Daniel Koehn*[2], *Renaud Toussaint*[3], *Piotr Szymczak*[4] and *Einat Aharonov*[5]

[1] Energy Safety Research Institute, College of Engineering, Swansea University, Swansea, UK, [2] School of Geographical and Earth Sciences, University of Glasgow, Glasgow, UK, [3] Institut de Physique du Globe de Strasbourg, Centre National de la Recherche Scientifique, University of Strasbourg/EOST, Strasbourg, France, [4] Institute of Theoretical Physics, Faculty of Physics, University of Warsaw, Warsaw, Poland, [5] Institute of Earth Sciences, Faculty of Mathematics and Sciences, Hebrew University of Jerusalem, Jerusalem, Israel

Keywords: porous media, granular materials, fracturing, pattern formation, capillary, friction, dissolution, two-phase flow

The Editorial on the Research Topic

Flow and Transformation in Porous Media

Fluid flow in transforming porous rocks, fracture networks, and granular media is subject to considerable current interdisciplinary research activity in Physics, Earth Sciences, and Engineering. Examples of natural and engineered processes include hydrocarbon recovery, carbon dioxide geo-sequestration, soil drying and wetting, pollution remediation, soil liquefaction, landslides, dynamics of wet or dry granular media, dynamics of faulting or friction, volcanic eruptions, gas venting in sediments, karst development and speleogenesis, ore deposit development, and radioactive waste disposal.

Hydrodynamic flow instabilities and pore scale disorder typically result in complex flow patterning. In *transforming media*, additional mechanisms come into play: compaction, de-compaction, erosion, segregation, and fracturing lead to changes in permeability over time. Dissolution, precipitation, and chemical reactions between solutes and solids may gradually alter the composition and structure of the solid matrix, either creating or destroying permeable paths for fluid flow. A complex, dynamic feedback thus arises where, on the one hand, the fluid flow affects the characteristics of the porous medium, and on the other hand the changing medium influences the fluid flow.

This Research Topic Ebook presents current research illustrating the depth and breadth of ongoing work in the field of flow and transformation in porous media through 15 papers by 72 authors from around the world. The body of work highlights the challenges posed by the vast range of length- and time-scales over which subsurface flow processes occur. Importantly, phenomena from each scale contribute to the larger-scale behavior. The flow of oil and gas in reservoirs, and the flow of groundwater on catchment scale is sensitively linked to pore scale processes and material heterogeneity down to the micrometer scale. The geological features of the same reservoirs and catchments evolved over millions of years, sometimes as a consequence of cracking and fracture growth occurring on the time scale of microseconds. The research presented by the authors of this Research Topic represents a step toward bridging the separation of scales as well as the separation of scientific disciplines so that a more unified picture of flow and transformation in porous media can start to emerge.

The first four papers in the Ebook focus on pore scale effects associated with capillary pressure, pore flow, and intergranular forces. Flovik et al. present a pore network model where a wettability

OPEN ACCESS

Edited by:
Alex Hansen, Norwegian University of Science and Technology, Norway

Reviewed by:
Daniel Bonamy, French Alternative Energies and Atomic Energy Commission, France

***Correspondence:**
Bjørnar Sandnes
b.sandnes@swansea.ac.uk

Specialty section:
This article was submitted to Interdisciplinary Physics, a section of the journal Frontiers in Physics

Received: *24 August 2016*
Accepted: *13 October 2016*
Published: *28 October 2016*

Citation:
Sandnes B, Koehn D, Toussaint R, Szymczak P and Aharonov E (2016) Editorial: Flow and Transformation in Porous Media. Front. Phys. 4:42. doi: 10.3389/fphy.2016.00042

altering agent is introduced to two-phase fluid flow. The model captures the intricate feedback between the changes in wettability and the evolving flow patterns. The authors are able to quantify the time dependent increase in oil fractional flow as trapped oil clusters are mobilized due to the change in wetting angle toward water-wetness. David et al. conduct a detailed experimental study of pore filling by imbibition of water into dry porous rocks. The authors use a combination of methods to characterize the motion of the capillary front. X-ray tomography imaging was performed in combination with ultrasound monitoring as a means of directly comparing the motion of the front with the acoustic signatures picked up by the ultrasound sensors.

Misztal et al. present a novel lattice Boltzmann simulation on unstructured grids of pollutant dispersion in the complex pore geometries of limestone samples discretized from X-ray tomography scans. The authors find that diffusive transport dominates over advective transport in pore spaces with high geometrical complexity. The results have implications for pollution remediation practices, suggesting that on/off cycles of flushing are more effective at removing pollutants compared to continuous flushing in the case of diffusion dominated systems. Marks et al. focus on the transmission of stress through grain-grain contacts in compacting granular packings. The authors use Discrete Element Method (DEM) simulations to show that propagation of stress to confining walls leads to exponentially increasing boundary stresses as the compaction front thickens.

The next five papers focus on medium scale processes and pattern formation. Kelka et al. present a micro-scale model of the formation of bands in ore-bearing dolomites. The zebra pattern of white and dark stripes develops during mineral replacement and grain boundary migration that is influenced by second phase pinning. Grains in dark bands with a high concentration of impurities remain small whereas grains in white bands are almost impurity free and can develop large crystals. Eriksen et al. look at the formation of viscous fingering and fracturing patterns when two non-miscible fluids flow in a confined, but mobile, granular medium. The finger thickness and fractal dimension change significantly depending on whether deformable or un-deformable boundary conditions are imposed, and whether or not the outer boundary is semi-permeable or free.

Turkaya et al. link observable granular deformation and fracture events to acoustic emissions in lab scale multiphase flow experiments associated with air injection. The authors are able to identify specific acoustic signatures associated with both the channel-creating fracturing events themselves, and aftershock emissions released during slow relaxation in compacted regions after the system has reached its final fractured state. Oppenheimer et al. present lab scale experiments on gas transport through high-viscosity, particle-rich suspensions serving as magma analogs. The authors demonstrate that an increased outgassing efficiency through fractures occurs when the crystal fraction is high, explaining why crystal-rich magmas are often observed to have depleted volatiles. Varas et al. present results from experiments of vertical gas venting through a submerged bed of grains where the granular material is fluidized within a parabolic-shaped process zone surrounding the rising gas column. The authors find a transition from intermittent to steady flow depending on gas flow rate and reservoir volume, and identify a new peculiar flow pattern where a gas "finger" extends vertically upwards to a critical height, above which the gas transport occurs through fractures in the granular packing.

The last six papers in this Research Topic deal with flow and transformation in reservoir scale geological systems. Keszthelyi et al. present a model to understand subsidence in the Ekofisk reservoir in the North Sea. The authors derive a micromechanical model combining microscopic processes of fracturing (pore failure) and creep (pressure solution) and upscale the model through fracture densities to understand reservoir scale behavior. Nermoen et al. present an experimental study of the effects of stress and temperature on chalk dissolution. In their long term experiments they flood core specimens of chalk with $MgCl_2$ brine in a 3D deformation cell under stress and evaluate the mineralogical changes. Their experiments show an increase in exchange between Mg^{2+} and Ca^{2+} where the rock samples retain magnesium and lose calcium. This transformation is enhanced with an increase in stress and temperature.

Petrus and Szymczak present a numerical model of the development of solution pipes by CO_2 saturated water flowing through limestone rocks and show how the pipes are influenced by layering in the soil. In their model the pipes develop through a reaction-infiltration instability that focuses flow due to a positive feedback between flow rate and dissolution driven porosity generation. The presence of low-porosity layers in the rock increases the competition between pipes so that flow focuses faster in single pipes and changes the shapes of the pipes locally, producing widening of pipes between the layers and narrowing of pipes in layers. Parez and Aharonov present simulations of sliding granular material to understand the run-off behavior of landslides. The authors show that the collapse of the landslides during their rapid travel results in a very low angle of repose, which leads to a long apparent runout even without any special low friction conditions at their base. Based on the simulations a scaling law is derived to connect landslide size with run-out and the authors show that this scaling is in accordance with data from natural examples.

Finally, there are two contributions on the evolution of fracture networks. Ghani et al. present a hydro-mechanical numerical model to simulate fluid driven fracturing in reservoirs with a special emphasis on layered systems. The authors present proxies to separate tectonically driven fracturing, with well-spaced and oriented networks of fractures, from fracturing that are driven mainly by fluid pressure gradients, which show breccia like patterns with variable fracture orientation. Sachau et al. present a numerical model of crustal scale hydraulic fractures and dynamic fluid movements. In their model, hydraulic fractures develop from an over-pressured source, travel upwards to release fluids and heal according to a viscous law. The authors explore the dynamics of their system and show that high healing rates lead to a very dynamic and pulse like fluid flow whereas low healing rates stabilize and result in constant flow.

The collective work presented by the authors demonstrate the growing interest in flow and transformation in porous media.

The research field is progressing at an accelerating rate driven by the needs of industry and society, and by recent advances in experimental and theoretical tools. Researchers are now able to characterize pore geometries with unprecedented resolution using X-ray micro-tomography, produce micromodels of controllable porous media characteristics, and detect large scale events using remote sensing. Advances in high performance computing have made simulation of pore flow processes down to sub-pore resolution possible. Using a combination of experimental and theoretical methods, the researchers are starting to unravel the sensitive coupling between pore scale events and large-scale flow and transport processes. The sheer complexity of flow in transforming porous media manifested as evolution of preferential flow paths, pattern formation, intermittent dynamics, anomalous transport, and material fracturing poses enormous challenges, but problems once thought intractable are now starting to yield to scientific enquiry.

AUTHOR CONTRIBUTIONS

All authors listed, have made substantial, direct and intellectual contribution to the work, and approved it for publication.

FUNDING

This work has received funding from the European Union's Seventh Framework Programme for research, technological development, and demonstration under grant agreement no 316889. BS acknowledges support from EPSRC Grant No. EP/L013177/1 and Sêr Cymru National Research Network in Advanced Engineering and Materials Grant No. NRN141.

ACKNOWLEDGMENTS

We thank all authors, reviewers, and editors that have contributed to this Research Topic.

Conflict of Interest Statement: The authors declare that the research was conducted in the absence of any commercial or financial relationships that could be construed as a potential conflict of interest.

frontiers in Physics

ORIGINAL RESEARCH
published: 10 November 2015
doi: 10.3389/fphy.2015.00086

Dynamic Wettability Alteration in Immiscible Two-phase Flow in Porous Media: Effect on Transport Properties and Critical Slowing Down

Vegard Flovik[1]*, *Santanu Sinha*[2]* and *Alex Hansen*[1]*

[1] Department of Physics, Norwegian University of Science and Technology, Trondheim, Norway, [2] Department of Physics, University of Oslo, Oslo, Norway

The change in contact angles due to the injection of low salinity water or any other wettability altering agent in an oil-rich porous medium is modeled by a network of disordered pores transporting two immiscible fluids. We introduce a dynamic wettability altering mechanism, where the time dependent wetting property of each pore is determined by the cumulative flow of water through it. Simulations are performed to reach steady-state for different possible alterations in the wetting angle (θ). We find that deviation from oil-wet conditions re-mobilizes the stuck clusters and increases the oil fractional flow. However, the rate of increase in the fractional flow depends strongly on θ and as $\theta \rightarrow 90^{\circ}$, a critical angle, the system shows critical slowing down which is characterized by two dynamic critical exponents.

Keywords: wettability, porous media, porous media flow, fluid transport, two-phase flow in porous media, two-phase flow, capillary forces, critical slowing down

OPEN ACCESS

Edited by:
Renaud Toussaint, University of Strasbourg, France

Reviewed by:
Piotr Szymczak, University of Warsaw, Poland
Peter Lehmann, ETH Zurich, Switzerland

***Correspondence:**
Vegard Flovik
vegard.flovik@ntnu.no;
Santanu Sinha
santanu.sinha@ntnu.no;
Alex Hansen
alex.hansen@ntnu.no

Specialty section:
This article was submitted to Interdisciplinary Physics, a section of the journal Frontiers in Physics

Received: *23 July 2015*
Accepted: *23 October 2015*
Published: *10 November 2015*

Citation:
Flovik V, Sinha S and Hansen A (2015) Dynamic Wettability Alteration in Immiscible Two-phase Flow in Porous Media: Effect on Transport Properties and Critical Slowing Down. Front. Phys. 3:86. doi: 10.3389/fphy.2015.00086

1. INTRODUCTION

The world's primary energy demand is predicted to increase by one-third between 2011 and 2035, where 82% of it comes from fossil fuels [1]. In this scenario, the fact that some 20–60% of the oil remains unrecovered in a reservoir after the production is declared unprofitable, is a challenge of increasing importance [2]. The main reason for this loss is the formation of oil clusters trapped in water and held in place by capillary forces, which in turn are controlled by the wetting properties of the reservoir fluids with respect to the matrix rock. The production from complex oil reserves that today are considered immobile or too slow compared to the cost is therefore an important area of research. In this context, the role of formation wettability is a focus area within the field of Enhanced Oil Recovery (EOR) [3].

Different reservoir rocks have widely different wetting characteristics [4]. Wettability may vary at the pore level from strongly oil wet through intermediate wetting to strongly water wet. Carbonate reservoirs contain more than half of the world's conventional oil reserves, but the oil recovery factor (a number between zero and unity representing the fraction of recoverable oil [5]) is very low compared to sandstone reservoirs [6]. This is due to the complex structure, formation heterogeneity and more chemically active wettability characteristics of the carbonate reservoirs, which leads to uncertainty in the fluid flow and oil recovery [7]. Sandstone is strongly water wet before oil migrates from a source rock into the reservoir. When oil enters a pore, it displaces the water which leaves behind a water film sandwiched between the oil and rock surface. This happens as a result of balancing van der Waals and electric double layer forces, capillary pressure and grain

curvature [8]. A permanent wettability alteration is then believed to take place by adsorption of asphaltenes from the crude oil to the rock, and leads to high but slow recovery through continuous oil films [9, 10]. As the oil saturation drops, these films can become discontinuous, leaving immobile oil clusters held in place by capillary forces.

After drilling a well into a reservoir, the natural pressure inside can force only around 10% of the total available volume of oil to reach the surface, which is called the primary recovery stage [5]. To maintain the pressure for further recovery, water or gas is injected by another injection well which is known as secondary recovery. This allows around 30% further production of oil depending on fluid properties and reservoir parameters. To recover the huge amount of oil left inside the reservoir after the secondary recovery, different techniques beyond the simple secondary injection are implemented, which constitutes the tertiary or EOR stage. In this stage wettability is the most important petrophysical property which plays a key role in the fluid transport properties of both conventional (permeabilities in milli-Darcy to Darcy range) and unconventional (low porosity and low permeability in nano to milli-Darcy range, e.g., shale) reservoirs [11] and there is great potential to improve the oil recovery efficiency by altering the wetting properties [12]. Main factors which can alter the pore wettability are: lowering the salinity [13, 14], adding water-soluble surfactants [15, 16] or adding oil-soluble organic acids or bases [17]. Increasing the reservoir temperature also increases water-wetness [4, 18]. There are some correlations with the wetting behavior to the electrostatic forces between the rock and oil surfaces [19], but there is no consensus on the dominating microscopic mechanism behind the wettability alteration. It is known from laboratory experiments and field tests that a drift from strongly oil-wet to water-wet or intermediate-wet conditions can significantly improve the oil recovery efficiency [17]. The amount of change in the wetting angle is a key factor here [20, 21] which not only decides the increase in oil flow but also the speed of the process. An improper change in the wetting angle can also make the recovery very slow and not profitable.

Given there is a certain change in the wetting angle due to a brine, the next important factor is the flow pathways in the matrix rock which transports the oil and brine. One cannot expect any change in the wetting angle of a pore if there is no flow of the brine through it. The flow pathways depend on several different factors: the porous network itself, oil saturation, capillary number and also on the present wettability conditions. A change in the wettability will cause a perturbation in the flow distribution of the system. This will in turn again affect the wettability change through the altered flow pathways, causing further changes in the flow distribution. The dynamics of wettability alterations is therefore controlled by a strongly correlated process.

There are some studies of wettability alterations in two-phase flow by equilibrium-based network models [22] for capillary dominated regimes where viscous forces are negligible. Wettability alterations by network models with film-flow has been studied [23] to find residual oil saturation as functions of contact angle. However, investigation of the time-scale of dynamics lacks attention in such models which is extremely important for practical reasons. In this article, we present a detailed study of wettability alterations in two-phase flow considering a network model of disordered pores transporting two immiscible fluids where a dynamic wettability alteration mechanism, correlated with the flow-pathways, is implemented. We will focus on the transport properties due to the change in the wettability as well as on the time scale of the dynamics.

We study in the following the effect of wettability changes on immiscible two-phase flow based on a network model [24–26]. In Section 2, we present the model and how we adapt it to incorporate the dynamic wettability changes. In Section 3, we present our results. Initially, we let the two phases settle into a steady state where the averages of the macroscopic flow parameters no longer evolve. At some point, we then introduce the wettability altering agent, so that it starts changing the wetting angle. The wetting angle alteration depends on the cumulative volume of the wettability altering fluid that has flowed past a given pore. This induces transient behavior in the macroscopic flow properties and we measure the time it takes to settle back into a new steady state. We find that there is a critical point at a wetting angle of 90° and we measure its dynamical critical exponents; the exponents are different whether one approaches the critical point from smaller or larger angles. In Section 4 we summarize and conclude.

2. MODEL

We model the porous medium by a network of tubes (or links) oriented at 45° relative to the overall flow direction. The links contain volumes contributed from both the pore and the throat, which then intersect at volume-less vertices (or nodes). Any disorder can be introduced in the model by a proper random number distribution for the radius r of each link, and we choose a uniform distribution in the range $[0.1\,l, 0.4\,l]$ here, where l is the length of each tube. It is possible to consider any other distribution of pore sizes without any further change in the model. The network transports two immiscible fluids (we name them as oil and water), one of which is more wetting than the other with respect to the pore surface. The pores are assumed to be in between particles, and the pore shape is thus approximated to be hour-glass shaped, which introduces capillary effects in the system. The model is illustrated in **Figure 1**.

Due to the hour glass shape of the pore, the capillary pressure at a menisci separating the two fluids is not constant, and depends on the position x of the menisci inside the pore. The capillary pressure $p_c(x)$ at position x inside the ith pore is then calculated from a modified form of the Young Laplace equation [24, 27],

$$p_c(x) = \frac{2\gamma \cos\vartheta_i}{r_i}\left[1 - \cos\left(\frac{2\pi x}{l}\right)\right]. \tag{1}$$

where γ is the interfacial tension between the fluids and ϑ_i is the wetting angle for that pore. As an interface moves in time, $p_c(x)$ changes. The capillary pressure is zero at the two ends ($x = 0$ and l) and it is maximum at the narrowest part of the pore. It makes the model closer to the dynamics of drainage dominated flow, where the film flow can be neglected. When there are multiple

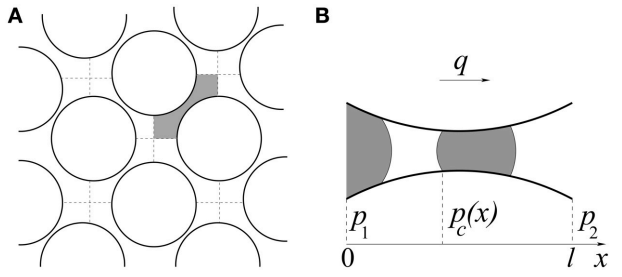

FIGURE 1 | (A) Illustration of the pore network model, constructed by links (tubes) with random radii connected to each other via nodes at the intersection of the dashed lines. One single link in the network is highlighted by gray which is again shown in **(B)** filled with two fluids. The wetting and non-wetting fluids are colored by white and gray, respectively. p_1 and p_2 are the pressures at the two ends of the link and q is the local flow-rate. There are three menisci inside and capillary pressure difference at a menisci is indicated as $p_c(x)$.

menisci in a pore, the total capillary pressure inside the ith pore is obtained from the vector sum $(\sum_i p_c(x))$ over all the menisci in that pore. The flow is driven by maintaining a constant total flow rate Q throughout the network, which introduces a global pressure drop. The instantaneous local flow rate q_i inside the ith link between two nodes with pressures p_1 and p_2 follows the Washburn equation of capillary flow [28],

$$q_i = -\frac{\pi r_i^2 k_i}{\mu_i^{\text{eff}} l}\left[\Delta p_i - \sum_i p_c(x)\right], \tag{2}$$

where $\Delta p_i = p_2 - p_1$. $k_i = r_i^2/8$ is the permeability of cylindrical tubes. Any other cross-sectional shape will only lead to an additional overall geometrical factor. $\mu_i^{\text{eff}} = \mu_o s_i + \mu_w(1-s_i)$, is the volume averaged viscosity of the two phases inside the link, which is a function of the oil saturation s_i in that link. Here μ_o and μ_w are the viscosities of oil and water, respectively.

The flow equations for the tube network are solved using a conjugate gradient method [29]. These are the Kirchhoff equations balancing the flow, where the net fluid flux through every node should be zero at each time step, combined with the constitutive equation relating flux and pressure drop across each tube. The system of equations is then integrated in time using an explicit Euler scheme with a discrete time step and all the menisci positions are changed accordingly. Inside the ith tube, all menisci move with a speed determined by q_i. When any menisci reach at the end of a tube, new menisci are formed in the neighboring tubes. Consequently, wetting and non-wetting bubbles are snapped-off from the links having flow toward a node and enters in neighboring links having outward flow. Here, the total volume of the fluids entering to a node are distributed according to the flow rates of the neighboring tubes. Moreover, it is not allowed to increase the number of menisci inside any tube infinitely and therefore we implement coalescence process by merging two nearest menisci. In this article, we considered a maximum of four menisci inside one pore which can be tuned depending on the experimental observations. When this maximum number is exceeded, the two nearest menisci are merged keeping the volume of each fluid conserved. In this way bubble snap-off and coalescence are introduced in the model. The absolute details of these processes in the simulation can be found in Knudsen et al. [25]. We did not consider film-flow in the present study. This is because wettability alteration techniques are important for reservoirs with low oil-saturation and when oil-saturation drops, the continuous oil films [9, 10] in a oil-wet network are expected to become discontinuous leaving immobile oil clusters stuck due to capillary forces.

The simulations are started with an initial random distribution of two fluids in a pure oil-wet network. Bi-periodic boundary conditions are implemented in the system, which effectively makes flow on a torus surface. The flow can therefore go on for infinite time, keeping the saturation constant and the system eventually reaches to a steady state. In the steady state, both drainage and imbibition take place simultaneously and fluid clusters are created, merged and broken into small clusters. One can consider this as the secondary recovery stage. Once the system reaches the steady-state in a oil-wet network, the dynamic wettability alterations are implemented, which may be considered as the tertiary recovery stage or EOR. In the following we discuss this in detail.

2.1. Dynamic Wettability Alteration

We now introduce a dynamic wettability alteration mechanism to simulate any wetting angle change, decided by the oil-brine-rock combination and the distribution of the flow channels in the system. In a previous study [26], a simplified static wettability alteration mechanism was studied, where the alteration probability was considered equal for all pores without any correlation with the flow of brine inside a pore. However, for wettability alterations to occur, the wettability altering agent (e.g., low-salinity water or surfactant) needs to be in contact with the pore walls. Thus, the wettability alteration should follow the fluid flow pathways and any change in the wetting angle inside a pore should depend on the cumulative volumetric flow of brine through that pore. This claim is rather trivial, as one can not expect any wettability change in a pore if the altering agent is not present. This means that if a certain pore is flooded by large amounts of brine, the wetting angle should change more in that pore than the one which had very little water flooded through. This is implemented in the model by measuring the cumulative volumetric flux $V_i(t)$ in each individual pore with time t,

$$V_i(t) = \sum_{\tilde{t}=t_0}^{t} q_i(\tilde{t})(1 - s_i(\tilde{t}))\Delta\tilde{t}, \tag{3}$$

where t_0 is the time when the injection of low salinity water is initiated, $\Delta\tilde{t}$ is the time interval between two simulation steps and $(1-s_i(\tilde{t}))$ is the water saturation. $V_i(t)$ is then used to change the wetting angle for each tube continuously, updated at every time step after $t = t_0$. The wetting angle ϑ_i of the ith pore can change continuously from 180° to 0° as $V_i(t)$ changes from 0 to ∞. Correspondingly, the $\cos\vartheta_i$ term in Equation (1) will change from -1 to 1 continuously. This continuous change of the

wetting angle with the variation of $V_i(t)$ is modeled by a function $G_i(t)$ given by,

$$G_i(t) = \frac{2}{\pi}\tan^{-1}\left[C\left(\frac{V_i(t)}{V_i^{\text{th}}} - 1\right)\right] \tag{4}$$

which replaces the $\cos\vartheta_i$ term in Equation (1). As, to our knowledge, there is no consensus in the literature about the exact functional dependence of the wetting angle on the volumetric flow of brine at the pore level, we have chosen a function which starts the wetting angles from oil-wet conditions ($\vartheta_i \approx 0^\circ$) at $V_i(t) = 0$ and then asymptotically approaches to water-wet conditions ($\vartheta_i \approx 180^\circ$) as $V_i(t) \to \infty$. The pre-factor $2/\pi$ is a normalization constant to set the range of the function. The parameter C can be tuned to adjust the slope during the transition from oil wet to water wet and can also change the initial wetting angle from 180°. As our model does not include film flow, the wetting angles are not likely to reach either 0 or 180° for circular cross-section of pores. We have chosen $C = 20$ for our simulations which sets the starting wetting angle $\vartheta_i = 165.5^\circ$ when $V_i(t) = 0$. This leads to the change in the wetting angle as a function of $V_i(t)$ as shown in **Figure 2**.

As a larger pore will need more brine to be flooded in order to have a similar change in the wetting angle than a smaller pore, a threshold value V_i^{th} is introduced, which is proportional to the volume of that pore,

$$V_i^{\text{th}} = \eta\pi r_i^2 l. \tag{5}$$

At $V_i(t) = V_i^{\text{th}}$, the wetting angle reaches to 90° in that pore and $p_c(x)$ essentially becomes zero. Here η is a proportionality constant which decides how many pore volumes of water is needed to reach $V_i(t) = V_i^{\text{th}}$ for the ith pore. This parameter can possibly be adjusted against future experimental results, but is considered as a tuning parameter in this study. The expression for the capillary pressure at a menisci from Equation (1) then takes the form,

$$p_c(t) = \frac{2\gamma G_i(t)}{r_i}\left[1 - \cos\left(\frac{2\pi x}{l}\right)\right]. \tag{6}$$

The maximum amount of wetting angle that can be changed depends on the combination of brine, oil and rock properties [20, 21]. We therefore set a cut-off θ in the wetting angle change, such that any pore that has reached to a wetting angle $\vartheta_i = \theta$, can not be changed further. The model thus includes all the essential ingredients of wettability alteration study–it is a time dependent model where the wettability alteration is correlated with the flow pathways of the brine, and can be used to study any oil-brine-rock combination decided by θ.

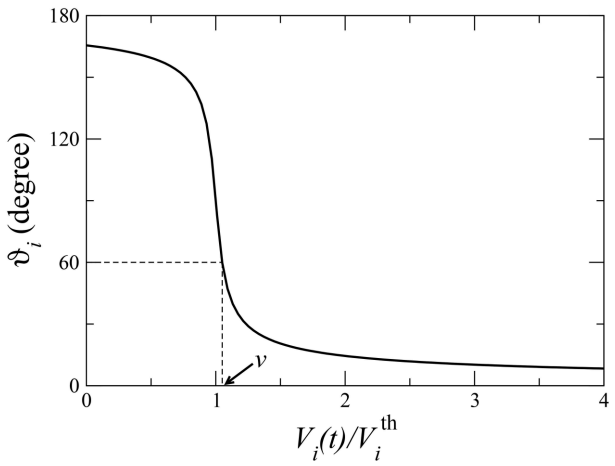

FIGURE 2 | Variation of the wetting angle ϑ_i in the ith link given by $G_i(t)$ (Equation 4) as a function of the cumulative volume of water $V_i(t)$ (Equation 3) passed through that link. V_i^{th} is the water volume needed to reach the wetting angle to 90° in that pore. When there is a cut-off (θ) in the maximum change in the wetting angle, ϑ_i is not allowed to change anymore as soon as $\vartheta_i = \theta$. An example of a cut-off 60° is shown by dashed lines, in this case as soon as $\vartheta_i = 60^\circ$ or $V_i(t) = vV_i^{th}$, ϑ_i is not changed anymore. The time (t) needed to reach the cut-off value therefore varies from pore to pore and depends on the value of V_i^{th}.

3. RESULTS

Simulations are started with a random distribution of oil and water in an oil-wet network, where $\theta = 165.5^\circ$ for all links. First, the oil-wet system is evolved to a steady state before any wettability alteration is started. This will allow us to compare the change in the steady-state fractional flow of oil (F) with a change in the wetting angle. The oil fractional flow (F) is defined as the ratio of the oil flow-rate (Q_{oil}) to the total flow-rate (Q) given by, $F = Q_{\text{oil}}/Q$. The flow rate (Q) is kept constant throughout the simulation, which sets the capillary number $\text{Ca} = \mu_{\text{eff}}Q/(\gamma A)$, where A is the cross-sectional area of the network. A network of 40 × 40 links are considered, which is sufficient to be in the asymptotic limit for the range of parameters used [25]. An average over 5 different realizations of the network has been taken for each simulation. As the simulation continues, both drainage and imbibition take place simultaneously due to bi-periodic boundary conditions and the system eventually evolves to a steady state, with a distribution of water and oil clusters in the system. In **Figure 3**, F is plotted against the number of pore volumes passed (N) through the network. As we run the system with constant flow-rate, N is directly proportional to the time t, $N = tQ/v$ where v is the total volume of the network. The initial 200 pore volumes are for an oil-wet network, where it reaches to a steady state with $F \approx 0.235$. We then initiate the dynamic wettability alteration which resembles the flow of a wettability altering brine and F starts to drift. Here we run simulations for different values of η, defined in Equation (5), and the results are plotted in different colors. $\theta = 0^\circ$ in these simulations, which means any pore can change to pure water-wet depending upon the flow of brine through it. One can see that F approaches to a new steady-state with $F \approx 0.308$ due to the wettability alteration. The initialization of steady state is defined as the instant when the average fractional flow stops changing with time and essentially stays within its fluctuation. The time (τ) required to initialize the steady state after wettability alteration is started is measured in terms of the pore-volumes and plotted in the inset of **Figure 3**

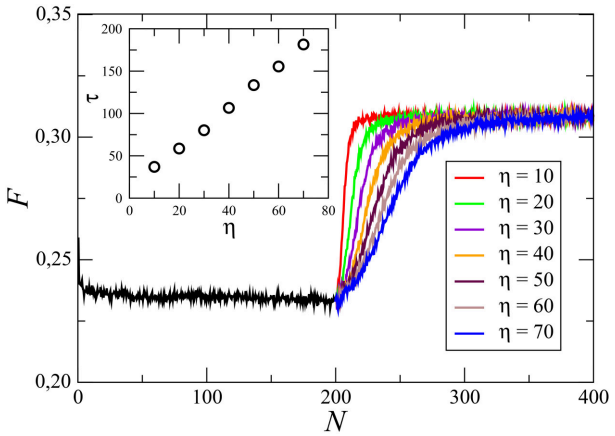

FIGURE 3 | (Color online) Change in the oil fractional-flow (*F*) during the simulation as a function of the number of network pore-volumes (*N*) of fluids passed through any cross-section of the network. Here the network is of size 40 × 40 links with oil saturation $S = 0.3$ and $\text{Ca} = 10^{-1}$. The initial part of the plot ($N < 200$) shows the change in F in an oil-wet system where it approaches to a steady state with $F \approx 0.235$. The wettability alteration starts at $N = 200$, where results for different simulations with different values of η (the number of pore volumes of *water* needed to pass through one pore to reach the wetting angle to 90° in that pore) are plotted in different colors. The system evolves to a new steady-state where F fluctuates around a higher average value. Different values of η only affects the rate of change in F but leads to the same average F. In the inset we plot τ, the number of network pore-volumes of fluids passed through the network to reach the steady-state after wettability alteration is initiated, as a function of η. τ is proportional to the total time to reach steady state which increases linearly with η as seen in the inset. A higher value of η results in a longer time to reach the new steady-state.

as a function of η and a simple linear dependency is observed. Therefore, different values of η only make the simulation faster or slower, but it reaches to the same steady state. In order to save computational time, we therefore use $\eta = 10$ in all our following simulations.

How the two fluids and the local flow-rates are distributed in the network in the two steady-states before and after the wettability alteration are shown in **Figure 4**. The network size is 64×64 links here with an oil-saturation $S = 0.3$ and the capillary number $\text{Ca} = 10^{-2}$. All the links are hour-glass shaped in the actual simulation with disorder in radii, but shown as a regular network for simplicity in drawing. The upper row shows the distribution of oil bubbles drawn in black. The left column (**Figure 4A**) shows the steady state in a oil-wet network and the right column (**Figure 4B**) shows the steady-state after the wettability alteration is initiated with maximum possible wetting angle change $\theta = 0°$. A closer look in these bubble distributions shows more clustered oil bubbles in **Figure 4A** than in **Figure 4B** where they are more fragmented. A more interesting picture can be seen in the local flow-rate distribution in the bottom row, which shows a more dynamic scenario. The left (**Figure 4C**) and right (**Figure 4D**) figures are for the same time-steps before and after wettability alteration as in **Figures 4A,B**, respectively. Here the local flow-rates in each pore, normalized in between 0 and 1, are shown in gray scale. Interestingly, in the oil-wet system (**Figure 4C**), the flow is dominated in a few channels (black lines) where the flow-rates are orders of magnitude higher than the rest of the system. Other than those channels, the system has negligible flow, indicated by white patches which means the fluids are effectively stuck in all those areas. This situation happens when the difference in the saturation of the two fluids is large, where the phase with higher saturation (water here) tries to percolate in paths dominated by a single phase with less number of interfaces. This is not favorable in oil-recovery, as it leaves immobile fluid in the reservoir. In the flow distribution after the wettability alteration (**Figure 4D**), the flow is more homogeneous and distributed over the whole system, indicating higher mobility of the fluids. However, one should remember that when the wettability alteration is started in a system shown in **Figure 4C**, the wettability alteration starts taking place only in those pores with active flow. But then it perturbs the flow-field and starts new flow paths and eventually the system drifts toward a more homogeneous flow with time, as shown in **Figure 4D**.

We now present the results when the wetting angle of any pore can change all the way down to zero degree ($\theta = 0°$). In **Figure 5** the steady-state oil fractional-flow in an initial oil-wet system (F) is compared with that in the steady-state after wettability alteration (F'). Results are plotted as a function of S for two different capillary numbers, (**Figure 5A**) $\text{Ca} = 10^{-1}$ and (**Figure 5B**) $\text{Ca} = 10^{-2}$. The diagonal dashed line in the plots corresponds to $F = S$. If the fluids are miscible and there is no capillary forces at the menisci then both the fluids will flow equally and F will be exactly equal to S. But the presence of capillary forces at the interfaces lead to the deviation of the fractional-flow curve from the diagonal line. A lower capillary number (higher capillary forces) therefore results in more deviation from the $F = S$ line. For low oil saturation, the oil fractional-flow is lower than S, i.e., under the diagonal and for high S, F is higher than S, i.e., above the diagonal. Roughly, the phase with higher volume fraction gains and it flows faster than the other. At some point, the curve crosses the diagonal and it is the point where no phase gains. The crossover point is not at 50% saturation which clearly shows the asymmetry between the two phases [30]. As F stays below the $F = S$ line for low S, the flow of oil becomes lower and lower as oil saturation drops resulting small but stuck oil clusters. Interestingly, when wettability alterations are implemented, a significant increase in F can be observed for the full range of oil-saturation. Moreover, increase in F is higher for the lower capillary number, indicating that wettability alteration is very significant in the case of oil recovery, as Ca can go as low as 10^{-6} in the reservoir pores. Fractional flow also obeys the symmetry relation $F'(S) = 1 - F(1 - S)$ [26] which implies that, if the wetting angle of any pore is allowed to change all way down to zero degree ($\theta = 0°$), the system will eventually become pure water-wet with time.

As noted earlier, the maximum change in wetting angle for a system, depends on the properties of the reservoir rock, crude oil and brine, and also on the temperature. Existing wettability alteration procedures generally turns the oil-wet system into intermediate wet, rather than to pure water-wet. Some examples of the change in the wetting angle for different rock materials and brine can be found in Kathel and Mohanty [20] and Nasralla et al. [21]. In our simulation this is taken care of by the parameter

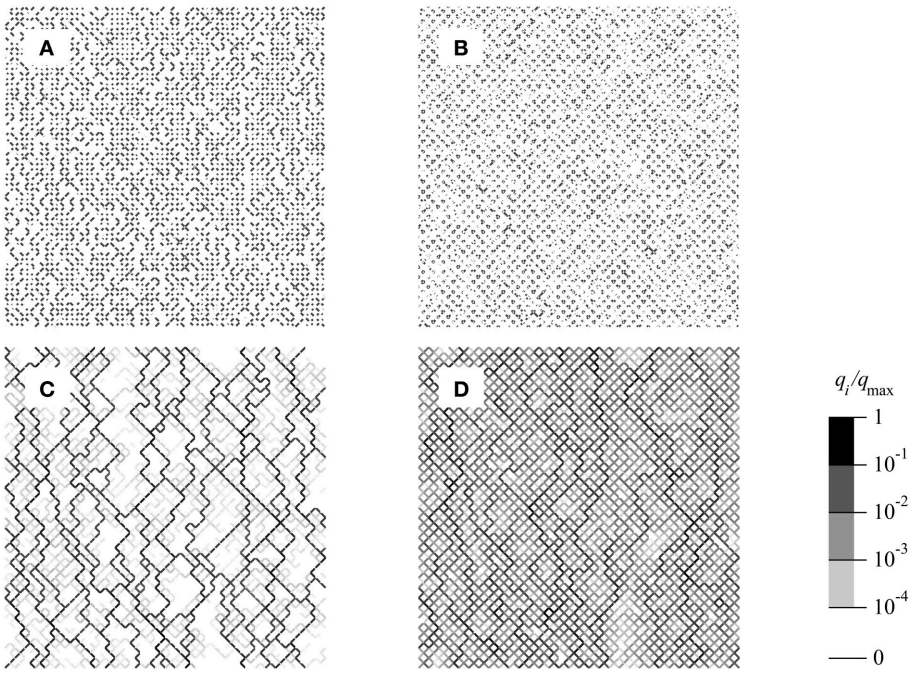

FIGURE 4 | Distribution of fluid bubbles (top row) and local flow rates (bottom row) in steady state in a network of 64 × 64 links with oil saturation $S = 0.3$ and $Ca = 10^{-2}$. The left column is for the steady state in a oil-wet network and the right column is the new steady state after wettability alteration takes place. In **(A,B)**, the oil bubbles are drawn in black. In **(C,D)**, the normalized local flow-rates q_i/q_{max} are drawn in gray scale.

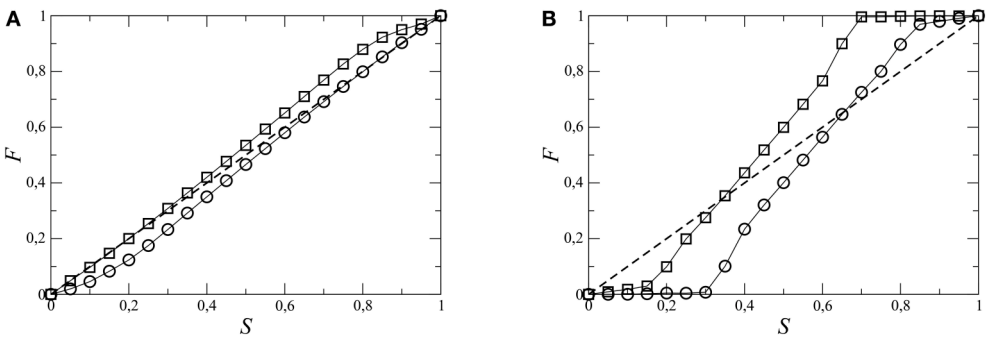

FIGURE 5 | Oil fractional-flow (*F*) in the steady state at different oil saturation (*S*) in the initial oil-wet system (○) and after the wettability alteration (□). There is no cut-off in the wetting angle change in these simulations and therefore $\theta = 0^\circ$ here. Individual simulations are performed for all *S* values at two different capillary numbers **(A)** $Ca = 10^{-1}$ and **(B)** $Ca = 10^{-2}$. *F* is higher after wettability alteration for the whole range of *S*. The diagonal dashed line represents $F = S$ curve, miscible fluids without any capillary pressures at the menisci would follow that line.

θ, which decides the maximum change in the wetting angle ϑ_i for any pore. One should remember that, we are not forcibly changing the wetting angles ϑ_i to θ, rather the change in ϑ_i is decided independently for individual pores by the amount of brine passed through it (by Equations 3–6), and there is a maximum allowed change in any ϑ_i. As before, simulations are started with a pure oil-wet system to reach a steady state and then wettability alteration is started and simulation continues until the system reaches to a steady state again. Independent simulations have been performed for different values of θ. The proportionate change in the oil fractional-flow due this wettability change from the oil-wet system, $\Delta F/F = (F' - F)/F$ is measured for different simulations and plotted in **Figure 6** against θ. There are a few things to notice. First, as one can immediately see, fractional flow increases with the decrease of oil-wetness, $\theta \rightarrow 0^\circ$. The maximum increase in F is higher for lower Ca, about 86% for $Ca = 10^{-2}$ and about 32% for $Ca = 10^{-1}$. This is because the change in wetting angle affects the capillary pressures at the menisci, so the change in F is larger when the capillary forces are higher. Secondly, the major change in F happens in the intermediate wetting regime, upto $\theta \approx 60^\circ$, and then it becomes almost flat afterwards. Moreover, this increase in F is

more rapid for lower value of Ca. All these facts points toward an optimal range of wetting angle change to increase the oil flow. This is an important observation for practical reasons, as it is not necessary to change the wetting angle further. Thirdly, there is a discontinuity in the curve exactly at $\theta = 90^\circ$, as we will discuss later.

Increase in the oil fractional-flow with the increase in the water-wetness may seem to be obvious and reported by many experiments and field tests. But, the most important concern for the oil industry is the rate of increase, or the time required to achieve a significant increase in the oil production. If the increment in oil flow is very slow compared to the cost of the process, then the oil recovery is declared as not profitable and the reservoir may be considered to be abandoned. As per our knowledge, there are very few systematic studies reported in the literature predicting the time scale to change the oil flow due to the wettability change by two-phase flow of brine and oil in a porous media. We observe that, due to the correlations between the flow paths and the wetting angle change, the time scale of the process varies dramatically with θ. This is illustrated in **Figure 7**, where F is plotted as a function of pore volumes (N) of fluid passed through the system. The initial 400 pore volumes are for an oil-wet system and then results of few different simulations with $\theta = 85$, 88, 89, 90, 91, 92 and 94° are plotted. Interestingly, the rate at which the system reaches a new steady-state, varies significantly depending on the value of θ. For example, after the wettability alteration is started, it needs to flow less than 100 pore volumes to reach the new steady state for $\theta = 94^\circ$ whereas more than 300 pore volumes are needed to reach a steady state for $\theta = 91^\circ$. Therefore, even if the final steady-state fractional flow is higher for $\theta = 91^\circ$ than for $\theta = 94^\circ$, it might not be profitable to alter the wetting angles to 91° because of the slow increase in F. In general, the process becomes slower and slower as $\theta \rightarrow 90^\circ$ from both sides. Such kind of slow increase in oil recovery as $\theta \rightarrow 90^\circ$ is also observed in experiments [20, 21]. This slowing down of the process is an combined effect of two factors. First, the fact that wettability only can change in the pores where there is flow of brine and the second is the value of θ. All the pores were initially oil-wet ($\vartheta_i \approx 165^\circ$) and when it reaches the steady state, the flow finds the high mobility pathways depending on the mobility factor of the pores and the capillary pressures at the menisci. When the wettability alteration is started, the wetting angles of the existing flow pathways start decreasing. As a result, capillary pressures at menisci in those channels first decreases as $\vartheta_i \rightarrow 90^\circ$ and then it increase afterwards as $\vartheta_i \rightarrow 0^\circ$. This creates a perturbation in the global pressure field and correspondingly viscous pressures start changing with time which changes the flow field. However, capillary pressures at the zero-flow regimes are now higher than the high-flow regimes which makes it difficult to invade the zero-flow regimes causing a slower change in the flow field as ϑ_i approaches 90°. An interesting feature is observed exactly at $\theta = 90^\circ$, where the average fractional flow does not change at all after the wettability change. At exactly $\theta = 90^\circ$, capillary pressures in all the pores in the existing flow pathways essentially become zero, making them the lowest resistive channels with zero capillary barriers. As a result, the fluids keep flowing in the existing

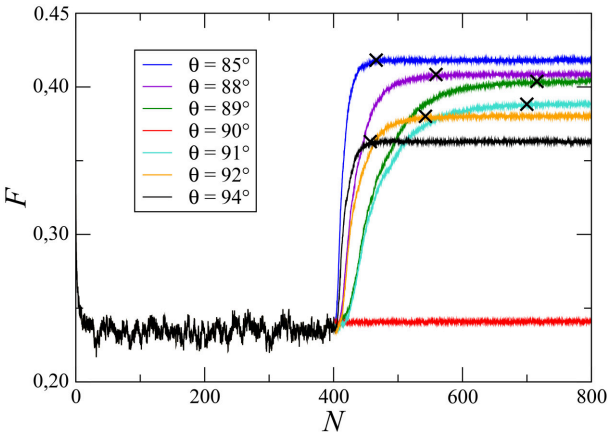

FIGURE 7 | Change in the oil fractional-flow *F* during the simulation for different values of maximum allowed wetting angle θ. The wettability alteration started at $N = 400$ pore-volumes. The initialization of the steady-states for different θ values are marked by crosses on the respective plots.

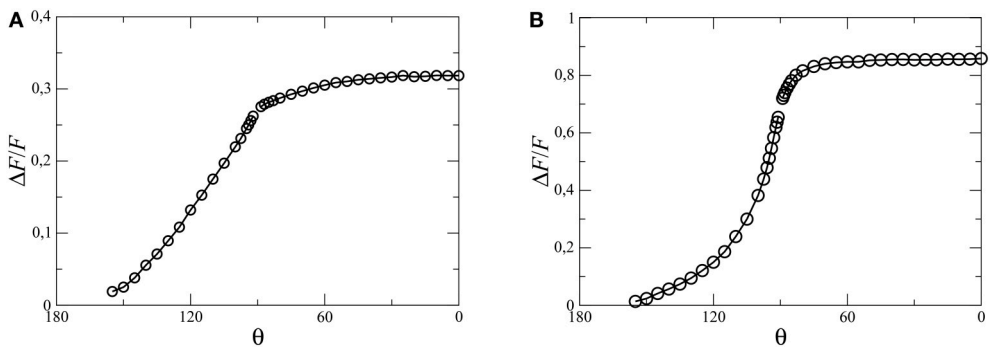

FIGURE 6 | Proportionate change in the steady-state oil fractional-flow ($\Delta F/F$) due to wettability alteration as a function of maximum wetting angle θ. For **(A)** the capillary number $Ca = 10^{-1}$ with oil-saturation $S = 0.3$ and for **(B)** $Ca = 10^{-2}$ with $S = 0.4$.

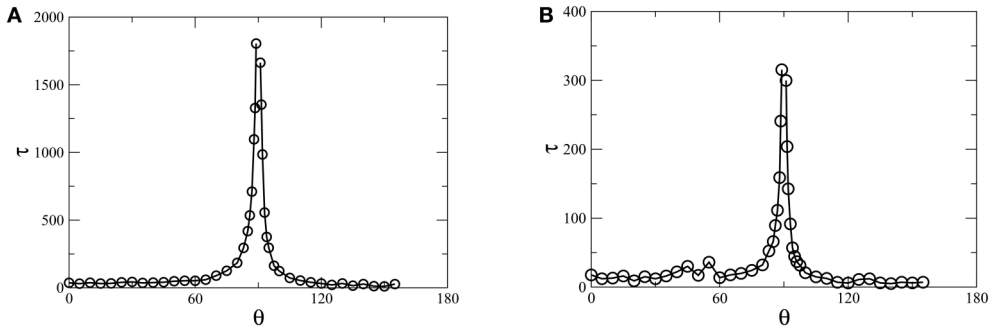

FIGURE 8 | Variation of steady-state initialization time τ (measured in pore-volumes) as a function of maximum allowed wetting angle θ in any pore. For **(A)** Ca $= 10^{-1}$ with oil saturation $S = 0.3$ and for **(B)** Ca $= 10^{-2}$ with $S = 0.4$. τ diverges rapidly as $\theta \rightarrow 90^{\circ}$, which is the critical wetting angle (θ_C).

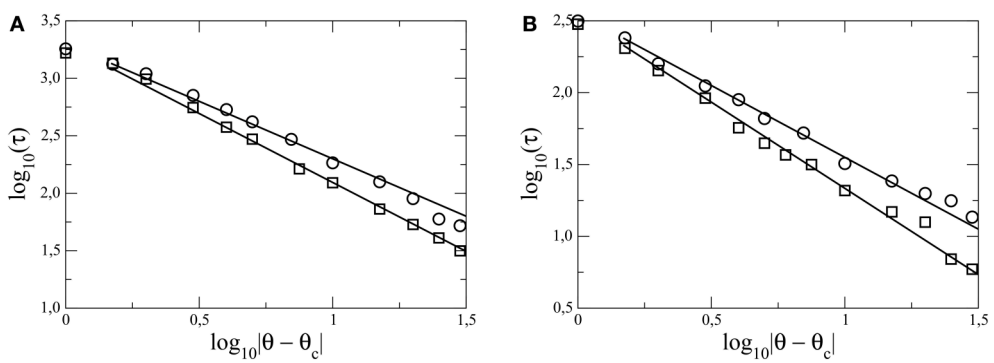

FIGURE 9 | Plot of $\log\tau$ vs. $\log|\theta - \theta_C|$, where θ is the final allowed wetting angle in any pore, $\theta_C = 90^{\circ}$ and τ is steady-state initialization time (measured in pore-volumes) after wettability alteration is initiated. For **(A)** the capillary number Ca $= 10^{-1}$ with oil saturation $S = 0.3$ and for **(B)** Ca $= 10^{-2}$ with $S = 0.4$. From the slopes, the value of the dynamic critical exponent α is obtained as $\alpha = 1.0 \pm 0.1$ for $\theta < \theta_C$ (circles) and $\alpha = 1.2 \pm 0.1$ for $\theta > \theta_C$ (squares).

channels forever and the system stays in the same steady-state. The time taken to reach another new steady-state is therefore infinite at $\theta = 90^{\circ}$ and it therefore is a critical point for the system.

We now measure the steady-state initialization time τ, defined as the moment when the average of the fractional flow stops changing with time and becomes horizontal with the x axis. This is shown In **Figure 7**, where the initialization of steady states is marked by crosses on the respective plots. As the simulations are performed with constant Q, τ is proportional to the fluid volume passed through the system and therefore we measure τ in the units of N. τ for different simulations with different values of the maximum wetting angle (θ) is plotted in **Figure 8A** for Ca $= 10^{-1}$ with $S = 0.3$ and in **Figure 8B** for Ca $= 10^{-2}$ with $S = 0.4$. One can see that τ diverges rapidly as θ approaches $\theta_c = 90^{\circ}$ from both sides, $\theta > 90^{\circ}$ and $< 90^{\circ}$. This divergence of the steady-state time τ as $\theta \rightarrow \theta_c$ indicates the *critical slowing down* of the dynamics, which is a characteristics of critical phenomena. The critical slowing down is the outcome of the divergence of correlations at the critical point and can be characterized by a dynamic critical exponent z defined as $\tau \sim \xi^z$, where ξ is the correlation length [31]. As $\theta \rightarrow \theta_c$, the correlation length ξ diverges as $|\theta - \theta_c|^{-\nu}$ where ν is the correlation length exponent. The divergence of the steady-state time τ can therefore be expressed as $\tau \sim |\theta - \theta_c|^{-\alpha}$, where $\alpha = z\nu$. In **Figure 9**, τ is plotted vs. $|\theta - \theta_c|$ in log-log scale which gives two different slopes for $\theta > \theta_c$ and $\theta < \theta_c$. We then find the value of the dynamic exponents α as $\alpha = 1.2 \pm 0.1$ for $\theta > \theta_c$ and $\alpha = 1.0 \pm 0.1$ for $\theta < \theta_c$. However, they are the same within error bar for different capillary numbers and saturations (**Figure 9**). The value of the dynamic critical exponents depend on the underlying dynamics and on the model [32]. In this case, wettability alteration was started from an oil-wet system with $\vartheta_i = 165^{\circ}$ for all the pores. So for the simulations with $\theta < 90^{\circ}$, the wetting angles cross the critical point (90°) when the capillary forces change directions. This might cause the system to mobilize the clusters somewhat faster than for $\theta > 90^{\circ}$ when the capillary forces does not change any direction. As a result, α becomes smaller for $\theta < 90^{\circ}$ than for $\theta > 90^{\circ}$.

We like to point out that a 2-dimensional (2D) pore network is considered in this study, but the model is equally applicable to any 3-dimensional (3D) network without any further change. However, as critical exponents depend on the spatial dimensionality of the system, values of the exponents measured for a 3D network are expected to be different.

4. CONCLUSIONS

In this article we have presented a detailed computational study of wettability alterations in two-phase flow in porous media, where the change in the wetting angle in a pore is controlled by the volumetric flow of the altering agent through it. When the wetting angles are allowed to alter toward water-wetness, the stuck oil clusters start to mobilize and oil-fractional flow increases. However, due to the correlations in the wetting angle change with the flow pathways, the time-scale of the dynamics strongly depends on the maximum allowed change in the wetting angle. We find that, as the final wetting angle is chosen closer to 90°, the system shows a critical slowing down in the dynamics. This critical slowing down is characterized by two dynamic critical exponents. The critical point we are dealing with is an equilibrium critical point as the system is in steady state. The dynamical critical exponents measure how long it takes to go from one steady state to a new one. To our knowledge, this is the first example of there being *different values* for the exponents on either side of the critical point. Our findings are in agreement with experimental observations reported in literature, and are extremely important for application purposes like oil recovery, where the time scale of the process is a key issue.

ACKNOWLEDGMENTS

We thank E. Skjetne for introducing us to the subject of this study. We have benefited from discussions with D. Bideaux, E. G. flekkøy, S. Kjelstrup, and K. J. Måløy. This work has been supported by the Norwegian Research Council. We furthermore thank the Beijing Computational Sciences Research Center and its Director, H. Q. Lin for hospitality during the final stages of this work.

REFERENCES

1. International Energy Agency. *World Energy Outlook*. Paris: IEA (2014). doi: 10.1787/weo-2013-en
2. Roberts P. *The End of Oil: On the Edge of a Perilous New World*. New York, NY: Houghton Mifflin (2005).
3. Abdallah W, Buckley JS, Carnegie A, Edwards J, Herold B, Fordham E. Fundamentals of wettability. *Schlumberger Oilfield Rev.* (2007) **19**:44. Available online at: http://www.slb.com/resources/publications/industry_articles/oilfield_review/2007/or2007sum04_wettability.aspx
4. Skauge A, Spildo K, Høiland L, Vik B. Theoretical and experimental evidence of different wettability classes. *J Pet Sci Eng.* (2007) **57**:321–33. doi: 10.1016/j.petrol.2006.11.003
5. Dake LP. *Fundamentals of Reservoir Engineering*. Amsterdam: Elsevier (1998).
6. Sheng JJ. Comparison of the effects of wettability alteration and IFT reduction on oil recovery in carbonate reservoirs. *Asia-Pac J Chem Eng.* (2013) **8**:154. doi: 10.1002/apj.1640
7. Chilingar GV, Yen TF. Some notes on wettability and relative permeabilities of carbonate reservoir rocks, II. *Energy Sources* (1983) **7**:67. doi: 10.1080/00908318308908076
8. Israelachivili J. *Intermolecular and Surface Forces, 3rd Edn.* Amsterdam: Academic Press (2011).
9. Kovscek AR, Wong H, Radke CJ. A pore-level scenario for the development of mixed wettability in oil reservoirs. *AlChe J.* (1993) **39**:1072. doi: 10.1002/aic.690390616
10. Kaminsky R, Radke CJ. Asphaltenes, water films, and wettability reversal. *SPE J.* (1997) **2**: 485. doi: 10.2118/39087-PA
11. Kidnay AJ, Parrish WR, McCartney DG. *Fundamentals of natural gas processing, 2nd Edn.* Florida, FL: CRC Press; Taylor & Francis Group (2011).
12. Alvarez JO, Neog A, Jais A, Schechter DS. Impact of surfactants for wettability alteration in stimulation fluids and the potential for surfactant EOR in unconventional liquid reservoirs. *Soc. Pet. Eng.* (2014). doi: 10.2118/169001-MS
13. Tang GQ, Morrow NR. Salinity, temperature, oil composition, and oil recovery by waterflooding. *SPE Reserv Eng.* (1997) **12**:269. doi: 10.2118/36680-PA
14. Tang GQ, Morrow NR. Influence of brine composition and fines migration on crude oil/brine/rock interactions and oil recovery. *J Pet Sci Eng.* (1999) **24**:99. doi: 10.1016/S0920-4105(99)00034-0
15. Standnes DC, Austad T. Wettability alteration in chalk: 2. Mechanism for wettability alteration from oil-wet to water-wet using surfactants. *J Pet Sci Eng.* (2000) **28**:123. doi: 10.1016/S0920-4105(00)00084-X
16. Mohan K, Gupta R, Mohanty KK. Wettability altering secondary oil recovery in carbonate rocks. *Energy Fuels* (2011) **25**:3966. doi: 10.1021/ef200449y
17. Tweheyo MT, Holt T, Torsæter O. An experimental study of the relationship between wettability and oil production characteristics. *J Pet Sci Eng.* (1999) **24**:179. doi: 10.1016/S0920-4105(99)00041-8
18. Schembre JM, Tang GQ, Kovscek AR. Wettability alteration and oil recovery by water imbibition at elevated temperatures. *J Pet Sci Eng.* (2006) **52**:131. doi: 10.1016/j.petrol.2006.03.017
19. Buckley JS, Takamura K, Morrow NR. Influence of electrical surface charges on the wetting properties of crude oils. *SPE Reserv Eng.* (1989) **4**:332. doi: 10.2118/16964-PA
20. Kathel P, Mohanty KK. EOR in tight oil reservoirs through wettability alteration. *Soc. Petro. Eng.* (2013). doi: 10.2118/166281-MS
21. Nasralla RA, Bataweel MA, Nasr-El-Din HA. Investigation of wettability alteration and oil-recovery improvement by low-salinity water in sandstone rock. *Soc. Petro. Eng.* (2013). doi: 10.2118/146322-PA
22. Blunt MJ. Physically-based network modeling of multiphase flow in intermediate-wet porous media. *J Pet Sci Eng.* (1998) **20**:117. doi: 10.1016/S0920-4105(98)00010-2
23. Ryazanov AV, van Dijke MIJ, Sorbie KS. Two-phase pore-network modelling: existence of oil layers during water invasion. *Transp Porous Med.* (2009) **80**:79. doi: 10.1007/s11242-009-9345-x
24. Aker E, Måløy KJ, Hansen A, Batrouni GG. A two-dimensional network simulator for two-phase flow in porous media. *Transp Porous Med.* (1998) **32**:163. doi: 10.1023/A:1006510106194
25. Knudsen HA, Aker E, Hansen A. Bulk flow regimes and fractional flow in 2D porous media by numerical simulations. *Transp Porous Med.* (2002) **47**:99. doi: 10.1023/A:1015039503551
26. Sinha S, Grøva M, Ødegården TB, Skjetne E, Hansen A. Local wettability reversal during steady-state two-phase flow in porous media. *Phys Rev E* (2011) **84**:037303. doi: 10.1103/PhysRevE.84.037303
27. Dullien FAL. *Porous Media: Fluid Transport and Pore Structure.* San Diego, CA: Academic Press (1992).
28. Washburn EW. The dynamics of capillary flow. *Phys Rev.* (1921) **17**:273. doi: 10.1103/PhysRev.17.273
29. Batrouni GG, Hansen A. Fourier acceleration of iterative processes in disordered systems. *J Stat Phys.* (1988) **52**:747. doi: 10.1007/BF01019728

30. Knudsen HA, Hansen A. Relation between pressure and fractional flow in two-phase flow in porous media. *Phys Rev E* (2002) **65**:056310. doi: 10.1103/PhysRevE.65.056310
31. Bellac ML, Mortessagne F, Batrouni GG. *Equilibrium and Non-Equilibrium Statistical Thermodynamics*. Cambridge: Cambridge University Press (2004).
32. Nightingale MP, Blöte HWJ. Dynamic exponent of the two-dimensional Ising model and Monte Carlo computation of the subdominant eigenvalue of the stochastic matrix. *Phys Rev Lett.* (1996) **76**:4548. doi: 10.1103/PhysRevLett.76.4548

Conflict of Interest Statement: The authors declare that the research was conducted in the absence of any commercial or financial relationships that could be construed as a potential conflict of interest.

frontiers in Physics

METHODS
published: 28 July 2015
doi: 10.3389/fphy.2015.00053

Detection of moving capillary front in porous rocks using X-ray and ultrasonic methods

Christian David[1]*, *Delphine Bertauld*[1,2], *Jérémie Dautriat*[2], *Joël Sarout*[2], *Beatriz Menéndez*[1] and *Bassem Nabawy*[3]

[1] Laboratoire Géosciences et Environnement Cergy, Université de Cergy-Pontoise, Cergy-Pontoise, France, [2] CSIRO, Energy Flagship, Perth, WA, Australia, [3] Department of Geophysical Sciences, National Research Center, Cairo, Egypt

Several methods are compared for the detection of moving capillary fronts in spontaneous imbibition experiments where water invades dry porous rocks. These methods are: (i) the continuous monitoring of the mass increase during imbibition, (ii) the imaging of the water front motion using X-ray CT scanning, (iii) the use of ultrasonic measurements allowing the detection of velocity, amplitude and spectral content of the propagating elastic waves, and (iv) the combined use of X-ray CT scanning and ultrasonic monitoring. It is shown that the properties of capillary fronts depend on the heterogeneity of the rocks, and that the information derived from each method on the dynamics of capillary motion can be significantly different. One important result from the direct comparison of the moving capillary front position and the P wave attributes is that the wave amplitude is strongly impacted before the capillary front reaches the sensors, in contrast with the velocity change which is concomitant with the fluid front arrival in the sensors plane.

Keywords: capillary imbibition, X-ray CT scanning, ultrasonic monitoring, sandstones, carbonates

OPEN ACCESS

Edited by:
Renaud Toussaint, University of Strasbourg, France

Reviewed by:
Laurent Olivier Louis, New England Research, USA
Yannick Peysson, IFP Energies Nouvelles, France
Yves Gueguen, Ecole Normale Supérieure, France

***Correspondence:**
Christian David, Laboratoire Géosciences et Environnement Cergy, Université de Cergy-Pontoise, 5 mail Gay-Lussac, F-95031 Cergy-Pontoise, France
christian.david@u-cergy.fr

Specialty section:
This article was submitted to Interdisciplinary Physics, a section of the journal Frontiers in Physics

Received: *30 April 2015*
Accepted: *10 July 2015*
Published: *28 July 2015*

Citation:
David C, Bertauld D, Dautriat J, Sarout J, Menéndez B and Nabawy B (2015) Detection of moving capillary front in porous rocks using X-ray and ultrasonic methods. Front. Phys. 3:53. doi: 10.3389/fphy.2015.00053

Introduction

Multiphase flow is ubiquitous in nature, and it is of fundamental importance to understand fluid displacement processes in porous media. A simple way to tackle this problem is to perform laboratory imbibition experiments, where a wetting fluid (e.g., water) spontaneously displaces a non-wetting phase (e.g., air) present in the pore space, or conversely drainage experiments where a non-wetting fluid (e.g., oil) is pushed under pressure to displace a wetting phase (e.g., water) present in the pore space [1]. It has been shown in previous works [2–4] that the geometry of the interface between the wetting and the non-wetting phase in imbibition experiments can be quite complex; the dynamics of fluid displacement is strongly controlled by the rock microstructure. These conclusions were drawn from the analysis of X-ray CT scan images obtained at various stages during water imbibition tests using a medical CT scanner. Imaging pore microstructures has proven to provide valuable quantitative information for the modeling of fluid flow processes in geomaterials. Nevertheless, imaging is not always possible, and one needs to rely on indirect techniques to characterize changes in stress state or fluid content in reservoirs rocks under *in situ* conditions for example. Obviously seismic techniques are good candidates for achieving a remote monitoring of reservoirs at depth, leading 4D seismic studies to have been widely used in the last decade [5]. It is still an open question to know at which extent seismic studies are reliable enough to detect accurately fluid motion or fluid substitution occurring in reservoirs at depth,

for instance during hydrocarbon production or CO_2 storage operations [6]. Experimental studies aiming to simultaneously image the fluid flow processes and monitor the seismic response are mostly welcome. We achieved this at the laboratory scale, by conducting water imbibition tests under a medical CT scanner with continuous recording of waveforms for P waves traveling across the tested rock samples. Doing so, it is possible to link the modification of the wave propagation signature with the fluid substitution. In this paper we will address the following questions. What primary information can be obtained from capillary imbibition tests in the lab? How accurate are seismic recordings to detect fluid motion in reservoir rocks? Which attribute of the seismic signal is the most reliable and accurate for such detection?

This paper will mainly focus on methods. Through a review of different applied techniques to study capillary imbibition processes: standard weight increase measurement, X-ray imaging, ultrasonic monitoring, we will investigate the reliability of ultrasonic monitoring by a direct comparison between wave attributes (amplitude, travel time, and spectral content) at different stages of the imbibition process, and the corresponding images of the fluid distribution in the rock, obtained by continuous X-ray CT scanning.

Standard Method for Capillary Imbibition Studies

Capillary imbibition experiments are commonly used in petrophysics to get information on porous geomaterials, as they are quite straightforward to conduct and inexpensive to implement. The standard technique to measure capillary rise in porous rocks consists in weighing a sample and/or in visually determining the height of the water front during imbibition (e.g., Siebold et al. [7]). To get a continuous data set, the sample is hooked under an electronic balance and a video recording device captures the water front rising along the sample surface while the bottom end of the sample is placed in contact with a water tank [8]. Knowing the rock porosity and the water saturation during imbibition, a reasonable agreement is found between the direct observation of the height reached by the rising water front and the one derived from the mass increase [3]. The detection of the moving front position from the mass intake involves as well the assumption that the interface between dry and wet parts of the tested sample is flat, figuring a kind of piston-like imbibition process. An example of such a study will now be presented.

Material and Methods

The data presented in this section have been obtained on a set of Paleozoic-Mesozoic Nubia sandstone samples selected from different locations in Egypt which were followed up and sampled through a cross section extending over more than 300 km through the north of the Eastern Desert and Sinai in Egypt. Four areas are studied in this cross section, namely Gebel Somr El-Qaa in the Eastern Desert, and Gebel Abu Durba, Wadi Soal (at Gebel El-Rome) and Wadi Watir (at Bir Sanafir) in Sinai Peninsula. In the studied sites, the Nubia sandstones are represented by Araba, Naqus, Abu Durba, and Malha Formations (collectively called the Nubia sandstones). More details on the geological background and rock composition will be given in a paper in preparation [Nabawy et al., under review]. Several petrophysical properties were measured on a large number of samples [9]. Among all this exhaustive characterization, capillary imbibition tests were conducted on a set of eight core samples with diameter 4 cm and length ranging between 6 and 8 cm. The selected samples presented different microstructural attributes from very fine to coarse grains and are composed mostly of brown to yellow, well sorted or sometimes ill sorted, very fine to coarse sandstones, mostly quartz arenite. These samples will be called hereafter NBS-1 to NBS-8. The dry rock samples are hooked under an electronic balance (precision 0.001 g), and at time zero the bottom end of the samples is immersed over a very short length (typically 1 mm) in a tank filled with water. Water is constantly supplied to the tank in order to maintain a constant water level. At this very early stage, several processes take place: (i) a meniscus water layer will form along the sample edge in contact with water (ii) buoyancy force in the immerged rock volume will oppose the gravity force. These effects need to be corrected in order to get the mass of water present in the pore space during capillary rise [3, 10]. For such experiments, the standard way to represent the data is to plot the water mass intake as a function of the square root of time. Doing so one would obtain a straight line if the porous rock would be replaced by a single pipe with constant radius r. The pore space of rocks being intrinsically heterogeneous, this linearity would never be observed for natural rocks. Nevertheless, it is possible to define the so-called coefficient of capillarity C [called W_s in David et al. [3]] from the mean slope of the mass vs. square root of time plot:

$$C = \frac{1}{\pi R^2} \frac{dm}{d\sqrt{t}} \tag{1}$$

where m is the water mass intake and R is the sample radius. Another important feature of capillary imbibition experiments is that full saturation is never reached during spontaneous imbibition experiments. The dynamics of capillary fluid motion in porous materials with heterogeneous pore size distributions induces indeed air-trapping. It is not possible to get the water saturation at intermediate stages during capillary rise without knowing the geometry and position of the capillary front, whereas it is easy to get a mean saturation value once the water front has reached the top of the sample.

Results

As stated above, we report in **Figure 1** the water mass intake plotted vs. the square root of time for eight tested samples. The values for the coefficient of capillarity C and the corresponding correlation coefficient for the linear regression (**Table 1**) show that, overall, the linear approximation is very satisfying. The coefficient of capillarity C varies by one order of magnitude ($0.006–0.07\ g/cm^2/s^{1/2}$). Porosity (17.7–22.4%), permeability (42–269 mD) and final saturation after the imbibition test (47–61%) are also reported in **Table 1**. Based on the analysis of a limited number of rocks, David et al. [3] expected a correlation between the permeability k and the capillary coefficient C, as

both parameters involve fluid displacement within the pore space. To verify this assumption on a larger dataset, capillarity-permeability data of the present study along with those of recent studies on oolitic limestones [11], dolostones [12], sandstones and carbonates [3] and a variety of sedimentary rocks [13] are reported in **Figure 2**. An overall positive correlation between C and the rock permeability is observed: a narrow elliptic envelope encompasses 97% of the data allowing the prediction of the rock permeability with a maximum error of about one order of magnitude. The dashed line corresponds to a power-law with exponent 2, the experimental correlation is then consistent with a simple relationship $k = \alpha C^2$ where α is a constant. From **Figure 2** we derived $\alpha = 1.38\ 10^{-12}$, k and C being in SI units. A similar relationship has been proposed recently by Benavente et al. [13] for the prediction of permeability from capillarity and microstructural data:

$$k = \alpha C^2 \ with\ \alpha = \frac{\eta r}{4\phi\rho^2\gamma cos\theta} \quad (2)$$

where η, ρ, and γ are the fluid viscosity, density and surface tension respectively, θ is the contact angle, ϕ is the porosity and r is the threshold pore radius which can be derived from mercury injection tests. A better correlation could probably be found if each of these parameters is known. In addition, the scatter in **Figure 2** can be explained by the variability of all these parameters, especially the threshold radius and the rock porosity. Such correlation allowing the prediction of permeability from capillarity data justifies the interest for the development of inexpensive capillary imbibition tests in the lab.

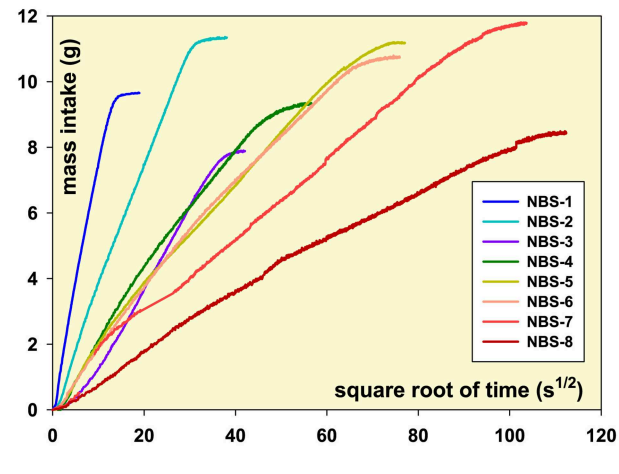

FIGURE 1 | Water mass intake evolution of the eight Nubia sandstone samples as a function of square root of time.

X-ray Imaging of Moving Capillary Fronts

The geometry of capillary fronts can be inferred by performing capillary rise experiments under a X-ray Computerized Tomography "CT" medical scanner. However, the concomitant measurement of the water mass intake with a balance is not possible during this experiment. Indeed, one cannot place metallic objects in the field of the X-ray beam without significantly downgrade the resulting image. Multiple X-ray beams crossing the rock sample during the CT scan allows one to get a map of X-ray attenuation that can be correlated to the density, which reveals the density contrast between the dry rock and the volume where water has invaded the pore space. It is then possible to get the position and the shape of the capillary front during imbibition. Classically several parameters can be retrieved from such experiments: (i) the maximum height and (ii) the minimum height of the capillary front, (iii) the curvature of the interface when the capillary front has a smooth shape which can be approximated by an arc of a circle [3].

Material and Methods

We present the results obtained on the same eight Nubia sandstone samples presented in the previous section. As mentioned above, the key point here is to scan the cored plugs using a medical scanner: this has been done in the framework of a collaboration with IFP Energies nouvelles (IFPEN). The dry samples are placed on a stand under the X-ray CT scanner to image the fluid flow patterns and their evolution with time. The stand is located in a container filled by a continuous flux of water which allows the water surface to always be in direct contact with the bottom end of the sample. As for the previous experiments, capillary forces induce the rise of water through the pore space. We start to image the sample as soon as water enters into the rock, until it reaches the top end of the sample. The

TABLE 1 | Petrophysical properties and coefficient of capillarity *C* of the Nubia sandstone samples obtained with the mass intake method.

Sample	Porosity (%)	Permeability (mD)	Mass intake method			
			C (g/s$^{1/2}$/cm^2)	Coeff corr.	Final saturation (%)	Quality of linearity
NBS-1	22.4	269	0.06957	0.998	61	Good linearity
NBS-2	20.5	136	0.02926	0.999	54	Good linearity
NBS-3	18.2	50	0.02189	0.999	47	Excellent linearity
NBS-4	19.6	129	0.01514	0.994	49	Poor at beginning
NBS-5	19.5	74	0.01265	0.999	58	Poor at beginning
NBS-6	19.3	57	0.01199	0.995	55	Poor linearity
NBS-7	21.9	135	0.00977	0.999	53	Excellent linearity
NBS-8	17.7	42	0.00606	0.994	48	Poor beginning—bumpy

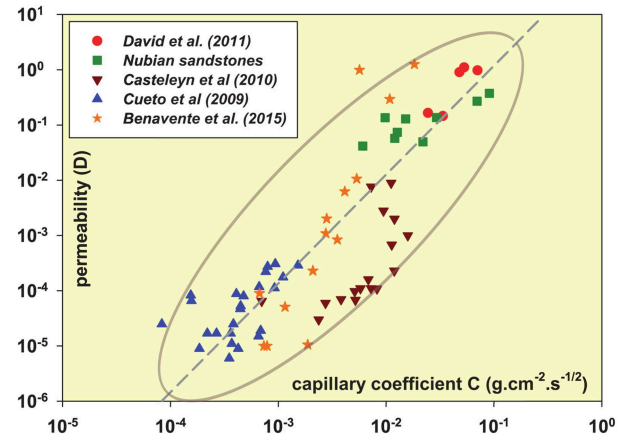

FIGURE 2 | Correlation between the coefficient of capillarity and permeability obtained in this study and by previous authors.

CT scanner requires a minimum time between two snapshots of 2.5 s. The typical total duration of a run is about 10 min which enables to obtain an average total number of 240 images per experiment. Only one axial slice or radiograph is taken each time, so that the geometry of the moving front is only investigated on a fixed plane: the 3D geometry of the interface cannot be obtained due to the limitation of the apparatus. The resolution of the obtained image is 0.4 mm × 0.4 mm per pixel. Following the method described in David et al. [3], image processing allows one to highlight the contrast between the dry and the wet parts of the sample, by subtracting to each image a reference image obtained on the dry rock. From these high contrasted images, it is then possible to measure automatically the maximum height H and the minimum height h reached by the water front at each time increment using an image analysis routine. The calculated heights do not correspond necessarily to the heights at the center or the border of the samples. Like for the mass intake plot, these parameters are generally plotted vs. the square root of time, and it is possible to define another capillary parameter A related to the evolution of the height:

$$A = \frac{dH}{d\sqrt{t}} \tag{3}$$

This parameter has been estimated in the linear part of the plot related to the maximum height. In this case also, if the rock would be replaced by a single pipe with constant radius, this parameter would be constant and the capillary plot would give a straight line.

Results

Heights H (solid circles) and h (open circles) are plotted vs. the square root of time for the eight Nubia sandstone samples (**Figure 3**). Different background colors and symbols are used to qualitatively characterize the shape of the water front: a green background means a concave upward curvature, a red background means a concave downward curvature, and a blue background means that the interface is flat. A large variety of

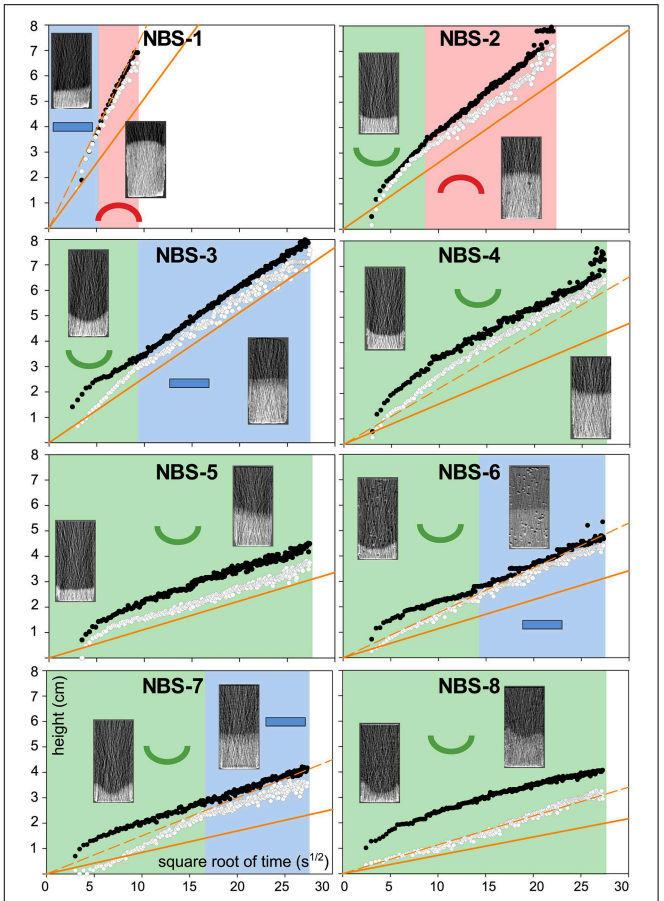

FIGURE 3 | Heights evolution of the water front as a function of square root of time. Solid and open circles correspond to the maximum and minimum heights, respectively. The shape of the front (upward/downward concave, flat) is represented with different symbols and background colors (respectively green, red, and blue). The solid and dashed lines correspond to the prediction from capillarity coefficient C using the final saturation and an *ad hoc* saturation respectively.

situations can be found, with the shape of the water front evolving during capillary rise. An example of the processed images at an intermediate stage for each sample is inserted in **Figure 3**: the upper dark zone on each image correspond to the dry part of the sample not invaded by water. Overall the quality of the linear fit is reasonably good (correlation coefficients higher than 0.97) and qualitatively the results for both capillary parameters A and C are in good agreement (**Table 2**). In a first approximation it is possible to make the link between both parameters assuming (i) a homogeneous water saturation in the water invaded part and (ii) a flat interface of the capillary front (not observed except for three samples in the ultimate stage). Doing so it is possible to predict the value for A knowing the value of C:

$$A_{pred} = \frac{C}{\rho\phi S_w} \tag{4}$$

where S_w is the water saturation in the invaded region, assumed to be the same everywhere. For this calculation we used the final

TABLE 2 | Capillary parameter *A* of the Nubia sandstone samples obtained with the height method using CT scan images, and qualitative description of the capillary front geometry.

Sample	Height method using CT scan images						
	A (cm/s$^{1/2}$)	Coeff. Corr.	Inferred slope from mass (cm/s$^{1/2}$)	Inferred saturation (%)	Beginning stage	Intermediate stage	Final stage
NBS-1	0.812	0.987	0.510	38	Slightly inclined	Slightly concave downward	Slightly concave downward
NBS-2	0.336	0.986	0.262	42	Concave upward	Slightly concave upward	Concave downward
NBS-3	0.259	0.998	0.256	46	Concave upward	Slightly concave upward	Straight horizontally
NBS-4	0.224	0.989	0.159	35	Concave upward	Slightly concave upward	Slightly wavy
NBS-5	0.121	0.990	0.112	54	Concave upward	Slightly wavy	Inclined
NBS-6	0.183	0.987	0.114	34	Concave upward	Slightly concave upward	Straight horizontally
NBS-7	0.148	0.971	0.085	30	Concave upward	Slightly wavy	Straight horizontally
NBS-8	0.124	0.983	0.072	28	Concave sharply upward	Smiley and wavy	Smiley and wavy

saturation value (**Table 1**). For three samples (NBS-2, NBS-3, and NBS-5), the slope of the predicted evolution is in good agreement with the observations on the CT scan images (**Figure 3**), but for the other five samples the height evolution is significantly different from the predicted one (**Table 2**). To account for this discrepancy, one can estimate from Equation (4) the water saturation that would be needed on the right hand side in order to get a predicted value equal to the measured one on the left hand side. Doing so, the inferred saturation values are given in **Table 2**, and the predicted height evolution corresponds to the dashed lines in **Figure 3**. As expected the slope of the predicted height agrees well with the measured ones. The saturation values need to be systematically lower in Equation (4), down to 28% in the worst case (NBS-8 in **Table 2**). However, these estimations need to be taken with caution because of the assumption of piston flow and uniform saturation in the invaded area, which might probably be an oversimplification of the actual situation.

Ultrasonic Method for the Detection of Moving Capillary Fronts

In order to get more information on capillary imbibition processes, it is possible to combine the classical weight measurement technique with a system allowing for the recording of ultrasonic acoustic signals. Pairs of ultrasonic sensors can be glued at different locations on the sample surface, and the travel time for elastic waves traveling from the emitter to the receiver can be recorded at given times. This allows one to monitor the rise of capillary fronts during imbibition tests. Both seismic velocities and attenuation are sensitive to the passage of fluid fronts [14]. In the following we present the experimental device available in the rock physics lab at Cergy-Pontoise University, and we present some results obtained on two carbonate rocks.

Material and Methods

For this study the selected rocks were the Majella grainstone (30% porosity) from the central Apennines, Italy, and the Saint-Maximin limestone (37% porosity) from the Paris basin, France. Information on the mineralogical and petrophysical properties of both carbonate rocks can be found in David et al. [15] and Baud et al. [16]. As explained in Section Material and Methods (Section Standard Method for Capillary Imbibition Studies), the rock sample is hanging under an electronic balance (**Figure 4**). Two ultrasonic transducers were fixed with phenyl salicylate glue at 30 mm from the bottom of the sample, across a diameter. AE sensors VS600-Z1 from Vallen Company were chosen for their small size (diameter 4.75 mm) and broad bandwidth (200–850 kHz). Both sensors are connected to a Panametrics 5058PR high voltage pulse-receiver which delivers to the emitter a high voltage pulse (max. 900 V) with a frequency of about 1 MHz. This device amplifies also the signal of the receiving sensor with a maximum gain of 60 dB. The waveform captured by the receiver is sent to a digital oscilloscope Agilent 2014A which has a 100 MHz sampling frequency. During each experiment, the received waveform is manually recorded on a USB stick every 5 s. After the experiment, the waveforms are analyzed thanks to an automatic procedure implemented using the Scilab freeware. Two parameters are retrieved from the recorded waveforms: (i) the arrival time of the P wave and (ii) the amplitude of the first peak. For picking automatically the first arrival, we used the Akaike Information Criterion (AIC method), a robust technique commonly used is seismology. Additional information on the dynamics of fluid front propagation can be obtained if one plots on the same graph all the waveforms recorded during the experiment. Finally the analysis of the spectral content of the waveforms at selected times during the imbibition process was carried out. To this end, spectrograms of the selected waveforms have been constructed using the S-transform described in detail by Pinnegar [17].

Results

The evolution of the normalized P wave velocity and first peak amplitude as a function of time during capillary imbibition tests on Majella grainstone (left) and Saint-Maximin limestone (right) are shown in **Figure 5**. The dashed lines represent the mass increase due to water intake during imbibition: we can observe that the imbibition kinetics is significantly faster in the Saint-Maximin limestone than in the Majella grainstone, probably due to the broader pore size distribution, larger internal surface

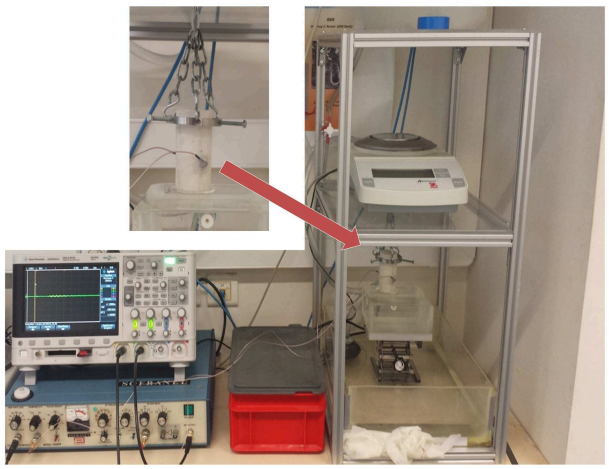

FIGURE 4 | Experimental device for imbibition experiments coupling ultrasonic measurements with mass intake method. The sample is hanging under an electronic balance, above a water tank and ultrasonic sensors are connected to a high voltage pulse-receiver and an oscilloscope.

area, smaller particle size and larger throat size (derived from mercury injection) in the former [16]. For both rocks the velocity and wave amplitude have been normalized to the value of the dry rock, before imbibition starts: for Majella grainstone, the initial P wave velocity is 2750 m/s and the first peak amplitude is −16.6 mV, while the initial P wave velocity is 2810 m/s and the first peak amplitude is −3.1 mV for Saint-Maximin limestone. From the comparison of the results for both rocks (**Figure 5**), common features but also striking differences can be highlighted. Firstly the arrival of the capillary front results in a decrease of the P wave velocity and amplitude in both samples. However, a much sharper drop in amplitude compared to velocity is systematically observed. The amplitude of the first peak seems to be more sensitive to fluid substitution than the velocity and should therefore be preferred for the detection of the capillary front arrival. Secondly the departure from the initial values of velocity and amplitude does not occur simultaneously, and the order is actually different from one rock to the other: for the Majella grainstone the amplitude decreases first, then the velocity, and the reverse is observed for the Saint-Maximin limestone. We are not able to provide further explanation on this behavior without detailed information on the capillary front position. In this kind of experiment, we can only speculate on the position and geometry of the water front inside the rock sample. Notice that for Saint-Maximin limestone we could derive the amplitude and velocity evolution only at the early stage of the imbibition process. Once the water front approaches the location of the ultrasonic sensors, the waveforms are strongly attenuated, the amplitude of the first peak becomes then so weak that the signal-to-noise ratio becomes vanishingly small and the AIC method does not work anymore. The gray boxes on the time axis correspond to the time interval when the height of the water front at the sample surface is moving from 2 mm below the sensors to 2 mm above the sensors (visual observation during the experiment). Whereas, for the Saint-Maximin limestone the passing through fluid front between the transducers is associated with major changes in the P wave amplitude and velocity, for the Majella grainstone those fluctuations are observed well before the fluid front reaches the transducer plane. This probably reveals the complex geometry of the capillary front inside the rock sample, which cannot be estimated from the observation of the sample surface. Again without a detailed knowledge of the capillary front geometry, it is not possible to get a comprehensive understanding of the waveform evolutions.

The evolution of the waveforms recorded during both experiments on Majella grainstone and Saint-Maximin limestone are reported in **Figure 6**. We highlighted two end-members: the red waveform is obtained at the beginning of the test when the rock is dry, and the dark blue one corresponds to the end of the test when the capillary front is well above the plane where the ultrasonic transducers are located. A drastic change in the waveform attributes is observed: the amplitude is strongly reduced and the frequency is lowered after imbibition. However, the comparison of the continuous evolution of the waveforms between the two end-members highlights a striking difference between both rocks. For Majella, a smooth transition is observed from one waveform to the other with a monotonic reduction of both amplitude and frequency, the waveform envelope being only slightly modified and the correlation remaining strong. Conversely for Saint-Maximin the evolution is more complex and characterized by a first increase of the amplitudes in the intermediate steps followed by a decrease in both amplitude and frequency.

Additional insight on the frequency content of the waveforms can be gained by studying the spectrograms at three different stages:

Stage #1. corresponds to the start of the test when the rock is completely dry (red waveform);
Stage #2. corresponds to the intermediate stage where the properties are evolving quickly (**Figure 5**)—i.e., the capillary front is close to the transducers;
Stage #3. the moving front is well above the plane of the transducers (dark blue waveform).

Again we observe large differences between both rocks. The red color corresponds to the arrival of wavelets with the highest energy plotted with the same time scale as the waveforms in the upper plot. For Majella, two wavelets with high energy are actually present in the early stages, but one of them vanishes at Stage #3. The first arrivals carry the highest energy, and this is why the automatic detection of velocities and first peak amplitudes gives good results (**Figure 5**). A decrease in the frequency of the wavelet accompanied by a delay in arrival time is observed when going from Stage #1 to #3. For Saint-Maximin, the first arrivals carry very little energy, which explains why the automatic (and manual) detection of velocities and first peak amplitudes gave poor results (**Figure 5**). The highest energy is associated with a wavelet arriving much later, with a frequency higher than what was found for Majella. When imbibition proceeds, the first arrivals are still very weak, and there is no clear wavelet which can be identified, but rather consistent oscillations at slightly higher frequencies that spread

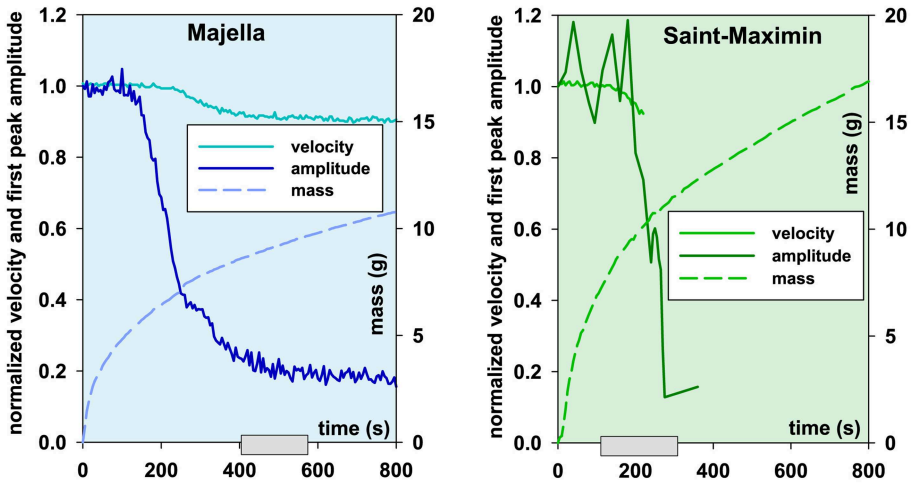

FIGURE 5 | Results from the imbibition experiments coupling ultrasonic measurements with the mass method for the Majella grainstone and the Saint-Maximin limestone: the velocity and first peak amplitude are normalized to their respective value in the dry state.

over almost the entire length of the recordings. The picture is thus very different from what we have observed on the Majella grainstone: the complexity found in the Saint-Maximin limestone is probably due to the heterogeneity of this rock. To go further in the analysis of the recorded signals, one would need to do some wave propagation simulation taking into account the geometry of the propagation and the heterogeneity in the tested rocks.

Combined X-ray Imaging and Ultrasonic Monitoring

Finally we designed an experiment where we combine imbibition tests with acoustic monitoring and imaging under an X-ray CT scanner. The comparison of the density maps with the acoustic measurements allows one to explore how the physical properties of the tested rock are affected by fluid substitution with direct assessment of the position and geometry of the capillary front during imbibition.

Material and Methods

Two samples available in CSIRO were tested, the Saint-Maximin grainstone and the Savonnières limestone. The Saint-Maximin used for the test was different from the one presented in Section Ultrasonic Method for the Detection of Moving Capillary Fronts, however the tested samples had a similar porosity (37%, Baud et al. [16]) and permeability (2.1 D). The Savonnières limestone is a relatively homogeneous clean biogenic limestone (98% of calcite) with a porosity of 31.6% and a moderate permeability of 51.2 mD. The tested plug came from the same block used by Lopes et al. [18] and Pimienta et al. [19]. Both samples were cored in the direction parallel to bedding.

We used techniques similar to those presented in Section X-ray Imaging of Moving Capillary fronts: the sample is placed on a X-ray transparent stand providing a constant water level at the bottom end of the cylindrical rock specimen. The rock samples have a diameter of 38.1 mm and a length of 68.3 mm and 76.2 mm for the Saint Maximin and the Savonnières, respectively. Two pairs of ultrasonic sensors are glued with cyanoacrylate at two different heights (**Figures 7B,C**). The external diameter of the ultrasonic transducers is 9 mm. They are made of piezoceramic disks 5 mm in diameter, with a central resonant frequency of ∼0.5 MHz. The surface of the transducers in contact with the rock is machined concave so as to match the cylindrical lateral surface of the specimen. Several ray paths were investigated (**Figure 7C**): plane 1 is the lower horizontal path (blue); plane 2 is the upper horizontal path (orange); inter-planes 1-2 (green) and 2-1 (purple) are oblique paths across planes 1 and 2. The P-wave arrival time, the amplitude of the first peak and the spectral content were analyzed on each recorded waveform using the same tools as in Section Ultrasonic Method for the Detection of Moving Capillary Fronts.

During the imbibition test, the sample's volume is continuously scanned with an X-ray CT scanner (Siemens SOMATOM Dual Energy 64 slices, **Figure 7A**) following a helical pattern with an axis parallel to the specimen's axis. In this experiment, we used a 140 kV/300 mA single X-ray energy beam and a typical acquisition set is made of 32 parallel and simultaneous slices separated by 0.6 mm in the central part of the sample. To avoid artifacts related to the transducers interacting with the X-ray beams, the sample is imaged along vertical planes normal to the plane defined by the positions of the four transducers (**Figures 7B,C**). In contrast with the results reported in Section X-Ray Imaging of Moving Capillary Fronts, the 32 slices acquired with this apparatus can be reconstructed to generate a 3D image of the central part of the specimen at each scanning stage during the imbibition. The investigated volume is therefore a truncated cylinder 18.6 mm in width and 68.3 mm and 76.2 mm in height for Saint Maximin and Savonnières, respectively. Each scanning stage lasts 1 s and is repeated every 5 s. Note that during each 3D volume scanning (32 simultaneous slices), the capillary front keeps rising. The pixel size in each

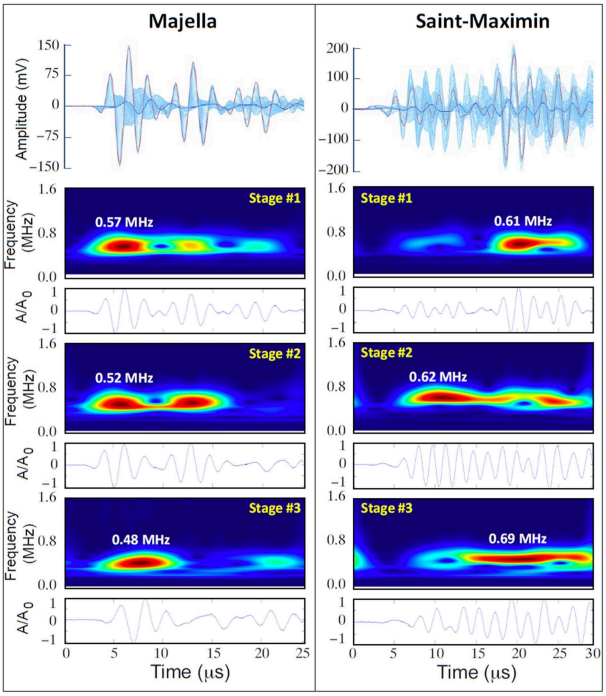

FIGURE 6 | Superimposition of transmitted signals during imbibition tests on Majella and Saint-Maximin samples (the first waveform is displayed in red and corresponds to the dry sample and the last one is displayed in dark blue) and spectrograms with corresponding waveforms at different stages (stage #1: beginning of the test, stage #2: arrival of the water front near the sensor plane, stage #3: end of the test).

reconstructed image is 0.15 × 0.15 mm. ImageJ software package has been used to stack the longitudinal images for a selected set of reconstructed volumes. Out of each stacked volume, two slices normal to the sample axis at heights corresponding to the ultrasonic transducer planes are extracted. The mean gray level in a rectangular crop (185 × 125 pixels) of these slices is computed for selected scanning stages to assess, during the imbibition process, the local change in density of the specimen associated with water invasion.

At each X-ray scanning stage, waveforms transmitted through the rock specimen between the source and receiving ultrasonic transducers are recorded according to the ray paths described above.

Results

For the Saint-Maximin grainstone (**Figure 8**), waveforms corresponding only to horizontal ray paths have been recorded. The P-wave attributes (velocity and amplitude of the first peak) were normalized to their initial value in the dry state (Vp = 2740 m/s). The variations of the gray level within the transducer planes with respect to the initial (dry) state were calculated. Based on the velocity, amplitude and gray level variation with time in the Saint-Maximin specimen, seven noticeable imbibition stages were selected for further analysis, and the following observations can be made:

Stage #1. The amplitude of the P wave in plane 1 is the first parameter to be impacted (sharp decrease) by the moving capillary front. The decrease occurs when the capillary front appears to be ∼6 mm below the location of the ultrasonic sensors (accounting for their actual diameter);

Stage #2. Both the velocity (decrease) and the gray level in plane 1 (increase) are impacted by the capillary front reaching plane 1;

Stage #3. Once the capillary front is about 10 mm above the sensors plane 1 (accounting for their diameter), the gray level, the P-wave velocity and amplitude remain constant;

Stage #4. The amplitude of the P wave in plane 2 decreases while the capillary front appears to still be located below the sensors;

Stage #5. Once the capillary front reaches the sensors in plane 2, both the P wave velocity and the gray level decrease;

Stage #6. The P wave velocity stabilizes while the capillary front appears located just above the sensors;

Stage #7. From that time on, all parameters are nearly constant in plane 2 except the gray level, which keeps on increasing slowly. The final P wave velocity after imbibition is $Vp = 2630$ m/s.

The waveforms recorded in planes 1 and 2 are shown in **Figure 8**, with the same color coding as in **Figure 6**. Higher absolute P wave amplitudes were recorded in plane 2 compared to plane 1. Interestingly, except for the amplitude, the first periods of the waveforms recorded in planes are remarkably similar. However, the magnitude of the change in normalized P wave amplitude associated with the imbibition process is similar in both planes. A half period time shift is observed between the beginning (dry state) and the end of the imbibition process with only little change in frequency.

A similar analysis was carried out for the experiment on the Savonnières limestone (**Figure 9**). For this specimen, two additional oblique ray paths were recorded and analyzed (inter-plane rays 1-2 and 2-1). For sake of clarity we separated in **Figure 9** the velocity plot from the amplitude/gray level plot. The first striking difference with the Saint-Maximin grainstone is that the Savonnières limestone exhibits no significant variation in P wave velocity which remains close to 3200 m/s. The second important difference is that the time scale for this experiment is much longer (2.5 h compared to 6 min). The fact that imbibition was much faster in the Saint-Maximin compared to the Savonnieres can be attributed to a difference in their microstructure, which impacts their macroscopic properties such as permeability (40 times lower for Savonnières) and therefore the balance between capillary and gravity forces [18]. Here five noticeable imbibition stages were selected for further analysis, and the following observations can be made:

Stage #1. The amplitude of the P wave in plane 1 decreases sharply once the capillary front appears to be ∼3 mm below the sensors in the 3D images;

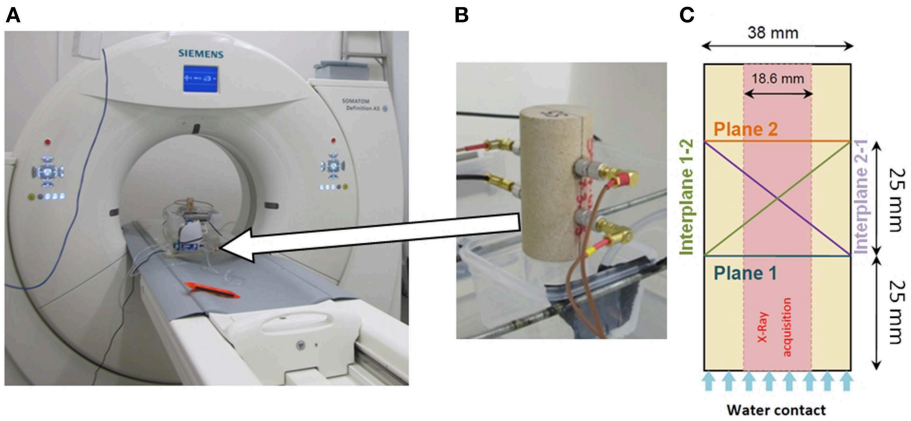

FIGURE 7 | Experimental device used for imbibition tests coupling ultrasonic measurements with X-ray imaging. (A) X-ray CT scanner. **(B)** Sample on the water tank with four sensors glued on the lateral surface. **(C)** Scheme of the equipped sample: studied ray paths for ultrasonic monitoring and area covered by X-ray acquisition. Ultrasonic paths are in a plane perpendicular to X-ray cross-sections (32 cross-sections separated by 0.6 mm are simultaneously recorded during each acquisition).

Stage #2. At this point the velocity along the inter-plane rays 1-2 and 2-1 as well as the gray level in plane 1 are impacted by the passage of the capillary front;

Stage #3. Once the capillary front appears to reach plane 1, the gray level and wave amplitude variations in that plane slow down;

Stage #4. When the capillary front appears to be located few millimeters above plane 1, the amplitude of the P wave reaches a plateau whereas the gray level keeps on increasing slowly;

Stage #5. The amplitude of the P wave in plane 2 decreases while the capillary front appears to be located a few millimeters below the sensors. Notice also that the amplitude of the P wave along both oblique paths decreases almost linearly between stages #2 and #5 and are very similar.

Consistently with the other tested rock (**Figure 8**), the P wave attributes, velocity and/or amplitude, are impacted by the water front approaching the sensors planes, before actually reaching it, as seen on the CT images.

The waveforms recorded in planes 1 and 2, and inter-planes 1-2 and 2-1 are shown in **Figure 9**. In plane 1, there is no significant change in the velocity during imbibition, only the amplitude of the arches is decreasing (no significant time shift). In plane 2, the amplitude remains nearly constant except at the very end of the experiment when the capillary front approaches the sensor plane. The shape of the waveforms recorded along both oblique paths, specially the first periods, remain remarkably similar during the imbibition process.

Figure 10 shows the spectrograms and associated normalized waveforms recorded on plane 1 for both samples at three different stages:

Stage #1. corresponds to the start of the test when the rock is completely dry (red waveforms on **Figures 8**, **9**);

Stage #2. corresponds to an intermediate stage where the properties are evolving quickly—i.e., the capillary front is close to the transducers;

Stage #3. the moving front is well above the plane of the transducers (dark blue waveforms on **Figures 8**, **9**).

For Saint-Maximin, two wavelets with high energy are actually present in the stage #1, three wavelets can also be identified in the signal coda. The first wavelet carries the highest energy. When the water reaches the transducer plane, a slight migration of the second wavelength to lower flight time is observed and this feature tends to prevail in the later stage. However, the energy of the coda vanishes significantly in presence of water. The frequency content variation of the waveform allows in this case to clearly identify the water arrival. In contrast, the impact of the water front on the spectrogram of the Savonnières is not so obvious. The signal is indeed not significantly modified between stages #1 and #3. A slight migration of the highest energy from the second to the first wavelength can be noticed but the overall spectral signature of the waveform is unaffected by the water front. Again, it is difficult to state on the origin of these striking differences without proceed to wave propagation simulation accounting for the intrinsic sample heterogeneities and those induced by the fluid migration. In the Saint-Maximin experiment, the coda analysis may however provide insights on the front propagation.

The simultaneous acquisition of 32 slices on a truncated cylindrical volume (**Figure 7C**) every 5 s gives the opportunity to perform three-dimensional reconstructions of the capillary front at selected times. A single X-ray scanning lasts about 1 s, and water keeps rising along the specimen during this time so that the reconstructed 3D images are not strictly speaking static. If the velocity of the moving front is slow enough, i.e., the water/air interface is less than 0.15 mm/s (pixel size/time to acquire an image), we can consider that the geometry derived from CT scanning provides a realistic image of the capillary

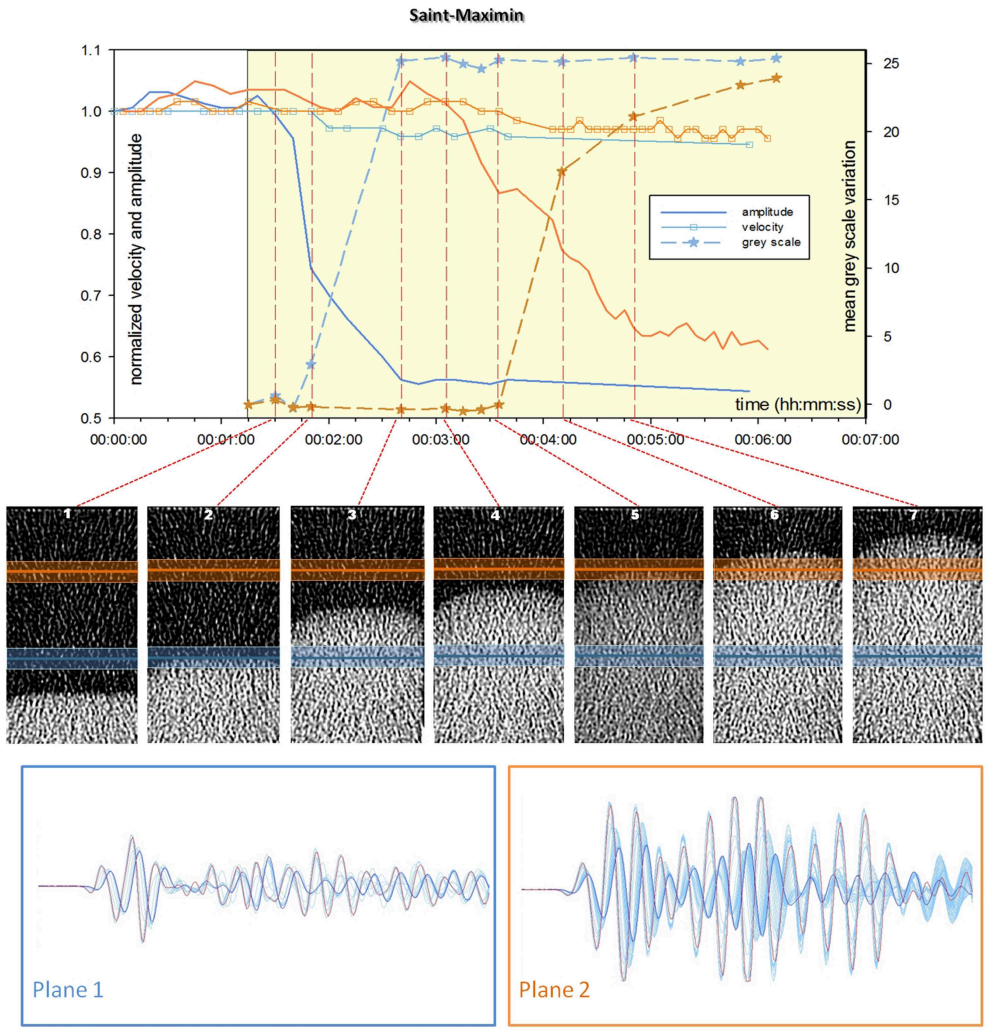

FIGURE 8 | Results for the imbibition test on Saint-Maximin grainstone: evolution as a function of time of normalized velocity and first peak amplitude recorded on planes 1 and 2 and mean gray level value calculated along these planes on selected CT volume. Processed X-ray cross section located in the middle of the sample highlighting water front shape and position. Water is in contact with the bottom of the sample at 00:01:15. The lower part of the figure is a superimposition of transmitted signals during the test for planes 1 and 2 (the first waveform obtained on the dry sample is displayed in red, and the last one is displayed in dark blue).

front at a given time. For the Saint-Maximin grainstone we chose to image the front using the data set obtained at the time corresponding to snapshots 1, 3, and 7 in **Figure 8**, and the results are shown in **Figures 11A–C**, respectively. For the Savonnières limestone, we selected the data sets corresponding to snapshots 1, 3, and 5 in **Figure 9**, and the results are shown in **Figures 11D–F**, respectively. **Figure 11** shows at each selected time the geometry of the volume invaded by water, with the upper surface corresponding to the capillary front. To our knowledge it is the first time that such data on the three-dimensional geometry of capillary fronts are reported. For Saint-Maximin, we observe that during capillary rise the curvature of the front increases, but not symmetrically. This observation is in good agreement with the sharp decrease of the P wave amplitudes observed on plane 1 contrasting with a more progressive diminution on plane 2 (**Figure 8**). The other important information derived from such analysis is the "roughness" of the capillary front, which tends also to increase during water rise. This roughness can probably be associated to local fluctuations in capillary forces linked to the heterogeneous nature of the pore network in the rock. For Savonnières similar observation can be made. The geometry of the rising front is clearly evolving with time, and the "roughness" of the capillary front seems to be higher compared to Saint-Maximin.

Discussion and Conclusion

This paper reports several experimental methods to monitor the dynamics of spontaneous capillary imbibition of water into dry porous rock samples.

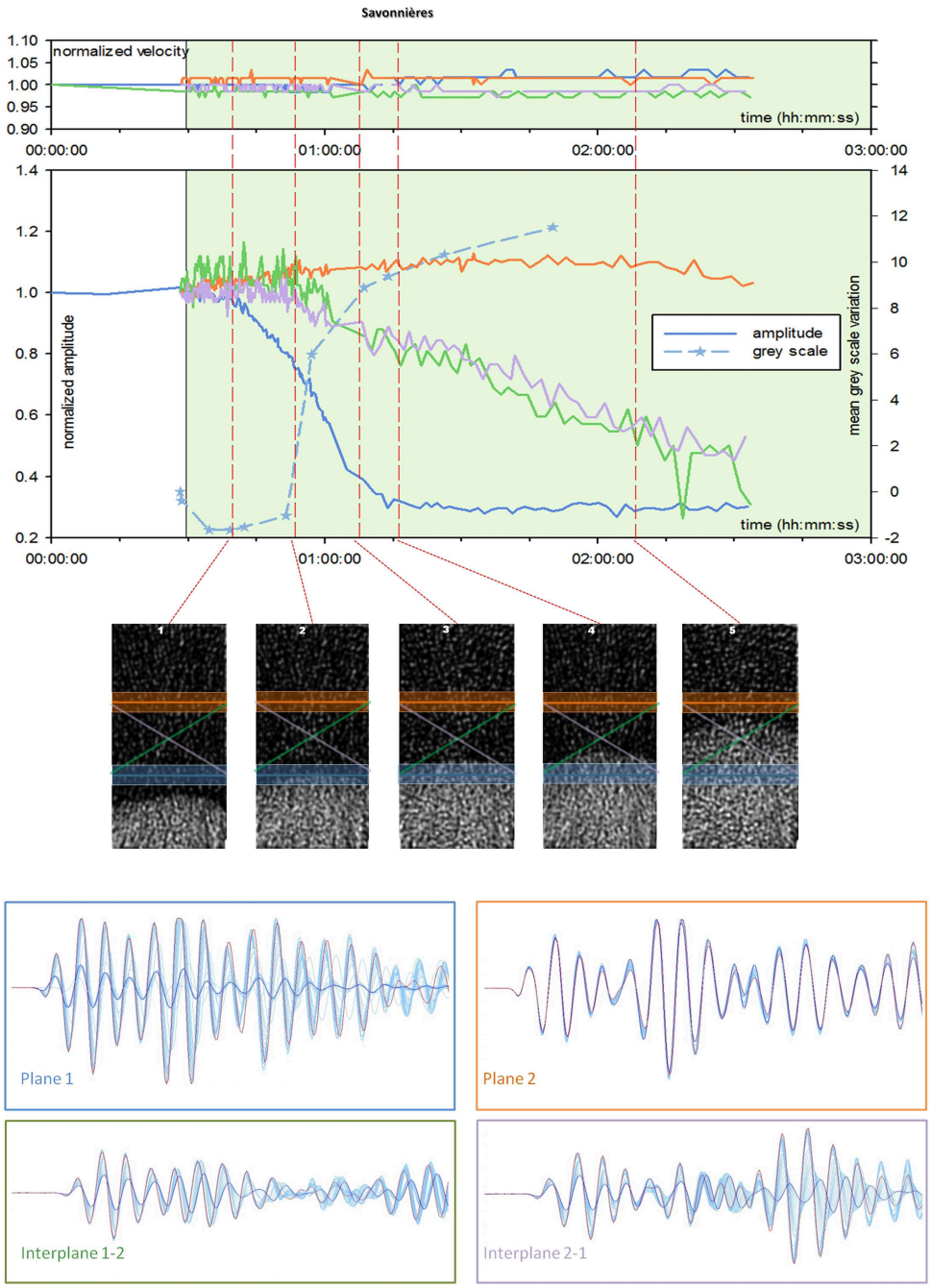

FIGURE 9 | Results for the test on Savonnières limestone: evolution as a function of time of normalized velocity and first peak amplitude recorded on planes 1 and 2 and on interplanes 1→2 and 2→1 and mean gray level value calculated along plane 1 on selected CT volume. Water is in contact with the bottom of the sample at 00:29:20. The lower part of the figure is a superimposition of transmitted signals during the test for all planes and interplanes (the first waveform obtained on the dry sample is displayed in red and the last one is displayed in dark blue).

(i) The standard weight method characterizes the mass intake dynamics. However, no detailed information is obtained on the geometry of the capillary front, except from observation of the dry-wet contact line at the sample surface. The coefficient of capillarity C can be estimated, and it was shown on a large data set that this parameter correlates reasonably well with permeability: an empirical relationship is proposed, $k = 1.38\ 10^{-12}\ C^2$ with k in m^2 and C in $kg/m^2/s^{1/2}$.

(ii) The X-ray CT scan method characterizes the capillary front dynamics and geometry, providing information on the inner part of the sample during imbibition. We used a

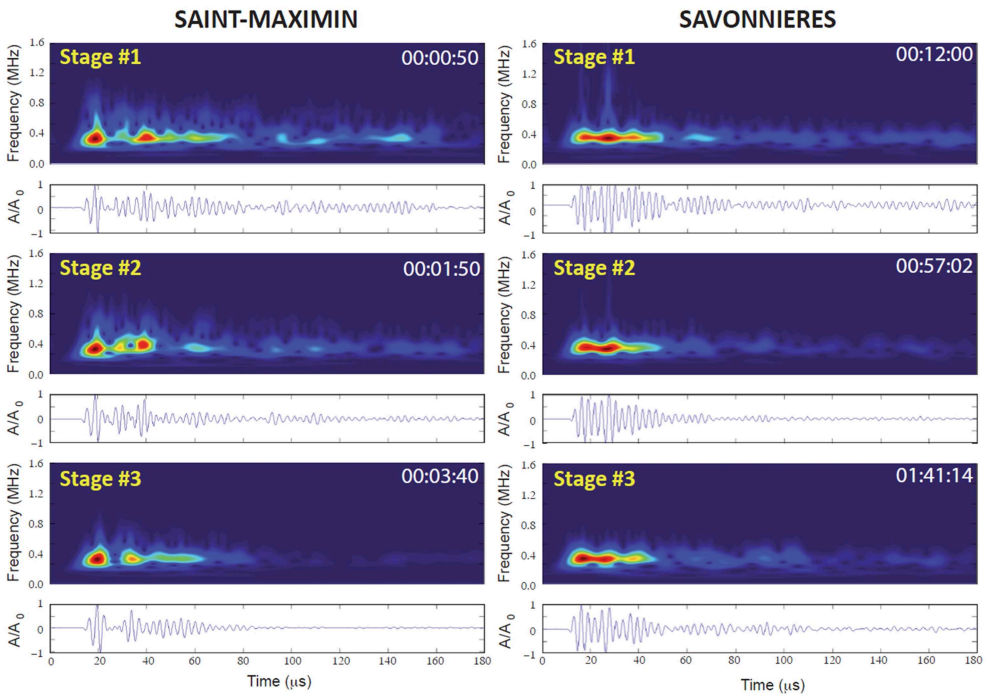

FIGURE 10 | Spectrograms and corresponding normalized waveforms obtained at different reported times on plane 1 for the Saint-Maximin and Savonnières samples.

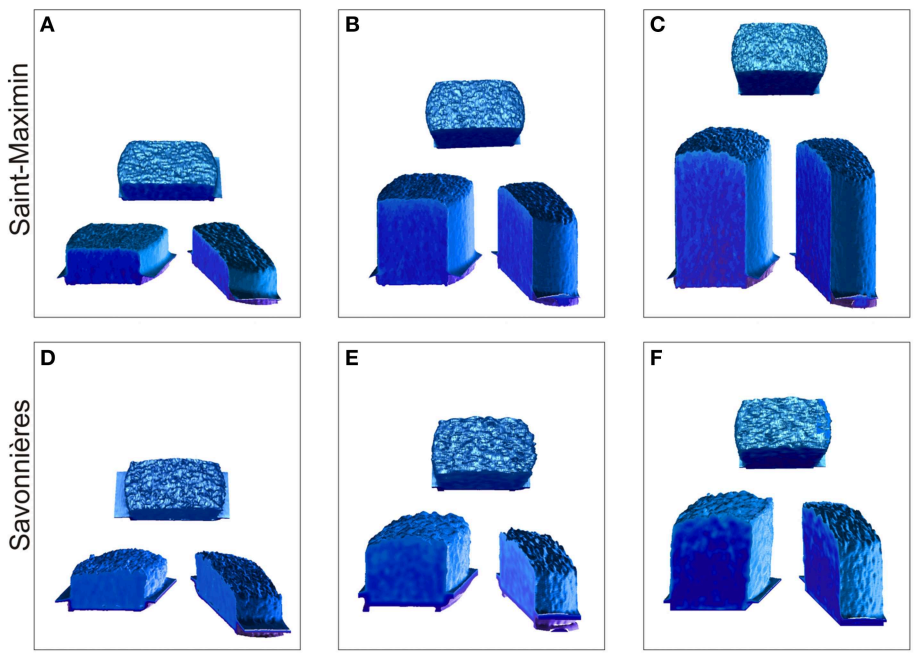

FIGURE 11 | 3D side and top views of the region invaded by water at different times during imbibition in the Saint-Maximin (A–C) and the Savonnières (D–F) samples.

standard medical scanner to obtain one centered radiograph every 2.5 s. Another capillary parameter *A* which quantifies the kinetics of the fluid front motion is derived from such images. Knowing the water saturation and assuming a flat capillary front, it is then possible to relate *A* and *C*. However, these assumptions are not fulfilled in general. We show indeed that the geometry of the capillary front is rarely flat and that both the saturation and the geometry of the water front are evolving during capillary rise. Unfortunately it is not possible to combine the weight increase monitoring while X-ray CT scanning.

(iii) The ultrasonic monitoring method consists in recording waveforms between ultrasonic sensors glued at the sample surface during imbibition. Both the velocity and the amplitude of the P waves are impacted by the passage of the capillary front near the transducers plane. For both carbonate rocks tested in this study we found that velocity and amplitude of the first peak decrease when the water front approaches the sensors, but not simultaneously. In addition capillary rise impacts first the velocity for one rock, and the amplitude for the other. Spectrograms reveal that the frequency content is changing significantly during imbibition. This method can be coupled to the weight method.

(iv) The combined X-ray imaging and ultrasonic monitoring permits to precisely identify the impact of capillary rise on the evolution of ultrasonic wave attributes (velocity, amplitude, and spectral content). The position and geometry of the moving front can be assigned to each variation observed for one of these parameters. Our measurements show that the P wave amplitude (first peak) is impacted first and significantly, when the maximum height of the capillary front is well below the wave path. In a second time, a slight velocity decrease occurs. It is associated with the increase of the average gray level, i.e., of the sample density, along the sensor plane, which reveals the arrival of water. The last generation of X-ray CT scanner permits fast acquisition of multiple slices and allows to build 3D reconstructions of the volume invaded by the water, and therefore to get an image of the topology of the capillary front in 3D space.

Monitoring the waveforms during imbibition tests in the laboratory is definitely a powerful tool for detecting fluid motion in porous rocks. The sensitivity of the different wave attributes to such fluid motion is not the same: on the carbonate rocks tested here, the variation of the P wave amplitude is a clear precursory signal for the arrival of the fluid front, whereas velocity variations (with smaller magnitude) occur only when the front actually reaches the measurement planes. A possible explanation for this behavior is that the P wave amplitude might be affected by vapor adsorption on the minerals which changes the surface energy and the elastic moduli [20], therefore the ultrasonic velocities and possibly their amplitudes. Our results show that the P wave amplitude starts to decrease sharply when the capillary front is at a distance between 3 (for Savonnières) and 6 mm (for Saint-Maximin) from the ultrasonic sensors. Interestingly this distance is of the same order of magnitude as the size of the first Fresnel zone defined in wave propagation theory [21, 22]. This zone can be approximated for homogeneous and isotropic media by an ellipsoid with a major axis equal to the distance between the sensors D and two equivalent minor axes corresponding approximately to the wavelength λ of the P wave propagating in our rocks ($\lambda \sim 6$ mm). This gives a half-width for the Fresnel clearance zone equal to about 3 mm below the sensor planes. Ray paths will be disturbed by the presence of "heterogeneities" in the Fresnel zone, like the arrival of the capillary front. The observed distances at which imbibition starts to impact the P wave propagation is of the same order as the size of the Fresnel zone estimated here. However, it is still an open question why the amplitude is impacted more and before the velocity. New results (currently being processed) from experiments done recently on other rocks confirm this observation. More work needs to be done to elucidate this particular point.

The methods applied in this paper rely on imbibition experiments on dry samples at ambient room conditions. Obviously, it remains an ideal case study but still far from *in-situ* conditions for which remote seismic monitoring is required. This study prefigures experimental programs aiming to simulate CO_2 injection, underground storage of hydrocarbon and/or Enhanced Oil Recovery operation under stress and temperature where CT-imaging cannot be used. The results presented here provide primary information on the reliable attribute of ultrasonic signals to detect fluid motions in multiphase situation, such as amplitude evolution or modification of the waveform frequency content.

Acknowledgments

We thank Marie Claude Lynch for her help with the CT scanner at IFPEN, Lionel Esteban for his help with the CT scanner at CSIRO and Maxim Lebedev for discussions and technical support. We also acknowledge Linda Stalker from the National Geosequestration Laboratory (NGL) to authorize the use of the Dual-Beam CT Scanner. We have benefited from discussions on seismic wave propagation with Christophe Barnes (GIM-labs). The work on Nubia sandstones was possible thanks to Ville de Paris who granted a post-doctoral fellowship to BN during his stay at Cergy-Pontoise and ENS Paris. Finally many thanks to the reviewers.

References

1. Dullien FAL. *Porous Media: Fluid Transport and Pore Structure*. San Diego: Academic Press (1979).
2. David C, Menendez B, Mengus J-M. The influence of mechanical damage on fluid flow patterns investigated using CT scanning imaging and acoustic emissions techniques. *Geophys Res Lett.* (2008) **35**:L16313. doi: 10.1029/2008GL034879
3. David C, Menendez B, Mengus JM. X-ray imaging of water motion during capillary imbibition in porous rocks. Part 1: methods, microstructures and mechanical deformation. *J Geophys Res.* (2011) **116**:B03204. doi: 10.1029/2010JB007972

4. Pons A, David C, Fortin J, Menendez B, Stanchits S, Mengus JM. X-ray imaging of water motion during capillary imbibition in porous rocks. Part 2: influence of compaction bands. *J Geophys Res.* (2011) **116**:B03205. doi: 10.1029/2010JB007973
5. Avseth P, Mukerji T, Mavko G. *Quantitative Seismic Interpretation: Applying Rock Physics Tools to Reduce Interpretation Risks*. Cambridge, UK: Cambridge University Press (2005).
6. Lumley D. 4D seismic monitoring of CO_2 sequestration. *Leading Edge* (2010) **29**:150–5. doi: 10.1190/1.3304817
7. Siebold A, Walliser A, Nardin M, Oppliger M, Schultz J. Capillary rise for thermodynamic characterization of solid particle surface. *J Colloid Interface Sci.* (1997) **186**:60–70. doi: 10.1006/jcis.1996.4640
8. Olafuyi OA, Cinar Y, Knackstedt MA, Pinczewski WV. Spontaneous imbibition in small cores. *Int J Pet Sci Technol.* (2009) **3**:65–82. doi: 10.2118/109724-MS
9. Nabawy B. *Mechanical, Petrophysical and Magnetic Fabrics of the Nubia Sandstones in North Eastern Desert and Sinai and their Impacts on the Preferred Interstitial Fluid Paths.* In: Internal Report, Ecole Normale Supérieure Paris (2010).
10. Labajos-Broncano L, Gonzalez-Martin ML, Bruque JM, Gonzalez-Garcia CM. Influence of the meniscus at the bottom of the solid plate on imbibition experiments. *J Colloid Interface Sci.* (2001) **234**:79–83. doi: 10.1006/jcis.2000.7244
11. Casteleyn L, Robion P, Collin PY, Menendez B, David C, Desaubliaux G, et al. Interrelations of the petrophysical, sedimentological and microstructural properties of the Oolithe Blanche formation (Bathonian, saline aquifer of the Paris basin). *Sediment Geol.* (2010) **230**:123–38. doi: 10.1016/j.sedgeo.2010.07.003
12. Cueto N, Benavente D, Martinez-Matrinez J, Garcia-del-Cura MA. Rock fabric, pore geometry and mineralogy effects on water transport in fractured dolostones. *Eng Geol.* (2009) **107**:1–15. doi: 10.1016/j.enggeo.2009.03.009
13. Benavente D, Pla C, Cueto N, Galvan S, Martinez-Martinez J, Garcia-del-Cura MA. Predicting water permeability in sedimentary rocks from capillary imbibition and pore structures. *Eng Geol.* (2015). doi: 10.1016/j.enggeo.2015.06.003. (in press).
14. Wulff AM, Mjaaland S. Seismic monitoring of fluid fronts: an experimental study. *Geophysics* (2002) **67**:221–9. doi: 10.1190/1.1451622
15. David C, Louis L, Menendez B, Pons A, Fortin J, Stanchits S, et al. X-ray imaging of fluid flow in capillary imbibition experiments – Influence of compaction and localized deformation. In: Alshibli KA, Reed AH, editors. *Advances in Computed Tomography for Geomaterials – GeoX 2010.* London: ISTE-Wiley (2010). p. 262–269.
16. Baud P, Vinciguerra S, David C, Cavallo A, Walker E, Reuschlé T. Compaction and failure in high porosity carbonates: mechanical data and microstructural observations. *Pure Appl Geophys.* (2009) **166**:869–98. doi: 10.1007/s00024-009-0493-2
17. Pinnegar CR. Time-frequency and time-time filtering with the S-transform and TT-transform. *Digit Signal Process.* (2005) **15**:604–20. doi: 10.1016/j.dsp.2005.02.002
18. Lopes S, Lebedev M, Muller TM, Clennell MB, Gurevich B. Forced imbibitions into a limestone: measuring P-wave velocity and water saturation dependence on injection rate. *Geophys Prospect.* (2014) **62**:1126–42. doi: 10.1111/1365-2478.12111
19. Pimienta L, Esteban L, Sarout J, Liu K, Delle Piane C, Clennell MB. Experimental evidence of calcite dissolution and induced precipitation during supercritical CO2 residence. In: *76th EAGE Conference and Exhibition 2014.* Amsterdam: RAI (2014a).
20. Pimienta L, Fortin J, Guéguen Y. Investigation of elastic weakening in limestone and sandstone samples from moisture adsorption. *Geophys J Int.* (2014b) **199**:335–47. doi: 10.1093/gji/ggu257
21. Spetzler J, Snieder R. The Fresnel volume and transmitted waves. *Geophysics* (2004) **69**:653–63. doi: 10.1190/1.1759451
22. Cerveny V, Soares JEP. Fresnel volume ray tracing. *Geophysics* (1992) **57**:902–15. doi: 10.1190/1.1443303

Conflict of Interest Statement: The authors declare that the research was conducted in the absence of any commercial or financial relationships that could be construed as a potential conflict of interest.

frontiers in Physics

METHODS
published: 08 July 2015
doi: 10.3389/fphy.2015.00050

Simulating anomalous dispersion in porous media using the unstructured lattice Boltzmann method

Marek K. Misztal[1], Anier Hernandez-Garcia[1], Rastin Matin[1], Dirk Müter[2], Diwaker Jha[2], Henning O. Sørensen[2] and Joachim Mathiesen[1]*

[1] Biocomplexity, Niels Bohr Institute, University of Copenhagen, Copenhagen, Denmark, [2] Department of Chemistry, Nano-Science Center, University of Copenhagen, Copenhagen, Denmark

Flow in porous media is a significant challenge to many computational fluid dynamics methods because of the complex boundaries separating pore fluid and host medium. However, the rapid development of the lattice Boltzmann methods and experimental imaging techniques now allow us to efficiently and robustly simulate flows in the pore space of porous rocks. Here we study the flow and dispersion in the pore space of limestone samples using the unstructured, characteristic based off-lattice Boltzmann method. We use the method to investigate the anomalous dispersion of particles in the pore space. We further show that the complex pore network limits the effectivity by which pollutants in the pore space can be removed by continuous flushing. In the smallest pores, diffusive transport dominates over advective transport and therefore cycles of flushing and no flushing, respectively, might be a more efficient strategy for pollutant removal.

Keywords: lattice Boltzmann method, flow in porous media, dispersion in porous media, unstructured grids, numerical modeling

OPEN ACCESS

Edited by:
Renaud Toussaint, University of Strasbourg, France

Reviewed by:
Francisco Welington Lima, Universidade Federal do Piauí, Brazil
Laurent Talon, Université Paris XI, France
Amélie Neuville, International Research Institute of Stavanger, Norway

****Correspondence:***
Marek K. Misztal, Niels Bohr Institute, University of Copenhagen, Blegdamsvej 17, Copenhagen DK-2100, Denmark
misztal@nbi.ku.dk

Specialty section:
This article was submitted to Interdisciplinary Physics, a section of the journal Frontiers in Physics

Received: *30 April 2015*
Accepted: *25 June 2015*
Published: *08 July 2015*

Citation:
Misztal MK, Hernandez-Garcia A, Matin R, Müter D, Jha D, Sørensen HO and Mathiesen J (2015) Simulating anomalous dispersion in porous media using the unstructured lattice Boltzmann method. Front. Phys. 3:50. doi: 10.3389/fphy.2015.00050

1. Introduction

Recent numerical simulations of flow in porous media in both two and three dimensions have revealed highly non-trivial flow patterns. Particles passively advected by the flow in the pore-space, so-called Lagrangian particles, follow trajectories with periods of almost stagnation punctuated by bursts of fast fluctuating motion [1–3]. In a Berea sandstone sample, it was shown by a three dimensional simulation that this intermittent behavior was equally significant in both longitudinal (the mean flow direction) and transverse directions [3]. The chaotic Lagrangian dynamic emerges despite the fact that the inertia of the fluid is negligible in many natural and industrial settings, i.e., the flow happens at low Reynolds numbers. Nonetheless, the flow might exhibit a complicated spatio-temporal behavior owing to the high heterogeneity of the pore space. The heterogeneity in fact gives rise to anomalous (non-Fickian) transport properties similar to those typically associated to high Reynolds number flow [4]. The anomalous transport has implications for the local dispersion of particles in a porous medium. It can alter the reaction rates of transported reactants or accelerate the small scale dispersion of pollutants.

In addition to the strong intermittent behavior, it has been found in both two and three dimensional simulations that the velocity autocorrelation, as a function of space, is short ranged while as a function of time the longitudinal velocity exhibits long time correlations. In the three dimensions, it was found [3] that the transverse velocity autocorrelation decays faster, though the

absolute value is strongly correlated in time, a feature also observed in turbulent flows [5]. These remarkable properties have led to the suggestion that the Lagrangian particle velocities is given by a Markov process in space (at equidistant positions along the Lagrangian trajectories) and not in time [6, 7]. In a Markov process the particle motion can be seen as a correlated continuous time random walk (CTRW). Using a correlated CTRW, several signatures of anomalous transport behavior were accurately reproduced such as the long tails of the first passage time distribution [6], the non-linear scaling of the second centered moment of the particles longitudinal and transverse displacements [3, 6, 8], the probability distribution function of the Lagrangian velocity increments for different time lags among others [1].

Interesting results were also obtained in the study of scalar mixing in two dimensional porous media with different structural disorder [9]. Numerical simulations showed that the scalar concentration forms, at advanced time, a fractal-like structure composed of stripes of high concentration and with high lacunarity. The probability distribution function of the pair separation of advecting particles was fitted to a log-normal distribution and the averaged squared separation was found to grow with time as a power law whose exponent depends on the geometry. For weak and strong heterogeneities of the porous sample the exponents were found to be 1.8 and 2.8, respectively. Remarkably, we can see that the second exponent is very close to the Richardson dispersion law, characteristic of the separation of particles whose distance lie in the inertial range interval in turbulent flows. The authors proposed a stochastic model based on *ad hoc* arguments to describe the behavior of the pair separation of advecting particles $l(t)$, which reflects the multiplicative nature of the stretching processes and accounts for the observed short range temporal correlations of the Lagrangian stretching rates.

Here we formulate a version of the lattice Boltzmann method on unstructured grids to efficiently simulate flow in complex pore geometries. We use the method to assess the Lagrangian dynamics of flows in the pore space of limestone samples computed by x-ray tomography. In order to faithfully compute the broadly distributed fluid velocities, it is required to represent the pore boundaries with a high resolution. Compared to classical lattice Boltzmann methods on regular grids, the unstructured grids offer a superior resolution and adaptivity [10]. We further analyze the impact of the complex pore geometry on pollutant removal from the pore space.

2. Materials and Methods

2.1. Porous Rock Samples

We have performed our pollutant dispersion studies on two different, natural porous samples, discretized using tetrahedral elements (the properties of the tetrahedral meshes are presented in **Table 1**).

Sample A (**Figure 1**) is chalk from off-shore drilling in the North Sea region (Hod chalk #15). *Sample B* (**Figure 2**) came from an outcrop of bryozoan chalk in Rødvig, Denmark. The digital 3D images were obtained by x-ray nanotomography [11] measured at beamline ID22 at the European Synchrotron Radiation Facility, France. The reconstructed volume of Sample A had a voxel size of 25 nm and an optical resolution about 150 nm. Details about the data collection and reconstruction can be found in Müter et al. [12]. The reconstructed images were corrected for ring artifacts [13] before segmentation by a dual filtering and Otsu thresholding procedure [14]. For the LBM calculations we used a subvolume of 100^3 voxels, which gives a side length of 2.5 microns. Sample B was reconstructed and segmented in the same way as Sample A. The only difference is that it was reconstructed with a voxel size of 50 nm leading to an optical resolution of about 300 nm. The LBM calculations were performed on a subvolume of 400^3 voxels (side length of 20 microns). In Sample A, the diameter of the pore throats corresponds to at least 6 voxel sizes, while the typical pore diameter is 30–40 voxels. In Sample B, the smallest pore throats are about 5 voxels, however, the flow is dominated by a large, well connected pore system, where the pore diameter is 50 voxels and above.

In order to construct the tetrahedral meshes, the initial triangular surface meshes were produced using the marching cubes isosurface as implemented in ImageJ [15]. The resolution of those surface meshes is the same as in the corresponding tomographic data (1 voxel accounting for 1-2 triangles). A tetrahedral volume mesh was constructed from the surface mesh using Tetgen [16].

2.2. Unstructured Lattice Boltzmann Method

The appeal of the lattice Boltzmann method to the geophysics research lies in its ability to model and simulate several types of phenomena related to reactive fluid flow in porous rocks: single and multiphase flows [17], unsteady flows [18], flows in complex geometries [19, 20] at a wide range of Reynolds numbers, as well as chemical processes, such as dissolution and precipitation [21]. For our experiments, we have used a variant of the finite element, off-lattice Boltzmann method [22], which uses the characteristic

TABLE 1 | Properties of the tetrahedral meshes used in the simulations and the wall-clock time spent per 5000 iterations of the unstructured lattice Boltzmann simulation (Intel® Xeon® 2.6 GHz).

	No. elements	No. vertices	Edge lengths (LB)			Side length (LB)	Node valency			Simulation time
			Avg.	Min.	Max.		Avg.	Min.	Max.	per 5000 iterations
Sample A	538,818	122,923	1.48	0.082	3.4	100	11.7	4	44	7 min 30 s
Sample B	19,011,599	4,131,911	1.51	0.22	68.0	400	12.3	4	39	4 h 30 min

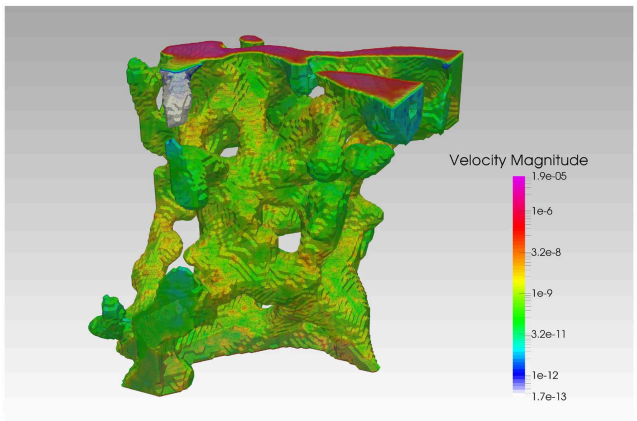

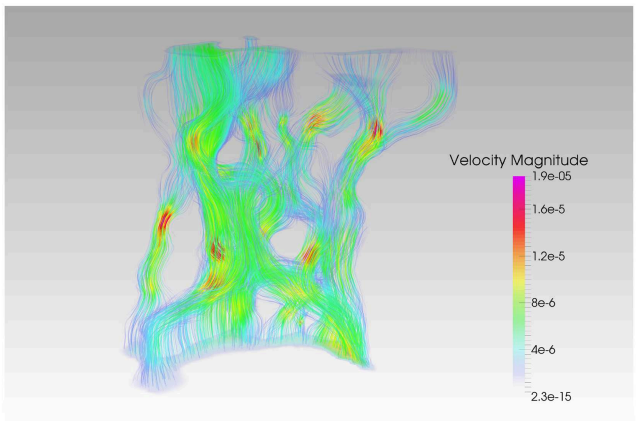

FIGURE 1 | Left: The surface plot of the investigated volume of Sample A, colored according to the surface velocities. The values on the solid boundary are at least three orders of magnitude lower than the values on the outlet (top surface of the mesh). **Right:** The streamlines of the steady-state velocity field, generated for $\tau = 0.02$, $\Delta\rho = 2.5 \cdot 10^{-6}$. Both images were generated using ParaView 4.3.1. [32].

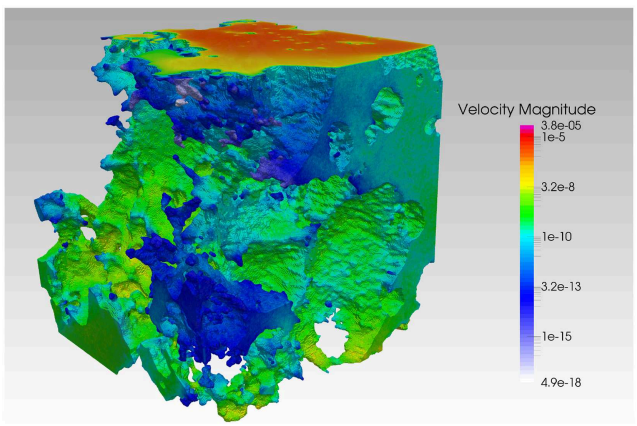

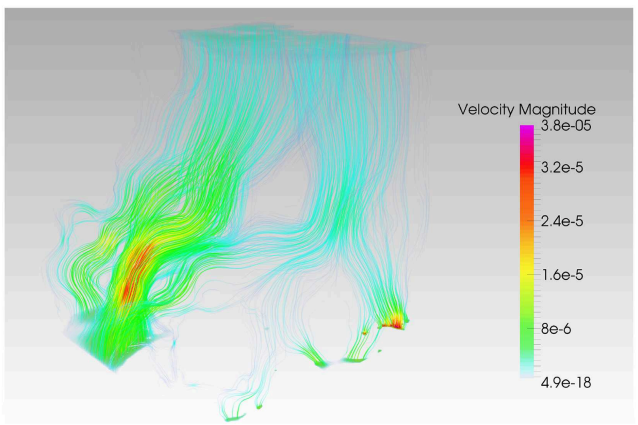

FIGURE 2 | Left: The surface plot of the investigated volume of Sample B, colored according to the surface velocities. The values on the solid boundary are at least three orders of magnitude lower than the values on the outlet (top surface of the mesh). **Right:** The streamlines of the steady-state velocity field, generated for $\tau = 0.1$, $\Delta\rho = 2.5 \cdot 10^{-6}$. Both images were generated using ParaView 4.3.1. [32].

based integration, first proposed by Zienkiewicz and Codina [23]. We chose this method over the finite volume approach [10, 24] due to its improved stability. The characteristic based, off-lattice Boltzmann method has been specifically designed to remove the coupling between the positions of the computational grid's nodes and the discrete set of velocities, while retaining the stability of the standard, regular grid-based approach. The new scheme is derived directly from the spatio-temporal continuous formulation of the lattice Boltzmann equation

$$\frac{\partial f_i}{\partial t} + \mathbf{c}_i \cdot \nabla f_i = \Omega_i(f(\mathbf{x}, t)), \tag{1}$$

where $f_i(\mathbf{x}, t)$ is the particle velocity distribution along the i-th discrete direction, $\mathbf{c}_i$ is the associated discrete velocity, and Ω_i is the collision operator, accounting for the rate of change of f_i due to collision. We have employed the two relaxation time collision (TRT) operator [19, 25], which is a special case of a multi relaxation time collision operator (MRT, [26]), most commonly used in the lattice Boltzmann studies of porous flow due to its improved treatment of the solid boundary conditions in comparison to the standard, single relaxation time Bhatnagar-Gross-Krook (BGK) operator [19].

2.2.1. Integration Along Characteristics

Integrating Equation (1) along the characteristic curves and approximating the right-hand side yields

$$f_i^{n+1}(\mathbf{x} + \mathbf{c}_i\delta t) = f_i^n(\mathbf{x}) + \delta t \left(\theta\Omega_i^{n+1}(f^{n+1}(\mathbf{x} + \mathbf{c}_i\delta t)) + (1-\theta)\Omega_i^n(f^n(\mathbf{x}))\right), \tag{2}$$

where n denotes the time step (iteration number), $0 \leq \theta \leq 1$ refers to the choice of the time integration method for the collision operator (0 for fully explicit, 1 for fully implicit, 0.5 for

Crank-Nicolson), $f_i^n(\mathbf{x}) = f_i(\mathbf{x}, t^n)$, and $f_i^{n+1}(\mathbf{x}) = f_i(\mathbf{x}, t^n + \delta t)$. In the general case of a MRT collision operator $\Omega_i\left(f(\mathbf{x}, t)\right) = \sum_j A_{ij}(f_j^{eq} - f_j)$ [26] the implicit character of Equation (2) can be removed by introducing new variable

$$g_i(\mathbf{x}, t) = f_i(\mathbf{x}, t) - \delta t\theta\, \Omega_i(f(\mathbf{x}, t)), \tag{3}$$

and expressing the collision operator in terms of g [22]

$$\Omega(f(\mathbf{x}, t)) = (\mathbf{I} + \delta t\theta\mathbf{A})^{-1}\Omega(g(\mathbf{x}, t)). \tag{4}$$

As the collision operator preserves both mass and momentum, the moments of g_i equal corresponding moments of f_i, $\sum_i g_i = \rho$, $\sum_i g_i\mathbf{c}_i = \rho\mathbf{u}$, hence also $g_i^{eq} = f_i^{eq}$. Finally, Equation (2) becomes

$$g_i^{n+1}(\mathbf{x} + \mathbf{c}_i\delta t) = g_i^n(\mathbf{x}) + \delta t \sum_j \hat{A}_{ij}(g_j^{eq,n}(\mathbf{x}) - g_j^n(\mathbf{x})), \tag{5}$$

where the modified collision matrix reads $\hat{\mathbf{A}} = (\mathbf{I} + \delta t\theta\mathbf{A})^{-1}\mathbf{A}$. By substituting $\mathbf{A}$ by $\mathbf{A}_{BGK} = \tau^{-1}\mathbf{I}$, which corresponds to the single relaxation time BGK collision operator, one readily obtains $\hat{\mathbf{A}}_{BGK} = (\tau + \theta\delta t)^{-1}\mathbf{I}$. The resulting shift in the effective relaxation time $\hat{\tau} = \tau + \theta\delta t$ accounts for the unconditional stability of the Crank-Nicolson method and the implicit Euler method, since the condition $\delta t < 2\hat{\tau}$ is always fulfilled as long as $\theta \geq \frac{1}{2}$ and $\tau > 0$. The standard Courant-Friedrichs-Lewy restriction on δt still applies.

2.2.2. Finite Element Scheme

In order to solve Equation (5) numerically on an unstructured grid, one has to be able to express the value of g_i^{n+1} at a given point $\mathbf{x}^*$ in terms of the value of g_i^n (and its derivatives) evaluated one time step earlier, at the same point. In order to enhance stability, this is typically done by the second order Taylor expansion of $g_i^n(\mathbf{x}^* - \mathbf{c}_i\delta t)$ [22, 23]

$$\begin{aligned} g_i^n(\mathbf{x}^* - \mathbf{c}_i\delta t) &= g_i^n(\mathbf{x}^*) - \delta t c_{ir}\partial_r g_i^n(\mathbf{x}^*) \\ &\quad + \frac{\delta t^2}{2} c_{ir}c_{is}\partial_s\partial_r g_i^n(\mathbf{x}^*) + \mathcal{O}(\delta t^3). \end{aligned} \tag{6}$$

After applying the same approximation to the equilibrium distribution function, Equation (5) takes the following form

$$\begin{aligned} g_i^{n+1} &= g_i^n - \delta t\left(c_{ir}\partial_r g_i^n - \sum_j \hat{A}_{ij}(g_i^{eq,n} - g_i^n)\right) \\ &\quad + \frac{\delta t^2}{2} c_{ir}\partial_r\left(c_{is}\partial_s g_i^n - 2\sum_j \hat{A}_{ij}(g_i^{eq,n} - g_i^n)\right) \\ &\quad + \frac{\delta t^3}{2} c_{ir}c_{is}\partial_s\partial_r\left(\sum_j \hat{A}_{ij}(g_j^{eq,n} - g_j^n)\right), \end{aligned} \tag{7}$$

which is now suitable for discretization in space using the Galerkin finite element method. Here, the spatial decomposition using linear, tetrahedral elements has been applied. The modified particle distribution functions are sampled at the nodes (vertices) of the tetrahedral mesh, and interpolated at other points

$$\tilde{g}_i^n(\mathbf{x}) = \boldsymbol{\phi}(\mathbf{x})^T\tilde{\mathbf{g}}_i^n \tag{8}$$

where $\tilde{g}_i^n$ is the approximate solution, $\tilde{\mathbf{g}}_i^n = \left[\tilde{g}_i^n(\mathbf{v}_1), \tilde{g}_i^n(\mathbf{v}_2), \ldots, \tilde{g}_i^n(\mathbf{v}_{N_V})\right]^T$ is the vector storing the values of $\tilde{g}_i^n$ at all vertices in the mesh, whose positions are $\mathbf{v}_1, \mathbf{v}_2, \ldots, \mathbf{v}_{N_V}$. Furthermore, $\boldsymbol{\phi}(\mathbf{x})^T = \left[\phi^1(\mathbf{x}), \phi^2(\mathbf{x}), \ldots, \phi^{N_V}(\mathbf{x})\right]$, where $\phi^k(\mathbf{x})$ is a piecewise-linear shape function (also known as a *hat* or *tent* function) associated with the vertex k, i.e., $\phi^k(\mathbf{v}_j) = \delta_{jk}$, and ϕ^k is linear over each tetrahedral element. By applying the Bubnov-Galerkin method, we finally obtain the discrete, weak form of Equation (7)

$$\begin{aligned} \mathbf{M}(\tilde{\mathbf{g}}_i^{n+1} - \tilde{\mathbf{g}}_i^n) = \left(-\delta t\mathbf{C}_i - \delta t^2\mathbf{D}_i\right)\tilde{\mathbf{g}}_i^n + \left(\delta t\mathbf{M} - \delta t^2\mathbf{C}_i - \delta t^3\mathbf{D}_i\right) \\ \sum_j \hat{A}_{ij}(\tilde{\mathbf{g}}_j^{eq,n} - \tilde{\mathbf{g}}_j^n), \end{aligned} \tag{9}$$

where matrices $\mathbf{M}, \mathbf{C}_i, \mathbf{D}_i \in \mathbb{R}^{N_V \times N_V}$ are defined as

$$\begin{aligned} \mathbf{M} = \int_{\mathcal{D}} \boldsymbol{\phi}\boldsymbol{\phi}^T dV, \quad \mathbf{C}_i &= \int_{\mathcal{D}} \boldsymbol{\phi}c_{ir}\partial_r\boldsymbol{\phi}^T dV, \\ \mathbf{D}_i &= \frac{1}{2}\int_{\mathcal{D}} \partial_s\boldsymbol{\phi}c_{is}c_{ir}\partial_r\boldsymbol{\phi}^T dV. \end{aligned} \tag{10}$$

2.2.3. Boundary Conditions

The quality of any lattice Boltzmann simulation hinges on the choice of the boundary conditions used both on the solid and open boundaries. In this work, we have used a recent formulation of the solid boundary conditions for high Reynolds number flows, first proposed by Chikatamarla and Karlin [27]. Similarly to the popular bounce back method, the first step is to determine the subset $\bar{D}$ of the discrete directions that are corresponding to the "missing" populations (i.e., point away from the solid phase and into the fluid phase). The procedure for finding such subset in an unstructured grid setting is described in detail in Misztal et al. [10]. By setting the target values of the density ρ_{tg} and velocity $\mathbf{u}_{tg}$ at the boundary node, the local populations are recovered using the following rules

$$f_i \longleftarrow \begin{cases} 2f_i^{eq}(\rho_{tg}, \mathbf{u}_{tg}) - f_i^{eq}(\rho, \mathbf{u}), & i \in \bar{D} \\ f_i + f_i^{eq}(\rho_{tg}, \mathbf{u}_{tg}) - f_i^{eq}(\rho, \mathbf{u}), & i \notin \bar{D} \end{cases}, \tag{11}$$

where $\rho = \sum_{i\in\bar{D}} f_i^{eq}(\rho_{tg}, \mathbf{u}_{tg}) + \sum_{i\notin\bar{D}} f_i$, and $\rho\mathbf{u} = \sum_{i\in\bar{D}} \mathbf{c}_i f_i^{eq}(\rho_{tg}, \mathbf{u}_{tg}) + \sum_{i\notin\bar{D}} \mathbf{c}_i f_i$. In our simulations we assumed no-slip boundary condition on the static, solid walls, corresponding to $\mathbf{u}_{tg} = 0$. The value of ρ_{tg} can be estimated either by using the bounce back method or, if the former approach fails (depending on the local geometry of the solid boundary), by extrapolating the values of density from the neighboring bulk nodes. We have observed that this choice of the solid boundary condition formulation yields significantly more stable simulations of flows with lower values of the kinetic

viscosity and higher Reynolds number, compared to the bounce back method.

The boundary conditions at the inlet and at the outlet can also be implemented using the same procedure. We have chosen to use pressure boundary conditions, specified by the constant pressure values: p_{in} at the inlet, and p_{out} at the outlet; $p_{in} > p_{out}$. Since $p = c_s^2 \rho$ in the lattice Boltzmann method, this is equivalent to setting $\rho_{tg} = p_{in}/c_s^2$ at the inlet and $\rho_{tg} = p_{out}/c_s^2$ at the outlet (like most authors, we use $c_s^2 = 1/3$). The values of $\mathbf{u}_{tg}$ at the open boundary nodes can be approximated using the averaged values of the velocity at the neighboring bulk nodes.

3. Results

The unstructured lattice Boltzmann method allows us to robustly compute single phase flow fields in arbitrary, complex channel networks for a wide range of flow parameters. In this section, we apply this method to study the flow in each of the natural porous samples described in Section 2.1. We then use the precomputed flow fields to study pollutant dispersion in the samples.

3.1. Steady-State Flow Computation

Our first goal is to compute the steady state flow in each porous rock sample due to applying a constant pressure difference between the inlet and the outlet planes. The particle distribution functions are initialized with the equilibrium distributions corresponding to $\rho = 1$, $\mathbf{u} = 0$ in the entire mesh. For a given time step δt, relaxation time τ, and constant inlet and outlet densities $\rho_{in} = 1+\Delta\rho$ and $\rho_{out} = 1$, we run the lattice Boltzmann simulation until the steady state is reached. In order to detect when steady-state has been reached, we compute the inlet flow rate Q_{in} by evaluating the following integral numerically at every time step t^n

$$Q_{in} = \int_{A_{in}} \mathbf{u} \cdot d\mathbf{A} \approx \sum_{T_k = \langle pqr \rangle} \frac{\mathbf{u}_p + \mathbf{u}_q + \mathbf{u}_r}{3} \cdot \mathbf{n}_k A_k, \qquad (12)$$

where the sum on the right-hand side is over each inlet triangle T_k; $\mathbf{u}_p$, $\mathbf{u}_q$, $\mathbf{u}_r$ are its nodal velocities, $\mathbf{n}_k$ is the unit-length normal vector to T_k, and A_k is its area. The outlet flow rate Q_{out} is evaluated the same way. The simulation ends when $|Q_{in}(t^{n+1}) - Q_{in}(t^n)| < \epsilon |Q_{in}(t^n)|$ and $|Q_{out}(t^{n+1}) - Q_{out}(t^n)| < \epsilon |Q_{out}(t^n)|$, where $\epsilon = 10^{-5}$.

Examples of the obtained velocity fields in each of the porous samples are shown in **Figures 1**, **2**. In **Figure 3** we present the typical convergence plots for Q_{in} and Q_{out} in our simulations. The initial oscillations are caused by the discontinuous initial conditions, as well as the formulation of the open boundary conditions; setting $\rho_{in} = 1 + \Delta\rho$ gives rise to a shock wave, which first travels to the outlet, and gets reflected off the outlet and inlet planes, while its amplitude decays exponentially. Once the pressure wave vanishes, the values of Q_{in} and Q_{out} continue to converge exponentially to the steady state values Q_{in}^{∞} and Q_{out}^{∞}. We expect these values to be equal, however, since the expression (12) is only first-order accurate, we observe a small difference between these two values, which is particularly evident in case of the more coarsely meshed Sample A. We have performed steady-state flow computation for $\Delta\rho$ ranging from $2.5 \cdot 10^{-7}$ to $2.5 \cdot 10^{-3}$, and relaxation times $\tau = 0.01 - 0.1$, and we have obtained stable results obeying the Darcy's law, which states that under steady-state flow conditions, the flow rate Q through a given cross section is proportional to the pressure drop $\Delta p = c_s^2 \Delta\rho$ that drives the fluid.

These simulation results shown in **Figures 1**, **2** correspond to a Reynolds number approximately equal to 0.01. The velocity in the figures is expressed in lattice Boltzmann units u_{LB}. By dimensional analysis we can express the velocity in another arbitrary system of units according to the following transformation

$$u_{SU} = u_{LB} \frac{l_{LB}}{l_{SU}} \frac{\nu_{SU}}{\nu_{LB}}, \qquad (13)$$

where the l_{LB} and ν_{LB} are the system size and kinetic viscosity in lattice Boltzmann units, l_{SU} and ν_{SU} are the same quantities

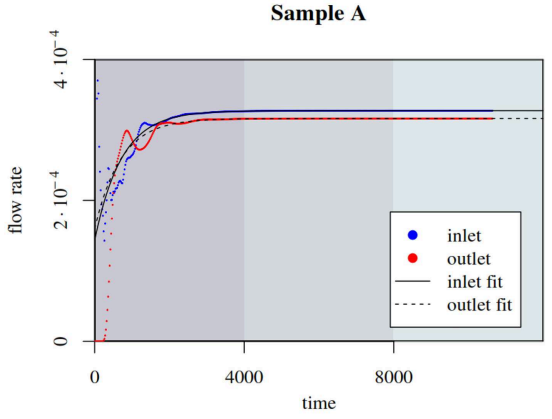

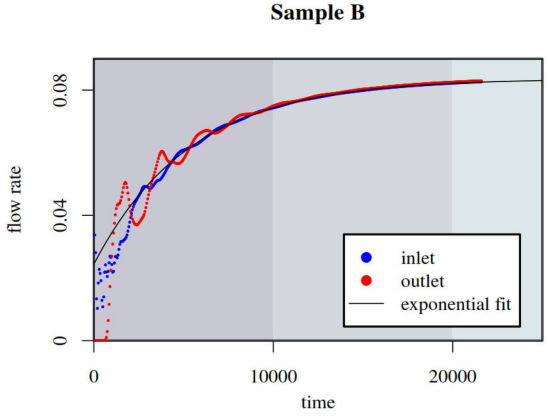

FIGURE 3 | Convergence plot for the steady-state computation in Sample A (on the left, $\tau = 0.02$, $\Delta\rho = 10^{-6}$) and in Sample B (on the right, $\tau = 0.1$, $\Delta\rho = 2.5 \cdot 10^{-6}$). The exponential fits are computed in R, using robust nonlinear regression, after weighting out the initial, oscillatory phase (flow rates and time are given in lattice Boltzmann units).

expressed in another system of units. If the fluid is water, substituting the real-world parameters into Equation (13) yields the following scaling formulas for the real-world velocities in the SI system of units: $u_{SI} = u_{LB} \cdot 6000 \frac{\mathrm{m}}{\mathrm{s}}$ in Sample A, and $u_{SI} = u_{LB} \cdot 600 \frac{\mathrm{m}}{\mathrm{s}}$ in Sample B.

3.2. Dispersion in Porous Samples

Having computed the steady state flow field in each of the porous rock samples, we obtain the Lagrangian trajectories of passive tracers, which satisfy

$$\dot{\mathbf{x}}_k(t) = \mathbf{u}(\mathbf{x}_k(t)), \tag{14}$$

in the absence of molecular diffusion. The solution of the above equation is fixed by the initial position $\mathbf{x}_k(0)$. From these Lagrangian trajectories we study the statistics of the separation $\mathbf{d}_{kj}(t) = \mathbf{x}_k(t) - \mathbf{x}_j(t)$ between two fluid particles, which initially are close to each other. The separation of particles obeys the differential equation

$$\dot{\mathbf{d}}_{kj}(t) = \mathbf{u}(\mathbf{x}_k(t)) - \mathbf{u}(\mathbf{x}_j(t)). \tag{15}$$

The constraints imposed by the porous heterogeneous structure may cause non-smooth velocity fields due to the intrinsic branching of channel connectivity, leading to broad distribution of velocities and absence of decorrelation in time. For non-smooth velocity fields we might have, for instance, that the velocity difference between two points scales as $|\mathbf{u}(\mathbf{x}_k(t)) - \mathbf{u}(\mathbf{x}_j(t))| \propto |\mathbf{x}_k(t) - \mathbf{x}_j(t)|^\beta = d_{kj}^\beta$, with $\beta < 1$, as in the inertial range in turbulent flows. Multiplying the left and right hand sides terms in Equation (15) by $\mathbf{d}_{kj}(t)$ and substitution of the latter scaling lead to

$$\dot{d}^2 = 2\,\mathbf{d}_{kj} \cdot \left[\mathbf{u}(\mathbf{x}_k(t)) - \mathbf{u}(\mathbf{x}_j(t))\right] \propto d^{1+\beta}, \tag{16}$$

whose solution for finite time gives the behavior

$$\left(\frac{d(t)}{d_0}\right)^2 \propto t^{\frac{2}{1-\beta}}. \tag{17}$$

As seen in **Figure 4**, we find from a flow simulation in Sample A that $\beta \approx 1/3$, which coincides with Richardson dispersion law. Of course, such spatial scaling should not be associated to the classical Richardson-Kolmogorov cascade picture. Instead, the anomalous dispersion originates from the high degree of heterogeneity in Sample A and the broad distributions of pore sizes. This is further confirmed by the simulations performed in Sample B, here we see a particle separation in time, which is consistent with ballistic motion of particles in a more simple geometry. This is due to the fact, that the flow in Sample B is dominated by one large pore and the heterogeneity of the much smaller neighboring pores is only having a negligible impact on the averaging (see **Figure 4**).

3.3. Evacuation of Particles through Advection and Diffusion

In our final experiment, we apply the previously obtained steady state velocity field $\mathbf{u}(\mathbf{x})$ in a study of pollutant removal from Sample A. In particular, we perform a comparative, qualitative study of particle evacuation rate from the porous sample, using two different flushing strategies: through continuous steady flow and through the use of rectangular pulses of equal width and amplitude, increasing period and decreasing duty cycle (see **Figure 5**).

As the first step of this numerical experiment, we randomly seed a large number of particles N_0 (in our experiments $N_0 = 250,000$), uniformly distributed in the pore space of the sample. We assume that the particles are passively advected by the fluid, but also undergo molecular diffusion. The motion of such passive tracers is described by the following Langevin equation

$$\dot{\mathbf{x}}_k(t) = \bar{\mathbf{u}}(\mathbf{x}_k(t), t) + \boldsymbol{\eta}_k(t), \tag{18}$$

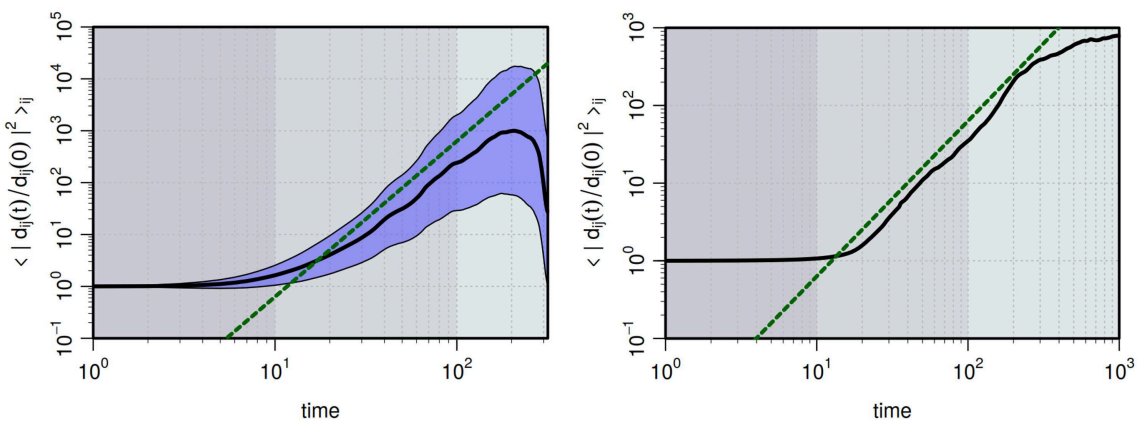

FIGURE 4 | The black line shows the change with time of the average of the squared distance of particles, which initially are closer than 1% of the system size (the linear size). In the left panel, we show data from Sample A. The green dashed line is proportional to t^3 and is consistent with the Richardson dispersion law. Despite the limited scaling region, we see an anomalous dispersion, where particles separates faster than in a ballistic regime. The envelope surrounding the black line shows the standard deviation of individual particle pairs. In the right panel, we show similar data for Sample B. The dashed line is here proportional to t^2 and is therefore consistent with a ballistic separation of particles.

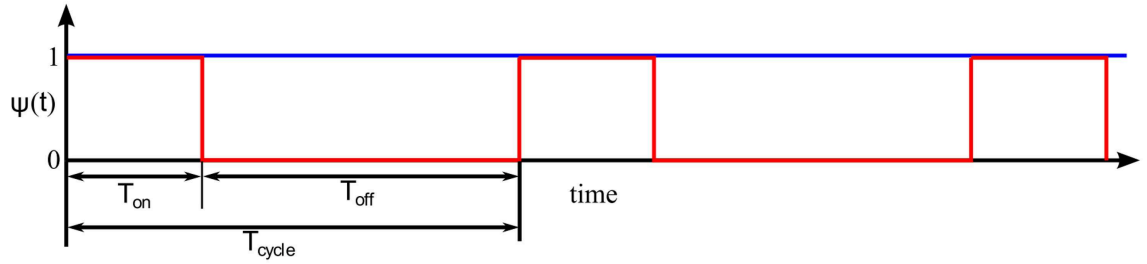

FIGURE 5 | Continuous (blue) and rectangular pulse envelope (red). The pulse width T_{on} is constant in all our particle evacuation simulations, and we run the simulations with three different pulse separation times T_{off}. The duty cycle is defined as $d = T_{on}/T_{cycle}$. The pulse separation time T_{off} is on the order of 10% of the diffusive time, defined as R^2/D, where R is the characteristic pore size, and D is the diffusivity.

where $\mathbf{x}_k(t)$ is the position of the kth particle at time t, and $\bar{\mathbf{u}}(\mathbf{x}_k(t), t) = \mathbf{u}(\mathbf{x}_k(t))\psi(t)$ is the fluid's velocity evaluated at particle's position at time t; $\psi(t)$ is the pulse envelope function. Here we assume that the frequency of the pulses is smaller than the inverse of the characteristic time in which viscous effect are propagated inside the porous sample. The latter can be estimated as R^2/ν, where R is on the order of the largest channel width. The final term, $\boldsymbol{\eta}_k(t) = \sqrt{2D}\boldsymbol{\xi}(\mathbf{x}_k(t), t)$, is the random "kick" function, where D is the diffusivity and $\boldsymbol{\xi}_k(t)$ is a vector-valued Gaussian noise with mean amplitude equal to unity, whose correlation is given by $\langle \boldsymbol{\xi}_k(t)\boldsymbol{\xi}_{k'}(t')\rangle = \delta_{kk'}\delta(t - t')$. The above equation for passive tracers can be obtained in the limit of vanishing Stokes time from the following system of Langevin equations describing the Brownian motion of inertial particles in a moving fluid [28]

$$\dot{\mathbf{x}}_k(t) = \mathbf{v}_k(t), \quad \dot{\mathbf{v}}_k(t) = \frac{1}{\tau}\left(-\mathbf{v}_k(t) + \bar{\mathbf{u}}(\mathbf{x}_k(t), t) + \boldsymbol{\eta}_k(t)\right), \tag{19}$$

in which τ is the Stokes time. We integrate Equation (18) for each particle using the forward Euler method. Additionally we assume elastic collisions between the particles and the solid wall, and that the particles which cross the outlet plane are removed from the system. Then, we track the number N of particles remaining in the pore space as a function of the total volume of fluid flushed through the system

$$V(t) = \int_0^t \left(\int_{A_{in}} \bar{\mathbf{u}}(\mathbf{x}, t) \cdot d\mathbf{A}\right) dt. \tag{20}$$

The results of our experiments for Sample A are presented in **Figure 6**. The parameters were chosen so that the effective Péclet number Pe $\approx$ 1600. Evidently, continuous flushing is the least efficient in terms of the amount of resources used (water, energy) in order to remove a given fraction of pollutant from the sample. Increasing the separation between the pressure pulses yields increasingly more efficient use of resources. This is due to the fact that the water flow through the sample quickly decreases the particle concentration in the main channel network, however, some pores are inaccessible to the flow, i.e., $\mathbf{u} = 0$ in such spaces. The only way for the particles to be released from these pores is through diffusion, and, as it is a slower process, increasing the pulse separation increases the time for diffusion to act on. In contrast, as the particle concentration in the main channel network decreases, the efficiency of continuous flushing quickly drops.

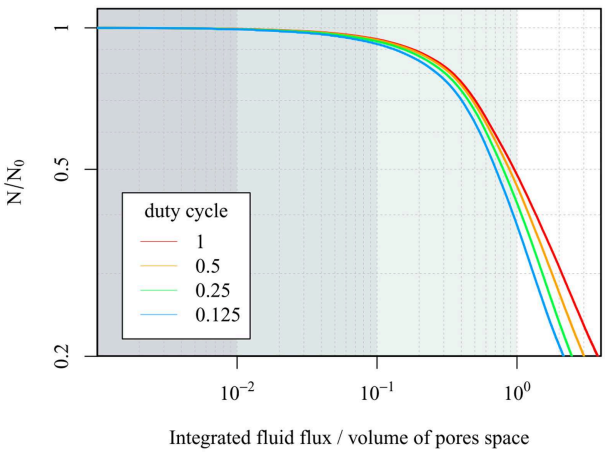

FIGURE 6 | The fraction of the pollutant left inside Sample A as a function of the total volume of water that passed through the sample (given as a fraction of the pore space volume), using continuous flushing (duty cycle $d = 1$) and increasingly separated, constant width, rectangular pressure pulses.

4. Discussion

4.1. Evaluation of the ULBM

Our choice to use the unstructured lattice Boltzmann method, as opposed to the regular grid based approaches, was dictated by the higher flexibility and accuracy of the unstructured meshes at representing complex solid boundaries. Unlike regular grids, unstructured meshes allow for locating the nodes precisely at the boundary, yielding the boundary approximation error on the order of h^2, as opposed to h in case of regular grids, where h is the grid spacing (or local edge length, in case of unstructured meshes). This error can be decreased further, without significantly increasing the problem size, by employing

adaptive meshes, i.e., using higher precision (lower h) to resolve fine features, while keeping the mesh coarser in the regions where the boundary is almost flat, or where the flow field is approximately linear. Furthermore, unstructured meshes do not introduce extra memory overhead related to the storage of the solid phase elements, which is particularly beneficial in case of samples with low porosity. Overall, the number of volumetric elements required to represent a porous structure with precision h on the boundary scales like $h^{-2}\log h^{-1}$, as opposed to h^{-3} in case of basic regular grids. Certain techniques, such as the immersed boundary method [29] and hierarchical voxel structures [30], allow regular grid based approaches reach the effective storage efficiency similar to that of unstructured meshes. However, they increase the complexity of the fluid simulation method, and the lack of coupling between the nodal positions and the precise location of the solid boundary persists. As a consequence, boundary features finer than the minimum grid spacing cannot be represented correctly and, in the worst case scenario, the topology of the channel network might be ambiguous or inaccurate. In contrast, unstructured grids yield much simpler formulation of the boundary conditions, allow for a faithful representation of arbitrarily fine surface details, and reproduce the channel network topology exactly (although, in our case, the accuracy of the representation is still limited by the resolution of the tomographic data).

The benefits of the ULBM come at a cost of increased number of computations per grid node. At each time step, at a given node, regular grid based LBM requires a single evaluation of the collision term, one assignment (copy) operation and a single addition per each discrete direction. ULBM also requires just a single evaluation of the collision term per node, at every time step, however, the streaming and collision steps require averaging the values of f_i and Ω_i from all neighboring nodes, yielding $2(v+1)$ additions and multiplications per each discrete direction, where v is the valency of the node. In the meshes used in our simulations, the average valency $\langle v\rangle \approx 12$ (**Table 1**). Finally, lattice Boltzmann methods compute the full temporal evolution of the flow and, when applied to the problem of finding the steady-state flow with constant pressure boundary condition, it converges asymptotically to the solution. Consequently, in this particular application, it can be outperformed by implicit, finite-element Stokes solvers, which typically require fewer sparse matrix multiplications (due to a lower number of variables, and a higher convergence rate). However, implicit Stokes solvers are unsuitable for simulations of unsteady flows, such as: multiphase flows, turbulent flows, flows influenced by moving solid boundaries or by oscillating pressure differences, all of which do not pose a great difficulty for the LBM. Furthermore, the LBM's convergence rate could be improved by employing more refined open boundary conditions, for example by specifying the velocity profile at the inlet, and using Grad's approximation [31] at the outlet.

5. Concluding Remarks

The complex pore geometry of most porous media is a significant obstacle for efficient numerical simulation of flow. We have here discussed the unstructured lattice Boltzmann method for fluid flow. We have used the method on a couple of rock samples and have in the sample with a more complex geometry observed an anomalous dispersion of Lagrangian particles without any particle diffusion introduced. One sample with a less complex pore space showed no sign of anomalous dispersion. We further showed that in the more complex parts of the pore space, diffusive transport might dominate over advective transport and therefore the evacuation of a pollutant might be, from a resource point of view, more effective if cycles of flushing water through the sample are used. Further simulations however would be needed to establish the most efficient strategy for pollutant removal.

Funding

Provided through the grant *Earth Patterns* from the Villum Foundation and by the Innovation Fund Denmark and Maersk Oil and Gas A/S through the P^3 project. The Danish National Research Council (via Danscatt) provided support for the experimental work. AH acknowledges funding from the European Unions Seventh Framework Programme for research, technological development and demonstration under grant agreement no 316889. DM acknowledges funding from the People Programme (Marie Curie Actions) of the European Unions Seventh Framework Programme FP7/2007-2013/ under REA grant no 297921.

Acknowledgments

We thank B. Vinter and J. Avery for help with improving the performance of the ULBM implementation, and S. Pedersen, K. N. Dalby and H. Suhonen for help with the experimental work at beamline ID22 at the European Synchrotron (ESRF).

References

1. de Anna P, Le Borgne T, Dentz M, Tartakovsky AM, Bolster D, Davy P. Flow intermittency, dispersion, and correlated continuous time random alks in porous media. *Phys Rev Lett.* (2013) **110**:184502. doi: 10.1103/PhysRevLett.110.184502
2. Lester DR, Metcalfe G, Trefry MG. Is chaotic advection inherent to porous media flow? *Phys Rev Lett.* (2013) **111**:174101. doi: 10.1103/PhysRevLett.111.174101
3. Kang PK, de Anna P, Nunes JP, Bijeljic B, Blunt MJ, Juanes R. Pore-scale intermittent velocity structure underpinning anomalous transport through 3-D porous media. *Geophys Res Lett.* (2014) **41**:6184–90. doi: 10.1002/2014GL061475
4. Benson DA, Wheatcraft SW, Meerschaert MM. Application of a fractional advection-dispersion equation. *Water Res Res.* (2000) **36**:1403–12. doi: 10.1029/2000WR900031
5. Mordant N, Delour J, Léveque E, Arnéodo A, Pinton JF. Long Time correlations in lagrangian dynamics: a key to intermittency in turbulence. *Phys Rev Lett.* (2002) **89**:254502. doi: 10.1103/PhysRevLett.89.254502
6. Le Borgne T, Dentz M, Carrera J. Lagrangian statistical model for transport in highly heterogeneous velocity fields. *Phys Rev Lett.* (2008) **101**:090601. doi: 10.1103/PhysRevLett.101.090601

7. Le Borgne T, Dentz M, Carrera J. Spatial Markov processes for modeling Lagrangian particle dynamics in heterogeneous porous media. *Phys Rev E.* (2008) **78**:026308. doi: 10.1103/PhysRevE.78.026308
8. Lester DR, Metcalfe G, Trefry MG. Anomalous transport and chaotic advection in homogeneous porous media. *Phys Rev E.* (2014) **90**:063012. doi: 10.1103/PhysRevE.90.063012
9. Le Borgne T, Dentz M, Villermaux E. Stretching, coalescence, and mixing in porous media. *Phys Rev Lett.* (2013) **110**:204501. doi: 10.1103/PhysRevLett.110.204501
10. Misztal MK, Hernandez-Garcia A, Matin R, Sørensen HO, Mathiesen J. Detailed analysis of the lattice Boltzmann method on unstructured grids. *J Comput Phys.* (2015) **297**:316–39. doi: 10.1016/j.jcp.2015.05.019
11. Cloetens P, Ludwig W, Baruchel J, Van Dyck D, Van Landuyt J, Guigay J, et al. Holotomography: quantitative phase tomography with micrometer resolution using hard synchrotron radiation x rays. *Appl Phys Lett.* (1999) **75**:2912–4. doi: 10.1063/1.125225
12. Müter D, Sørensen H, Jha D, Harti R, Dalby K, Suhonen H, et al. Resolution dependence of petrophysical parameters derived from X-ray tomography of chalk. *Appl Phys Lett.* (2014) **105**:043108. doi: 10.1063/1.4891965
13. Jha D, Sørensen HO, Dobberschütz S, Feidenhans R, Stipp SLS. Adaptive center determination for effective suppression of ring artifacts in tomography images. *Appl Phys Lett.* (2014) **105**:143107. doi: 10.1063/1.4897441
14. Müter D, Pedersen S, Sørensen HO, Feidenhans'l R, Stipp SLS. Improved segmentation of X-ray tomography data from porous rocks using a dual filtering approach. *Comput Geosci.* (2012) **49**:131–9. doi: 10.1016/j.cageo.2012.06.024
15. Schneider CA, Rasband WS, Eliceiri KW. NIH Image to ImageJ: 25 years of image analysis. *Nat Meth.* (2012) **9**:671–5. doi: 10.1038/nmeth.2089
16. Si H. TetGen, a delaunay-based quality tetrahedral mesh generator. *ACM Trans Math Softw.* (2015) **41**:11:1–11:36. doi: 10.1145/2629697
17. Huang H, Wang L, Lu XY. Evaluation of three lattice Boltzmann models for multiphase flows in porous media. *Comput Math Appl.* (2011) **61**:3606–17. doi: 10.1016/j.camwa.2010.06.034
18. Pazdniakou A, Adler PM. Dynamic permeability of porous media by the lattice Boltzmann method. *Adv Water Res.* (2013) **62**, Pt B:292–302. doi: 10.1016/j.advwatres.2013.06.001
19. Pan C, Luo LS, Miller CT. An evaluation of lattice Boltzmann schemes for porous medium flow simulation. *Comput Fluids.* (2006) **35**:898–909. doi: 10.1016/j.compfluid.2005.03.008
20. Chang C, Liu CH, Lin CA. Boundary conditions for lattice boltzmann simulations with complex geometry flows. *Comput Math Appl.* (2009) **58**:940–9. doi: 10.1016/j.camwa.2009.02.016
21. Kang Q, Zhang D, Chen S. Simulation of dissolution and precipitation in porous media. *J Geophys Res.* (2003) **108**:2505. doi: 10.1029/2003jb002504
22. Bardow A, Karlin IV, Gusev AA. General characteristic-based algorithm for off-lattice Boltzmann simulations. *Europhys Lett.* (2006) **75**:434–40. doi: 10.1209/epl/i2006-10138-1
23. Zienkiewicz OC, Codina R. A general algorithm for compressible and incompressible flow–Part I. the split, characteristic-based scheme. *Int J Numer Meth Fluids.* (1995) **20**:869–85. doi: 10.1002/fld.1650200812
24. Rossi N, Ubertini S, Bella G, Succi S. Unstructured lattice Boltzmann method in three dimensions. *Int J Num Methods Fluids.* (2005) **49**:619–33. doi: 10.1002/fld.1018
25. Talon L, Bauer D, Gland N, Youssef S, Auradou H, Ginzburg I. Assessment of the two relaxation time Lattice-Boltzmann scheme to simulate Stokes flow in porous media. *Water Resour Res.* (2012) **48**:W04526. doi: 10.1029/2011WR011385
26. d'Humieres D, Ginzburg I, Krafczyk M, Lallemand P, Luo LS. Multiple-relaxation-time lattice boltzmann models in three dimensions. *Philos Trans Math Phys Eng Sci.* (2002) **360**:437–51. doi: 10.2307/3066323
27. Chikatamarla SS, Karlin IV. Entropic lattice Boltzmann method for turbulent flow simulations: Boundary conditions. *Phys A Statis Mech Appl.* (2013) **392**:1925–30. doi: 10.1016/j.physa.2012.12.034
28. Cardy J, Falkovich G, Gawedzki K, Nazarenko S, Zaboronski OV. *Non-equilibrium Statistical Mechanics and Turbulence.* Cambridge: Cambridge University Press (2008). doi: 10.1017/CBO9780511812149
29. Chen DJ, Lin KH, Lin CA. Immersed boundary method based lattice boltzmann method to simulate 2d and 3d complex geometry flows. *Int J Modern Phys C.* (2007) **18**:585–94. doi: 10.1142/S0129183107010826
30. Stiebler M, Tölke J, Krafczyk M. Advection-diffusion lattice Boltzmann scheme for hierarchical grids. *Comput Math Appl.* (2008) **55**:1576–84. doi: 10.1016/j.camwa.2007.08.024
31. Chikatamarla SS, Ansumali S, Karlin IV. Grad's approximation for missing data in lattice Boltzmann simulations. *Europhys Lett.* (2006) **74**:215. doi: 10.1209/epl/i2005-10535-x
32. Ayachit U. *The ParaView Guide: A Parallel Visualization Application.* Kitware (2015).

Conflict of Interest Statement: The authors declare that the research was conducted in the absence of any commercial or financial relationships that could be construed as a potential conflict of interest.

frontiers in Physics

ORIGINAL RESEARCH
published: 09 June 2015
doi: 10.3389/fphy.2015.00041

Compaction of granular material inside confined geometries

Benjy Marks[1,2]*, *Bjørnar Sandnes*[2], *Guillaume Dumazer*[1], *Jon A. Eriksen*[1,3] and *Knut J. Måløy*[1]

[1] Condensed Matter Physics, Department of Physics, University of Oslo, Oslo, Norway, [2] College of Engineering, Swansea University, Swansea, UK, [3] Centre National de la Recherche Scientifique, Institut de Physique du Globe de Strasbourg, University of Strasbourg/Ecole et Observatoire des Sciences de la Terre, Strasbourg, France

In both nature and engineering, loosely packed granular materials are often compacted inside confined geometries. Here, we explore such behavior in a quasi-two dimensional geometry, where parallel rigid walls provide the confinement. We use the discrete element method to investigate the stress distribution developed within the granular packing as a result of compaction due to the displacement of a rigid piston. We observe that the stress within the packing increases exponentially with the length of accumulated grains, and show an extension to current analytic models which fits the measured stress. The micromechanical behavior is studied for a range of system parameters, and the limitations of existing analytic models are described. In particular, we show the smallest sized systems which can be treated using existing models. Additionally, the effects of increasing piston rate, and variations of the initial packing fraction, are described.

Keywords: granular material, Janssen stress, boundary effects, confinement, deformable media, hele-shaw cell, discrete element method, micromechanics

OPEN ACCESS

Edited by:
Daniel Bonamy, Commissariat à l'Énergie Atomique et aux Énergies Alternatives, France

Reviewed by:
Eric Josef Ribeiro Parteli, University of Erlangen-Nuremberg, Germany
Ferenc Kun, University of Debrecen, Hungary

***Correspondence:**
Benjy Marks, Condensed Matter Physics, Department of Physics, University of Oslo, Sem Sælands Vei 24, Fysikkbygningen, Oslo 0371, Norway
benjy.marks@fys.uio.no

Specialty section:
This article was submitted to Interdisciplinary Physics, a section of the journal Frontiers in Physics

Received: *20 April 2015*
Accepted: *27 May 2015*
Published: *09 June 2015*

Citation:
Marks B, Sandnes B, Dumazer G, Eriksen JA and Måløy KJ (2015) Compaction of granular material inside confined geometries. Front. Phys. 3:41. doi: 10.3389/fphy.2015.00041

1. Introduction

When granular materials are placed in confined geometries, we often observe a significant portion of the stress being redirected toward the confining boundaries. This phenomenon has been systematically studied for many systems [1–3], most notably in silos, beginning with Janssen [4]. Force redirection has been attributed to the granular nature of the material, and has in many cases been shown to be well represented by a constant coefficient, known as the Janssen coefficient K, defined in one spatial dimension as

$$K = \sigma_r/\sigma_n,$$

where σ_r is the redirected stress due to some applied normal stress σ_n. Here we investigate the development of stresses within a granular packing, confined vertically between two horizontal plates, with no walls in the remaining directions, subjected to a rigid piston impacting it from one side. As the piston moves, granular material is compacted near the piston, and with increasing displacement of the piston, the size of the packing increases. Such an accumulation process is known to occur in the petroleum industry, where sand is liberated from the host rock during extraction, altering the underground morphology of cracks [5, 6]. This may also be relevant for understanding proppant flowback in propped fractures [7]. Additionally, this geometry is representative of a number of recent experimental studies in Hele-Shaw cells [8–11] where the validity of Janssen stress redirection has not been ascertained.

There are a number of interesting patterns which form when a granular material is displaced by a flexible interface in such a geometry [9, 11]. The nature of the patterns have been shown to depend on many factors, primarily the initial packing fraction and the rate of displacement [10]. For this reason, we here investigate the microstructural and mechanical evolution of such a system under these conditions. To reduce the complexity of the system, we consider only a rigid piston.

We are interested in systems which are highly confined. In common experiments with granular material inside Hele-Shaw cells, there are in general fewer than 20 grain diameters between the two Hele-Shaw plates, typically down to around 5 grain diameters [10]. As the confinement increases, i.e., as the gap spacing decreases, we expect a transition from three dimensional behavior toward a behavior governed by the boundaries, as demonstrated for vertical silos in Bratberg et al. [12]. It is then of interest to study the changes that result from increasing confinement. We expect that altering the confinement will affect the force redistribution. A transition may occur for extremely confined systems where such an assumption concerning force redirection may not be valid.

Existing analytic models for the micromechanics of such a system generally reduce the problem to one spatial dimension (x), assuming that variations in both remaining directions (y and z) are small, although recently curved interfaces have also been described [8]. For simplicity, we consider a flat interface, and validate the analytic description with a discrete element model.

Firstly, in Section 2 describe the numerical model that has been used to simulate this system. In Section 3, we establish continuum properties which correspond to the analytic formulation, and show comparisons between the two. In particular, the limitations of current analytic models are identified. Finally, a parameter set is proposed that best fits the analytic theories for a wide range of system variables.

2. Materials and Methods

This paper is an investigation into the micromechanics of a system which is highly constrained by external boundaries. For this reason, it is ideal to use a particle based method to model the behavior, as the total number of grains in the system is small. Toward this end, we use a conventional soft sphere discrete particle approach, implemented in the open source code MercuryDPM (www.mercurydpm.org) [13, 14]. The geometry considered here, shown in **Figure 1**, consists of a rigid piston, oriented in a space $r = \{x, y, z\}$, with normal along the x axis, which pushes particles between two rigid plates, separated by a spacing D and having normals in the $\pm z$ directions, with two periodic boundaries in the remaining perpendicular direction, y. The coordinate system moves with the piston, such that it is located at $x = 0$ at all times. As the piston moves horizontally at a velocity u toward the grains, its displacement at any time t is then $s = ut$.

We work in a system of non-dimensionalized units with the following properties; length and mass have been non-dimensionalized by the length d'_m and mass m'_m of the largest particle in the system, respectively, where the prime indicates that the quantity has dimension. The particle diameters, d, we use are therefore $d \leq 1$, with material density defined by $4\pi(1/2)^3\rho_p/3 = 1$, or $\rho_p = 6/\pi$. Time is non-dimensionalized by the time taken for the largest particle to fall from rest its own radius under the action of gravity, so that a unit time is $t = \sqrt{d_m/g}$, which requires that $g = 1$. Other values are non-dimensionalized by a combination of these three scales, for example stress is non-dimensionalized by $m'_m g'/d'^2_m$.

Particles are filled into the available space by assigning them to positions on a regular hexagonally close packed lattice, dimensioned such that particles of diameter 1 would be in contact. In all cases we use particles distributed uniformly in the range $0.5 \leq d \leq 1$ to avoid crystallization, and to mimic the size range used in Sandnes et al. [10]. Variable particle filling is

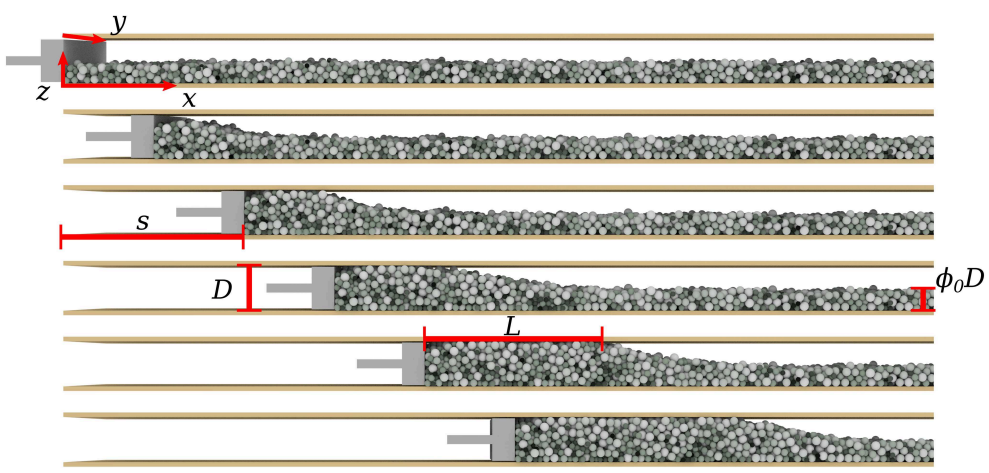

FIGURE 1 | Particle positions during a single test, shown at six piston displacements s. Top to bottom: $s = 0, 10, 20, 30, 40,$ and 50. Labels refer to the coordinate system x, y, and z, the gap height D, the plug length L and the initial packing fraction ϕ_0. Particles are colored by size, darker colors representing smaller particles.

facilitated by changing the number of layers of the grid, such that the initial packing fraction, ϕ_0 defined in Equation (3), is approximately constant throughout the cell. From $t = -10$ to $t = 0$, gravity in the $-z$ direction is increased from $g = 0$ to $g = 1$ to settle the grains in a loose packing. From $t = 0$ the piston begins to move at velocity u.

As shown in **Figure 2**, the particles' material properties are described by normal, tangential and rolling damped spring sliders [13, 15] with the properties contained in **Table 1**. These values have previously been calibrated to mimic 20 micron silica beads [16]. Here we neglect the role of adhesion between particles, which will become increasingly important as the physical size of the particles reduces. The walls are implemented such that they are rough; when a particle contacts a wall, the piston, or both, it is prohibited from rotating, i.e., $\mu_r = 1$. Otherwise, the interaction properties are the same as between two particles, except that the walls and piston are of infinite mass. We therefore have a well defined macroscopic sliding friction of $\mu = 0.4$ that does not depend on the rate of loading.

In the following Section we will firstly detail the important macroscopic quantities measured from a single simulation. We will then investigate the effect of three controlling parameters on the evolution of the system: the Hele-Shaw spacing D, the initial packing fraction ϕ_0 and the velocity of the piston, u. The piston

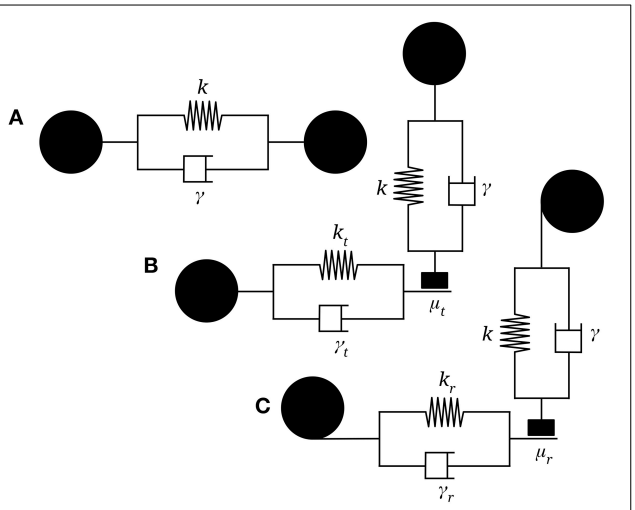

FIGURE 2 | Contact laws used in the discrete element model. Interactions are characterized by **(A)** normal, **(B)** tangential and **(C)** rolling laws, parameterized by stiffnesses k, k_t and k_r, viscous dissipation γ, γ_t and γ_r and friction coefficients μ_t and μ_r. Full details are given in Luding [15].

TABLE 1 | Material properties of the spheres.

Direction	Stiffness, k $\left(\frac{\text{kg/s}^2}{m'_m/(g'd'_m)}\right)$	Dissipation, γ $\left(\frac{\text{kg/s}}{m'_m/\sqrt{g'd'_m}}\right)$	Coefficient of friction, μ
Normal	1,00000	1000	–
Tangential	80,000	0	0.4
Rolling	80,000	0	10^{-3}

rate, however, is not *a priori* a governing quantity, so we choose to control the piston rate via the inertial number, I, which is defined as $I = \dot{\gamma} d_m/\sqrt{P/\rho_p}$, which is the ratio of inertial to imposed stresses, where P is a typical pressure and $\dot{\gamma}$ is a typical shear strain rate [17]. Taking $\dot{\gamma} = u/D$, and $P = \rho_p g D$, gives

$$I = \frac{u d_m}{D^{3/2} g^{1/2}} = u D^{-3/2}.$$

3. Results

As depicted in **Figure 1**, three distinct regions exist inside the system. These are termed the *plug zone*, where particles are densely packed near to the piston ($x \leq L$), the *undisturbed zone*, far from the plug, and the *transition zone*, where the plug is accumulating. To define these regions systematically, we must first measure the solid fraction, $\nu = V_s/V_t$, which is a local measure of the ratio of the volume of solids to the total volume. The solid fraction is coarse grained in one spatial dimension, x, as

$$\nu(x, t) = \frac{1}{WD} \sum_{i=1}^{N} V_i \mathcal{W}(x - x_i(t)), \tag{1}$$

where N is the number of grains in the system, W is the width of the system, V_i is the volume of the i-th grain, x_i its center of mass and $\mathcal{W}$ is the coarse graining function, chosen in this case to be a 1D normalized Gaussian function [14, 18]. Such a coarse graining method allows the coarse graining width to be defined, so that either the macro- or micro-structure is visible. We choose to use a coarse graining width equal to the maximum particle diameter, such that small scale variations are minimized, and smooth continuum fields are obtained [19]. All other continuum quantities are defined using the same coarse graining technique, presented in Goldhirsch [18], Weinhart et al. [14]. Using the definition (1), we denote the maximum solid fraction, ν_m, as an average over the solid fraction close to the wall at some time when the transition zone is far from the piston as

$$\nu_m = \frac{1}{5D} \int_{5D}^{10D} \nu(x)\, dx, \tag{2}$$

where in practice a numerical integration is done over the discrete coarse grained cells, and the limits of $5D$ and $10D$ are chosen arbitrarily. We define the normalized packing fraction, $\phi(x, t)$, as $\phi = \nu/\nu_m$, and note that in the absence of volumetric expansion or dilation of the granular material, ϕ is directly proportional to the height of the packing between the Hele-Shaw walls. The undisturbed zone is that which is maintained at the initial packing fraction ϕ_0, which is defined at time $t = 0$ as

$$\phi_0 = \frac{1}{5D} \int_{5D}^{10D} \phi(x, t = 0)\, dx.$$

To delineate the plug, transition and undisturbed zones, at each time t we use linear regression to find the best linear fit to the

points in the range $\phi = \phi_0 + 0.1$ to $\phi = 0.9$, such that $\phi D \approx b - x\tan\theta$, for some value of b and slope angle θ. Five examples of this are shown in **Figure 3A**. Using this best fit, we can define the point at which the plug zone meets the transition zone as the intersection of the best fit regression line and $\phi = 1$, such that $L = (b - D)/\tan\theta$, as shown in **Figure 3A**. The value of L grows monotonically with piston displacement, as shown in **Figure 3B**. Conservation of mass implies that on average, if there is no volumetric change in the packing, and no slip between the grains and the walls, this relationship can be expressed as

$$\frac{L}{s} = \frac{\phi_0}{1 - \phi_0}, \tag{3}$$

which is shown as the dashed line in **Figure 3B**. For all cases reported here, the value of θ does not appear to vary with increasing plug length L. The point at which the undisturbed zone meets the transition zone can then be defined in a similar manner as above, by the intersection of the best fit regression line with $\phi = \phi_0$. The coordination number, Z, (average number of contacts per particle), is fairly constant in the plug zone, (**Figure 3C**), increasing with compaction, as rearrangement occurs. Additionally, at large values of L the stresses are high enough to cause significant overlap of the particles (up to 1%). In the transition zone, significant particle rearrangement lowers the coordination number.

Coarse graining techniques in general cause measured fields to converge toward zero near boundaries [14]. While it is feasible to reconstruct these fields in general near individual boundaries, near the piston we have three distinct boundaries which all interact. To access stresses in this region, it is then preferable to directly measure the forces applied to the rigid boundaries of the system. Toward this end, we denote σ_n^p as the normal stress measured at the piston. This is shown as a function of piston displacement in **Figure 3D**. The stresses measured from coarse graining within the packing are shown in **Figure 3E**. In both cases, the stresses grow exponentially both with increasing

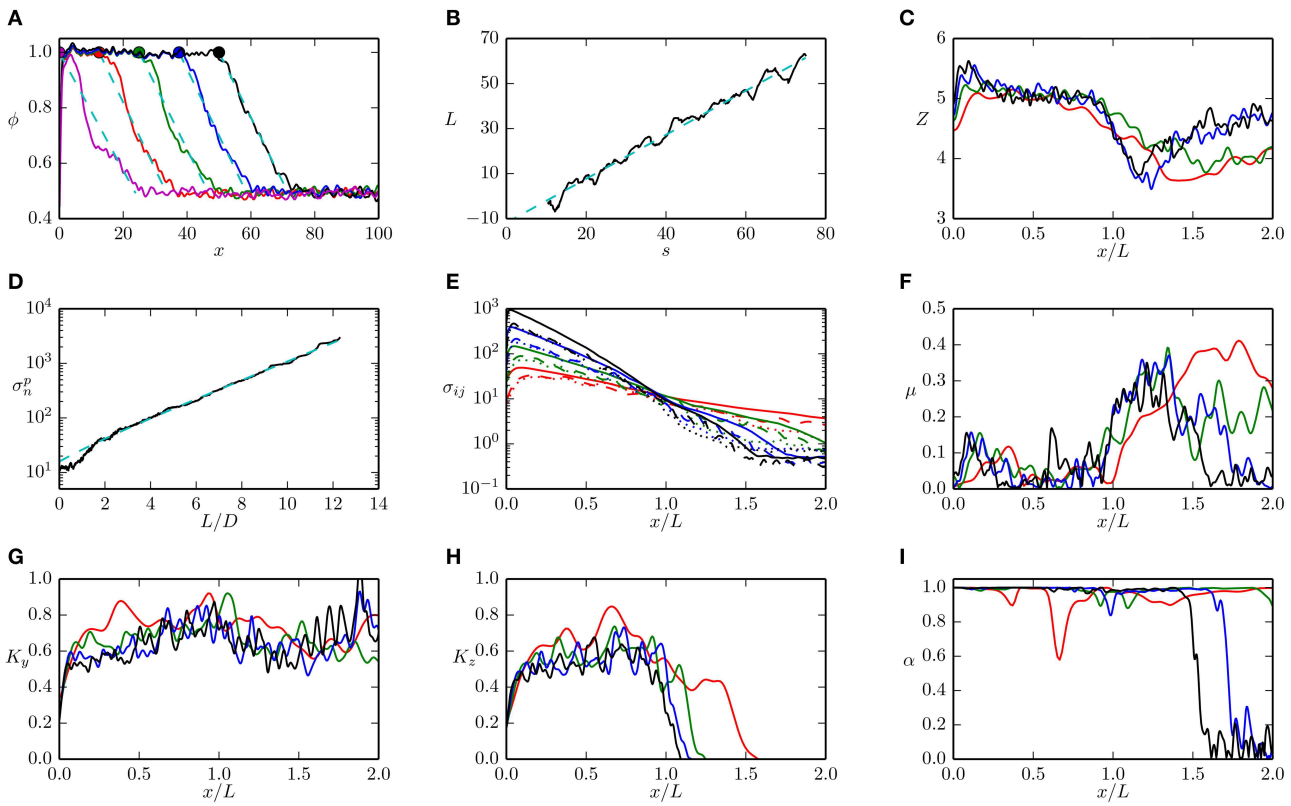

FIGURE 3 | Evolution of coarse grained properties of the system with increasing piston displacement, s, for $D = 5$, $\phi_0 = 0.5$ and $I = 0.01$. (A) Five examples of the normalized packing fraction of the particles, ϕ. The magenta, red, green, blue, and black lines indicate displacements which correspond to $L = 0, 12.5, 25, 37.5$, and 50 respectively. The same color scheme is used for each subsequent plot in this Figure unless stated otherwise. A filled circle indicates the measured value of L, and the cyan dashed line indicates the linear best fit measurement of the transition zone. **(B)** Evolution of the measured value of L with increasing displacement s drawn in black. The cyan line indicates the best linear fit to these points. **(C)** The coordination number, Z, as a function of normalized distance from the piston head, x/L. **(D)** Normal stress measured at the piston is shown in black. The cyan dashed line indicates the best fit estimate of Equation (6). **(E)** Normal stress distributions within the packing. Solid lines indicate σ_{xx}, dashed σ_{yy} and dotted σ_{zz}. **(F)** Apparent friction coefficient measured within the packing, $\mu = |\sigma_{xz}|/\sigma_{zz}$. **(G)** Out of plane Janssen coefficient measured within the packing, $K_y = \sigma_{yy}/\sigma_{xx}$. **(H)** In plane vertical Janssen coefficient measured within the packing, $K_z = (\sigma_{zz} - \rho_p v g D/2)/\sigma_{xx}$. **(I)** Absolute value of the x component of the eigenvector of the major principal stress.

L and decreasing x, as shown by the linearity in a semilog space in **Figures 3D,E**.

An analytic expression to describe this stress evolution was first derived in Knudsen et al. [9], assuming that: (a) the stress redirection in the z direction is described by a constant $K_z = \sigma'_{zz}/\sigma_{xx}$, where $\sigma'_{zz} = \sigma_{zz} - D\rho_p v_m g/2$ is the component of the vertical stress not due to gravity and (b) friction at the side walls is $\mu = \sigma_{xy}/\sigma_{zz}$. It can be shown using force balance in the x direction that under these conditions, if there is no net acceleration,

$$\frac{d\sigma_{xx}}{dx} = -\frac{2\mu K_z}{D}\sigma_{xx} - \mu\rho_p v_m g.$$

By further assuming that the stress at $x = L$ is a constant, i.e., $\sigma_T \equiv \sigma_{xx}(x = L)$,

$$\sigma_{xx} = \left(\sigma_T + \frac{D\rho_p v_m g}{2K_z}\right) e^{2\mu K_z(L-x)/D} - \frac{D\rho_p v_m g}{2K_z}. \quad (4)$$

Previously, the threshold stress σ_T has been modeled as either estimated from experimental data [8], or as a constant by assuming sliding of a wedge of material [9, 11]. Here, we choose to model the threshold stress σ_T as a ϕ_0 dependent quantity by considering limit equilibrium of a wedge of material being displaced into the undisturbed zone, as shown in **Figure 4**. We assume a noncohesive Coulomb failure of the material internally, along a failure plane parallel to and meeting the surface of the transition zone. We additionally assume that the internal friction angle is also defined by μ. Limit equilibrium in the x direction can then be expressed using the notation defined in **Figure 4** as $F_x = T_b + T_i \cos\theta$, where $F_x = D\sigma_T$, $T_b = \mu W_0 = \mu D^2 \rho_p v_m g/(2\tan\theta)$ and $T_i = \mu W_1 \cos\theta = \mu D^2 \rho_p v_m g \phi_0^2 \cos\theta/(2\tan\theta)$ per unit length in the y direction. After some rearrangement this implies that

$$\sigma_T = \frac{\mu D \rho_p v_m g}{2\tan\theta}(1 + \phi_0^2 \cos^2\theta). \quad (5)$$

This assumption of the failure surface introduces no new parameters into the model, and as will be shown in the following, closely predicts the measured value of σ_T for a large range of system parameters. In the limit where $\phi_0 \to 0$, this definition reduces to that used in Knudsen et al. [9] and Sandnes et al. [11]. Including this new definition of the threshold stress, Equation (5), in Equation (4) gives

$$\sigma_{xx} = \frac{D\rho_p v_m g}{2K_z}\left(\left(\frac{\mu K_z}{\tan\theta}(1 + \phi_0^2\cos^2\theta) + 1\right)e^{2\mu K_z(L-x)/D} - 1\right). \quad (6)$$

A best fit estimate is used to find K_z from Equation (6), and is shown as the dashed line in **Figure 3D** at $x = 0$, using the measured values of v_m, θ and ϕ_0, which adequately captures the behavior of the system past $L/D = 2$. Before this limit, stress redistribution has not saturated, and σ_{xx} is less than the predicted value. We find the same transition value of $L/D \approx 2$ for all cases reported here.

The measured value of apparent friction $\mu = \sigma_{xz}/\sigma_{zz}$ inside the packing, shown in **Figure 3F** shows that the system is far from failure inside the plug zone, and increasingly unstable in the transition zone. The out of plane Janssen coefficient, $K_y = \sigma_{yy}/\sigma_{xx}$, shown in **Figure 3G**, has large variations in x, but is not significantly affected by the formation of the plug. The in plane Janssen coefficient (**Figure 3H**), $K_z = \sigma'_{zz}/\sigma_{xx}$, however, is strongly influenced by the formation of the plug, and is relatively constant with increasing L inside the plug zone.

An underlying assumption of the Janssen stress redistribution is that when averaging over the width of the system (here in the y and z directions), the principal stress directions are parallel to the system geometry [4]. For this reason we measure α, the absolute value of the x component of the eigenvector of the major principal stress, which is shown in **Figure 3I**. When $\alpha \approx 1$ the major principal stress points along the x-axis, and when $\alpha \approx 0$, the principal stress lies in the yz plane. For $x \leq L$ we find that the major principal stress is collinear with the system geometry, and the Janssen stress model fits well. In a traditional silo problem, gravity acts parallel to the applied stress, and averaging across the width of a silo ensures the validity of this assumption. For this case, however, because the direction of gravity has broken the inherent symmetry of the silo problem, its validity is not ensured [20]. We do, however, find that this assumption holds well for this and all simulations reported here.

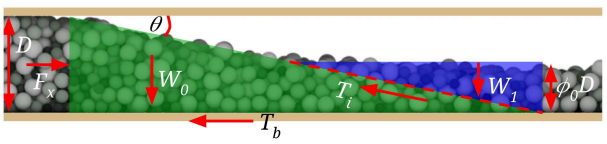

FIGURE 4 | Limit equilibrium of the transition zone. For the pile to be displaced by a force F_x, two forces must be overcome; T_b, the basal traction due to the weight W_0 of the green region, and the x component of the internal sliding traction T_i along the assumed failure surface denoted by the dashed line, due to the normal component of the weight above the failure surface, W_1, of the blue region.

3.1. Gap spacing

As motivated in Equation (6), the gap spacing D largely controls the magnitude of the stresses within the system. For this reason, we here vary this spacing systematically from $D = 1$ to $D = 15$, while maintaining $\phi_0 = 0.5 \pm 0.05$ and $I = 0.01$ (except for the case of $D = 1$, where $\phi_0 \approx 0.66$), as depicted for four values of D in **Figure 5**. To make a reasonable comparison between these simulations, in each case the area of the piston is kept constant, such that its area is $WD = 100$. Select measures of the behavior of the system are shown in **Figure 6**. Slope angles, θ, are averaged over the times corresponding to $2D \leq L \leq 10D$, whilst K and σ_T are averaged temporally over values in the range $2D \leq L \leq 10D$, where at each time we measure spatially in the range $L/4 \leq x \leq 3L/4$. In **Figures 6A,B**, we observe increasing solid fraction in the plug, v_m, and slope angle, θ, with increasing gap spacing, as the effect of the boundaries on the system decreases.

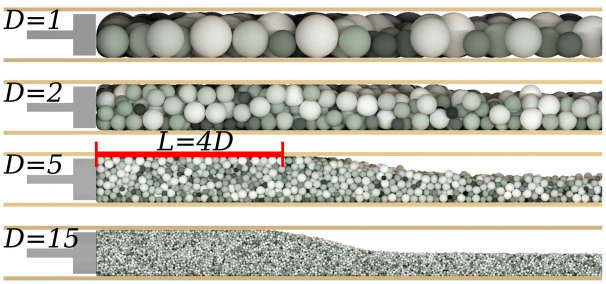

FIGURE 5 | Particle positions for four simulations with varying gap spacing. Top to bottom: $D = 1, 2, 5$, and 15. For all cases, $\phi_0 \approx 0.5$, $I = 0.01$ and the simulation is displayed at the time corresponding to $L = 4D$. Particles are colored by size, darker colors representing smaller particles.

For each simulation, the measured normal stress at the piston, σ_n^p, is fitted with Equation (6), and a best fit estimate of K_z is shown as crosses, with the standard deviation of the error of the regression used as error bars, in **Figure 6C**. The mean and standard deviation of the measured values of K_z and K_y from the continuum data between $L = 2D$ and $L = 10D$ are shown as dots and triangles, respectively. For $D \geq 2$ we find that both the measured values of K_z and K_y are independent of D, and have mean values of $K_y = 0.67 \pm 0.04$ and $K_z = 0.58 \pm 0.05$. Best fit estimates of K_z are also independent of D, with mean values of $K_z = 0.56 \pm 0.07$. **Figure 6D** shows the mean of σ_T also from $L = 2$ to $L = 10$. Triangles represent the prediction from Equation (5) using the measured values of ν_m, θ and ϕ_0. In all cases, we find the measured and fitted values of K_z to be in agreement, whereas the values of σ_T agree only with $D \geq 3$. We note, however, that σ_T depends strongly on θ, and we have as yet no means for predicting this quantity. The dependence of σ_T on θ is in contrast to studies on fold and thrust belts [21], where there is no confinement vertically above the material.

3.2. Initial Packing Fraction

Existing models [8, 9] for the evolution of the stresses in similar geometries have neglected any effect of the initial packing fraction ϕ_0. To test this assumption, we here vary ϕ_0 from 0.1 to 0.6, while maintaining $D = 5$ and $I = 0.01$. As shown in **Figures 7A,B**, the packing fraction inside the plug and the slope of the transition zone are independent of the initial packing fraction. In **Figure 7C**, we observe that the measured and best fit values of K_z are in agreement for a wide range of ϕ_0, and that these values are lower than the measured values of K_y. The prediction of threshold stress from Equation (5), which includes a dependence on ϕ_0, slightly under-predicts the threshold stress at $\phi_0 = 0.1$. Nevertheless, both the measured and predicted values of the threshold stress in **Figure 7D** are in agreement with observations from Eriksen et al. [8], where a non-dimensional threshold stress of $\sigma_T = 10.7$ was found to reproduce the observed pattern formation behavior in the quasi-static limit, at $D = 5$, for a range of values of $\phi_0 \leq 0.5$.

3.3. Inertial Number

Finally, we wish to comment on inertial effects in such a system. Toward this end we systematically vary the inertial number I from 10^{-2} to 10 while maintaining $D = 5$ and $\phi_0 = 0.5 \pm 0.05$. As shown in **Figure 8**, a transition occurs at $I \approx 0.1$, where the quasistatic behavior begins to be dominated by inertial effects, and the system is fluidized. In **Figure 8A**, we notice a jump in the maximum solid fraction, as the particles begin to flow and rearrange due to the increased piston velocity. This is accompanied by an increase in the slope angle θ (**Figure 8B**), and a decrease in the accumulation rate (**Figure 8C**, as the grains begin to slip relative to the walls. With increasing piston velocity, the anisotropy of the system is lost, as shown in **Figure 8D**, and both K_y and K_z tend toward a mean value of 0.56 ± 0.02 for $I \geq 1$. As shown in **Figure 8E**, the threshold stress, σ_T, also diverges above $I = 0.1$ away from the theoretical prediction. For values of $I \geq 0.1$, we have therefore used the measured value of σ_T in the best fit estimation of K_z shown in **Figure 8D**, rather than the value predicted from Equation (5), as used in all other cases.

4. Conclusions

We have here described a large number of simulations of granular materials which have been compacted in a confined geometry. For all cases, we observed that the stress distribution within the packing is well approximated by previous models, once a more rigorous definition of the threshold stress is used. This is true for a wide range of gap spacings, initial filling fractions and piston rates.

In this study we have used a rough boundary condition, where macroscopic friction at the piston and walls is equal to the inter-particle friction. However, in many systems we expect the roughness at the boundaries to be lower than that between particles. It is unclear how this difference will affect either the accumulation of material near the piston head, or the stress distribution within the packing.

Below a gap spacing of 3 particle diameters, the stress distribution is not well represented by this model. We conclude that $D = 3$ represents the smallest system size which may reasonably be described by the one dimensional Janssen stress model. In addition, at inertial numbers of $I \geq 0.1$, we find that there is significant slip at the boundary, and the threshold stress diverges from the model prediction. In all cases, we cannot as yet predict the slope of the free surface in the transition zone, but we observe that this slope approaches the angle of repose for large systems at low piston rates. Janssen stress coefficients for this system are well represented by $K_z = 0.6 \pm 0.1$ and $K_y = 0.7 \pm 0.1$ for a wide range of system parameters. A model for the threshold stress has been presented using limit equilibrium, and this holds well for systems with $D \geq 3$ and $I < 0.1$.

The slope angle, θ, has been measured for different system parameters to lie in the range of 2°–18°. *A priori*, we could only assume that this angle must be smaller than or equal to the angle of repose, which for these grains is approximately 20°. The wide variability of θ is as yet unexplained, and is in contrast to the case where a top boundary does not exist, for example in fold and thrust belts [21], bulldozing [22] and additive manufacturing using loose powders [23]. We do note, however, that at large values of D the slope angle approaches the angle of repose.

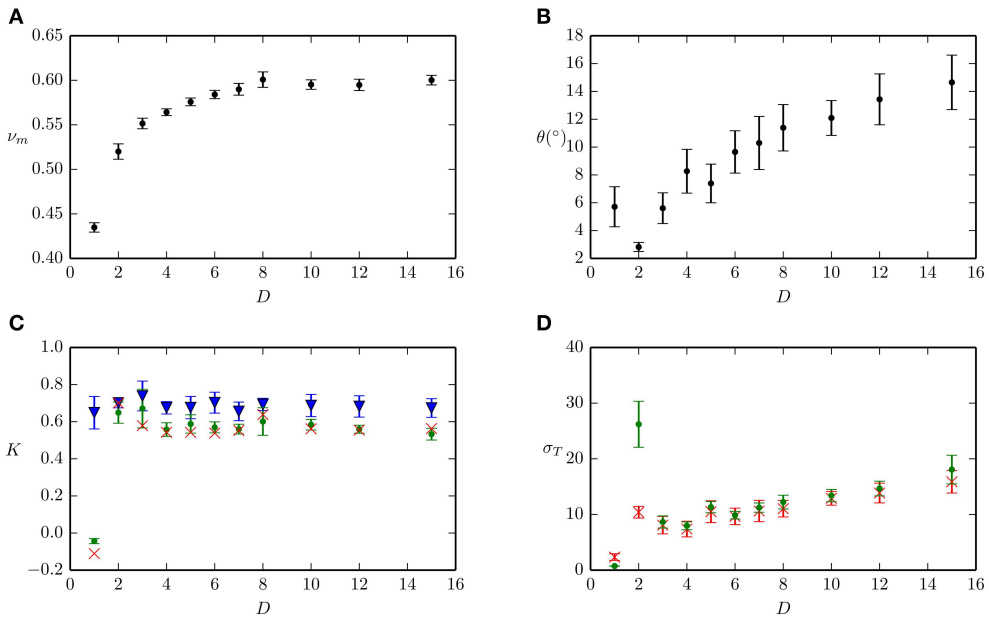

FIGURE 6 | Descriptors of the system with varying gap spacing *D*. Error bars in each plot represent one standard deviation of the measured value. **(A)** Average solid fraction within the plug zone, ν_m. **(B)** Slope of the pile in the transition zone, θ. **(C)** Crosses represent best fit value of K_Z from measurement of the stress on the piston head, σ_n^p using Equation (6). K_Z and K_y, represented by dots and triangles respectively, are calculated directly from the coarse grained granular packing. **(D)** Threshold stress σ_T. Dots represent the mean value of the coarse grained continuum field σ_{xx} at $x = L$, and crosses represent predicted values from Equation (5) using measured values of ν_m, θ and ϕ_0.

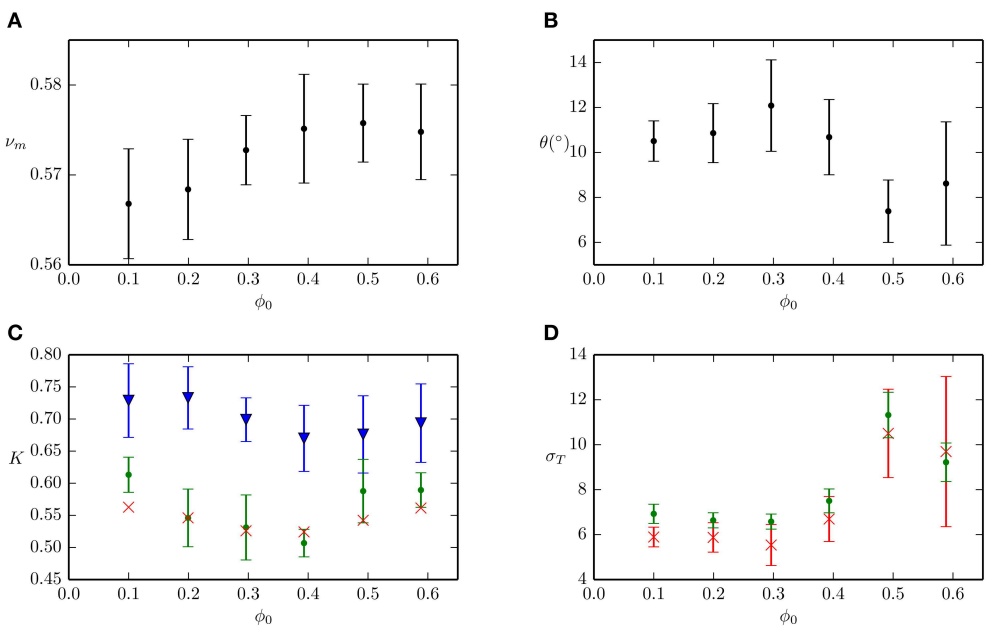

FIGURE 7 | Descriptors of the system with varying initial packing fraction ϕ_0. Error bars in each plot represent one standard deviation of the measured value. **(A)** Average solid fraction within the plug zone, ν_m. **(B)** Slope of the pile in the transition zone, θ. **(C)** Crosses represent best fit value of K_Z from measurement of the stress on the piston head, σ_n^p using Equation (6). K_Z and K_y, represented by dots and triangles respectively, are calculated directly from the coarse grained granular packing. **(D)** Threshold stress σ_T. Dots represent the mean value of the coarse grained continuum field σ_{xx} at $x = L$, and crosses represent predicted values from Equation (5) using measured values of ν_m, θ and ϕ_0.

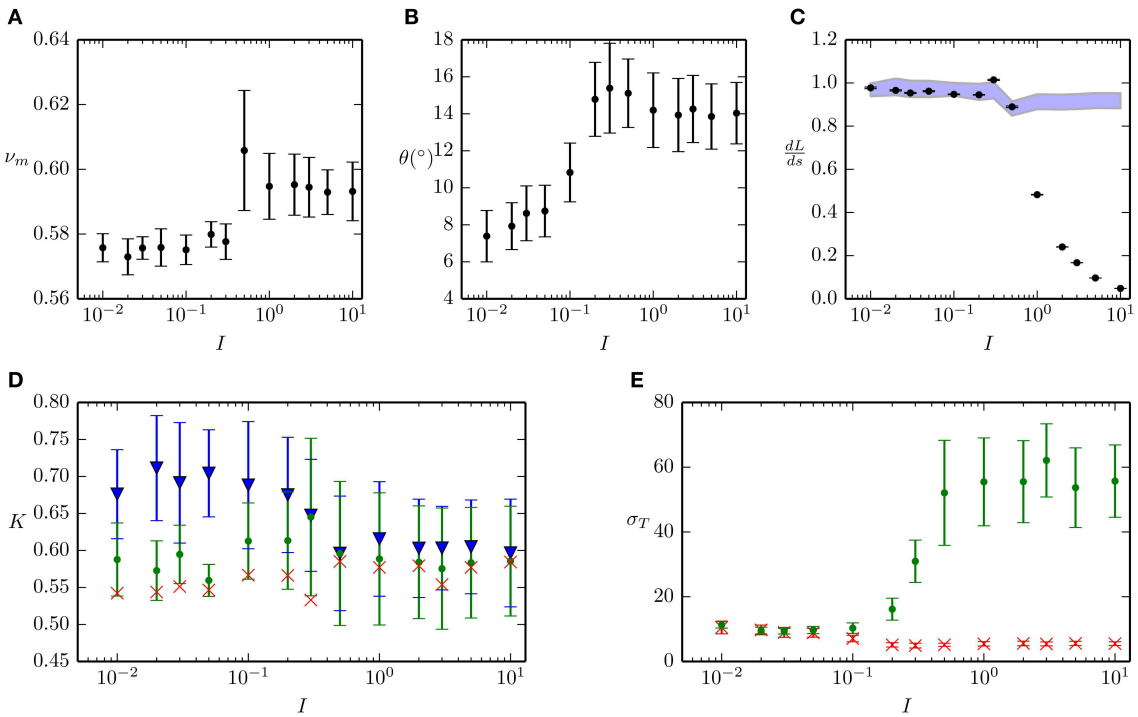

FIGURE 8 | Descriptors of the system with varying inertial number *I*. Error bars in each plot represent one standard deviation of the measured value. **(A)** Average solid fraction within the plug zone, ν_m. **(B)** Slope of the pile in the transition zone, θ. **(C)** Slope of the best fit value of $L(s)$ denoted by black dots against prediction using incompressibilty shown as the shaded region, which denotes ± one standard deviation around the mean value for each case. **(D)** Crosses represent best fit value of K_z from measurement of the stress on the piston head, σ_n^p using Equation (6). K_z and K_y, represented by dots and triangles respectively, are calculated directly from the coarse grained granular packing. **(E)** Threshold stress σ_T. Dots represent the mean value of the coarse grained continuum field σ_{xx} at $x = L$, and crosses represent predicted values from Equation (5) using measured values of ν_m, θ and ϕ_0.

With regards to the two Janssen parameters, we can clearly distinguish the values of K_y and K_z in **Figures 6C**, **7C**, **8D**, for $I < 0.1$. The reason for the difference between these two quantities may either be due to anisotropy in the granular packing, or due to the differing boundaries in the y and z directions. As the Janssen parameters are relatively insensitive to the gap spacing D, we conclude that this anisotropy is due to the accumulation process, which creates a preferential direction within the packing. This distinction is important when considering models which account for more complex geometries, such as in Eriksen et al. [8]. For industrial applications, such as propped fractures or sand production, the stresses within a plug of grains in a horizontal crack are expected to be a function not only of the relative size of the grains to the crack width, but also the rate of accumulation of the grains.

Author Contributions

BM conducted the simulations, post-processing and authored the paper. BS conceived the idea for the simulations. BS, GD, JE, and KM assisted with the interpretation and analysis of the simulations, and editing of the manuscript.

Acknowledgment

The authors would like to acknowledge grants 213462/F20 and 200041/S60 from the NFR.

References

1. Bräuer K, Pfitzner M, Krimer DO, Mayer M, Jiang Y, Liu M. Granular elasticity: stress distributions in silos and under point loads. *Phys Rev E* (2006) **74**:061311. doi: 10.1103/PhysRevE.74.061311
2. Landry JW, Grest GS, Silbert LE, Plimpton SJ. Confined granular packings: structure, stress, and forces. *Phys Rev E* (2003) **67**:041303. doi: 10.1103/PhysRevE.67.041303
3. Sperl M. Experiments on corn pressure in silo cells–translation and comment of Janssen's paper from 1895. *Granular Matter* (2006) **8**:59–65. doi: 10.1007/s10035-005-0224-z
4. Janssen HA. Versuche über getreidedruck in silozellen. *Zeitschr d Vereines Deutscher Ingenieure* (1895) **39**:1045–9.
5. Tronvoll J, Fjaer E. Experimental study of sand production from perforation cavities. *Int J Rock Mech Mining Sci Geomech Abstr.* (1994) **31**:393–410. doi: 10.1016/0148-9062(94)90144-9

6. Veeken CAM, Davies DR, Kenter CJ, Kooijman AP. Sand production prediction review: developing an integrated approach. In: *SPE Annual Technical Conference and Exhibition. Society of Petroleum Engineers*. Dallas, TX, (1991). p. 335–46.
7. Milton-Tayler D, Stephenson C, Asgian MI. Factors affecting the stability of proppant in propped fractures: results of a laboratory study. In: *SPE Annual Technical Conference and Exhibition. Society of Petroleum Engineers*. Dallas, TX, (1992). p. 569–79.
8. Eriksen JA, Marks B, Sandnes B, Toussaint R. Bubbles breaking the wall: two-dimensional stress and stability analysis. Phys. Rev. E. (2015) **91**:052204. doi: 10.1103/PhysRevE.91.052204
9. Knudsen HA, Sandnes B, Flekkøy EG, Måløy KJ. Granular labyrinth structures in confined geometries. *Phys Rev E.* (2008) **77**:021301. doi: 10.1103/PhysRevE.77.021301
10. Sandnes B, Flekkøy EG, Knudsen HA, Måløy KJ, See H. Patterns and flow in frictional fluid dynamics. *Nat Commun.* (2011) **2**:288. doi: 10.1038/ncomms1289
11. Sandnes B, Knudsen HA, Måløy KJ, Flekkøy EG. Labyrinth patterns in confined granular-fluid systems. *Phys Rev Lett.* (2007) **99**:038001. doi: 10.1103/PhysRevLett.99.038001
12. Bratberg I, Måløy KJ, Hansen A. Validity of the Janssen law in narrow granular columns. *Eur Phys J E* (2005) **18**:245–52. doi: 10.1140/epje/e2005-00030-1
13. Thornton AR, Weinhart T, Luding S, Bokhove O. Modeling of particle size segregation: calibration using the discrete particle method. *Int J Modern Phys C* (2012) **23**:1240014. doi: 10.1142/S0129183112400141
14. Weinhart T, Thornton AR, Luding S, Bokhove O. From discrete particles to continuum fields near a boundary. *Granular Matter.* (2012) **14**:289–94. doi: 10.1007/s10035-012-0317-4
15. Luding S. Cohesive, frictional powders: contact models for tension. *Granular Matter* (2008) **10**:235–46. doi: 10.1007/s10035-008-0099-x
16. Fuchs R, Weinhart T, Meyer J, Zhuang H, Staedler T, Jiang X, et al. Rolling, sliding and torsion of micron-sized silica particles: experimental, numerical and theoretical analysis. *Granular Matter* (2014) **16**:281–97. doi: 10.1007/s10035-014-0481-9
17. GDR MiDia. On dense granular flows. *Eur Phys J E* (2004) **14**:341–65. doi: 10.1140/epje/i2003-10153-0
18. Goldhirsch I. Stress, stress asymmetry and couple stress: from discrete particles to continuous fields. *Granular Matter* (2010) **12**:239–52. doi: 10.1007/s10035-010-0181-z
19. Weinhart T, Hartkamp R, Thornton AR, Luding S. Coarse-grained local and objective continuum description of three-dimensional granular flows down an inclined surface. *Phys Fluids* (2013) **25**:070605. doi: 10.1063/1.4812809
20. Nedderman RM. *Statics and Kinematics of Granular Materials.* Cambridge: Cambridge University Press (2005).
21. Davis D, Suppe J, Dahlen FA. Mechanics of fold-and-thrust belts and accretionary wedges. *J Geophys Res.* (1983) **88**:1153–72. doi: 10.1029/JB088iB02p01153
22. Sauret A, Balmforth NJ, Caulfield CP, McElwaine JN. Bulldozing of granular material. *J Fluid Mech.* (2014) **748**:143–74. doi: 10.1017/jfm.2014.181
23. Parteli EJR. DEM simulation of particles of complex shapes using the multisphere method: application for additive manufacturing. *AIP Conf Proc.* (2013) **1542**:185–8. doi: 10.1063/1.4811898

Conflict of Interest Statement: The authors declare that the research was conducted in the absence of any commercial or financial relationships that could be construed as a potential conflict of interest.

frontiers in Physics

ORIGINAL RESEARCH
published: 09 September 2015
doi: 10.3389/fphy.2015.00074

Zebra pattern in rocks as a function of grain growth affected by second-phase particles

Ulrich Kelka, Daniel Koehn and Nicolas Beaudoin*

School of Geographical and Earth Sciences, University of Glasgow, Glasgow, UK

Alternating fine grained dark and coarse grained light layers in rocks are often termed zebra patterns and are found worldwide. The crystals in the different bands have an almost identical chemical composition, however second-phase particles (e.g., fluid filled pores or a second mineral phase) are concentrated in the dark layers. Even though this pattern is very common and has been studied widely, the initial stage of the pattern formation remains controversial. In this communication we present a simple microdynamic model which can explain the beginning of the zebra pattern formation. The two dimensional model consists of two main processes, mineral replacement along a reaction front, and grain boundary migration affected by impurities. In the numerical model we assume that an initial distribution of second-phase particles is present due to sedimentary layering. The reaction front percolates the model and redistributes second-phase particles by shifting them until the front is saturated and drops the particles again. This produces and enhances initial layering. Grain growth is hindered in layers with high second-phase particle concentrations whereas layers with low concentrations coarsen. Due to the grain growth activity in layers with low second-phase particle concentrations these impurities are collected at grain boundaries and the crystals become very clean. Therefore, the white layers in the pattern contain large grains with low concentration of second-phase particles, whereas the dark layers contain small grains with a large second-phase particle concentration. The presence of the zebra pattern is characteristic for regions containing Pb-Zn mineralization. Therefore, the origin of the structure is presumably related to the mineralization process and might be used as a marker for ore exploration. A complete understanding of the formation of this pattern will contribute to a more accurate understanding of hydrothermal systems that build up economic mineralization.

Keywords: banding, dolomitization, grain growth, second-phase particles, zebra dolomite, zener drag

OPEN ACCESS

Edited by:
Wei-Xing Zhou,
East China University of Science and Technology, China

Reviewed by:
Eric Josef Ribeiro Parteli,
University of Erlangen-Nuremberg, Germany
Veerle Vandeginste,
Imperial College London, UK

****Correspondence:***
Ulrich Kelka,
School of Geographical and Earth Sciences, University of Glasgow, Gregory Building, Lilybank Gardens, Glasgow, G12 8QQ Scotland, UK
ulrich.kelka@glasgow.ac.uk

Specialty section:
This article was submitted to Interdisciplinary Physics, a section of the journal Frontiers in Physics

Received: *30 May 2015*
Accepted: *24 August 2015*
Published: *09 September 2015*

Citation:
Kelka U, Koehn D and Beaudoin N (2015) Zebra pattern in rocks as a function of grain growth affected by second-phase particles. Front. Phys. 3:74. doi: 10.3389/fphy.2015.00074

1. Introduction

The zebra texture is a periodic pattern which is encountered worldwide in geological formations and is often associated with hydrothermal mineralization. Zebra banding occurs in claystones [1], siderite ores [2, 3], and sphalerite mineralization [4]. The process of the zebra pattern formation varies depending on the rock hosting this structure. Here we focus on the origin of zebra banding occurring in dolostones that is often found in the vicinity of Pb-Zn mineralization. The banding

consists of alternating dark and light layers which are built up by a single mineral phase, namely dolomite. Despite the color the only macroscopically recognizable difference is the grain size, which can differ by several orders of magnitude between the coarse grained light and the fine grained dark regions. The pattern appears very symmetric and the layers comprise of monotonic thickness and spacing at the local scale (**Figure 1**). On a microscale other differences become visible between the dark and the light regions (**Figure 1**). The fine grained areas are always accompanied by a high density of opaque second-phase material. Furthermore, the crystals in the fine grained layers exhibit lobate grain boundaries whereas the grain boundaries in the light regions display a more polygonal geometry. The overall structure of the coarse grained layers is very similar to the type of veins or crack fillings where the crystals grow toward the central part of the opening and thus form a median line.

In order to be able to compare the outcome of our numerical simulations with natural specimens, representative samples on which analytical analysis can be performed were collected at the San Vicente mine in Central Peru. This location is a good general example of an ore deposit where numerous of the described zebra textures occur with a high diversity of layer spacing and thickness. The San Vicente mine is a case example of an ore deposit with many typical characteristics of hydrothermal Pb-Zn mineralization which is associated with the zebra textures where ore occurs along and within the bands [5]. The San Vicente mine is hosted in dolomitized platform carbonates in basin flanks in a foreland thrust belt in front of the Andean mountains with larger ore bodies bound to specific lithological units.

Different theories about the origin of the zebra textures in dolostones have been formulated. It is widely accepted that the formation of the structure consists of several phases of which the dark fine grained dolomite is the first one. This first phase represents the replacement of the initial limestone by dolomite [5–15]. What exactly triggers the development of the subsequent phases, which build up the coarse grained regions and are responsible for the final appearance of the pattern, is still a point of debate.

A selection of existing models will be presented in this paragraph. Zebra dolomites occurring in Northern Canada can be related to pre-existing structures in the initial limestone [14]. Prior to the dolomitization the limestone comprised of rhythmic sedimentary structures with a higher porosity/permeability. During the replacement of the limestone by dolomite the fluid flow was focused in these high permeability zones leading to higher dissolution and dolomitization rates and the formation of layers. Studies carried out on zebra dolomites in Belgium, Spain and Canada concluded that the pattern evolved during fracturing due to tectonic stress [8, 9] or hydrofracturing during the pulsed influx of dolomitizing brines [12, 13, 15]. The light coarse grained dolomite bands are interpreted as being at least partly void filling cements which precipitated into extensional fractures [12]. Based on the high symmetry of the banding it has been stated that the process which leads to the formation of the zebra texture has to involve self-organization [7, 10, 11]. The pattern of the zebra dolomite is found to be much too cyclic to be related solely to pre-existing sedimentary features [7]. The concept of self-organization can produce symmetric or rhythmic patterns out of an initially unordered system. An example of such a self-organizing process which produces equidistant concentric banding are the Ostwald-Liesegang rings which evolve during a reaction-diffusion process [16]. The necessary conditions for self-organization processes were found to be present in rocks hosting the zebra patterns [7]. The rhythmic pattern may evolve during dolomitization due to cyclic dissolution/precipitation processes focused in the white layers [7]. Another self-organizing concept which may explain the monotonic thickness and equidistant occurrence of the zebra patterns was introduced by Merino et al. [10] and Merino et al. [11]. In this model the crystals in the light layers displace the host rock during growth (displacive vein growth). The growth of this second dolomite phase not only pushes away the primary dolomite in the dark bands, but

FIGURE 1 | Examples of zebra textures at different scales. The left picture shows an outcrop in the area of the San Vicente mine. On the right side a hand specimen and two thin sections are shown. The area of the displayed thin sections is 1 cm^2 which is equivalent to the area of the simulation. The two micrographs show zebra banding with different spacing between the dark and the light layers.

also induces a stress field around the light layers. This stress field, which arises from the crystallization stress, is thought to prevent the growth of new material in the direct vicinity [11]. A more general model for the development of banded structures in rocks is the crystal zoning model [3]. In this model a phase transition front collects impurities during its propagation. If a critical value of collected material is reached, the front switches from collecting to releasing particles. This approach can generate a periodic layered distribution of impurities similar to mud bands in snow sediments or the opaque second-phase material in the fine grained layers of the zebra dolomite. Even though this theory does not account for the difference in grain size between the dark and light regions, it may be regarded as a possible process which triggers the formation of the zebra pattern.

It can be summarized that several different models of zebra dolomite formation exist which are either based on focused fracturing or dissolution, self-organizational concepts or simply link the textures to preexisting structural features in the dolomitized limestone. A consensus has therefore not been found yet, and the suggested models sometimes contradict each other. Because the dolomitizing fluids which are likely to be linked to the pattern formation are capable of delivering the metal content to the respective deposit, a general model of the zebra texture formation can widen the understanding of hydrothermal systems that build up economic Pb-Zn mineralization.

Pattern formation in geological systems is often related to self-organization processes. The pattern emerges out of an initially unordered system which is out of equilibrium and in which feedback reactions occur [17, 18]. Especially the genesis of a rhythmic pattern like the one discussed in this paper are likely to involve some kind of self-organization [7]. The concept of self-organization applies to a broad range of scientific problems like Biology [19], Chemistry [20], Geochemistry [17, 18], and Mechanics [21]. Especially when dealing with two phase systems like a fluid saturated rock were mechanical and/or chemical reactions take place, self-organization is likely to occur. As the concept of self-organization is a general approach, findings achieved in one scientific field may also be applicable to another. That self-organization occurs in the type of hydrological system studied in this communication was already proposed by Ortoleva et al. [18], where banded Pb-Zn mineralization was linked to geochemical self-organization.

In this communication we present a simple generic model which can explain the differences in color and grain size in the layers of the zebra pattern. Our model starts with the replacement of the initial impurity rich limestone by dolomite according to the crystal zoning model where the scattered second-phase is redistributed along the propagation direction of the reaction front. The complete dolomitization is followed by a grain growth process that is influenced by second-phase particle densities. This simulation setup involves feedback between the redistribution of second-phase material and grain growth. Moreover, the hydrological system has to be assumed to be out of equilibrium. As already pointed out by Fontbote [7] the host rock and the infiltrating dolomitizing fluid will account for the "out-of-equilibrium condition." These are general principles which are present during self-organized pattern formation [17, 18].

2. Numerical Model

2.1. Setup

The numerical simulations were carried out in 2D at the scale of a thin section (1 cm^2) using the modeling environment "*ELLE*." In our simulations two grids are mapped onto each other (**Figure 2**). The background is represented by nodes distributed on a hexagonal grid that is stationary and records impurity content, concentration and mineralization. The second grid is a mobile boundary-model consisting of line segments that are connected by nodes, where the line segments represent grain boundaries of growing crystals. The two grids are linked to each other so that the impurity content in the hexagonal grid can influence the simulation of grain boundary migration in the boundary model.

During the simulation of the pattern formation two main processes are active, an initial replacement of calcite by dolomite along a reaction front and a subsequent coarsening of grains as a function of variations in surface energy. Both processes affect impurity distributions whereas the grain growth process itself is also affected by the redistributed scatter of impurities.

2.2. Dolomitization and Second-phase Redistribution

The dolomitization in our model is simulated as a replacement of the initial calcite ($CaCO_3$) by dolomite ($CaMg(CO_3)_2$) due to a concentration change of Mg^{2+} in the nodes of the hexagonal grid. Usually the replacement process in large hydrothermal systems involves convective fluid flow but because the area of our

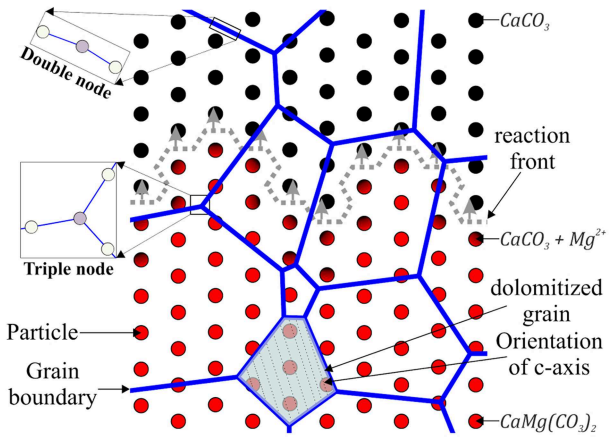

FIGURE 2 | Schematic section of the model showing the basic elements used to simulate the dolomitization and the grain growth. The nodes which are distributed on a hexagonal lattice build up the background of the simulation. The nodes have a value of Mg^{2+}-concentration and the parameters of the second-phase (radius and densities) assigned to them. The later influences the migration rate of the grain boundaries. The top layer is built up by the boundary model consisting of connected nodes (either double or triple) which represent the grains. Only grains which are dolomitized can grow whereas the driving force for migration is derived from the surface energy, which is a function of the orientation of the *c*-axis of the considered crystal and the adjacent grains.

simulation is comparatively small we assume that on such a scale convection can be neglected and a general transport equation can be applied:

$$\left(\frac{\partial c}{\partial t}\right)_x = v_D \left(\frac{\partial c}{\partial x}\right)_t + D_f \left(\frac{\partial^2 c}{\partial x^2}\right)_t \quad (1)$$

This expression describes the change in concentration (c) in the x-direction over time (t) due to advection (v_D) and diffusion (D_f) of a specimen. As a simplification we assume the diffusivity to be constant and isotropic. If we consider the transport of a specimen in the saturated zone with non-turbulent flow ($Re < 1$) we can calculate the advection part of Equation(1) using Darcys law:

$$v_D = \frac{\kappa}{\phi} \cdot \Delta P \quad (2)$$

The velocity in this equation is a function of the pressure gradient (ΔP) in the respective environment, the permeability (κ) and the porosity (ϕ) of the considered medium. Compared to the advection speed the diffusivity usually contributes only a small amount to the overall concentration change and therefore the Darcy velocity will be the critical term in Equation (1). As a consequence the propagation of the reaction front is mainly governed by the Darcy velocity. In order to apply Equations (1) and (2) to our simulation we initially set a constant pressure gradient, a randomly distributed porosity and an initial concentration in the hexagonal grid. These parameters are then used to calculate the concentration change in the nodes due to the propagation of a fluid supersaturated with Mg^{2+}. The associated concentration change in the nodes is proportional to the calculated Darcy velocity combined with the constant diffusivity. The Darcy velocity itself is calculated using the initially defined pressure gradient and the local porosity/permeability. A threshold for the concentration of Mg^{2+} was set, above which we consider the node to be completely dolomitized. In addition the porosity increases by about 13% [22] when a node is changed completely to dolomite. Once a grain becomes dolomitized the slower grain growth process can start. However, the grain boundary migration only begins in the considered grain if the adjacent grains are also dolomitized as we assume grain growth to appear along dolomite/dolomite boundaries (**Figure 2**).

The initial scatter of impurities is alternated by the advancing reaction front similar to the crystal zoning model [3]. The reaction front in our model is capable of collecting second-phase particles whereas the collected amount is inversely proportional to the size of the impurities and proportional to the concentration change between two time steps (Equation 3). For the collection process we applied a size dependent step-function [$f(r_p)$] assuming that the mobility of second-phase particles during replacement is similar to the mobility associated with grain boundary migration described by Gottstein and Shvindlerman [23]. Furthermore, we chose a function [$f(c)$] which relates the amount of collected impurities to the concentration change between two time steps which is directly proportional to the replacement rate. The impurities should become mobile during replacement as the calcite/dolomite transition is accompanied by an increase of the crystallographic order. The originating dolomite crystals will prefer a low internal energy state and therefore tend to build in fewer impurities in their lattices. This cleansing process of the crystals can be compared to the generation of impurity free crystals from melt during industrial zone melting [3] even though the transition in our model is between two mineral phases and not a change of the state of matter. The Equation(3) outlines how we calculated the amount of particles collected by the advancing front, if the threshold for collection is not exceeded.

$$\begin{aligned} m &= C_{1/2} \cdot f(r_p) \cdot f(c); \quad S = [0;1] \\ f(r_P) &= 1 - tanh(r_P) \quad r_P < r_{crit} \\ f(c) &= 2 \cdot (c_1 - c_0) \quad c_{0/1} < 0.5 \end{aligned} \quad (3)$$

Here m_p is the amount of the second-phase which is collected by the reaction front, r_p is the radius of the second-phase particles, r_{crit} is the threshold of the particle size, c_0 is the concentration of the contaminant in the previous time step and c_1 is the concentration in the current time step, respectively. The factor $C_{1/2}$ is used to control the amount of particles collected or released by the front. As the threshold for dolomitization in our simulation was set to 0.5, the maximum solution of $f(c)$ is 1 but will usually be much lower. Once the loading-threshold of the reaction front is reached the collecting force of the front breaks down and the process switches to releasing particles [acc. [3]]. The release of second-phase particles in our model is a function of particle size and concentration change according to:

$$\begin{aligned} f(r_P) &= tanh(r_p) \quad r_p < r_{crit} \\ f(c) &= 1 - \left(2 \cdot (c_1 - c_0)\right) \quad c_{0/1} < 0.5 \end{aligned}$$

2.3. Grain Growth

Static grain growth can be divided into normal and abnormal grain growth. During normal grain growth the coarse grains grow and small grains shrink [24]. The driving force for this process is usually derived from the specific surface energy (γ) of the material and the local radius of curvature (r) of the grain boundary. This driving force is proportional to the reduction of the Gibbs free energy (ΔG) [25].

The energy for grain boundary migration derived from the reduction of the Gibbs free energy is largest for surfaces with a small radius of curvature (Equation 8). In general the reduction of the surface free energy of the crystals tends to generate curved boundaries and the direction of the migration depends on the curvature of the considered crystal. Typically the grain boundary will migrate toward its center of curvature [26]. If the reduction of the Gibbs free energy is the main driving force and the surface energy of the crystals is isotropic, the grain boundaries tend to produce a polygonal pattern with straight boundaries. Once all the grains have roughly the same size, the resulting structure is a so-called foam structure with angles of $\approx 120^\circ$ at triple junctions [27].

In this study we simulated grain growth where grain boundaries interact with a dispersed second-phase. In order to find a kinetic rate-law governing the propagation of boundaries

we chose a first order rate law for dissolution/precipitation based on transient state theory [28]. The general form of the applied equation is:

$$D_r = k_r V_s \left[1 - exp \left(\frac{C_A}{C_A^{eq}} \right) \right] \tag{4}$$

In this expression D_r is the dissolution rate $[m/s]$, k_r is a rate constant $[molm^{-2}s^{-1}]$ at a given temperature and pH , V_s is the molar volume $[m^3mol^{-1}]$, C_A is the concentration of the specimen in the fluid and C_A^{eq} is the equilibrium concentration of the solute. If we use the expression for the equilibrium constant K_{eq}:

$$C_A^{eq} \approx K_{eq} = K_0 exp \left(\frac{\Delta P_n V_s}{RT} \right) exp \left(\frac{\Delta \Psi_s}{RT} \right) \tag{5}$$

and assume an equilibrium saturation and no stress acting on the crystal surface, we can derive an expression for the dissolution or precipitation rate at constant fluid pressure under saturated conditions as Koehn et al. [29, 30]:

$$D_r = k_r V_s \left[1 - exp \left(-\frac{\Delta \Psi_s}{RT} \right) \right] \tag{6}$$

where R is the universal gas constant and T is the temperature $[K]$. We then get a temperature dependent rate law for dissolution/precipitation processes using the Helmholtz free energy change $\Delta\Psi_s$. Further details on the derivation can be found in Koehn et al. [29, 30]. If we now substitute $\Delta\Psi_s$ with ΔG we can describe the process by means of Gibbs free energy reduction. This energy change is closely related to the change of the radius of curvature (Δr) of the considered grain. If this energy reduction is the main driving force for grain boundary migration, the velocity of a point on the grain boundary can be calculated using the surface energy (γ), the grain boundary mobility (m) and the radius of curvature (r) as:

$$\Delta r \approx \left(\frac{-m\gamma}{r} \right) \leftrightarrow v = \frac{\partial r}{\partial t} = \frac{-m\gamma}{r} \tag{7}$$

Based on Equation(7) the velocity of a grain boundary (v) is a function of the reduction of r over time or the grain boundary mobility (m) and the surface free energy (γ, respectively [31]. We can simplify this expression and determine the energy of a point on the grain boundary by:

$$\Delta E_r = \frac{\gamma}{r} \tag{8}$$

This expression can be regarded as the apparent activation energy and we substitute the energy change in Equation(6) by ΔE_r. Hereby it is possible to formulate a general rate law depending on the reduction of the Gibbs free energy with a temperature dependent Arrhenius term which is often used to describe grain growth processes. To compute the migration rate of a grain boundary in our simulation we then applied:

$$v_{gb} = k_r V_s \left[1 - exp \left(-\frac{\Delta E_r}{RT} \right) \right] \tag{9}$$

By implementing a uniform surface energy γ, isotropic grain growth will be simulated and the developing grains will generate a foam structure. In order to resemble grain boundary migration which produces a more dolomite-like crystal shape we adopted a function for anisotropic grain growth developed by Bons et al. [27], in which the surface energy of the grains is a function of the *c*-axis orientation of the considered- and the adjacent grain. By relating the surface energy to the angle between the grain boundary and the *c*-axis, the problem is reduced to a function of γ over 90° (Figure A1a). The shape of this function determines to a certain extent the geometry of the developing grains. The energy state of the considered boundary segment is a function of four angles for any node on a boundary but will be a function of six angles for a node at a triple junction. The value of the surface energy of a single node is derived by adding up the energies of the adjacent boundary segments and accounting for the length of every segment. The energy state of a single segment is the product of its length and the sum of the energy values according to the function in Figure A1a. The process developed by Bons et al. [27] also accounts for low energy boundaries related to coincident side lattices. In Figure A1b the distribution of the calculated surface energy of a simulation consisting of 10.000 time step is shown. The distribution of the surface energies shows two distinct peaks at ≈0.2 and ≈0.5 Jm^{-2}. This bimodal distribution is caused by the underlying function (Figure A1a).

In contrast to normal grain growth, abnormal grain growth can occur in aggregates where some large grains exist in an otherwise fine grained matrix. The larger grains will then grow at the cost of many small grains which will shrink or disappear [25].

In this work we mainly focus on normal static grain growth, but depending on the distribution of the developing grain sizes, abnormal grain growth may occur at later stages of the simulations. The shift from normal to abnormal grain growth might be caused by the anisotropic distribution of surface energies [32] or by the distribution of impurities.

2.4. Drag Force of Mobile Particles

Fluid films, inclusions, melt, pore size, and the chemical composition of fluids can all change the grain boundary mobility [24, 25, 33]. In our simulation we focus on the interaction of a second-phase volume fraction with a migrating grain boundary. This second-phase can for example be fluid filled pores or a different mineral phase [23–25, 33–35]. The interaction between the grain boundary and an impurity, which results in reduction of the driving force for migration, can be quantified by the so-called Zener drag. Zener formulated equations to calculate the influence of second-phase particles on a moving grain boundary based on laboratory experiments [36]. That the results achieved during laboratory studies can approximate the interaction of crystal growth and a dispersion of second-phase particles in geological systems was shown by Mas and Crowley [34], who achieved a quantitative analysis of the relationship between second-phases and the grain size in marble. It was found that already volume fractions of ≈5% will have a significant effect on the grain size in natural systems and even a very fine grained second-phase can have a remarkable effect on

the growth rate as long as the volume fraction is sufficiently high enough.

When a moving grain boundary encounters a single, coherent, spherical second-phase particle, this obstacle initially applies an attraction force to the crystal surface. In order to migrate over the obstacle, the grain boundary has to increase its area proportional to the size of the impurity. During progressive boundary migration the particle will then exert a drag force on the surface (**Figure 3A**). The area increase of the grain boundary and the drag force both result in additional energy needed for further grain boundary migration, whereas the effective drag force is primarily dependent on the size of the considered particle [25]. In order to calculate the drag force of a single second-phase particle the assumption has to be made that the surface tensions of the particle and the grain boundary are in equilibrium. If this is assumed and the grain boundary meets the obstacle at an angle of 90°, the two tensions will cancel out leaving only one surface tension (γ) [36]. This surface tension is the internal energy of the matrix/matrix boundary and not of the matrix/particle interface [25]. The general equation of the Zener drag (F_Z) is then

$$F_z = 2\pi\gamma r_p \cdot cos\Theta \cdot sin\Theta \tag{10}$$

where γ is the resulting surface tension, r_p is the radius of the particle and Θ is the angle between the tangent to the pinned matrix boundary at its intersection with the particle and the tangent to the boundary when no particle is present. The maximum pinning force occurs at $\Theta = 45°$. In this case the product of the two trigonometric functions equals 1/2, leaving:

$$F_z = \pi\gamma r_p \tag{11}$$

which is the equation for the maximum Zener-force of a single coherent spherical particle, disregarding the shape of the actual grain boundary [36].

It is very unlikely that there is just one single particle at one grain boundary in a natural system. It is more reasonable to consider a dispersion of particles with different radii (r_p). The effective driving force for grain growth (F_{eff}) will then be reduced by the cumulative attraction forces of all particles with the same radius (r_p). This can be written as

$$\Delta F_{eff} = F_{eff} - \sum_{i=1}^{n_p} n_i F_{z_i} \tag{12}$$

with n_i being the number of particles with the radius r_p, n_p the maximum number of these particles and F_{zi} the Zener drag of a particle with the considered radius [23].

In order to simulate the drag force of several particles on a grain boundary we chose Equation(13), which gives a good estimate for the drag force resulting from a volume fraction of particles. This equation is based on the assumption that the particles contributing to the drag force all have the same radius. A zone of interaction between the particles and the grain boundary (R_{gb}) has to be defined (**Figure 3B**), which has approximately the diameter of a single particle ($2r_p$). Furthermore, only second-phase particles which are in the interaction zone (R_{gb}) behind the moving grain boundary will contribute to the drag force because the impurities in the particle-boundary interaction zone (R_{gb}) in front of the boundary will produce an attractive force. Finally it is assumed that the volume distribution of particles equals the area distribution (f) on the grain boundary. The equation to calculate the drag force resulting from a volume distribution of second-phase particles is:

$$P_z = \frac{3}{2} f \frac{\gamma}{R_{gb}} \quad R_{Gb} \approx 2r_p \tag{13}$$

We simplified the process of calculating the impurity-depending drag force by computing the volume fraction of impurities in one node of the hexagonal grid and introducing this value as the area fraction of second-phase particles in Equation(13) (**Figure 3B**).

To simulate the interaction of a grain boundary with a fraction of impurities we calculated the drag force resulting from the scatter of second-phase particles in the background of the model. The derived drag force reduces the apparent activation energy or driving force for grain boundary migration according to:

$$D_r = k_r V_s \left[1 - exp\left(- \frac{\left[\left(\gamma \frac{1}{r}\right) - \left(\frac{3}{2} f \frac{\gamma}{R_{gb}}\right) \right]}{RT} \right) \right] \tag{14}$$

This is the equation on which our simulation of anisotropic grain growth hindered by a dispersed second-phase is based. The final

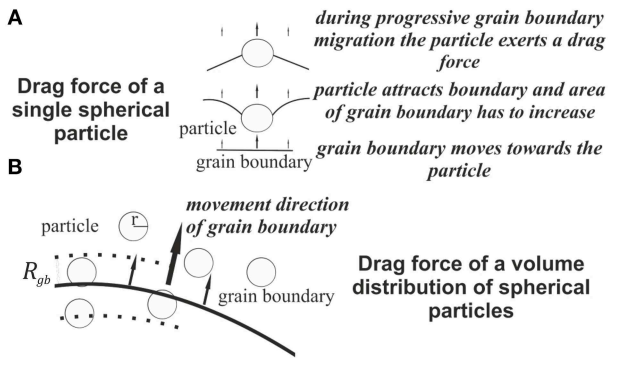

FIGURE 3 | (A) Basic concept of the Zener drag applied to a grain boundary by a single coherent, spherical particle. In the first stage when the grain boundary encounters a particle it will be attract by it. In order to move over the particle the grain boundary has to increase its area which is associated with a higher energy needed for further migration. During progressive grain boundary migration the particle will exert a drag force on the particle. This force is highest for angles of 45° between the bend grain boundary and an imaginary undeformed boundary. The area increase and the applied drag force from particle result in a higher energy needed for grain boundary migration and therefore slow down or even inhibit further grain boundary migration [after Nes et al. [36]]. **(B)** Concept of the Zener pressure applied to a grain boundary by multiple spherical, coherent particles of the same radius. The Zener pressure is the drag force of a distribution of particles which are present in the particle-boundary interaction-zone (R_{gb}). The assumption for the validity of this concept is that the volume fraction of particles equals the area fraction of particles on the grain boundary [after Nes et al. [36]].

average and the maximum grain size are both affected by the size and number of impurities present in a volume [23, 33, 35–41].

In addition to applying a drag force on grain boundaries, second-phase particles are not stationary during grain growth. A moving grain boundary can capture particles and shift them in its propagation direction if the grain boundary migration rate is sufficiently low and the diameter of the second-phase particles is small enough. During continuous grain growth the grain boundary will be loaded with progressively more particles that are smaller than a critical size [23]. As the value of the grain boundary velocity derived from the driving force is crucial to the loading process, it is also possible that a loaded grain boundary detaches itself from the particles when the driving force increases. At this point the grain boundary velocity will have the value of a boundary without any particle. Grain boundary migration can therefore take place in two regimes, an impurity controlled regime, with a slow grain boundary migration and an impurity-free regime with a fast grain boundary migration [26]. According to the theory of mobile particles by Gottstein and Shvindlerman [23] we chose a threshold for the radius of the second-phase and for the velocity of the migrating boundary. The amount of the second-phase particles that are redistributed by a moving grain boundary is inversely proportional to the particle size and to the velocity of the grain boundary according to:

$$\begin{aligned} m_p &= C_1 \cdot f(r) \cdot f(v_{gb}) \quad S = [0;1] \\ f(r) &= 1 - tanh(r_p) \quad r_p < r_{crit} \\ f(v_{gb} &= 1 - tanh(v_{gb}) \quad v_{gb} < v_{crit} \end{aligned} \tag{15}$$

It can be inferred that the maximum drag force and therefore the maximum grain size achieved during grain growth are both a function of the size and the dispersion of the second-phase [25, 35]. In order to quantify this relationship Equation(16) can be used to estimate the maximum achievable grain size.

$$A_{max} = C^{'(m)} \cdot \frac{d_p}{f} \tag{16}$$

Where A_{max} is the maximum grain area, d_p is the initial grain size, f is the volume fraction of the second-phase and $C^{'(m)}$ is a constant that depends on the model assumptions. The dispersion of the second-phase particles has a high impact on final grain size whereby the smallest grain size is reached when the particles are not randomly dispersed and most of them lie on grain corners [25].

3. Results

3.1. Initial Setup

Prior to every simulation a constant pressure gradient, a random distribution of porosity, second-phase particle radii and densities were assigned to the nodes of the hexagonal grid. Particle distributions are aligned horizontally in order to mimic an initial sedimentary layering with graded beds. Such a sedimentary layering can often be found in limestones and may be caused by cyclic sedimentary deposition. Banding in calcareous rocks might as well be of biological origin of which Stromatolites, Stromatoporoids or algae mats are good examples. In addition compaction during diagenesis might form a layered distribution of impurities resulting from pressure solution and subsequent precipitation. An example of a banded dolomite which was found in the Upper Silesian Pb-Zn district in Poland compared with the initial impurity scatter in our model is shown in Figure A2. The Upper Silesian ore deposit is of the same type as the one hosting the San Vicente mine in Peru but a zebra pattern is not frequently observed in this region.

The *c*-axis orientation of grains varies randomly throughout the model (Figure A1c). We chose the area of the model as being equivalent to 1 cm^2, the time scale of a single time step was set to 1 h for the dolomitization and once the volume was completely dolomitized the time scale was switched to 10*a* in order for grain growth to occur. According to the chosen spatial scale one node in the hexagonal grid is thought to equal a spherical volume with a diameter of $\approx 45\ \mu m$ in which a fraction of impurities can be present.

3.2. Dolomitization and Second-phase Redistribution

Initially a reaction front progresses through the material. This front changes calcite to dolomite, a reaction that includes an increase in porosity (up to 13%). The reaction is induced by an influx of fluid from the lower boundary of the model and is calculated using an advection-diffusion algorithm (see Section 2.2). We use intermediate Péclet and Damköhler numbers to avoid too pronounced fingering in the front. This setup leads to a wavy front in the simulations (**Figure 4A**) with an intermediate width. During the progression of the reaction the second-phase particles are collected within the front and move with the front until a threshold is reached and the front

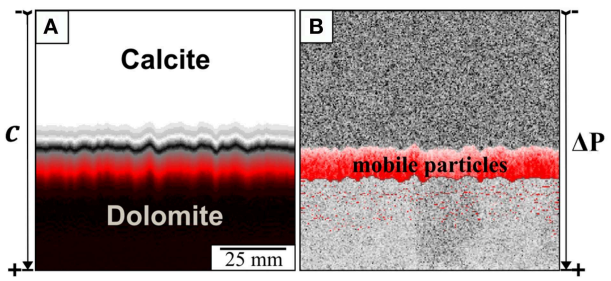

FIGURE 4 | Simulated reaction front after 2500 time steps. (A) Concentration (c) of Mg^{2+}. The Bottom part is already dolomitized (black) and the grain growth process could already start. Different layers of concentration change are visible and these different bands of Mg^{2+} could be interpreted as metastable phase in the transition from pure calcite to dolomite. The fluid flow follows the initially set pressure gradient (ΔP). **(B)** The advancing dolomitization front collects second-phase material along its propagation direction. The amount of captured particles depends on the size of the particles and the concentration change in the front between two time steps. The mobile particles (red) are moving together with the advancing front and represent the amount of second-phase material which is released from the crystal lattices by the dolomitization process.

loses particles again. Behind the front the particle densities are generally lower unless the front is oversaturated and releases particles. The progressing reaction front enhances the initial second-phase distribution (horizontal sedimentary layering). A zonation in concentration change is clearly visible in **Figure 4A**. The development of channels is minimal but the shape of the front is clearly irregular. The second-phase particle loading process (Equation 3) is displayed in **Figure 4B**. The highest densities of mobile particles are present close to the actual replacement where the concentration change nearly exceeds the threshold for dolomitization. Once the reaction front has changed the material to dolomite grain boundary migration becomes active (**Figure 2**).

3.3. Grain Growth with Zener Pressure

Based on the analyzed natural samples, in which saddle dolomite is present in the coarse layers, we assumed a temperature of at least 80°C [22, 42]. This temperature regime is also found in the literature for the area of the San Vicente mine where the involved fluids are characterized as brines with a temperature of ≈75–160°C and a *pH* of ≈5 [11, 43, 44]. The *pH* in the work of Spangenberg et al. [44] was determined through geochemical analyses on sulfates giving the hydrogeochemical parameters of the mineralizing brine. The dolomitizing brine probably percolated through the same underlying detrital rocks generating a similar slightly acidic fluid. The *in situ pH* of general dolomitizing brines presented in the work of Merino and Canals [11] is also 5. However, a change in *pH* and/or *T* will accelerate or slow down the precipitation rate of dolomite as both affect the dissolution constant (k_r) used in Equation(14). We estimated the value of k_r trough an extrapolation to *pH* 5 from a series of experiments carried out by Gautelier et al. [45]. The measurement of the steady-state dolomite dissolution rate in the work of Gautelier et al. [45] was performed at a maximum temperature of 80°C and is in the temperature range we consider appropriate for our simulations. The value of the surface free energy for limestone is 0.27 Jm^{-2} [46] whereas the value for dolomite is poorly known. We therefore based the distribution of the surface energy in our model on the work of Austen et al. [47]. Although the simulated process is thought to be situated in a burial environment with an average depth of 2 km, we neglected the pore pressure and the stresses acting on the crystals assuming that these play only a minor role.

We first tested the implementation of Equation(9) with the chosen constants by comparing the analytical solution with the outcome of the simulation. In Figures A3a,b the derived velocities for different surface energies (0.2–0.8 Jm^{-2}) are plotted against an increasing radius of curvature. The theoretical solution (Figure A3b) and the values computed during the simulation (Figure A3a) fit well. The boundary velocity is inversely proportional to the radius of curvature (r) and proportional to the surface energy (γ) in accordance to theory [27, 31]. We further tested the reliability of our applied rate law by simulating the shrinking of a single circular grain (Figure A3c). The radius of curvature will decrease with time and the time steps can therefore be related to a relative radius. As the energy for grain boundary migration is a function of the radius of curvature and the surface energy in our simulation, the different surface energies (0.2–0.8 Jm^{-2}) can be related to different grain boundary mobility. A linear decrease of the grain area over time is expected for an isotropic surface energy distribution and the shrinking rate should be proportional to the grain boundary mobility [27], which is the case for the outcome of our simulation.

The maximum grain size and the reduction of grain numbers in our simulation are different for isotropic grain growth, anisotropic grain growth and anisotropic grain boundary migration influenced by second-phase particles (**Figure 5**). The reduction of the grain number shows an exponential decrease in all three cases, whereas the actual rate is highest for the isotropic case. The difference in the average grain size between anisotropic grain growth and the impurity-controlled growth seems small but is still significant considering that either one or no impurity was assigned to every node in the hexagonal grid, which gives a small volume fraction. Furthermore, the distribution of the surface energy along grain boundaries according to Figure A2a results in grain shapes which are similar to the ones observed in the natural samples. In contrast to the foam structure achieved by isotropic grain growth the angles at triple junctions differ significantly from 120° and the grain shapes are more irregular. In the case of impurity-controlled growth the shapes become even more irregular and the average grain size is slightly smaller.

Figure 6 shows simulations with different particle densities with initial distributions shown in Figure A4a. The maximum grain size depends inversely on the particle densities with larger grains in aggregates with lower second-phase densities (**Figure 6**). There is a large difference in the maximum grain size between a simulation with one or zero mobile impurity and a simulation with a maximum of 15 second-phase particles per node. Grain growth stops and a stable grain size is achieved at time step 2500 in the simulation with 15 mobile impurities per node whereas in the simulation with fewer impurities the maximum grain size is still increasing at time step 7500.

Abnormal grain growth appeared during the simulation with a maximum of 10 impurities assigned to every node in the hexagonal grid (**Figure 6**). This process is likely to be caused by

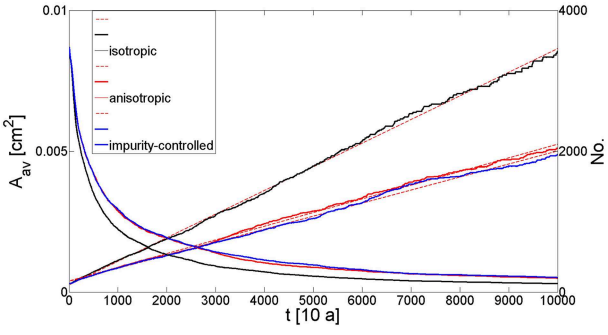

FIGURE 5 | Graph showing the number of grains and the average grain size during simulations with 10.000 time steps (100 ka). The exponential decrease of grain numbers is visible in all three simulation. The maximum grain size is achieved by isotropic grain growth and the smallest maximum grain size is found in the impurity controlled regime. This area increase is inverse proportional to the number of grains at the end of the simulation.

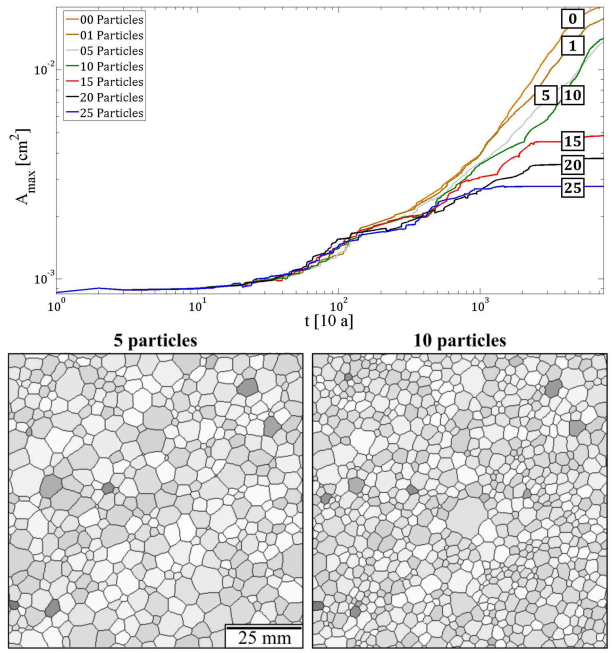

FIGURE 6 | Top: Graph showing the evolution of the maximum grain size during simulations of 7500 time steps. **Bottom**: The grain size distribution for the case of 5 and the case for 10 impurities per point in the hexagonal grid.

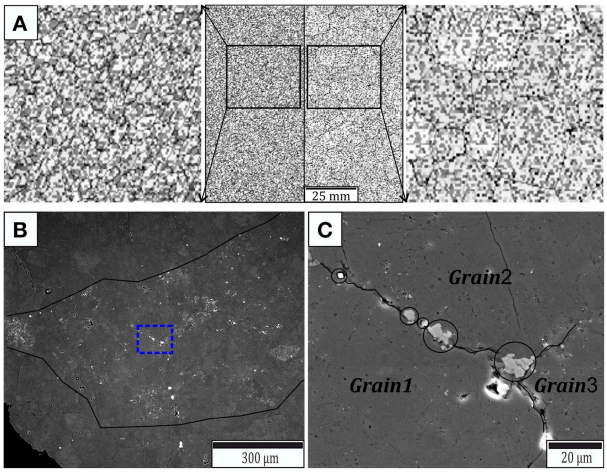

FIGURE 7 | (A) Particle redistribution during the simulation of anisotropic grain growth shown in **Figure 5**. The left picture in **(A)** shows the initial impurity distribution and the right image shows the second-phase particle scatter after 10,000 time steps of the simulation. **(B)** Backscattered SEM image showing a fine grained layer in the center. The highest particle densities occur in the fine grained part which is indicated by the black line. **(C)** Combined backscattered and second-electron image showing the area indicated by the blue dotted line in **(B)**. Larger second-phase particles are lined up along the grain boundary (black circles) and the highest density of impurities is visible at the triple junction.

the redistribution of second-phase particles during grain growth in combination with a energetic advantageous orientation of the *c*-axis in the large grain compared to its adjacent neighboring crystals. The anhedral shape of the grain boundaries of the large grain leads to an additional driving force, which is probably the reason for the abnormal grain growth of those crystals.

The redistribution of second-phase particles during a simulation with exclusively mobile particles is shown in **Figure 7**. Every node in the hexagonal grid had either one or zero particles assigned to it and the distribution of the impurity radii is shown in Figure A4a. At the end of the simulation the highest particle densities occur on grain boundaries and especially at triple junctions. This is in good agreement with the simulations carried out by Shelton and Dunard [39] and with our observations on natural samples. In thin sections the grain boundaries in the fine grained layers of the zebra dolomite appear dark, which implies that the grain boundaries captured particles. This can be seen in **Figure 7B** where an electron-backscattered image of a fine grained band in between two coarse grained bands is shown. The second-phase particle distribution appears to be non-random, with highest particle densities in the fine grained layer and specifically along grain boundaries (**Figure 7C**). In accordance with the simulations the highest particle densities in the real samples occur at the triple junctions.

3.4. Pattern Formation

To model the formation of the zebra texture we combined the simulation of the dolomitization and associated impurity redistribution with the simulation of grain growth influence by second-phase particle densities. The initial distribution of the impurities (Figure A4b) represents graded bedding with one sedimentary cycle consisting of 15 single layers with a change in the mean grain size of 0.05 μm from one to the subsequent layer (**Figure 8**). The reaction front moves from the bottom to the top of the simulation following a predefined pressure gradient and redistributes the impurities along its way.

The advancing reacting front collects the second-phase particles whereas the amount of particles depends on the radius of the impurities (Equation 3). The width of the front expands successively with time and the amount of particles collected by the front rapidly increases as soon as the front enters regions with smaller second-phase particle radii. Areas with larger particles sizes are not cleared as effective as areas with smaller particles sizes (Equation 3). The dolomitizing front leaves layers with high particle densities behind and releases impurities in small patches when the loading threshold of the front is exceeded (top of **Figure 8**). Since the amount of collected particles is related to the concentration change between two time steps (Equation 3) the loading process is also related to the development of fingers in the front so that the critical loading value is reached faster in regions between pronounced fingers (**Figure 8**).

Once the dolomitization front has passed through the sample the time scale is changed so that grain growth becomes active. Due to the layered distribution of second-phase particle densities, which were superimposed by the dolomitization front, high grain boundary migration rates only occur in regions with low impurity densities. This produces larger and potentially more isotropic grains, whereas areas with high particle densities only

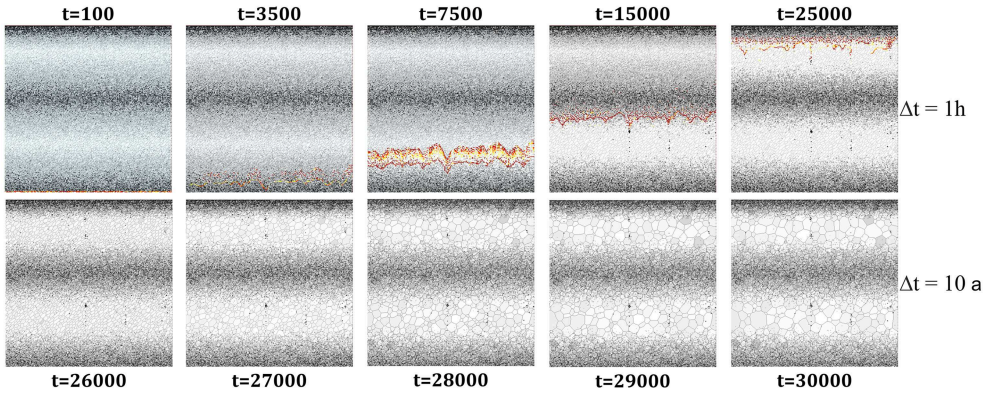

FIGURE 8 | Simulation of the zebra pattern formation by combining the simulation of the dolomitization and the grain growth. Both simulated processes redistribute the initial impurity scatter. The bifurcation is achieved because the initial set graded bedding distribution of particle size is superimposed by the size-dependent shift of the reaction front. A secondary redistribution is then performed during the propagation of the grain boundaries.

show minor grain growth. Because of the bifurcation of growth rates due to the impurity concentrations a pattern consisting of layers with a large, and layers with a smaller grain size develops. The grain growth process itself will then also account for the secondary redistribution of particle densities and leads to a secondary cleaning of the growing grains. As an additional result of the bifurcation of the growth rate, the larger grains in the low density second-phase areas are cleaned more effectively by the grain boundary migration as this process is much longer active in these grains than in the grains located in regions with high impurity densities. The stable grain size achieved in the light and dark layers is in good agreement with the natural samples (**Figure 9**). The grain sizes are found to vary between 80 and 150 μm in the dark and 0.5–5 mm in the light layers [12]. The crystals in the simulations have final grain sizes ranging from $\approx$ 200 μm in the impurity rich to 2 mm in the impurity free layers.

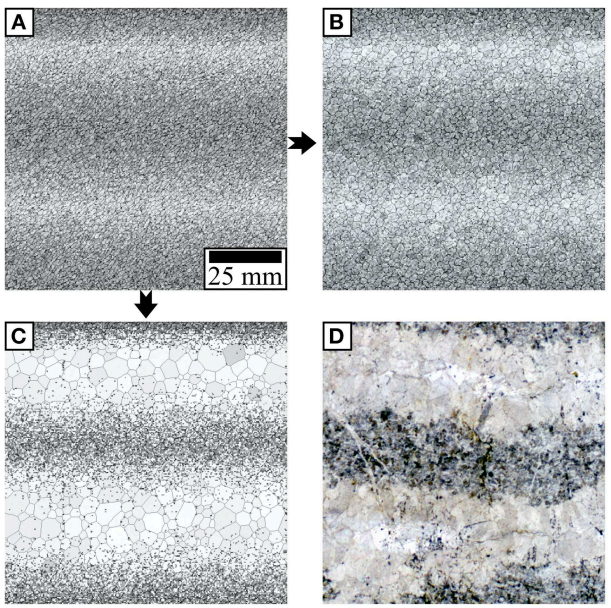

FIGURE 9 | (A) Initial distribution of second-phase particles for the simulations in **(B,C)**. **(B)** Result of a grain growth simulation without the redistribution performed by the reaction front after 3500 time steps. A stable grain size is reached and no pronounced banding is observable. **(C)** Result of s simulation of dolomitization followed by grain boundary migration after 30,000 time steps. The redistribution of the second-phase material leads to a bifurcation in grain growth rates and this causes banding. **(D)** Scan of a thin section. The area of the scan is equivalent to the area of the simulation. The location of the dark and light layers as well as the grain size differences are in good agreement with the result of the simulation shown in **(B)**.

4. Discussion

A combination between second-phase particle redistribution by a replacement front and subsequent grain growth can generate patterns similar to zebra textures observed in natural samples. We therefore put forward a process of pattern formation based on the bifurcation of the overall grain boundary migration rate, where this dichotomy in grain boundary mobility is caused by a layered distribution of second-phase particle densities.

Our simulation of the calcite-dolomite replacement governed by a general transport equation can produce instabilities in the reaction front leading to fingering. This is due to the increasing porosity which accompanies the replacement process and can be compared to the general process of reactive infiltration instabilities [48]. Even though our simulation of the dolomitization is a simplified model of the natural process it is sufficient to simulate the impurity redistribution mechanism which we assume to be crucial for the textural evolution. The basis for the second-phase rearrangement is the crystal zoning model [3] combined with the theory of particle mobility during grain boundary migration [23]. We had to estimate the parameters for the impurity-loading process of the reaction front because the actual values have not yet been determined experimentally. We applied general laws for second-phase particle mobility during the replacement because we assumed that the process is similar to the shifting of particles during

grain boundary migration. The mechanism which is of high importance for the pattern formation is the impurity size dependent shift as it superimposes the initial graded bedding distribution in our simulations. The size dependence of the impurity sweep can superimpose a graded bedding structure and build up a layered scatter of impurities. The particle collecting and precipitating reaction front will cleanse areas consisting of second-phase particles with a smaller grain size more efficiently. The resulting structure will consist of equidistant, almost particle free layers alternating with high particle density layers. Thus, the initial layering controls where the respective bands will be formed. We propose that this process produces a basic conditions for formation of banded structures in rocks.

We could further show that our model can reliably calculate grain boundary velocities in a system with mobile second-phase particles (Equation 14). Particle numbers and maximum grain size relationships (Equation 16) are in good agreement with the general theory of grain boundary motion in the presence of impurities [23, 25, 49]. Our simulation can show that during progressive grain boundary migration the impurities will line up along grain boundaries [38, 39, 49] and that surviving grains comprise of a core which is not affected by grain growth [50]. Both simulated processes comprise of some simplification but reflect the natural processes to the extent needed to show how a layered pattern can be generated by combining these two mechanisms.

Based on our simulations we can suggest a general hypothesis for the development of the initial zebra textures or the development of banded structures in crystalline materials. The crucial point in our theory is the development of an equidistant layered distribution of impurity densities. Without the redistribution of the initial impurity scatter by the reaction front no bifurcation in grain growth rates is observed (**Figure 9**). If the differences in second-phase particle radii and densities are high enough grain growth rate bifurcation might also be observable without the redistribution by the reaction front. However, the dolomitization front will always enhance the banding. Based on that we propose that the layered scatter of the second-phase can either evolve by superimposing a pre-existing structure (like a graded bedding distribution in our model), it could be generated out of an initially random distribution of particles which has been shown be the crystal zoning model developed by [3] or could even be solely of sedimentary origin. The model shown in this communication generates structures which are similar to the ones observed in the natural samples. Even on a microscale the simulations give results which are in good agreement with the samples. The noticeable high densities of opaque material along grain boundaries in the thin sections are also observable in our simulations and are generated by the mobility of the second-phase particles during grain growth. We can therefore conclude that the crucial parameters needed for zebra texture evolution are the initial porosity of the limestone, the saturation of the hydrothermal fluid with respect to dolomite and the porosity change associated with the calcite-dolomite replacement. We would like to point out that the actual redistribution process of second-phase material in our simulation is a strong simplification of the natural process. Pattern formation in natural materials, especially when it happens on a localized scale often involves self-organization [17, 18]. If the process of impurity redistribution as it is simulated in our model is active in every environment where an impurity rich limestone is replaced by dolomite, zebra textures would occur in much more regions than they actually do. Therefore, some critical parameters must be present which produce the layered distribution of second-phase material.

On the large scale these critical parameters could be related to the geometry of the specific tectonic environment and over-pressured fluid systems in which large hydrothermal Pb-Zn mineralization are formed, whereas on the small scale variations in porosity or impurity content could trigger banding or not.

Our model may represent the initial trigger of the pattern formation but can not explain all features, like the elongated shape of the light crystals and the sometimes observed macropores along the median line. It is conceivable, that after the formation of the two maximum grain sizes in our model another process might become active. The final pattern could be formed by one of the existing models (see Section 1). For instance, the grain coarsening could lead to a feedback with the fracturing as the yield stress will drop with increasing grain size leading to a late fracturing of median lines or preferred dissolution along them. The initial sedimentary bedding related anisotropy is in good agreement with the work of Morrow [14]. As suggested by Fontbote [7] a self-organization process is expected to be crucial for the pattern formation. However, whether hydrofracturing, focused dissolution or crystal growth accompanied by the displacement of the fine grained bands is the final stage of pattern formation cannot be said with certainty. Further research is needed to combine the model introduced in this work with either one of the pre-existing theories or with an additional process which has not yet been regarded.

Funding

This work has received funding from the European Union's Seventh Framework Programme for research, technological development and demonstration under grant agreement no 316889.

Acknowledgments

We would like to thank Peter Chung for the help with the SEM measurements and Piotr Szymczak for organizing the field trip to the Pb-Zn district in Poland. The comments of the two reviewers helped a lot to improve this paper in terms of accuracy and illustrative examples.

Supplementary Material

The Supplementary Material for this article can be found online at: http://journal.frontiersin.org/article/10.3389/fphy.2015.00074

References

1. Loughnan FC, Roberts FI. Composition and origin of the 'zebra rock' from the East Kimberley region of Western Australia. *Aust J Earth Sci.* (1990) **37**:201–5. doi: 10.1080/08120099008727920
2. Strmić Palinkaš S, Spangenberg JE, Palinkaš LA. Organic and inorganic geochemistry of Ljubija siderite deposits, NW Bosnia and Herzegovina. *Miner Deposita* (2009) **44**:893–913. doi: 10.1007/s00126-009-0249-z
3. Krug HJ, Brandstädter H, Jacob KH. Morphological instabilities in pattern formation by precipitation and crystallization processes. *Int J Earth Sci.* (1996) **85**:19–28.
4. Wallace MW, Both RA, Morales Ruano S, Hach-Ali F, Lees T. Zebra textures from carbonate-hosted sulfide deposits; sheet cavity networks produced by fracture and solution enlargement. *Econ Geol.* (1994) **89**:1183–91. doi: 10.2113/gsecongeo.89.5.1183
5. Leach DL, Taylor RD, Fey DL, Diehl SF, Saltus RW. Chap. A of mineral deposit models for resource assesment, Scientific Investigation Report 2010-5070-A. In: *A Deposit Model for Mississippi Valley-Type Lead-Zinc Ores*. Reston, VA: U.S. Geological Survey (2010). p. 52.
6. Fontboté L, Gorzawski H. Genesis of the Mississippi Valley-type Zn-Pb deposit of San Vicente, Central Peru: geologic and isotopic (Sr, O, C, S)evidence. *Econ Geol.* (1990) **85**:1402–37. doi: 10.2113/gsecongeo.85.7.1402
7. Fontboté L. Self-organization fabrics in carbonate-hosted ore deposits: the example of digenetic crystallization rhythmites (DCRs). In: Fenoll Hach-Ali P, Torres-Ruiz J, Gervilla F, editors. *Current Research in Geology Applied to Ore Deposits, Proceedings of the Second Biennial SGA Meeting*. Granada (1993). pp. 11–4. Available online at: http://archive-ouverte.unige.ch/unige:29376
8. López-Horgue MA, Iriarte E, Schröder S, Fernandéz-Mendiola PA, Caline B. An example on the tectonic origin of zebra dolomites: the San Martín beach outcrop (Santoña, North Spain). *Geol Acta* (2009) **47**:85–8.
9. López-Horgue MA, Iriarte E, Schröder S, Fernandéz-Mendiola PA, Caline B, Corneyllie H, et al. Structurally controlled hydrothermal dolomites an Albian corbonates of the Asón valley, Basque Cantabrian Basin, Northern Spain. *Mar Petrol Geol.* (2010) **27**:1069–92. doi: 10.1016/j.marpetgeo.2009.10.015
10. Merino E, Canals A, Fletcher RC. Genesis of self-organized zebra textures in burial dolostones: displacive veins, induced stress, and dolomitization. *Geol Acta* (2006) **4**:383–93.
11. Merino E, Canals A. Self-accelerating dolomite-for-calcite replacement: self-organized dynamics of burial dolomitization and associated mineralization. *Am J Sci.* (2011) **311**:573–607. doi: 10.2475/07.2011.01
12. Nielsen P, Swennen R, Muchez PH, Keppens E. Origin of Dinantian zebra dolomites south of the Brabant-Wales Massif, Belgium. *Sedimentology* (1998) **45**:727–43. doi: 10.1046/j.1365-3091.1998.00171.x
13. Swennen R, Vandegisnste V, Ellam E. Genesis of zebra dolomites (Cathedral Formation: Canadian Cordillera Fold and Thrust Belt, British Columbia. *J Geochem Explor.* (2003) **78–9**:571–7. doi: 10.1016/S0375-6742(03)00065-7
14. Morrow DW. Zebra and boxwork fabrics in hydrothermal dolomites of northern Canada: indicators for dilational fracturing, dissolution or *in situ* replacement? *Sedimentology* (2014) **61**:915–51. doi: 10.1111/sed.12094
15. Vandeginste V, Swennen R, Gleeson SA, Ellam RM, Osadetz K, Roure F. Zebra dolomitization as a result of focused fluid flow in the Rocky Mountains Fold and Thrust Belt, Canada. *Sedimentology* (2005) **52**:1067–95. doi: 10.1111/j.1365-3091.2005.00724.x
16. Cartwright JHE, Garca-Ruiz JM, Villacampa AI. Pattern formation in crystal growth: Liesegang rings. *Comput Phys Commun.* (1999) **121-2**:411–3. doi: 10.1016/S0010-4655(99)00370-7
17. Ortoleva P. Macroscopic self organization at geological and other first order phase transitions. In: Vidal C, Pacault A, editors. *Non-Equilibrium Dynamics in Chemical Systems - Proceedings of the International Symposium*. Bordeaux (1984). doi: 10.1007/978-3-642-70196-2_14
18. Ortoleva P, Merino E, Moore C, Chadam J. Geochemical self-organization I: reaction-transport feedbacks and modeling approach. *Am J Sci.* (1987) **287**:979–1007. doi: 10.2475/ajs.287.10.979
19. Karsenti E. Self-organization in cell biology: a brief history. *Nat Rev Mol Cell Biol.* (2008) **9**:255–62. doi: 10.1038/nrm2357
20. Taylor AF, Tinsley MR. Chemical self-organization: a path to patterns. *Nat Chem.* (2009) **1**:340–1. doi: 10.1038/nchem.310
21. Parteli EJR, da Silva LR, Andrade Jr JS. Self-organized percolation in multi-layered structures. *J Stat Mech.* (2010) **2010**:p03026. doi: 10.1088/1742-5468/2010/03/p03026
22. Machel HG. Concepts and models of dolomitization: a critical reappraisal. *Geol Soc Lond Spec Pub.* (2004) **235**:7–63. doi: 10.1144/GSL.SP.2004.235.01.02
23. Gottstein G, Shvindlerman LS. Theory of grain boundary motion in the presence of mobile particles. *Acta Metall Mater.* (1993) **41**:3267–75. doi: 10.1016/0956-7151(93)90056-X
24. Davis NE, Newman J, Wheelock PB, Kronenberg AK. Grain growth kinetics of dolomite, magnesite and calcite: a comparative study. *Phys Chem Miner.* (2011) **38**:123–38. doi: 10.1007/s00269-010-0389-9
25. Evans B, Renner J, Hirth G. A few remarks on the kinetics of static grain growth in rocks. *Int J Earth Sci.* (2001) **90**:88–103. doi: 10.1007/s005310000150
26. Urai JL, Means WD, Lister GS. Dynamic recrystallization of minerals. In: Hobbs BE, Heard HC, editors. *Mineral and Rock Deformation: Laboratory Studies: The Paterson Volume*. American Geophysical Union (1986). pp. 161–200. doi: 10.1029/GM036p0161
27. Bons PD, Jessell MW, Evans L, Barr T, Stüwe K. Modelling of anisotropic grain growth in minerals. In: *Tectonic Modeling: A Volume in Honor of Hans Ramberg* . Vol. 193 . Geological Society of America Memoirs (2000). pp. 1–11.
28. Lasaga AC. *Kinetic Theory in the Earth Sciences*. Princeton: Princeton University press (1998). doi: 10.1515/9781400864874
29. Koehn D, Arnold J, Jamtveit B, Malthe-Sørenssen A. Instabilities in stress corrosion and the transition to brittle failure. *Am J Sci.* (2003) **303**:956–71. doi: 10.2475/ajs.303.10.956
30. Koehn D, Renard F, Toussaint R, Passchier CW. Growth of stylolite teeth patterns depending on normal stress and finite compaction. *Earth Planet Sci Lett.* (2007) **257**:582–95. doi: 10.1016/j.epsl.2007.03.015
31. Bons PD, Jessell MW, Becker J. Grain boundary migration. In: Bons PD, Koehn D, Jessell M, editors. *Microdynamics Simulation*. Berlin; Heidelberg: Springer (2008). pp. 115–26. doi: 10.1007/978-3-540-44793-1
32. Hwang NM. Simulation of the effect of anisotropic grain boundary mobility and energy on abnormal grain growth. *J Mater Sci.* (1998) **33**:5625–9. doi: 10.1023/A:1004472400615
33. Freund D, Rybacki E, Dresen G. Effect of impurities on grain growth in synthetic calcite aggregates. *Phys Chem Miner.* (2001) **28**:737–45. doi: 10.1007/s002690100196
34. Mas DL, Crowley PD. The effect of second-phase particles on stable grain size in regionally metamorphosed polyphase calcite marbles. *J Metamorph Geol.* (1996) **14**:155–62. doi: 10.1046/j.1525-1314.1996.05805.x
35. Olgaard DL, Evans B. Effect of second-phase particles on grain growth in calcite. *J Am Ceram Soc.* (1986) **69**:C-272–7.
36. Nes E, Ryum N, Hunderi O. On the Zener drag. *Acta Metall.* (1985) **33**:11–22. doi: 10.1016/0001-6160(85)90214-7
37. Brimhall JL, Klein MJ, Huggins RA. Influence of a finely dispersed second phase on recrystallization. *Acta Metall.* (1966) **14**:459–66. doi: 10.1016/0001-6160(66)90313-0
38. Harun A, Holm EA, Clode MP, Miodownik MA. On computer simulation methods to model Zener pinning. *Acta Mater.* (2006) **54**:3261–73. doi: 10.1016/j.actamat.2006.03.012
39. Shelton RK, Dunard DC. Computer modeling of particle pushing and clustering during matrix crystallization. *Acta Mater.* (1996) **44**:4571–85. doi: 10.1016/1359-6454(96)00082-1
40. Urai JL, Jessell M. Recrystallization and grain growth in minerals: recent developments. In: Gottstein G, Molodov D, editors. *Recrystallization and Grain Growth, Proceedings of the first Joint International Conference, RWTH Aachen*. Aachen: Springer Verlag (2001). pp. 87–96.
41. Weygand D, Bréchet Y, Lépinoux J. Inhibition of grain growth by particle distribution: effect of spatial heterogeneities and of particle strength dispersion. *Mater Sci Eng A* (2000) **292**:34–9. doi: 10.1016/S0921-5093(00)00990-4
42. Warren J. Dolomite: occurrence, evolution and economically important associations. *Earth Sci Rev.* (2000) **52**:1–81. doi: 10.1016/S0012-8252(00)00022-2

43. Spangenberg JE, Macko SA. Organic geochemistry of the San Vicente zinclead district, eastern Pucará Basin, Peru. *Chem Geol.* (1998) **146**:1–23. doi: 10.1016/S0009-2541(97)00158-7
44. Spangenberg JE, Fontboté L, Macko SA. An evaluation of the inorganic and organic geochemistry of the San Vicente mississippi valley-type zinc-lead district, central Peru; implications for ore fluid composition, mixing processes, and sulfate reduction. *Econ Geol.* (1999) **94**:1067–92. doi: 10.2113/gsecongeo.94.7.1067
45. Gautelier M, Oelkers EH, Schott J. An experimental study of dolomite dissolution rates as a function of pH from -0.5 to 5 and temperature from 25 to 80°C. *Chem Geol.* (1999) **157**:13–26. doi: 10.1016/S0009-2541(98)00193-4
46. Clark SPJ. *Handbook of Physical Constants*. New York, NY: Geological Society of America (1966).
47. Austen KF, Wrigth K, Slater B, Gale JD. The interaction of dolomite surfaces with metal impurities: a computer simulation study. *Phys Chem Chem Phys.* (2005) **7**:4150–6. doi: 10.1039/b510454h
48. Chadam J, Hoff D, Merino E, Ortoleva P, Sen A. Reactive infiltration instabilities. *J Appl Math.* (1986) **36**:207–21. doi: 10.1093/imamat/36.3.207
49. Moelans N, Blanpain B, Wollants P. Phase field simulations of grain growth in two-dimensional systems containing finely dispersed second-phase particles. *Acta Mater.* (2006) **54**:1175–88. doi: 10.1016/j.actamat.2005.10.045
50. Jessell MW, Kostenko O, Jamtveit B. The preservation potential of microstructures during static grain growth. *J Metamorph Geol.* (2003) **21**:481–91. doi: 10.1046/j.1525-1314.2003.00455.x

Conflict of Interest Statement: The authors declare that the research was conducted in the absence of any commercial or financial relationships that could be construed as a potential conflict of interest.

List of Symbols

A	Grain area
A_{av}	Average grain area
A_{max}	Maximum grain area
c	Concentration of specimen
c_0	Concentration
c_1	Concentration
$C'(m)$	Modelling constant
c_γ	Surface energy factor
$C_{1/2}$	Modelling parameter
C_A	Concentration of specimen in fluid
C_A^{eq}	Equilibrium concentration of specimen
d_p	Initial grain size
D_c	Diffusion coefficient
D_r	Dissolution rate
f	Volume fraction of particles
k_r	Steady-state dissolution constant of dolomite
K_0	Rate constant
K_{eq}	Equilibrium constant
m	Grain boundary mobility
m_p	Amount of second-phase particles
n_p	Number of particles
No	Number of grains
r	Radius of curvature
r_{crit}	Critical particle radius
r_P	Radius of particle
R	Ideal gas constant 8.314 $\frac{J}{mol \cdot K}$
R_{gb}	Particle-grain-boundary interaction zone
S	Solution of equation
t	Time
T	Temperature
v_{crit}	Critical grain boundary velocity
v_D	Darcy velocity
v_{gb}	Velocity of grain boundary
V_S	Molar volume
α	Angle between c-axes and grain boundary
γ	Surface free energy
κ	Permeability
ϕ	Porosity
Θ	Angle between tangent of grain boundary and particle surface
ΔG	Gibbs Potential
$\Delta \Psi$	Helmholtz potential
$\Delta \Psi_S$	Pressure gradient
ΔP_n	Change in normal pressure on surface

frontiers in Physics

ORIGINAL RESEARCH
published: 02 October 2015
doi: 10.3389/fphy.2015.00081

Invasion patterns during two-phase flow in deformable porous media

Fredrik K. Eriksen[1,2]*, *Renaud Toussaint*[1], *Knut J. Måløy*[2] and *Eirik G. Flekkøy*[2]

[1] *Institut de Physique du Globe de Strasbourg, Université de Strasbourg/EOST, Centre National de la Recherche Scientifique, Strasbourg, France,* [2] *Department of Physics, University of Oslo, Oslo, Norway*

We study the formation of viscous fingering and fracturing patterns that occur when air at constant overpressure invades a circular Hele-Shaw cell containing a liquid-saturated deformable porous medium—i.e., during the flow of two non-miscible fluids in a confined granular medium at high enough rate to deform it. The resulting patterns are characterized in terms of growth rate, average finger thickness as function of radius and time, and fractal properties. Based on experiments with various injection pressures, we identify and compare typical pattern characteristics when there is no deformation, compaction, and/or decompaction of the porous medium. This is achieved by preparing monolayers of glass beads in cells with various boundary conditions, ranging from a rigid disordered porous medium to a deformable granular medium with either a semi-permeable or a free outer boundary. We show that the patterns formed have characteristic features depending on the boundary conditions. For example, the average finger thickness is found to be constant with radius in the non-deformable (ND) system, while in the deformable ones there is a larger initial thickness decreasing to the ND value. Then, depending on whether the outer boundary is semi-permeable or free there is a further decrease or increase in the average finger thickness. When estimated from the flow patterns, the box-counting fractal dimensions are not found to change significantly with boundary conditions, but by using a method to locally estimate fractal dimensions, we see a transition in behavior with radius for patterns in deformable systems; In the deformable system with a free boundary, it seems to be a transition in universality class as the local fractal dimensions decrease toward the outer rim, where fingers are opening up like fractures in a paste.

Keywords: two-phase flow, drainage, deforming porous media, viscous fingering, fracturing

OPEN ACCESS

Edited by:
Antonio F. Miguel, University of Evora, Portugal

Reviewed by:
Sujata Tarafdar, Jadavpur University, India
Christopher William MacMinn, University of Oxford, UK

***Correspondence:**
Fredrik K. Eriksen, Institut de Physique du Globe de Strasbourg, 5 Rue René Descartes, 67084 Strasbourg Cedex, France
eriksen@unistra.fr

Specialty section:
This article was submitted to Interdisciplinary Physics, a section of the journal Frontiers in Physics

Received: *03 June 2015*
Accepted: *18 September 2015*
Published: *02 October 2015*

Citation:
Eriksen FK, Toussaint R, Måløy KJ and Flekkøy EG (2015) Invasion patterns during two-phase flow in deformable porous media. Front. Phys. 3:81. doi: 10.3389/fphy.2015.00081

Introduction

Multi-phase flow in porous and granular materials are complex processes in nature and industry, and the understanding of the involved mechanisms is an ongoing challenge. In early research on the flow of two immiscible fluids in thin cells (Hele-Shaw cells), it was found that the invasion by a less viscous fluid into a more viscous fluid results in a displacement instability where viscous fingering patterns form [1]. This means that the invading fluid displaces the more viscous one in separated finger-like intrusions, while leaving the fluid inbetween the fingers less or not displaced. Following an increased interest in this phenomenon, two-phase flow have been widely studied in quasi-2-dimensional porous media confined in thin cells with circular and rectangular geometries [2–14]. In horizontal cells containing rigid disordered porous media,

the unstable invasion patterns during drainage are found to be fractal and either form an invasion percolation cluster [15] in the capillary fingering regime [16, 17], or long thin fingers resembling DLA patterns in the viscous fingering regime [18, 19]. The flow regime during drainage of a horizontal porous medium is dependent on the ratio between the driving and stabilizing forces involved in flow and pore-invasion, usually described by the dimensionless capillary number Ca [3, 5]. The capillary number is the ratio of viscous pressure drop over capillary pressure drop at the characteristic pore scale, and can be found by

$$Ca = \frac{\mu v a^2}{\gamma \kappa}, \tag{1}$$

where μ is the viscosity of the saturating fluid, v is a characteristic velocity (flux/injection cross section), a is the bead diameter, γ is the interface tension between the invading and defending fluid and κ is the permeability of the porous medium. For low capillary numbers ($Ca \ll 1$) capillary fingering dominates and for higher capillary numbers ($Ca \rightarrow 1$) there is a crossover to viscous fingering. The stabilizing mechanism is provided by a network of capillary pressure thresholds situated at the pore-necks along the fluid-fluid interface. The capillary thresholds arise from the surface tension γ between the immiscible fluids and is described by

$$p_{cap} = \frac{\gamma}{R_1} + \frac{\gamma}{R_2}, \tag{2}$$

where R_1 and R_2 are the smallest possible radii of curvature for the interface meniscus in the vertical and horizontal directions. In a perfect wetting situation, the radii are half the height of the pore-neck and half the width of the pore-neck. The capillary pressure thresholds at each pore is thus determined by the pore geometry. The consequence of Equation (2) is that the pressure difference dP between the invading and saturating fluids has to overcome a certain threshold before a given pore is invaded, i.e., $dP > p_{cap}$. At low enough capillary numbers, at very low constant injection flow, we will see pore-by-pore invasions where the fluid takes the path of least resistance (larger pores have lower thresholds), leaving some pores trapped and/or never invaded. At higher capillary numbers, flow may be driven on a sample scale by a viscous pressure gradient over the saturating fluid. The filtration velocity (interstitial fluid velocity times the porosity) v through a porous medium with permeability κ is described by Darcy's law as

$$v = -\frac{\kappa}{\mu}\nabla P \approx \frac{\kappa}{\mu}\frac{\Delta P}{r}, \tag{3}$$

where μ is the viscosity of the saturating fluid, ΔP is the pressure difference between the invading fluid and the cell outlet, and r is the distance from the invading fluid to the cell outlet. At high enough capillary numbers, since the pressure can be considered constant within the invading fluid cluster [19], Equation (3) shows that the parts of the cluster that are closer to the outside of the cell flow faster than less advanced parts. In addition, the pressure distribution is given by the Laplace equation ($\nabla^2 P = 0$) such that the longest fingers are "screening" the pressure gradient from the less advanced fingers [19]. Due to this instability and the geometry of the pore-space, an invasion bubble will become perturbed early and we will see the onset of viscous fingers from the most advanced parts of the interface, growing on expense of the less advanced parts. In addition, the flow path of fingers is influenced by random capillary thresholds at the interface.

In similar systems where air is injected with high enough overpressure into dry and dense deformable porous media in thin cells, granular fingering patterns emerge as a result of hydraulic fracturing of the dense packing [20–24]. This granular fingering is also observed in liquid saturated dense porous media where the same fluid is injected [25]. An interesting observation in these cases is that despite the absence of surface tension, the granular fingering patterns resemble viscous fingering. This fingering formation is driven by momentum exchange between the flowing fluid and particles, and becomes unstable like viscous fingers when the fluid-solid interface is perturbed. The stabilizing mechanism during granular fingering was found to be particle-particle and particle-plate friction, which builds up in stress-chains during compaction of the multi-layered packing and prevents further particle displacement.

Moreover, combinations of two-phase and granular flow in thin cells have been studied. In e.g., [26–28] it was found that a range of different patterns emerge when air is injected in granular suspensions in thin cells. Invasion patterns such as frictional fingering, viscous fingering, fluidized fronts and stick-slip bubbles were observed depending on bead fraction and injection rate. The resulting patterns depend on whether the invading fluid overcomes frictional or capillary thresholds first, i.e., bead displacement occurs when the capillary threshold is highest and pore-invasion when the frictional threshold is highest. Experiments with air injection into saturated deformable porous media placed under a confining pressure was studied in Holtzman et al. [29]. For a given interface tension γ and friction coefficient μ_f, the crossover from fingering to fracturing during constant flow rates was found to depend only on the confining pressure P_c and particle size d, and that fracturing tends to occur if the particle size is below a critical value $d_c = (\gamma/\mu_f){P_c}^{-1}$. In other words, opening of pore-necks and fracturing was observed when capillary forces could overcome frictional thresholds and rearrange particles. Flow induced deformation in a monolayer of deformable porous media has also been studied in the absence of surface tension, during fluid injection into a soft granular media saturated with the same fluid [30]. During injection, the beads were observed to be displaced radially outwards due to the pressure gradient in the flow, and an empty cavity formed around the injection center. In these experiments, no fingers emerged and the central cavity stabilized at a certain size since the beads were confined within the cell.

In this paper we present an exploratory study where we further experiment with the combination of two-phase and granular flows by performing air injection into saturated monolayers of beads. It is part of fundamental research on pattern morphology in various deforming systems, which is important for increased understanding of flow in any deformable porous medium.

By injecting air at a constant overpressure into a deformable saturated monolayer, we have a system where particles may be displaced by a viscous pressure gradient and/or capillary forces between the two fluids. Since it is a single layer of beads without imposed confining pressure, granular stress is expected to depend on the boundary condition and number of particles in contact ahead of the flow, rather than build-up of normal stress against the plates. The outer boundary can be set to either allow or prevent decompaction of the medium. As a result of competition between viscous and capillary forces, and build-up/relaxation of friction during flow, we expect to see transitions between finger opening and pore invasion in the viscous fingering regime, for example during initial compaction or outer decompaction. We aim to characterize these flow patterns and porous media deformations, depending on imposed boundary conditions and injection pressure.

Increased knowledge of the mentioned processes may have applications in earth science and industry where multiphase flow and solid deformation occur. Examples are oil and gas production [31–33], carbon sequestration [34], enhancement of water well- and geothermal energy production [35–37]. There may also be applications in natural flow, especially in the field of subsurface sediment mobilization, where formations like sand injectites, mud diapirs, and mud volcanoes occur due to pore-fluid overpressure [38–43].

Materials and Methods

Three different types of porous media samples are created by preparing them with the different boundary conditions referred to as non-deformable (ND), confined deformable (CD), or open deformable (OD). These three sample types are presented after a brief introduction to the general experimental setup which is common for all the experiments.

Experimental Setup

In general, the porous samples are created by forming a single layer of 1.0 mm diameter glass beads between the transparent plates of a horizontal and circular Hele-Shaw cell. The bead size has a tolerance of ±10%, but beads are sifted, resulting in a distribution between 1.0 and 1.1 mm. The diameter of the cell is 40 cm, and the 10 mm thick plates are clamped together with a vertical plate separation of 1.0 mm in the ND case and 1.4 mm in the deformable cases. This setup results in obtained volume fractions of 32.7 ± 0.9% beads in the ND cell, and 29.4 ± 1.8% beads in the cell for the deformable systems. If we only consider the volume occupied by the monolayers, the deformable systems have $\sim 10^5$ beads with a volume fraction that is 68.2 ± 4.2% of η_{hcp}, where $\eta_{hcp} = 60.5\%$ is the volume fraction of the densest possible bead configuration in the cell if the plate separation is 1.0 mm (i.e., a hexagonal close packing with $\sim 1.45 \cdot 10^5$ beads). The ND systems have $\sim 8 \cdot 10^4$ beads and a volume fraction that is 54.2 ± 1.4% of η_{hcp}. The reason for the different monolayer volume fractions arise from the different filling procedures for the ND and CD/OD systems, which are described in the next section. The fluid inlet to the sample is a 10 mm diameter hole in the center of the bottom disk, and the outlet is the open perimeter along the rim of the cell. After a sample is prepared, its pore-space is saturated with a viscous water-glycerol solution consisting of 20% water and 80% glycerol by mass, with a viscosity of 0.045 Pa·s. The saturating fluid is wetting the beads as well as the cell disks. **Figure 1** shows a cross-sectional illustration of the experimental setup.

The experimental procedure is also common for all the sample types; the air overpressure to be applied at the cell inlet is pre-set with a pressure regulator situated between a pressurized air reservoir and the cell inlet. The experiment starts when the inlet valve is opened, allowing air to invade the sample with a maintained and constant overpressure. As the overpressure is kept constant at a pressure in the range from 25 to 100 hPa (hPa = mbar), the air cluster will grow and drain the sample radially outwards until it breaks through at the rim. Breakthrough of the air cluster was seen in all our experiments and marks the end of the experiment. The cell is illuminated by flicker free white light from below, and a Photron SA5 high-speed camera positioned above the cell captures optical data at a framerate of 125 frames per second (fps) during the experiment.

Three Cases of Boundary Conditions

The porous matrix of a ND sample is rigid, single-layered and disordered. This sample type is prepared on the bottom disk before assembling the cell; first, the top surface of the bottom disk is coated with an adhesive, thin and transparent plastic film. Then, beads are poured onto the adhesive surface, which will cause them to attach at random positions on the bottom disk. The process is continued until no more beads are able to hit the bottom disk surface, i.e., when the longest distance between

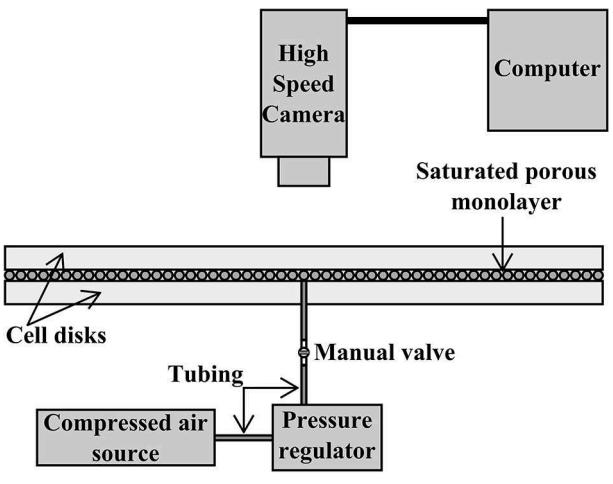

FIGURE 1 | Sketch of the experimental setup for the two-phase flow experiments: The horizontal cell consists of **two** transparent disks of 40 cm in diameter, clamped together (not shown) but separated by a small gap. The gap is big enough to accommodate a saturated porous monolayer of 1.0 mm beads. This sketch represents the non-deformable system, however the setup is the same for the other boundary conditions as well. A compressed air source is connected to an injection hole in the center of the bottom disk, and a pressure regulator is used to adjust the constant injection pressure between 25 and 100 hPa. During air injection, the high speed camera situated directly above the cell captures the invasion at a framerate of 125 frames per second.

beads in the monolayer is shorter than a bead diameter. Pores that are slightly smaller than a bead can occur, so this filling procedure generates a rather loose packed random layer. After removing excess beads of a beginning second layer, the top disk, also adhesive, is put onto the resulting monolayer and clamped together with the bottom disk. The disk separation therefore equals the bead diameter of 1.0 mm.

The porous matrix of a CD sample is a random close packed monolayer of beads which can be displaced within the cell volume, but are prevented to leave the cell by a semi-permeable border. This sample type is prepared partially before and after assembling the cell. First, the rim of the bottom disk is fitted with a semi-permeable belt made of foam rubber (it can be seen in **Figure 2A**). This belt, which is permeable to fluids and impermeable to beads, is 5 mm wide. Next, the top disk is placed onto the bottom disk and they are clamped together. The disk separation is controlled with 1.4 mm thick spacers between the disks at the clamp positions, and ensures the possibility of bead displacement as well as keeping the bead packing approximately single-layered. The gap above the beads (0.4 mm) is still smaller than the large interparticle nearest distance in the system (1 mm), and we observed no significant invasion occurring over several bead lengths in the gap above the beads. When clamped between the plates, the semi-permeable belt with an elastic stiffness of 1.5 kPa is imposed a 47% compressive strain, and has an estimated permeability of 10^{-5} cm^2. Finally, beads are injected into the cell through the central injection hole until they form a monolayer that fills the confined volume. Since the beads may rearrange during the filling procedure, this method results in a more close packed random layer than achieved with the ND method.

The OD sample is prepared in the same way as the CD sample, but with a temporary semi-permeable border at the rim which is removed before experiments. This means that the OD porous matrix is a deformable monolayer where the beads can be displaced and also pushed out of the cell at the open perimeter. Thus, on one side of the scale we have the ND boundary condition where nothing is deformed in the porous medium, and on the other end of the scale we have the OD boundary condition where most of or all of the sample is deformed. Somewhere in between we have the CD boundary condition.

Performed Experiments

Ten experiments are considered in this study. They lasted between 0.9 and 9.7 s, where two of them were ND, four were CD and four were OD. The two ND experiments, used as reference for no deformation, were both injected with an air overpressure of 25 hPa and are labeled ND1 and ND2. Patterns in this system will appear similar for higher injection pressures since we already are in the viscous fingering regime. The CD experiments are referred to as CD25, CD50, CD75, and CD100 since the injection pressures were set as 25, 50, 75, and 100 hPa, respectively. The injection pressures in the OD experiments were selected in the same way, so these experiments are referred to as OD25, OD50, OD75, and OD100. Approximate capillary numbers Ca were calculated for each experiment, based on the equation

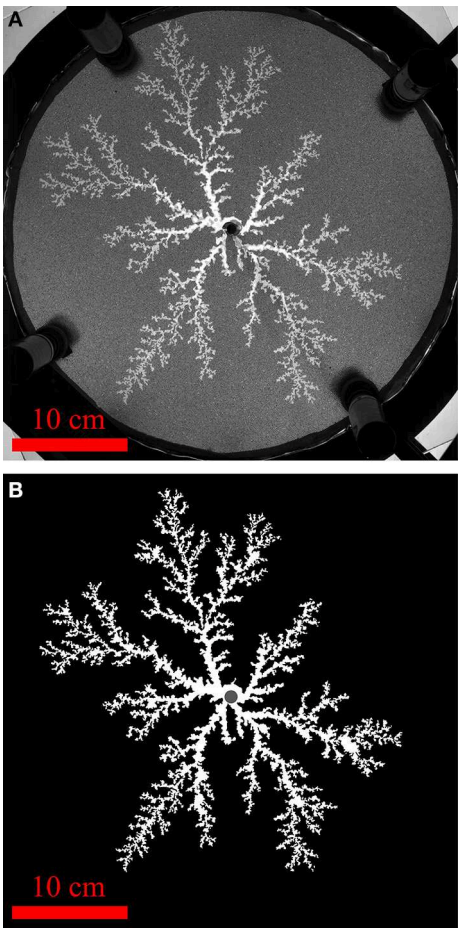

FIGURE 2 | The raw data breakthrough image of the confined deformable experiment with 75 hPa injection pressure (A), and the resulting binary image after segmentation of the air cluster (B), where the active pixels belonging to the cluster is shown in white and the inactive background pixels are shown in black. The dark injection region where it is difficult to separate saturated and invaded parts is indicated in gray, and is excluded from our analysis. In the raw data image we can also see the 0.5 cm thick semi-permeable belt surrounding the porous medium.

$$Ca = \frac{\Delta P a^2}{\gamma R}, \tag{4}$$

which is obtained by combining Equations (1) and (3), where $a = 1$ mm is the typical pore size, $\gamma = 65.7$ μN/mm is the interfacial tension between the fluids, $R = 20$ cm is the cell radius and ΔP is the imposed overpressure. The approximate capillary numbers are found to be $Ca = 0.2$, 0.4, 0.6, and 0.8 for $\Delta P = 25$, 50, 75, and 100 hPa, respectively, and independent of boundary conditions. These capillary numbers confirm that the displacement flow in all our experiments is dominated by viscous forces (viscous fingering regime), as seen in e.g., Løvoll et al. [3] for $Ca = 0.22$. A characteristic permeability for the systems is estimated with the Kozeny-Carman relation [27],

$$\kappa = \frac{a^2 \phi^3}{180(1-\phi)^2}, \tag{5}$$

where a is the bead diameter and ϕ is the porosity. For the ND system with a porosity of 0.673, we get $\kappa = 1.22{\cdot}10^{-4}$ cm^2, and for the deformable systems with a porosity of 0.706 we get $\kappa = 2.26{\cdot}10^{-4}$ cm^2 (initially, before deformation). In the CD system, the permeability of the outer belt is one order of magnitude lower than the initial permeability of the porous medium, however we observed no significant influence on the flow regime due to that. For a characteristic filtration velocity, the pressure drop along a distance L is given by $\Delta P = \mu v L/\kappa$. Even if κ is smaller in the belt than in the cell, its extent L along the flow is much smaller than the radius of the cell. Thus, the characteristic pressure drop, which scales like L/κ, is much larger in the cell than in the belt—explaining why it does not seem to significantly affect the pattern.

The raw data from each experiment is a sequence of grayscale images with a spatial resolution of 1024 × 1024 pixels, where the side of one pixel corresponds to 0.4 mm. The framerate yields high temporal resolution with a snapshot every 8 ms, and each image contains information about the instantaneous configuration of the air cluster and the porous medium. A raw data snapshot is shown in **Figure 2A**.

Flow Pattern Analysis

The raw images are transformed into binary images of the air clusters, i.e., every pixel being a part of the air cluster, defined as having an intensity value above a certain threshold, is given the pixel-value "1" (white) while all the other pixels are assigned the pixel-value "0" (black). An example is shown in **Figure 2B**. In the images of ND experiments, beads have been removed by subtracting the graymap field of the initial image from the graymap field of the current image - a process called image subtraction technique (as e.g., in Løvoll et al. [3], Niebling et al. [12]). Later on, trapped liquid clusters within fingers are replaced by white pixels, considering them as parts of the finger. In the images of deformable experiments, beads have been removed by deleting small white clusters not connected to the large white pattern. A dark central region of 10 mm in diameter is caused by shadow from the injection tubing, so image data here is not considered (the air cluster cannot be distinguished from the liquid). There are different features of the flow patterns that we want to analyze, such as their shape, growth, and fractal dimension. This information is obtained from the binary images with various image processing methods.

To get a visual overview of the shape and growth of a flow pattern over time we create a figure of the breakthrough pattern where colors indicate the time when a pixel was invaded by air. Such a figure is made by summing together all the binary images in the sequence (obtained as explained above), creating a matrix where the elements indicate the number of timesteps during which the considered pixel has been invaded: A value more than 1 means that invasion occurred earlier than breakthrough, 1 is at breakthrough and 0 means that this pixel is never invaded. This matrix is then converted to a figure where colors represent the time of invasion at each pixel of the air cluster, and shown in **Figure 3** for each of the experiments.

In addition to a visual characterization of the patterns, we obtain some quantities to describe the growth of the clusters over time. To investigate the growth of the clusters we plot the radius of the most advanced finger and the radial variation of finger thicknesses as function of time. The longest finger radius as function of time is found by assigning values to the pixels in the binary patterns according to their distance from the injection center, and then record the highest value of each image in the sequence. For the investigation of radial finger thickness variation we look at the average finger thickness as a function of radius from the injection center. This is found by counting the number of active pixels within a small window (plus minus one pixel) around each integer radius, giving the total sum of finger widths per radius. These values are then divided by the corresponding number of fingers per radius (the number of active pixel-segments at each radius), giving the average finger thickness per radius.

Fractal analysis is a commonly used method to describe a two-phase flow pattern since its fractal dimension, when it exists, reveals information about how the pattern fills the space it occupies. There are different ways to estimate the fractal dimension of a pattern [44, 45]. We will look at the mass- and box fractal dimensions, and compare them with local fractal dimensions of intersections at different radii. The mass-radius relation of a pattern is found by counting the number of active pixels (mass) contained within each radius from the injection center. If the log-log plot of the mass-radius relation is linear, such that it follows a power law

$$N(r) \propto r^{D_m}, \tag{6}$$

the fractal mass-dimension D_m of the pattern is found as the slope of the plot. Figure A1 in the Supplementary Material shows the mass-radius relations for the breakthrough patterns from each experiment. The fractal box-dimension of a pattern is estimated by counting the number of squares needed to cover the pattern as a function of the side length of the square. As boxes we use grids of equal squares, where the pattern center is always in the center of a square. Starting with a square larger than the image size, a box count is performed before decreasing the box size. This is repeated until the smallest square covering the entire pattern is found. Then, the smallest box covering the entire pattern is divided into equal but increasingly smaller squares for each box count. The procedure of subsequent box size decreasing and counting is continued until the lower size limit of one pixel is reached. For a fractal, the number of boxes N as function of side length l follows a power law

$$N(l) \propto l^{-D_b}, \tag{7}$$

The value of the fractal box-counting dimension D_b is found as the opposite of the slope of the number of boxes as function of side length in a log-log plot. The slope is fitted between the lower box size cutoff at 1 mm (typical pore size), and the upper cutoff at the largest box size where at least one box does not cover the pattern. Figure A2 in the Supplementary Material shows these plots for each experiment. Finally, a local fractal dimension D_L is estimated as function of radius by intersecting the pattern with a one pixel thick, concentric ring at each radius and do

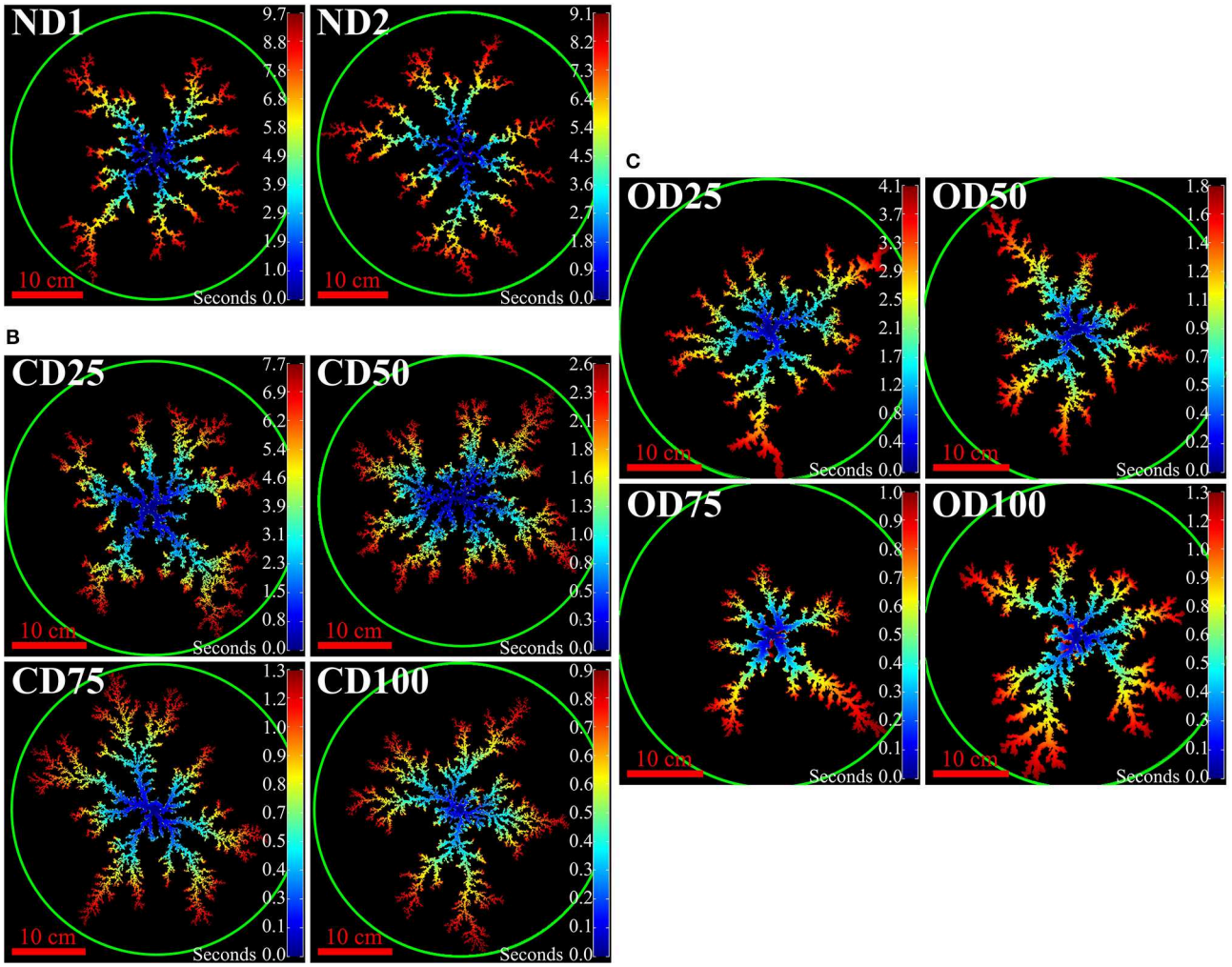

FIGURE 3 | Breakthrough patterns for the non-deformable experiments (A), confined deformable experiments (B), and open deformable experiments (C). Both ND experiments have an injection pressure of 25 hPa, while for the CD and OD experiments the number in the experiment name (top left corners) gives the injection pressure in hPa. The color code indicates the time of air invasion in seconds after start, where blue is at the start and dark red is at breakthrough. The green circles indicate the cell rims.

1-dimensional box counts along the rings. At each radius, the ring is divided into equal arc segments and the number of arc segments that intersect the pattern are counted as function of arc length as the arc length is decreased. The number of arc segments intersecting the pattern is plotted in a log-log plot as a function of arc length, and we find the local fractal dimension as the opposite of the value of the slope as shown in **Figure 4**. The local dimension slopes have one upper and one lower cutoff length at each radius. The upper cutoff length is approximately the separation distance between fingers along the ring, and the lower cutoff length is approximately the average thickness of the fingers. We set the lower cutoff constant as the average finger thickness for the ND patterns, which is found to be approximately 0.4 cm (see Section Pattern Characteristics). The upper cutoff length is set at each radius as the maximum arc length where at least one of the arc segments does not intersect the pattern and is not counted. It is assumed that the flow patterns have an isotropic pattern morphology such that the local fractal dimensions are independent on the angular offset of the arcsegment cuts. In order to compare D_L with D_m and D_b we use Mandelbrot's rule of thumb for intersecting fractal sets [46, 47]. It states that the codimension of a set of intersection points equals the sum of codimensions of the individual intersecting sets. In our case, in the image plane (with dimension $E = 2$), the intersecting sets are the air cluster of codimension 2-D and a ring of codimension 2-1. This gives

$$\begin{aligned} (2 - D) + (2 - 1) &= 2 - D_L \\ \Downarrow& \\ D &= D_L + 1, \end{aligned} \tag{8}$$

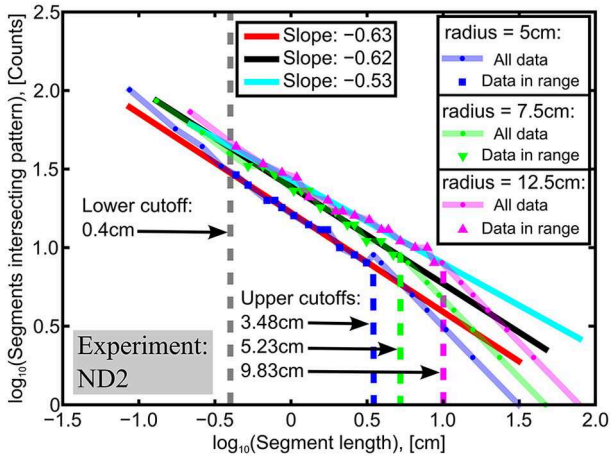

FIGURE 4 | Results of 1-dimensional box counts of the ND2 pattern along a radius of 5, 7.5, and 12.5cm. The slopes that are used to determine the local fractal dimension are fitted to the data points in the range between the lower cutoff of 0.4cm (average finger width) and the upper cutoffs where the pattern appears space filling (indicated by arrows). We see that the upper cutoff, which is approximately the separation between fingers, increase for increasing radius. Local dimension as function of radius is found as the negative value of such slopes, estimated at each pixel radius (approximately every 0.04 cm) outside the injection region. However, at radii where there are <10 data points between cutoffs, the local dimensions are not included for analysis.

where D is the fractal dimension of the pattern and D_L is the local fractal dimension. In a physical view, if the mass within a circle of thickness dr is given by $dr{\cdot}\alpha(2\pi r)^{D_L}$ where α is a constant pre-factor, the total mass inside a radius R is given by

$$N(R) = \alpha \cdot (2\pi)^{D_L} \int_0^R r^{D_L} dr = \frac{\alpha \cdot (2\pi)^{D_L}}{(D_L + 1)} \cdot R^{D_L+1} \propto R^{D_L+1}, \tag{9}$$

if D_L is independent of r. For a perfect fractal cluster $N(R) \sim R^D$, so if $D_L(r)$ is constant we have a perfect fractal with fractal dimension $D = D_L + 1$.

Deformation Analysis

We quantify the deformation of a porous medium by processing the sequence of raw images with a Digital Image Correlation (DIC) software called Ncorr, which by cross-correlation of subsequent frames estimates both direction and magnitude of bead displacements. Closer discussions of this DIC algorithm is found in Blaber et al. [48], Hariral et al. [49]. A qualitative assessment of deformations in the different sample types is done by comparing figures representing the porous media where values of radial displacement components at each pixel is represented by a color code. In addition, areas of compaction or decompaction are identified in figures where the volumetric strains ε_v are represented at each pixel. The volumetric strains are found by Vable [50]

$$\varepsilon_v = \varepsilon_{xx} + \varepsilon_{yy}, \tag{10}$$

assuming that $\varepsilon_{zz} = 0$ in the direction normal to the plates, corresponding to the fixed character of the side plates. The strains ε_{xx} and ε_{yy} at a pixel are estimated from the gradients of the displacement fields around that pixel. In order to reduce noise, least-squares fits are made to the displacement fields within an approximate 2 mm radius around the evaluated pixel, and the slopes of the fits are considered as the displacement gradients.

Results

Pattern Characteristics

The flow patterns from all ten experiments are shown in **Figure 3**, where the color of a pixel indicates the time taken from experiment start until the area of the pixel became invaded by air (For readers who wants a closer look, a larger image is included in the Supplementary Material). In **Figure 3A**, we see that the flow patterns in ND media have long and thin fingers, and the thickness of the fingers appears constant at all radii outside the injection center. The flow patterns in CD media are shown in **Figure 3B**, and they typically feature centrally few and thick fingers that cross over to thinner and more numerous fingers with increasing radius. For the flow patterns in OD media, shown in **Figure 3C**, we see centrally few and thick fingers that cross over to more numerous and thinner fingers at intermediate radii, which then cross back to few thick fingers near the cell outlet. The intermediate region where the fingers are thinner seems to decrease in length for increasing injection pressure. In all the systems the growth of fingers is mainly in the radial direction, favored on the finger tips, and more advanced fingers grow on expense of less advanced fingers.

Figure 5 shows plots of the longest finger radius as function of time for all the experiments, as well as breakthrough times as function of overpressure. The experiments and their breakthrough times are also listed in **Table 1**.

Both the ND experiments were performed with a constant injection pressure of 25 hPa, and we see that the time required to reach breakthrough of the air cluster is similar for both experiments. In the CD experiments we see that the time until breakthrough decreases for increasing injection pressure. This is also seen in the OD boundary condition, except for OD100 which breaks through slower than OD75. The patterns seem to grow with a roughly constant rate over time with some deviations, e.g., a faster growth rate initially for the CD25 and CD50 cases, and OD75 with an increasing growth rate in the second half of the experiment.

In **Figure 6**, plots of the average finger thickness as function of radius are shown in several snapshots during the experiments. For both the ND experiments in **Figure 6A** we see that, over time, the average finger thickness approaches a limiting curve with a more or less constant value around 0.4 cm. For the CD experiments in **Figure 6B** we again see the average finger thickness approach a limiting curve over time, but in this system there is a continuous decrease in average finger thickness with increasing radius. For the CD25, CD75, and CD100 breakthrough patterns the average finger thickness starts at 1.0–1.5 cm near the injection center and quickly decreases to the ND value of 0.4 cm. The CD50 breakthrough pattern already has

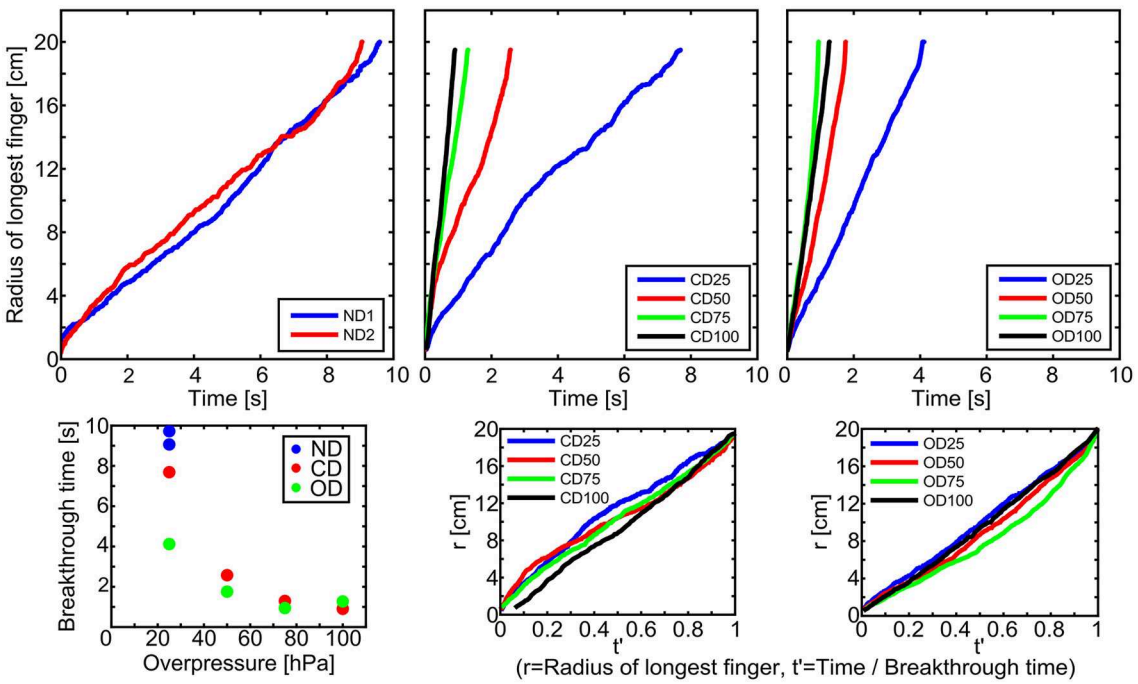

FIGURE 5 | Radius of longest finger as function of time for all the experiments, grouped by boundary condition. From top left to top right: non-deformable, confined deformable, and open deformable. The injection pressure in both ND experiments is 25 hPa, while the number in the experiment names for the CD and OD experiments gives the injection pressure in hPa. In the bottom plots below the deformable experiments, time is divided by breakthrough time to compare the shape of the curves, and the bottom left plot shows the breakthrough times as function of overpressure for all the experiments.

TABLE 1 | Breakthrough times for the experiments.

ND experiment	Breakthrough time [s]	CD experiment	Breakthrough time [s]	OD experiment	Breakthrough time [s]
ND1	9.7	CD25	7.7	OD25	4.1
ND2	9.1	CD50	2.6	OD50	1.8
		CD75	1.3	OD75	1.0
		CD100	0.9	OD100	1.3

an average finger thickness of 0.4 cm initially. However, for all the patterns, when the average finger thickness has decreased to 0.4 cm it will continue to decrease slowly toward 0.2 cm over the remaining radial length of the sample. In the plots for the OD experiments in **Figure 6C**, we also see that the average finger thickness approach a limiting curve over time. In this system, the limiting curves have initially larger average finger thicknesses which decrease and approach the ND constant value of 0.4 cm with increasing radius. Then, after remaining at a thickness of around 0.4 cm over an intermediate range, the average finger thickness increases again when approaching the cell rim. The intermediate range where the average finger thickness is similar to the ND flow patterns seems to decrease in size for increasing injection pressure.

The different fractal dimensions found for the breakthrough patterns are shown in **Figure 7**; **Table 2**.

Having used Equation (8), the local dimensions are plotted as $D_L(r) + 1$, and the mass dimensions D_m and box dimensions D_b are indicated as lines with uncertainties. The uncertainty intervals for the fractal dimensions are determined as the difference between the steepest and least steep slope that can be fit within a 95% confidence interval around the best fits in the log-log plots. In **Figure 7A**, we see that the ND1 and ND2 mass dimensions are virtually equal to their corresponding box dimensions since they have overlapping uncertainty intervals. The mass and box dimensions also correspond well with the local fractal dimensions according to Mandelbrot's rule of thumb, since $D_L(r) + 1$ fluctuates around the corresponding D_m and D_b values. A sharp decrease in local dimensions is seen close to the rim, and is due to finite size effects of the clusters. In **Figure 7B** we see the fractal dimensions found for the CD patterns. Except for the CD50 pattern where the mass dimension is equal to the box dimension within the uncertainties, the mass dimensions are significantly lower than the obtained box dimensions. The box dimensions correspond better to the local dimensions than the mass dimensions do. As for the ND patterns the CD25 and CD50

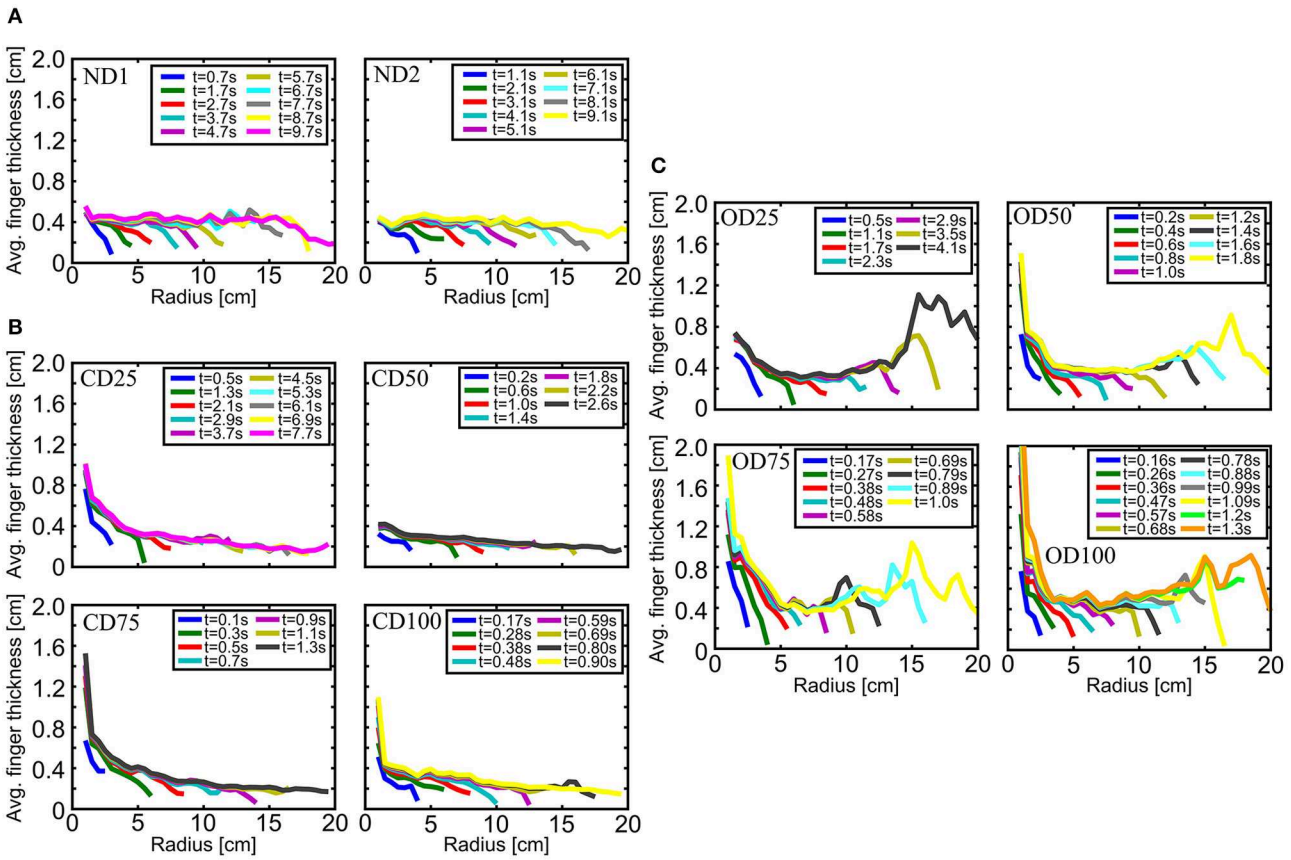

FIGURE 6 | Average finger thickness as function of radius plotted at several snapshots for the non-deformable experiments (A), confined deformable experiments (B), and open deformable experiments (C). The injection pressure in both ND experiments is 25 hPa, while the number in the experiment names for the CD and OD experiments gives the injection pressure in hPa.

local dimensions fluctuate around the box dimension values, before the outer finite size effects make the local dimensions decrease. For the higher injection pressures, CD75 and CD100, we see an inner region with higher local dimensions, before the local dimensions approach values fluctuating around the corresponding box dimensions, and finally decrease due to the finite size effects. The obtained dimensions for the OD breakthrough patterns are plotted in **Figure 7C**. All of the patterns show a decreasing trend in local dimensions for increasing radius. The mass dimensions are significantly lower than the obtained box dimensions, and the box dimensions seem to best correspond to the local dimensions for intermediate radii. Inner regions show higher local dimensions, with $D_L(r) + 1$ starting on 1.8–1.9, indicating emptier inner structures.

Figure 8A shows examples of mass-radius relations at several snapshots of growing clusters in each boundary condition. For the boundary conditions probed, the mass-radius relations are seen to grow toward a limiting curve over time. The flat regions seen at larger radii are outside the current pattern, and they give the total mass at that time. We check whether the mass dependence on time and radius can be collapsed onto a master curve according to a Family-Vicsek relationship [51]. Indeed, such a relationship is common in many growth phenomena, as e.g., in rough interface evolution during two-phase flow in Hele-Shaw cells [52], interface depinning models [53], fracture front growth [54] and thermal roughening of dipolar chains [55, 56]. **Figure 8B** shows Family-Vicsek scaling of the same mass-radius relations as in **Figure 8A**, and show how they scale over time. We have assumed that the total mass N and longest finger r of a pattern scales with time as

$$N(t) = N_b \cdot (t/t_b)^{\alpha} \quad , \quad r(t) = r_b \cdot (t/t_b)^{\beta}, \tag{11}$$

where N_b, r_b, and t_b are breakthrough values of mass, radius and time, respectively. It is a reasonable assumption once the fingering instability is established, i.e., after the patterns had grown to a mass of around 10% of N_b. The plots are shown in Figure A3 in the Supplementary Material. Since, in addition, the mass-radius relation is assumed to follow Equation (6), the scaled mass-radius relation should be on the form

$$\frac{N(r,t)}{N_b \cdot (t/t_b)^{\alpha}} = \left(\frac{r}{r_b \cdot (t/t_b)^{\beta}} \right)^{D_m}, \tag{12}$$

where D_m is the mass dimension of the pattern. We find the scaling exponent α from the slope of the log-log plot of $(N(t)/N_b)$

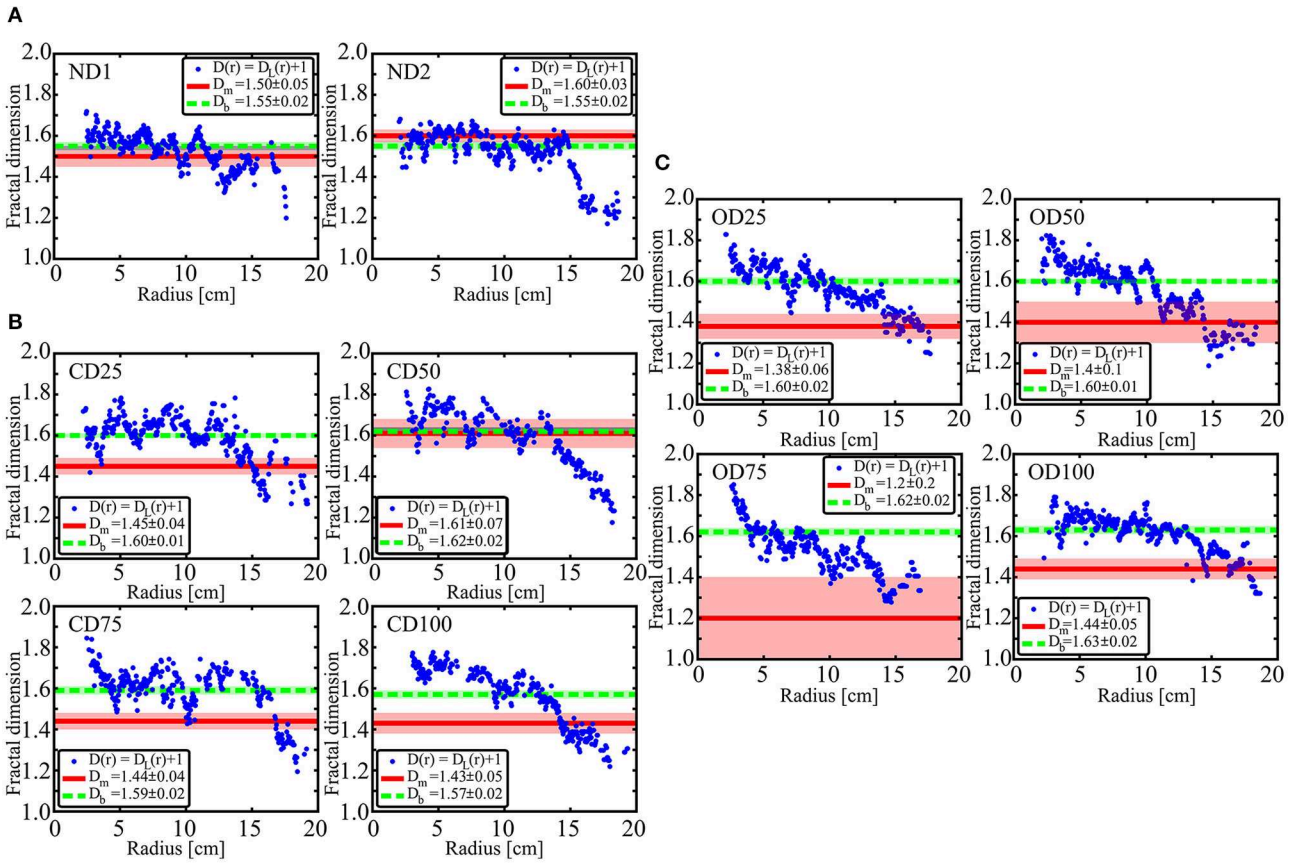

FIGURE 7 | The blue dots represent local fractal dimensions plotted as ($D_L + 1$) as function of radius for the non-deformable breakthrough patterns (A), confined deformable breakthrough patterns (B), and open deformable breakthrough patterns (C). The estimated mass dimensions D_m are indicated as solid red lines with uncertainties shown as light red bands, and the box dimensions D_b are indicated as dotted green lines with uncertainties shown as light green bands. Overlaps of the D_m and D_b uncertainties are colored gray. The injection pressure in both ND experiments is 25 hPa, while the number in the experiment names for the CD and OD experiments gives the injection pressure in hPa.

TABLE 2 | The fractal mass dimensions D_m and box dimensions D_b for the breakthrough patterns.

	ND1	ND2	CD25	CD50	CD75	CD100	OD25	OD50	OD75	OD100
D_m	1.50 ± 0.05	1.60 ± 0.03	1.45 ± 0.04	1.61 ± 0.07	1.44 ± 0.04	1.43 ± 0.05	1.38 ± 0.06	1.40 ± 0.10	1.20 ± 0.20	1.44 ± 0.05
D_b	1.55 ± 0.02	1.55 ± 0.02	1.60 ± 0.01	1.62 ± 0.02	1.59 ± 0.02	1.57 ± 0.02	1.60 ± 0.02	1.60 ± 0.01	1.62 ± 0.02	1.63 ± 0.02

as function of (t/t_b), and the scaling exponent β from the slope of the log-log plot of $(r(t)/r_b)$ as function of (t/t_b), following Equation (11). The estimated values for α and β are presented in **Table 3**, and the corresponding plots are shown in Figure A3 in the Supplementary Material.

For the ND boundary condition we see that the scaled curves collapse fairly well on top of each other, except for an inner part which has a slightly lower mass-radius slope. The slopes are however limited to the estimated mass dimension. For both the deformable boundary conditions we see that the scaled curves collapse well on top of each other and along the estimated mass dimensions. Although, there are inner parts with slopes close to 2 falling down from the collapsed curves. This effect is most obvious in the OD plots.

Deformations

Deformation of the porous media is illustrated in **Figure 9** for selected snapshots of the confined and OD experiments with an injection pressure of 100 hPa. The radial displacements and volumetric strains are shown at an early stage, around mid-experiment, at a later stage and at breakthrough. Radial displacement of beads in the CD boundary condition, seen in **Figure 9A**, are directed outwards from the injection center. In the initial stage, the displacements do not reach all the way to the rim of the cell, but over time the displaced area grows toward a final size and magnitude, which goes toward zero near the rim. The corresponding volumetric strains are shown in **Figure 9B**, and show that the porous medium is increasingly compacted with time outside the invasion cluster.

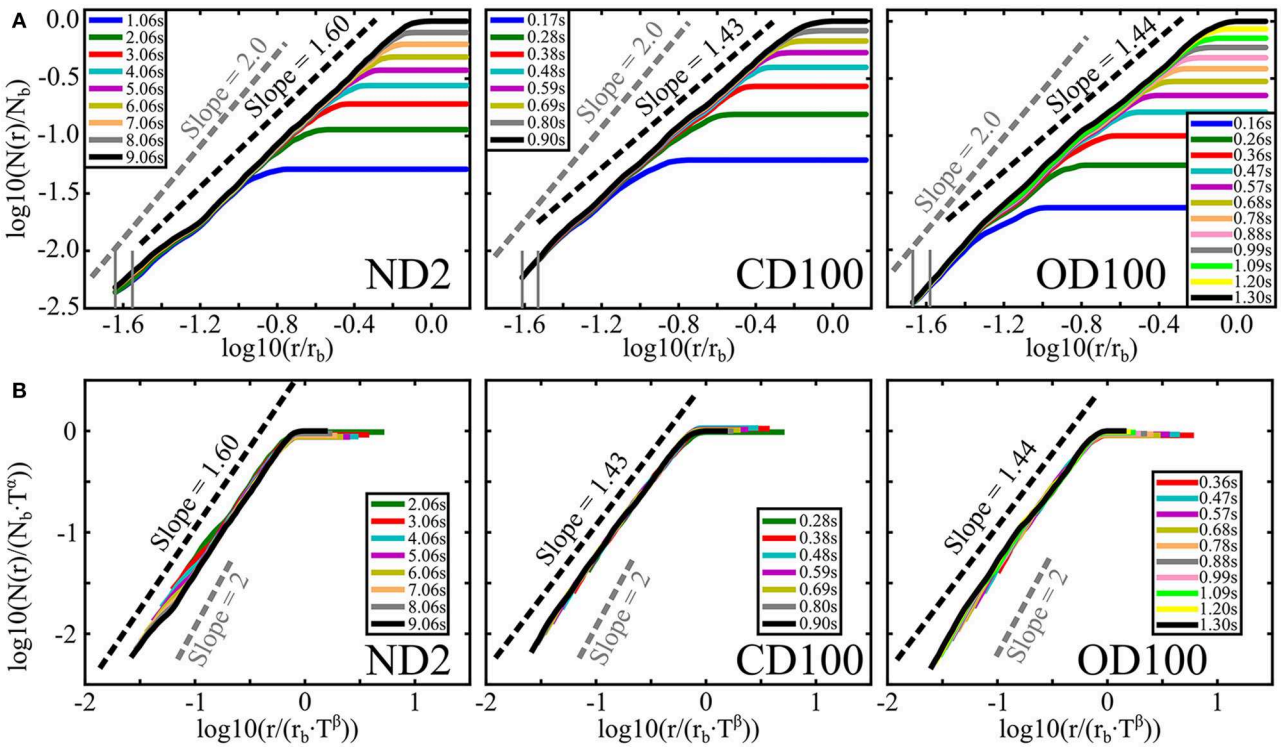

FIGURE 8 | (A) Examples of mass-radius relations at several snapshots for a non-deformable experiment at 25 hPa (left), a confined deformable experiment at 100 hPa (middle), and an open deformable experiment at 100 hPa (right). At the start of the curves, the leftmost gray vertical lines mark the lower radius cutoff, which is just outside the injection region, and the gray vertical lines to the right mark a distance of 1 mm outside the lower cutoff. The black dotted lines show the estimated mass dimensions for the breakthrough patterns. The gray dotted lines has slopes of 2 to indicate the space filling dimension of an emptied bubble. **(B)** Family-Vicsek scaling of the same mass-radius relations as above, except for the smallest clusters with a total mass <10% of the breakthrough mass. On the axes, $T = (t/t_b)$ is the ratio of time over breakthrough time, r is radius, r_b is breakthrough radius, $N(r)$ is mass within radius r, N_b is total mass at breakthrough, and α and β are scaling exponents. Here, for ND2: $\alpha = 1.45$ and $\beta = 0.80$, for CD100: $\alpha = 1.58$ and $\beta = 1.02$, and for OD100: $\alpha = 1.73$ and $\beta = 1.10$.

Finger opening, i.e., parts of the air cluster empty of beads, is observed in regions where the volumetric strain exceeds 0.05. Thus, there is a crossover from finger opening to pore invasion in the latter half of the experiment. Radial displacements at different snapshots for the OD100 experiment are shown in **Figure 9C**. We see a similar behavior as in the CD case initially, where the inner beads are displaced radially outwards from the injection center while the outer beads are not yet displaced. With time, the radial displacements increase in magnitude outside the growing cluster and eventually reach out to the rim where beads leave the cell. The corresponding volumetric strains for the OD snapshots are shown in **Figure 9D**. Initially, there is compaction outside the growing air cluster, and with time there is increasing decompaction of the outer portion of the medium. Again, finger opening is observed in regions with volumetric strain above 0.05 and we see that it goes on until breakthrough in this experiment.

The tangential displacements were found to look similar for both boundary conditions, and is illustrated for a 40 ms interval in **Figure 10**. The displacements are directed away from the sides of the fingers, and are higher in magnitude for larger fingers. Outside the air cluster, where radial displacement dominates, tangential displacement magnitudes are small.

TABLE 3 | The scaling exponents α and β found for the experiments ND2, CD100, and OD100.

	α	β	$D_m = \alpha/\beta$
ND2	1.45 ± 0.18	0.80 ± 0.17	1.81 ± 0.35
CD100	1.58 ± 0.12	1.02 ± 0.13	1.55 ± 0.25
OD100	1.73 ± 0.10	1.10 ± 0.04	1.57 ± 0.14

Discussion

When we examine the flow patterns in **Figure 3**, we find that they have both common features across boundary conditions and typical characteristics depending on the boundary conditions. In common, they all have the dendritic branching structure that spreads out from the center, similar to DLA [18], where longer fingers grow on expense of less advanced fingers. This behavior is expected for viscous fingering in a porous medium since the invasion flow follows Darcy's law (3), with the pressure distribution given by the Laplace equation outside the air cluster (of constant pressure) such that the pressure gradient is screened inside the longest fingers [19]. We do observe in **Figures 6**, **8** that spatial properties of the structures grow toward limiting curves

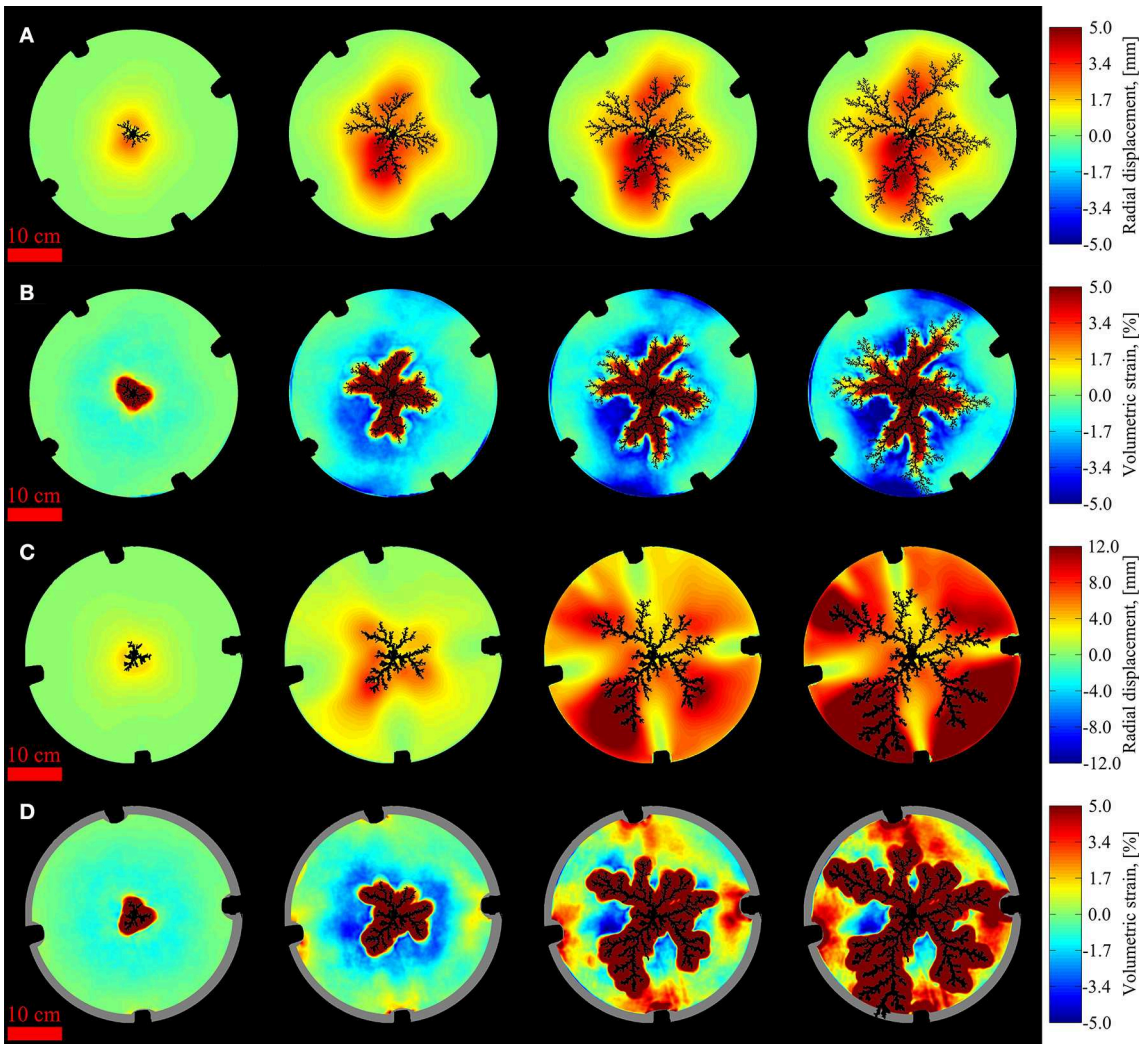

FIGURE 9 | Visualization of accumulated deformation at different snapshots during experiments: Radial displacements **(A)** and volumetric strains **(B)** in the confined deformable experiment with 100 hPa injection pressure. The radial displacements **(C)** and volumetric strains **(D)** are for the open deformable experiment with 100 hPa injection pressure. Time is increasing from left to right, where the snapshots in **(A,B)** are taken at 176, 488, 696, and 904 ms (i.e., 20, 54, 77, and 100% of the breakthrough time). The snapshots in **(C,D)** are taken at 232, 544, 960, and 1272 ms (i.e., 18, 43, 75, and 100% of the breakthrough time). For the radial displacements **(A,C)**, red color means that displacements are directed outwards and blue means inwards. For the volumetric strains **(B,D)**, red color means decompaction and blue means compaction. The air clusters and areas outside of the cell are shown in black, and the black bumps at the cell rim are due to the clamps. The gray areas in **(D)** indicate omitted data where boundary effects of beads leaving the cell influence the strain calculations.

over time, and in **Figure 7** that the local fractal dimensions show a sudden decrease at the outermost radii, i.e., the active growth zone. This confirms that growth dynamics of the patterns follow a behavior where an outer active growth zone surrounds an internally developed and frozen pattern, as described in similar linear systems [3, 4]. The fundamental similarity in the growth dynamics of the structures is reflected by their similar global appearance across boundary conditions. This is also indicated by the fractal box dimensions, which are all observed in the range from 1.55 to 1.63, consistent with earlier observed values of e.g., 1.53 [4] and 1.62 [19] for viscous fingers in ND porous media. The breakthrough times, shown in **Figure 5**, are generally observed to decrease with increased deformability and injection pressure, while the growth rates generally seem to have a linear trend with some fluctuations.

Typically, as seen in **Figures 3A**, **6A**, invasion patterns in the ND system has long thin fingers with approximately the same finger thickness at all radii. In the deformable systems, typical invasion patterns have initially an air bubble emptied of grains, as observed in Johnsen et al. [21]. The empty bubble seems larger for higher injection pressure and deformability, but in all cases it branches rather quickly into few and thick fingers. In the CD system (**Figures 3B**, **6B**) the few thick fingers cross over to increasingly numerous and thinner fingers with radius, while in the OD system (**Figures 3C**, **6C**), typical invasion patterns goes from the few thick fingers into more numerous and thinner

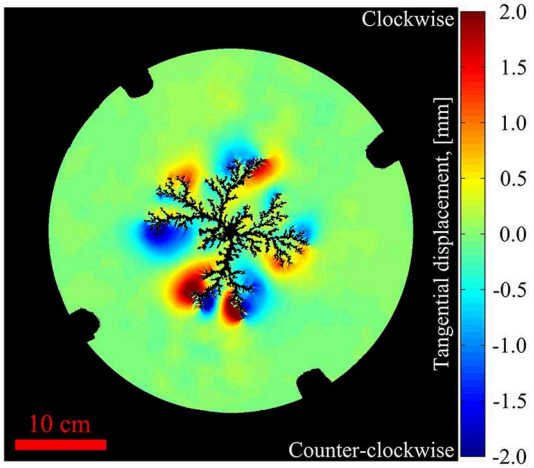

FIGURE 10 | Example of tangential displacement behavior taken from the interval of 448–488 ms (50–54% of breakthrough time) for the confined deformable experiment with 100 hPa injection pressure. Blue color means counter-clockwise displacements and red means clockwise displacements. The air cluster and area outside of the cell are shown in black, and the black bumps at the cell rim are due to the clamps.

fingers before crossing back to few and thick fingers close to the rim. The key difference between the deformable systems is visualized in **Figures 9B,D**. The porous medium in the CD system is increasingly compacted as the cluster grows, while the porous medium in the OD system is centrally compacted and then decompacted near the rim as the cluster grows. Inside the longest finger radius, displacements are observed to be directed out from the side of fingertips as in **Figure 10**, while outside the invasion cluster, radial displacements dominate.

The radial displacements outside the invasion cluster are driven by a viscous pressure gradient, as in the experiments by MacMinn et al. [30] where a saturated granular material is injected with the same fluid. We assume that radial displacement occurs outside the invasion cluster when

$$\Delta p > \sigma_g, \tag{13}$$

where Δp is the viscous pressure drop across a bead and σ_g is the granular stress opposing bead displacement. In the OD boundary condition, decompaction at the rim is believed to initiate when the pressure drop across the outer layer of beads overcome the pressure necessary to move one bead out of the cell, $\Delta p > \sigma_b$.

The displacements away from fingertips correspond to opening of fractures by capillary forces, as e.g., discussed in Holtzman et al. [29]. A typical capillary threshold in our deformable systems is found from Equation (2) as

$$p_{cap} = \gamma \left(\frac{2}{a} + \frac{2}{b} \right), \tag{14}$$

where a is the typical bead size and b is the plate separation, giving $p_{cap} = 225.26$ Pa. Since the lowest injection pressure in our experiments is 2500 Pa, we can always expect pore invasions if fracturing does not occur. However, if

$$p_{cap} > \sigma_g \text{ and } \Delta p_\perp > \sigma_g, \tag{15}$$

where $\Delta p_\perp$ is the pressure drop perpendicular to fingers across beads, fracturing is assumed to occur. Limiting mechanisms for fracturing can then be an increase in σ_g due to compaction and accumulated friction, or a decrease in $\Delta p_\perp$ due to pressure screening from the longest fingers.

In the CD system fracturing occurs initially, but since the granular stress increase as the medium compacts over time, we observe a crossover from fracturing to pore invasions. In the OD system, fracturing occurs initially and may cross over to pore invasions in the intermediate compacted region due to compaction and accumulated friction. Later on, when the fingers approach the open rim, the medium decompacts and friction is relaxed such that fracturing re-initiates. This results in a new instability as fingers are sensitive to the proximity of the open rim, and we observe 1–2 fingers grow to breakthrough on expense of the others. The outer fingers appear similar to fractures in a paste [57]. During the outer fracturing instability for the higher injection pressures, we also see an increased number of branches on the longest fingers. This could be a consequence of outer decompaction of the media, in the sense that the pore sizes increase along the fingers and become more easily invaded.

The local fractal dimensions in **Figure 7A** are more or less constant inside the frozen region, and correspond well to the global mass- and box dimensions by Mandelbrot's rule of thumb (8). Thus, the ND patterns have fairly well defined fractal dimensions on a global scale, between 1.5 and 1.6, consistent with earlier observed values. The local fractal dimensions in **Figure 7B**, for the CD experiments, are observed to be approximately constant in the frozen part of the patterns, similar to the ND case for the lower injection pressures (CD25, CD50). However, for higher injection pressures we see slightly higher local dimensions initially, influenced by the central emptied structures and thick fingers. The local dimensions for the structures in the OD system, **Figure 7C**, are more or less decreasing with radius. In addition, mass dimensions for the deformable patterns generally do not correspond well with the local dimensions due to finite size effects. In other words, the less developed outer parts contribute to a decrease in the mass-radius slope. For the CD100 and OD experiments the box dimension only corresponds with a part of the local dimensions. This indicates that the patterns in the most deformable systems does not have a well-defined global fractal dimension, but have locally defined fractal dimensions and transitions of universality class with radius. The initial emptied and thick finger regions seem to have local dimensions corresponding to around 1.7 which is the measured fractal dimension for invasion patterns in empty cells and DLA [58, 59]. In an intermediate region, the local dimensions correspond well to the measured box dimensions around 1.6, indicating viscous fingering. For the outer parts in the OD system, the local dimensions decrease toward 1.4, which is similar to the measured box dimension of 1.43 for fractures in a paste [57].

After pattern growth develops into viscous fingering, the mass-radius relations as function of time are found to scale according to a Family-Vicsek scaling relation, where $N(t) = N_b \cdot (t/t_b)^{\alpha}$ and $r(t) = r_b \cdot (t/t_b)^{\beta}$. The dynamic scaling exponents α for the invaded area over time $N(t) \sim t^{\alpha}$ are observed to increase with the deformability of the porous media. When considering that

$$\frac{dN(t)}{dt} \sim t^{\alpha-1}, \tag{16}$$

we see that higher values of α imply that the invaded area changes at a faster rate. To the knowledge of the authors, a dynamic scaling exponent for invasion area over time for two-phase flow in deformable porous media is not discussed in earlier papers. Thus, we present a new measured exponent which calls for theoretical evaluation and comparison with theoretical models. When mass dimensions of the patterns in the deformable systems are estimated from the scaling law, $D_m = \alpha/\beta$, we get the values 1.55 ± 0.25 for CD100 and 1.57 ± 0.14 for OD100, which is similar to the respective box dimensions as well as observed fractal dimensions of patterns in ND systems.

Acknowledgments

This project has received funding from the European Union's Seventh Framework Programme for research, technological development and demonstration under grant agreement no. 316889, ITN FlowTrans. We acknowledge the support of the University of Strasbourg and the IDEX program through the award "Hope of the University of Strasbourg," and the University of Oslo. We thank Mihailo Jankov for technical support.

Supplementary Material

The Supplementary Material for this article can be found online at: http://journal.frontiersin.org/article/10.3389/fphy.2015.00081

References

1. Saffman PG, Taylor G. The penetration of a fluid into a porous medium or Hele-Shaw cell containing a more viscous liquid. *Proc R Soc Lond A Math Phys Sci.* (1958) **245**:312–29. doi: 10.1098/rspa.1958.0085
2. Lenormand R. Pattern growth and fluid displacements through porous media. *Physica A*. (1986) **140**:114–23.
3. Løvoll G, Méheust Y, Toussaint R, Schmittbuhl J, Måløy KJ. Growth activity during fingering in a porous Hele-Shaw cell. *Phys Rev E.* (2004) **70**:026301. doi: 10.1103/PhysRevE.70.026301
4. Toussaint R, Løvoll G, Méheust Y, Måløy KJ, Schmittbuhl J. Influence of pore-scale disorder on viscous fingering during drainage. *Europhys Lett.* (2005) **71**:583. doi: 10.1209/epl/i2005-10136-9
5. Toussaint R, Måløy KJ, Méheust Y, Løvoll G, Jankov M, Schäfer G, et al. Two-phase flow: structure, upscaling, and consequences for macrosopic transport properties. *Vadoze Zone J.* (2012) **11**:3. doi: 10.2136/vzj2011.0123
6. Huang H, Zhang F, Callahan P, Ayoub J. Granular fingering in fluid injection into dense granular media in a Hele-Shaw cell. *Phys Rev Lett.* (2012) **108**:258001. doi: 10.1103/PhysRevLett.108.258001
7. Kong XZ, Kinzelbach W, Stauffer F. Morphodynamics during air injection into water-saturated movable spherical granulates. *Chem Eng Sci.* (2010) **65**:4652–60. doi: 10.1016/j.ces.2010.05.007
8. Varas G, Vidal V, Géminard JC. Morphology of air invasion in an immersed granular layer. *Phys Rev E.* (2011) **83**:061302. doi: 10.1103/PhysRevE.83.061302
9. Vinningland JL, Johnsen Ø, Flekkøy EG, Toussaint R, Måløy KJ. Granular Rayleigh-Taylor instability: experiments and simulations. *Phys Rev Lett.* (2007) **99**:048001. doi: 10.1103/PhysRevLett.99.048001
10. Frette V, Feder J, Jøssang T, Meakin P. Buoyancy-driven fluid migration in porous media. *Phys Rev Lett.* (1992) **68**:3164. doi: 10.1103/PhysRevLett.68.3164
11. Völtz C, Pesch W, Rehberg I. Rayleigh-Taylor instability in a sedimenting suspension. *Phys Rev E.* (2001) **65**:011404. doi: 10.1103/PhysRevE.65.011404
12. Niebling MJ, Flekkøy EG, Måløy KJ, Toussaint R. Mixing of a granular layer falling through a fluid. *Phys Rev E.* (2010) **82:**011301. doi: 10.1103/PhysRevE.82.011301
13. Birovljev A, Furuberg L, Feder J, Jøssang T, Måløy KJ, Aharony A. Gravity invasion percolation in two dimensions: experiment and simulation. *Phys Rev Lett.* (1991) **67**:584. doi: 10.1103/PhysRevLett.67.584
14. Méheust Y, Løvoll G, Måløy KJ, Schmittbuhl J. Interface scaling in a two-dimensional porous medium under combined viscous, gravity, and capillary effects. *Phys Rev E.* (2002) **66**:051603. doi: 10.1103/PhysRevE.66.051603
15. Wilkinson D, Willemsen JF. Invasion percolation: a new form of percolation theory. *J Phys A Math Gen.* (1983) **16**:3365–76.
16. Chandler R, Koplik J, Lerman K, Willemsen JF. Capillary displacement and percolation in porous media. *J Fluid Mech.* (1982) **119**:249–67.
17. Lenormand R, Zarcone C. Capillary fingering: percolation and fractal dimension. *Transp Porous Media*. (1989) **4**:599–612.
18. Paterson L. Diffusion-Limited Aggregation and two-fluid displacements in porous media. *Phys Rev Lett.* (1984) **52**:1621–4. doi: 10.1103/PhysRevLett.52.1621
19. Måløy KJ, Feder J, Jøssang T. Viscous fingering fractals in porous media. *Phys Rev L.* (1985) **55**:2688.
20. Lemaire E, Abdelhaye YOM, Larue J, Benoit R, Levitz P, van Damme H. Pattern formation in noncohesive and cohesive granular media. *Fractals* (1993) **1**:968–76. doi: 10.1142/S0218348X93001040
21. Johnsen Ø, Toussaint R, Måløy KJ, Flekkøy EG. Pattern formation due to air injection into granular materials confined in a circular Hele-Shaw cell. *Phys Rev E.* (2006) **74**:001301. doi: 10.1103/PhysRevE.74.011301
22. Cheng X, Xu L, Patterson A, Jaeger HM, Nagel SR. Towards the zero-surface-tension limit in granular fingering instability. *Nat Phys.* (2008) **4**:234–7. doi: 10.1038/nphys834
23. Johnsen Ø, Toussaint R, Måløy KJ, Flekkøy EG, Schmittbuhl J. Coupled air/granular flow in a linear Hele-Shaw cell. *Phys Rev E.* (2008) **77**:011301. doi: 10.1103/PhysRevE.77.011301
24. Niebling MJ, Toussaint R, Flekkøy EG, Måløy KJ. Dynamic aerofracture of dense granular packings. *Phys Rev E.* (2012) **86**:061315. doi: 10.1103/PhysRevE.86.061315
25. Johnsen Ø, Chevalier C, Lindner A, Toussaint R, Clément E, Måløy KJ, et al. Decompaction and fluidization of a saturated and confined granular medium by injection of a viscous liquid or gas. *Phys Rev E.* (2008) **78**:051302. doi: 10.1103/PhysRevE.78.051302
26. Chevalier C, Lindner A, Leroux M, Clément E. Morphodynamics during air injection into a confined granular suspension. *J NonNewton Fluid Mech.* (2009) **158**:63–72. doi: 10.1016/j.jnnfm.2008.07.007
27. Sandnes B, Flekkøy EG, Knudsen HA, Måløy KJ, See H. Patterns and flow in frictional fluid dynamics. *Nat Commun.* (2011) **2**:288. doi: 10.1038/ncomms1289
28. Eriksen JA, Marks B, Sandnes B, Toussaint R. Bubbles breaking the wall: two-dimensional stress and stability analysis. *Phys Rev E.* (2015) **91**:052204. doi: 10.1103/PhysRevE.91.052204

29. Holtzman R, Szulczewski ML, Huanes R. Capillary fracturing in granular media. *Phys Rev Lett.* (2012) **108**:264504. doi: 10.1103/PhysRevLett.108.264504
30. MacMinn CW, Dufresne ER, Wettlaufer JS. Fluid-driven deformation of a soft granular material. *Phys Rev X.* (2015) **5**:011020. doi: 10.1103/PhysRevX.5.011020
31. Montgomery CT, Smith MB. Hydraulic fracturing: history of an enduring technology. *J Pet Technol.* (2010) **62**:26–32. doi: 10.2118/1210-0026-jpt
32. Department of Energy, Hydraulic fracturing white paper (2004), EPA 816-R-04-003, Appendix A.
33. Naik GC. *Tight Gas reservoirs - An Unconventional Natural Energy Source for the Future* (2003). Available online at: http://www.pinedaleonline.com/socioeconomic/pdfs/tight_gas.pdf (Accessed 11, 2014).
34. Johnson SM, Morris JP. Hydraulic fracturing mechanisms in carbon sequestration applications. In: *43rd U.S. Rock Mechanics Symposium and 4th U.S. - Canada Rock Mechanics Symposium*. Asheville, NC: American Rock Mechanics Association (2009).
35. Williamson WH, Wooley DR. *Hydraulic Fracturing to Improve the Yield of Bores in Fractured Rock*. Canberra, ACT: Australian Government Publishing Service (1980).
36. Rummel F, Kappelmayer O. The Falkenberg geothermal frac-project: concepts and experimental results. *Hydraul Fract Geotherm Energy*. (1983) **5**:59–74. doi: 10.1007/978-94-009-6884-4_4
37. Clark L. Energy company plans to frack volcano. In: *Wired Science* (2012). Available online at: http://www.wired.com/wiredscience/2012/10/newberry-volcano-fracking (Accessed 11, 2014).
38. Hurst A, Cartwright J, Duranti D. Fluidization structures produced by upward injection of sand through a sealing lithology. In: Van Rensbergen P, Hillis RR, Maltman AJ, Morley CK, editors. *Subsurface Sediment Mobilization*. London: Geological Society (2003), Special Publications 216. pp. 123–38.
39. Løseth H, Wensaas L, Arntsen B, Hovland M. Gas and fluid injection triggering shallow mud mobilization in the Hordaland Group, North Sea. In: Van Rensbergen P, Hillis RR, Maltman AJ, Morley CK, editors. *Subsurface Sediment Mobilization*. London: Geological Society (2003), Special Publications 216. pp. 139–57.
40. Van Rensbergen P, Poort J, Kipfer R, De Batist M, Vanneste M, Klerkx J, et al. Near-surface sediment mobilization and methane venting in relation to hydrate destabilization in southern Lake Baikal, Siberia. In: Van Rensbergen P, Hillis RR, Maltman AJ, Morley CK, editors. *Subsurface Sediment Mobilization*. London: Geological Society (2003), Special Publications 216. pp. 207–21.
41. Talukder AR, Comas MC, Soto JI. Pliocene to recent mud diapirism and related mud volcanoes in the Alboran Sea (Western Mediterrenean). In: Van Rensbergen P, Hillis RR, Maltman AJ, Morley CK, editors. *Subsurface Sediment Mobilization*. London: Geological Society (2003), Special Publications 216. pp. 443–59.
42. Pralle N, Külzer M, Gudehus G. Experimental evidence on the role of gas in sediment liquefaction and mud volcanism. In: Van Rensbergen P, Hillis RR, Maltman AJ, Morley CK, editors. *Subsurface Sediment Mobilization*. London: Geological Society (2003), Special Publications 216. pp. 159–71.
43. Deville E, Battani A, Griboulard R, Guerlais S, Herbin JP, Houzay JP, et al. The origin and processes of mud volcanism: new insights from Trinidad. In: Van Rensbergen P, Hillis RR, Maltman AJ, Morley CK, editors. *Subsurface Sediment Mobilization*. London: Geological Society (2003), Special Publications 216. pp. 475–90.
44. Feder J. *Fractals*. New York, NY: Plenum Press (1988).
45. Barabási AL, Stanley HE. *Fractal Concepts in Surface Growth*. Cambridge: Cambridge University Press (1995).
46. Mandelbrot BB. The fractal geometry of nature. New York, NY: W. H. Freeman and company (1982).
47. Feder J. *Fractals*. New York, NY: Plenum Press (1988).
48. Blaber J, Adair B, Antoniou A. Ncorr: open-source 2D digital image correlation matlab software. *Exp Mech.* (2015) **55**:1105–22. doi: 10.1007/s11340-015-0009-1
49. Hariral R, Ramji M. Adaption of open source 2D DIC Software Ncorr for solid mechanics applications. In: *9th International Symposium on Advanced Science and Technology in Experimental Mechanics, New Delhi* (2014).
50. Vable M. *Mechanics of Materials*, *2nd Edn*. Michigan Technological University (2014). Available online at: http://www.me.mtu.edu/~mavable/MoM2nd.htm
51. Family F, Vicsek T. Scaling of the active zone in the Eden process on percolation networks and the ballistic deposition model. *J Phys A Math Gen.* (1985) **18**:L75–81. doi: 10.1088/0305-4470/18/2/005
52. Horváth VK, Family F, Vicsek T. Dynamic scaling of the interface in two-phase viscous flows in porous media. *J Phys A Math Gen.* (1991) **24**:L25–9. doi: 10.1088/0305-4470/24/1/006
53. Makse HA, Nunes Amaral LA. Scaling behavior of driven interfaces above the depinning transition. *Europhys Lett.* (1995) **31**:379–84. doi: 10.1209/0295-5075/31/7/007
54. Tallakstad KT, Toussaint R, Santucci S, Schmittbuhl J, Måløy KJ. Local dynamics of a randomly pinned crack front during creep and forced propagation: an experimental study. *Phys Rev E.* (2011) **83**:046108. doi: 10.1103/PhysRevE.83.046108
55. Toussaint R, Helgesen G, Flekkøy EG. Dynamic roughening and fluctuations of dipolar chains. *Phys Rev Lett.* (2004) **93**:108304. doi: 10.1103/PhysRevLett.93.108304
56. Toussaint R, Flekkøy EG, Helgesen G. Memory of fluctuating Brownian dipolar chains. *Phys Rev E.* (2006) **74**:051405. doi: 10.1103/PhysRevE.74.051405
57. Lemaire E, Levitz P, Daccord G, Van Damme H. From viscous fingering to viscoelastic fracturing in colloidal fluids. *Phys Rev Lett.* (1991) **67**:2009. doi: 10.1103/PhysRevLett.67.2009
58. Sharon E, Moore MG, McCormick WD, Swinney HL. Coarsening of viscous fingering patterns. *Phys Rev Lett.* (2003) **91**:205504. doi: 10.1103/PhysRevLett.91.205504
59. Davidovitch B, Levermann A, Procaccia I. Convergent calculation of the asymptotic dimension of diffusion limited aggregates: scaling and renormalization of small clusters. *Phys Rev E.* (2000) **62**:R5919–22. doi: 10.1103/PhysRevE.62.R5919

Conflict of Interest Statement: The authors declare that the research was conducted in the absence of any commercial or financial relationships that could be construed as a potential conflict of interest.

frontiers in Physics

ORIGINAL RESEARCH
published: 08 September 2015
doi: 10.3389/fphy.2015.00070

Bridging aero-fracture evolution with the characteristics of the acoustic emissions in a porous medium

Semih Turkaya[1], Renaud Toussaint[1], Fredrik K. Eriksen[1,2], Megan Zecevic[3], Guillaume Daniel[3], Eirik G. Flekkøy[2] and Knut J. Måløy[2]*

[1] Centre National de la Recherche Scientifique, Institut de Physique du Globe de Strasbourg, Université de Strasbourg, Strasbourg, France, [2] Department of Physics, University of Oslo, Oslo, Norway, [3] Magnitude, Sainte Tulle, France

The characterization and understanding of rock deformation processes due to fluid flow is a challenging problem with numerous applications. The signature of this problem can be found in Earth Science and Physics, notably with applications in natural hazard understanding, mitigation or forecast (e.g., earthquakes, landslides with hydrological control, volcanic eruptions), or in industrial applications such as hydraulic-fracturing, steam-assisted gravity drainage, CO_2 sequestration operations or soil remediation. Here, we investigate the link between the visual deformation and the mechanical wave signals generated due to fluid injection into porous medium. In a rectangular Hele-Shaw Cell, side air injection causes burst movement and compaction of grains along with channeling (creation of high permeability channels empty of grains). During the initial compaction and emergence of the main channel, the hydraulic fracturing in the medium generates a large non-impulsive low frequency signal in the frequency range 100 Hz–10 kHz. When the channel network is established, the relaxation of the surrounding medium causes impulsive aftershock-like events, with high frequency (above 10 kHz) acoustic emissions, the rate of which follows an Omori Law. These signals and observations are comparable to seismicity induced by fluid injection. Compared to the data obtained during hydraulic fracturing operations, low frequency seismicity with evolving spectral characteristics have also been observed. An Omori-like decay of microearthquake rates is also often observed after injection shut-in, with a similar exponent $p \approx 0.5$ as observed here, where the decay rate of aftershock follows a scaling law $dN/dt \propto (t - t_0)^{-p}$. The physical basis for this modified Omori law is explained by pore pressure diffusion affecting the stress relaxation.

Keywords: fracturing, lamb waves, acoustic emissions, power spectral evolution, Hele-Shaw cell

OPEN ACCESS

Edited by:
Ferenc Kun, University of Debrecen, Hungary

Reviewed by:
Takahiro Hatano, The University of Tokyo, Japan
Loic Vanel, Université Claude Bernard Lyon 1, France

****Correspondence:***
Semih Turkaya, Centre National de la Recherche Scientifique UMR 7516, Institut de Physique du Globe de Strasbourg, Université de Strasbourg, 5 Rue Rene Descartes, 67084 Strasbourg, France turkaya@unistra.fr

Specialty section:
This article was submitted to Interdisciplinary Physics, a section of the journal Frontiers in Physics

Received: *29 June 2015*
Accepted: *21 August 2015*
Published: *08 September 2015*

Citation:
Turkaya S, Toussaint R, Eriksen FK, Zecevic M, Daniel G, Flekkøy EG and Måløy KJ (2015) Bridging aero-fracture evolution with the characteristics of the acoustic emissions in a porous medium. Front. Phys. 3:70. doi: 10.3389/fphy.2015.00070

1. Introduction

Fluid flow [1, 2], rock deformation [3] and granular dynamics [4] by themselves are very large scientific domains to investigate individually [5]. However, the idea of putting them together via a system of deformable porous medium with a fluid flow makes the phenomena even harder to understand. Rapid changes in the porosity of the medium due to fluid flow, channeling and fracturing via momentum exchange with the flow make understanding the mechanics of the system a challenge [6–9]. Hydraulic fracturing of the ground is a good example for this coupled behavior of solid and fluid phases. First, the pressure of the flow creates fissures and cracks which

changes the permeability of the initial rock. Then, a flowing mixture of fine sand and chemicals helps maintain this cracked state by penetrating the newly opened areas. By jamming and/or cementing the newly-formed channels and cracks, possible relaxation after injection is prevented. Thus, a more permeable state of the rock is preserved after injection for various types of industrial applications. Recently, various well-stimulation projects have attempted to use pressurized gas (N_2, CO_2), instead of water, to trigger fracturing within reservoirs for several reasons (e.g., to avoid wasting water, to sequestrate CO_2, environmental risks due to chemicals etc.) [10–12]. In this study, contrary to conventional fracturing methods, the fractures are induced using air injection.

Monitoring, predicting and controlling fracture evolution during hydraulic-fracturing, steam-assisted gravity drainage, or CO_2 sequestration operations is a key goal [13–16]. One possibility for monitoring is to use generated acoustic emissions during those operations. In the hydraulic fracturing industry, the typical monitoring devices consist of geophones and seismometers. However, the interpretation of the signals during fast deformations of porous media due to fast fluid flow is not simple. Particularly, the measurements of deformations are usually difficult to achieve in an opaque medium, and the source of the seismic waves and acoustic emissions can be complex. The study of microseismicity during well operations is routinely done in the industry, but its interpretation is often delicate [17–19].

In this paper, we present an experimental study using a purpose-built setup allowing channeling and fracturing due to fluid flow, where we can observe the deformations optically using a fast camera and transparent setup, and simultaneously record the mechanical waves emitted by the complex channels and fractures created. Both signals, optical and acoustic/microseismic, are then analyzed. They display a complex evolution of the source geometry, and of the spectral characteristics. The experimental setup designed to achieve this consists of a rectangular Hele-Shaw cell filled with 80 microns diameter grains, mixed with fluid (air). The linear cell has three lateral sealed boundaries and a semi-permeable one enabling fluid (but not solid) flow. During the experiments, air is injected into the system from the side opposite to the semi-permeable boundary so that the air penetrates into the solid and at high injection pressures makes a way to the semi-permeable boundary via the creation of channels and fractures - or at low injection pressures, directly using the pore network.

For a similar system of aerofractures in a Hele-Shaw cell, a numerical model was conducted by Niebling et al. [20]. These models were also compared with experiments for further development and validation [20–24]. Same kind of experiments—but without acoustic monitoring—with a Hele-Shaw cell have also been conducted. Johnsen et al. worked on the coupled behavior by air injection into the porous material both in fluid saturated and non-saturated cases to study multiphase flow numerically and experimentally [23, 25, 26]. Aero-granular coupling in a free falling porous medium in a vertical Hele-Shaw cell was studied numerically and experimentally by Vinningland et al. [27–29]. Varas et al. conducted experiments of air injection into the saturated porous media in a Hele-Shaw cell [30, 31] and in a cylinder box [32]. Eriksen et al. and McMinn et al. worked on injecting gas into a saturated deformable porous medium [Eriksen et al., submitted; 33]. Sandnes et al. classified different regimes of fingering of porous media in a Hele-Shaw cell [34]. Rust et al. developed a closed-system degassing model using volcanic eruption data [35]. Holtzman et al. also studied air induced fracturing where they identified different invasion regimes [36]. Furthermore, a recent study was conducted by Eriksen et al. where the air injection causes bubbles in a fluid-grain mixture [37].

The equivalent of microseismicity monitoring in the lab is the tracking of acoustic events. Hall et al. compared recorded acoustic emissions with the digital image correlation to track crack propagation in the rock samples [38]. Valès et al. used acoustic emissions to track strain heterogeneities in Argilite rocks [39]. Some studies have started to look at sources directly, both optically and acoustically, in various problems to characterize the different source mechanisms [40–44]. Farin et al. conducted some experimental studies on rockfalls and avalanches where he monitors those phenomena using acoustic emissions [45]. Stojanova et al. worked on fracture of paper using acoustic emissions created during crack propagation [46–48]. During the current experiments, acoustic signals are recorded using different sensors (shock accelerometers and piezoelectric sensors). Those signals are compared and investigated further in both time and frequency domains. Furthermore, during the experiments, photos of the Hele-Shaw cell are taken using a high speed camera. Thus, it is possible to visualize the complex branched patterns arising due to the solid-fluid interaction and to process images to gather information about the strain and strain rates, and investigate the mechanical properties of the solid partition.

2. Experimental Setup

A Hele-Shaw cell is made of two glass plates (80 × 40 cm) placed on top of the other, separated by 1.5 mm distance. The plates are separated via aluminum spacers placed close to the edges to provide equidistant spacing across the cell. For the experiments particular to this study, we completely sealed three boundaries of the Hele-Shaw cell and made one semi-permeable boundary using 50 μm steel mesh which allows fluid to exit the system but keeps the solid grains inside the cell. One of the plates has an inlet, which is used for injection of pressurized air, located at the bottom end of the plate, midway from the long edges 3 cm inside from one of the clamps close to the shorter edge (**Figure 1A**). The cell is filled with non-expanded polystyrene grains (80 μm diameter ±1%) called Ugelstad spheres (see details in Toussaint et al. [49]). The density of the spheres is 1.005 g/cm^3. A mass of 170 g of grains is required to fill the cell, corresponding to an initial solid fraction of 52 ± 5% which is close to the 57% random loose pack for monodispersed grains [50]. Solid fraction of the grains in similar systems was investigated thoroughly by Johnsen et al. and found to be as low as 44% [23]. The difference between our experimental value and the theoretical value for an infinite box could be due to finite size of the cell which causes steric effect between the grains and the flat boundaries of the container, making the solid fraction 10–15% less [51]. Additionally, the

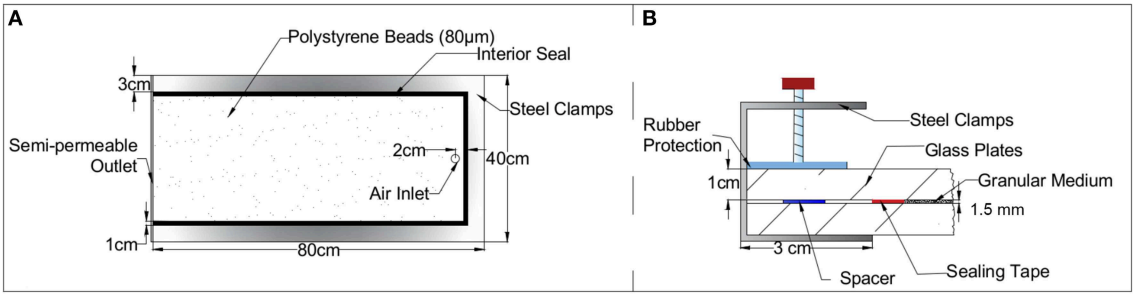

FIGURE 1 | Schematic diagram of the Hele-Shaw cell including the dimensions. (A) Top view of the Hele-Shaw cell including its dimensions. The cell is made of two glass plates which are placed on top of the other with 1.5 mm spacing between them. A porous medium is placed inside the cell. Three sides of the cell are sealed and the 4th boundary is sealed with a semi-permeable filter. **(B)** Side view of the Hele-Shaw cell showing clamp details. To protect the glass plates from point loading, a rubber sheet is placed in between the screw and the plate. Aluminum spacers are placed in between the plates to provide equivalent spacing everywhere in the cell.

measurement of 1.5 mm plate separation is subject to an error of 10% which has a direct effect on the solid fraction error bar. Electrostatic forces and humidity are also effective for real experimental beads and not for theoretical hard spheres, which can lower the solid fraction.

Some of the grains are colored with Indian ink to provide markers and texture, allowing a better resolution of the displacement measurements based on optical data. Images taken via high speed camera are used for digital image correlation to have full field measurements of displacement, velocity, strain rate etc. [21, 52–54]. The solid-air interface is placed 1-2 cm away from the inlet to avoid pressure localization close to the inlet. A schematic diagram of the Hele-Shaw cell is shown in **Figure 1**. The sides of the Hele-Shaw cell are clamped using steel clamps after sealing with double-sided rubber sealing tape. To protect the glass plates from stress focus on the clamping points, rubber sheets are placed between the clamp screws and the glass plates. Before placing the semi-permeable boundary, the cell is placed vertically and grains are poured inside. Following this, a semi-permeable filter is placed on the 4th edge. Then, the Hele-Shaw cell is positioned vertically, in a way that the semi-permeable boundary stays at the bottom side to decompact grains and homogenize the solid fraction through the cell. Another important goal of this rotation process is to provide a small rectangular buffer empty of grains around the air injection inlet to avoid having point injection force over the medium. After the filling phase, the Hele-Shaw cell is placed horizontally.

Air injection is started and ceased via an electrovalve placed on the pipe very close to the air inlet, (**Figure 2**). This air pressure is provided via a pressurized air tank. Injection pressure over time is constant. It starts like a step function and is monitored using a pressure sensor placed on the air inlet allowing to check if the real injection pressure is within 5% of the value required during the experiment.

During the experiments, acoustic signals are recorded using different sensors. The data recorded on the piezoelectric sensors which are mostly sensitive in the range (200–900 kHz) are amplified with a Signal Preamplifier. The data recorded on the shock accelerometers which are mostly sensitive in the range (1 Hz–26 kHz) are amplified with a Brüel and Kjaer Nexus Charge Amplifier—Type 2692-A. The amplified/conditioned signal is transmitted to the computer via a Ni-DAQ mx PCI-6133 acquisition card with multiple channels at 1 MHz sampling rate (**Figure 2**). In addition, synchronized with the acoustical data, images of the Hele-Shaw cell are taken via a Photron SA5 high speed camera transferred and stored numerically. A TTL signal is used as a trigger to initiate the injection and the data acquisition via the camera and the acoustic sensors, thus, enabling time synchronization between the apparatus. Ambient lab noise is also recorded for reference and investigated using camera and accelerometer recordings prior to air injection. After recording, the signals are corrected by using the response function of the accelerometers provided by the manufacturer and cross-checked at the lab.

3. Experimental Observations

At large enough injection pressures, the fluid makes its way by creating channels and fractures toward the semi-permeable boundary as seen in **Figure 3**. In the beginning, the solid-air interface of the porous medium (closest to the injection point) moves more or less homogeneously, with the appearance of only large scale curvature of the interface (**Figure 3B**). Then after roughly 150 ms, some thin finger-like carved formations of thickness around 2 mm start to appear at several points (marked with yellow circles in **Figure 3C**). As injection continues, those fingers penetrate further in the medium. They get larger and wider with the help of the air pressure (**Figure 3D**). In addition to that enlargement, fingers branch out into thinner fingers. In the end, a tree-like branched channel network is created inside the porous medium. As a result of those fractures and channels, the surrounding material is displaced and the porous medium is compacted. Fracturing, channeling and fluid interaction inside the porous medium has its effects on the granular part of the medium. These interactions also result in granular transportation and compaction which involves inter-granular interactions as well as interactions of the solid grains with the confining glass plates. Initially the solid fraction is homogenous inside the plate.

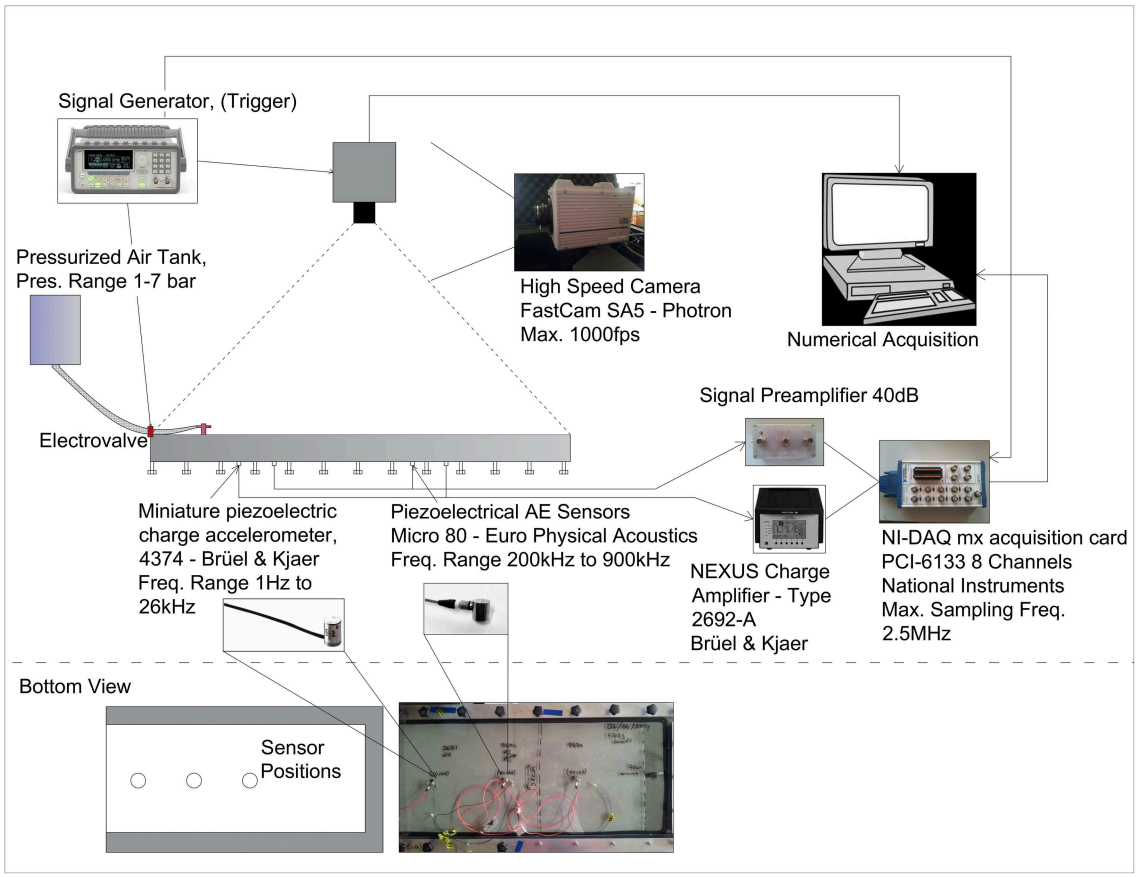

FIGURE 2 | The acquisition chain of the aero-fracturing experiments with a Hele-Shaw cell. The signal acquisition card, camera and the electrovalve connected to the air pump are triggered at the same time via a TTL sent from the signal generator to have synchronized optical and acoustic data. The sensors are placed on the bottom glass plate of the Hele-Shaw cell.

However, during the experiment the solid fraction of the grains increases in the close vicinity of the channels and fractures (up to the maximum possible solid fraction up to 63% for loose packed medium [50]. As observed in numerical models of such system in Niebling et al. [24], this solid fraction may decrease with distance from the fingers. After the experiment, depending on the pressure duration, initial solid fraction, and overpressure, some parts of the medium may have remained at the initial solid fraction, in other words may not have been compacted at all.

The acoustic events recorded during the experiments arise presumably due to sources of various types. While some vibrations are happening solely due to the air pressure fluctuation inside the channels, some others are generated by the stress increases on the plates due to granular compaction, intra-porous air pressure vibrations, granular shocks and variation of the friction forces. These sources excite the confining plates, transporting mechanical waves to the sensors, i.e., the source types that are convoluted with the response of the Hele Shaw cell structure. Eventually, what is recorded is not just a signal created by a simple source, but a systemic response (i.e., signals interacting with plates and clamps, reflecting from edges, refracting through interfaces and eventually having different characteristic properties) to the many individual processes happening inside the plate during the whole period of the experiment. Signature of the signals recorded during experiments did not depend significantly of the sensor type and location.

Even though many individual acoustic events are superposed in time in the recorded signals, and are influenced by a systemic response, this does not mean that their specific signature is lost. Superposed signals may hide their signatures in the time domain, however their influence in the power spectrum may still be noticeable. In the following section, the evolution of the power spectral signature with varying solid-fluid interactions (e.g., compaction of the solid with fluid pressure, channeling, diffusion of the overpressure of the injected fluid through the pore spaces etc.) is shown. First, the power spectrum of several snapshots in time (i.e., Fast Fourier Transform, FFT), taken from different experimental stages, are presented. Then, they are analyzed and compared with each other. The flowchart in **Figure 4** describes the analysis procedure.

4. Results

4.1. Power Spectral Evolution

The first time window analyzed, occurred prior to injection (i.e., at a state of rest). **Figure 3** shows an image of the Hele-Shaw cell,

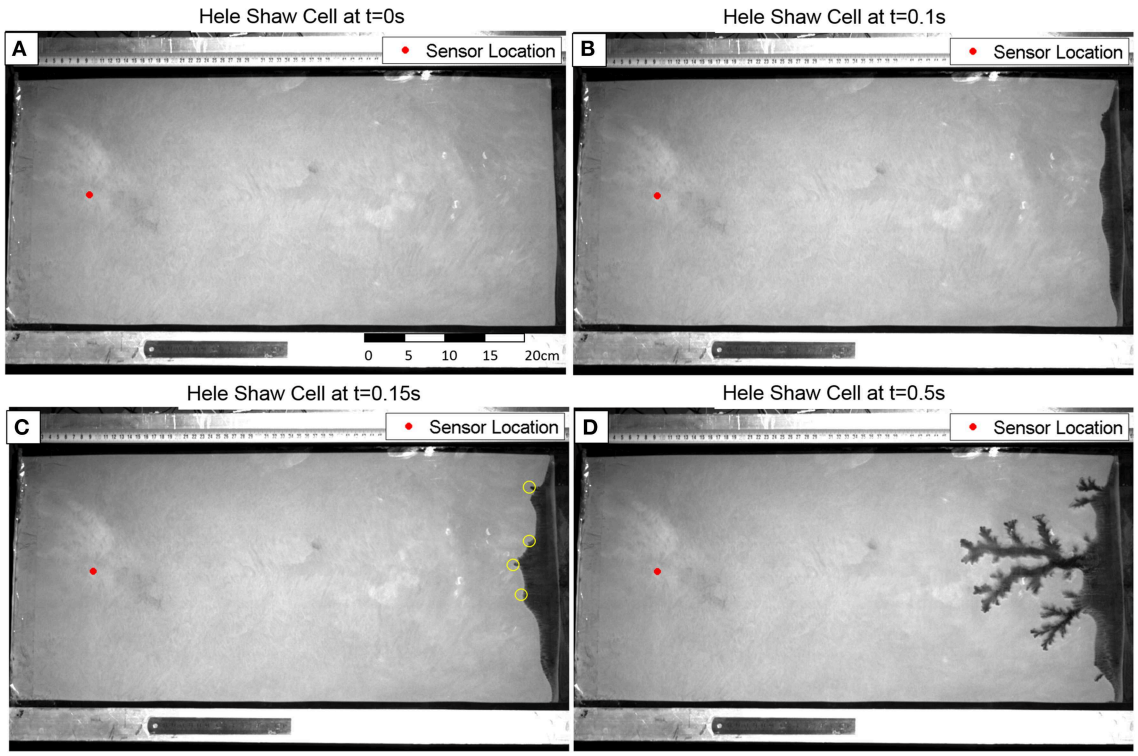

FIGURE 3 | Image of the Hele-Shaw Cell prior to injection (A), during quasi-homogenous compaction (B) and during channeling (C–D). Red dot shows the position of the acoustic sensor (accelerometer). Yellow circles in **(C)** represent the locations of the first finger-like carved formations.

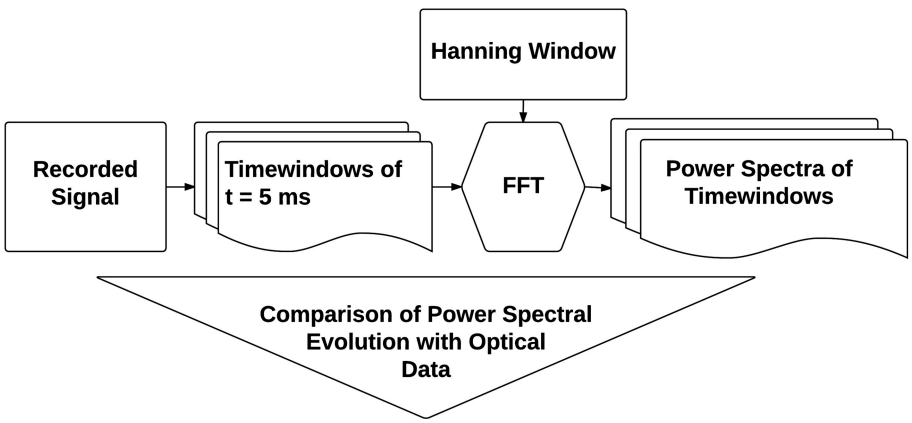

FIGURE 4 | Flowchart showing the acoustic-emission analysis procedure. Snapshots of the experimental signal is taken. Then, they are first converted to the fourier domain to obtain the power spectra. Afterwards, power spectra are compared with each other to understand differences.

acquired via the fast speed camera. The acoustic recordings at the same time step are shown in **Figure 5**. The air injection starts at $t = 0$ s.

Before injection, only ambient electrical noise in the recording system is present. Its power spectrum is flat (**Figure 5**, Right, Blue Curve). After correction with the sensor response the mechanical response (**Figure 5**, Right, Red Curve) is obtained. This noise represents the minimum mechanical vibration level which can be captured by the sensors without being hidden by the electrical noise. Aside from the ambient noise within the lab, no other signal is present. The red strip (time window of 0.005 s) on the experimental signal (**Figure 5**, Top-Left) shows the time window of signal when the picture in **Figure 3A** is taken. The FFT is applied to this time window to obtain the power spectrum which is presented in the right panel of **Figure 5**.

Compaction starts when the fluid (air) pressure is sufficiently large to move the solid grains. In **Figure 6A**, 150 ms after the

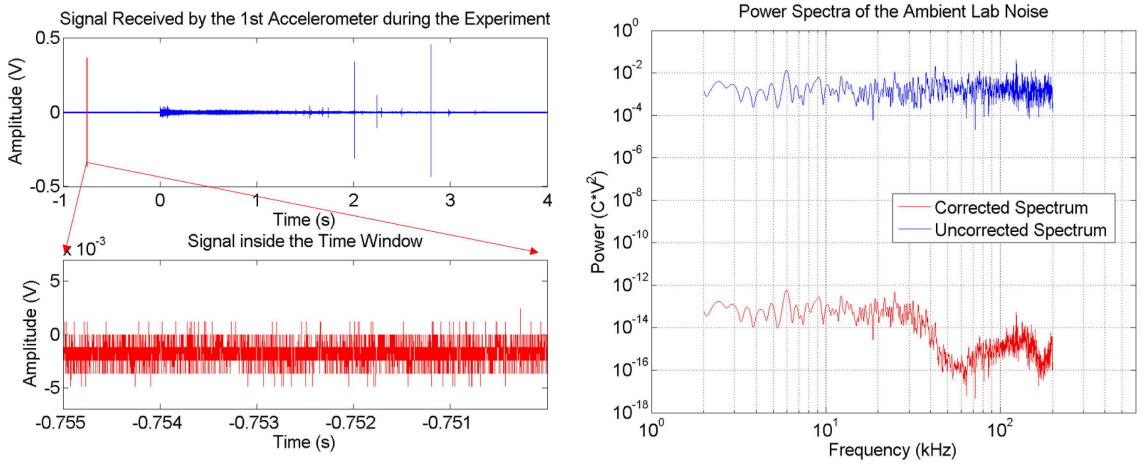

FIGURE 5 | Ambient Lab Noise recorded prior to experiment. The red strip in the top left panel (time window of 0.005 s) and its zoomed version **(Bottom left panel)** corresponds to the snapshot that the power spectra **(Right)** occurred at. **Right panel:** The uncorrected (blue) and corrected with sensor response (red) power spectra of the ambient lab noise.

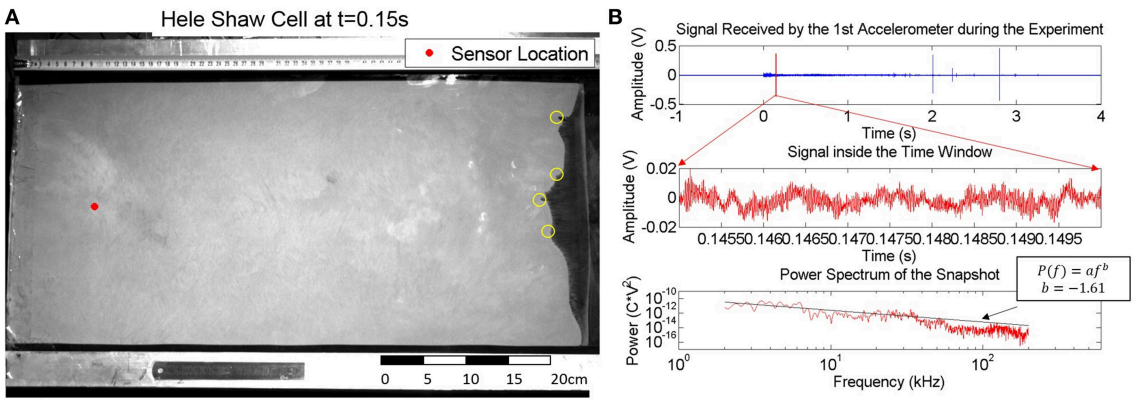

FIGURE 6 | Optical (A) and acoustic (B) experimental recordings just before channeling. Yellow circles on the left image shows the initiation points of the channeling. The red dot on the left image illustrates the sensor location where the signal on the right is recorded. Top Right panel: Acoustic signal recorded throughout the entire experiment. The red strip (time window of 0.005 s) corresponds to the snapshot that the image **(A)** and power spectrum (Bottom Right) occurred at.

start of the injection, channel initiation can be observed at several points, as highlighted by the yellow circles. Due to the interaction between the solid and fluid phases inside the Hele-Shaw cell, some mechanical signals are generated. The power spectrum of the signal recorded during this snapshot is presented in the bottom right panel of **Figure 6**. As channeling continues, the bulk movement of the grains takes place together with fluid motion. This causes emergent acoustic emissions which are predominantly in the low frequency range (less than 10 kHz). Vibration of the plates, granular friction and stress differences on the plates due to compaction create waves that are also in the power spectrum. All those contributions from different source mechanics gives a shape to the presented power spectra, similar to a power law decay having an exponent $b = -1.61$.

In addition to this slope, it is possible to find the mean frequency of the power spectra using Equation (1).

$$\langle f \rangle = \frac{\int f |a(f)|^2 df}{\int |a(f)|^2 df} \tag{1}$$

This will show the dominant frequency range within the signal. In the following **Figure 7**, it can be seen that the mean frequency starts very low and then increases with increasing energy in the high frequency range. As the channel network develops, we see that the mean frequency reaches to its maximum value. Using cubic fitting, this mean frequency curve is estimated and compared with the optically obtained curves. An inflection point of the fitted curve is observed around time $t_0 = 1.49$ s after injection. This corresponds to the point where the finger

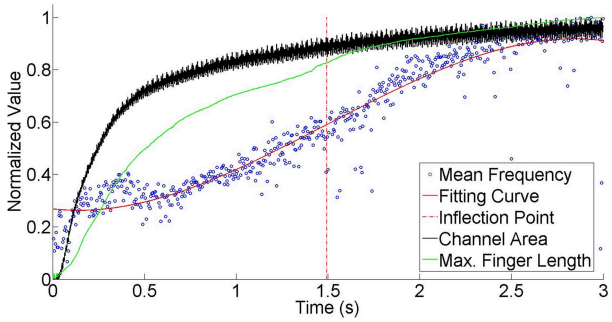

FIGURE 7 | Mean frequency evolution (normalized with the maximum value 200 kHz) during injection. As the channel network develops progressively the energy percentage in the low frequency range f <10 kHz diminishes, and the mean frequency gets higher. A cubic polynomial curve (red) is fitted to the mean frequency data to simplify the comparison and discussions. The location of the inflection point of this curve is indicated by the (red) dash dot strip ($t_0 = 1.49$ s). In this curve the normalized maximum finger length (green, maximum value is approximately 35 cm) and the carved area (black, maximum value is approximately 270 cm^2) is also presented.The area saturates to a maximum at a time close to t_0. The length still increases slightly after t_0, in particular, a small step in finger length (high slope of the length curve, corresponding to a large stick slip event connected to the finger) can be noticed around t_0.

development stops and the regime inside the Hele-Shaw cell changes to a slow relaxation stage with slow fluid overpressure diffusion detailed in the discussion section.

4.2. Acoustic Events

It is possible to link the information received from the small scale lab experiments with large scale data, and vice-versa. In the experiments, we noted that the number of acoustic events occurring inside the Hele-Shaw cell is related to the empty channel area. However, after the fractured area reaches the final channel network shape, stress relaxation events are observed. These events are investigated further using event counting methods based on the ratio of Short Term Average over Long Term Average (STA/LTA) for event detection and compared with the evolution of the channel area inside the Hele-Shaw cell.

4.2.1. Event Detection

Detecting the number of events occurring during fracturing is a good indicator of the compaction level within the material. As long as there is motion of granular particles with the fast fluid flow it is very probable to detect some acoustic events in the experimental recording. However, it is very important to analyze and understand which part of the recording can be labeled an event and which part can not. STA/LTA threshold method is commonly used in seismic data interpretation [55–58]. If the parameters are selected carefully, it is very easy to use and is very robust [59]. While LTA considers the average temporal noise to have an idea of the general behavior of the site, STA looks for intense changes in the signal in a small time window to detect acoustic events. Thus, it makes the ratio of those two parameters sensitive to the more complex events as well. When this STA/LTA ratio passes a pre-defined threshold, it is considered as an event (**Figure 8**), and the event counter is incremented. As long as the ratio stays above the threshold, it does not trigger again. Right after the ratio goes below the threshold, the algorithm can be triggered again for the next event to be counted. This algorithm (for one time window) can be generalized as follows:

$$\frac{(STA)}{(LTA)} = \frac{\frac{1}{N_s}\sum_i^{i+N_s}(s(i)^2)}{\frac{1}{N_l}\sum_i^{i+N_l}(s(i)^2)} \tag{2}$$

$$\Psi = \frac{(STA)}{(LTA)} \rightarrow \Psi > T \rightarrow Event \tag{3}$$

where $s(i)^2$ is the squared raw signal in the time domain (if necessary, a filtered signal $s'(i)^2$ can be used for different characteristic events), N_s and N_l are the length of the short (0.05 ms) and long time (1 ms) windows respectively and T is the predefined threshold for an event. The threshold to detect events may change between different datasets or different types of acoustic events.

4.2.2. Event Classification

One important thing that should be mentioned about the STA/LTA counting method is the frequency range used. After detailed analysis, it has become apparent that two different types of events exist within the experimental dataset. The first type of events are the non-impulsive low frequency (less than 10 kHz, similar to **Figure 6**) events (Type 1) which are related to the fluid flow and to the fluid-grain interactions rearranging the grains and producing major deformations and channeling. These events begin at the moment when the air injection starts and continue until a fully developed channel network is reached. It is possible to determine accurately this period from the optically acquired data, simply by calculating the area of the channel (estimated via the number of dark pixels in a binarized image) that saturates to a maximum value before the end of the acoustic emissions. Interestingly, in our findings, the number of Type 1 acoustic events follows a similar trend in time as the evolving emptied channel area within the Hele-Shaw cell (**Figure 9**). To enable the detection algorithm to distinguish between the different types of events, frequency filters are applied. To detect Type 1 events, a butterworth bandpass filter with corner frequencies 100 Hz and 10 kHz is applied to the raw signal $s(i)$ before the STA/LTA event detection is applied.

The second type is the aftershock-like events, Type 2. Unlike the Type 1 events, in power spectrum their energy is spread over a wide frequency range similar to the one presented in **Figure 10**. These events are similar to the stick-slip relaxation events following a big earthquake in real scale. Compacted grains are rearranging their positions to have a more compacted state due to continuous air injection which results in some of their energy being released as acoustic emissions. To detect Type 2 events, a highpass filter for frequencies higher than 100 kHz is applied to the raw signal $s(i)$ before the STA/LTA event detection is applied. In **Figure 11** the evolution in the power spectrum with time is presented. In the figure, a Type 2 event occurred at $t = 2.8$ s is also presented.

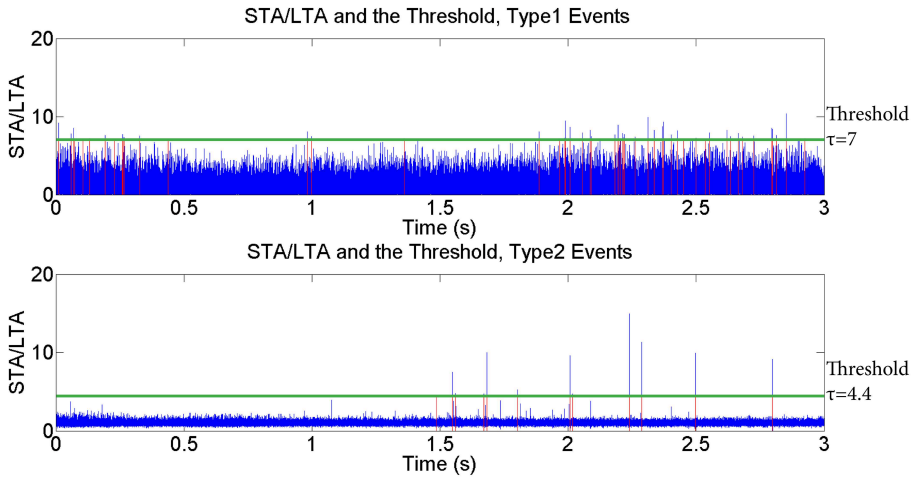

FIGURE 8 | STA/LTA detection plots for Type 1 (upper figure) and Type 2 (lower figure) events. Top: The raw signal is filtered by using a butterworth bandpass filter with corner frequencies 100 Hz and 10 kHz before computation. **Bottom:** The raw signal is filtered by using a highpass filter for frequencies higher than 100 kHz before computation. We found that some of the Type 2 events can be classified as Type 1 events since they have energy in the low frequency higher than the threshold.

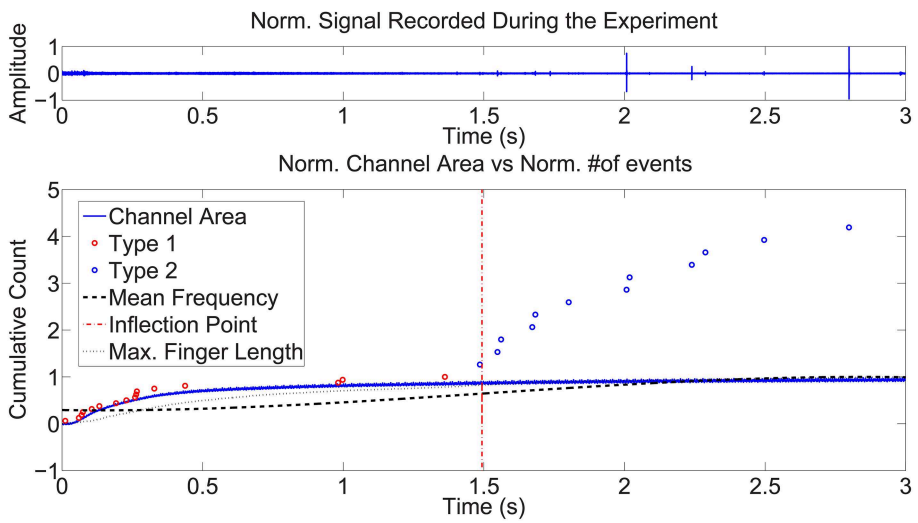

FIGURE 9 | Top: Signal recorded during the experiment. **Bottom:** Blue curve shows dark pixel counting over the image to compare compacted area with the number of different acoustic events occurred. Circles represent cumulative number of events normalized with maximum number of Type 1 events (i.e., 17 events). Cumulative number of Type 1 events (red points) are fitting well to the normalized channel area with time presented in the lower plot. First Type 2 (blue) event occurs very close to the inflection point of the mean frequency curve. Type 2 events are very impulsive and noticeable in the top panel as well.

After investigating further, we also noticed that the occurrence frequency of these events decay with time, similar to the Omori Law [60, 61]. In the following section, curve fitting to the number of Type 2 acoustic emissions assuming an Omori Law decay (**Figure 12**) will be discussed.

4.2.3. Omori Law

Omori [60, 61] worked on the half-day and monthly frequencies of aftershocks of the 1891 Nobi earthquake in Japan [60, 61] . He found that the frequency of aftershocks $n(t')$ at time t' can be expressed as:

$$n(t') = K(t' + c)^{-1} \tag{4}$$

and the same equation for the cumulative number of aftershocks is given as

$$N(t') = \int_0^{t'} n(s)ds = Kln(t'/c + 1), \tag{5}$$

where c is a characteristic time, small and positive, K is the slope of the fit in the semi-logarithmic domain and $N(t')$ is the number of cumulative aftershocks up to time t'. Following

Omori, Utsu (1957) emphasized that the real aftershock activity decays with time differently than the originally derived Omori Law and proposed the equation for the frequency of aftershocks, with another fitting exponent p, as Utsu [62, 63]:

$$n(t') = K'(t' + c')^{-p} \tag{6}$$

and called this the Modified Omori Law (MOL). The corresponding equation for the cumulative number of aftershocks is given as:

$$N(t') = \frac{K'}{(p-1)}\left(c'^{1-p} - (t' + c')^{1-p}\right) \tag{7}$$

where c' is a characteristic time and K' is the slope having the dimension of time$^{(p-1)}$.

Using these approaches Omori Parameters K, c and p are estimated on our experimental catalog of Type 2 events, using time $t' = t - t_0$, where t_0 is the time defined in Section 4.1, that corresponds to the end of the channel formation and to the inflection point of the mean frequency recorded (**Figure 12**). A bin size to find frequency of occurrence of the events is selected as 0.2 s. However, it is more robust to use cumulative number of aftershocks (Equations 5 and 7) to avoid choosing an additional parameter for binning which can vary. Fitting is computed with 95% confidence bounds (i.e., two standard deviations away from the mean of the estimated value) to show the quality of fitting. Fitting parameters are calculated by a linear regression in the semi-logarithmic space of the cumulative number of events as $K = 4.89 \pm 1.33$ and $c = 0.13 \pm 0.8$ s. The Root Mean Square Error (RMSE) - average of the residual of the fit - is calculated to be 0.57 in this particular fit using the Equation (5).

Using the Modified Omori Law (i.e., Equation 7) fitting parameters are found as $K' = 5.34 \pm 1.52$ s$^{-0.45}$, $c' = 0.0066 \pm 0.55$ s, $p = 0.55 \pm 0.38$ and RMSE is calculated to be 0.53 and the error bar is evaluated as the standard error [64]. The dashed lines in the **Figure 12** represents two RMSE from the fitted curves.

5. Discussion

5.1. Discussion of the Experimental Results

The power spectrum of the mechanical signal at the different time windows show that the interactions inside the Hele-Shaw cell are evolving with continuous injection. In the beginning, there is a bulk movement of the grains due to the compaction caused by air injection. In **Figure 6B** it can be seen that the power spectrum follows a power law trend with an

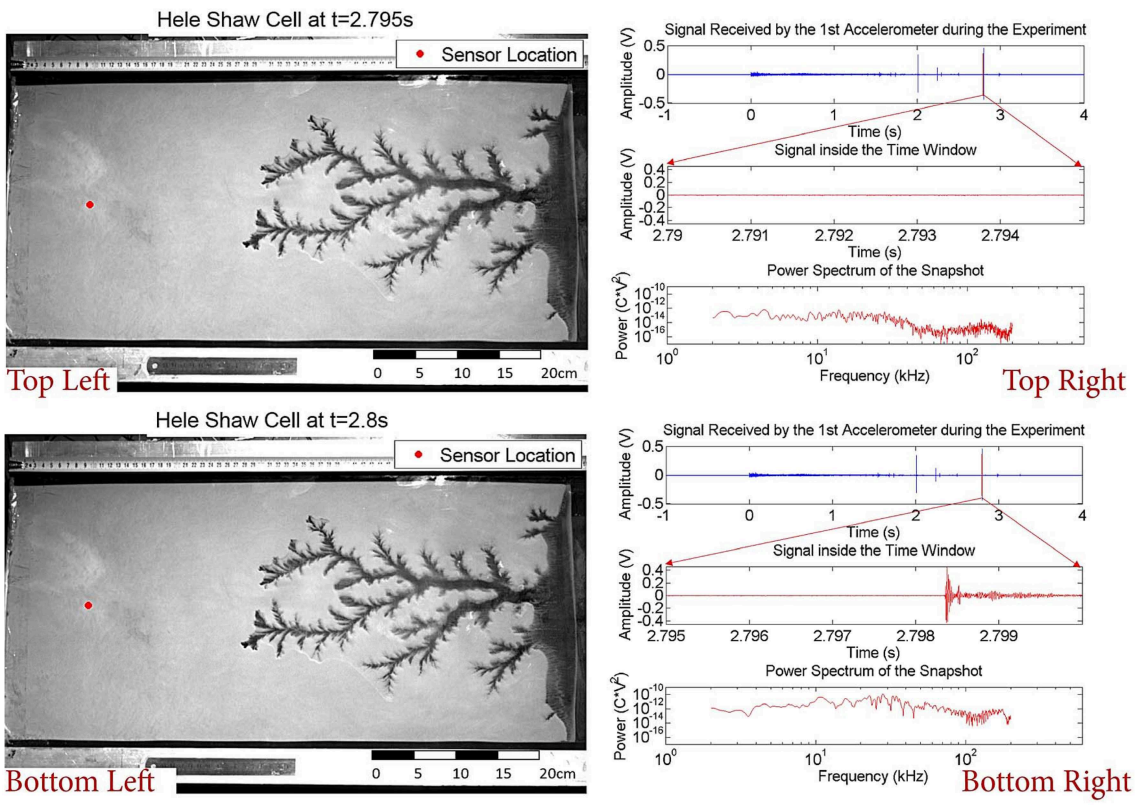

FIGURE 10 | Optical (Left) and acoustic (Right) experimental recordings just before (Top) and during (Bottom) an aftershock like event. The red dot on the left image illustrates the sensor location where the signal on the right is recorded. **Top Right:** Acoustic signal recorded throughout the entire experiment. The red strip (time window of 0.005 s) corresponds to the snapshot that the image **(Left)** and power spectrum **(Right)** occurred at.

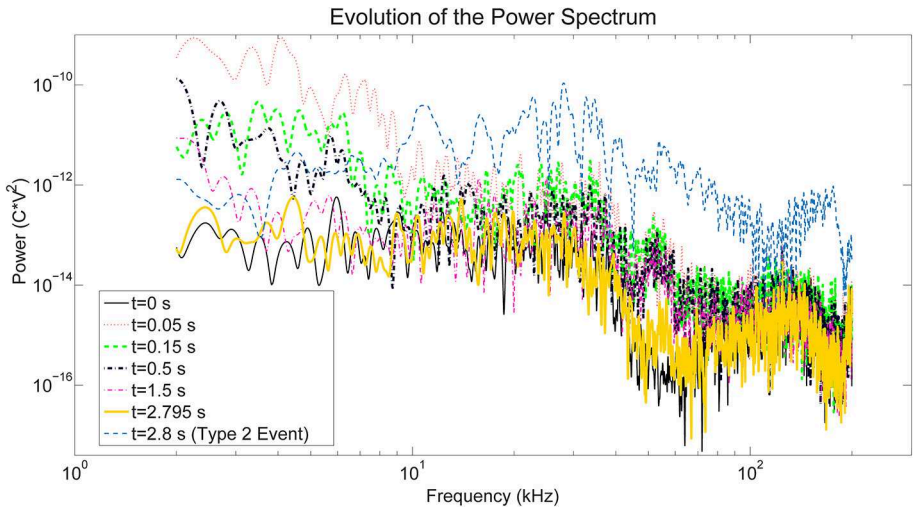

FIGURE 11 | The evolution of power spectrum over different time windows are presented. With time, the power is decreasing until finally reaching back to the initial level. However, during Type 2 events the spectrum has a completely different signature.

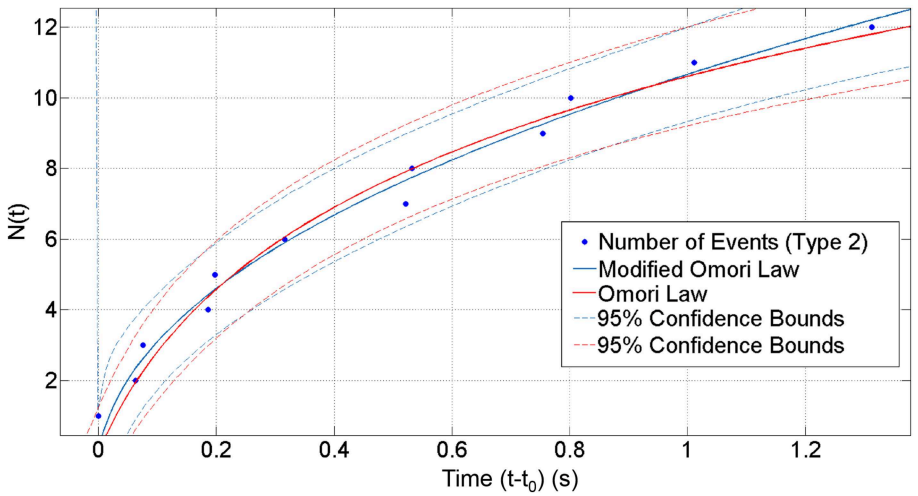

FIGURE 12 | Conventional and Modified Omori Law Fits of the cumulative number of events. The circles represent the cumulative number of events and the solid lines represent the fitting curves given by the Equations (5) and (7). $t' = 0$ in this representation corresponds to time $t_0 = 1.49$ s after the start of the air injection.

exponent equal to −1.61 without any major peak. This indicates, although there are many different phenomena with various characteristic frequencies happening at the same time (e.g., bulk compaction, interactions between solid and fluid phase, stress redistribution among the medium etc.), that a scale-free mechanical phenomenon—probably related to the developing branching pattern—is dominating the emissions. Since the low frequency has higher energy, it can be seen that the mean frequency of the initial part $t < 1.5$ s is low as well (**Figure 7**). As the channeling and fingering starts, the mean frequency is shifting from lower frequencies $f < 10$ kHz to the higher frequencies. Moreover, this evolution can be seen in **Figure 11**. Rising mean frequency is also seen in the signals recorded during some volcanic processes, as e.g., the 2004 eruption process of the Arenal volcano, Costa Rica, and was interpreted as related to the stress increase with time due to the fluid pressure [65]. Additionally, the rate of this increase decreases as the channel network establishes. The trend which represents the channel area and also increasing permeability due to fracturing, is given in **Figure 9** by checking the dark pixels in the images through time. Occurrence frequency of low frequency earthquake-like events (described as Type 1) decreases with increased permeability due to fingering and fracturing indicated in the work of Frank et al. about real scale events seen in Mexico [66].

The inflection point (**Figure 7** red dash dot line) of the mean frequency curve ($t_0 = 1.49$ s) shows the point where the power spectra evolves from a power law trend (**Figure 6B**) to stick-slip aftershock like events (**Figure 10**, Bottom Right) whose

power spectra consists of several peaks in the frequencies higher than 10 kHz (**Figure 11**) which causes the increase in the mean frequency. This inflection point occurs almost at the same time as the small step in the maximum finger length curve (high slope of the length curve, **Figure 7** green) can be noticed around t_0. This small step shows a stick slip motion in the most advanced finger tip. The inflection point also corresponds to the start of occurrence of the first Type 2 event which is presented in **Figure 9**. We can thus attribute it to a change in dynamics of the pneumatic fracture process: the main tree of channels stabilizes, and a slower stress relaxation process starts in the bulk around the channels, which leads to different type of acoustic event signatures, associated to the appearance of the impulsive Type 2 events.

The presence of this inflection point in the average frequency of the power spectrum, and the appearance of impulsive events (Type 2), can be suggested as the interesting signatures of the stabilization of the main channel during the monitoring of field scale hydrofracture or pneumatic fracture: these clear signatures can be detectable even in opaque field scale microseismic monitoring studies. This change of event types can also be seen in **Figure 9** which shows the event detection using STA/LTA event detection procedure. As presented in the bottom panel of **Figure 8**, Type 2 events are detected starting from the inflection point of the mean frequency curve ($t_0 = 1.49$ s). Furthermore, we noticed that the cumulative number of Type 2 events are following an Omori Law trend which is shown in the **Figure 12**. This is due to the similarity between the aftershocks which is observed in real life and the Type 2 events in the medium which are due to the local stress relaxations. $K = 4.89 \pm 1.33$ and $c = 0.13 \pm 0.8$ s for the Omori Law and $K' = 5.34 \pm 1.52$ $s^{-0.45}$, $c' = 0.0066 \pm 0.55$ s, $p = 0.55 \pm 0.38$ for the Modified Omori Law are computed as fitting parameters. It can be said that the Modified Omori Law—Equation (7)—gives slightly better fitting results to this dataset (RMSE is 0.57 for Omori Law and 0.53 for Modified Omori Law) due to the application of another parameter which is making the fitting procedure more sensitive.

The obtained p-value in this study ($p = 0.55$) corresponds to the p-value range for earthquakes studied by different scientists (i.e., 0.6–1.6 [63], or 0.3–2.0 [67]). There are several studies for different types of earthquake mechanisms with varying p-values. Utsu [63] presented some of them: $p = 0.9 \pm 0.1$ is found for the 1962 Westport earthquake in New Zealand, $p = 1.4$ is found for the 1965 Hindu Kush intermediate-depth ($h = 214$ km) earthquake, and $p = 0.84$ is found for the aftershocks following a rock fracture event in a mine causing a low magnitude earthquake ($M = -2$). This variability has been attributed to the variations in the state of stress, temperature, structural heterogeneities, material parameters, etc., in different tectonic regimes. However, a single, dominant factor controlling this parameter has not yet been identified [68].

In different examples, post-injection fluid-induced seismic events at various injection sites such as Fenton Hill, USA, and Soultz-sous-Forêts, France, appear to decay with an Omori-like fashion [69]. The rate of the post-injection seismic events in these cases has not been analyzed using the conventional MOL, thus a direct comparison between the obtained p-values cannot be carried out. In other examples, Nur and Booker [70] found that the decay of earthquakes following a step in the pore fluid pressure obeys a Modified Omori Law (MOL) with $p = 0.5$, which was consistent with a pore fluid diffusion law. Similarly, Yamashita worked on a model linking the fault slip and fluid flow in a system preloaded in shear. He found that the p-value is 0.48 for an early time period in a sequence of induced secondary aftershocks [71]. This link was also derived by Shapiro et al. [72–74] and Rozhko et al. [75] for the events related to pressure changes in operation wells. Their formulation relates the rate of acoustic events to the temporal change in pore pressure. This is very similar to the p-value obtained by fitting the MOL to our experimental results.

5.2. Physical Explanation of the Experiments

The observed p-value in our experiments is also consistent with the derivations and approximations carried out in the models derived by Niebling et al. [20, 24] or Johnsen et al. [25] for systems related to the one currently studied. The exponent of this Modified Omori Law and its prefactor can be directly related to the stress relaxation due to the diffusion of fluid pressure with the following approximations - that will be validated a posteriori by the agreement between the exponent and prefactor derived and the one that can be measured directly.

After the initial fast stage where the large empty channel is created, the compressibility of the fluid induces a slower seepage into the surrounding material. The boundary conditions can be considered as fixed for the granular material along the channel: owing to the large permeability of the channel, the boundary condition along the channel corresponds to an approximately homogeneous fluid pressure equal to the imposed inlet pressure, which also corresponds to the total stress since no grains are present in the channel, and the total pressure and pore pressure correspond on this boundary. The outlet boundary conditions can be considered as fixed pore pressure equal to the atmospheric one, and fixed displacement due to the semipermeable grid. The boundary conditions along the plates correspond to no flux for the fluid, and no normal displacement for the particles.

Since no large motion occurs in the following relaxation stage, the total stress field in the medium can be approximated as constant. This total stress $\sigma^{\mathbf{T}}$ is the sum of the solid stress $\sigma^{\mathbf{s}}$ arising from the forces transmitted in the grain-grain and grain-plate contacts, and the pore pressure $\mathbf{p}$:

$$\sigma^{\mathbf{T}} = \sigma^{\mathbf{s}} + \mathbf{pId}, \tag{8}$$

where $\mathbf{Id}$ is the identity matrix. This general formulation of summing the solid-bearing and fluid-bearing parts of the stress is for example demonstrated by Jackson [76], and is valid as long as the large scale shear stress due to fluid-solid momentum exchange is negligible. It was shown to hold, for example, in sheared saturated granular layers [77].

The total stress being fixed with fixed boundary conditions, the balance between solid-bearing and fluid-bearing stress changes as the fluid seeps in due to pore pressure relaxation. For every grain-grain contact and grain-plate contact, the stick/slip

criterion can be described using a Coulomb friction criterion according to which slip occurs when the equality is reached:

$$\sigma_s^s \geq \mu \sigma_n^s, \tag{9}$$

where σ_n^s and σ_s^s are respectively the norms of the normal and shear (frictional) solid stress transmitted by the contact considered, and μ is the friction coefficient depending on the characteristics of the contacting elements (grains and plates).

The fluid can be explicitly considered by expressing this law in terms of total stress and fluid pressure, using Equations (8, 9) which leads to a formulation corresponding to Terzaghi's 1936 effective stress formulation [77, 78]:

$$\sigma_s^T \geq \mu(\sigma_n^T - p), \tag{10}$$

where p is the pore fluid pressure. With fixed total stress, Equation (10) can be reformulated in terms of fluid pressure required for the grain pairs to slide:

$$p > \sigma_n^T - \frac{\sigma_s^T}{\mu}. \tag{11}$$

We assume a random distribution for the local total stress values, σ_s^T and σ_n^T, and call ξ the density of contacts per unit surface of the plates that will break with an acoustic emission due to sufficiently high pore fluid pressure. According to the above criterion, when p rises from the initial value to the final one a slip, during which micro acoustic events are produced, happens. The rate of events can be derived as follows: the system is considered to have a quasi one dimensional geometry where the grains ahead of the channel in the average flow direction correspond to $x > 0$. The initial value of the overpressure (i.e., pressure above the atmospheric pressure) is approximated as $P = P_{max}$ for $x < 0$ and $P = 0$ for $x > 0$. This holds if the initial channel creation was fast compared to pressure diffusion, so that the pressure skin depth stayed small with respect to the system size during channel creation, which was verified numerically by Niebling et al. [20].

The variation of the pore pressure over time is thus the key factor in this system to change stability of the porous medium. This pore pressure can be expressed using the fluid pressure diffusion into the porous medium. Considering that the grains are not moving, the pore velocity v_d of the fluid (local velocity in the pores) and the Darcy velocity v_D, can be computed from Darcy's law. As presented e.g., in Niebling's work [22] or Johnsen's [26]:

$$v_d = \frac{v_D}{\phi} = -\frac{\kappa}{\phi\mu}\nabla P \tag{12}$$

where κ is the local permeability, ϕ is the local porosity of the granular medium, μ is the fluid viscosity and P is the pressure gradient driving the flow. Implementing this equation into conservation of mass we have:

$$\partial_t(\phi\rho(P)) + \nabla(\phi\rho(P)v_d) = 0 \tag{13}$$

where $\rho(P)$ is the updated mass density of air, obtained assuming the state equation of a perfect gas which is following the relation $\rho(P) = \rho_0 \frac{P}{P_0}$ which is valid for this type of setups since the pressure is not varying by orders of magnitude with no strong density changes over the cell. When the pressure dependence of the density is included in the analysis which is indeed more correct, the diffusion equation becomes nonlinear. It can be treated numerically, Niebling et al. [20]. As shown by Niebling et al., no qualitative changes are noted in this kind of regime though and the same kind of scaling law for the growth of the skin depth is observed. In this equation, ρ_0 is the density of air and P_0 is the atmospheric pressure. This puts Equation (13) into the form:

$$\frac{\rho_0}{P_0}\partial_t(\phi P) - \nabla(\rho_0 \frac{\kappa}{\mu}\nabla P) = 0. \tag{14}$$

Considering that porosity ($\phi = \phi_0$) and local permeability ($\kappa = \kappa_0$) does not change with time, after some simplification Equation (14) will become:

$$\frac{\phi_0}{P_0}\partial_t(P) - \frac{\kappa_0}{\mu}\nabla^2 P = 0. \tag{15}$$

Then, from Equation (15) we can derive the diffusion equation as:

$$\partial_t(P) = \frac{\kappa_0 P_0}{\phi_0 \mu}\nabla^2 P \tag{16}$$

where the part before the pressure gradient of Equation (16) can be described as diffusivity constant of overpressure in a porous medium, corresponding to the slow Biot wave [79]:

$$D = \frac{\kappa_0 P_0}{\phi_0 \mu}. \tag{17}$$

The local permeability κ_0 can be computed using Carman-Kozeny equation [22]:

$$\kappa_0 = \frac{d^2}{180}\frac{\phi^3}{(1-\phi)^2} \tag{18}$$

where $d = 80\,\mu$m is the diameter of the grains and ϕ, the porosity of the medium, is around 48% which is typical for this kind of preparation. The results of Niebling et al. [20] show that in this kind of system, fast forming aerofractures are formed, followed by a slow diffusion of overpressure away from the large channels - our slow relaxation stage.

He modeled the behavior of the aerofractures with two different stages, with initially a fast channel formation in the beginning due to the high fluid pressure and following, close to the injection point, a thick compaction front which satisfies Equation (11).

As the overpressure diffuses in the medium, the grains can slip and rearrange, possibly giving rise to the acoustic events. The fundamental solution of Equation (16) is derived with an approximated 1D boundary condition, having an initial condition $P = 0$ at $t = t_1$ describing the finger tip as a flat boundary at $x = 0$, and the space ahead of it as $x > 0$. Then, the initial condition for the overpressure is $\Delta P = 0$ for $x > 0$ and $t = t_1$ (when the finger stops and the overpressure has not

yet penetrated far from the boundary). Furthermore, boundary conditions corresponding to the imposed overpressure are $\Delta P = P_{max}$ at $x = 0$ (the finger boundary), and $\Delta P = 0$ at $x \to +\infty$ (far ahead of the finger). The solution of the diffusion Equation (16) gives the overpressure at distance x ahead of the tip of the empty channel, and at time $t > t1$, after the end of the channel formation [25]:

$$\begin{aligned}\Delta P(x,t) &= P_{max}\mathrm{erfc}\left(\frac{x}{2\sqrt{D(t-t_1)}}\right)\\ &= P_{max}\frac{2}{\sqrt{\pi}}\int_{x/2\sqrt{D(t-t_1)}}^{\infty} e^{-y^2}dy \end{aligned} \quad (19)$$

where t_1 is the time when the end of channel growth stops, P_{max} is the saturation level of pressure. As it is described in Equation (11) fluid pressure is directly effective on the number of failing contacts.

This exponentially decreasing pressure field, for order of magnitude estimates, can be approximated as a zone of (skin) depth $2\sqrt{D(t-t_1)}$ ahead of the finger tip experimenting a significant overpressure rise close to the maximum overpressure P_{max}, and a negligible overpressure in the zone ahead of it. Since ξ contacts break—with an acoustic emission—per unit area when the overpressure rises from 0 to P_{max}, the cumulative number of contacts failing (i.e., the cumulative number of acoustic emissions) can be approximated via the equation below:

$$N(t) = 2L\xi\sqrt{D(t-t_1)} = \sqrt{(t-t_1)/\tau} \quad (20)$$

where L is the width of the cell. Furthermore, there is a characteristic time related to the pore pressure diffusion and density of contacts breaking due to this pore pressure increase,

$$\tau = 1/(4DL^2\xi^2). \quad (21)$$

This time τ is different from the other characteristic time t_1, that corresponds to the start of the diffusive behavior for the pore pressure.

Equating Equations (7) and (20) (and recalling that the time t' is measured with respect to t_0 in this last equation), we obtain the prediction:

$$((t-t_1)/\tau)^{0.5} = \frac{K'}{1-p}((t'+c')^{(1-p)} - c'^{(1-p)}), \quad (22)$$

which predicts that $1-p = 0.5$, i.e., $p = 0.5$, $t - t_1 = t' + c'$, $c' = 0$ which leads to $t - t_1 = t'$. Considering $t' = t - t_0$, this becomes $t_1 = t_0$ and finally Equation (22) turns into $K'/(1-p) = \tau^{-(1-p)}$.

This is indeed the case up to the error bars: $t_1 = t_0 - c'$, with $c' = 0.0066 \pm 0.55$ s, i.e., the start of the diffusive regime $t = t_1$ corresponds to the end of the growth of the finger $t = t_0$ up to the error bar, and p is found to be $p = 0.55 \pm 0.38$, equal to 0.5 up to the error bar. The prefactor of the MOL, found with the central p-value of 0.55 to be $K' = 5.34 \pm 1.52$ s$^{-0.45}$, allows to evaluate the characteristic diffusion time

$$\tau = (K'/(1-p))^{1/(p-1)} = (5.34/0.45)^{(-1/0.45)} = 0.004\,\mathrm{s}. \quad (23)$$

The frequency of occurrence of events is the time derivative:

$$\frac{dN}{dt} = \frac{1}{2\sqrt{\tau(t-t_1)}}. \quad (24)$$

The present study thus suggests that $p = 0.5$ in the Modified Omori Law is the signature of the slow stress relaxation due to the diffusion of the overpressure in the medium surrounding the cavities.Presumably, this p-value may decrease if the fluid injected slowly enough so that the diffusion skin depth becomes large with respect to the channel width during the injection, which is a contrary to the situation depicted here [20]. Also, large injection pressure may lead to subcritical crack growth and change p-value [40, 42, 80].

The prefactor of this law, corresponding to the characteristic time $\tau = 0.004$ s for this diffusion, can thus be related to the porosity and permeability of the medium around the channels, the viscosity and compressibility of the fluid, and the density of failing sites leading to events.

Putting τ back into the Equation (21) it is possible to calculate ξ via the following equation:

$$\xi = \frac{1}{2L\sqrt{D\tau}} \quad (25)$$

Recalling the expressions Equations (17) and (18), we obtain for this medium a diffusivity

$$D = \frac{d^2\phi^2 P_0}{180(1-\phi)^2\mu} = 0.20\ \mathrm{m}^2/\mathrm{s} \quad (26)$$

where we have used the air viscosity, $\mu = 1.810^{-5}$ Pa s, and the atmospheric pressure value $P_0 = 10^5$ Pa.

These two last equations, Equations (25) and (26), allow to express the density of the triggered seismogenic contacts, with $L = 0.4$ m, as:

$$\xi = \frac{1}{2L\sqrt{D\tau}} \simeq 45/\mathrm{m}^2 \quad (27)$$

for this presented experimental setup. This indicates that around 45 contacts per square meter can give rise to strong events due to overpressure rise (which is far lower than the total number of contacts $\approx 2.3 \times 10^{10}$ for the grains and cell thickness considered). This shows that just a small subfraction of contacts give rise to strong events.

It is also very consistent within the order of magnitude with the fact that 12 events of Type 2 were observed during this relaxation in the system of size around 50 cm ahead of the main finger by 40 cm width, i.e., of size 0.2 m^2 corresponding to a density around 50 m^{-2} microseismogenic events happening during this stress relaxation.

6. Conclusion

A purpose-built Hele-Shaw cell experiment was designed to enable both optical and acoustic recordings associated with controlled fracturing of a porous medium via air injection.

The optical and acoustic recordings are analyzed together to obtain a further understanding of the type of deformation occurring within the cell. Based on the evolution of the power spectrum and mean frequency of the acoustic data with time, together with the growing channel network, it can be determined that the low frequency content $f < 10$ kHz of the acoustic emissions is directly related to the permeability state of the medium. Low frequencies dominate the power spectrum as long as the medium has not reached its final fractured state. After this state is reached, aftershock-like events seem to release the stress from the medium in the post-fractured phase. These aftershock-like events have a broadband spectrum where the energy is not focused on the low frequency but spread on a wide span of frequencies. These events occur right after reaching the final fractured state and their frequency of occurrence decays with time. Both power spectra evolution and diminishing frequency of occurrence are present in real scale microseismic data. In addition, it is possible to estimate the number of aftershocks by using Modified Omori Law in experimental and microseismic data. These signatures, inflection point in the average frequency, appearance of impulsive events of high frequency, and starting point of an Omori Law, can be used straightforwardly in large scale microseismic monitoring of fluid injection and well stimulation. The permeability of the medium can also be directly estimated from the prefactor of the Omori Law.

Acknowledgments

We would like to thank Alain Steyer and Miloud Talib for their technical support during experimental campaigns. We would also like to thank Maxime Farin for stimulating discussions during this work. This project has received funding from the European Union's Seventh Framework Programme for research, technological development and demonstration under grant agreement no 316889, from the REALISE program of the Alsatian research network, from the Universities of Oslo and Strasbourg via a gjesteforsker program and an IDEX Espoirs award.

References

1. Guyon E, Hulin JP, Petit L. *Hydrodynamique Physique.* Savoirs Actuels, EDP Sciences (2001). Available online at: http://books.google.fr/books?id=ma8Me9pe1-MC
2. Spurk JH. *Fluid Mechanics. Problems and Solutions.* Springer Verlag (1997).
3. Craig RF. *Craig's Soil Mechanics, 7th Edn.* Taylor & Francis (2004). Available online at: http://books.google.fr/books?id=pfK66ZiuWMcC
4. Duran J, Reisinger A, de Gennes PG. *Sands, Powders, and Grains: An Introduction to the Physics of Granular Materials.* Partially Ordered Systems. New York, NY: Springer (2012). Available online at: https://books.google.no/books?id=x9TiBwAAQBAJ
5. Herrmann HJ, Hovi JP, Luding S. *Physics of Dry Granular Media.* NATO Advanced Science Institutes Series. Series E, Applied Sciences. Springer (1998). Available online at: http://books.google.fr/books?id=TZyOKD8bJRgC
6. Gidaspow D. *Multiphase Flow and Fluidization: Continuum and Kinetic Theory Descriptions.* Academic Press (1994). Available online at: http://books.google.fr/books?id=vYVexK0-tooC
7. Kunii D, Levenspiel O. *Fluidization Engineering. Butterworth-Heinemann Series in Chemical Engineering.* Butterworth-Heinemann (1991). Available online at: http://books.google.fr/books?id=ZVnb17qRz8QC
8. Goren L, Aharonov E, Sparks D, Toussaint R. Pore pressure evolution in deforming granular material: a general formulation and the infinitely stiff approximation. *J Geophys Res Solid Earth* (2010) **115**:B09216. doi: 10.1029/2009JB007191
9. Goren L, Aharonov E, Sparks D, Toussaint R. The mechanical coupling of fluid-filled granular material under shear. *Pure Appl Geophys.* (2011) **168**:2289–323. doi: 10.1007/s00024-011-0320-4
10. Schuring JR, Kosson DS, Fitzgerald CD, Venkatraman S. *Pneumatic Fracturing and Multicomponent Injection Enhancement of in Situ Bioremediation.* U.S. Patent No. 5,560,737. Google Patents. (1996) Available online at: http://www.google.com/patents/US5560737
11. US. Environmental Protection Agency. *Accutech Pneumatic Fracturing Extraction and Hot Gas Injection, Phase One: Applications Analysis Report.* Cincinnati, OH: DIANE Publishing Company (1994).
12. Gao F, Xie H, Zhou F, Ju Y, Xie L, Liu Y, et al. *Pneumatic Fracturing Method and System for Exploiting Shale Gas.* U.S. Patent App. 14/335,935. Google Patents (2014). Available online at: https://www.google.com/patents/US20140326450
13. Charléty J, Cuenot N, Dorbath L, Dorbath C, Haessler H, Frogneux M. Large earthquakes during hydraulic stimulations at the geothermal site of Soultz-sous-Forłts. *Int J Rock Mech Mining Sci.* (2007) **44**:1091–105. doi: 10.1016/j.ijrmms.2007.06.003
14. Cuenot N, Dorbath C, Dorbath L. Analysis of the microseismicity induced by fluid injections at the EGS site of soultz-sous-forłts (Alsace, France): implications for the characterization of the geothermal reservoir properties. *Pure Appl Geophys.* (2008) **165**:797–828. doi: 10.1007/s00024-008-0335-7
15. Dorbath L, Cuenot N, Genter A, Frogneux M. Seismic response of the fractured and faulted granite of Soultz-sous-Forłts (France) to 5 km deep massive water injections. *Geophys J Int.* (2009) **177**:653–75. doi: 10.1111/j.1365-246X.2009.04030.x
16. Aochi H, Poisson B, Toussaint R, Schmittbuhl J. Induced seismicity along a fault due to fluid circulation: conception and application. In: *Japan Geoscience Union Meeting 2011.* Chiba (2011).
17. Valkó P, Economides MJ. *Hydraulic Fracture Mechanics.* Wiley (1995). Available online at: https://books.google.com.tr/books?id=zcFTAAAAMAAJ
18. Cornet F, Helm J, Poitrenaud H, Etchecopar A. Seismic and aseismic slips induced by large-scale fluid injections. In: *Seismicity Associated with Mines, Reservoirs and Fluid Injections.* Basel: Springer (1998). p. 563–83.
19. Cornet FH. *Elements of Crustal Geomechanics.* Cambridge University Press (2015). Available online at: https://books.google.fr/books?id=GdXeBgAAQBAJ
20. Niebling MJ, Toussaint R, Flekkøy EG, Måløy KJ. Dynamic aerofracture of dense granular packings. *Phys Rev E* (2012) **86**:061315. doi: 10.1103/physreve.86.061315
21. Niebling MJ, Flekkøy EG, Måløy KJ, Toussaint R. Mixing of a granular layer falling through a fluid. *Phys Rev E* (2010) **82**:011301. doi: 10.1103/physreve.82.011301
22. Niebling MJ, Flekkøy EG, Måløy KJ, Toussaint R. Sedimentation instabilities: impact of the fluid compressibility and viscosity. *Phys Rev E* (2010) **82**:051302. doi: 10.1103/PhysRevE.82.051302
23. Johnsen Ø, Toussaint R, Måløy KJ, Flekkøy EG. Pattern formation during air injection into granular materials confined in a circular hele-shaw cell. *Phys Rev E* (2006) **74**:011301. doi: 10.1103/physreve.74.011301
24. Niebling MJ, Toussaint R, Flekkøy EG, Måløy KJ. Numerical studies of aerofractures in porous media. *Rev Cubana Fis.* (2012) **29**:1E66–70. Available online at: http://www.fisica.uh.cu/biblioteca/revcubfis/files/Archivos/2012/Vol29-No1E/RCF-29-1E-66.pdf
25. Johnsen Ø, Toussaint R, Måløy KJ, Flekkøy EG, Schmittbuhl J. Coupled air/granular flow in a linear hele-shaw cell. *Phys Rev E* (2008) **77**:011301. doi: 10.1103/PhysRevE.77.011301
26. Johnsen Ø, Chevalier C, Lindner A, Toussaint R, Clément E, Måløy KJ, et al. Decompaction and fluidization of a saturated and confined granular medium by injection of a viscous liquid or gas. *Phys Rev E* (2008) **78**:051302. doi: 10.1103/physreve.78.051302

27. Vinningland JL, Johnsen Ø, Flekkøy EG, Toussaint R, Måløy KJ. Granular rayleigh-taylor instability: experiments and simulations. *Phys Rev E* (2007) **99**:048001. doi: 10.1103/PhysRevLett.99.048001
28. Vinningland JL, Johnsen Ø, Flekkøy EG, Toussaint R, Måløy KJ. Experiments and simulations of a gravitational granular flow instability. *Phys Rev E* (2007) **76**:051306. doi: 10.1103/physreve.76.051306
29. Vinningland JL, Johnsen Ø, Flekkøy EG, Toussaint R, Måløy KJ. Size invariance of the granular rayleigh-taylor instability. *Phys Rev E* (2010) **81**:041308. doi: 10.1103/physreve.81.041308
30. Varas G, Vidal V, Géminard JC. Dynamics of crater formations in immersed granular materials. *Phys Rev E* (2009) **79**:021301. doi: 10.1103/PhysRevE.79.021301
31. Varas G, Géminard JC, Vidal V. Air invasion in a granular layer immersed in a fluid: morphology and dynamics. *Granular Matter* (2013) **15**:801–10. doi: 10.1007/s10035-013-0435-7
32. Varas G, Vidal V, Géminard JC. Venting dynamics of an immersed granular layer. *Phys Rev E* (2011) **83**:011302. doi: 10.1103/PhysRevE.83.011302
33. MacMinn CW, Dufresne ER, Wettlaufer JS. Fluid-driven deformation of a soft granular material. *Phys Rev X* (2015) **5**:011020. doi: 10.1103/PhysRevX.5.011020
34. Sandnes B, Flekkøy E, Knudsen H, Måløy K, See H. Patterns and flow in frictional fluid dynamics. *Nat Commun.* (2011) **2**:288. doi: 10.1038/ncomms1289
35. Rust A, Cashman K, Wallace P. Magma degassing buffered by vapor flow through brecciated conduit margins. *Geology* (2004) **32**:349–52. doi: 10.1130/G20388.2
36. Holtzman R, Szulczewski ML, Juanes R. Capillary fracturing in granular media. *Phys Rev Lett.* (2012) **108**:264504. doi: 10.1103/PhysRevLett.108.264504
37. Eriksen JA, Marks B, Sandnes B, Toussaint R. Bubbles breaking the wall: two-dimensional stress and stability analysis. *Phys Rev E* (2015) **91**:052204. doi: 10.1103/PhysRevE.91.052204
38. Hall SA, de Sanctis F, Viggiani G. Monitoring fracture propagation in a soft rock (Neapolitan Tuff) using acoustic emissions and digital images. *Pure Appl Geophys.* (2006) **163**:2171–204. doi: 10.1007/s00024-006-0117-z
39. Valès F, Bornert M, Gharbi H, Nguyen M, Eytard JC. Micromechanical investigations of the hydro-mechanical behaviour of argillite rocks, by means of optical full field strain measurement and acoustic emission techniques. In: *Proc. Int. Soc. Rock Mechanics.* Lisbon (2007).
40. Grob M, Schmittbuhl J, Toussaint R, Rivera L, Santucci S, Måløy K. Quake catalogs from an optical monitoring of an interfacial crack propagation. *Pure Appl Geophys.* (2009) **166**:777–99. doi: 10.1007/s00024-004-0496-z
41. Grob M, van der Baan M. Inferring *in-situ* stress changes by statistical analysis of microseismic event characteristics. *Leading Edge* (2011) **30**:1296–301. doi: 10.1190/1.3663403
42. Lengliné O, Toussaint R, Schmittbuhl J, Elkhoury JE, Ampuero J, Tallakstad KT, et al. Average crack-front velocity during subcritical fracture propagation in a heterogeneous medium. *Phys Rev E* (2011) **84**:036104. doi: 10.1103/PhysRevE.84.036104
43. Lengliné O, Schmittbuhl J, Elkhoury J, Ampuero JP, Toussaint R, Måløy KJ. Downscaling of fracture energy during brittle creep experiments. *J Geophys Res Solid Earth* (2011) **116**. doi: 10.1029/2010jb008059
44. Lengliné O, Elkhoury J, Daniel G, Schmittbuhl J, Toussaint R, Ampuero JP, et al. Interplay of seismic and aseismic deformations during earthquake swarms: an experimental approach. *Earth Planet Sci Lett.* (2012) **331**:215–23. doi: 10.1016/j.epsl.2012.03.022
45. Farin M, Mangeney A, Roche O. Fundamental changes of granular flow dynamics, deposition, and erosion processes at high slope angles: insights from laboratory experiments. *J Geophys Res Earth Surf.* (2014) **119**:504–32. doi: 10.1002/2013JF002750
46. Stojanova M, Santucci S. Acoustic emissions in fracturing paper. In: *ICF13.* Beijing (2013).
47. Stojanova M, Santucci S, Vanel L, Ramos O. The effects of time correlations in subcritical fracture. An acoustic analysis. In: *21ème Congrès Français de Mécanique, 26 au 30 août 2013.* Bordeaux (2013).
48. Stojanova M, Santucci S, Vanel L, Ramos O. High frequency monitoring reveals aftershocks in subcritical crack growth. *Phys Rev Lett.* (2014) **112**:115502. doi: 10.1103/PhysRevLett.112.115502
49. Toussaint R, Flekkøy EG, Helgesen G. The memory of fluctuating brownian dipolar chains. *Phys Rev E* (2006) **74**:051405. doi: 10.1103/PhysRevE.74.051405
50. Scott GD. Packing of spheres: packing of equal spheres. *Nature* (1960) **188**:908–9. doi: 10.1038/188908a0
51. Ciamarra MP, Coniglio A, de Candia A. Disordered jammed packings of frictionless spheres. *Soft Matter* (2010) **6**:2975–81. doi: 10.1039/c001904f
52. Hild F, Roux S. Digital image correlation: from displacement measurement to identification of elastic properties a review. *Strain* (2006) **42**:69–80. doi: 10.1111/j.1475-1305.2006.00258.x
53. Viggiani G, Hall SA. Full-field measurements, a new tool for laboratory experimental geomechanics. In: *Fourth Symposium on Deformation Characteristics of Geomaterials,* Vol. 1. Amsterdam: IOS Press (2008). p. 3–26.
54. Travelletti J, Delacourt C, Allemand P, Malet JP, Schmittbuhl J, Toussaint R, et al. Correlation of multi-temporal ground-based optical images for landslide monitoring: application, potential and limitations. *ISPRS J Photogramm Remote Sens.* (2012) **70**:39–55. doi: 10.1016/j.isprsjprs.2012.03.007
55. Allen RV. Automatic earthquake recognition and timing from single traces. *Bull Seismol Soc Am.* (1978) **68**:1521–32.
56. Baer M, Kradolfer U. An automatic phase picker for local and teleseismic events. *Bull Seismol Soc Am.* (1987) **77**:1437–45.
57. Earle PS, Shearer PM. Characterization of global seismograms using an automatic-picking algorithm. *Bull Seismol Soc Am.* (1994) **84**:366–76.
58. Wong J, Han L, Bancroft J, Stewart R. Automatic time-picking of first arrivals on noisy microseismic data. *CSEG* (2009) **1**:1–4.
59. Trnkoczy A. Understanding & setting sta/lta trigger algorithm parameters for the k2. *Appl Note* (1998) **41**:16–20.
60. Omori F. On after-shocks. *Rep Imp Earthq Inv Corn.* (1894) **2**:103–38.
61. Omori F. On after-shocks of earthquakes. *J Coll Sci Imp Univ Tokyo* (1894) **7**:111–200.
62. Utsu T. Magnitudes of earthquakes and occurrence of their aftershocks. *Zisin* (1957) **2**:35–45.
63. Utsu T, Ogata Y, Matsu'ura RS. The centenary of the Omori formula for a decay law of aftershock activity. *J Phys Earth* (1995) **43**:1–33. doi: 10.4294/jpe1952.43.1
64. Press WH, Teukolsky SA, Vetterling WT, Flannery BP. *Numerical Recipes 3rd Edition: The Art of Scientific Computing, 3rd Edn.* New York, NY: Cambridge University Press (2007).
65. Almendros J, Abella R, Mora MM, Lesage P. Array analysis of the seismic wavefield of longperiod events and volcanic tremor at arenal volcano, Costa Rica. *J Geophys Res Solid Earth* (2014) **119**:5536–59. doi: 10.1002/2013JB010628
66. Frank WB, Shapiro NM, Husker AL, Kostoglodov V, Bhat HS, Campillo M. Along-fault pore-pressure evolution during a slow-slip event in Guerrero, Mexico. *Earth Planet Sci Lett.* (2015) **413**:135–43. doi: 10.1016/j.epsl.2014.12.051
67. Helmstetter A, Sornette D. Diffusion of epicenters of earthquake aftershocks, Omori's law, and generalized continuous-time random walk models. *Phys Rev E* (2002) **66**:061104. doi: 10.1103/PhysRevE.66.061104
68. Lindman M, Lund B, Roberts R, Jonsdottir K. Physics of the Omori law: inferences from interevent time distributions and pore pressure diffusion modeling. *Tectonophysics* (2006) **424**:209–22. doi: 10.1016/j.tecto.2006.03.045
69. Langenbruch C, Shapiro SA. Decay rate of fluid-induced seismicity after termination of reservoir stimulations. *Geophysics* (2010) **75**:MA53–62. doi: 10.1190/1.3506005
70. Nur A, Booker JR. Aftershocks caused by pore fluid flow? *Science* (1972) **175**:885–7. doi: 10.1126/science.175.4024.885
71. Yamashita T. Regularity and complexity of aftershock occurrence due to mechanical interactions between fault slip and fluid flow. *Geophys J Int.* (2003) **152**:20–33. doi: 10.1046/j.1365-246X.2003.01790.x
72. Shapiro SA, Huenges E, Borm G. Estimating the crust permeability from fluid-injection-induced seismic emission at the KTB site. *Geophys J Int.* (1997) **131**:F15–8. doi: 10.1111/j.1365-246X.1997.tb01215.x

73. Shapiro SA, Audigane P, Royer JJ. Large-scale *in situ* permeability tensor of rocks from induced microseismicity. *Geophys J Int.* (1999) **137**:207–13. doi: 10.1046/j.1365-246x.1999.00781.x
74. Shapiro SA, Rothert E, Rath V, Rindschwentner J. Characterization of fluid transport properties of reservoirs using induced microseismicity. *Geophysics* (2002) **67**:212–20. doi: 10.1190/1.1451597
75. Rozhko AY, Podladchikov YY, Renard F. Failure patterns caused by localized rise in pore-fluid overpressure and effective strength of rocks. *Geophys Res Lett.* (2007) **34**:L22304. doi: 10.1029/2007GL031696
76. Jackson R. *The Dynamics of Fluidized Particles. Cambridge Monographs on Mechanics.* Cambridge University Press (2000). Available online at: https://books.google.fr/books?id=wV9ekwf-fA8C
77. Goren L, Toussaint R, Aharonov E, Sparks DW, Flekkøy EG. A general criterion for liquefaction in granular layers with heterogeneous pore pressure. *Poromechanics V.* (2013) 415–424. doi: 10.1061/9780784412992.049
78. Terzaghi VK. The shearing resistance of saturated soils and the angle between the planes of shear. In: *Proceedings of the 1st International Conference on Soil Mechanics and Foundation Engineering,* Vol. 1. Cambridge, MA: Harvard University Press (1936). p. 54–6.
79. Masson YJ, Pride SR, Nihei KT. Finite difference modeling of Biot's poroelastic equations at seismic frequencies. *J Geophys Res Solid Earth* (2006) **111**:B10305. doi: 10.1029/2006JB004366
80. Santucci S, Vanel L, Ciliberto S. Slow crack growth: models and experiments. *Eur Phys J Spec Top.* (2007) **146**:341–56. doi: 10.1140/epjst/e2007-00192-9

Conflict of Interest Statement: The authors declare that the research was conducted in the absence of any commercial or financial relationships that could be construed as a potential conflict of interest.

frontiers in Physics

ORIGINAL RESEARCH
published: 12 August 2015
doi: 10.3389/fphy.2015.00060

Gas migration regimes and outgassing in particle-rich suspensions

Julie Oppenheimer[1]*, *Alison C. Rust*[1], *Katharine V. Cashman*[1] and *Bjornar Sandnes*[2]

[1] School of Earth Sciences, University of Bristol, Bristol, UK, [2] College of Engineering, Swansea University, Swansea, UK

Understanding how gasses escape from particle-rich suspensions has important applications in nature and industry. Motivated by applications such as outgassing of crystal-rich magmas, we map gas migration patterns in experiments where we vary (1) particle fractions and liquid viscosity (10–500 Pa s), (2) container shape (horizontal parallel plates and upright cylinders), and (3) methods of bubble generation (single bubble injections, and multiple bubble generation with chemical reactions). We identify two successive changes in gas migration behavior that are determined by the normalized particle fraction (relative to random close packing), and are insensitive to liquid viscosity, bubble growth rate or container shape within the explored ranges. The first occurs at the random loose packing, when gas bubbles begin to deform; the second occurs near the random close packing, and is characterized by gas migration in a fracture-like manner. We suggest that changes in gas migration behavior are caused by dilation of the granular network, which locally resists bubble growth. The resulting bubble deformation increases the likelihood of bubble coalescence, and promotes the development of permeable pathways at low porosities. This behavior may explain the efficient loss of volatiles from viscous slurries such as crystal-rich magmas.

Keywords: three-phase suspension, porosity, permeability, outgassing, bubble deformation, granular material, rheology, crystal-rich magma

OPEN ACCESS

Edited by:
Wei-Xing Zhou, East China University of Science and Technology, China

Reviewed by:
Kunal Bhattacharya, Birla Institute of Technology and Science, Pilani, India
Christopher William MacMinn, University of Oxford, UK

***Correspondence:**
Julie Oppenheimer, Volcanology Group, School of Earth Sciences, University of Bristol, Queen's Rd, BS8 1RJ Bristol, UK
julie.oppenheimer@bristol.ac.uk

Specialty section:
This article was submitted to Interdisciplinary Physics, a section of the journal Frontiers in Physics

Received: *01 May 2015*
Accepted: *27 July 2015*
Published: *12 August 2015*

Citation:
Oppenheimer J, Rust AC, Cashman KV and Sandnes B (2015) Gas migration regimes and outgassing in particle-rich suspensions. Front. Phys. 3:60. doi: 10.3389/fphy.2015.00060

Introduction and Background

Volcanic eruptions provide a striking example of the importance of outgassing in natural viscous suspensions. Erupting magmas are suspensions of bubbles and crystals in silicate melt, and eruptions are driven by the exsolution and expansion of the gas phase. Therefore, the mobility of bubbles strongly influences eruption dynamics, and, more fundamentally, the ability of magma to erupt at all [e.g., 1]. Intriguingly, crystal-rich magmas are often found with depleted volatiles [e.g., 2, 3], suggesting an effective—and yet unknown—mechanism for gas loss. It is this conundrum that has motivated our research.

Analog experiments are commonly used to study gas migration behavior in particle-rich suspensions, where both the morphology and migration rate of injected gas can be used to identify distinct behavioral regimes [e.g., 4–6]. The simplest experimental configuration utilizes Hele-Shaw cells, parallel plates clamped together and separated by a small gap, where fluid flow is laminar [7]. Under these conditions, gas intruded into a more viscous liquid migrates in the shape of fingers due to the Saffman-Taylor instability [8]. Adding particles to the invaded liquid creates a spectrum of gas phase geometries that arise from interactions between gas bubbles, liquid and

particles [e.g., 9, 10]. If the particles are density matched, increasing the particle fraction causes fingers to thin and branch, due to an increase in effective viscosity, and local perturbations from discrete particles [11, 12]. When the suspension approaches the random close packing (RCP, also called maximum random packing), fracture-like patterns may form [12–17]. The transition from fingering to fracturing has been placed at a packing fraction of 0.9 * RCP [10, 12]. At RCP, gas migration patterns depend on the confining pressure [15, 17, 18]. Specifically, low confining stress allows continued fracturing, while increasing the confining stress causes the granular material to become rigid, and forces the gas to invade the pore space in the form of capillary or viscous fingering.

In suspensions approaching RCP, the particles are likely to touch. Therefore, a key control on gas migration through particle suspensions is the interactions between solid particles, which also undergo regime changes. The random loose packing (RLP < RCP) is "the loosest possible random packing that is mechanically stable" [19]. Below RLP, a particle suspension generally behaves like a liquid, but at RLP, the suspension becomes capable of jamming [or developing a yield strength; 20, 21]. Furthermore, since a large number of particles are in contact with each other, suspensions of hard spheres become dilatant in response to shear [19]. Indeed, to accommodate an applied shear force, the particles must dislocate around other particles. This inefficient sliding requires space, and causes the whole suspension to dilate; particles transmit the displacement to their neighbors until the successive displacements reach the particles at the boundary. Dilation has important implications for the rheology of particle suspensions. Because the particles are in contact with each other, particle-particle contacts can transmit stress and build force chains, or networks, that extend from the source of shear to the suspension boundaries [22, 23]. Again, confining stress matters: if the boundaries can deform freely, then the particles at the edge will intrude the surface without transmitting stress to their neighbors. However, even a small resistance from the boundary will allow stress build-up in the particle network, which can then resist shear [24]. At the random close packing, the percentage of particles in contact with each other is at its highest (for a randomly packed suspension), and even suspensions of frictionless particles develop a yield strength [21, 25, 26].

We hypothesize that the fields of research synthesized above (finger-to-fracture transition in Hele-Shaw cells, dilation, and jamming) are linked and, together, can explain outgassing of particle-rich suspensions. To this purpose, we extend existing work on gas pattern formation in Hele-Shaw cells to (1) viscous suspending liquids (motivated by application to magmas), and (2) container shapes that approach fully three-dimensional systems. This work is detailed in Part I. In Part II, we assess the role of gas distribution by generating bubble growth throughout the suspension. By combining observations from these diverse experiments, we then explore the likely mechanisms that control both spatial gas migration patterns and outgassing efficiency in particle-rich suspensions.

Part I: Injection of Single Bubbles

Materials and Methods

To study bubble-particle interactions in three-phase suspensions, we ran several suites of experiments that used continuous air injection into suspensions sandwiched between two glass plates. Plate gap distance, liquid viscosity and particle fraction were varied. These experiments were performed in open parallel plate geometries (**Figure 1**); the mixtures of liquid and particles could spread freely laterally, but were confined within a small gap vertically. The set-up procedure was as follows: a suspension was placed upon a solid glass plate (dimensions $40 \times 40 \times 2$ cm), then covered with another glass plate of equal dimensions, allowing the mixture to spread under the weight of the top plate. The two confining plates were clamped together and held apart by separators. During the experiments, an inlet of diameter 1.35 cm in the center of the top plate allowed gas injection into the center of the suspensions. A T joint screwed into this hole connected a pressure gauge on one end (Edwards ASG 2000 mbar), and a 50 mL air-tight syringe on the other via a brass tube of length 31.5 cm and diameter 2.4 mm (**Figure 1**). The air flow from the syringe was controlled with a Becton Dickinson Programme 2 syringe pump that slid the plunger at a constant rate. The total air volume initially contained in the tubing, the T joint and the syringe was 57.6 mL. The pressure at the inlet was recorded in MATLAB at sampling frequencies of 2500 and 5000 Hz. A light box was placed over the top plate and the whole set-up was surrounded by a light-blocking curtain, so that the experiments were lit homogeneously and from above only. Time-lapse images were taken from below, every 2 s.

The materials used were sugar syrup (Tate and Lyle golden syrup), and poly-disperse soda-lime glass beads (Guyson co.) of ∼100 μm diameter (with a range of 75–125 μm). The syrup is Newtonian with a viscosity of ∼60 Pa s at 20°C and surface tension of ∼80 mN/m [27]. We achieved viscosities of 10 Pa s to >600 Pa s (**Table 1**) by respectively diluting the syrup

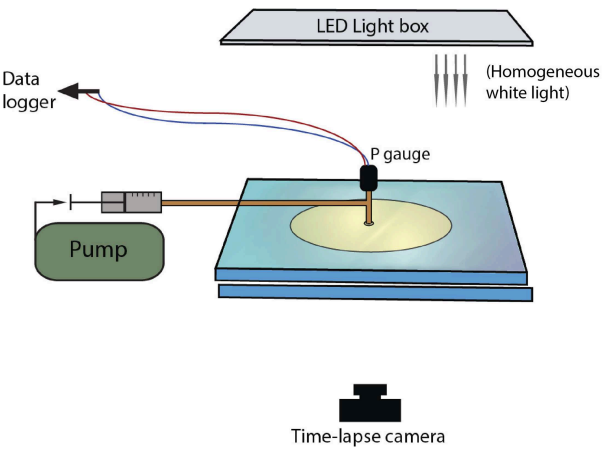

FIGURE 1 | Experimental set-up for injection of single bubbles into particle suspensions sandwiched between parallel plates.

TABLE 1 | Experimental conditions explored in this study.

Nr of experiments	Viscosity (Pa s)	Viscosity ratio*	Geometry	Particle fraction (vol%)	Gas influx (mL/h)
EXPERIMENTS WITH INJECTION OF SINGLE BUBBLES					
19	9–12	$5.0–6.7 \times 10^5$	Small gap	0, 20, 40, 45, 50, 53, 54	52
34	40–80	$2.2–4.4 \times 10^6$	Small gap	0, 10, 20, 30, 35, 40, 45, 50, 52, 53, 54	52
14	51–80	$2.8–4.4 \times 10^6$	Large gap	20, 52, 53, 54, 60, 62, 63, 64	52, 93
7	600–850	$3.3–4.7 \times 10^7$	Large gap	30, 50, 55, 58, 63	52
Nr of experiments	**Viscosity (Pa s)**	**Viscosity ratio**	**Geometry**	**Particle fraction (vol%)**	**Reagents (g/mL) Citric acid |sodium bicarb.**
EXPERIMENTS WITH BUBBLES GENERATED BY CHEMICAL REACTIONS					
9	45–72	$3.0–4.8 \times 10^6$	Small gap	0, 40, 50, 54	0.051 |0.054
25	40–62	$2.7–4.1 \times 10^6$	Cylinder	0, 30, 40, 45, 50, 53, 55, 58, 60, 63	0.051 |0.054

*A detailed list can be found in Supplementary Material. *The viscosity ratio (η_{liq}/η_{gas}) was calculated using viscosities of 1.8×10^{-5} Pa s for air, and 1.5×10^{-5} Pa s for carbon dioxide.*

with 5 vol% water, and reducing the room temperature to 5°C. Nonetheless, viscosity ratios between the suspending liquid and injected gas remain high, within the range $5–500 \times 10^5$ (calculated as η_{liq}/η_{gas}, with η the viscosity). Since gas viscosity in our experiments remains relatively constant, we hereafter focus on liquid viscosity, so as to highlight the possible effects of viscous forces within the particle suspension. We express all particle and syrup contents in vol% of the original bubble-free suspensions. The relative volumes of syrup and particles were determined by weighing both components and correcting for density. The syrup density was measured by weighing 100 mL of syrup, and the glass bead density was measured by immersion in water. There is a substantial density difference between glass beads (2452 kg/m^3) and sugar syrup (1412 kg/m^3). However, for glass beads in pure syrup, Stokes terminal velocities predict a particle settling of 0.2–0.4 mm in 1 h. Hindered settling in dense particle suspensions further slows settling [only 15 vol% solids can halve settling velocities; 28, 29]. We therefore assume that settling is negligible compared to gap thickness for experiment durations <1 h. Settling may become significant for low viscosity experiments (terminal velocity ≈ 2 mm/h), although these experiments were shorter because of higher flow rates.

The gap between plates was varied to explore the effect of confining geometry on gas migration patterns.

(1) "Small-gap parallel plate" (Hele-Shaw cell)

This set of experiments was performed with 0.48 mm plate spacing. Due to the higher resistance to spreading in such a small gap, the setup for experiments with high particle contents and more viscous liquids required weights to be placed on the top plate, and gentle movement of the top plate (with short back-and-forth pivoting motions) to facilitate spreading. As a result, the suspensions in these experiments occasionally had irregular outer edges. Experiments were performed with a constant suspension volume of 4 mL. Since the viscosity ratios are high between the liquid and injected gas, gas migration in this geometry is within the highly unstable displacement regime [e.g., 30], and therefore occurs in the shape of fingers. We defined different regimes by observing the direction and advance rate of the gas front and the overall gas geometry, and quantified regime transitions by measuring the bulk growth of the suspension, bubble shape parameters and average finger widths in ImageJ [31]. Key experiments were repeated three times and measurements on repeat experiments were averaged.

Bulk growth was measured from binary images, which allowed measurement of the total area of the gas + suspension. The image background was separated from the bulk suspension using a color intensity threshold. However, this method was applicable only when fingers grew in all directions. When one finger dominated, outgassing occurred prematurely when the dominant finger breached the outer boundary of the suspension, and bulk estimates ceased to be representative. In these cases, finger width was a better indicator of regime categories. Initial analysis of trial experiments showed that the finger width varied with time, especially at the very beginning (first appearance) and the very end (outgassing event) of the gas migration history. For this reason, finger widths were measured when they reached half the distance to the edge of the disk. The average finger thickness was determined by subtracting a Euclidean distance map from the skeleton of each finger, which provided a measure of the distance to the nearest edge from each point along the center of the finger (**Figure 2**). The method assumes a symmetric finger and may therefore underestimate finger width by up to two pixels (<0.15 mm with our image resolutions).

Particle Image Velocimetry (PIV) provided insights into the local interactions between the fingers and the particle suspension. PIV analyses were performed on the entire suspension using the "PIVLab" tool in MATLAB [32]. This method tracks the darker elements of the image, and thus the movement of particle clusters and small bubbles trapped within the suspension, which appear darker to the camera due to refractive index contrasts. To compare particle mobilization caused by advancing fingers in the different migration regimes, we chose pairs of images taken 2 s apart, starting with the image selected for finger width analysis described above.

(2) "Large-gap parallel plate":

A second set of experiments was performed with the confining plates held apart by separators 4.94 mm high. Initial suspension volume was kept constant at 40 mL, but a subset of experiments

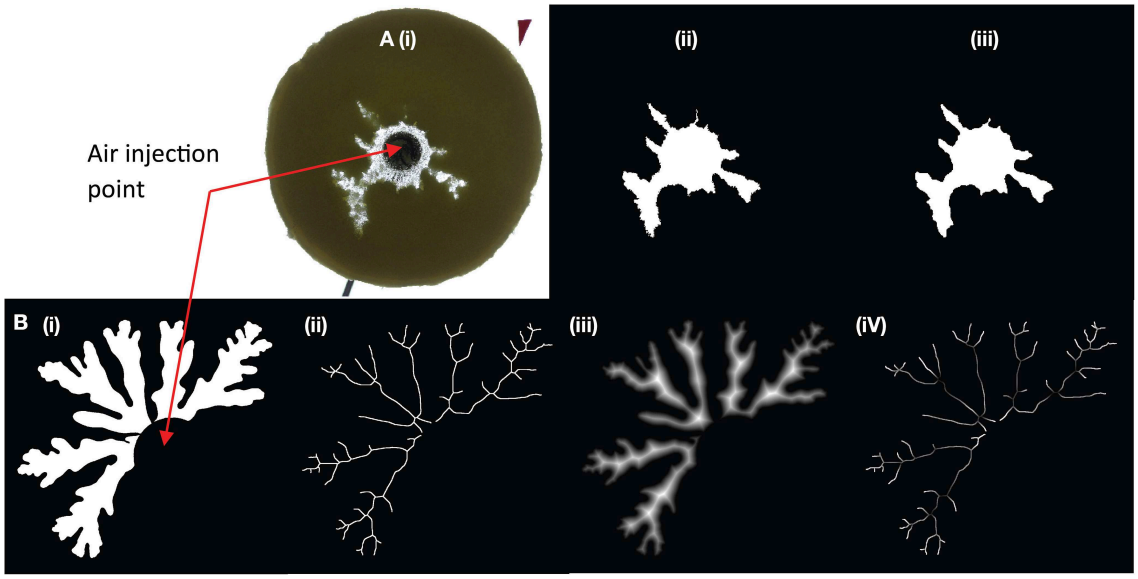

FIGURE 2 | Two examples of finger analysis in (A) a large gap parallel plate experiment, and (B) a small gap Hele-Shaw cell. (A) treatment of a large gap experiment at 63% particles, ~700 Pa s. The original image (i) is thresholded (ii) then smoothed with a median filter (iii). Some details are lost in the fracture-like areas, but the artificial edge roughness is removed. **(B)** Experiments in small gap Hele-Shaw cells (here 45 vol% particle content, 11 Pa s) needed further processing to determine finger widths. The image is first thresholded as in **(A)**, then skeletonized (ii) and a distance map is extracted (iii). The distance map records the distance from the center of the finger by incrementing gray scale values. The distance map is then subtracted from the skeleton (white values = 255) to calculate a "distance skeleton" where the gray scale value represents the distance in pixels from the skeleton to the first background pixel (iv). The resulting finger width was calculated as 2*(gray scale in pixels/number of pixels per unit length). In this example, brightness and contrast were increased to better visualize the variations in gray scale. The diameter of the black circle outlining the injection point is 1.9 cm.

were performed with a volume of 70–90 mL. Regime categories were again characterized visually, then separated using shape (morphometric) analysis in ImageJ. Because these experiments formed round or deformed bubbles (gas pockets), image analysis was performed on entire bubbles, rather than individual branches. The bubbles were isolated with a color intensity threshold and smoothed using a median filter (**Figure 2**). We classified bubble shapes using both circularity $C = 4\pi A/P^2$ where A is bubble area and P is perimeter, and solidity $S = A/(Convex\ Hull)$. The convex hull is determined using a "gift wrapping algorithm" [31].

To compare results from different experiment geometries, we used the normalized packing fraction, ϕ, which was measured by dividing the particle concentration (by volume) in an experiment by the random close packing (RCP) in that geometry:

$$\phi = \frac{particle\ volume\ fraction}{RCP}. \quad (1)$$

RCP was determined experimentally for each confining geometry by measuring the packing fraction of dry grains after shaking/tapping the containers for approximately 3 min. RCP was thus established at 54 ± 2% for the 0.48 mm gap, and at 63 ± 0.8% for the 4.94 mm gap; the discrepancy is due to the relative inefficiency of packing near walls.

Results

For small gap geometries, it is well established that injection of air into a more viscous liquid generates air fingers that grow from Saffman-Taylor instabilities. We observe in **Figure 3A** that the average finger thickness decreases with increasing particle content [increasing effective viscosity; e.g., 12, 33], which is consistent with the decrease in finger width for Saffman-Taylor instabilities with increasing host liquid viscosity (8, 12). At particle fractions above 45 vol% (normalized particle fractions $\phi > 0.83$), however, the slope steepens; addition of particles causes stronger thinning of the fingers. At 54 vol% particles ($\phi \approx 1$) gas advances in a fracture-like manner. In contrast to the continuous advance and expansion of Saffman-Taylor fingers, the fractures are characterized by a gas front that advances intermittently and a constant fracture width. Fractures that reach the edge of the suspension can open and reseal repeatedly, or another fracture may develop and outgas in another direction. Consequently, outgassing is irregular, and often occurs in multiple bursts (**Figure 4**, green curve). Near the transition to fractures, small variations in particle fractions can strongly affect results, and even spatial variations within a suspension can cause fractures to turn into fingers, or fingers to fractures.

In large-gap parallel plate experiments (**Figure 3B**), the bubble is round for gas injected into syrup ($\phi = 0$); increasing particle content produces successive regimes of rounded bubbles, deformed bubbles above 54 vol% particles ($\phi > 0.86$) and fractures at 63 vol% particles ($\phi \approx 1$). Hence the transitions occur

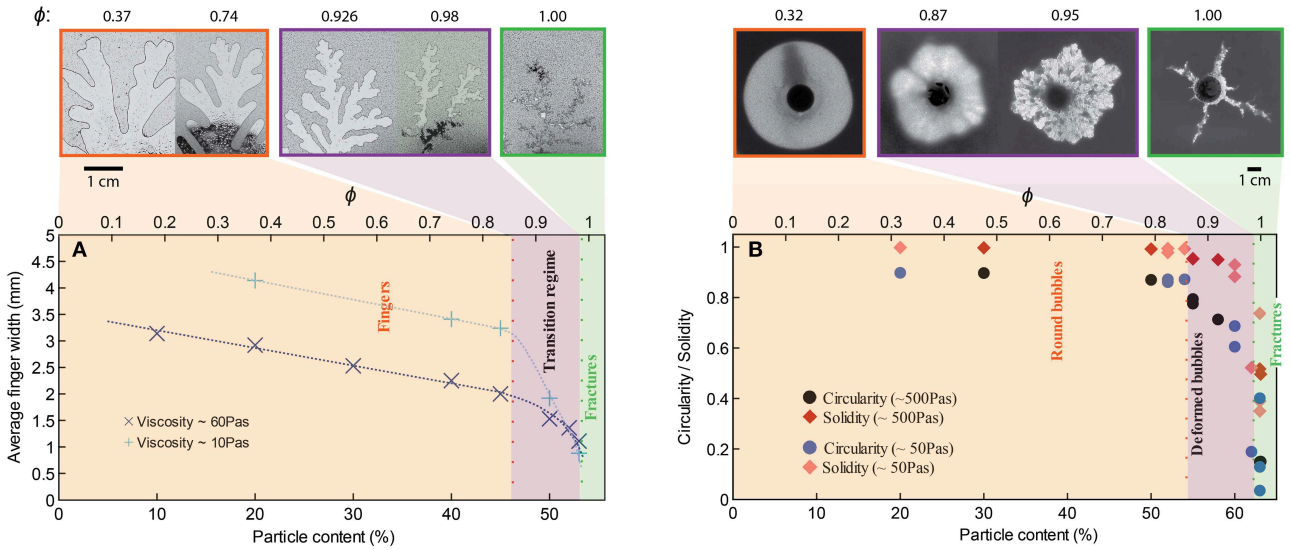

FIGURE 3 | Change in bubble morphology with particle content for experiments with bubble injection in (A) small-gap parallel plate geometry, and (B) large-gap parallel plate geometry. Injection rate is 52 mL/h for all experiments, although a few additional experiments in graph **(B)** have an injection rate of 93 mL/h (at 59, 62, and 63% particles). The example experiments displayed above the graphs have a liquid viscosity of ~10 Pa s (small-gap), and ~50 Pa s (large-gap geometry). In all geometries and for all liquid viscosities, a change in bubble morphology occurs around $\phi \approx 0.86$.

at different absolute particle volume fractions in the small- and large-gap geometries but at approximately the same values of ϕ.

Variations in liquid viscosity and injection rate do not appear to affect the transition ϕ values within the experimental range studied here. Indeed, increasing the liquid viscosity from 10 Pa s to > 600 Pa s yields the same transitional ϕ values. However, bubbles expanding in the lower viscosity suspensions have lower internal bubble pressures for the same air injection rate. Fracture morphology also varies, with straighter and longer fractures observed in lower viscosity liquids. Experiments at 10 Pa s in the small gap geometry also have wider fingers at low particle fractions, due to the viscosity-dependence of Saffman-Taylor instabilities [8]. There is no observable change in bubble morphology with viscosity in the large gap experiments, although the viscosity ratio between liquid and gas is consistently high. Air injection rate was not specifically investigated, but some faster experiments (93 mL/h) in large-gap parallel plates did not affect results (**Figure 3B**). A preliminary experiment in the small-gap geometry with injection rate 1 mL/h and 54 vol% particles generated thin fingers (instead of fractures) of width comparable to those at 53 vol% particles (just before the transition) under "normal" conditions. Therefore, the regime transitions appear insensitive to injection rate over two orders of magnitude.

The bulk response to bubble growth is also subject to regime transitions. Bulk expansions (gas volume fractions, V_{gas}/V_{total}) are plotted in **Figure 4A** for experiments in the small gap geometry that expanded symmetrically. For $\phi > 0.83$, the maximum bulk growth decreases with increasing particle fractions, yet the onset of bubble expansion (or bulk growth) occurs with a significant delay. Since gas is injected at a constant rate, this delay suggest that an increase in pressure occurs before bubble growth begins in particle-rich experiments, which reflects a significant bulk resistance to bubble growth. Indeed experiments at $\phi > 0.83$ accumulate higher internal bubble pressures before outgassing (at which point the pressure drops; **Figure 4B**), and maintain a lower bubble volume than particle-poor experiments (**Figure 4A**).

Particle Image Velocimetry (**Figure 5**) shows displacements caused by the advance of the gas fingers. While the entire suspension is mobilized in experiments with low particle contents, the mobilized area reduces considerably at $\phi > 0.83$ (>45 vol% particles), and is limited to the very tip of the gas front in the fracturing regime, where most of the suspension remains static.

Key Insights from Part I

Gas injection experiments performed in parallel plate geometries reveal the fundamental interactions that occur when a bubble grows in a particle-rich suspension. Experiments in both small-gap and large-gap geometries show the same transition at a critical normalized particle fraction $\phi_{def} \approx 0.86$, where fingers in small gap experiments become narrower, and bubbles in large gap experiments begin to deform. We refer to this as the "bubble deformation regime."

At the random close packing ($\phi_{fr} \approx 1$), the bubble migration behavior changes again: the gas front migrates episodically, in the form of fractures that do not widen with time or distance. We refer to this as the fracture regime because the gas morphology resembles fractures in a solid medium; we note, however, that there are no cohesive forces between the grains, and thus the term is applied loosely. In both large-gap and small-gap experiments, the transition from bubble deformation to fractures occurs progressively, with fingers that thin as ϕ increases (**Figure 3**). Thus, in many cases, the onset of the fracture regime was defined

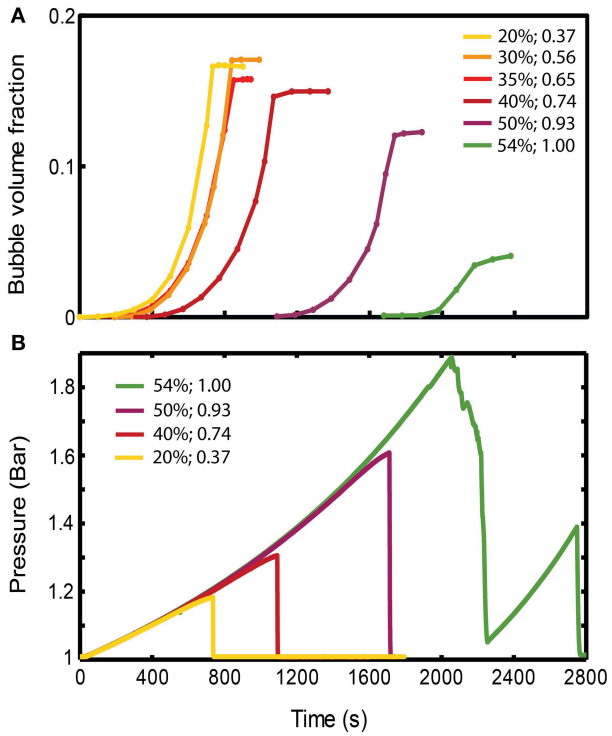

FIGURE 4 | (A) Evolution of gas volume fraction at various particle concentrations for bubble injection experiments in small-gap Hele-Shaw cells. The gas volume fraction, calculated as V_{gas}/V_{total}, is a measure of bulk growth normalized by the total volume. The plateau indicates that a finger has reached the edge, creating an open channel for gas flow, and the gas volume fraction in the experiment cannot grow any further. (Viscosity ≈ 50 Pa s, gas influx = 52 mL/h, experiments with ~symmetrical fingers). **(B)** Pressure values at the inlet, reflecting the delay in outgassing experienced by the more particle-rich experiments. The outgassing event is characterized by a sudden drop in pressure. Experiments are the same as in **(A)**. The figure legend shows particle volume fraction (first column), and ϕ (second column).

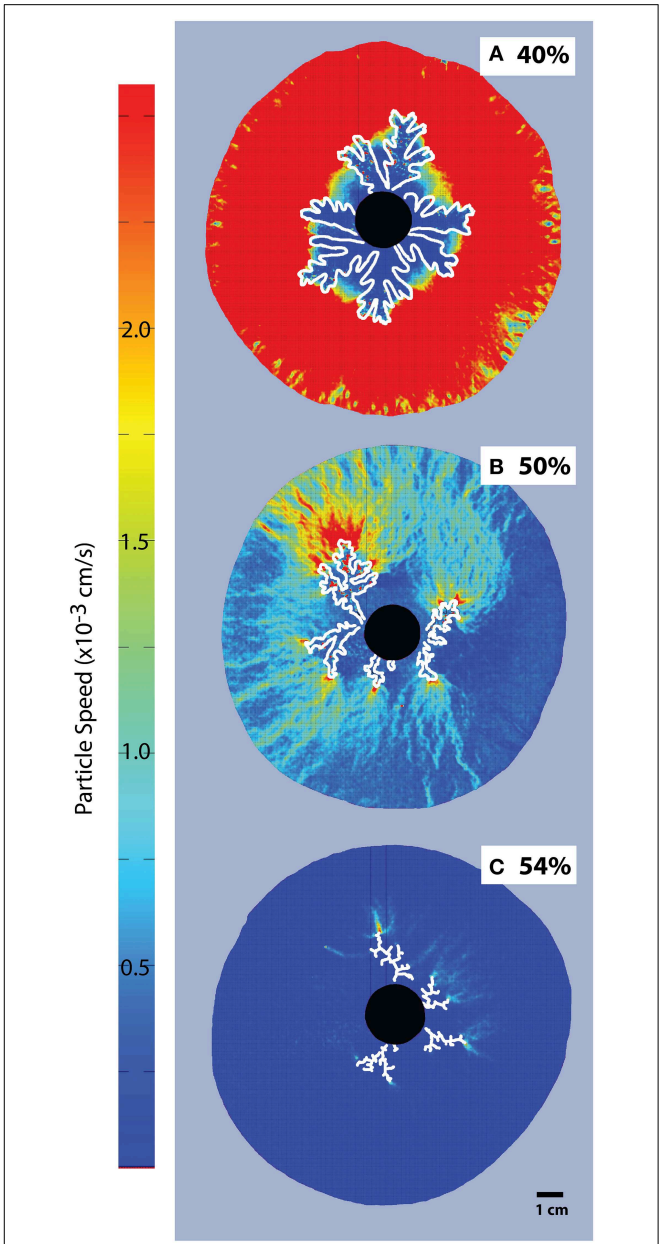

FIGURE 5 | Particle Image Velocimetry on bubble injection experiments in a small-gap parallel plate geometry. Particle concentrations are **(A)** 40% or $\phi = 0.74$, **(B)** 50% or $\phi = 0.93$, and **(C)** 54%, or $\phi = 1$. The black disk in the center is the injection point, and fingers grow radially (outlined in white). The color scale is constant for all images, for better comparison. The areas with most displacement appear red and the dark blue areas are essentially immobile (Viscosity ≈ 10 Pa s, air influx = 52 mL/h).

visually, using characteristics such as intermittent advance of the gas front and the morphology of individual gas branches.

Previous experiments in Hele-Shaw cells (small gap geometry) describe only a single transition at $\phi = 0.9$ where fingers change to fractures [10, 12]. Liquid viscosities in these experiments are lower (0.005–0.1 Pa s), but the viscosity ratios (order of 10^2–10^3) still place them in the highly unstable displacement regime [e.g., 30]. Therefore, Saffman-Taylor instabilities cause bubbles to form finger-like shapes, and the thinning of fingers in the bubble deformation regime resembles fractures. Thus, the distinction between regimes (bubble deformation and fractures) is subtle. In our large gap parallel plate experiments, bubble shape analyses (such as solidity measurements, **Figure 3**) can be used to locate the fracture regime more precisely; in this geometry, the gradual elongation of bubbles into fracture-like fingers occurs over a smaller range of particle fractions ($\sim 0.96 < \phi_{fr} \leq 1$), where it is accompanied by a sharp decrease in solidity from ~0.8 to <0.5.

We suggest, therefore, that these two gas migration regimes are likely important in three-dimensional settings. They do not depend on liquid viscosity or container shape, but are strongly dependent on particle fraction. In the following section, we test this hypothesis by extending our experiments to another three-dimensional geometry: vertical cylinders. Furthermore, to determine how these regime transitions affect outgassing, and by analogy with magmatic systems, we also investigate conditions where bubbles are generated internally, by chemical reactions, rather than externally, by injection.

Part II: *In situ* Bubble Growth Generated by Chemical Reactions

Materials and Methods

These experiments were designed to examine the effect of the regime transitions described in part I on outgassing behavior of three-phase suspensions where the gas phase is dispersed in the granular suspension. The experiments were performed using the materials described in part I, with the exception that bubbles were generated *in situ* by chemical reactions between powders of citric acid ($C_6H_8O_7$) and sodium bicarbonate ($NaHCO_3$). The resulting exsolution of CO_2 generated bubble nucleation and growth throughout the suspension.

Experiments began ($t = 0$ in data analysis) when the reactants were mixed into the suspension of syrup and particles. The initial concentration of reactants in the syrup was kept constant for all experiments at 0.051 g/mL ($C_6H_8O_7$) and 0.054 g/mL ($NaHCO_3$). This allowed relative changes in bubble content and outgassing rates to be studied for different particle contents. All experiments were allowed to run for 24–48 h, due to the low bubble growth rates, but only the first 10–15 h of the experiments were analyzed in detail, to limit the likelihood of significant particle settling. The rate of bubble exsolution decreased with time due to exhaustion of reactants, and reaction rates were sensitive to temperature (Figure S1, Supplementary Material). To minimize error, we kept room temperature at 22.0 ± 0.5°C for all experiments that were directly compared. For simplicity, all particle and syrup volume contents are expressed in vol% of the original bubble-free suspension, and bubble volume contents at time t are expressed by dividing the bubble volume by the bulk volume at time t (V_b/V_{tot}).

Two container geometries were used:

(1) "Small-gap parallel plate" (Hele-Shaw cell):

This set of experiments was performed in the same parallel plate geometry as described in part I, held apart by separators 0.48 mm high, with images captured from below (**Figure 6**). The liquid+particle suspension volume was always 6.0 ± 0.5 mL. Bubbles began to form before the mixture was enclosed between the rigid plates, thus affecting the initial bubble concentrations in the confined geometry. However, the experiment durations were much longer than the set-up time and most of the gas expansion occurred in the confined environment. This near-2D set-up permitted analysis of bubble geometry, shape and position from time lapse images taken every 10 s. Bulk (three-phase suspension) growth rates were estimated by measuring the area of thresholded images, multiplied by the gap width between plates to obtain a volume. Bubble size and shape (circularity, aspect ratio) were measured using binary (thresholded) images, for bubbles of diameter >0.1 mm.

(2) "Cylinder":

Mixtures of syrup and particles were inserted in a graduated cylinder of diameter 28 mm and capacity 100 mL (**Figure 6**). A light box was placed behind a set of three cylinders, and bulk growth was monitored with time-lapse videos. Experiments were performed at a constant initial volume of 15.5 ± 1.0 mL. The cylinder geometry did not allow direct observations of outgassing paths or bubble morphologies. Instead, bulk growth rates were tracked by measuring total suspension volumes from time-lapse images taken every 30 s. The particle-rich experiments formed a convex upper surface, so the total volume was calculated as a cylinder using the average heights of the highest central point and the contact between the suspension and the cylinder walls.

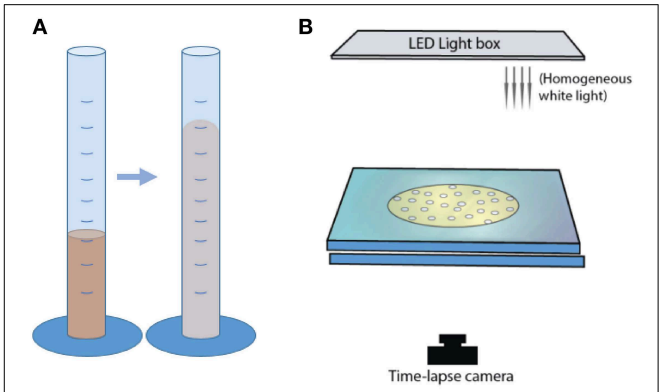

FIGURE 6 | Experimental set-up for *in situ* bubble growth using chemical reactions, in (A) graduated cylinders, and (B) parallel-plate geometry.

As in part I, the results from different geometries were compared by using the normalized packing fraction, ϕ, calculated as the ratio of the particle fraction by the random close packing in the geometry used. The random close packing of particles was measured experimentally at 54 ± 2% for small gap parallel plates, and at 63 ± 0.7% for graduated cylinders. This latter value is close to the empirical value of 64% for monodispersed spheres [e.g., 34].

Results

Bubble Behavior in Small-gap Parallel Plates

The small gap (Hele-Shaw) set-up allows observations of bubble behavior through time. Three stages of foam development were identified in both particle-rich and particle-free experiments (**Figure 7**):

(1) Isolated bubbles: At the beginning, the bubbles were distributed sufficiently far apart to not interact with each other. Bubbles in the center were smaller than those at the edges.
(2) Bubble coalescence and deformation: When enough bubbles had formed, they began to interact and coalesce. When bubbles broke the surface at the edge and outgassed, the bubbles immediately behind them visibly expanded due to a local pressure decrease.
(3) Bursting foam: In this final stage, bulk spreading slowed and outgassing occurred in large, apparently random events of cascading bubble ruptures that propagated from the edge toward the center of the suspension.

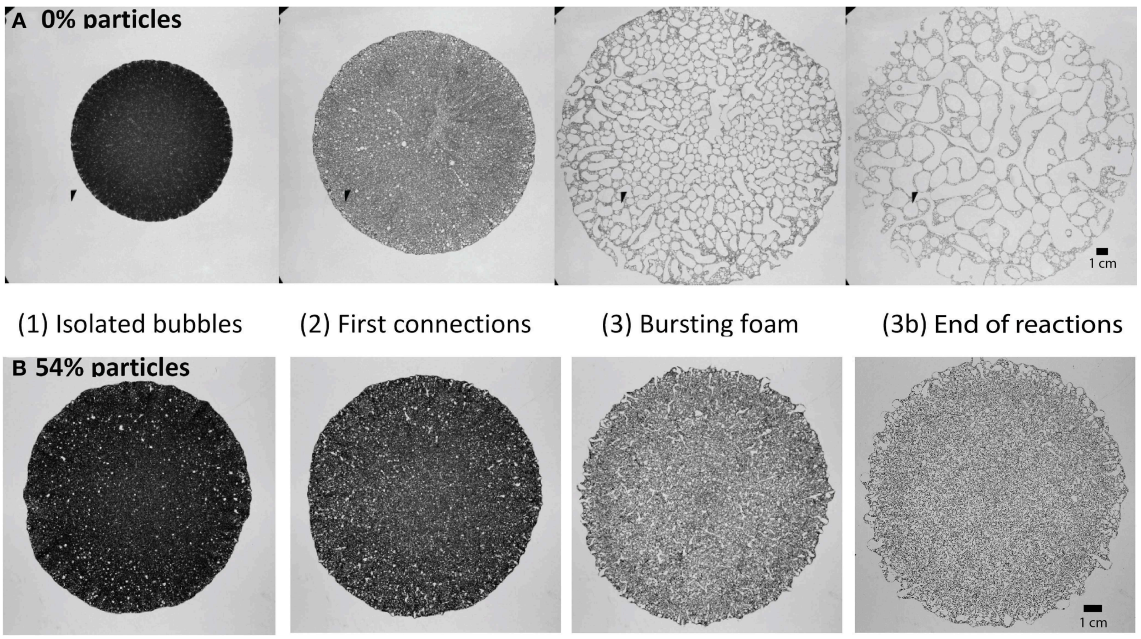

FIGURE 7 | Four phases of foam build-up for (A) a particle free experiment, and (B) a particle rich experiment containing 54 vol% particles ($\phi \approx 1$). For all cases, syrup viscosity is 45–49 Pa s. Videos of these two experiments are available in Supplementary Material.

The particle-poor experiments were characterized by relatively large bulk expansion. In early stages, the flow of liquid, bubbles and particles was fastest in radial channels, which gave lobate outer edges to the expanding mixture. These channels remained stable throughout stages (1) and (2) of the experiment (see Video 1 in Supplementary Material). Bubble coalescence and outgassing initiated at the edges of the suspension, where populations of small bubbles accumulated and grew. As the whole suspension expanded, the outgassing events progressively reached farther into the suspension. In this way, the experiment slowly evolved toward the bursting foam stage, with coalescence events involving bubbles in locations that span the entire radial range of the suspension. Individual bursts, however, occurred slowly due to depleted reactants, and ultimately the bubbles became large and convoluted.

In contrast, particle-rich experiments showed little expansion. Instead, the lateral flow of liquid, bubbles and particles that developed in the first two phases was quickly replaced by gas expulsion (see Video 2 in Supplementary Material). The short ($\leq$30 min) phase of bubble coalescence and deformation was terminated by sudden coalescence and outgassing events throughout the suspension that narrowed the bubble size distribution. This transition to the bursting foam stage initiated rapid and frequent bursting events that lasted until the end of the experiment (when the chemical reactions stop). It occurred earlier in experiments with higher ϕ, and corresponded with a substantial reduction in bulk expansion rate. The bubbles remained small throughout the experiment, although they tended to elongate into long, thin and winding fingers in the final stages.

The interactions between bubbles and their environment changed significantly when particle fractions increased. Bubble size and bubble deformation increased with time in both the particle-free and particle-rich cases (**Figure 8**). However, while particle-free experiments showed large increases in bubble size, particle-rich experiments retained very small bubbles, and rapidly reached a stable bubble size distribution, which remained constant throughout the experiment (**Figure 8A**). Bubble shapes were also dramatically different, with particle-free experiments bearing mostly rounded bubbles (concave cumulative circularity distributions; **Figure 8B**), and particle-rich experiments containing more deformed bubbles (convex cumulative circularity distributions; **Figure 8B**).

Bulk Behavior in Cylinders

In graduated cylinders, suspension height and volume are proportional, since the suspension can only expand upward. Thus, the time history of the suspension height, plotted in **Figure 9**, illustrates gas exsolution in the experiment. Gas exsolution initially triggered a rapid growth phase, which slowed down as the experiments progressed. After a time that varied with particle concentration, the surface level of the column began to oscillate, and bulk growth ceased. For experiments that contain less than 55 vol% particles ($\phi < 0.87$), this phenomenon often coincided with the appearance of larger bubbles (on the scale of the cylinder width) that rose through the foam at a faster rate than the other (smaller) bubbles. As the experiments progressed, the amplitude of the surface oscillations increased, until the whole column slumped back toward its original volume (i.e., outgassing was complete). Large bubbles were not observed in experiments

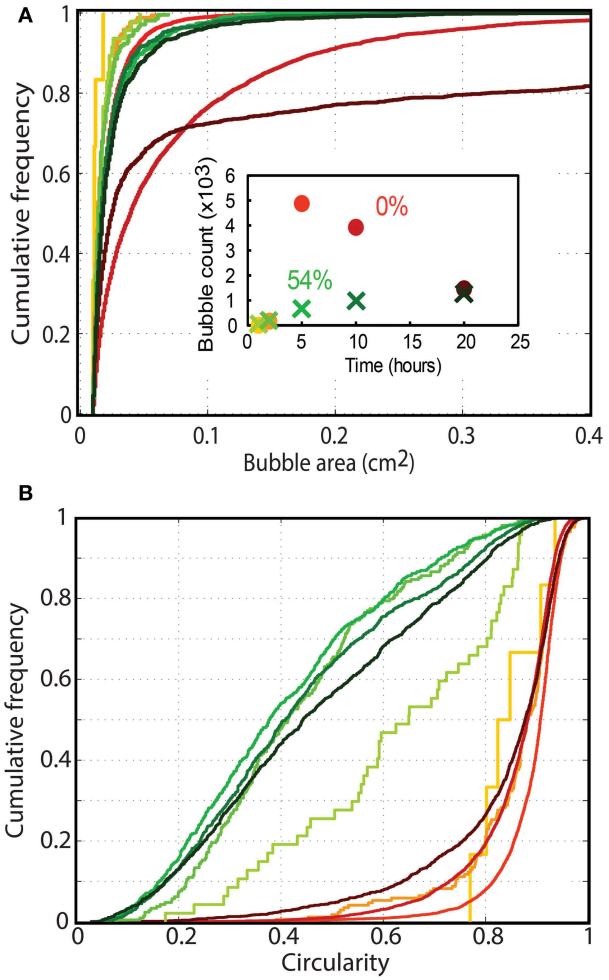

FIGURE 8 | Cumulative frequency distribution of (A) bubble circularity and (B) bubble sizes in particle rich (green; 54 vol% or $\phi = 1$) and particle free (orange; $\phi = 0$) foam generation experiments. The color gradient shows the migration of distributions with time at $t = 1$, 2, 5, 10, and 20 h (as shown in the inset graph). Only bubbles larger than 0.01 cm^2 are considered, and the first lines in each series appear jagged because they are built from measurements on few bubbles. The number of bubbles considered in each measurement is shown in the inset graph (colors are consistent with **Figures 7A,B**). The profiles clearly differ for particle-rich (small, highly deformed bubbles) and particle-free experiments (rounder bubbles that continually grow with time).

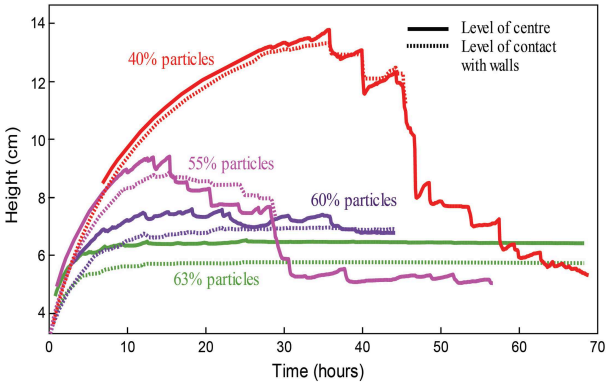

FIGURE 9 | Tracks of column height with time over the full lifespan of four experiments with foams (generated via chemical reactions) in cylinder geometries, with particle fractions of 40, 55, 60, and 63%. Note that the 55% line shows characteristics of both regimes: early onset oscillations and low maximum growth, as well as large oscillations (accompanied by the rise of large bubbles) and a final deflation.

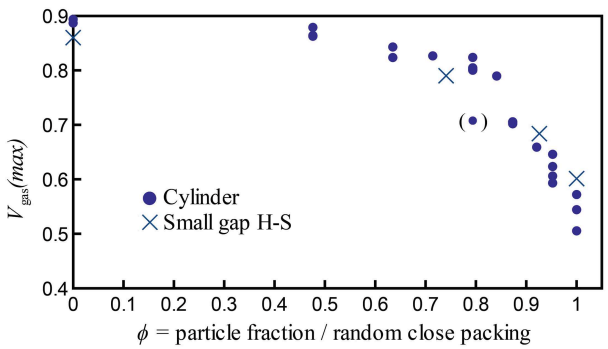

FIGURE 10 | Maximum bubble volume fractions $V_{gas}(max) = V_{gas}/V_{total}$ achieved in all experiments with bubbles generated by chemical reactions, including experiments at all temperatures tested (19–23°C). The outlier at $\phi = 0.79$ is indicated in parentheses, because four additional experiments at the same ϕ value all reached a larger maximum bubble volume fraction of $V_{gas}/V_{tot} \approx 0.8$.

with particle fractions above 55 vol%, although these experiments were more opaque and thus individual gas pockets were less visible. Furthermore, experiments with higher particle fractions did not exhibit a final deflation, but instead maintained a gas volume fraction close to their peak values even after all chemical reactions had stopped (**Figure 9**, green and purple curves). Since chemical concentrations in the syrup were kept constant in all experiments, suspensions with higher particle fractions (lower syrup fractions) contained less reactants, therefore simple measurements of column growth can be misleading. However, normalizing the bulk growth by the syrup volume yields a similar result (Figure S2), and **Figure 10** shows that, for $\phi > 0.84$, the maximum bubble capacity decreases rapidly with increasing ϕ, far beyond the decrease in available chemicals.

Bulk Growth and Outgassing

Figure 10 shows the maximum growth (maximum bubble content) reached by individual experiments, calculated as $V_{gas}(max) = V_{gas}/V_{tot}$. The data from both parallel plate and cylinder geometries are comparable when particle fractions are normalized by the random close packing: they collapse onto a single trend with a change in slope at a critical packing fraction $\phi_C \approx 0.84$–0.87, where the maximum bubble capacity decreases rapidly with increasing ϕ. This suggests an increase in gas expulsion at high particle fractions that is valid in both geometries. Moreover, this transition is remarkably stable despite small variations in experimental conditions (such as room temperature).

Key Insights from Part II

The *in situ* bubble growth experiments show a dramatic increase in gas expulsion above a critical particle fraction ($\phi_C \approx$ 0.84–0.87). Outgassing occurs through large-scale coalescence events (bursting foam) that begin earlier in the more particle-rich experiments. The transition ϕ value is constant in both cylinder and small-gap parallel plate (Hele-Shaw) geometries, two dramatically different geometries. Importantly, foams in graduated cylinders grow vertically and are constrained laterally, so that outgassing occurs in the direction of buoyancy. In contrast, experiments in horizontal Hele-Shaw cells are constrained vertically and expand laterally, hence the flow of bubbles is perpendicular to gravitational forces. The fact that both experiments yield similar results indicates that the main outgassing mechanism does not occur by buoyant rise of bubbles through the suspension. Instead, particle-rich foams appeared to have a lower capacity for bubble retention (**Figure 10**), and bubbles that were smaller and more deformed. A likely explanation involves an increase in bubble connectivity with increasing particle concentrations, which will be discussed in detail in the next section.

General Discussion

Gas Migration Regimes are Governed by ϕ

The three geometries used (cylinders, large- and small- gap parallel plates) offer varying levels of confinement, but the normalized particle fraction (ϕ) allows comparison between the different geometries (see Supplementary Material for details). **Figure 11** shows a regime diagram based on (**Figure 11A**) bubble shapes observed in single bubble experiments (part I), and (**Figure 11B**) maximum bulk growth of foams generated by chemical reactions (part II). The most striking feature is that the ϕ marking the onset of bubble deformation in single bubble experiments corresponds with the substantial decrease in gas retention observed in experiments involving *in situ* foam generation. The behavioral transition to the "bubble deformation regime" (named after the bubble shapes) occurs in both experiment types at a critical normalized packing fraction $\phi_{def} = 0.86 \pm 0.03$. This value is calculated using the average transition (black line in **Figure 11**) and the maximum observed offset between experiments immediately adjacent to the transition in both experiment types (single bubble vs. *in situ* foam generation, in the large gap and cylinder geometries). The error value also includes the error on random close packing. This correlation suggests that (1) bubble deformation and gas expulsion are closely linked, and (2) this first behavioral transition is not affected by the amount of bubbles already in suspension.

Considering the many variations of experiments performed in part I and part II, this transition at ϕ_{def} is remarkably consistent. It is insensitive to container shape, to the direction of outgassing, to the amount of bubbles in suspension, and to liquid viscosity. It is also insensitive to bubble growth rate, as demonstrated by the consistent behavior of experiments involving chemical reactions and those involving gas injection. Indeed, bubble growth rates in chemical reaction experiments average 2–3 mL/h initially and progressively decrease during the experiment, while single bubble experiments have a gas injection rate of 52 mL/h or 93 mL/h, an order of magnitude higher. Surface tension (σ) also has little effect on the particle fraction at which bubble deformation begins, as illustrated by consistent results in experiments performed with silicone oil [$\sigma = 21$ mN/m; 12], water/glycerin mixtures ($\sigma \sim 68$ mN/m; 10), and sugar syrup ($\sigma \sim 80$ mN/m; our data). We conclude that the normalized particle volume fraction (ϕ) controls the threshold that separates regimes in bubble shape (round to deformed) and outgassing behavior (bubble growth to gas expulsion).

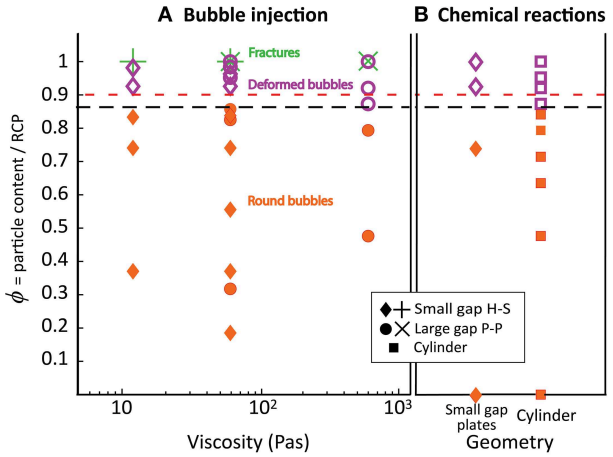

FIGURE 11 | Regime diagram separating the round bubble regime (filled orange shapes), the bubble deformation regime (purple open symbols) and the fracture regime (green crosses). The red dashed line indicates the transition from fingering to fracturing in Sandnes et al. [10] and Chevalier et al. [12] at viscosities of 0.01, and 0.005–0.2 Pa s. The black line indicates ϕ_{def}, determined from regime changes in part I and II. **(A)** Bubble injection experiments in small-gap parallel plates (diamonds) and large-gap parallel plates (disks), with bubble growth rates of 52 and 93 mL/h; **(B)** Chemical reaction experiments in small-gap parallel plates (diamonds) and cylinder geometries (squares), with bubble growth rates that average 2–3 mL/h in the first few hours of the experiments.

Experiments with single bubbles underwent a second transition, from deformed bubbles to fractures, at $\phi_{fr} \approx 1$. This transition was also insensitive to container shape and liquid viscosity, but did not occur in experiments with *in situ* bubble growth, suggesting that suspensions of deformable bubbles affect the formation of fractures. The effect of bubble growth rate on the transition to fractures was not tested, however this transition occurred at the same particle fraction during bubble injection at 52–93 mL/h, and our low rate experiment (1 mL/h) was indicatively close to the regime transition. Again, particle volume fraction (ϕ) appears to control this transition in gas migration regimes.

The Role of Particles on Regime Transitions

PIV analysis of single bubble experiments [**Figure 5**; 12] shows that at low particle fractions, bubble advance fronts mobilize the entire suspension. When the bubble deformation regime is reached, the mobilized area shrinks until, in the fracture regime, only the area in the direct vicinity of the gas front is mobilized. This behavior indicates an intrinsic resistance to flow within the

suspension, which develops in the deformation regime and can be explained by local jamming phenomena because of particle interactions in a frictional system [12].

The importance of particle interactions is further demonstrated by the rigidity of particle-rich foams in vertical cylinder experiments. While foams with few particles tend to slump back to their original volume at the end of an experiment, particle-rich foams ($\phi > \phi_{def}$) maintain their peak bulk volume, 2–3 times their original bubble-free volume, even after gas exsolution ends (**Figure 9**). In this case, foams with high particle concentrations appear to be stabilized by a rigid structure of local solid-solid particle contacts.

The transition to bubble deformation at $\phi_{def} = 0.86 \pm 0.03$ lies close to the random loose packing (RLP) of monodisperse spheres at 55.5 ± 0.5 vol% [$\phi = 0.867 \pm 0.008$, using 64% as the close packing of spheres; 19, 35]. This RLP value also marks the onset of shear-dilation [19]. Hence the bubble deformation regime occurs within the limits of RLP and random close packing (RCP). These dense suspensions dilate in response to shear, and can therefore develop a normal force against their boundaries and build force-bearing networks of particles. The strength of the particle networks is determined by the number of particles in contact with each other [22], the friction between particles [36], and the magnitude of the forces that resist particle displacement / dilation, such as the flexibility of the boundaries against which the force chains rest [24, 37], or the applied pressure [e.g., from gravitational loading; 17].

In our experiments, the forces that resist dilation include frictional interaction with the rigid plates or cylinder walls, the internal bubble pressure and the interfacial tension at the gas-liquid boundary. We suggest that the bubbles and particles both act on- and react to- each other. The growing bubbles displace the whole suspension, and are therefore the source of shear stress that causes dilation. They create strong force chains inside the suspension that, in turn, locally resist bubble growth. The growing bubble must then deform around this "backbone," preferentially displacing areas in the suspension with unconnected or weakly connected particles, where the stress opposing motion is lowest. As a result, the bubble deforms into a lobate or finger-like pattern ("bubble deformation regime" in **Figure 11**).

The stress that opposes bubble growth increases as particle fractions increase toward RCP, where fracture propagation begins ($\phi_{fr} \approx 1$). Previous research shows that at $\phi \approx 1$, if confining pressures are high, the particle network can lock. Under these conditions, the gas front cannot mobilize the particles, because the mechanical forces that resist particle displacement are stronger than those generated by bubble expansion, and the gas must advance by invading the pore-space [15, 17, 18]. Importantly, the fracture regime was not observed in experiments with *in situ* bubble generation. In these three-phase suspensions, compressible bubbles increased the bulk deformability, which may have affected fracture formation. Therefore, it appears that the suspension must be neither too rigid nor too deformable for the fracture regime to occur.

This frustrated dilation model fits well with our observations, where regime transitions are controlled by particle interactions, and are not affected by liquid viscosity, bubble growth rate or container shape. Interestingly, frustrated dilation, as well as the dependence of suspension behavior on ϕ (when $\phi > \phi_{def}$), are also consistent with discontinuous shear-thickening, the rapid increase of a suspension's bulk viscosity over a short range of applied shear [23, 24].

Consequence for Outgassing

We propose that the interactions that occur between the densely packed particles create particle force chains that resist bubble growth, and cause the gas front to deform around the areas that offer the larger resistance. This causes bubble deformation on two scales, and bubble compression.

Large-scale Bubble Deformation

The increase in outgassing efficiency with increasing particle fraction at $\phi > \phi_{def}$ in the experiments involving chemical reactions coincides with the onset of bubble deformation observed in parallel plate geometries (**Figure 11**). Similarly, in experiments involving chemical reactions in small-gap parallel plates, bubble deformation is significantly greater, and bubble sizes significantly smaller, in experiments above ϕ_{def} than in those below ϕ_{def} (**Figure 8**). In particle-rich experiments, regular gas release maintains a relatively constant bubble size distribution. Hence bubble deformation and bulk permeability appear to be linked. Indeed, bubble deformation enhances the likelihood of bubble contact and coalescence, and thus the likelihood of forming a bubble network that reaches the edge of the suspension [38, 39]. When a network of touching bubbles breaches the edge of the suspension, a large-scale outgassing episode ensues, until the network seals again and other bubbles expand. As a consequence, the gas flux exiting the suspension is episodic and expressed as sudden and dispersed bursting events. This episodic gas release also characterizes the transition to fractures, since in single bubble experiments, thin fingers and fractures open and seal intermittently, releasing gas in puffs (**Figure 4B**).

Small-scale Perturbation of Bubble Walls

Particles also affect the coalescence of bubbles on the scale of inter-bubble films. Previous work on foam stability (mostly in colloidal suspensions) focuses on static foams, where bubbles are not formed *in situ*, and the bubble volume fraction does not increase with time [e.g., review by 40–42]. In these foams, particles that are wetting and density-matched increase foam stability by (a) increasing the viscosity and thus stabilizing thick films, (b) obstructing gravitational drainage, and (c) limiting coarsening, the diffusion of volatiles from smaller bubbles toward larger bubbles. We compare this expectation with our cylindrical experiments with internally nucleated bubbles. In accordance with these results, after the chemical reactions ended (static foam), particle-rich foams retained their peak bubble volumes, displaying an ability to resist gravitational collapse (**Figure 9**). However, while the bubbles were growing (dynamic foam), experiments with $\phi > \phi_{def}$ showed increased gas expulsion. Particle-rich foams reached a maximum bubble capacity early on in the experiment (**Figures 9**, **10**) and had markedly smaller

bubbles than particle-poor foams (**Figure 8**). Therefore, particles appear to weaken bubble walls in a dynamic foam.

The most important distinction between a static and dynamic foam is that as the bubbles grow, the films between bubbles elongate and thin with time. Inefficient particle packing in a bubble film causes the film surface to deform around the protruding particles, as shown in gravitational drop detachment experiments. In these experiments, drops with higher particle fractions detached earlier, at a shorter filament length and at larger filament diameters [43, 44]. An additional detachment regime was observed, whereby the air intrudes in the gaps between particle clusters until a short-lived particle-free filament separates two particle rich bodies [45]. A similar mechanism likely occurs in planar films between bubbles in a foam. If the film can rupture earlier, and at shorter elongation, then bubble coalescence will also occur earlier and at smaller bubble sizes.

Bubble Compression

As particle fractions increase above ϕ_{def}, the areas mobilized by the expanding bubble localize to the bubble edge, where the shear stress is highest (**Figure 5**). This localization illustrates the increase in stress necessary to deform the suspension as the force-bearing particle chains transmit force to the confining plates, thereby increasing the opposing frictional stress experienced by the moving interface. As a result, the suspension can resist larger internal bubble pressures with minimal bulk deformation, and limit bubble expansion. Because this stiffening occurs in conjunction with bubble deformation, the small pressurized bubbles are also more likely to outgas. This is best illustrated in **Figure 4**, where air injection in particle-rich suspensions ($\phi >$ 0.86) caused less bulk growth than in particle-poor suspensions, despite substantially higher internal bubble pressures.

General Conclusions

We have identified two successive changes in gas migration regime that occur in particle-rich suspensions. The first transition, predominant in all sets of experiments, occurs when particle fractions reach the random loose packing. At this packing fraction, dilation of the granular network develops in response to shear, and creates a local resistance to bubble growth, causing the bubbles to deform. At the random close packing, gas migration can occur in a fracture-like manner if the suspension is somewhat deformable and does not contain too many bubbles. Parameters such as liquid viscosity (or viscosity ratios), container geometry, or gas inflow rate may affect certain aspects of bubble migration (internal pressure, front velocity, or bubble shapes within individual regimes), but they did not affect regime transitions within the ranges tested. Instead, the transitions were entirely dependent on particle interactions.

Furthermore, we establish a link between the onset of bubble deformation in particle-rich suspensions and increased outgassing with increasing particle fractions. The particle-particle interactions that occur in such densely packed suspensions promote outgassing by (1) deforming bubbles into long fingers and fractures that reach far into the suspension, (2) causing perturbations at the bubble walls facilitating coalescence of neighboring bubbles, and (3) compressing the bubbles (limiting bulk expansion). As a result, a new gas migration regime occurs. It is characterized by an increase in permeability whereby the gas escapes through pathways formed by coalesced bubbles. This type of outgassing occurs in bursts or puffs, through transient apertures that open and seal intermittently.

Because liquid viscosity does not significantly affect these gas migration regimes, they are likely applicable to most granular deformable media, including crystal-rich magmas. Severely deformed bubbles are commonly observed in such magmas [e.g., 46, 47], therefore our results give a compelling explanation for the efficient outgassing of these particle-rich slurries.

Acknowledgments

We would like to thank Mr Charles Clapham for his help with building the set-up. The research leading to these results has received funding from the People Programme (Marie Curie Actions) of the European Union's Seventh Framework Programme (FP7/2007-2013) under the project NEMOH, REA grant agreement n° 289976. KVC acknowledges the AXA Research Fund for their support.

Supplementary Material

The Supplementary Material for this article can be found online at: http://journal.frontiersin.org/article/10.3389/fphy.2015.00060

References

1. Cashman KV, Sparks RSJ. How volcanoes work: a 25 year perspective. *Geol Soc Am Bull.* (2013) **125**:664–90. doi: 10.1130/B30720.1
2. Pinkerton H, Wilson L, Macdonald R. The transport and eruption of magma from volcanoes: a review. *Contemp Phys.* (2002) **43**:197–210. doi: 10.1080/00107510110097756
3. Cashman KV. Volatile controls on magma ascent and degassing. The state of the planet: frontiers and challenges in geophysics. *Am Geophys Union Monogr.* (2004) **150**:109–24. doi: 10.1029/150GM10
4. Mena PC, Ruzicka MC, Rocha FA, Teixeira JA, Drahoš J. Effects of solids on homogeneous-heterogeneous flow regime transition in bubble columns. *Chem Eng Sci.* (2005) **60**:6013–26. doi: 10.1016/j.ces.2005.04.020
5. Kong XZ, Kinzelbach W, Stauffer F. Morphodynamics during air injection into water-saturated movable spherical granulates. *Chem Eng Sci.* (2010) **65**:4652–60. doi: 10.1016/j.ces.2010.05.007
6. Mota A, Vicente AA, Teixeira J. Effects of spent grains on flow regime transition in bubble column. *Chem Eng Sci.* (2011) **66**:3350–7. doi: 10.1016/j.ces.2011.01.042
7. Hele-Shaw HS. Flow of Water. *Nature* (1898) **58**:34–6.
8. Saffman PG, Taylor G. The penetration of a fluid into a porous medium or Hele-Shaw cell containing a more viscous liquid. *Proc R Soc Lond Ser Math Phys Sci.* (1958) **245**:312–29. doi: 10.1098/rspa.1958.0085
9. Knudsen HA, Sandnes B, Flekkøy EG, Måløy KJ. Granular labyrinth structures in confined geometries. *Phys Rev E* (2008) **77**:021301. doi: 10.1103/PhysRevE.77.021301

10. Sandnes B, Flekkøy EG, Knudsen HA, Måløy KJ, See H. Patterns and flow in frictional fluid dynamics. *Nat Commun.* (2011) **2**:8. doi: 10.1038/ncomms1289
11. Chevalier C, Lindner A, Clément E. Destabilization of a saffman-taylor fingerlike pattern in a granular suspension. *Phys Rev Lett.* (2007) **99**:4. doi: 10.1103/PhysRevLett.99.174501
12. Chevalier C, Lindner A, Leroux M, Clément E. Morphodynamics during air injection into a confined granular suspension. *J Non-Newtonian Fluid Mech.* (2009) **158**:63–72. doi: 10.1016/j.jnnfm.2008.07.007
13. Shin H, Santamarina JC. Fluid-driven fractures in uncemented sediments: underlying particle-level processes. *Earth Planet Sci Lett.* (2010) **299**:180–9. doi: 10.1016/j.epsl.2010.08.033
14. Varas G, Vidal V, Géminard JC. Morphology of air invasion in an immersed granular layer. *Phys Rev E* (2011) **83**:7. doi: 10.1103/physreve.83.061302
15. Holtzman R, Szulczewski ML, Juanes R. Capillary fracturing in granular media. *Phys Rev Lett.* (2012) **108**:4. doi: 10.1103/PhysRevLett.108.264504
16. Varas G, Geminard JC, Vidal V. Air invasion in a granular layer immersed in a fluid: morphology and dynamics. *Granular Matter* (2013) **15**:801–10. doi: 10.1007/s10035-013-0435-7
17. Islam A, Chevalier S, Sassi M. Experimental and numerical studies of CO2 injection into water-saturated porous medium: capillary to viscous to fracture fingering phenomenon. *Energy Procedia* (2013) **37**:5511–19. doi: 10.1016/j.egypro.2013.06.471
18. Holtzman R, Juanes R. Crossover from fingering to fracturing in deformable disordered media. *Phys Rev E* (2010) **82**:5. doi: 10.1103/PhysRevE.82.046305
19. Onoda GY, Liniger EG. Random loose packings of uniform spheres and the dilatancy onset. *Phys Rev Lett.* (1990) **64**:2727–30. doi: 10.1103/PhysRevLett.64.2727
20. Pica Ciamarra M, Nicodemi M, Coniglio, A. Recent results on the jamming phase diagram. *Soft Matter* (2010) **6**:2871–4. doi: 10.1039/b926810c
21. Silbert LE. Jamming of frictional spheres and random loose packing. *Soft Matter* (2010) **6**:2918–24. doi: 10.1039/c001973a
22. Bi DP, Zhang J, Chakraborty B, Behringer RP. Jamming by shear. *Nature* (2011) **480**:355–8. doi: 10.1038/nature10667
23. Brown E, Jaeger HM. Shear thickening in concentrated suspensions: phenomenology, mechanisms and relations to jamming. *Rep Prog Phys.* (2014) **77**:23. doi: 10.1088/0034-4885/77/4/046602
24. Brown E, Zhang HJ, Forman NA, Maynor BW, Betts DE, Desimone JM, et al. Shear thickening and jamming in densely packed suspensions of different particle shapes. *Phys Rev E* (2011) **84**:11. doi: 10.1103/PhysRevE.84.031408
25. Liu AJ, Nagel SR. Granular and jammed materials. *Soft Matter* (2010a) **6**:2869–70. doi: 10.1039/c005388k
26. Liu AJ, Nagel SR. The jamming transition and the marginally jammed solid. In: Langer JS, editor. *Annual Review of Condensed Matter Physics, Vol. 1.* Palo Alto: Annual Reviews (2010b). p. 347–69. doi: 10.1146/annurev-conmatphys-070909-104045
27. Llewellin EW, Mader HM, Wilson SDR. The rheology of a bubbly liquid. *Proc R Soci Math Phys Eng Sci.* (2002) **458**:987–1016. doi: 10.1098/rspa.2001.0924
28. Richardson JF, Zaki WN. Sedimentation and fluidisation: part I. *Trans Inst Chem Eng.* (1954) **32**:35–53.
29. McGhee TJ. *Water Resources and Environmental Engineering*. New York, NY: McGraw-Hill (1991).
30. Lenormand R, Touboul E, Zarcone C. Numerical models and experiments on immiscible displacements in porous media. *J Fluid Mech.* (1988) **189**:165–87. doi: 10.1017/S0022112088000953
31. Schneider CA, Rasband WS, Eliceiri KW. NIH Image to ImageJ: 25 years of image analysis. *Nat Methods* (2012) **9**:671–5. doi: 10.1038/nmeth.2089
32. Thielicke W, Stamhuis EJ. *PIVlab – Towards User-friendly, Affordable and Accurate Digital Particle Image Velocimetry in MATLAB. J Open Res Soft.* (2014) **2**:e30. doi: 10.5334/jors.bl
33. Stickel JJ, Powell RL. Fluid mechanics and rheology of dense suspensions. *Ann Rev Fluid Mech.* (2005) **37**:129–49. doi: 10.1146/annurev.fluid.36.050802.122132
34. Kamien RD, Liu AJ. Why is random close packing reproducible? *Phys Rev Lett.* (2007) **99**:155501. doi: 10.1103/PhysRevLett.99.155501
35. Jerkins M, Schröter M, Swinney HL, Senden TJ, Saadatfar M, Aste A. Onset of mechanical stability in random packings of frictional spheres. *Phys Rev Lett.* (2008) **101**:018301–4. doi: 10.1103/PhysRevLett.101.018301
36. Seto R, Mari R, Morris JF, Denn MM. Discontinuous shear thickening of frictional hard-sphere suspensions. *Phys Rev Lett.* (2013) **111**:5. doi: 10.1103/PhysRevLett.111.218301
37. Brown E, Jaeger HM. The role of dilation and confining stresses in shear thickening of dense suspensions. *J Rheology* (2012) **56**:875–923. doi: 10.1122/1.4709423
38. Walsh SDC, Saar MO. Numerical models of stiffness and yield stress growth in crystal-melt suspensions. *Earth Planet Sci Lett.* (2008) **267**:32–44. doi: 10.1016/j.epsl.2007.11.028
39. Saar MO, Manga M, Cashman KV, Fremouw S. Numerical models of the onset of yield strength in crystal-melt suspensions. *Earth Planet Sci Lett.* (2001) **187:**367–79. doi: 10.1016/S0012-821X(01)00289-8
40. Hunter TN, Pugh RJ, Franks GV, Jameson GJ. The role of particles in stabilising foams and emulsions. *Adv Colloid Interface Sci.* (2008) **137**:57–81. doi: 10.1016/j.cis.2007.07.007
41. Dickinson E. Food emulsions and foams: stabilization by particles. *Curr Opin Colloid Interface Sci.* (2008) **15**:40–9. doi: 10.1016/j.cocis.2009.11.001
42. Fameau AL, Salonen A. Effect of particles and aggregated structures on the foam stability and aging. *C. R. Phys.* (2014) **15**:748–60. doi: 10.1016/j.crhy.2014.09.009
43. Bonnoit C, Bertrand T, Clement E, Lindner A. Accelerated drop detachment in granular suspensions. *Phys Fluids* (2012) **24**:14. doi: 10.1063/1.4704801
44. Bertrand T, Bonnoit C, Clement E, Lindner A. Dynamics of drop formation in granular suspensions: the role of volume fraction. *Granular Matter* (2012) **14:**169–74. doi: 10.1007/s10035-012-0318-3
45. Roche M, Kellay H, Stone HA.Heterogeneity and the role of normal stresses during the extensional thinning of non-brownian shear-thickening fluids. *Phys Rev Lett.* (2011) **107**:5. doi: 10.1103/PhysRevLett.107.134503
46. Bacon CR. Magmatic inclusions in silicic and intermediate volcanic rocks. *J Geophys Res.* (1986) **91**:6091–112. doi: 10.1029/JB091iB06p06091
47. Cashman KV, Thornber C, Kauahikaua JP. Cooling and crystallization of lava in open channels, and the transition of Pahoehoe Lava to ʻAʻa. *Bull Volcanol.* (1999) **61**:306–23.

Conflict of Interest Statement: The authors declare that the research was conducted in the absence of any commercial or financial relationships that could be construed as a potential conflict of interest.

frontiers in Physics

ORIGINAL RESEARCH
published: 19 June 2015
doi: 10.3389/fphy.2015.00044

Flow and fracture in water-saturated, unconstrained granular beds

Germán Varas[1], *Gabriel Ramos*[1], *Jean-Christophe Géminard*[2] *and Valérie Vidal*[2]*

[1] *Instituto de Física, Pontificia Universidad Católica de Valparaíso, Valparaíso, Chile,* [2] *Laboratoire de Physique, École Normale Supérieure - Centre National de la Recherche Scientifique, Université de Lyon, Lyon, France*

The injection of gas in a liquid-saturated granular bed gives rise to a wide variety of invasion patterns. Many studies have focused on constrained porous media, in which the grains are fixed in the bed and only the interstitial fluid flows when the gas invades the system. With a free upper boundary, however, the grains can be entrained by the ascending gas or fluid motion, and the competition between the upward motion of grains and sedimentation leads to new patterns. We propose a brief review of the experimental investigation of the dynamics of air rising through a water-saturated, unconstrained granular bed, in both two and three dimensions. After describing the invasion pattern at short and long time, a tentative regime-diagram is proposed. We report original results showing a dependence of the fluidized zone shape, at long times, on the injection flow rate and grain size. A method based on image analysis makes it possible to detect not only the fluidized zone profile in the stationary regime, but also to follow the transient dynamics of its formation. Finally, we describe the degassing dynamics inside the fluidized zone, in the stationary regime. Depending on the experimental conditions, regular bubbling, continuous degassing, intermittent regime or even spontaneous flow-to-fracture transition are observed.

Keywords: granular media, saturated beds, three-phase flows, fluidization, patterns, fracture

OPEN ACCESS

Edited by:
Renaud Toussaint, University of Strasbourg, France

Reviewed by:
Takahiro Hatano, The University of Tokyo, Japan
Bjornar Sandnes, Swansea University, UK
Michael Julian Niebling, Schlumberger Limited, Norway

***Correspondence:**
Valérie Vidal, Laboratoire de Physique, École Normale Supérieure - Centre National de la Recherche Scientifique, Université de Lyon, 46 Allée d'Italie, 69364 Lyon, France
valerie.vidal@ens-lyon.fr

Specialty section:
This article was submitted to Interdisciplinary Physics, a section of the journal Frontiers in Physics

Received: *23 April 2015*
Accepted: *02 June 2015*
Published: *19 June 2015*

Citation:
Varas G, Ramos G, Géminard J-C and Vidal V (2015) Flow and fracture in water-saturated, unconstrained granular beds. Front. Phys. 3:44. doi: 10.3389/fphy.2015.00044

1. Introduction

A fluid (liquid or gas) crossing an immersed granular medium is a process widely encountered in nature, and often referred to as "venting." It includes a large variety of phenomena such as methane venting [1], hydraulic fractures [2–4], pockmarks [5–7], hydrothermal complexes [8, 9], kimberlite pipes [10–12] or mud volcanoes [13–16]. Since the 90's, the technique of air sparging has also been developed. It consists of injecting gases into the saturated zone in the subsurface, in order to remove water contamination by volatile compounds [17–21]. Understanding these processes is important not only for economy and ecology, but also for the mitigation of natural hazards. Indeed, quick fluidization due to fluid venting is often associated with catastrophic events such as soil liquefaction [22], volcaniclastic events [10, 11] or, at a larger scale, global warming [23, 24].

Many studies have been performed in two-phase systems to analyze the mechanisms at play in the fluid venting process, either for dry (gas/grains) [25, 26] or wet (liquid/grains) [16, 22, 27, 28] beds. For unconstrained beds, where the grains are likely to move and their free surface to deform, different patterns have been thoroughly described when changing the fluid injection flow-rate, Q, in the granular matrix. For low flow-rate, the grains remain at rest and the fluid percolates the medium—as a rigid porous medium. For intermediate Q, the granular bed deforms and develops instabilities and microchannels, but the macroscopic

flow-rate still obeys Darcy's law. Finally, for high flow-rate, the sample exhibits hydraulic failure, with pipe formation leading to a partial liquefaction of the system [16, 22, 27, 28]. However, many natural phenomena involve a three-phase flow. Typical examples are gas discharge by submarine mud volcanoes [29], or pockmarks [6]. In both cases, gas escapes from a saturated granular matrix—seafloor sediments for pockmarks or dense particle suspension for mud volcanoes. Extensive modeling for gas injection in a saturated, rigid porous medium has been performed in the last 20 years, both with and without the presence of heterogeneities in the system (see for instance [2, 30–35], a tentative phase diagram by Geistlinger et al. [36], and references within). When the medium is deformable, however, complex patterns may arise from the interaction between the fluid flow and the grains motion [37, 38]. In particular, in the dense regime, frictional contacts play a central role, and govern the macroscopic behavior of the granular bed.

Laboratory experiments are ideal tools to investigate the parameters governing the complex dynamics of three-phase systems. In the recent years, a thorough description of the patterns and hydrodynamic regimes have been reported for systems where gas is injected in a saturated granular medium. For injection at a fixed overpressure and grain compacity in a quasi-bidimensional (Hele-Shaw) cell, a transition has been reported between the viscous and frictional regimes [39], or between a Saffman-Taylor instability, dense suspension fracturing and fingering in a fixed porous medium [40]. When the compacity is not constrained, and the cell gap varies, more regimes can be found, exhibiting a strong coupling between the fluid and grain flows, as well as an expansion and fluidization of the granular bed [41]. Gravity, however, did not play a strong role in these systems, consisting mainly of a horizontal Hele-Shaw cell.

In this work, we investigate the dynamics of buoyancy-driven, unconstrained, three-phase systems. First, we summarize previous results describing the different regimes when air is injected at the bottom of a vertical Hele-Shaw cell filled with a granular material immersed in water [18, 21, 37, 38, 42–44], and propose a tentative regime diagram. As already reported in the literature, the fluidized zone exhibits a parabolic shape, in the stationary regime, for most of the experimental parameters. However, contrary to previous results, we report a dependence of this shape on the air injection flow-rate and grain size, for larger grains. In addition, the final shape departs from the classical parabola for the largest grains. After a brief description of the transient, we focus on the air dynamics inside the fluidized zone, in the stationary regime. We propose a regime diagram for 3D systems, and report a peculiar flow-to-fracture transition in the 2D cell. Finally, we discuss the dimensionless numbers previously introduced in the literature, predicting the dynamics of the system. We underline the major role played by the polydispersity in the invasion process.

2. Materials and Methods

The experimental setup (**Figure 1**) consists of a 3D cell (plexiglas cylinder, 7.4 cm in diameter) or 2D vertical Hele-Shaw cell (glass plates 40×30 cm, gap 2 mm). The cell is filled with spherical glass beads (USF Matrasur or Wheelabrator), sieved to achieve typical diameter ranges from 200–250 μm up to 710–965 μm (the grain diameter ranges are given for each result in the next sections). For each batch, we systematically measure the grain size distribution by means of a microscope. Typically, a thousand grains are considered for each batch, and the grain size distribution is fitted by a gaussian, which fairly accounts for the shape of the distribution for most grain batches. The central value provides the typical grain diameter, d, whereas the standard deviation quantifies the typical size dispersion. Measurements are given in **Table 1** for the grains used in the 2D experiment. Note that in the following, we refer either to the grain batch (e.g., "250–425 μm") or to the typical grain size (e.g., "318 $\pm$ 44 μm"). The granular layer is immersed under water. In the 3D experiment, we stir the grains vigorously with a paddle to remove the gas bubbles trapped

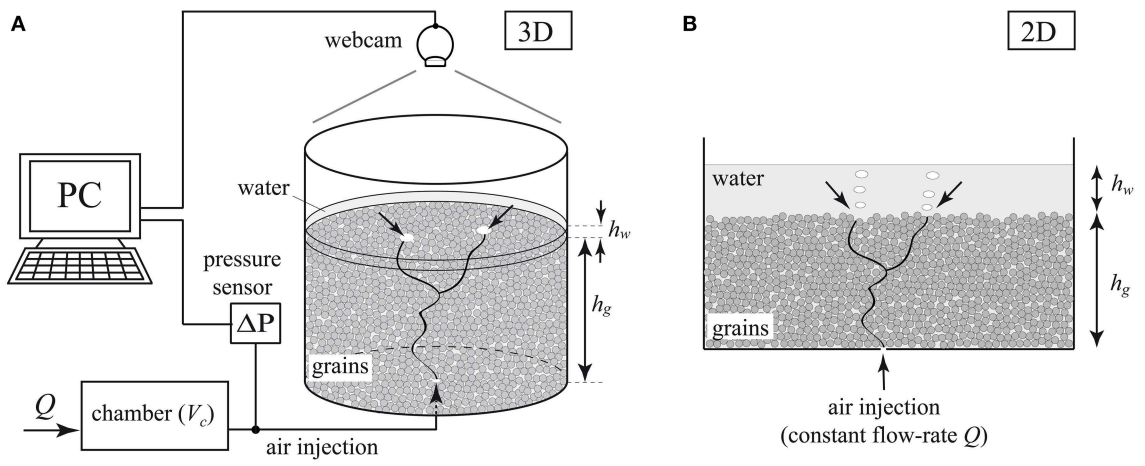

FIGURE 1 | Experimental setup, 3D (A) or 2D (B). Air is injected at constant flow rate, Q, through a nozzle at the base of the immersed granular bed, via a dry chamber (volume V_C). Direct visualization from top (3D) or side (2D) is achieved by means of webcams. In some experiments, we can monitor simultaneously the overpressure ΔP in the chamber, which provides indication on the system dynamics.

in the bed. In the 2D experiment, the cell is completely filled with water, then closed and turned upside-down. Right before a total sedimentation, it is flipped back to its original position, and the water is removed up to a given height. The free surface of the grains is then smoothed gently with a thin pole (in 2D) or a squegee (in 3D). h_g denotes the grain layer height, and h_w the water layer height above the grains free surface, respectively (**Figure 1**). In all the experiments, $h_w \simeq 2$ cm, small enough to avoid grain advection over large distances in the water layer, and the subsequent crater formation at the bed free surface [45].

Air is injected at constant flow-rate, Q, into a dry chamber (volume V_c), connected to a nozzle of inner diameter 1 mm, localized at the bottom center of the cell. The constant flow-rate is set either by means of a valve and capillary tube ($1.5 \leq Q \leq 4.3$ mL/s) or with a mass-flow controller (Bronkhorst, Mass-Stream Series D-5111, $0.17 \leq Q \leq 3.3$ mL/s). In some experiments, the pressure variations in the chamber is also monitored with a pressure sensor (MKS Instruments, 223 BD-00010 AB) connected to an acquisition board (National Instruments, PCI-6251), with a sensitivity of about 10 Pa. Illumination of the surface (in 3D) or the bulk (in 2D) is achieved with a transparency flat viewer (Just NormLicht, Classic Line) or with an array of LED lights, which ensure a homogeneous light. Images are recorded by a webcam (Logitech QuickCam Express, 2D experiment and Logitech QuickCam S7500, 3D experiment) or by a camera PixeLINK, model PL-B741U, 1280 × 800 px^2. Continuous or time-lapse acquisition is performed to capture either the quick degassing dynamics or the evolution of the system over long time-scales, by means of either a free software (Astra Image Webcam Video Grabber), or the PixeLINK camera software. The images are then analyzed with Matlab (MathWorks®).

TABLE 1 | Grain size and theoretical predictions for the characteristic length *D* describing the extension of the fluidized zone (2D experiment).

Grain batch [μm]	d [μm] (Measured)	χ (Estimated)	D [cm] (From theory)
200–250	218 ± 17	15–150	0.3–3.3
250–425	318 ± 44	7–70	0.2–2.2
600–710	631 ± 37	2–18	0.1–1.1
710–960	802 ± 68	1–11	0.09–0.9

3. Results

3.1. Invasion Patterns

3.1.1. Tentative Regime Diagram

First, we focus on the 2D experiment, which makes it possible to directly visualize the air patterns in the immersed granular bed. At short times, two different invasion patterns are observed, depending on the injected flow-rate Q. At low flow-rate, the pressure and/or buoyancy in the system is not enough to lift the grains and the air percolates the immersed granular layer, without moving significantly the grains (**Figure 2**, bottom left picture). The pattern develops several branches, which can reach the surface. The pressure loss in the percolating channels is much larger than the pressure drop associated with a bubble emission at the surface. Consequently, we can observe simultaneous bubble emissions at the free surface. At high flow-rate, a fracture opens, which propagates quickly toward the surface (**Figure 2**, top left picture). The side branches of this pattern are less pronounced, as the upper fracture tip always propagates at a larger speed, due to the strong vertical pressure gradient between the finger tip and the free surface. When reaching the surface, the bubble emission generates a large pressure drop in the fracture, and a subsequent collapse of its walls. Under continuous injection, another fracture opens, not necessarily following the same path.

It is interesting to note that the transition between percolation and fracture, at short times, is not clearly defined. Indeed, for

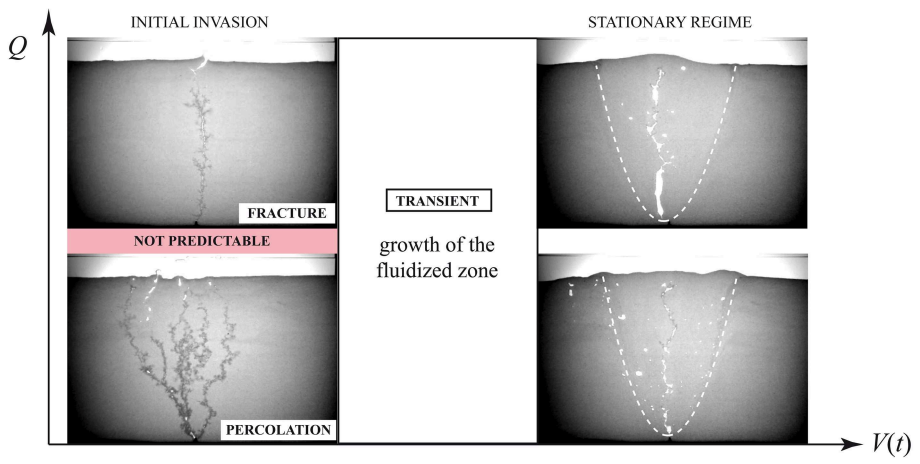

FIGURE 2 | Tentative regime diagram of the invasion pattern dynamics as a function of the injected flow-rate, *Q*, and the total volume of gas *V*(*t*) which has crossed the system at time *t*. The light red zone indicates the region where the initial invasion regime (percolation or fracture) cannot be predicted [images from the grain batch 250–425 μm, $h_g = 22$ cm, $h_w = 2$ cm, $Q = 0.43$ mL/s (bottom images) and $Q = 2.17$ mL/s (top images); the white dashed lines indicate the fluidized zone boundary].

a given range of intermediate Q, it is not possible to predict the invasion pattern. This indetermination, already reported in Varas et al. [44] with a tilted experimental cell, is due to the local heterogeneities in the system. Indeed, both the polydispersity of the grains batch and the layer preparation (resulting in different local packing fraction) make the system slightly different from one experiment to the other, although the grains sample and the global packing fraction are the same.

At long time (typically, between a few hours and a few tens of hours, depending on the flow-rate), a fluidized zone is formed at the center of the cell [38], clearly visible in the 2D Hele-Shaw cell (**Figure 2**, right). Although it is not possible to visualize it directly in the 3D experiment, mapping the air location at the free surface of the granular layer also provided a good description of the region invaded by the air, as a function of the bed height [42]. For most experiments, the stationary shape of the fluidized zone is a parabola. This parabolic shape has already been described in the literature [17, 21, 37, 46], although for many years a cone-shape invasion zone has also been reported [17]. More recent works have pointed out the robustness of the parabolic shape, whichever the initial invasion regime, i.e., whichever the injection flow-rate, both in 2D and 3D experiments [42–44]. Based on these results and our experiments, we propose the tentative diagram displayed in **Figure 2**, where for a given immersed granular bed, the state of the system will be mainly governed by the injection flow rate, Q, as well as the volume of gas $V(t)$ which has crossed the grain layer at time t.

A simple analytical model can account for the final parabolic shape [42] and its independence on the flow rate. It points out that the dynamics of the system is governed by a single dimensionless parameter:

$$\chi = \frac{\sigma_p}{\rho g d} \tag{1}$$

where ρ is the water density, g the gravitational acceleration and d the typical grain diameter; σ_p is the width of the distribution of the capillary overpressures in the system. In other words, the parameter χ compares the width of the distribution of the capillary overpressure associated with the passage of air between the immersed grains, σ_p, to the typical hydrostatic pressure variation over the grain size, $\rho g d$. The width of the distribution of the capillary overpressure in the system can be written $\sigma_p \sim w\gamma/d$, where w is the typical relative variation of the pores size and γ is the air-water surface tension. Therefore,

$$\chi = \frac{w\gamma}{\rho g d^2} \ . \tag{2}$$

The geometry of the air paths in the system are well-reproduced by a 2D numerical model [43], which captures both the branches morphology as a function of the parameter χ, and the typical contour of the region invaded by the gas. For a given batch of grains, when the parameter χ increases, the air path extends laterally and the typical contour of the invaded region widens. We do not detail here these results that are thoroughly discussed in previous articles [43, 44]. In Section 4, we further discuss the parameter χ and compare it to the classical Bond and modified Bond numbers, previously introduced in the literature to describe the dynamics of fluid invasion in porous media.

3.1.2. Dependence on *Q* and *d*

The experiments reported in this article explore a larger range of grains diameter than in former studies. In order to detect precisely the contour of the fluidized zone, we propose a new method based on the global tracking of motion in the system, for the 2D experiment. We consider the absolute difference in the intensity of two consecutive images, $\mathrm{M}_k = |\mathrm{I}_{k+1} - \mathrm{I}_k|$. The matrix M_k can contain either zero (no motion) or non-zero elements, the latter corresponding to regions where a motion occurred in the system—due either to air or grain motion. The generation of the fluidized zone can be seen as a cumulative process due to the continuous emission of gas through the system. Therefore, its dynamics is generally slow, and requires to accumulate information over time to enhance the contrast and detect correctly its contour. We define the *flow density*, $\rho_n(x, z)$, as the sum of consecutive image differences M_k:

$$\rho_n(x,z) = \sum_{k=1}^{n-1} \mathrm{M}_k = \sum_{k=1}^{n-1} \left|\mathrm{I}_{k+1} - \mathrm{I}_k\right| . \tag{3}$$

The normalized flow density, $\overline{\rho} = \rho_n/\max(\rho_n)$, provides a quantification of the average motion in the granular bed. The contour of the fluidized zone is then determined by imposing a low threshold value, typically $\overline{\rho} < 0.1$, which makes it possible to detect the boundary between the outer zone, where the grains do not move significantly, and the central fluidized zone.

Figure 3 displays the flow density for all the grain diameters and flow rates used in our experiments (16 experiments in total, one final flow density image per experiment). For almost all experiments, the stacking of successive image difference was performed over 4000 images (time interval between successive images $\Delta t = 10$ s, see legend in **Figure 3**). Note that it does not represent an equal total volume crossing the medium for the different flow rates, but rather a similar experiment duration. Once the system is in stationary regime, the time over which the images stacking is performed does not change much the result—the longer the time, the better the contrast, but the contour of the fluidized zone (FZ) remains the same. Interestingly, when the grain size is increased (typically, for $d > 250$ μm), the contour of the fluidized zone becomes slightly dependent on the flow-rate Q. For the largest grain size ($d = 710$–965 μm), no fluidized zone is formed at all for the lowest flow rate (see bottom left picture, **Figure 3**). This can be explained by the fact that for larger grains, the pore size increases, which favors percolation of the granular bed by the air. In that case, it is harder to trigger the grain motion and at low flow-rate, the medium resembles a rigid porous medium.

Previous studies have described the fluidized zone (FZ) parabolic contour by the equation $|x| = \sqrt{Dz}$, where D can be seen as the analog of a diffusion coefficient—here, D is a characteristic "diffusive" length [42]. Typically, in similar experiments, D was found of the order of 4 cm [44]. **Figure 4** displays an example of how to extract D from the experimental data. In **Figure 4A**, the (x, z) FZ profile is shown for the grain

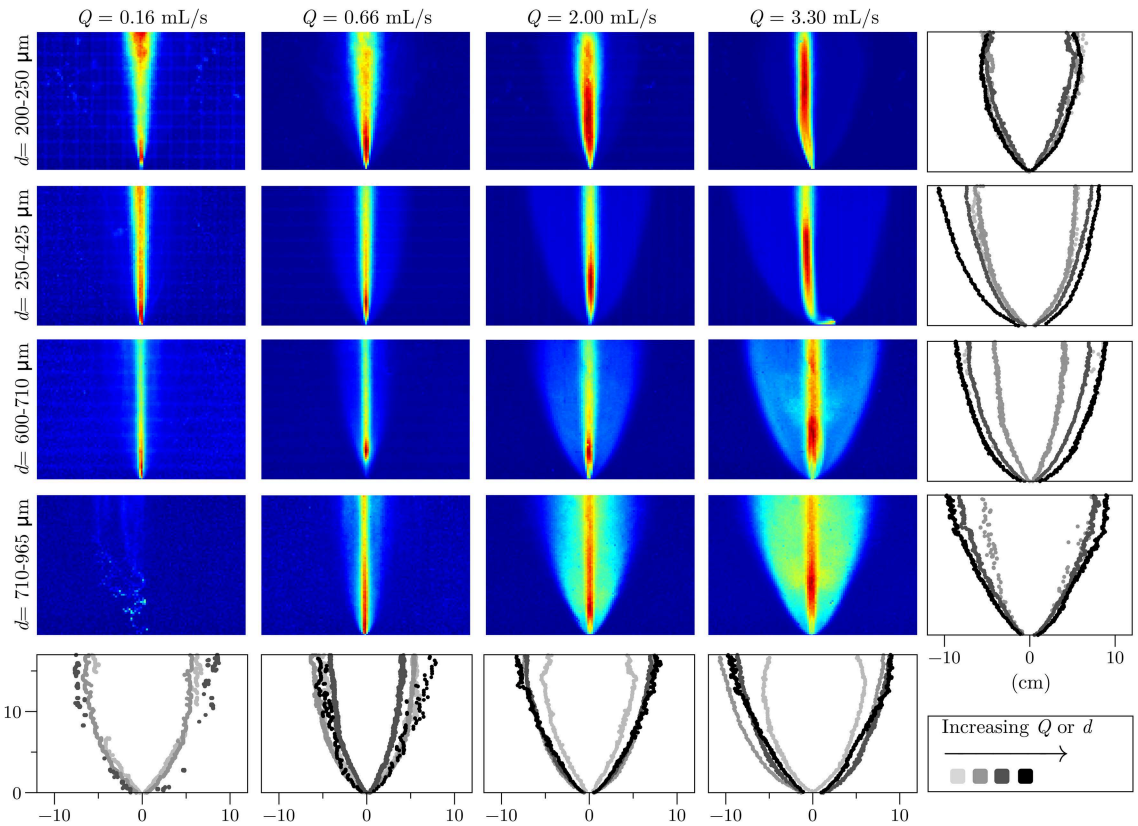

FIGURE 3 | Normalized flow density, $\overline{\rho}$, for all the parameters used in our experiments. Each flow density image displayed here corresponds to one experiment (16 experiments in total) [$h_g = 17$ cm, stacking over 4000 images (all except the bottom-left flow density image) or 8000 images (bottom-left density image), $\Delta t = 10$ s between successive images]. The color ranges from 0 (dark blue) to 1 (dark red). *Right and bottom:* Fluidized zone boundary [threshold $\overline{\rho} = 0.1$, light gray to black: increasing Q or d]. Note that for the large grains ($d =$ 710–965 μm), no fluidized zone is formed at low flow rate ($Q = 0.16$ mL/s).

batch 250–425 μm, and a flow-rate $Q = 0.16$ mL/s. The FZ contour is obtained by considering a threshold value for its boundary, here $\overline{\rho} = 0.1$. The horizontal distance to the injection point at the center, $|x|$, is then displayed as a function of $\sqrt{z}$ for both the right and left FZ contour (**Figure 4B**), and a linear fit gives the value of D. Note that the determination of D excludes a small region close to the air inlet ($z < 2$ mm), and just below the free surface ($z > 12$ cm). Indeed, in these regions, boundary effects are observed (blue regions, **Figure 4**). The coefficient D is then calculated for all experiments.

The results are displayed in **Figure 5**. Note that the grain sizes displayed in the figure correspond to the typical grain sizes (and standard deviations) found from the gaussian fit of the grain size distributions corresponding to each batch (see Section 2 and **Table 1**). For smaller grains (batch 200–250 μm), $D \sim 3$–4 cm and no significant variation is found as a function of the flow-rate (**Figure 5A**), in agreement with previous results [44]. Note that it is difficult to interpret the value of D for very low flow-rate ($Q < 0.5$ mL/s). Indeed, in that case, the air invasion is mainly percolation and no clear grain motion is observed in the fluidized zone, even over long time-scale. Nonetheless, up to grain size of about 700 μm, the flow density images, obtained by stacking the successive image differences, displays a parabolic contour (**Figure 3**). For the large grains, however, no parabolic region is observed over the experimental observations—in that particular case, the stacking was performed up to 8000 images, corresponding roughly a 22 h experiment (**Figure 3**, bottom left flow density image). For these parameters, therefore, the coefficient D is undetermined.

For larger grain size ($d > 250$ μm) and larger flow-rate ($Q > 0.5$ mL/s), we report an increase of the fluidized zone extension as a function of the flow-rate (**Figure 5A**). **Table 1** gives the range of χ and D expected from the theory, by using Equation (2) and $D \sim d\chi$ as given by numerical simulations [43]. For a granular bed made of polydisperse grains, w is usually of the order of the relative width of the size distribution [42]. This value, however, is difficult to quantify precisely, and may strongly vary from one batch to the other. We consider here a typical relative variation of pore sizes ranging between $w = 0.1$ to 1. The upper limit of D expected from the theory is of the order of the experimental observations at low flow-rate ($Q < 1$ mL/s). Note that, for $Q = 0.66$ mL/s, we observe a widening of the fluidized zone (increase of D) when the grain size decreases, as predicted by the model with similar w for all batches. Variations of w depending on the

grain batch may explain the value of the coefficient D larger for $d = 710$–$960\,\mu$m than for $d = 600$–$710\,\mu$m. For other flow-rates, no clear dependence is observed as a function of the average grain size. The dependence on the flow-rate is not predicted by the model.

Figure 5B summarize the results in the (d, Q) phase diagram, where the marker size is proportional to the value of D. Although a parabolic contour is always observed in the flow density images (except for the larger grains and lower flow-rate), it is interesting to note that the dynamics in the granular bed varies a lot. For small grains (typically, $d < 425\,\mu$m), in the stationary regime, the fluidized zone is characterized by two convection rolls, which entrain the grains upward in the central zone (together with the air crossing the layer), and downward on both sides. The fluidization, and thus the overall motion in the FZ, is homogeneous. However, for larger grains ($d > 600\,\mu$m), a more complex dynamics is observed. The fluidization is heterogeneous, with lateral fracture opening intermittently—which explains the increase in the flow density value inside the central zone (see for example **Figure 3**, bottom right image). In that case, a local fluidization, limited to a region right above the injection point (typically, a couple of centimeters), is observed, while the motion above mostly happens either through percolation, or intermittent fracture opening. This dynamics strongly resembles the formation of a *"fluidized cavity"* reported by Philippe and Badiane [47], who injected liquid in liquid-saturated grains (two-phase system), with grain size above 3 mm. The transition between a fluidized zone dynamics mainly governed by grain

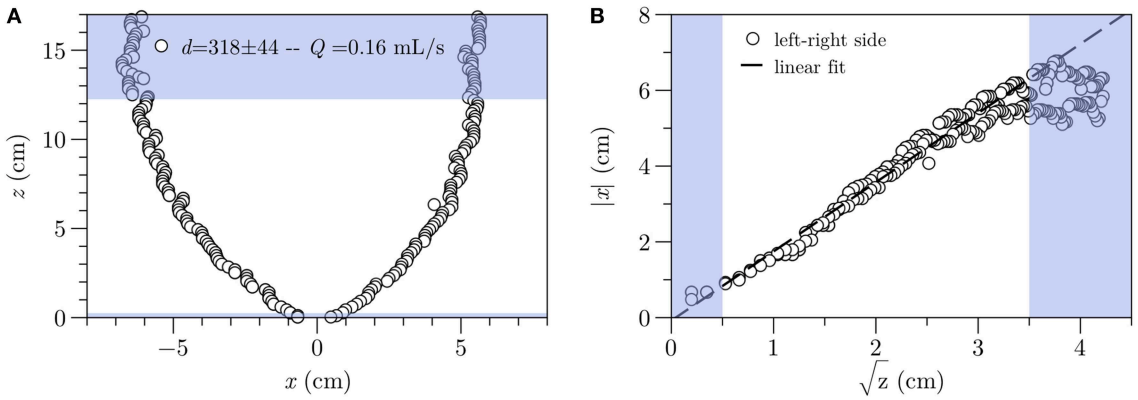

FIGURE 4 | Determination of the coefficient D characterizing the parabolic shape of the fluidized zone, $|x| = \sqrt{Dz}$ [grain batch 250–425 μm, corresponding to a typical grain size $d = 318 \pm 44\,\mu$m, estimated with a gaussian fit (see text); $Q = 0.16$ mL/s]. (A) Automatic contour detection from the normalized flow density images shown in **Figure 3** [threshold $\overline{\rho} = 0.1$]. The lower ($z < 2$ mm) and upper ($z > 12$ cm) zones (in blue) are excluded for the following fit, to avoid boundary effects (mainly close to the surface). **(B)** Linear fit of the experimental data, $|x|$ as a function of $\sqrt{z}$ [same data than **(A)**]. The right and left sides of the fluidized zone are superimposed, and a single fit is performed. We only take into account the experimental points in the central, white region. The parabola coefficient, D, is directly extracted from the slope—here $\sqrt{D}$.

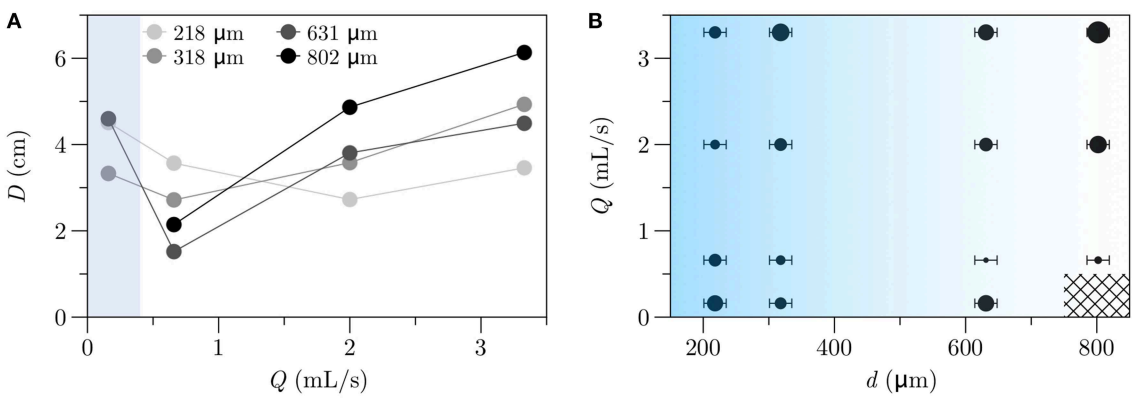

FIGURE 5 | (A) Coefficient D as a function of the injection flow-rate, Q, for different grain size (only the average grain size is indicated here). **(B)** Diagram of the parabolic contour determination (coefficient D) as a function of the governing parameters, the injection flow-rate Q and the grain size d. The marker size is proportional to D, and the horizontal error bar indicates the grain size standard deviation for each batch. The blue shade indicates a transition between a dynamics governed by a homogeneous grain convection in the fluidized zone, for small grains ($d < 425\,\mu$m) to a more complex regime where the fluidization is heterogeneous, and intermittent, lateral fracture is observed in the fluidized zone ($d > 600\,\mu$m). The hatched zone corresponds to parameters for which no fluidized zone formation was observed over the experimental time.

convection, or a local fluidization plus percolation and fracture above, is not clear, and would require a more detailed study. It is indicated qualitatively by the blue shade in **Figure 5B**.

3.2. Transient Dynamics: Growth of the Fluidized Zone

After having characterized the properties of the fluidized zone in the stationary regime, we briefly describe its formation in the 2D experiment. For grain size of 250–425 μm, Varas et al. [44] have shown that the fluidized zone develops from the free surface, and grows downward until reaching the injection nozzle. The authors reported a logarithmic growth of both the horizontal and vertical extent of the fluidized central region. For larger grains ($d = 400$–$600\ \mu$m), Kong et al. [38] pointed out the existence of a threshold flow-rate, above which the fluidized region indeed grows from the grains free surface, and reaches the orifice—in that case, the authors state that the fluidization region accesses the whole region initially explored by the tree-like percolation pattern. Below this threshold flow-rate, the fluidization stops *"somewhere between the top of the packing and the orifice."* The precise motion, however, is difficult to detect on the direct images, and has to be guessed from the accelerated movie of the experiment (see for instance **Figure 5A** of Varas et al. [44]). The *flow density* determination, as described in Section 3.1, makes it possible to clearly observe the transient dynamics of fluidized zone formation (**Figure 6**).

At short time, it is interesting to note that the motion is not limited to the later fluidized zone contour, but extends to a wider region, mostly close to the surface. This is due to the formation of microchannels or instabilities close to the free surface, when the air explores the system at the beginning of the injection. Later on, the motion concentrates in the central zone, until being exclusively limited to this latter. The large motion at the center is due to the repetitive air rise, which does not explore anymore a wide region, but behaves as air rising in a fluid—the central region can then be assimilated to a liquid-like granular suspension. Note that this behavior is observed only for grain diameter below 425 μm (see above section).

In the following section, we will focus on the dynamics of air crossing the fluidized zone, in the stationary regime.

3.3. Degassing in the Stationary Regime

3.3.1. Bubbles or Channels?

Few experiments have previously reported the dynamics of gas rising in an unconstrained, saturated porous medium, although the different patterns for rigid porous media have been thoroughly discussed in the *in-situ* air sparging (ISAS) literature [48]. In sand-sized porous media, Ji et al. [46] reported experimentally that gas formed channels rather than discrete bubbles or percolation (dendritic) networks. The formation of air channels, as well as their migration, in unconstrained media has been described by Kong et al. [37] in grains saturated with a glycerine-water solution. A later work by the same authors evidenced the existence of a meandering single channel, at the center of the fluidized zone [38]. This irregular, oscillating channel is formed by *"several discrete elongated bubbles [...] driven by their buoyant forces."* In a first attempt to characterize better the air dynamics through the fluidized region, we analyzed the signal monitored by the pressure sensor, close to the injection nozzle, in the 3D experiment (**Figure 1A**). Two different signals are registered. For low flow-rate, the pressure signal exhibits a sawtooth shape, characteristic of successive pressure increase, followed by bubble emission, which triggers a sharp pressure drop (**Figure 7A**, up). For higher flow-rate, bubble emission is still observed (sawtooth-shaped signal), but from time to time, the pressure remains at a constant value (**Figure 7A**, down). This is the signature of a channel, opening from the injection nozzle through all the granular layer, and emitting air continuously through the bed [49]. The pressure value in this state can vary, depending on the pressure loss in the channel, and can exhibit slow temporal variations, if the channel remains open for a long time (up to a couple of minutes in our experiments). After a time ranging from less than a second up to a couple of minutes, the channel collapses and the bubbling regime restarts. In this regime, channels formation and collapse are observed intermittently.

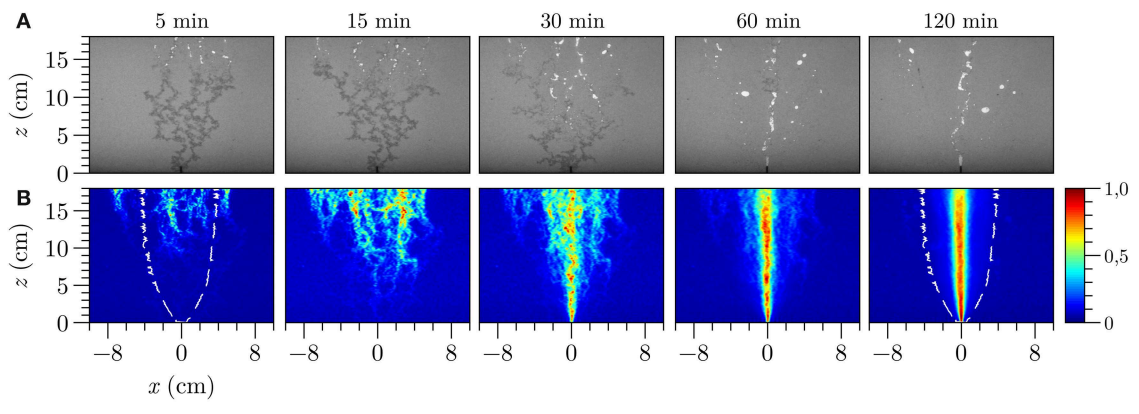

FIGURE 6 | Formation of the fluidized zone [$Q = 0.66$ mL/s, d =250–425 μm]. (A) Direct images from the experiment. **(B)** Normalized flow density $\overline{\rho}$ obtained by stacking successive image differences from the beginning of the experiment up to the time indicated above each image. The white dashed line indicate the contour of the fluidized zone, found by using the threshold $\overline{\rho} = 0.1$ in the final image.

This dynamics strongly resembles the degassing dynamics, in the same experimental conditions (constant injection flow-rate), through a layer of shear-thinning, viscoelastic fluid [50–52].

In **Figure 7B**, we propose a regime diagram summarizing the behavior of the system depending on the injection flow-rate, Q, and also the volume of the chamber, V_c in which the air flows before entering the nozzle at the bottom of the experiment (see **Figure 1A**). Note that V_c includes all the air volume between the gas flow controller and the injection point, and therefore takes into account the volume of the pipes which bring the air at the cell bottom. In most experiments (as in the 2D experiment presented in this work), there is no chamber in the system, but the tube length (in our case, about 0.03 mL in total) should be specified, as it may influence the degassing dynamics. Small V_c tend to favor an intermittent degassing regime, while large V_c favor the bubbling regime. This graph points out the importance of this parameter, often neglected or which value is not specified in similar experiments—although all experiments have injection tubes whose volume should be carefully determined.

3.3.2. Fingering and Fracturing

The previous determination of the bubble vs. intermittent regime is based on pressure signal analysis only. Indeed, in the 3D experiment, it is not possible to visualize directly the air pathway(s) through the immersed granular bed. In this last part, we report qualitative observations of a new regime, in the 2D experiment. For the smaller grains ($d < 425\,\mu$m), in a given range of flow-rate, a peculiar dynamics was observed in the stationary regime, inside the fluidized zone (**Figure 8**). In that case, an air finger grows vertically, until reaching a critical height h^*. Its velocity decreases up to this height. It then stops, but as continuous air flow-rate is injected to the system, the pressure increases in the finger, until the air suddenly fractures the above grain layer.

The transition height h^* between the fingering and fracturing dynamics is quite reproducible over time, as the air crosses the system. It is interesting to note that it coincides with a maximum in the normalized flow density $\overline{\rho}$, computed in the stationary regime (**Figure 8**, right). We are not able at present to provide an explanation for this spontaneous change of dynamics, which shall be at the center of a future work.

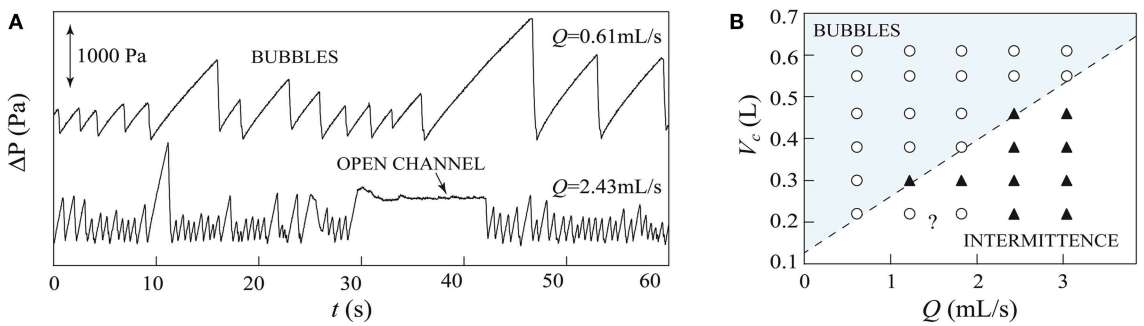

FIGURE 7 | Different degassing regimes through an immersed granular layer [3D experiment, $d = 315$–$400\,\mu$m, $h_g = 2$ cm, $h_w = 10$ cm]. (A) For low flow-rate, successive bubbles cross the medium; for high flow-rate, we report an intermittence between the bubbling and the open channel regime. **(B)** Regime diagram when varying the chamber volume V_C and the flow-rate Q [○ = bubbles, ▲ = intermittence]. The dashed line indicates the transition between the two regimes. Due to the finite acquisition time (1 min), it is sometimes difficult to infer the boundary with precision.

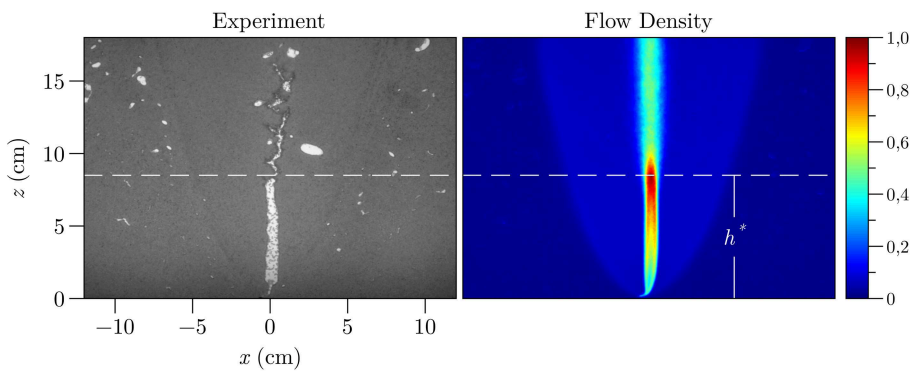

FIGURE 8 | Transition from an invading finger, and the fracturing of the above granular layer [$h_g = 17$ cm, $h_w = 2$ cm, $d = 250$–$425\,\mu$m, $Q = 2$ mL/s]. Left: Direct image showing the transition. **Right:** Normalized flow density $\overline{\rho}$ in the stationary regime, pointing out the coincidence between the fingering-to-fracturing transition, at height h^*, and the zone exhibiting the maximum of motion [stacking over 2000 images].

4. Discussion and Conclusions

A thorough description of two-phase flow patterns (gas-liquid) when injecting gas in a rigid, saturated porous medium has been provided in the literature (see for example [48], [21] and references within). These patterns—air bubbles, percolation networks or air channels—mainly depend on the grain size, and prediction attempts have been made by the *in-situ* air sparging (ISAS) community. Typically, bubbles are characteristic of water-filled media with pore size greater than about 4 mm, air channels form when the pore size is smaller than 0.5 mm, and dendritic invasion takes place for intermediate grain size [21]. Based on the Uniform Soil Classification System [53], which provides a classification of the different types of soils—in particular, their average size—the transition zone happens for the medium to coarse sands, making it possible to roughly predict the gas patterns in a given soil.

To account for the physical mechanisms at stake when considering three-phase, buoyancy-driven systems—in particular, the invasion of a non-wetting fluid into a wetting-fluid in a saturated porous medium under the influence of gravity, we have to consider the relative importance of the dominant forces in the system, i.e., buoyancy and capillary forces. The Bond number, also called Eötvös number, has been used traditionally to characterize multiphase flow in porous media, and is defined as the ratio between gravity over capillarity forces:

$$Bo = \frac{\Delta\rho g r_p^2}{\gamma} \tag{4}$$

where $\Delta\rho$ is the density difference between the liquid and gas, g the gravitational acceleration, r_p the characteristic pore size and γ the liquid-gas surface tension. However, the pore size r_p cannot account simultaneously for the largest buoyancy and the largest capillary overpressure to be overcome for the air to propagate in the system. Indeed, the largest capillary overpressure is governed by the narrowest interstice between grains, while the largest buoyancy force is given, at the contrary, by the wider pore space. Brooks et al. [48] proposed to introduce a modified Bond number, which compares the buoyancy forces in the so-called *pore body* (size r_b), to capillary forces in the *pore neck* (size r_n):

$$Bo^* = \left(\frac{\Delta\rho g}{\gamma}\right)\left(\frac{{r_b}^3}{r_n}\right) = \frac{Bo}{\alpha} \tag{5}$$

where $\alpha = r_n/r_b$ is the ratio of the pore neck size to pore body size, referred to as the aspect ratio [54]. In a crude approximation, the typical size of the pore body is often taken as the grain radius $d/2$, and $r_n = \alpha(d/2)$, which gives a modified Bond number $Bo^* = (\Delta\rho g d^2)/(4\gamma\alpha)$. Although this dimensionless parameter has been used previously to attempt a physical classification of the flow patterns [21, 48], it is not always easy to determine, due to the difficulty to determine the porous media aspect ratio [48]. Moreover, it does not take into account the pore size distribution, which can strongly vary from one grain sample to the other, even when the average size remains the same. It has already been pointed out in the literature, although qualitatively, that the soil heterogeneity—and not only the average grain size—may have a strong effect on the efficiency of air sparging [20].

The parameter χ, introduced in previous works and emphasized in Section 3.1, provides a way to quantify the importance not only of the average grain size, but also of its distribution [42–44]. Equation (1) shows that it is easy to estimate from the granular medium or soil granulometry. From its other formulation (Equation 2), it is possible to link it with the Bond number, as $\chi = w/Bo$, where w is the relative variation of the pore size. It cannot be compared to the modified Bond number, $Bo^* = Bo/\alpha$, as w here takes into account the heterogeneities in the medium (grain size distribution and local packing fraction) and their impact on the flow pattern, which is not the case for α. In other words, χ can be considered as a *polydisperse Bond number*. However, it is also based on the physics of rigid porous media. Even if it succeeds in providing a general description of the parabolic region explored by the gas, it does not account for the grain motion, and the resulting coupling between the solid, fluid and gas phase flow. A theoretical description of this interaction would require a more complex formulation, and is out of the scope of this article.

This work has reported new experimental results evidencing an increase of the central fluidized zone extension on the flow rate. In spite of the different physical mechanisms at stake—percolation, fracturing, localized fluidized zone above the injection nozzle or lateral fracture—in most experiments, the fluidized zone boundary is always parabolic. The only exception is for large grains ($d = 710$–$965\,\mu$m), at low flow rate. The exploration of the regime diagram for larger grains would be required to extend this description, and attempt to propose a mechanism to account for this difference.

We also introduced the normalized *flow density*, $\overline{\rho}$, which provides a quantification of the average motion in the granular bed. It proves to be a useful tool not only to accurately determine, in the stationary regime, the contour of the fluidized zone, but also to image its transient growth. The detailed analysis of this latter will be the topic of a future work. We evidenced different degassing dynamics in the stationary regime, inside the fluidized zone, and underline the importance of a parameter often hidden in the experimental systems, the volume of gas V_c available before the injection nozzle. For low flow-rate Q or large V_c, air bubbles cross the deformable medium. For large Q or small V_c, we observe an intermittence between air bubbles, and open channels connecting the air nozzle to the grains free surface. In this latter regime, a continues degassing is observed, until the channel walls collapse, back to a bubbling regime. Finally, a new regime was reported in the 2D experiment, with a transition between the growth of an air finger and the fracture of the above granular layer at a given height in the cell. Such patterns as fingering and fracturing have been reported in the literature in deformable, saturated porous media, when varying the grain volume fraction [40, 55, 56]. These patterns, however, were mainly described for horizontal Hele-Shaw cell, in which buoyancy does not govern the system dynamics. To our knowledge, it is the first time

that a spontaneous transition between fingering and fracturing is reported. Additional techniques of index-matching would be required to check if this peculiar dynamics is a consequence of the confinement by the lateral plates, or also occurs in the 3D experiment.

Author Contributions

GV and GR performed most of the experimental work related to Sections 3.1, 3.2, and 3.3.2. VV performed the experiments about the degassing regimes (Section 3.3.1). GV, JG, and VV provided the theoretical background, and all authors participated in the results analysis and interpretation. VV drafted the work, and all authors revised it and gave their final approval.

Funding

GV and VV acknowledge financial support from FONDECYT Project No.11121300. This work was supported by the *Programa de cooperación científica* ECOS/CONICYT C14E07 and by the LABEX iMUST (ANR-10-LABX-0064) of Université de Lyon, within the program "Investissements d'Avenir" (ANR-11-IDEX-0007) operated by the French National Research Agency (ANR).

Acknowledgments

The authors thank the editors of Frontiers Research Topic *"Flow and Transformation in Porous Media"* to ask them for this contribution. We acknowledge the three reviewers for interesting remarks and discussions which greatly improved the manuscript.

References

1. Naudts L, Greinert J, Artemov Y, Beaubien SE, Borowski C, De Batist M. Anomalous sea-floor backscatter patterns in methane venting areas, Dnepr paleo-delta, NW Black Sea. *Mar Geol.* (2008) **251**:253–67. doi: 10.1016/j.margeo.2008.03.002
2. Flekkøy EG, Malthe-Sørenssen A, Jamtveit B. Modeling hydrofracture. *J Geophys. Res.* (2002) **107**:2151. doi: 10.1029/2000JB000132
3. Cobbold PR, Rodrigues N. Seepage forces, important factors in the formation of horizontal hydraulic fractures and bedding-parallel fibrous veins ('beef' and 'cone-in-cone'). *Geofluids* (2007) **7**:313–22. doi: 10.1111/j.1468-8123.2007.00183.x
4. Boutt DF, Goodwin L, McPherson BJOL. Role of permeability and storage in the initiation and propagation of natural hydraulic fractures. *Water Resour Res.* (2009) **45**:W00C13. doi: 10.1029/2007WR006557
5. Hovland M, Talbot M, Olaussen S, Aasberg L. Recently formed methane-derived carbonates from the North Sea floor. In: Thomas BM, editor. *Petroleum Geochemistry in Exploration of the Norwegian Shelf.* London: Graham and Trottman (1985). p. 263–6.
6. Hovland M, Gardner JV, Judd AG. The significance of pockmarcks to understanding fluid flow processes and geohazards. *Geofluids* (2002) **2**:127–36. doi: 10.1046/j.1468-8123.2002.00028.x
7. Gay A, Lopez M, Cochonat P, Sérane M, Levaché D, Sermondadaz G. Isolated seafloor pockmarks linked to BSRs, fluid chimneys, polygonal faults and stacked OligoceneMiocene turbiditic palaeochannels in the Lower Congo Basin. *Math Geol.* (2006) **226**:25–40. doi: 10.1016/j.margeo.2005.09.018
8. Svensen H, Planke S, Jamtveit B, Pedersen T. Seep carbonate formation controlled by hydrothermal vent complexes: a case study from the Vøring Basin, the Norwegian Sea. *Geo-Mar Lett.* (2003) **23**:351–8. doi: 10.1007/s00367-003-0141-2
9. Svensen H, Jamtveit B, Planke S, Chevallier L. Structure and evolution of hydrothermal vent complexes in the Karoo basin, South Africa. *J Geol Soc.* (2006) **163**:671–82. doi: 10.1144/1144-764905-037
10. Walters AL, Phillips J, Brown RJ, Field M, Gernon T, Stripp G, et al. The role of fluidisation in the formation of volcaniclastic kimberlite: grain size observations and experimental investigation. *J Volcanol Geotherm Res.* (2006) **155**:119–37. doi: 10.1016/j.jvolgeores.2006.02.005
11. Gernon TM, Gilbertson MA, Sparks RSJ, Field M. Gas-fluidisation in an experimental tapered bed: insights into processes in diverging volcanic conduits. *J Volcanol Geotherm Res.* (2008a) **174**:49–56. doi: 10.1016/j.jvolgeores.2007.12.034
12. Gernon TM, Sparks RSJ, Field M. Degassing structures in volcaniclastic kimberlite: examples from southern African kimberlite pipes. *J Volcanol Geotherm Res.* (2008b) **174**:186–94. doi: 10.1016/j.jvolgeores.2007.12.035
13. Planke S, Svensen H, Hovland M, Banks DA, Jamtveit B. Mud and fluid migration in active mud volcanoes in Azerbaijan. *Geo-Mar Lett.* (2003) **23**:258–68. doi: 10.1007/s00367-003-0152-z
14. Mastalerz V, de Lange GJ, Dählmann A, Feseker T. Active venting at the Isis mud volcano, offshore Egypt: origin and migration of hydrocarbons. *Chem Geol.* (2007) **246**:87–106. doi: 10.1016/j.chemgeo.2007.09.005
15. Mazzini A, Svensen H, Akhmanov GG, Aloisi G, Planke S, Malthe-Sørenssen A, et al. Triggering and dynamic evolution of the LUSI mud volcano, Indonesia. *Earth Planet Sci Lett.* (2007) **261**:375–88. doi: 10.1016/j.epsl.2007.07.001
16. Mörz T, Karlik EA, Kreiter S, Kopf A. An experimental setup for fluid venting in unconsolidated sediments: New insights to fluid mechanics and structures. *Sediment Geol.* (2007) **196**:251–67. doi: 10.1016/j.sedgeo.2006.07.006
17. Reddy KR, Kosgi S, Zhou J. A review of *in-situ* air sparging for the remediation of VOC-contaminated saturated soils and groundwater. *Hazard Waste Hazard Mater.* (1995) **12**:97–118. doi: 10.1089/hwm.1995.12.97
18. Semer R, Adams JA, Reddy KR. An experimental investigation of air flow patterns in saturated soils during air sparging. *Geotech Geol Eng.* (1998) **16**:59–75. doi: 10.1023/A:1008884213834
19. Reddy KR, Semer R, Adams JA. Air flow optimization and surfactant enhancement to remediate toluene-contaminated saturated soils using air sparging. *Environ Manage Health* (1999) **10**:52–63. doi: 10.1108/09566169910257239
20. Reddy KR, Adams JA. Effects of soil heterogeneity on airflow patterns and hydrocarbon removal during *in situ* air sparging. *J Geotech Geoenviron Eng.* (2001) **3**:234–47. doi: 10.1061/(ASCE)1090-0241(2001)127:3(234)
21. Selker JS, Niemet M, McDuffie NG, Gorelick SM, Parlange JY. The local geometry of gas injection into saturated homogeneous porous media. *Transp Porous Med.* (2007) **68**:107–27. doi: 10.1007/s11242-006-0005-0
22. Wilhelm T, Wilmański K. On the onset of flow instabilities in granular media due to porosity inhomogeneities. *Int J Multiphase Flow* (2002) **28**:1929–44. doi: 10.1016/S0301-9322(02)00105-2
23. Svensen H, Planke S, Renssen AMS, Jamtveit B, Myklebust R, Eidem TR, et al. Release of methane from a volcanic basin as a mechanism for initial Eocene global warming. *Nature* (2004) **429**:542–5. doi: 10.1038/nature02566
24. Svensen H, Planke S, Chevallier L, Renssen AMS, Corfu F, Jamtveit B. Hydrothermal venting of greenhouse gases triggering Early Jurassic global warming. *Earth Planet Sci Lett.* (2007) **256**:554–66. doi: 10.1016/j.epsl.2007.02.013
25. Nermoen A, Raufaste C, deVilliers SD, Jettestuen E, Meakin P, Dysthe DK. Morphological transitions in partially gas-fluidized granular mixtures. *Phys Rev E* (2010a) **81**:061305. doi: 10.1103/PhysRevE.81.061305
26. Nermoen A, Galland O, Jettestuen E, Fristad K, Podladchikov Y, Svensen H, et al. Experimental and analytic modeling of piercement structures. *J Geophys Res.* (2010b) **115**:B10202. doi: 10.1029/2010JB007583

27. Rigord P, Guarino A, Vidal V, Géminard JC. Localized instability of a granular layer submitted to an ascending liquid flow. *Gran Matt.* (2005) **7**:191–7. doi: 10.1007/s10035-005-0214-1
28. Zoueshtiagh F, Merlen A. Effect of a vertically flowing jet underneath a granular bed. *Phys Rev E* (2007) **75**:056313. doi: 10.1103/PhysRevE.75.056313
29. Sauter EJ, Muyakshin SI, Charlouand JL, Schlüter M, Boetius A, Jerosch K, et al. Methane discharge from a deep-sea submarine mud volcano into the upper water column by gas hydrate-coated methane bubbles. *Earth Planet Sci Lett.* (2006) **243**:354–65. doi: 10.1016/j.epsl.2006.01.041
30. Vedvik A, Wagner G, Oxaal U, Feder J, Meakin P, Jøssang T. Fragmentation transition for invasion percolation in hydraulic gradients. *Phys Rev Lett.* (1998) **80**:3065–8. doi: 10.1103/PhysRevLett.80.3065
31. Løvoll G, Méheust Y, Toussaint R, Schmittbuhl J, Måløy KJ. Growth activity during fingering in a porous Hele-Shaw cell. *Phys Rev E* (2004) **70**:026301. doi: 10.1103/PhysRevE.70.026301
32. Toussaint R, Løvoll G, Méheust Y, Måløy KJ, Schmittbuhl J. Influence of pore-scale disorder on viscous fingering during drainage. *Europhys Lett.* (2005) **71**:583–9. doi: 10.1209/epl/i2005-10136-9
33. Stauffer F, Kong XZ, Kinzelbach W. A stochastic model for air injection into saturated porous media. *Adv Water Resour.* (2009) **32**:1180–6. doi: 10.1016/j.advwatres.2009.03.010
34. Løvoll G, Jankov M, Måløy KJ, Toussaint R, Schmittbuhl J, Schäfer G, et al. Influence of viscous fingering on dynamic saturation-pressure curves in porous media. *Transp Porous Med.* (2010) **86**:305–24. doi: 10.1007/s11242-010-9622-8
35. Fiori A, Jankovic I. On preferential flow, channeling and connectivity in heterogeneous porous formations. *Math Geosci.* (2012) **44**:133–45. doi: 10.1007/s11004-011-9365-2
36. Geistlinger H, Krauss G, Lazik D, Luckner L. Direct gas injection into saturated glass beads: transition from incoherent to coherent gas flow pattern. *Water Resour Res.* (2006) **42**:W07403. doi: 10.1029/2005WR004451
37. Kong XZ, Kinzelbach W, Stauffer F. Migration of air channels: an instability of air flow in mobile saturated porous media. *Chem Eng Sci.* (2009) **64**:1528–35. doi: 10.1016/j.ces.2008.12.028
38. Kong XZ, Kinzelbach W, Stauffer F. Morphodynamics during air injection into water-saturated movable spherical granulates . *Chem Eng Sci.* (2010) **65**:4652–60. doi: 10.1016/j.ces.2010.05.007
39. Sandnes B, Flekkoøy EG, Knudsen HA, Måløy KJ, See H. Patterns and flow in frictional fluid dynamics. *Nat Commun.* (2011) **2**:288. doi: 10.1038/ncomms1289
40. Chevalier C, Lindner A, Leroux M, Clément E. Morphodynamics during air injection into a confined granular suspension. *J Non-Newtonian Fluid Mech.* (2009) **158**:63–72. doi: 10.1016/j.jnnfm.2008.07.007
41. Johnsen Ø, Chevalier C, Lindner A, Toussaint R, Clément E, Måløy KJ, et al. Decompaction and fluidization of a saturated and confined granular medium by injection of a viscous liquid or gas. *Phys Rev E* (2008) **78**:051302. doi: 10.1103/PhysRevE.78.051302
42. Varas G, Vidal V, Géminard JC. Venting dynamics of an immersed granular layer. *Phys Rev E* (2011a) **83**:011302. doi: 10.1103/PhysRevE.83.011302
43. Varas G, Vidal V, Géminard JC. Morphology of air invasion in an immersed granular layer. *Phys Rev E* (2011b) **83**:061302. doi: 10.1103/PhysRevE.83.061302
44. Varas G, Géminard JC, Vidal V. Air invasion in a granular layer immersed in a fluid: morphology and dynamics. *Granular Matter* (2013) **15**:801–10. doi: 10.1007/s10035-013-0435-7
45. Varas G, Vidal V, Géminard JC. Dynamics of crater formations in immersed granular material. *Phys Rev E* (2009) **79**:021301. doi: 10.1103/PhysRevE.79.021301
46. Ji W, Dahmani A, Ahlfeld DP, Lin JD, Hill E. Laboratory study of air sparging: air flow visualization. *Ground Water Monit Rem.* (1993) **13**:115–26. doi: 10.1111/j.1745-6592.1993.tb00455.x
47. Philippe P, Badiane M. Localized fluidization in a granular medium. *Phys Rev E* (2013) **87**:042206. doi: 10.1103/PhysRevE.87.042206
48. Brooks MC, Wise WR, Annable MD. Fundamental changes in *in-situ* air sparging flow patterns. *Ground Water Monit Rem.* (1999) **19**:105–13. doi: 10.1111/j.1745-6592.1999.tb00211.x
49. Gostiaux L, Gayvallet H, Géminard JC. Dynamics of a gas bubble rising through a thin immersed layer of granular material: an experimental study. *Granular Matter* (2002) **4**:39–44. doi: 10.1007/s10035-002-0105-7
50. Divoux T, Bertin E, Vidal V, Géminard JC. Intermittent outgassing through a non-Newtonian fluid. *Phys Rev E* (2009) **79**:056204. doi: 10.1103/PhysRevE.79.056204
51. Divoux T, Vidal V, Ripepe M, Géminard JC. Influence of non-Newtonien rheology on magma degassing. *Geophys Res Lett.* (2011) **38**:L12301. doi: 10.1029/2011GL047789
52. Vidal V, Soubiran F, Divoux T, Géminard JC. Degassing cascades in a shear-thinning viscoelastic fluid. *Phys Rev E* (2011) **84**:066302. doi: 10.1103/PhysRevE.84.066302
53. ASTM. *Annual Book of ASTM Standards, Section 4 Construction, Vol. 04.08 Soil and Rock; Dimension Stone; Geosynthetics.* Philadelphia: ASTM (1993).
54. Chatzis I, Morrow NR, Lim HT. Magnitude and detailed structure of residual oil saturation. *Soc Petrol Eng J.* (1983) **23**:311–26. doi: 10.2118/10681-PA
55. Holtzman R, Juanes R. Crossover from fingering to fracturing in deformable disordered media. *Phys Rev E* (2010) **82**:046305. doi: 10.1103/PhysRevE.82.046305
56. Holtzman R, Szulczewski ML, Juanes R. Capillary fracturing in granular media. *Phys Rev Lett.* (2012) **108**:264504. doi: 10.1103/PhysRevLett.108.264504

Conflict of Interest Statement: The authors declare that the research was conducted in the absence of any commercial or financial relationships that could be construed as a potential conflict of interest.

frontiers in Physics

ORIGINAL RESEARCH
published: 16 February 2016
doi: 10.3389/fphy.2016.00004

Compaction of North-Sea Chalk by Pore-Failure and Pressure Solution in a Producing Reservoir

*Daniel Keszthelyi *, Dag K. Dysthe and Bjørn Jamtveit*

Physics of Geological Processes, University of Oslo, Oslo, Norway

The Ekofisk field, Norwegian North sea, is an example of a compacting chalk reservoir with considerable subsequent seafloor subsidence due to petroleum production. Previously, a number of models were created to predict the compaction using different phenomenological approaches. Here we present a different approach which includes a new creep model based on microscopic mechanisms with no fitting parameters to predict the strain rate at reservoir scale. The model is able to reproduce the magnitude of the observed subsidence making it the first microstructural model which can explain the Ekofisk compaction.

Keywords: compaction, creep, crack growth, pressure solution, subsidence, carbonates, Ekofisk

OPEN ACCESS

Edited by:
Renaud Toussaint, University of Strasbourg, France

Reviewed by:
Einat Aharonov, Hebrew University of Jerusalem, Israel
Marcus Ebner, OMV, Austria

****Correspondence:***
Daniel Keszthelyi
daniel.keszthelyi@fys.uio.no

Specialty section:
This article was submitted to Interdisciplinary Physics, a section of the journal Frontiers in Physics

Received: *30 April 2015*
Accepted: *29 January 2016*
Published: *16 February 2016*

Citation:
Keszthelyi D, Dysthe DK and Jamtveit B (2016) Compaction of North-Sea Chalk by Pore-Failure and Pressure Solution in a Producing Reservoir. Front. Phys. 4:4. doi: 10.3389/fphy.2016.00004

1. INTRODUCTION

The Ekofisk field is one of the largest petroleum fields in the Norwegian North Sea and the largest where oil is produced from chalk formations (map on **Figure 1**). The early stages of oil production caused considerable changes in pore fluid pressure [1] which led to a reservoir compaction. This was first identified in 1984 when subsidence of the overlying seafloor was discovered [2]. The extent of the subsidence was still smaller than the volume of produced petroleum but considerably larger than expected by elastic models developed by Geertsma [3] and Segall [4] using reasonable elastic parameters ([5], **Figure 1**, Data Sheet 1 in Supplementary Material). The reservoir compaction was initially ascribed to pore collapse due to the dramatic increase in effective stress associated with hydrocarbon production and fluid pressure reduction [6, 7], however the exact mechanism was not investigated.

After the identification of the subsidence, a new production scheme started by waterflooding the reservoir and thus increasing the pore pressure and decreasing the effective stress inside the reservoir. However, the subsidence continued even after the new production scheme was introduced and pore pressure was raised to the initial values. Currently, the total subsidence observed since the beginning of oil production at the Ekofisk field is 9 m at the center of the field [8]. The high value of subsidence made it necessary to raise the platform and storage facilities above the subsiding bowl [9].

Several compaction models were created in an attempt to predict reservoir compaction and seafloor subsidence (e.g., [6, 10–12]). These apply a number of different phenomenological approaches to model the compaction of chalk based on macroscopic continuum equation models where parameters are fitted to experiments and observations. The first models explained the compaction as being elastic until the porous chalk riches a critical stress when sudden pore collapse happens resulting in a considerable plastic strain. Later models (e.g., [10]) included the idea that shear failure due to the build-up of differential stresses is responsible for the compaction. Inspired by these ideas several constitutive models for chalk were created most of which included

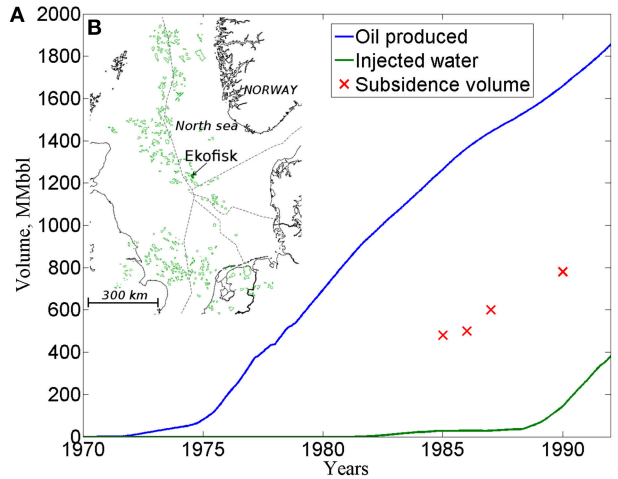

FIGURE 1 | (A) Comparison of produced and injected volume with estimated subsidence volume during the production and **(B)** the map of Norwegian Sea with petroleum fields showing the location of Ekofisk field.

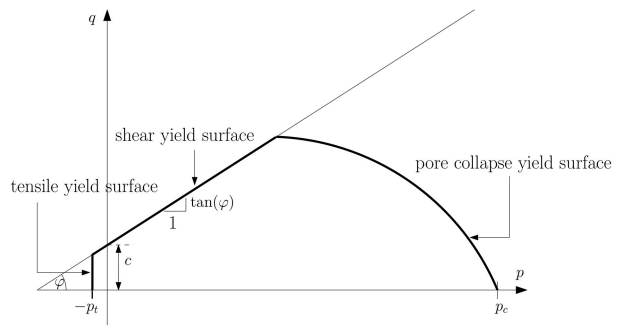

FIGURE 2 | A generalization of the constitutive models yield surfaces in p-q stress invariant plane: tensile, shear failure, and pore collapse mechanism have their distinct yield surfaces, the resulting surface is a closed union of these surfaces. The tensile yield surface is characterized by p_t critical tensile strength, the shear surface by φ friction angle and c cohesion and the pore collapse surface by p_C critical stress and the shape of the ellipse. Some models introduce smooth changes close to the intersections while the model of Papamichos et al. [13] creates a similar shape yield surface by formulating their model as one mechanism.

2–3 failure/yield mechanisms which they represented as separate failure surfaces intersecting each other. A generalized concept of the yield/failure surfaces is shown on **Figure 2**. With the introduction of water injection scheme the attention shifted toward the effect of water and how it decreases the material strength of chalk. This phenomenon is often referred as "water weakening" of chalk and several models were created to explain it (e.g., [14, 15]). A more detailed review of the previous models can be seen in Data Sheet 1 in Supplementary Material.

Here we present a different approach, based on microscopic mechanisms with no fitting parameters using a universal creep model which combines microscopic fracturing and pressure solution where the local fracture stress is related to pore size, and then use a statistical mechanical approach to scale it up and predict strain rate at reservoir scale. We apply the model to field data and find that it reproduces the observed magnitude of seafloor subsidence. An advatage of this model over previous models is that it follows a bottom-up physics-based approach and therefore it provides a thorough insight into the underlying physical phenomena giving a higher predictive value.

2. THE EKOFISK RESERVOIR

The Ekofisk field is an elongated anticlinal structure in the Southern part of the Norwegian North Sea with an aerial extent of about 6.8 by 9.3 km. The thickness of the overlying sediments is 2840 m in the central part of the field and increases toward the flanks [16]. Oil is produced from Ekofisk and the deeper Tor formation which are separated by a typically 15 m thick low porosity chalk layer, the so-called Ekofisk Tight Zone. The thickness of the Ekofisk formation varies between 100 and 150 m, while the thickness of the Tor formation varies between 75 and 150 m.

The reservoir rocks are high-porosity fine-grade chalk, a limestone composed of coccolith fragments, the skeletal debris of unicellar algae (Coccolithophorids). The reservoir rock's porosity ranges between 30 and 48%, while the Ekofisk Tight Zone has porosity between 10 and 20%. Even the high porosity chalk has relatively low matrix permeability (i.e., the permeability of the matrix itself) between 1 and 5 mD ($1 - 5 \cdot 10^{-15}$ m^2). Natural fractures give a high fracture permeability (i.e., the permeability caused by the macroscopic fractures) resulting in total chalk permeability between 10^{-13} and 10^{-14} m^2 (10 − 100 mD) [16].

The overburden is mainly composed of clays and shales with thin interlayered limestone or silty layers [11, 14]. The permeability is extremely low (10^{-18} – 10^{-21} m^2, 10^{-3} – 10^{-6} mD) [16]. These rocks have a very low cohesional strength which makes them difficult to sample and therefore there is sparse and uncertain data about their rock properties [17].

In the early stage of oil production, pore fluid pressure dropped and the reservoir compacted, leading to a seafloor subsidence of up to 0.4 m per year which corresponds to a mean strain rate of $5 \cdot 10^{-11}$ $\frac{\text{m}}{\text{s}}$. Later a new reservoir management program was introduced maintaining pore pressure [18], however compaction and sea-floor subsidence continued.

3. MODELING THE SUBSIDENCE

In this paper we predict subsidence history for the production phase before water injection using a very simple creep model (detailed in Keszthelyi et al. [19]). This model has the following simplifying assumptions:

- Prior to production, the reservoir rock is a non-reactive, elastic solid with a collection of pores with a probability distribution, $p(r)$ of pore radii r.
- The reservoir rock is subject to confining stress σ of overlying sediments and a pore fluid pressure, P. All deformations are controlled by the effective stress $\sigma_e = \sigma - P$.

- When the effective stress exceeds a threshold, microscopic fractures will start to propagate from all pores with radius larger than a threshold value r_{max}. This threshold is defined by linear elastic fracture mechanics: $r_{max} = \gamma E/\sigma_e^2$ where E is the Young's modulus of the rock and γ is the interfacial energy of the rock-pore fluid surface [20].
- The number of fractures created is proportional to the number of pores involved in the fracturing process. The fracture density ρ_f describes the abundance of the microscopic fractures and has the unit m/s. We calculate this by statistical means from pore size distribution $p(r)$ and initial porosity Φ_0.
- Fracturing is instantaneous and we neglect the strain in the solid due to the formation of these fractures and the poroelastic response of the rock.
- The new microscopic fractures are reactive sites where pressure solution takes place if there is water present. The fraction of water-wet fractures equals the water saturation S_w of the rock.
- The rate $\dot{\xi}$ of pressure solution at each reaction sites (expressed in m/s) can be calculated by any pressure solution model independently from any other part of thee creep model. In this article we compared two approaches: a theoretical approach presented in Zhang et al. [21] and Pluymakers and Spiers [22] where pressure solution rate is a function of initial porosity Φ_0, temperature T and effective stress σ_e. In the other approach pressure solution rate is calculated from long-term strain rates measured in creep experiments.

The equations of the compaction model are presented in Data Sheet 1 in Supplementary Material.

The change in rock volume $V = V_p + V_s$, where V_s is the solid volume and V_p the pore volume, with time t, is expressed by the volumetric strain rate:

$$\dot{\varepsilon}_v(t) = \frac{1}{V}\frac{\partial V}{\partial t} = S_w \cdot \rho_f \left(\sigma_e, p(r)\right) \dot{\xi}\left(\sigma_e, \Phi_0, T\right). \quad (1)$$

The input parameters of the creep model are: effective stress σ_e, initial porosity Φ_0, pore size distribution $p(r)$, temperature T and water saturation S_w. Except for the effective stress we use constants obtained from literature (see **Table 1**). For pore size distribution $p(r)$ we use a Weibull-type distribution with a shape parameter 1.5 and mean pore size of $r_{mean} = 2.2\,\mu$m as found in Japsen et al. [20]. Effective stress is calculated using the relation

$$\sigma_e = \sigma - P. \quad (2)$$

This is a much simpler definition for effective stress than used in some previous chalk compaction papers. In the following subsections we show that choosing this relation introduces only a small error in the result while the model is kept simple and physical. Then we present simple calculations to illustrate why the reservoir pressure P can be considered quasi equal to the pressure inside the boreholes. We then present a method used to calculate borehole pressures from production data and oil properties. Finally, we discuss how to calculate the other variable in the effective stress law: the confining stress σ.

TABLE 1 | Reservoir parameters used to calculate the subsidence history.

Initial porosity, Φ_0	Sulak and Danielsen [16]	37.5%
Reservoir temperature, T	Sulak and Danielsen [16]	150 °C
Water saturation, S_w	Sulak and Danielsen [16]	4.5%
Mean pore size, r_{mean}	Japsen et al. [20]	2.2 μm

3.1. Effective Stress Law

According to Coussy [23] effective stress definitions can be summerized in the following two equations assuming that deformations can be decomposed into a plastic and an elastic component:

$$\sigma'_{ij,e} = \sigma_{ij} - \alpha P\delta_{ij} \text{ and } \sigma'_{ij,p} = \sigma_{ij} - \beta_p P\delta_{ij}, \quad (3)$$

where $\sigma'_{ij,e}$ denotes the element of the effective elastic stress tensor which is the driving stress for elastic strains, while $\sigma'_{ij,p}$ is the element of the plastic stress tensor: the driving stress for plastic strains [23]. σ_{ij} is the element of the confining stress tensor, δ_{ij} is the Kronecker-delta function, P is the pore pressure, α is the Biot-coefficient and β_p is a plastic compressibility parameter.

The two constants (α and β_p) in the equations can vary between 0 and 1 and they describe how strain is distributed in the porous media between the solid matrix and the pore volume. $\alpha = 1$ means an elastically incompressible matrix and 0 corresponds to the case when the pore volume is incompressible and all the elastic strains originate from the elastic deformation of the matrix. Similarly, $\beta_p = 1$ means a plastically incompressible matrix and 0 corresponds to an incompressible pore volume and all plastic stains originating from the plastic deformation of the matrix.

There have been several studies on the determination of the Biot-coefficient of chalk. While some of them claim a coefficient as low as 0.7–0.8 [24, 25], other experiments indicated a Biot-coefficient of 1 [26]. Hickman [5] showed considerably smaller bulk modulus (1–3 GPa) for chalk samples in the Ekofisk porosity range than the 70 GPa bulk modulus of calcite [27]. This implies a Biot-coefficient close to 1. Vajdova et al. [28] found experimentally that some plastic deformation (e.g., twinning) of calcite occurs in deforming limestones, however microcracking is the dominant deformation mechanism which implying a plastic compressibility parameter close to 1.

As the determination of the exact Biot-coefficient and compressibility parameter is beyond the scope of this article we assume that both are 1.

$$\alpha = 1 \quad \text{and} \quad \beta_p = 1 \quad (4)$$

Furthermore, we assume that compaction is conrolled by the compressive stress:

$$\sigma = \frac{1}{3}\sum_i \sigma_{ii}. \quad (5)$$

With these assumptions we can apply the simplified definition of the effective stress:

$$\sigma_e(t) := \sigma' = \sigma - P(t). \quad (6)$$

TABLE 2 | Material and reservoir parameters (approximate values) for the estimation of pressure propagation characteristics.

Matrix permeability (Sulak and Danielsen [16])	k_m	$1-5$ mD
Total permeability (Sulak and Danielsen [16])	k	100 mD
Compressibility of reservoir fluid (Mackay [30])	β	$10^{-10}\,m^2N^{-1}$
Viscosity of reservoir fluid (Mackay [30])	μ	10 cP
Porosity (Sulak and Danielsen [16])	Φ	35%
Pressure dependence of porosity	$\frac{\partial\Phi}{\partial P}$	0

3.2. Pressure Propagation

Oil is produced from the reservoir layer through boreholes penetrating the layer. Inside the boreholes they introduce a lower pressure than in the surrounding reservoir layer to facilitate the flow of pore fluids toward the well. To characterize the pressure changes inside the reservoir layer away from boreholes we treat the problem as the boreholes were uniformly distributed and calculate the fluid density function $\rho(r, t)$ around a single well at a horizontal distance r from the borehole at time t after the pressure change inside the well took place.

The reservoir layer is treated as an axisymmetric layer with a finite thickness and with relatively high permeability compared to the surrounding (i.e., no fluid flow into or out from the layer). Its horizontal dimensions exceed the diameter of the reservoir field, the outer part is filled with water.

For the calculations we follow Muskat [29]'s approach based on the following two equations:

$$\text{Continuity equation} \quad div(\Phi\rho\vec{v}) = -\frac{\partial(\Phi\rho)}{\partial t} \tag{7}$$

$$\text{Darcy-law} \quad \Phi\vec{v} = -\frac{k}{\mu}\nabla P \tag{8}$$

where Φ is the porosity, k is the permeability of the rock, μ is the dynamic viscosity of the fluid, ρ denotes the fluid density and $\vec{v}$ is the Darcy speed.

Furthermore, we assume that the reservoir fluid is compressible and it has the pressure-density relation $\rho = \rho_0 \cdot exp(\beta P)$ where β is the compressibility of the fluid and ρ_0 is a reference density at $P = 0$ pressure. By assuming that the initial fluid pressure was p_0 throughout the reservoir, and that there exists an outer boundary at distance r_2 where the fluid pressure remains constant and a borehole radius r_w inside which the pressure equals to well pressure p_w we obtain:

$$\rho(r,t) = \rho_{stationary} + \rho_{scaling} \cdot e^{-\kappa\alpha_n^2 t}$$
$$\text{where} \quad \kappa = \frac{\mu\Phi}{k}\left(\beta + \frac{1}{\Phi}\frac{\partial\Phi}{\partial P}\right) \tag{9}$$

and α_n is a constant depending on the boundary conditions. For details see Data Sheet 1 in Supplementary Material.

We perform calculations with material parameters relevant to the Ekofisk field (see **Table 2**) with a range of borehole radii r_w and reservoir outer boundary values r_2 (**Figure 3**) to estimate the half-time of the pressure propagation: the time required for that the amplitude of the pressure change become the half of the difference between the initial and the steady-state solution after pressure perturbation was introduces inside the borehole. We consider borehole radius r_w as unknown since this radius corresponds to an extremely highly fractured region around the physical borehole. **Figure 3B** shows that pressure propagation half times are in the order of minutes or hours in most of the cases. Therefore, we assume that the pressure respond instantaneously following the pressure changes in the boreholes.

Based on this we calculated the pressure evolution during time from production data. The calculation assumes that the ratio between the produced gas and liquid phases at the surface depends on the gas and liquid fraction in the reservoir which is a function of the pressure inside the reservoir.

The stationary solution of the pressure propagation problem around a well is a conical pressure depression around the well where the center of the cone is the borehole where pressure is decreased. However, in the Ekofisk field hydrocarbons are produced from numerous wells penetrating into the reservoir and pressure is decreased in all of these wells. By 1980 forty wells were already producing from the reservoir. Given that the extent of the field is ∼9 by 4 km, this implies that boreholes are placed closer than 1 km to each other. Hence the pressure depression cones are overlapping and the pressure changes inside the reservoir between two boreholes are small. Therefore, if we neglect the permeability inhomogeneites in the reservoir on the large scale we can assume a constant pressure throughout the reservoir as in [16, 17].

3.3. Calculating Reservoir Pressure from Production Data

To estimate how our model performs in terms of predicting the subsidence during the years of production, historical reservoir pressure data were needed. We use publicly available production and crude oil property data to make an estimae of the reservoir pressure history. We use the widely accepted concept of reservoir engineering (e.g., [31]) that the fraction of hydrocarbon in the liquid and gas state depends on the current pressure: at high pressure light components tend to dissolve in the liquid phase implying that above a certain threshold pressure (called bubble point) all hydrocarbons are in liquid phase.

Initially, when the reservoir was highly pressurized all hydrocarbons were in liquid phase. As pore pressure was decreased the reservoir became more saturated until it reached its bubble point (5990 psi, 41.3 MPa) in 1976 [1]. Thereafter two phases were present in the reservoir and the concentration of dissolved gas decreased while pressure declined. This resulted in a relative increase in the volume of gaseous phase both due to the liberation of natural gas from the liquid phase and to the relatively higher volume increase of the gaseous phase during decompression.

The increasing amount of gas inside the reservoir was clearly reflected in production data. Initially, before reaching the bubble point, the ratio of produced gas and oil—commonly referred as GOR, gas-oil-ratio—was constant and reflected the amount of gas deliberated from the fluid phase as the hydrocarbons were exposed to surface pressure. However, as pressure declined below the bubble point, gas bubbles appeared in the liquid phase

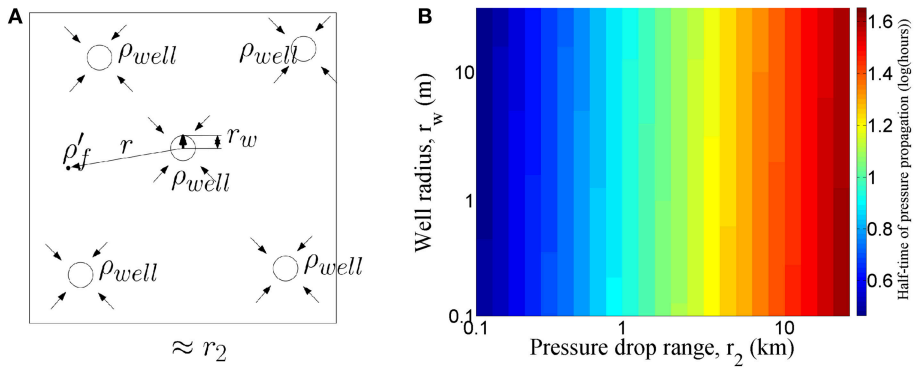

FIGURE 3 | (A) Model of pressure propagation characteristic time calculations. We are interested in the pressure changes around a well: at any point with a distance r from the borehole. As fluid is moving toward the well pressure decreases in the reservoir. For the calculations our assumptions was that there exist a finite radius inside which pressure and thus fluid density (ρ_{well}) is constant—the well radius r_w—and an outer finite radius r_2 outside which pressure is constant and equals to the initial pressure. **(B)** Half-time of pressure propagation: the time necessary to experience 50% of pressure change—defined as the integral of the pressure change along the whole field—from the initial to the final pressure profile.

and therefore the produced hydrocarbon contained considerably larger amount of gas which now were partly due to degassing from the liquid phase and partly due to the expansion of the gas bubbles originally present in the reservoir when they became exposed to surface conditions (see **Figure 4**).

Knowing the amount of dissolved and free gas at different pressure and the relative volume of the phases at different pressure [32] it is possible to inversely calculate the pressure history from published GOR history data ([33], see **Figure 5**). We also account for the effect of injected gas volume assuming that due to the fact that reservoir fluid is already saturated it will mainly increase the free gas volume after compression. The calculated pressures can be seen on **Figure 6**.

3.4. Overburden Behavior

A schematic view of the Ekofisk reservoir during production can be seen in **Figure 7**. The majority of reservoir scale simulations treat overburden as a linear elastic material which is fully coupled to the reservoir and therefore follows its subsidence.

However, it has been pointed out that the overburden has a certain rigidity compared to the reservoir [7, 16]. Hamilton et al. [36] suggested that fractures formed inside the overburden as a consequence of stress field change and they supported the idea with the argument that the overburden has a high smectite content which facilitate fracturing.

The existence and nature of fractures inside the overburden are not yet completely understood. Observations show that casing deformations inside the overburden are most pronounced inside those wells which have a horizontal position between the central and the peripheral part of the reservoir [17, 37]. This implies that a fracture network is present inside the overburden and the location of the fractures coincide with the sites where stress is maximal due to arching effect. To better understand the overburden behavior future work is necessary.

For simplicity, we assume that the overburden is completely soft and follows the motion of the compacting reservoir layer and we neglect the effect of shear. Therefore, the subsidence rate, $\dot{s}(t)$ of the field can be estimated as the product of the strain rate $\dot{\varepsilon}_v$ corresponding to the reservoir pressure $P(t)$ and the thickness of the reservoir h:

$$\dot{s}(t) = \dot{\varepsilon}_v\left(P(t)\right) \cdot h. \tag{10}$$

4. RESULTS

The model of Keszthelyi et al. [19] can be used to predict compaction and subsidence if the pore size distribution and the average porosity is known. However, the pore size distribution is somewhat uncertain. In the following we assume a Weibull distribution ([38], see subfigure in **Figure 8**) with 2.2 μm as mean pore size [20] that was fitted to SEM image data of chalk from wells in the same formation. We calculate microscopic fracture density as a function of effective stress (see **Figure 8**) with these input parameters. It can be seen that at lower effective stresses the fracture density is virtually zero. It rises very rapidly in a very narrow effective stress range and it flattens out at higher effective stress to an asymptotic value around 10^5 m^{-1}.

Due to the uncertainty of the pore size distribution data we calculate fracture densities for a range of mean pore sizes relevant to the Ekofisk field, while preserving the shape of the pore size distribution. We plotted the fracture density as a function of two variables: effective stress σ_e and mean pore size r_{mean} (see **Figure 9**). It can be seen that fracture density varies in a relatively narrow band of effective stress values, however, the interval where this band is exactly located is a non-linear function of the mean pore size: for smaller pores only larger stress produce fracturing, while for larger pores require smaller stresses can produce fracturing.

We also calculate the resulting strain rate in the same range of the variables by using both approaches for the pressure solution rate calculation (theoretical model: **Figure 10** and long-term model: **Figure 11**). Initial (pre-production) and maximal

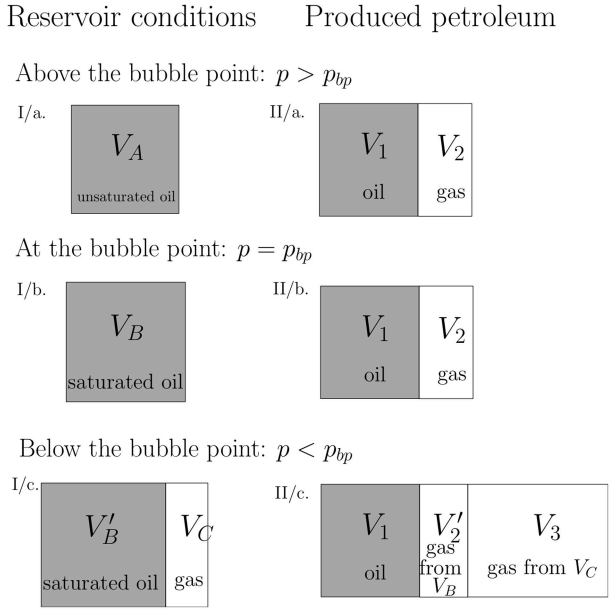

FIGURE 4 | Volumes and phase changes of hydrocarbons inside the reservoir and during production as reservoir pressure is changed corresponding to same volume V_1 of oil produced at the surface. **(I/a.)** Initially there is a V_A volume unsaturated oil. **(I/b.)** As pressure is decreased to the bubble point oil becomes saturated and meanwhile there is a small expansion of its volume to V_B. **(I/c.)** As pressure is further decreased a free gas phase will form with V_C volume which largely depends on the reservoir pressure. Meanwhile the saturated oil phase also expands to V'_B volume. The right side of the figure shows the composition of the produced petroleum: all volumes are relative to the amount of oil produced and for simplicity it is V_1 in all cases. **(II/a,b.)** At the bubble point pressure and above it the gas phase with V_2 volume is formed by the degassing due to pressure drop from reservoir to surface conditions. Note that the gas-oil ratio is the same in both cases since the degasing starts only at the bubble point pressure. **(II/c.)** If pressure is decreased below the bubble point the produced gas is partly due to degasing (V'_2) and partly to the free gas phase occupying a portion of the reservoir (V_C). V'_2 is slightly smaller than V_2 since V'_B contains slightly less dissolved gas than V_B, however $V_3 + V'_2 \gg V_2$. Note that the exact production volumes depend largely on reservoir pressure, larger reservoir pressures allow larger amount of petroleum to be produced, so in reality much less amount of oil is produced when pressure is lower. However, the dependence of produced petroleum to the reservoir pressure is controlled by the production technic, therefore, it is not show on this figure.

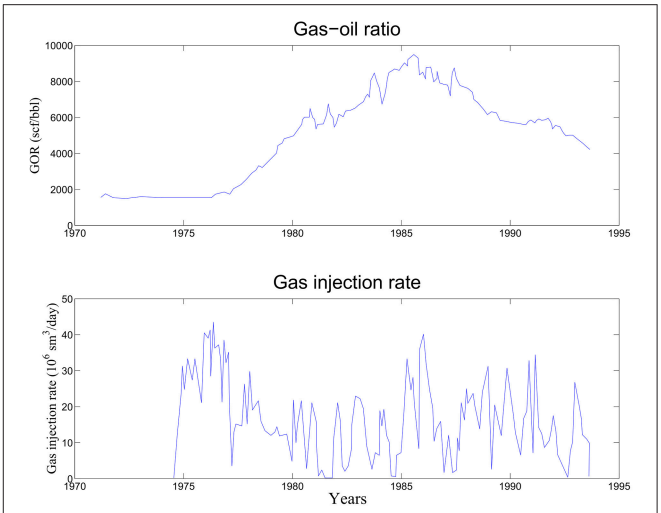

FIGURE 5 | Gas injection rates and gas-oil ratio during the first period of production at the Ekofisk field. Source of data: Jakobsson et al. [33]. 1 ft^3/barrel oil = 0.1781 sm^3/sm^3 oil. sm^3: m^3 at surface conditions.

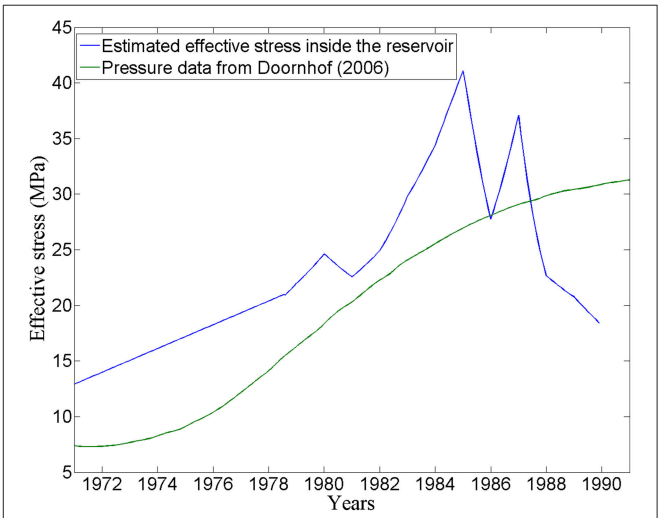

FIGURE 6 | Estimated reservoir pressure during the years of production. The estimation was constrained by some data from Rhett [12] and Mes et al. [34]. Pressure history data presented in Doornhof et al. [35] are also plotted. SI units are used, 1 MPa = 145 psi.

effective stress values are marked with horizontal lines and strain rates corresponding to the initial and maximal effective stress using 2.2 μm mean pore size value are also marked. An isoline at a strain rate of 10^{-11} s^{-1} corresponding to the average measured strain rate is also shown. In the theoretical model the dissolution rate depends on effective stress while in the long-term model dissolution rate remains constant and fracture density has the only pressure dependence.

In both cases, the initial effective stress corresponds to a negligible amount of compaction, while at maximum effective values we get realistic predicted strain rates, the average measured strain rate is between the initial and maximal values.

In order to compare model prediction with field data we calculate the subsidence rate and resulting subsidence for a 20 year long period (see **Figures 12**, **13**) using the estimated pressure history data calculated from the produced amount of hydrocarbons (see **Figure 6** and Section 3.3 for the principles of the calculation) and estimated pressure history curve from Doornhof et al. [35]. These calculations show that the theoretical model gives subsidence comparable to field observations, and by using the estimates from production curves the model prediction agrees very well with field observations, while the model based on the long-term compaction experiments somewhat underestimates the compaction, though it gives significantly better estimates than the poroelastic model of Segall [4].

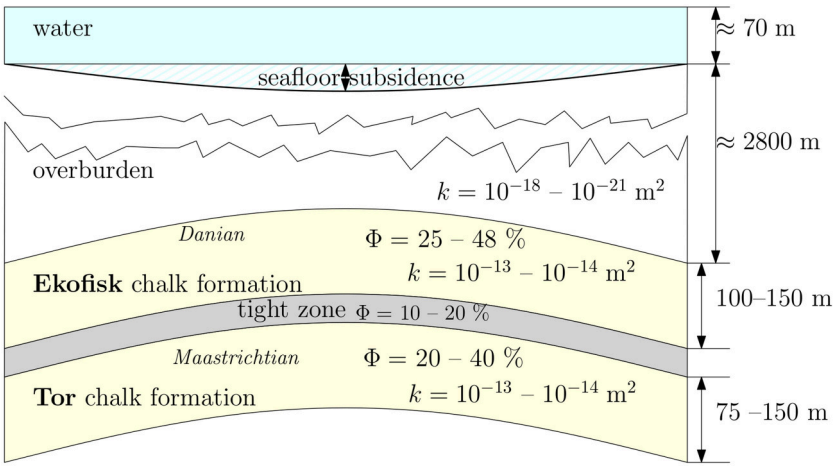

FIGURE 7 | Schematic view of the produced Ekofisk field showing the layering of the chalk reservoir, the thick overburden, and the shallow layer of seawater. The most important material parameters (k: permeability and Φ porosity) are shown on the figure. SI units are used, $9.87 \cdot 10^{-10}$ m^2 = 1 mD.

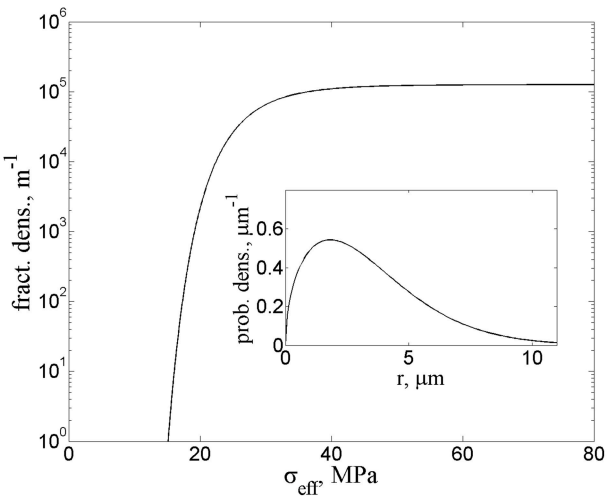

FIGURE 8 | Fracture density as function of effective stress if Weibull-type distribution and 2.2 μm average pore diameter is assumed. The pore size distribution's density function is shown in the inset. It is defined by the equation $p(r) = 1.5\lambda^{-1}\sqrt{r/\lambda} \cdot e^{-(r/\lambda)^{1.5}}$ where the shape factor $\lambda = 1.5$. SI units are used, 1 MPa = 145 psi.

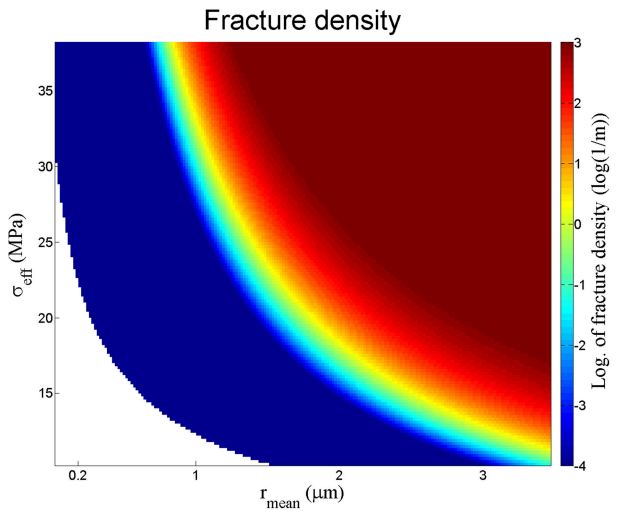

FIGURE 9 | Fracture density as a function of effective stress and mean pore diameter assuming a Weibull distribution (similar to Figure 8). The figure is color-coded representing the magnitude—logarithm—of the fracture density. SI units are used, 1 MPa = 145 psi.

5. CONCLUDING REMARKS

We were able to apply a micromechanical model of carbonate compaction which combines microscopic fracturing (pore failure) with creep (pressure solution) using upscaling to reservoir scale through the concept of fracture density. This model predicted surprisingly well the observed compaction and subsidence making it the first microstructural model which can explain the Ekofisk subsidence. The model contains a very small number of internal parameters: Young's modulus of chalk, the water-wet interfacial energy of calcite and reaction constants describing the dissolution-precipitation kinetics and diffusion of calcite all of which can be meausured with simple physical experiments independently. The input parameters are pore size distribution, water saturation, porosity and pressure history. Furthermore, the model is based on physical assumptions, eliminating the need of unphysical fitting parameters. We believe this results in a higher predictive power than previously used models with a large number of fine-tuned parameters.

The discrepancy between the model prediction and field observations is due to the uncertainty of input parameters and the simplifying assumptions during the application or inside the model.

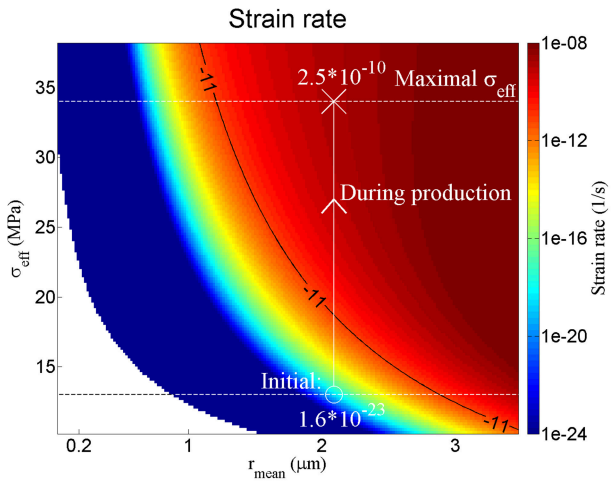

FIGURE 10 | Strain rate calculated assuming a Weibull distribution of pore size, using a range of mean pore size and effective stress values and dissolution rates calculated from the theoretical model. A line representing the modeled mean pore size for Ekofisk chalk (following Japsen et al. [20]) and average strain rate for this period is also plotted on the figure. The contour line crosses the line corresponding to Ekofisk chalk. SI units are used, 1 MPa = 145 psi.

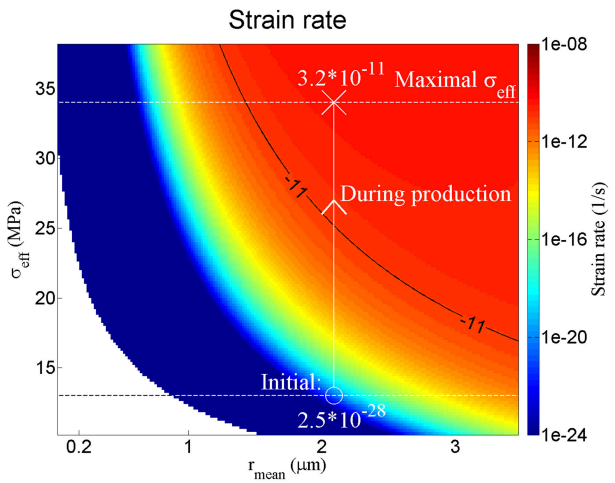

FIGURE 11 | Long-term strain rate calculated assuming a Weibull distribution of pore size, using a range of mean pore size and effective stress values and dissolution rates calculated from the long-term strain rates of Zhang et al. [21] experiments. A line representing the modeled mean pore size for Ekofisk chalk (following Japsen et al. [20]) and average strain rate for this period is also plotted on the figure. The contour line crosses the line corresponding to Ekofisk chalk. SI units are used, 1 MPa = 145 psi.

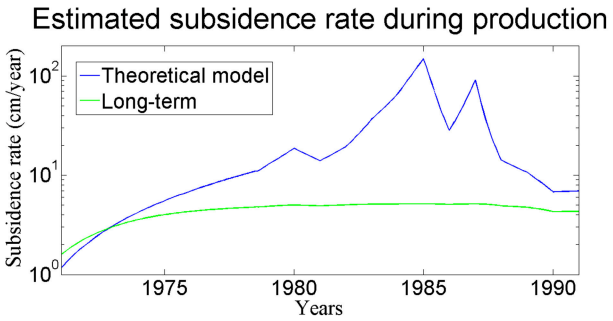

FIGURE 12 | Estimated subsidence rate according to the model using reservoir pressure history estimations (see Section 3.3). The resulting subsidence rate are similar to the observed rates.

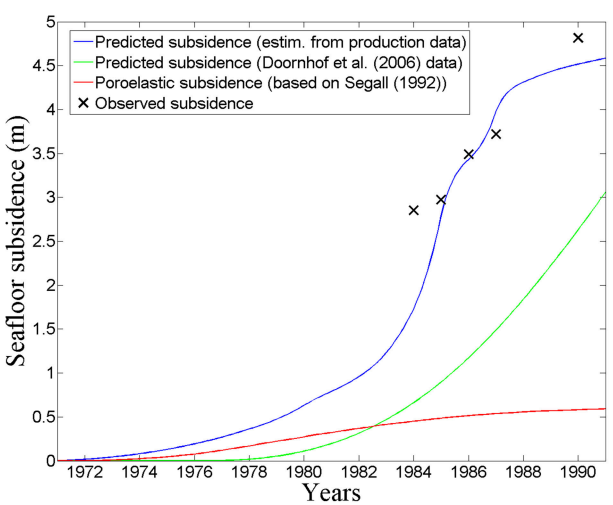

FIGURE 13 | Estimated subsidence during the first period of the production. Estimation based on pressure history calculations in Section 3.3 and on data from Doornhof et al. [35]. Predictions of the poroelastic model of Segall [4] is also plotted.

The model is very sensitive to the pore size distribution. Application of this model depends on reliable data for the actual situation to estimate the pore size distribution. Pore size distribution data can be obtained by accurate measurements: currently the most accurate being X-ray microtomography data, although only a few measurements exist currently. Mercury injection data are considerably more common and can be used as a less reliable source of pore size distribution measurements since it does not measure pore size distribution directly but pore throat distribution.

A previous study [20] found that the Weibull distribution fit observations reasonably well for chalk samples from wells close to the Ekofisk field. There have been several other measurements on chalks from different origin: Hellmann et al. [39] measured pore size distribution by mercury-injection on chalk samples from Paris basin and found a sigmoid-type cummulative pore size distribution with some larger pores in addition. Price et al. [40] investigated chalk samples from the Upper Chalk formation and found also a sigmoid-type cummulative pore size distribution function, however the mean pore size differs from that of Japsen et al. [20]. Being the closest analogue to the Ekofisk field we used Weibull distribution presented in Japsen et al. [20].

Investigating the effect of water saturation can presumably help to address the question of ongoing subsidence during

production with water injection when the pore pressure was increased to the original values. As water is pumped in and water saturation increases inside the reservoir the newly entering water can also flow into the initially oil-filled recent microscopic fractures triggering pressure solution there. This may cause the reservoir to compact after the start of injection, but to settle down as water saturation levels to equilibrium. The model also shows that there is a large potential of further subsidence if water saturations increase in the reservoir and thus it can serve as an explanation for "water weakening" effect of chalk.

Inhomogeneities inside the reservoir are present in every scale. Apart from the variability of material parameters (porosity, pore size distribution, and water saturation) a complicated network of macroscopic fractures makes the modeling difficult. While some part of the reservoir are extensively fractured and pressure changes can happen rapidly, other parts of the reservoir contain less macroscopic fractures slowing down pressure propagation and the whole compaction process. In order to characterize the compaction and subsidence in detail these variations should be considered.

The current micromechanical model keeps the model of the microscopic fracturing process simple and claims that compaction is mainly driven by vertical stress. This approach neglects the modifying effect of horizontal stresses which are present as far-field tectonic stresses, while laterial variations in the compaction process due to different reservoir parameters can also cause local build-up of horizontal stresses. Therefore, a 3-dimensional reservoir-scale model of compaction should take into account the effect of horizontal stresses and should be tested against a detailed data on the compaction process.

AUTHOR CONTRIBUTIONS

All authors listed, have made substantial, direct and intellectual contribution to the work, and approved it for publication.

ACKNOWLEDGMENTS

We gratefully acknowledge the support of the FlowTrans Marie-Curie ITN for the funding of the PhD grant of DK (under grant agreement no. 31688 in the European Seventh Framework Programme). Thanks to Anja Røyne and Amélie Neuville for their valuable comments and for the employees of ConocoPhilips Norway for the thoughtful discussions.

SUPPLEMENTARY MATERIAL

The Supplementary Material for this article can be found online at: http://journal.frontiersin.org/article/10.3389/fphy.2016.00004

REFERENCES

1. Hermansen H, Landa G, Sylte J, Thomas L. Experiences after 10 years of waterflooding the Ekofisk Field, Norway. *J Petrol Sci Eng*. (2000) **26**:11–8. doi: 10.1016/S0920-4105(00)00016-4
2. Boade R, Chin L, Siemers W. Forecasting of Ekofisk reservoir compaction and subsidence by numerical simulation. *J Petrol Technol.* (1989) **41**:723–8. doi: 10.2118/17855-PA
3. Geertsma J. Land subsidence above compacting oil and gas reservoirs. *J Petrol Technol.* (1973) **25**:734–44. doi: 10.2118/3730-PA
4. Segall P. Induced stresses due to fluid extraction from axisymmetric reservoirs. *Pure Appl Geophys*. (1992) **139**:535–60.
5. Hickman RJ. *Formulation and Implementation of a Constitutive Model for Soft Rock*. Ph.D. dissertation, Virginia Polytechnic Institute and State University (2004).
6. Johnson J, Rhett D. Compaction behavior of Ekofisk chalk as a function of stress. In: *European Petroleum Conference*. London (1986). doi: 10.2118/15872-MS
7. Sulak R, Thomas L, Boade R. 3D reservoir simulation of ekofisk compaction drive (includes associated papers 24317 and 24400). *J Petrol Technol*. (1991) **43**:1272–8.
8. Jones G, Kendall JM, Bastow I, Raymer D, Wuestefeld A. Characterization of fractures and faults: a multi-component passive microseismic study from the Ekofisk reservoir. *Geophys Prospect*. (2014) **62**:779–96. doi: 10.1111/1365-2478.12139
9. Gutierrez M. Fully coupled analysis of reservoir compaction and subsidence. In: *European Petroleum Conference*. London (1994). doi: 10.2118/28900-MS
10. Chin L, Boade R, Prevost J, Landa G. Numerical simulation of shear-induced compaction in the Ekofisk reservoir. *Int J Rock Mech Mining Sci Geomech Abstr*. (1993) **30**:1193–200.
11. Abdulraheem A, Zaman M, Roegiers JC. A finite-element model for Ekofisk field subsidence. *J Petrol Sci Eng*. (1994). **10**:299–310.
12. Rhett DW. Ekofisk revisited: a new model of Ekofisk reservoir geomechanical behavior. In: *EUROCK 98 Symposium*. Trondheim (1998). doi: 10.2118/47273-MS
13. Papamichos E, Brignoli M, Santarelli F. An experimental and theoretical study of a partially saturated collapsible rock. *Mech Cohesive-frictional Mater*. (1997) **2**:251–78.
14. Plischke B. Finite element analysis of compaction and subsidence-Experience gained from several chalk fields. *Rock Mech Petrol Eng*. Delft (1994). doi: 10.2118/28129-MS
15. Datcheva M, Charlier R, Collin F. Constitutive equations and numerical modelling of time effects in soft porous rocks. In: *Numerical Analysis and Its Applications*. Berlin; Heidelberg: Springer (2001). pp. 222–29.
16. Sulak R, Danielsen J. Reservoir aspects of Ekofisk subsidence. *J Petrol Technol*. (1989) **41**:709–16.
17. Chin L, Boade R, Nagel B, Landa G. Numerical simulation of Ekofisk reservoir compaction and subsidence: treating the mechanical behavior of the overburden and reservoir. *Rock Mech Petrol Eng*. Delft (1994). doi: 10.2118/28128-MS
18. Sylte J, Thomas L, Rhett D, Bruning D, Nagel N. Water induced compaction in the Ekofisk field. In: *SPE Annual Technical Conference and Exhibition*. Houston, TX (1999). doi: 10.2118/56426-MS
19. Keszthelyi D, Dysthe DK, Jamtveit B. Modeling of carbonate compaction by pore failure and pressure solution. *J Geophys Res.* (in review).
20. Japsen P, Dysthe D, Hartz E, Stipp SLS, Yarushina V, Jamtveit B. A compaction front in North Sea chalk. *J Geophys Res*. (2011) **116**:B11208. doi: 10.1029/2011JB008564
21. Zhang X, Spiers CJ, Peach CJ. Compaction creep of wet granular calcite by pressure solution at 28 C to 150 C. *J Geophys Res*. (2010) **115**:B09217. doi: 10.1029/2008JB005853
22. Pluymakers A, Spiers C. Compaction creep of simulated anhydrite fault gouge by pressure solution: theory v. experiments and implications for fault sealing. *Geol Soc Lond Spec Publ.* (2014) **409**:SP409–6. doi: 10.1144/SP409.6

23. Coussy O. *Poromechanics*. Chichester: John Wiley & Sons (2004).
24. Alam MM, Fabricius IL, Christensen HF. Static and dynamic effective stress coefficient of chalk. *Geophysics* (2012) **77**:L1–11. doi: 10.1190/geo2010-0414.1
25. Kristiansen TG, Plischke B. History matched full field geomechanics model of the Valhall Field including water weakening and re-pressurisation. In: *SPE EUROPEC/EAGE Annual Conference and Exhibition*. Barcelona: Society of Petroleum Engineers (2010). doi: 10.2118/131505-MS
26. Warpinski N, Teufel L. Determination of the effective stress law for permeability and deformation in low-permeability rocks. *SPE Form Eval.* (1992) **7**:123–31.
27. Dvorkin J, Prasad M, Sakai A, Lavoie D. Elasticity of marine sediments: rock physics modeling. *Geophys Res Lett*. (1999) **26**:1781–4.
28. Vajdova V, Baud P, Wu L, Wong Tf. Micromechanics of inelastic compaction in two allochemical limestones. *J Struct Geol*. (2012) **43**:100–17. doi: 10.1016/j.jsg.2012.07.006
29. Muskat M. *The Flow of Homogeneous Fluids through Porous Media,* Vol. 12. New York, NY: McGraw-Hill (1937).
30. Mackay D. *Ekofisk Crude Oil Properties*. Version 4, October 2007 to April 2008, Gatineau, QC: Environment Canada, Emergencies Science and Technology Division (1995).
31. Dake LP. *Fundamentals of Reservoir Engineering*. Amsterdam: Elsevier (1983).
32. NPD. *Norwegian Petroleum Directorate Technical Report: Reservoir Fluid Study for Phillips Petroleum Company - Norway, 2/4-2X well DST No. 6B Ekofisk field, North Sea, Norway* (1970). Available online at: http://www.npd.no/engelsk/cwi/pbl/wellbore_documents/97_05_2_4_3(2X)_Reservoir_Fluid_Study_DST_6.pdf
33. Jakobsson NM, Christian TM. Historical performance of gas injection of Ekofisk. In: *SPE Annual Technical Conference and Exhibition*. New Orleans, LA: Society of Petroleum Engineers (1994). doi: 10.2118/28933-MS
34. Mes MJ. Ekofisk reservoir pressure drops and seabed subsidence. In: *Offshore Technology Conference*. Houston, TX: Offshore Technology Conference (1990). doi: 10.4043/6241-MS
35. Doornhof D, Kristiansen TG, Nagel NB, Pattillo PD, Sayers C. Compaction and subsidence. *Oilfield Rev.* (2006) **18**:50–68.
36. Hamilton JM, Mailer AV, Prins MD. Subsidence-induced shear failures above oil and gas reservoirs. In: *The 33th US Symposium on Rock Mechanics (USRMS)*. Santa Fe, NM: American Rock Mechanics Association (1992).
37. Schwall G, Denney C. Subsidence induced casing deformation mechanisms in the Ekofisk field. *Rock Mech Petrol Eng.* Delft (1994). doi: 10.2118/28091-MS
38. Weibull, W. A statistical distribution function of wide applicability. *J. Appl. Mech.* (1951) **18**:293–297.
39. Hellmann R, Renders PJ, Gratier JP, Guiguet R. Experimental pressure solution compaction of chalk in aqueous solutions. Part 1. Deformation behavior and chemistry. In: Hellmann R and Wood SA, editors. *Water-Rock Interaction, Ore Deposits, and Environmental Geochemisty: A tribute to David A Crerar*, Vol. 7, (Washington, DC: Geochemical Society) (2002). pp. 129–52.
40. Price M, Bird M, Foster S. Chalk pore-size measurements and their significance. *Water Serv.* (1976) **80**:596–600.
41. Johnson J, Rhett D, Siemers W. Rock mechanics of the Ekofisk reservoir in the evaluation of subsidence. In: *Offshore Technology Conference*. Houston, TX (1988). doi: 10.4043/5621-MS
42. Shao J, Henry J. Development of an elastoplastic model for porous rock. *Int J Plast*. (1991) **7**:1–13.
43. Andersen M, Foged N, Pedersen H. The rate-type compaction of a weak North Sea chalk. In: *The 33th US Symposium on Rock Mechanics (USRMS)*. Santa Fe, NM: American Rock Mechanics Association (1992).
44. Andersen M, Foged N, Pedersen H. The link between waterflood-induced compaction and rate-sensitive behavior in a weak North Sea chalk. In: *Proceedings of 4th North Sea Chalk Symposium*. Deauville (1992).
45. Nagel N. Compaction and subsidence issues within the petroleum industry: from Wilmington to Ekofisk and beyond. *Phys Chem Earth A Solid Earth Geod*. (2001) **26**:3–14. doi: 10.1016/S1464-1895(01)00015-1
46. Du J, Olson JE. A poroelastic reservoir model for predicting subsidence and mapping subsurface pressure fronts. *J Petrol Sci Eng*. (2001) **30**:181–197. doi: 10.1016/S0920-4105(01)00131-0
47. De Gennaro V, Delage P, Cui YJ, Schroeder C, Collin F. Time-dependent behaviour of oil reservoir chalk: a multiphase approach. *Soils Found.* (2003) **43**:131–47. doi: 10.3208/sandf.43.4_131
48. Collin F, Cui YJ, Schroeder C, Charlier R. Mechanical behaviour of Lixhe chalk partly saturated by oil and water: experiment and modelling. *Int J Numerical Anal Methods Geomech*. (2002) **26**:897–924. doi: 10.1002/nag.229

Conflict of Interest Statement: The authors declare that the research was conducted in the absence of any commercial or financial relationships that could be construed as a potential conflict of interest.

frontiers in Physics

ORIGINAL RESEARCH
published: 02 February 2016
doi: 10.3389/fphy.2016.00002

How Stress and Temperature Conditions Affect Rock-Fluid Chemistry and Mechanical Deformation

Anders Nermoen[1,2], Reidar I. Korsnes[2,3], Olav Aursjø[1], Merete V. Madland[2,3], Trygve A. C. Kjørslevik[3] and Geir Østensen[3]*

[1] International Research Institute of Stavanger, Stavanger, Norway, [2] The National IOR Centre of Norway, University of Stavanger, Stavanger, Norway, [3] Institute of Petroleum Sciences, University of Stavanger, Stavanger, Norway

We report the results from a series of chalk flow-through-compaction experiments performed at three effective stresses (0.5, 3.5, and 12.3 MPa) and two temperatures (92 and 130°C). The results show that both stress and temperature are important to both chemical alteration and mechanical deformation. The experiments were conducted on cores drilled from the same block of outcrop chalks from the Obourg quarry within the Saint Vast formation (Mons, Belgium). The pore pressure was kept at 0.7 MPa for all experiments with a continuous flow of 0.219 M $MgCl_2$ brine at a constant flow rate; 1 original pore volume (PV) per day. The experiments have been performed in tri-axial cells with independent control of the external stress (hydraulic pressure in the confining oil), pore pressure, temperature, and the injected flow rate. Each experiment consists of two phases; a loading phase where stress-strain dependencies are investigated (approximately 2 days), and a creep phase that lasts for 150–160 days. During creep, the axial deformation was logged, and the effluent samples were collected for ion chromatography analyses. Any difference between the injected and produced water chemistry gives insight into the rock-fluid interactions that occur during flow through the core. The observed effluent concentration shows a reduction in Mg^{2+}, while the Ca^{2+} concentration is increased. This, together with SEM-EDS analysis, indicates that magnesium-bearing mineral phases are precipitated leading to dissolution of calcite. This is in-line with other flow-through experiments reported earlier. The observed dissolution and precipitation are sensitive to the effective stress and test temperature. Higher stress and temperature lead to increased Mg^{2+} and Ca^{2+} concentration changes. The observed strain can be partitioned additively into a mechanical and chemical driven component.

Keywords: chalk, physicochemical processes, tri-axial, compaction, flow-through experiments

OPEN ACCESS

Edited by:
Daniel Koehn,
University of Glasgow, UK

Reviewed by:
Renaud Toussaint,
University of Strasbourg, France
Francois Renard,
Joseph Fourier University, France

****Correspondence:***
Anders Nermoen
aner@iris.no

Specialty section:
This article was submitted to Interdisciplinary Physics, a section of the journal Frontiers in Physics

Received: *15 May 2015*
Accepted: *07 January 2016*
Published: *02 February 2016*

Citation:
Nermoen A, Korsnes RI, Aursjø O, Madland MV, Kjørslevik TAC and Østensen G (2016) How Stress and Temperature Conditions Affect Rock-Fluid Chemistry and Mechanical Deformation. Front. Phys. 4:2. doi: 10.3389/fphy.2016.00002

INTRODUCTION

The study of how the physicochemical interplay between fluids and rocks alters the mechanical behavior of porous materials has enhanced the understanding of long-term creep behavior of crustal rocks (e.g., [1–3]), and has found industrial applications in e.g., CO_2 sequestration, ore deposits, hydrology, pharmaceutical industries [4] as well as hydrocarbon migration, petroleum production, and reservoir engineering.

The mechanical integrity of reservoir chalks during seawater injection has been of significant interest to the scientific and industrial communities since the seabed subsidence and reservoir deformation was discovered in the Ekofisk (chalk) field in the 1980s [5]. Other examples include the Weyburn field in Canada that has undergone extensive monitoring during compaction (see e.g., [6] for a description). The primary production phase during hydrocarbon extraction is recognized by fluid over-pressure release (i.e., the pressure in addition to the hydrostatic stress). From the Terzaghi principle [7], expanded by the Biot theory [8, 9], the effective stress is given by the externally imposed load minus a fraction α (the Biot coefficient) of the pore pressure. In reservoirs, the external load is given by the principal stresses, typically related to the weight of the overburden rocks (vertical direction), and the horizontal stresses originating from tectonic processes and Poisson ratio. At Ekofisk, over-pressure depletion led to reservoir compaction which induced overburden deformation and seafloor subsidence which led to detrimental effects on the production equipment and to the platforms resting on the seafloor. In addition to that, when the pressure declined this led to significant reduction in the production rates during the late 1970's and early 1980's (see e.g., [10]). In the secondary production phase, recognized by seawater injection, pressure support was provided to maintain the pressure gradient through the oil-field and to reduce the effective stresses and corresponding compaction to pre-production times. Seawater injection has until now been a great financial success because, in addition to maintain a pressure gradient and to reduce the effective stress, the seawater imbibes from fractures into water-wet chalk matrix where it displaces the oil, an effect leading to increased oil production [11, 12]. However, for chalks, time-dependent creep effects are significant. At Ekofisk, for example, since the seawater injection started in the mid-1980s it took several years before the reservoir pressure and stress conditions were increased to pre-production level. Despite the re-pressurization, the compaction prevailed at approximately 1/3 of the peak compaction rate of 35 cm/year in the regions in contact with the injected seawater, an effect termed water weakening [13–15]. The prevailing compaction and seafloor subsidence after re-pressurization indicate that not only stress and pressure effects drive deformation, but also the chemical nature of the pore fluid.

Specially designed experiments have shown how the pore fluid composition (gases, water/brines, and oils) alters different aspects of the mechanical strength. For example, at temperatures above 90°C, injecting brines containing sulfate ions significantly reduces the elastic bulk modulus during loading (1 day interval) and while the magnesium ion enhances the rate of compaction during creep (10–100 days interval; see e.g., [16] and references there-in). In addition, the yield stresses, at which irreversible deformation occurs during stress-strain load experiments, are significantly altered by the chemistry of the pore fluids [16].

As such, the exact way in which pore fluid chemistry impacts chalk mechanics is multi-faceted, as both long-term and short-term chemical processes may occur simultaneously. For example adsorption processes occur at short time-intervals since it may occur within 1–2 pore volumes injected, while dissolution/precipitation is time-dependent occurring during injection for hundreds of pore volumes [17]. Rock-fluid interactions estimated from equilibrium calculations become increasingly important with temperatures above 100°C, reported in e.g., [18–20]. At these conditions they showed that when seawater is injected into chalk reservoirs it becomes supersaturated with respect to magnesium bearing minerals, e.g., dolomite, magnesite, huntite, and brucite. In addition, precipitation of the Mg-bearing carbonate minerals drives dissolution of calcium-carbonate, which subsequently leads to an excess amount of Ca-ions in the aqueous solution. These excess ions bind to the sulfate ions in the seawater to form calcium-sulfate, such as anhydrite. Chalks have a varying degree of $CaCO_3$-purity. The impurity is often associated with silicate-bearing minerals such as quartz and various forms of clay. When dissolution of pre-existing quartz is taken into account, the geochemical calculations show that magnesium-bearing silicates such as tremolite and talc are also formed. These predictions have been supported by direct XRD and SEM observations that were published recently by Zimmermann et al. [21]. As such, calculations and direct rock-observations have shown that chalk is prone to chemical rock-fluid reactions at high temperatures [17].

The rate of deformation with time is linked to mineral alteration (see e.g., [17]). Any dissolution related to solid-volume changes may affect the bulk volume directly. And, in addition, changes to grain volumes increase the probability for the grain to "un-lock" from its current configuration and shift into pores nearby, effectively reducing the pore space. Since these mineral reactions, expected when $MgCl_2$ are flooded through chalks, are associated with density increase, the total volumetric deformation can be partitioned into a solid volume and a pore volume component. Depending on how the solid volume and pore volume changes, the porosity may change in a non-intuitive way [17].

It is the chemical potential, related to the Gibbs free energy, which governs the chemical stability of minerals, with temperature and pressure as state variables. In granular systems, where there are large spatial variations in the local stress level, the difference between the externally applied forces over the bulk area may be significantly smaller than the stresses at the solid-solid contacts. The Biot coefficient, measured to be in the range of 0.80–0.99, is linked to the consolidated area, thereby leading to increased stresses at the grain contacts. These stresses may end up to be 5–100 times the externally imposed load (see later in this paper). However, the appropriate pressure to be used in the geochemical calculations may range from the pore pressure, in the lower end (typically 0.7 MPa to avoid boiling in many of the high temperature experiments reported), to 100 times the externally imposed load, in the upper. This range in the appropriate thermodynamic pressure at grain contacts are therefore significant, and may therefore lead to spatial differences in the solubility of the different minerals within the porous rock. The stress-driven dissolution at grain contacts is termed pressure solution and has been used to understand the long-term creep experiments (see [22, 23] for a review). Croize et al.

[24] performed single-indenter experiments on calcite crystals showing that measurable pressure solution occurs at stresses above approximately 400 MPa.

Sub-critical crack growth, where cracks propagate at imposed stresses below a critical level due to the chemical interplay between the fluids and rock surface close to the crack tip [25], may also be an effective driver of deformation and grain re-organization. In addition, the adsorption of sulfate in the diffusive double layer sets up a disjoining pressure at the grain contacts that leads to a reduction in the attractive van der Waals forces. This mechanism has been shown to significantly alter the mechanical properties and rates of deformation in chalks [16].

It is important to note that the deformation, due to grain re-organization and porosity reduction, alters the flow pattern. As the material deforms, fresh mineral surfaces are exposed to the non-equilibrium brine, which again increases the chemical reactions there. Hence, deformation could be important for the total chemical reaction measured in the ion concentration of the effluent water concentration.

In this paper we present the results from six experiments, probing two test temperatures and three effective stress levels (σ_p'). The chemical alteration, as measured from the effluent-brine analysis of the dissolved Ca^{2+} concentration and mass-and-rock analysis, is higher in the high stress experiments at 130°C. Such kind of stress-dependency is not observed for the 92°C temperature experiment. Many experiments from the University of Stavanger have been performed at these temperatures previously, since the temperature coincide with the temperature at Ekofisk and Valhall reservoir chalk fields at the Norwegian Continental Shelf.

METHODS

The Chalk

The experiments were performed on Upper Cretaceous outcrop chalk samples collected from the Obourg quarry in Belgium from the Saint Vast formation of the Mons basin (OBSV). Each experiment is denoted OBSV with a number suffix for identification.

Chalk is a sedimentary rock with high calcium carbonate ($CaCO_3$) content. The concentration of $CaCO_3$ for these chalks has been reported to be ranging from approximately 90 to 95% (see e.g., [16, 21, 26]). Cylindrical plugs were drilled from a chalk block, before being radially adjusted to diameters D_0 and cut to lengths L_0. The bulk volumes V_b were estimated according to the volume of a cylinder. Before testing, the plugs were dried at 100°C overnight and the initial dry mass $M_{s,0}$ was measured. The plugs were then placed in a vacuum cabinet before being saturated with distilled water, and the saturated weight of each plug was measured ($M_{sat,0}$). The difference between the saturated and dry mass was used to estimate the pore volume and thereby the porosity ϕ according to:

$$\phi = \frac{M_{sat} - M_s}{\rho_{dw} V_b}. \tag{1}$$

Here, ρ_{dw} is the density of distilled water. The porosity estimate from mass difference measurements was performed both before and after the experiment. Based on previous experience in related geochemistry, pycnometry, saturation and dry mass estimates, the porosity of connected pores is equal to the overall porosity of the chalk sample [17].

Helium gas pycnometer measurements, using the *Micromeritics Gas Pycnometer model AccuPyc II 1340,* were also employed to estimate the solid density ρ_s of tested and un-tested material. The solid density can be used to estimate the volume of the solids V_s, so that the porosity can be estimated (before and after test) according to:

$$\phi = 1 - \frac{V_s}{V_b} = 1 - \frac{M_s}{\rho_s V_b}. \tag{2}$$

The average mineral density was estimated from the dry mass divided by the solid volume. Lengths, diameters, densities, and other basic quantities, which were measured before and after the experiments, are reported in **Tables 1**, **2** for the 130 and 92°C experiments, respectively.

The Triaxial Cell and Experimental Setup

The chalk plugs were mounted into a triaxial cell that allowed for continuous measurements of the axial strains during the injection of reactive fluids at elevated stresses, pressures and temperatures (see **Figure 1**). The cell was equipped with a heating jacket and a regulating system (Omron E5CN) with precise temperature control (±0.1°C). The temperature was set to either 92 or 130°C, and monitored by a Pt-100RDT resistance temperature detector inside the cell. Three pumps were connected to the cell allowing for independent control of the piston pressure (P_{pist}), radial confining stress (σ_{rad}), and injection flow rate (q_{in}) (*Gilson Pump - Model 307 HPLC*). The pore pressure was controlled by a back-pressure regulator ensuring constant pore pressure at 0.7 MPa on the downstream side of the core. The back-pressure regulator allowed for continuous sampling of the effluent water throughout the test period. The axial stress σ_{ax} was calculated from the confining pressure P_{conf} (i.e., radial stress σ_{rad}), piston pressure P_{pist}, frictional pressure P_{fric} of the piston movement in the triaxial cell, and an area factor f_{area} for the piston-pressure chamber and the cross area of the plug, giving:

$$\begin{aligned} \sigma_{ax} &= P_{conf} + f_{area}\left(P_{pist} - P_{fric}\right), \text{ and} \\ \sigma_{rad} &= P_{conf} \end{aligned} \tag{3}$$

The triaxial cell has been designed to have a balanced piston, meaning that the confining oil pressure can migrate to a chamber above the piston [see confining pressure (outlet) in **Figure 1**] to inhibit piston movement unless an additional piston pressure, that overcomes the friction pressure, is added in the upper chamber. The piston friction and the area factor is not the same for all the triaxial cells used. The piston friction is measured in each case, typically depending on temperature and confining pressure, and it takes on values between 0.3 and 0.5 MPa. The area factor varies for the different chalk core

TABLE 1 | Basic quantities of the 130°C experiments.

σ'_p [MPa]	OBSV21 (163 days)		OBSV15 (162 days)		OBSV8 (160 days)	
	0.5		3.5		12.3	
	Before	After	Before	After	Before	After
M_{dry} [g]	121.13	117.37	127.26	122.90	126.16	121.94
Measured ΔM [g]	3.76 g		4.36 g		4.22 g	
Relative mass loss [%]	3.1		3.4		3.3	
M_{wet} [g]	152.01	149.87	160.03	155.148	159.11	146.66
Porosity [%]	40.77	42.98	41.00	41.54	41.31	35.66
Length [mm]	70.41	70.30	70.03	68.65	69.92	65.88
Avg. diameter [mm]	37.01	37.00	38.12	37.91	38.11	36.46
Bulk Volume [ml]	75.75	75.62	79.92	77.63	79.76	69.33
Correction factor, ξ	0.35		0.28		0.78	
ρ_S estimated [g/ml]	2.70	2.72	2.70	2.71	2.70	2.73
ρ_S pycnometer [g/ml]	2.68	2.71	2.69	2.71	2.68	2.71
Solid volume [ml]	44.86	43.12	47.15	45.39	46.81	44.60
Volume strain, unit 1	0.002		0.059		0.163	

The pore pressure was 0.7 MPa and the volume strain that was estimated from the measured volumes before and after the test [Equations (6) and (7)].

diameters and the design of each setup. It varies between the values of 1.2 and 1.3. The position of the piston, and hence the length L of the plug, was monitored by an external Linear Variable Differential Transducer (LVDT) placed on top of the piston.

The experiments were performed in the following steps:

(1) Loading the confining pressure to 1.2 MPa and the pore pressure to 0.7 MPa during flow of distilled water. The piston pressure was kept 0.2 MPa above the friction pressure of the piston (approximately 0.4 MPa). The 0.7 MPa pore pressure is used since it enables continuous water sampling and it is sufficient to avoid boiling of pore fluids within the core.
(2) Saturating the core with $MgCl_2$-brine.
(3) Raising the temperature from ambient to 92 or 130°C.
(4) Increasing the confining pressure at hydrostatic conditions to 3.5 or 12.3 MPa (except the 0.5 MPa effective stress experiments). The confining (hydrostatic) pressure σ_p was increased with a constant flow rate of the hydraulic oil surrounding the core which was encapsulated by the shrinkage sleeve. During this phase, elastic and plastic parameters were measured from stress-strain plots. The initial steps from (1) to (4) lasted 3 days.
(5) Creep at constant hydrostatic stress conditions for varying number of days, while injecting 0.219 M $MgCl_2$ brine at constant pore pressure and confining pressure.

Ion Chromatography (IC)

Samples of produced fluids downstream were collected approximately three times a week during the test period to quantify rock-fluid interactions. The samples were diluted 500 times with distilled water on a *Gilson GX-271* machine to meet the linear region of the calibration curve of the *Dionex ICS-3000* ion chromatograph. The concentration of four anions (*IonPac AS16* exchange column) and three cations (*IonPac CS12A* exchange column) were estimated from the areas under the chromatographic curves when compared to known standards. Here, we report the Mg^{2+} and Ca^{2+} concentrations.

Constitutive Relations for the Volume Evolution of Bi-Phase Materials

The bulk volume V_b of a bi-phase material equals the sum of the solid volume V_s and the pore volume V_p, i.e.:

$$V_b = V_p + V_s. \tag{4}$$

Any changes to the total volume are given by changes in pore volume and solid volume,

$$\Delta V_b = \Delta V_p + \Delta V_s. \tag{5}$$

After testing, the plug is non-homogenously deformed such that a more accurate estimates of the bulk volume is given by the sum of truncated circular cones:

$$V_b = \sum_i \frac{\pi h_i}{12}\left(D_i^2 + D_{i+1}^2 + D_i D_{i+1}\right), \tag{6}$$

where the diameter D_i is measured at intervals h_i along the length of the plug (see **Table 3**).

TABLE 2 | Basic quantities of the 92°C experiments.

σ'_p [MPa]	OBSV28 (160 days)		OBSV32 (162 days)		OBSV14 (151 days)	
	0.5		3.5		12.3	
	Before	After	Before	After	Before	After
M_{dry} [g]	121.16	118.68	120.03	117.56	127.87	125.35
Measured ΔM [g]	2.48		2.47		2.52	
Relative mass loss [%]	2.0		2.0		2.0	
M_{wet} [g]	151.98	150.25	151.26	149.08	160.22	151.03
Porosity [%]	40.81	41.84	41.32	42.00	40.52	35.84
Length [mm]	70.20	70.18	70.22	69.84	69.91	66.72
Avg. diameter [mm]	37.01	37.00	37.02	36.89	38.13	37.35
Bulk volume [ml]	75.52	75.46	75.58	74.87	79.83	71.63
Correction factor, ξ	0.95		0.65		0.61	
ρ_S estimated [g/ml]	2.71	2.71	2.71	2.71	2.69	2.72
ρ_S pycnometer [g/ml]	2.69	2.69	2.69	2.69	2.70	2.69
Solid volume [ml]	44.62	43.79	44.35	43.44	47.48	45.96
Volume strain [1]	0.001		0.009		0.103	

The pore pressure was 0.7MPa and the volume strain was estimated from the measured volumes before and after the test [Equations (6) and (7)].

Strain Measurements

Axial strains are estimated from length measurements according to:

$$\varepsilon_{ax} = -\frac{L - L_0}{L_0}, \tag{7}$$

where L is the length of the core during the experiment and L_0 is the original length. If the core keeps a cylindrical geometry, the volumetric strain ε_{vol} can be calculated from the axial strains according to:

$$\varepsilon_{vol} = (1 + 2\xi)\varepsilon_{ax} + 2\left(\xi + \xi^2\right)\varepsilon_{ax}^2 = -\frac{V_b - V_{b,0}}{V_{b,0}}. \tag{8}$$

Here, the conversion factor ξ is given by the radial strain ε_{rad} to axial strain ε_{ax} ratio measured directly on the core after the experiment, using that $\varepsilon_{rad} = \xi\varepsilon_{ax}$ (see **Tables 1**, **2**).

The Effective Stress and Stress-Strain Relations

The loading was performed by injecting hydraulic oil to the chamber surrounding the chalk core at a constant rate. Thus, the hydrostatic stress was increased from 0.5 to 3.5 MPa or 12.3 MPa with a hydrostatic stress rate ranging from 0.026 to 0.031 MPa/min. The loading phase lasted about 120 and 500 min, for the 3.5 and 12.3 MPa experiments, respectively. The effective stress of a porous material has been calculated from the Biot effective stress relation [8, 27]:

$$\sigma' = \sigma_p - \alpha P, \tag{9}$$

where the confining stress σ_p is reduced by a fraction α of the internal pore pressure P. Here, α is termed the Biot coefficient. For low pore pressures, as is the case here, the exact value of the Biot coefficient is not of great importance, and we equal it to one. In a drained hydrostatic experiment, the volumetric strain is linked to the effective stress σ' via the drained bulk compressibility of the rock framework K_{fr} [28], so that:

$$\sigma' = K_{fr}\varepsilon_{vol}. \tag{10}$$

Beyond a certain stress level during stress buildup, the observed strain dynamics deviate from the initial linear response. This is observed in the high-stress experiments. The onset of non-linearity signals the onset of irreversible deformation associated with grain-reorganization and pore-collapse. However, irreversible deformation could also occur at low stresses due to, e.g., the closure of micro-cracks that may originate from the rock sampling and preparation of the cores. When the extrapolated linear relation and the observed stress deviates above a threshold of 0.2 MPa, the onset of yield Y_o was defined. Values of the bulk elastic modulus and the onset of yield are reported in **Table 4**.

Estimating Changes in Solid Mass

The evolution of the solid mass over time within the plug is given by the difference in chemical flux into the core and out of the core. The chemical flux in and out of the core is monitored by measuring the effluent concentration of different ions over time. Over a time interval δt the difference in mass is given by:

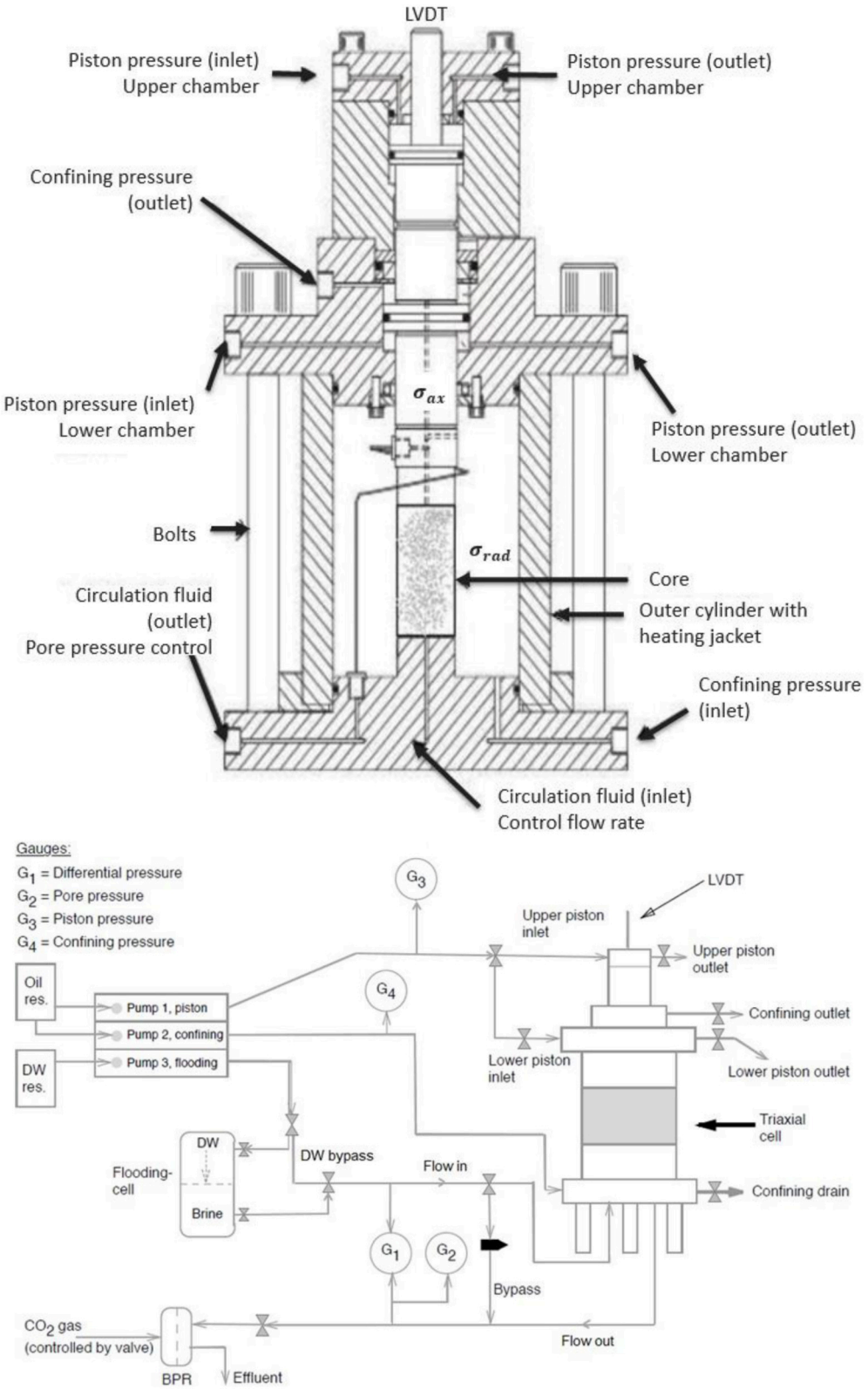

FIGURE 1 | (Top) Sketch of the tri-axial cell [17] and an overview of the gauges, pumps and flow-loop in the experimental setup (Bottom).

TABLE 3 | Lengths and diameters of the cores after test.

mm from inlet	OBSV28 [mm]	OBSV32 [mm]	OBSV21 [mm]	OBSV15 [mm]	OBSV8 [mm]	OBSV14 [mm]
Length	70.2	69.8	70.3	68.7	65.9	66.72
Inlet	37.0	36.8	37.0	37.9	36.7	37.55
5		36.7		37.4	34.9	36.80
10	37.0	36.7	37.1	37.4	35.1	
20	37.0	36.9	37.0	38.0	36.4	36.57
30	37.0	36.9	37.0	38.1	37.0	36.72
40	37.0	37.0	37.0	38.1	37.1	36.88
50	37.0	37.0	37.0	38.1	37.1	37.05
60	37.0	37.0	37.0	38.1	37.3	37.17
Outlet	37.0	37.0	37.0	38.1	37.6	37.79

$$\frac{\delta M_s}{\delta t} = \sum_j \left(c_{in,j} - c_{out,j}\right) q M_{wj}, \tag{11}$$

where $c_{in,j} - c_{out,j}$ is the difference in the ion concentration [mol/l], q is the flow rate [l/day], and M_{wj} is the molar weight [g/mol] of species j (magnesium and calcium ions). The molar weight of calcium and magnesium are 40.08 and 24.31 g/mol respectively. The accumulated mass change at any given time t throughout the test period is estimated from the integrated sum of all sample analyses:

$$\Delta M_s(t) = \int_0^t \frac{\delta M_s}{\delta t'} dt', \tag{12}$$

where the integrand is taken from Equation (11). Given knowledge about the density evolution of the solid constituent, we can now estimate the volume of solids through:

$$\Delta V_s(t) = \frac{M_s(t)}{\rho_s(t)} - \frac{M_{s,0}}{\rho_{s,0}}. \tag{13}$$

In Equation (13), the mass and the density before experiment, $M_{s,0}$ and $\rho_{s,0}$ respectively, are known quantities.

RESULTS AND DISCUSSION

Mechanical Deformation during Loading

The axial strains (LVDT-measurements) were converted to volumetric strain according to Equation (8) with the values of ξ as reported in **Tables 1**, **2**. The stress-strain curve during loading is shown in **Figures 2A,B** (for 92 and 130°C). The bulk modulus and yield stresses are given in **Table 4**. No direct dependency in the bulk modulus with respect to temperature can be drawn from the results, however the yield stress seem to be significantly reduced for the 130°C compared to the 92°C experiment. Significant variations in the elastic parameters can often be observed during direct loading (without cycling). The variation may e.g., be caused by defects that form during the core handling prior to the test, such that stress cycling are required to obtain more repeatable elastic properties as function of temperature. The authors are aware that several papers have been published on the temperature dependent elastic/plastic properties, see e.g., [29], but more work is required to understand the effect of temperature in these systems.

TABLE 4 | Mechanical parameters obtained during loading.

Test ID	Bulk modulus [GPa]	Yield onset [MPa]	Temp. [°C]
OBSV8	0.79 ± 0.04	5.8	130
OBSV 15	1.04 ± 0.02	n/a.	130
OBSV14	1.21 ± 0.02	9.2	92
OBSV32	0.73 ± 0.02	n/a.	92

Mechanical Creep Deformation at 92 and 130°C

After the hydrostatic loading to 3.5 or 12.3 MPa, the stress, the fluid pressure, and the temperature were held constant during a constant flowrate of 1 PV/day of 0.219 M $MgCl_2$ brine for the rest of the test. Since the individual cores had different initial pore volumes, the flow rates were different in each experiment (see **Tables 1**, **2**). As can be seen in **Figure 3**, the cores in the high stress experiment (12.3 MPa) deform significantly more than the 3.5 MPa experiment, which again deform more than the 0.5 MPa experiments. This applies to both 92 and 130°C. However, when comparing experiments at equal stress, the temperature effect becomes apparent. With time, the 130°C experiments creep more than experiments performed at 92°C. An additional experiment performed at 92°C and 12.3 MPa that failed after 127 days, has been included into **Figure 3** to display the repeatability in the experiments (dotted line).

For the 12.3 MPa experiments, the axial strain curves follow the approximately the same path for both 130 and 92°C until approximately 20–25 days. In this time interval (from 0 to 20 days), the creep rate of both 92 and 130°C is reduced with time (primary creep) and the temperature seems inconsequential to the observed creep dynamics. However, from 25 to 35 days the observed strain for the 130°C experiment enters an accelerating phase which is not observed for the 92°C experiment. Accelerated creep behavior were also reported by Madland et al. [19], Omdal [30], and Wang et al. [unpublished manuscript]. This may indicate how rock-fluid chemical processes at high temperatures impacts chalk mechanical deformation.

Interestingly, the same accelerating creep behavior is also observed for the 3.5 MPa effective stress experiment. In this experiment the acceleration occurs after 40–50 days, somewhat delayed compared to the 12.3 MPa experiment. The 3.5 MPa experiment was performed at stresses below yield (see **Table 4**) such that negligible strain was observed until 40 days. We see that the difference between creep curves at 130 and 92°C are the same for both the 3.5 and 12.3 MPa experiments. No temperature driven deformation is observed in the 0.5 MPa effective stress experiments.

Quantifying Primary Creep Dynamics

Creep is defined as the time-dependent irreversible/plastic deformation that occurs at constant stress conditions. For chalks, plastic creep is dominating the overall deformation at effective

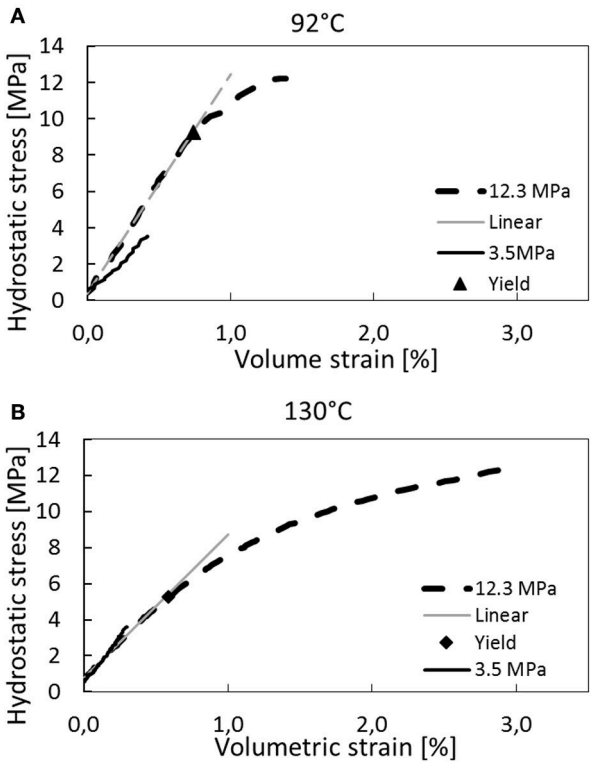

FIGURE 2 | Stress–strain curves during loading to hydrostatic confining pressures of 4.2 and 13.0 MPa (i.e., 3.5 and 12.3 effective stress). In **(A)** the 130°C tests are shown while the 92°C tests are displayed in **(B)**. The bulk modulus and onset of yield are shown in **Table 4**.

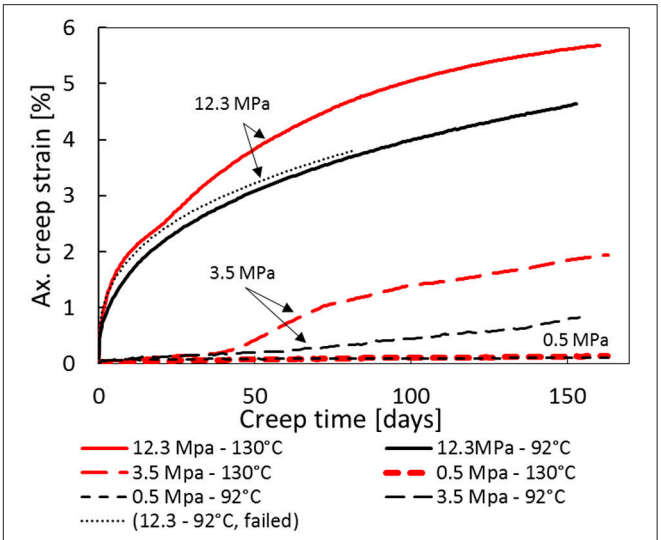

FIGURE 3 | Axial creep strain curve with time for 130and 92°C temperatures, and 0.5, 3.5, and 12.3 MPa effective stresses. In addition, a failed test performed at 12.3 and 92°C is included to display the repeatability of creep experiments.

stresses beyond the yield stress (see **Table 4** for yield values for 92 and 130°C). In this section we present, for the 12.3 MPa experiments, three simplified models to parametrize the creep curves. These models have been fitted to the observed creep curves at 92 and 130°C. This has been done to explore the functional form of the creep curve, and to visualize how chemical effects impact creep. Only the primary creep curve, recognized by a steadily declining creep rate, have been fitted since accelerated creep requires more sophisticated models that couple mechanical deformation and rock-fluid chemistry. For the 130°C experiment the primary creep applies to the first 20 days (after 20 days the creep rate accelerates) and the model fits are extrapolated beyond this time (see **Figure 4A**). Since no accelerated creep is observed in the 92°C experiment the whole creep curve is used (i.e., to 153 days; see **Figures 5A,B**). In **Figure 4B** the experimental and model-fitted strain rates are plotted together on log-log axis. **Figure 4B** shows that up to 20 days the creep rate declines with a constant slope in the log-log plot, indicating power-law behavior within this regime. From 20 to 30 days the strain rate increases, as can be seen by the red curve in **Figure 4B**. After the acceleration phase, from approximately 30 to 100 days, the curve attains the same slope as from 0 to 20 days. From approximately 100 to 160 days the log-log creep rate curve bends downwards, motivating using an exponential cut-off at finite times for the model fit.

Three models have been used to quantify primary creep dynamics: the de Waal model, the Griggs model and a power law model with exponential cut-off. The de Waal model was obtained from his dissertation in 1986 [31] where he was studying time-dependent deformation in sandstone reservoirs, and has been re-used by e.g., Andersen 1992 [32] to North-Sea chalks. The Griggs model is obtained from his original work from 1939 [33]. The aim of these three models is to couple time to the observed volumetric creep. They are expressed as:

$$\begin{aligned} \text{Power law with exponential cut-off: } \varepsilon_{pow} &= Bt^A e^{-\frac{t}{t_0}} \\ \text{De Waal: } \varepsilon_{z,dW} &= A\log(Bt+1) \\ \text{Griggs: } \varepsilon_{z,G} &= A\log(t+1)+Bt \end{aligned} \quad (14)$$

In the estimation of the factors A, B, and t_0, the residual strain is minimized. The residual strain is defined as the sum of all absolute differences between the observed axial strain and the strain from the fitting curves (ε_{mod}). The overall residual strain has been rescaled by the number of data-points (N) such that the total residual can be compared for the different experiments:

$$RES = \frac{1}{N}\sum |\varepsilon_{obs} - \varepsilon_{mod}| \quad (15)$$

The absolute values between the observed and the best fitted creep strain are shown in **Figures 4C**, **5C**, whereas the model parameters (A and B) and the residuals (RES) are shown in **Table 5**.

As can be seen in the reported residuals in **Table 5**, the power-law creep with a cut-off time of approximately 50,000 (infinity, which indicates no cut-off) fits better the observed creep curve compared to the de Waal and Griggs relations, with a

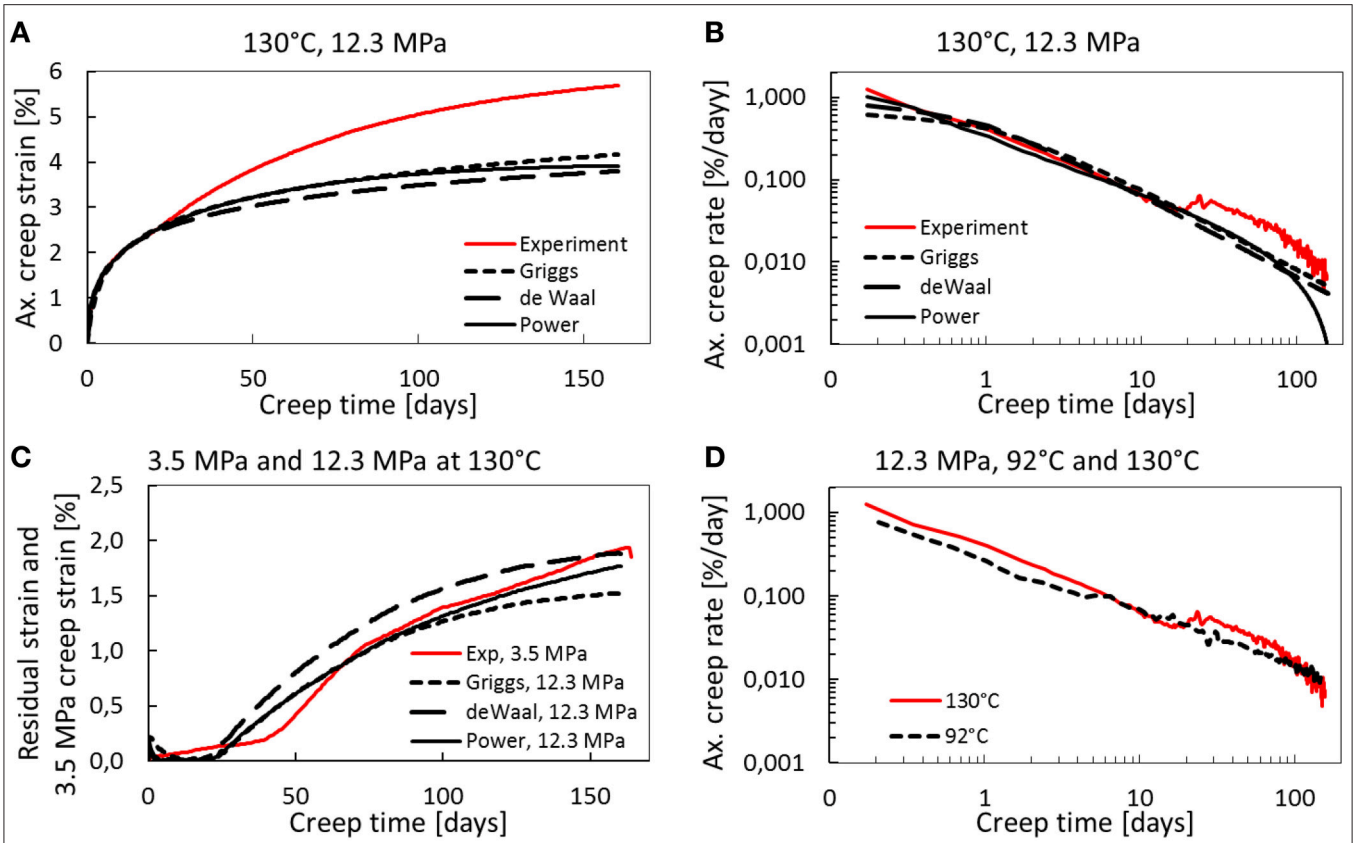

FIGURE 4 | (A) Creep curve for the 130°C and 12.3 MPa effective stress experiment compared to the best model fits. The fitting has been performed on the primary creep part (i.e., first 20 days) and extrapolated to visualize the effect of chemistry. **(B)** Log-log plot of strain rate (in %/day) vs. time. Accelerated creep observed when the red experimental curve deviates from the models. **(C)** The difference between the extrapolated strain and observed strain at a given time, is plotted through time for the 12.3 and 130°C experiment (black line) and compared to the 130°C and 3.5 MPa experiment creep (red stippled line). The deviation is interpreted to arise from chemical effects, which coincide with the creep dynamic of the experiment performed at 3.5 MPa (below yield). **(D)** Comparison of the axial creep strain rate for the 92 and 130°C experiment. The GRG-nonlinear regression tool in the Solver add-in in Excel 2013 was used to search for the optimal values of A, B, and t_0 to minimize the total residue.

residue of 1.5×10^{-2} compared to 6.7×10^{-2} and 3.7×10^{-2}, respectively, for the 92°C experiments (**Figure 5**). This is not the case for the 130°C experiment where the de Waal model seems to fit to the data in a more satisfactory way than the power-law model with a finite cut-off time (**Figure 4**). Based on the presented data, we cannot conclusively identify whether power law models with exponential cut-offs are more than the best fit out of three selected models, or if power laws models and self-organized criticality represent the best description of how nature works [34]. Special care should be taken before claiming that creep curves, which indeed are finite systems, exhibit scale-free behavior [35].

At 3.5 MPa effective stress it is expected that the mechanical component of the observed strain, associated with grain re-organization, should be negligible. In **Figure 4C** we plot the observed strain from the 3.5 MPa experiment (dashed) together with the residual strain from the 12.3 MPa experiment, i.e., the difference between the fitting models and the observed strain extrapolated into the accelerated phase, as a function of time. As can be seen, the 3.5 MPa experiment creep curve coincides with the residual strain. This may presumably indicate that the deviation between the extrapolated models and the observed deformation are caused by chemical reactions alone. As such, **Figure 4C** is significant to our interpretation, since it visualizes the effect of chemistry from the reactive flow on the volumetric strain for both the 3.5 and 12.3 MPa experiment. The additional strain increases monotonously to approximately 2% after 160 days. We can therefore suggest a simplified additive partitioning of the observed strain into a mechanical component and a chemical component.

In **Figure 4D** the creep strain rate for both the 92 and 130°C experiment is seen. Accelerated strain is not observed for the 92°C experiment, as also can be seen in **Figure 5A** where the axial creep strain is plotted with time for the experiment and the model fits. In **Figure 5B** we plot the creep strain rate and time on logarithmic axes, and in **Figure 5C** the residual strain are plotted with time.

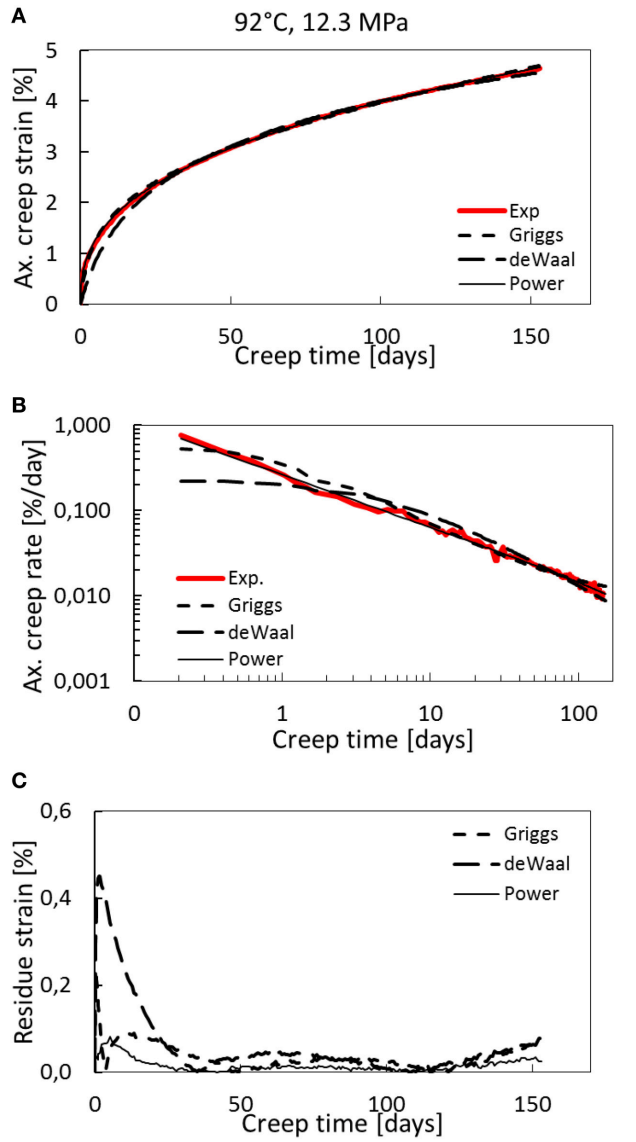

FIGURE 5 | Creep curves for the 92°C and 12.3 MPa effective stress experiment (OBSV25). (A) Axial creep strain curves compared to the best fit of power law with exponential cutoff, de Waal and Griggs models. **(B)** Logarithmic strain rate (in %/day) plotted with logarithmic time-axis. **(C)** Residual strain through time. The power law curve fits the data better than the de Waal and Griggs models.

The Chemical Interactions—Effluent Profiles

The observed creep dynamics in **Figure 3** shows that temperature is important during creep with flow of non-equilibrium brines as a temperature of 130°C leads to more strain than at 92°C.

In this section, we describe the results of the ion chromatography (IC) analysis of the effluent brine. Any changes between the injected concentrations and the effluent samples indicate to which extent rock-fluid interactions occurred in the core. In **Figures 6A,B**, the effluent Mg^{2+} and Ca^{2+} concentrations are shown. The injected concentration of Ca^{2+} and Mg^{2+} are 0 and 0.219 mol/l (dotted line). The larger the difference between the zero line and the Ca^{2+} concentration and the dotted line and the Mg^{2+} concentration, the more chemical reactions have taken place in the core. The effluent chemical profiles for the 92°C experiments (**Figure 6B**) indicate that less chemical reactions occur compared to the 130°C experiments (**Figure 6A**).

In **Figure 6C** the produced calcium concentration is shown for all experiments. Here, the produced Ca^{2+} concentration for the 92°C experiment overlap each other, indicating that the chemical reactions are in-sensitive to the stress level. This is not the case for the 130°C experiments in which more stress leads to more dissolution. As such, both stress and temperature are important for the chemical reactions. We split the discussion up into the early effluent dynamics from 0 to 20–30 days and intermediate and late effluent dynamics from 30 to 100 days and 100 to 160 days, respectively.

Early Effluent Dynamics

As can be seen in **Figure 6C**, the produced effluent Ca^{2+}-concentration is reduced from being initially being around 0.10–0.01 mol/l for the 92°C experiments and to 0.02–0.03 mol/l for the 130°C experiments. This transient behavior lasts approximately 2–3 days for the 92°C experiments and up to 3 weeks for the 130°C temperature experiments. The same trend is seen for the retention of Mg^{2+}-ions. The underlying reason for this behavior has been debated in the scientific literature (see e.g., [36]). One hypothesis has been associated with the migration of the finest particles through the porous chalk, see e.g., Karoussi and Hamouda [37]. They conclude that fine migration could be a mechanism for wettability alteration and enhanced oil recovery. We believe that fine migration is unlikely in the experiments presented here for two reasons: Firstly, if fine migration is the dominating mechanism for the initial transient behavior, why would this phenomenon be temperature dependent? Any fine migration is supposedly obstructed by the pore throat dimensions and dependent on the extent to which the grains attach to each other, rather than temperature vibrations of the smallest fines. Fine attachment could, however, be affected by temperature due to the electrostatic forces (sometimes named disjoining pressures) which depend on temperature [16]. A second reason why we believe fine migration is unlikely in some of these experiments, is that if fines are produced from the porous body it would be in the form of $CaCO_3$-minerals and thus the retention of Mg-ions should not be mirrored by the Ca-production. In **Table 6**, we estimated the amount of carbonate ions CO_3^{2-} produced from the core, based on the discrepancy between the total molar production of Mg^{2+} and Ca^{2+}. As can be seen in this table, stoichiometry is almost perfectly conserved for the high-temperature experiments (i.e., produce the same amount of Ca^{2+} as what is lost in Mg^{2+}). This indicates that Mg^{2+} ions are bound to the dissolved CO_3^{2-} to form magnesite ($MgCO_3$) and/or dolomite ($MgCa_2(CO_3)_2$), thus very low concentrations of CO_3^{2-} ions are produced in the experiments where the transient behavior is observed. Thus, based on Mg-Ca stoichiometry, fines of $CaCO_3$ that would increase the measured produced Ca^{2+} concentration

TABLE 5 | Fitting parameters for the primary creep curve, i.e., with monotonous decreasing strain rate, in the 12.3 MPa experiments.

	Power law + cutoff				de Waal			Griggs			Fitting interval [days]
	A	*B*	t_0 [days]	*RES* (10^{-2})	*A*	*B*	*RES* (10^{-2})	*A*	*B*	*RES* (10^{-2})	
92°C (failed)	0.34	0.86	50000	0.7	2.56	0.36	7.3	1.67	0.07	2.3	0–127 (failed)
92°C	0.38	0.69	47038	1.5	3.19	0.17	6.8	1.55	0.009	3.7	0–157
130°C	0.36	0.88	500	2.4	1.53	1.91	1.4	1.89	0	5.9	0–20

The numbers apply to unit days for creep-time and % for axial creep.

in the effluent, has not been produced. However, for the 92°C experiments stoichiometry is not conserved, i.e., more Ca^{2+} is produced than Mg^{2+} retained within the core (see **Table 6**). This indicate that CO_3^{2-} are produced from the core, possibly in the form of fines the first 2–3 days, but it cannot explain the 3 week transient behavior in the high temperature experiments.

Hiorth et al. [38] and Andersen et al. [39] propose, using geochemical simulations coupled to fluid flow dynamics, that the initial high value in the produced calcium concentration, observed in the IC-data, may be understood using a relatively high Mg-Ca ion exchange capacity. However, the slow transient decline in the calcium production (and increase in Mg-concentration) over the next 20 days (i.e., 20 pore volumes injected) cannot easily be explained by the use of common rate equations. An extension of this analysis has been presented by Pedersen et al. [36], where they describe how the slow transient behavior may be naturally captured by assuming an evolving pore geometry, thereby dynamically modifying the surface areas prone to chemical interplay.

Intermediate and Late Effluent Dynamics from 30 Days—Dissolution at Stressed Contacts

From approximately 20–30 to 80–100 days, the three 130°C experiments display several interesting features. As can be seen in **Figures 6B,C**, the effective stress level is important to the observed IC-data. The produced calcium concentration is successively higher for higher stress, i.e., it is higher at 12.3 MPa than at 3.5 MPa, and higher at 3.5 MPa than at 0.5 MPa. However, from 80 to 100 days and onwards the production of Ca^{2+} and the retention of Mg^{2+} reach the same values independent of stress within experimental the error.

The externally applied load σ_p is imposed onto the solid skeleton through the heat-shrinkable sleeve, separating the core material from the hydraulic oil in the tri-axial cell surrounding the core samples. The external stress is evenly distributed (**Figure 7A**) and it is carried by the force-chains transmitted through the grain contacts (**Figure 7B**). At the deformation rates reported in this paper, the permeability of these rocks is adequate to ensure drained conditions, i.e., the relative movement of the grains does not lead to build up of pore pressure within the sample, despite the fact that the pore pressure carries some of the externally imposed load according to the Terzhagi principle. When grains are partially cemented together at grain contacts, the effect of the pore pressure on the carrying capacity of the solid skeleton is reduced by the fraction termed the Biot coefficient.

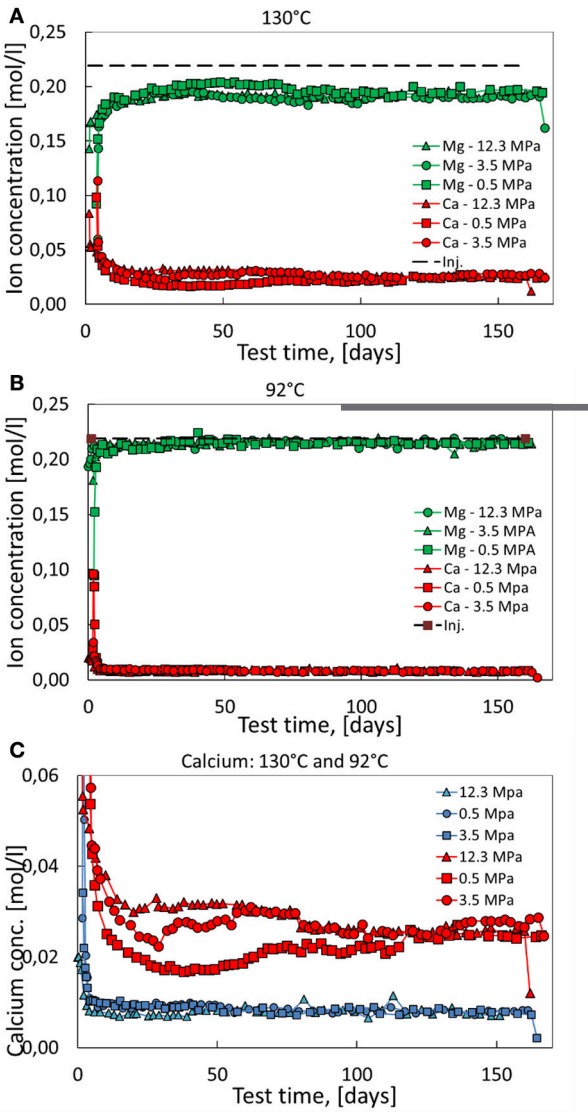

FIGURE 6 | Magnesium and calcium ion concentrations of the effluent at 92°C (A) and 130°C (B). The injected Mg^{2+}-concentration is shown as dashed line at 0.219 mol. **(C)** Comparing the calcium production dynamics from the 92°C and 130°C experiments.

These effects are included into the effective stress concept as shown in Equation (9). The Biot coefficient is, in this perspective, an indirect measure of the area of the fluid-solid contact area

TABLE 6 | Integrated effluent Ca^{2+} and Mg^{2+} concentrations.

Temp., °C	Stress MPa	$\Delta n(Mg^{2+})$ [mol]	$\Delta n(Ca^{2+})$ [mol]	$\Delta n(CO_3^{2-})$ [mol]	$\Delta m(Mg^{2+})$ [g]	$\Delta m(Ca^{2+})$ [g]	$\Delta m(CO_3^{2-})$ [g]	Δm_{tot} [g]	Δm_{meas} [g]
OBSV28 92°C 0.5 MPa	0.5	−0.030	0.044	0.014	−0.73	1.78	0.87	1.92	2.48
OBSV32 92°C 3.5 MPa	3.5	−0.030	0.040	0.010	−0.72	1.61	0.62	1.50	2.47
OBSV14 92°C 12.3 MPa	12.3	0.032	0.039	0.007	−0.78	1.56	0.42	1.20	2.52
OBSV21 130°C 0.5 MPa	0.5	−0.11	0.11	−0.00	−2.72	4.38	0	1.66	3.76
OBSV15 130°C 3.5 MPa	3.5	−0.16	0.15	−0.01	−3.86	5.91	(−0.6)	2.05	4.36
OBSV8 130°C 12.3 MPa	12.3	−0.15	0.15	−0.00	−3.72	6.13	0	2.41	4.22

When more Ca^{2+} is produced than Mg^{2+} this indicates dissolution of carbonate CO_3^{2-}. Positive sign is used when the produced fluid has a higher concentration than the injected concentration, i.e., $\Delta n = \int (c_{out} - c_{in})\, q\, dt$. The total produced and retained amount of each chemical component (in mol) are multiplied by the molar weight of Ca^{2+}, Mg^{2+}, and CO_3^{2-} to get their weights in grams. The estimated mass loss is compared to the mass loss measured on a scale.

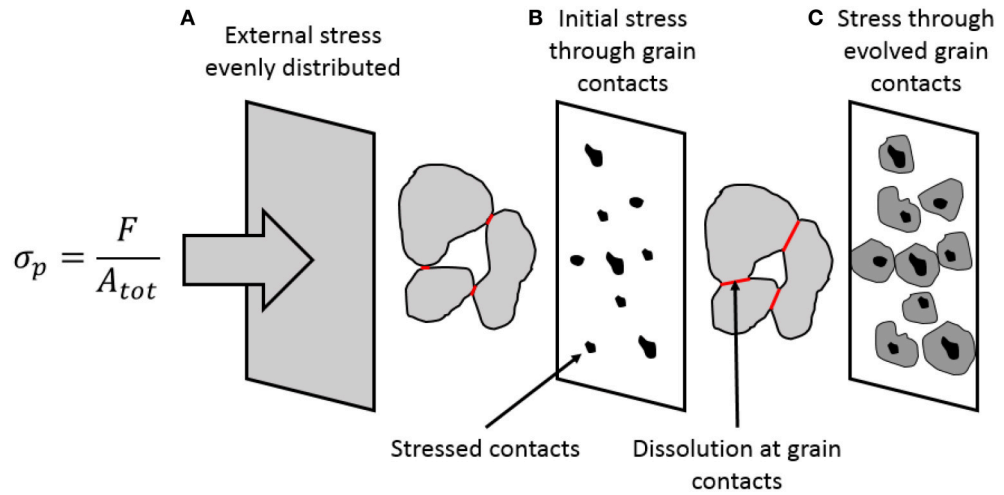

FIGURE 7 | (A) The external stress is evenly distributed over the plastic sleeve covering the whole plug. The stress is transmitted through the granular package through grain contacts. **(B)** Initially, the contact area is small compared to the total area , thus the contact stresses are large leading to localized dissolution either due to the electrochemical effects and-/or pressure solution at the grain contacts. **(C)** When the grain contacts evolve, and the relation of increase, this effect reduces the contact stresses thus reducing pressure solution effects with time.

$A_{f\to s}$ divided by the total area A_{tot} projected onto an arbitrary plane within the porous body:

$$\alpha = \frac{A_{f\to s}}{A_{tot}} = 1 - \frac{A_{s\to s}}{A_{tot}}. \tag{16}$$

Here, we have used that the total cross sectional area is the sum of the solid-to-solid contact areas $A_{s\to s}$ and the fluid-to-solid contact areas, $A_{tot} = A_{f\to s} + A_{s\to s}$. (For a discussion on the Biot coefficient see, e.g., [40]). In drained conditions, the pore fluids have ample time to escape the pore volumes during compaction, i.e., the deformation-rate is lower than the flow-rate such that the pore pressure is unaffected by the solid stresses ($\sigma_{f\to f} = 0$). Force balance considerations may be applied in static equilibrium. The externally imposed load is counteracted by the pore fluid pressure times the solid-fluid contact area plus the solid-solid skeleton stress times the solid-solid contact area (see e.g., [41, 42]). Thus:

$$\sigma_p A_{tot} = \sigma_{s\to s} A_{s\to s} + P A_{f\to s} \tag{17}$$

Re-arranging and using the Biot coefficient as defined in Equation (16), the magnitude of the solid-solid stress will be given as:

$$\sigma_{s\to s} = \frac{A_{tot}}{A_{s\to s}}(\sigma_p - \alpha P) = \frac{\sigma'}{1-\alpha}. \tag{18}$$

The Biot coefficient for the type of rocks tested here has been shown to vary between 0.8 and 0.99 (see e.g., [40, 43], and references therein), such that the contact stresses are a factor from 5 to 100 times larger than the effective stress imposed to the system. If this is the case then the contact stresses could be sufficient for pressure-solution of calcite grains to occur [22, 24].

With time pressure solution leads to localized dissolution, thereby increasing the solid-to-solid contact areas as sketched in **Figures 7B,C**, where granular contact areas have increase in size. This effect would then reduce the Biot stress coefficient α and this would reduce the solid-solid contact stresses that drive additional dissolution. Thus, the stress driven dissolution process

is reduced with time. It is exactly this effect that is observed in the continuous monitoring of the effluent brines in **Figure 6**, and especially in **Figure 6C** where the calcium concentration of the produced effluent attains the same value from approximately 80 days and onward. Thus, dissolution from the stressed contacts seem to stop. Remark that the stress-driven dissolution effect is only observed for the 130°C experiments.

Model of Chemo-Mechanical Creep Curve Dynamics

As was seen in Section Quantifying Primary Creep Dynamics, the data by itself cannot univocally identify with certainty the functional form of the observed creep as several models may fit the observed behavior equally well. In this section, we develop an analytical primary creep model from more basic principles from simple additive partitioning between the chemical and mechanical component, which is based on the coinciding residual for the 12.3 MPa experiment and the creep curve of the 3.5 MPa experiments at 130°C (see **Figure 4C**).

Assume that the observed strain may be partitioned into a pore volume and a solid volume component:

$$\varepsilon_{vol} = \varepsilon_p + \varepsilon_s \tag{19}$$

This assumption is always valid in a porous material of solids and voids where the pore volume reduction is associated with re-organization of grains, and the solid volume reduction is associated with rock-fluid interactions (dissolution and precipitation) changing the solid volume. In both [17, 21] the compositional changes have been documented displaying how $MgCl_2$ flooding of chalk leads to calcite—magnesite replacement. This again leads to density increase and mass loss which changes the solid volume. The assumption that the volume change is constant through time implies that there are adequate amounts of calcite surfaces available for reactions (unlike what was shown in [17]). In the partitioning above we make a further assumption that cross-terms are omitted i.e., how the grain re-organization would affect the solid volume development, and *vice versa*.

From Equations (4) and (8) we may rewrite the bulk volume rate as:

$$\frac{dV_b}{dt} = \frac{dV_p}{dt} + \frac{dV_s}{dt} = \phi\frac{dV_b}{dt} + V_b\frac{d\phi}{dt} - \beta, \tag{20}$$

where the pore volume at any time is given by the product of the porosity and the bulk volume ($V_p = \phi V_b$), and the change in solid volume is given by the factor β calculated from Equation (14) using the solid volume changes reported in **Tables 1**, **2** divided by time. Assuming constant solid volume rate, we get 0.01 ml/day for the 130°C experiments and 0.005 ml/day for the 92°C experiment.

In Equation (20) the time-dependent variables are the bulk volume and the porosity. During compaction and primary creep the porosity is decreasing through time. The simplest possible conjecture would be to introduce a rate of change in porosity which is proportional to the porosity itself, such that the compaction is more rapid for high porosity than for smaller porosities. Since grain reorganization cannot continue until zero porosity, a terminal porosity ϕ_c is introduced. The parameter ϕ_c will act as a fix-point for the differential equation. Under the assumption that $n > 0$ a porosity evolution equation:

$$\frac{d\phi}{dt} = -\alpha\left(\phi - \phi_c\right)^n \tag{21}$$

may be introduced. For $n = 1$ and $\phi_c = 0$, we have that $\phi = \phi_0 e^{-\alpha t}$ and an analytical solution:

$$V_b(t) = \frac{V_{b,0}\left(1-\phi_0\right)e^{\alpha t}}{e^{\alpha t} - \phi_0} - \frac{\beta t}{1 - e^{-\alpha t}} \tag{22}$$

exists for the bulk volume evolution. By using Equation (8) we obtain the creep function:

$$\varepsilon_{vol}(t) = \frac{\left(1-\phi_0\right)e^{\alpha t}}{e^{\alpha t} - \phi_0} - \frac{\beta t}{V_{b,0}\left(1 - e^{-\alpha t}\right)} - 1. \tag{23}$$

In this model the value of the parameter β is fixed from the experiments to (0.01 and 0.005 ml/day for the 130 and 92°C, respectively); while α remains a free variable. In **Figure 8**, the model described above is integrated numerically and matched (by hand) to the experimental data with values of n, α and ϕ_c as described in the caption for the two experiments performed at 92 and 130°C, with 12.3 MPa effective stress.

Compaction Exposes Fresh Reactive Mineral Surfaces

Deformation by grain re-organization and pore collapse alters the local porosity field through the rock. Most likely the deformation is non-uniform as the material parameters may vary through the core. This depends upon the mesoscale dimensions that locally defines the material. As such, also the permeability field may change both with time and space within the core. Alterations in the permeability field change the flow pattern. Given that dissolution/precipitation is limited by the flow and not the

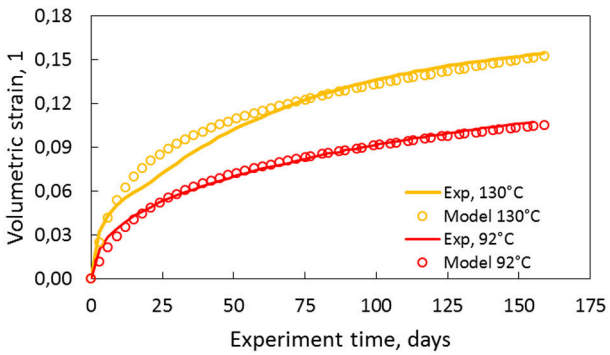

FIGURE 8 | Volume strain observed in solid lines for 130 and 92°C at 12.3 MPa effective stress. The open circles are the model proposed in the text where the values of $n = 3$, $\alpha = 6$, and $\phi_C = 0.375$ were used to match the 92°C experiment, and $n = 3$, $\alpha = 7$, and $\alpha = 0.355$ were used to match the 130°C experiment. The value of β is used obtained from the experiment. α describes the exponential porosity evolution decay rate, and hence the rate of pore volume reduction.

chemical kinetics, the amount of fluid passing through a volume of the core within a time interval determine the degree of chemical alteration. Since the reactions under investigation here reduce the solid volume, a positive feed-back mechanism may be proposed. If the flow is, for some reason, focused within a region of the porous body, this leads to enhanced chemical reaction in this region. Now, if the chemical reaction leads to solid volume reduction (and a local porosity increase), this would lead to further focusing of the flow through this region. This positive feed-back mechanism is often termed worm-holing [44] and has, e.g., been used to understand the destruction of dams.

However, when compaction is taken into consideration, this is often localized to regions of the core with higher porosity, because the grains there may re-organize more easily. When the grain volumes are reduced with time, the local porosity increases and compaction becomes more likely within the next time-interval [45]. Such a negative feed-back mechanism would distribute the flow over a larger region and inhibit worm-holing to occur. With time, it is therefore likely that in the high-stress experiments the injected brine comes in contact with all the reactive surfaces in the core. This leads to enhanced chemical reactions, compared to the low stress experiments where worm-holing would focus the chemical alteration to localized areas.

An example of worm-holing can be seen on the inlet side of the core shown in **Figure 9** for the experiment exposed to 130°C and 0.5 MPa effective stress. Since the injected brine is not in equilibrium with the rock, and since the brine is injected through holes in a drainage plate on the inlet side of the core, we have localized dissolution close to the inlet points, while the injected brine and the rock equilibrate chemically. Whether the spots seen on this image will grow or not, is determined by temperature, brine chemistry, and degree of compaction. When $MgCl_2$ is injected at 130°C we often see areas of filled half-spheres where the rock structure has been altered, most likely due to dissolution and re-precipitation of Mg-bearing minerals. Other experiments performed within our laboratories indicate that when, on the other hand, NaCl-brine is injected, void half-spheres form around the inlet points.

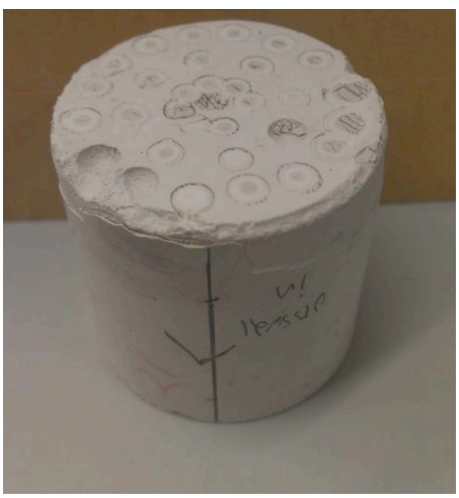

FIGURE 9 | Inlet side of the 130°C and 0.5 MPa effective stress (OBSV21) core after the experiment completed. In this experiment the stresses are too low to induce compaction and grain re-organization, although the temperature is high such that dissolution/precipitation occurs at the entry-points of the injected $MgCl_2$ fluids.

How Chemical Interactions Changes Rock Properties

In this section we present the rock observations that were made before and after the experiments were performed. The spatial dimensions of the plug were measured and the bulk volume was estimated. The axial to radial strain ratio for the different experiments was used to estimate the correction factor ξ (Equation 8). As can be seen in **Tables 1**, **2**, the radial strains are less than the strain in the axial direction (i.e., $\xi < 1$). The bulk volume changes depend significantly on the creep stress. In addition, the saturated and dry masses were measured before and after the experiment. Similarly, the porosity was estimated to be the difference between the dry and saturated mass divided by the bulk volume. For the low stress experiments (with almost zero deformation), the porosity increased by 2.16 and 1.03% for the 130 and 92°C experiments, respectively. This indicates that the solid volume has been reduced. Since the total volume is given as the solid volume together with the pore volume, the dry mass and porosity can be re-combined to estimate the average mineral density. These results show that the mineral density increased from approximately 2.69–2.70 g/ml, before the experiment, to 2.72, 2.71, and 2.73 g/ml after for the 0.5, 3.5, and 12.3 MPa experiments, respectively (130°C). Such density changes are not seen for the 92°C experiments. Typically, pore volume estimates based on dry and saturated cores combined with the bulk volume measurements vary within 0.01–0.02 g/ml. These estimates are in agreement with the gas adsorption pycnometry data that is also shown in **Tables 1**, **2**.

Interestingly, when comparing the dry mass of the core before and after the experiments, one observes a significant mass reduction. For the 130°C experiments, the mass losses are 3.72 g (3.1%), 4.34 g (3.4%), and 4.19 g (3.3%) for, respectively, the 0.5, 3.5, and 12.3 MPa experiments. The mass loss relative to the initial mass is given in parentheses. We see that more mass is lost for the high stress experiments (3.5 and 12.3 MPa) compared to the low-stress experiment (0.5 MPa). However, the relative mass loss measured on the scale is not seen to change significantly with stress, though the integrated $CaCO_3$ dissolution from IC data is stress dependent. Additional experiments are required to quantify if these observations are significant. In the 92°C experiments the mass loss is 2.48 g (2.1%), 2.47 g (2.0%), 2.52 g (2.0%) for the 0.5, 3.5, and 12.3 MPa effective stress experiments, respectively. We observe from the rock measurements conducted that the chemical interactions depend on temperature and stress, which is in accordance with what was reported in Section Quantifying Primary Creep Dynamics, and typically, higher temperature and higher stress lead to enhanced chemical reactions. The loss of mass and increased mass density leads to changes in the solid volume.

TABLE 7 | Summary of the results of all experiments performed at the two temperatures and the three stresses.

	0.5 MPa effective stress Δm[%], K, and Yield	**3.5 MPa effective stress Δm[%], K, and Yield**	**12.3 MPa effective stress (for α = 1), Δm[%], K and Yield**
92°C	(OBSV28)	(OBSV32)	(OBSV14)
	Δm = −2.48 g (−2%)	Δm = −2.43 g (−2%), K = 0.55 GPa	Δm = 2.52 g (−2%), K = 1.2GPa, Y_O = 9.2 MPa
	−1.92 g carbonate from IC	−1.50 g carbonate from IC	−1.20 g carbonate from IC
	−0.56 g silicate	−0.93 g silicate	−1.32 g silicate
	1.03% increase porosity	0.68% increase porosity	−4.68%decrease in porosity
	0.1% volume strain	0.9% volume strain	10.3% volume strain
	0.65 radial/axial strain ratio	0.95 radial/axial strain ratio	0.61 radial/axial strain ratio
130°C	(OBSV21)	(OBSV15)	(OBSV08)
	Δm = −3.79 g (−3.1%)	Δm = −4.36 g (−3.4%), K = 1.04 GPa	Δm = −4.22 g (−3.3%), K = 0.76 GPa, Y = 5.8 MPa
	−1.66 g carbonate	−2.05 g carbonate	−2.41 g carbonate
	−2.3 g silicate	−2.31 g silicate	−1.81 g silicate
	1.21% increase porosity	0.54% increase porosity	−5.65% decrease in porosity
	0.02 g/cc increase in density	0.01 g/cc increase in density	0.03 g/cc increase in density
	0.2% volume strain	5.9% volume strain	16.3% volume strain
	0.345 radial/axial strain ratio	0.292 radial/axial strain ratio	0.706 radial/axial strain ratio

The carbonate loss is estimated from the IC-data integrated in Equations (11) and (12). The rest is assumed to be related to silicate dissolution.

The solid-volume changes during flow of $MgCl_2$ brines in chalks have previously been shown to be related to the dissolution of $CaCO_3$ and the precipitation of Mg^{2+}-bearing minerals such as dolomite and magnesite (see e.g., [17, 21]). These minerals all have a density larger than calcium carbonate, which is in agreement with the gas adsorption measurements reported. For constant mass, this gives a reduction in the solid volume. When the mass is reduced, in addition to an increased density, this leads to a further decrease in solid volume.

Now, since the ion weight of Mg^{2+} and Ca^{2+} are 24.31 and 40.08 g/mol, respectively, any exchange between the production of Ca^{2+} and retention of Mg^{2+} would reduce the mass of the core. When integrating the amount of Mg^{2+} retained in the core (adds to the core weight) and the production of Ca^{2+} (reduces the core weight), we calculate a mass loss of 1.92, 1.50, and 1.20 g for the 92°C IC-data, and a loss of 1.66, 2.05, and 2.41 g for the 130°C experiments, for 0.5, 3.5, and 12.3 MPa effective stresses, respectively (see **Table 6**). These numbers can be compared to the mass loss measured by weighing the core on the scale after the experiment (see **Tables 1**, **2**, **6**). For the 92°C experiments, stoichiometry results are not perfectly satisfying, indicating that small amounts of CO_3^{2-} are produced from the core. The discrepancy between the weight loss measured on the scale (dry weight) and the one estimated from the IC-data indicates that not only dissolution of calcium carbonate occurs but also precipitation of magnesium carbonate. The same mass loss discrepancy has been reported and discussed earlier by Nermoen et al. [17] for $MgCl_2$ flow through Liège chalk. Equilibrium calculations indicate that the silicate minerals that are present in some of these chalks will dissolve when using $MgCl_2$ brines at these pressure and temperature conditions [18, 19]. Thus, dissolution of silicates (clays, quartz etc.) are expected. Further geochemical analyses of the rock chemistry (such as e.g., X-ray diffraction and whole rock geochemistry) are required to understand the presented mass loss discrepancy in this case.

Porosity Development

In a porous material the porosity is defined as the ratio of the pore volume to the bulk volume. Using the constituency relation in Equation (4) any changes in the bulk volume are caused by either changes in the solid/mineral volume and/or changes of the pore volume, thus the porosity become:

$$\phi(t) = \frac{\mathrm{V_{p,0}} + \Delta V_b(t) - \Delta V_s(t)}{V_{b,0} + \Delta V_b(t)}, \tag{24}$$

where we have used Equation (5) for the changes in ΔV_p. If we now divide by the initial bulk volume $V_{b,0}$ and use the definition of the volumetric strain in Equation (8) we arrive at a porosity evolution equation that takes into account both changes to the bulk volumetric strain and the solid volume changes:

$$\phi(t) = \frac{\phi_0 - \varepsilon_{vol}(t) - \frac{\Delta V_s(t)}{V_{b,0}}}{1 - \varepsilon_{vol}(t)} \tag{25}$$

Since neither the volume of solids nor the bulk volumes are conserved in these experiments, the porosity displays a rather complex behavior. Higher hydrostatic stress is linked to more reduction in the bulk volume. Simultaneously, the experiments have shown that the solid volume changes also increase with stress. With respect to porosity, increased stresses lead to volumetric compaction that are more important than how the stress alters the solid volume. For the tests at 130°C, more dissolution/precipitation is observed at 3.5 and 12.3 MPa than at 0.5 MPa. However, at 12.3 MPa the volumetric compaction leads to a porosity reduction from 41.31 to 35.66%,

since compaction dominates over dissolution/precipitation. At 3.5 MPa the chemical alteration and volumetric compaction are almost the same since the porosity only increases from 41.00 to 41.54%. At 0.5 MPa, compaction is insignificant compared to dissolution/precipitation since the porosity increases from 40.77 to 42.98%. In the experiments performed at 92°C the porosities change from 40.81% to 41.84%, 41.32% to 42.00%, and 40.52% to 35.84% for the 0.5, 3.5, and 12.3 MPa tests, respectively. When comparing the experiments performed for 3.5 MPa effective stress, the porosity increase is larger at 92°C than at 130°C (0.7 and 0.5% respectively). More dissolution and more strain are accumulated at 130°C than at 92°C, with volumetric compaction of 2.3 and 0.7 ml, and solid mass loss of 4.34 and 2.47 g respectively. For the 12.3 MPa experiment the situation is opposite with respect to temperature. Here, the porosity declined by −4.68% for the 92°C experiment while −5.65% for 130°C. Thus, when evaluating the porosity evolution during chemo-mechanical compaction both compaction, mass exchange and density alteration are tightly connected (see also [17]) as the relative importance of compaction and mass exchange are both temperature and stress dependent. See an overview in **Table 7**.

Changes to the Produced Solute Concentration

The effluent concentration is affected by mineral dissolution and precipitation. From Equation (4.66) in [46] a general rate law for the reaction rate (R), in units mole/L/s, can be written as:

$$R = \frac{dc}{dt} = \mathrm{k}\frac{A_0}{V_p}\left(\frac{n}{n_0}\right)^n g(C), \tag{26}$$

where the factor k is the specific rate (mole/m^2/s), A_0 is the initial total surface area of the solid (m^2), V is the volume of the solution (i.e., pore volume, m^3), and n/n_0 is the ratio of the current to initial moles of the reactive solids (i.e., $CaCO_3$) at a given time. Here, $g(C)$ depends on the distance from equilibrium, which incorporates the solution composition and the changes to the rock. The parameters above may evolve with time as the chemical components are transported through the core and hence lead to localized precipitation and dissolution. The primary result from the experiments is that the produced Ca-concentration is higher for the high-stress experiments than the low-stress experiments. In order to capture this observation we may simplify the physics described in Equation (25). In the high stress experiments, grain re-organization leads to reduction in the pore volume, and hence increased reaction rate, compared to the low-stress experiments. The pore volume at any given time is simply given by the product of the porosity evolution times the bulk volume from recasting Equation (8) into $V_b = V_{b0}(1-\varepsilon_b)$. Under the assumption that differences in, A_0, m/m_0, n, and $g(C)$ are small compared to the pore volume changes, we may re-scale Equation (25) to obtain the ratio of produced Ca- concentrations of the 12.3 MPa experiment to the concentrations in the 0.5 MPa experiment:

$$\frac{R_{12.3}(t)}{R_{0.5}(t)} = \frac{dc_{12.3}(t)}{dc_{0.5}(t)} \propto \frac{V_{p,0.5}(t)}{V_{p,12.3}(t)}\frac{V_{p,orig,12.3}}{V_{p,orig0.5}} \tag{27}$$

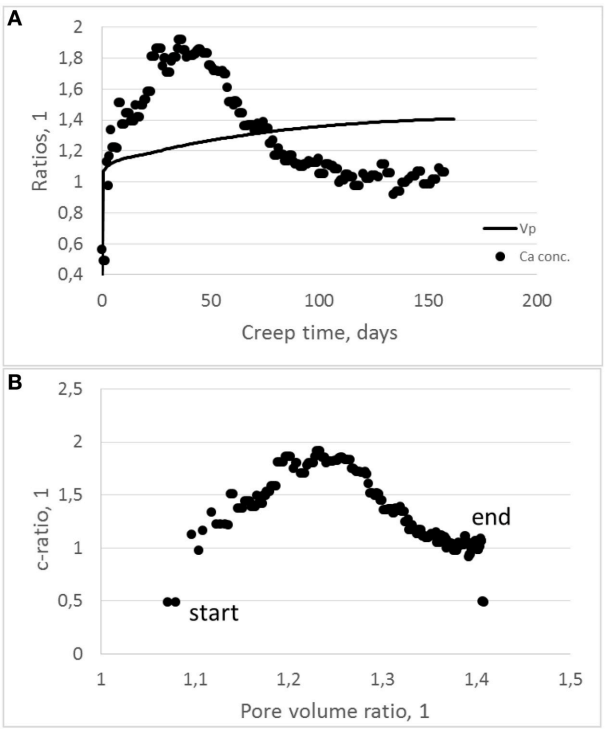

FIGURE 10 | (A) The pore volume ratio for the 0.5 divided by the 12.3 MPa development (solid line) plotted together with the calcium concentrations ratios for the same experiments (dots) as function of test time. **(B)** Displaying the correlation between the ratio of the effluent Ca-concentration divided by the pore volume ratio. As can be seen, a positive correlation is seen the first 30 (or so) days. The peak concentration ratio occurs after 30–40 days, before a negative trend is observed.

Please note that here we only address the effect of solute pore volume reduction and omit any differences in, e.g., n (which depends on the integrated concentrations). The comparison between the 0.5 and 12.3 MPa experiment is shown in **Figure 10**.

Microstructural Observations

Scanning electron microscopy (SEM) and energy dispersive spectroscopy (EDS), performed at University of Stavanger display the changes to the microstructure morphology and the element concentrations. All the SEM-EDS that are reported have been performed approximately 0.8 cm into the core from the inlet and approximately 0.2 cm from the center axis. This is because Zimmermann et al. [21] has shown how the replacement reaction varied throughout the core. The microstructural morphology varies spatially and heterogeneities can be observed on a variety of scales, see also [17]. SEM images of tested cores (a, b, and c) and un-tested (d) chalk can be seen in **Figure 11**. Comparing (a) and (b) we can see the effect of compaction. As is shown in **Table 7**, the 0.5 MPa at 130°C increased its porosity by 1.21% while the porosity decreased by 5.65% for the 12.3 MPa at 130°C test. The foraminifers and coccolith rings that can be seen in (d) are still visual in the tested cores (a, b, and c), although the overall morphology of the mineral structure seem less ordered because of

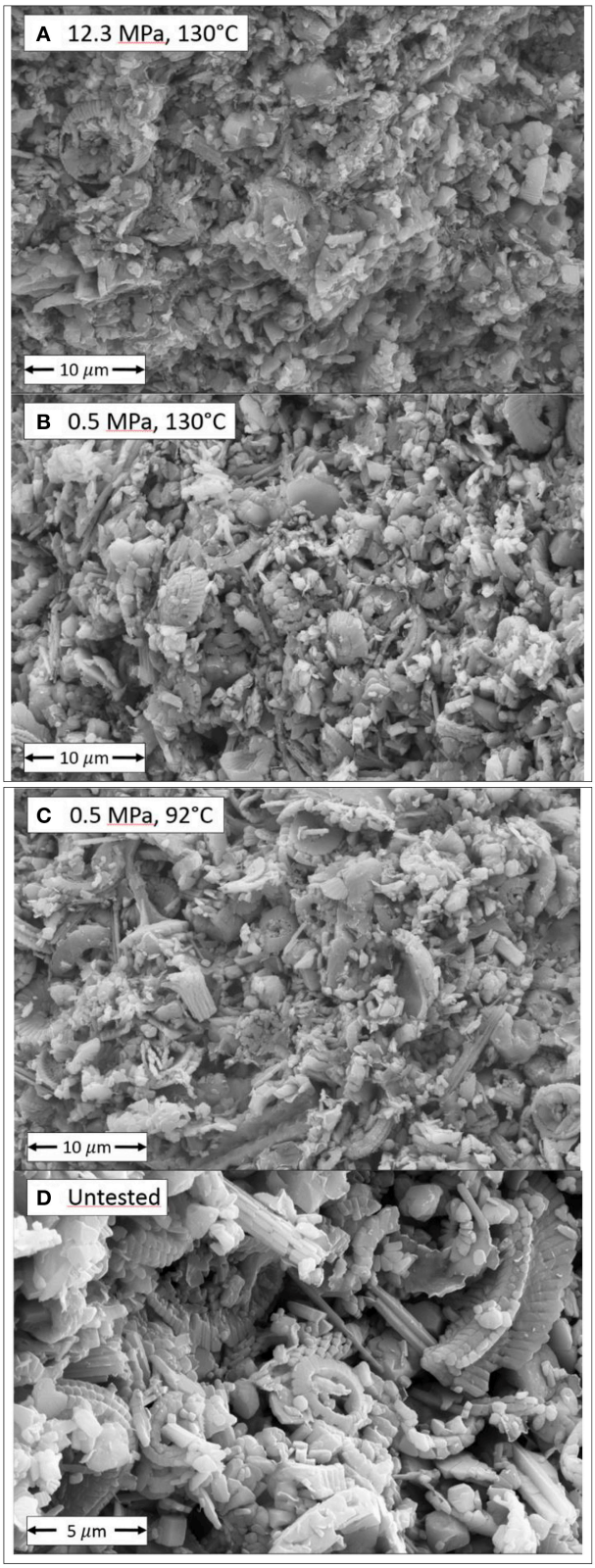

FIGURE 11 | High resolution SEM images of the microstructure of tested cores at varying effective stress and test temperature. Scale *(Continued)*

FIGURE 11 | Continued
bare is shown. Coccolith rings and foraminifers can be seen. In **(A)** the 130°C and 12.3 MPa experiment can be seen and compared to **(B)** in which the 130°C and 0.5 MPa experiment is observed. The microscopic morphology of the grain package seem denser at the high stress test **(A)** than the low stress test **(B)**. In **(C)** the 0.5 MPa and 92°C experiment is shown. The tested material can be compared to the untested core material shown in **(D)**.

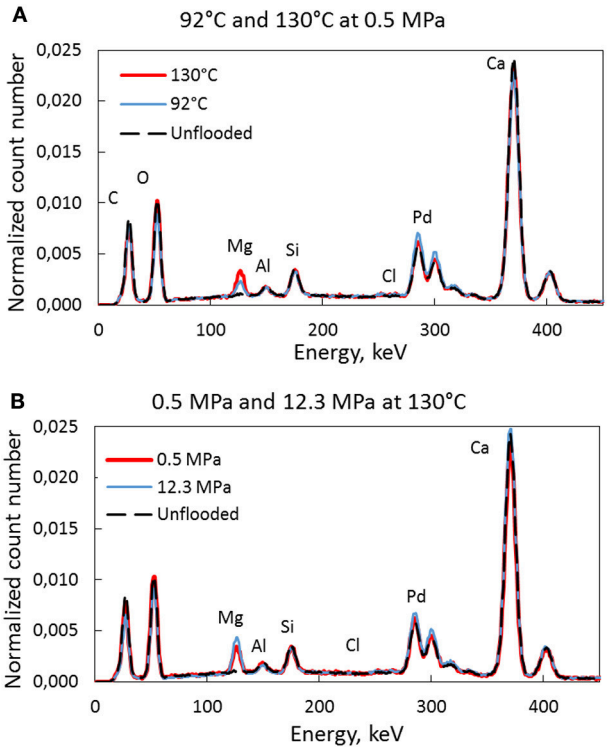

FIGURE 12 | EDS spectra of the tested core material with peaks for the different elements. The effect of temperature is shown in **(A)** where more Mg is seen for the high temperature test. This is the same trend as for the high-stress experiment compared to the low stress experiment in **(B)**.

the precipitate nucleation and growth. To what extent the grains are dissolved at grain boundary contacts, cannot be conclusively observed from the reported SEM images.

Figure 12A displays the differences of the EDS diagram for the 92 and 130°C test without stress. As can be seen, more Mg is observed in the core at higher temperature. Each EDS-curve is an average of two measurements and the number of counts at any energy are divided by the total number such that a direct comparison of the count—numbers can be made. In **Figure 12B** the effect of stress can be seen. Again, the amount of replaced Mg is higher for the high-stress experiment. Even though the Mg—trends are as expected from the IC-data, shown in **Figures 6A–C** care should be taken in the interpretation due to the uncertainty of these EDS measurements. When it comes to the other measured elements (C, O, Al, Si, Cl) they are unchanged while the Pd arise from the

coating (standard procedure in the preparation of the SEM samples). The Ca-concentration seems unchanged in the EDS spectra (**Figure 12**) even though Ca-ions were produced from the core.

CONCLUSIONS

The mechanical and chemical results from a series of flow-through experiments are reported. The test matrix consists of two temperatures (92 and 130°C) and three effective stresses (0.5, 3.5, and 12.3 MPa). The experiments have been performed on chalk obtained from a single chalk block from the Obourg Saint Vast quarry in Mons, Belgium. Twenty seven cores were produced and out of these, six cores of similar porosity were selected such that a one-to-one comparison could be made. The cores were continuously flooded with 0.219 M $MgCl_2$ brine at a rate of one initial pore volume per day.

The experiments were loaded and allowed to creep over time and total test duration ranged from 153 to 165 days, Basic quantities such as dry mass lost (relative to the initial mass) and volumetric strain could therefore be compared for all experiments.

We have shown that the produced Ca^{2+}-concentration vary with stress for the 130°C experiments. A similar stress dependency is not observed for the 92°C experiments. Mechanical deformation and stress may couple to the chemistry of mineral dissolution and precipitation in several ways. Several mechanisms have been discussed to explain the exact physicochemical mechanisms at play. A simplified creep model has been suggested based on a simple additive partitioning between the pore volume and solid volume development. Although, being simplified, this model paves the way for more realistic developments in the future where for instance full coupling between the two processes should be included: Chemical reactions trigger pore volume reduction, and stress conditions affects the rate of chemical reactions.

The perhaps most significant result from this paper is the documentation of how the effluent concentrations change with time for different stress and temperatures. Three mechanisms were suggested. First, we discussed the impact of pressure solution leading to dissolution in the stressed inter-granular contacts. We used the Biot stress coefficient to argue that the local stresses at grain contacts may be adequate for pressure solution to occur if the relevant thermodynamic pressure is the same as the skeleton stresses at grain contacts. Secondly, compaction and deformation alters the microscopic granular structure. This changes the way in which fluids are moving through the core. We believe that initially the flow is focused within volumes with the highest porosity, and within the next time interval, it is in these regions compaction and chemical effects occurs. The compaction by grain re-organization leads to local permeability loss, thereby diverting the fluids to other parts of the core. Thus, compaction would dynamically alter the fluid flow through the core such that the produced effluent concentrations are higher for the high-creep strain experiments. A third mechanism is related to how dissolution and precipitation alters the reactive surface area with time which is important for the effluent sample dynamics (see [17, 36]).

The integrated Mg^{2+}/Ca^{2+} stoichiometry is almost perfectly conserved for the 130°C experiments, but not at 92°C where more Ca^{2+} is produced from the core than the amount of Mg^{2+} that is retained (see **Table 6**). Since the chalk contains non-carbonate minerals and since rock-fluid interactions are temperature dependent, different minerals are involved in the dissolution/precipitation process. The non-stoichiometry at 92°C indicates that, e.g., CO_3^{2-} ions are produced. The observed discrepancy between the estimated mass loss (from IC data) and the mass loss measured on the scale strengthens the need for complete geochemical models such as those presented in [18]. More detailed geo-chemical investigations of the rocks, before and after experiments, are required to determine whether or not the production of non-carbonates, such as silicate bearing clays, can be at play. In Zimmermann et al. [21] they describe the compositional/mineralogical changes of a chalk for a $MgCl_2$ flow-through experiment. ICP analyses of the effluent brines would help to quantify the production of additional ions such as Fe, Si, Al, etc. It is important to note that the stress dependency almost disappears when considering the mass loss measured on a scale. We have shown that the mass loss estimated from the Mg^{2+} and Ca^{2+} ion dynamics is stress dependent at 130°C for the first 100 days or so.

AUTHOR CONTRIBUTIONS

All authors listed, have made substantial, direct and intellectual contribution to the work, and approved it for publication.

ACKNOWLEDGMENTS

We would like to thank Larry M. Cathles for offering constructive criticism and valuable comments to this work. We also thank Mona Minde for the SEM-EDS measurements obtained at University of Stavanger, Norway. The authors acknowledge the Research Council of Norway and the industry partners; ConocoPhillips Skandinavia AS, BP Norge AS, Det Norske Oljeselskap AS, Eni Norge AS, Maersk Oil Norway AS, DONG Energy A/S, Denmark, Statoil Petroleum AS, GDF SUEZ E&P NORGE AS, Lundin Norway AS, Halliburton AS, Schlumberger Norge AS, Wintershall Norge AS of The National IOR Centre of Norway for support.

REFERENCES

1. Fabricius IL. Burial stress and elastic strain of carbonate rocks. *Geophys Prospect*. (2014) **62**:1327–36. doi: 10.1111/1365-2478.12184
2. Amitrano D, Helmstetter A. Brittle creep, damage, and time to failure in rocks. *J Geophys Res Solid Earth* (2006) **111:**B11. doi: 10.1029/2005JB004252
3. Turcotte D, Schubert, G. *Geodynamics, 2nd Edn.* Cambridge: Cambridge University Press (2002).

4. Durand J. *Sands, Powders and Grains—An Introduction to the Physics of Granular Materials*. New York, NY: Springer (1997).
5. Nagel NB. Compaction and subsidence issues within the petroleum industry: from Wilmington to Ekofisk and Beyond. *Phys Chem Earth (A)* (2001) **26:**3–14. doi: 10.1016/S1464-1895(01)00015-1
6. Preston C, Monea M, Jazrawi W, Brown K, Whittaker S, White D, et al. IEDA GHG Weyburn CO_2 monitoring and storage project. *Fuel Proces Technol.* (2005) **86:**1547–69. doi: 10.1016/j.fuproc.2005.01.019
7. Terzaghi KV. Die berechnung der durchassgikeitsziffer des tones aus dem Verlauf der hydrodynamishen Spannungserscheinungen. *Sitzungsber Akad Wiss Wien Math Naturwiss Kl Abt*. (1923) **2A**:105.
8. Biot MA. General theory of three-dimensional consolidation. *J Appl Phys*. (1941) **12:**155–64. doi: 10.1063/1.1712886
9. Nur A, Byerlee JD. An exact effective stress law for elastic deformation of rock with fluids. *J Geophys Res.* (1971) **76:**6414–9.
10. Hermansen LK, Thomas JE, Sylte JE, Aasboe BT. Twenty five years of ekofisk reservoir management. In: *SPE Annual Technical Conference and Exhibition*. San Antonio, TX (1997). p. 873–85. doi: 10.2118/38927-MS
11. Thomas LK, Dixon TN, Evans CE, Vienot ME. Ekofisk waterflood pilot. *J Pet Technol.* (1987) **283**:221–32.
12. Hermansen H, Landa GH, Sylte JE, Thomase, LK. Experiences after 10 years of waterflooding the Ekofisk Field, Norway. *J Pet Sci Eng.* (2000) **26**:11–8.
13. Jensen TB, Harpole KJ, Østhus A. *EOR Screening for Ekofisk*. Paris: Society of Petroleum Engineers (2000).
14. Awan AR, Teigland R, Kleppe J. A survey of North Sea enhanced oil recovery projects initiated during the years of 1975 to 2005. *SPE Reserv Eval Eng.* (2008) **11**:497–512. doi: 10.2118/99546-PA
15. Spencer AM, Briskeby PI, Dyrmose Christensen L, Foyn R, Kjølleberg F, Kvadsheim E, et al. Petroleum Geoscience in Norden—exploration, production and organization. *Episodes* (2008) **31:**115–24.
16. Megawati M, Hiorth A, Madland MV. The impact of surface charge on the mechanical behaviour of high-porosity chalk. *Rock Mechan Eng.* (2012) **46**:1073–90. doi: 10.1007/s00603-012-0317-z
17. Nermoen A, Korsnes RI, Hiorth A, Madland MV. Porosity and permeability development in compacting chalks during flooding of non-equilibrium brines - insights from long term experiment. *J Geophys Res Solid Earth* (2015) **120**:2935–60. doi: 10.1002/2014JB011631
18. Hiorth A, Cathles L, Madland M. The impact of pore water chemistry on carbonate surface charge and oil wettability. *Transp. Porous Med.* (2010) **85:**1–21. doi: 10.1007/s11242-010-9543-6
19. Madland M, Hiorth A, Omdal E, Megawati M, Hildebrand-Habel T, Korsnes R, et al. Chemical alterations induced by rock-fluid interactions when injecting brines in high porosity chalks. *Transp Porous Med.* (2011) **87:**679–702. doi: 10.1007/s11242-010-9708-3
20. Cathles L. *Eq-Alt-Equilibrium Chemical Alteration in Combined Physical and Chemical Geofluids Modeling*. Windsor, ON: University of Windsor (2006).
21. Zimmermann U, Madland MV, Hildebrand-Habel NAT, Bertolino SAR, Hiorth A, Korsnes RI, et al. Evaluation of the compositional changes during flooding of reactive fluids using scanning electron microscopy, nano-secondary ion mass spectrometry, x-ray diffraction, and whole rock geochemistry. *AAPG Bull.* (2015) **99:**791–805. doi: 10.1306/12221412196
22. Hellmann R, Renders PJN, Gratier J-P, Guiguet DR. Experimental pressure solution compaction of chalk in aqueous solutions. Part 1. Deformation behavior and chemistry the geochemical society, special publication. *Water Rock Interact Depos Environ Geochem*. (2002) **7:**129–52.
23. Croize D, Rendard F, Gratier J-P. Compaction and porosity reduction in carbonates: a review of observations, theory and experiments. *Adv Geophys*. (2013) **54:**181–238. doi: 10.1016/B978-0-12-380940-7.00003-2
24. Croize D, Renard F, Bjørlykke K, Dysthe DK. Experimental calcite dissolution under stress: evolution of grain contact microstructure during pressure solution creep. *J Geophys Res.* (2010) **115**:B09207. doi: 10.1029/2010JB000869
25. Røyne A, Bisschop J, Dysthe DK. Experimental investigation of surface energy and subcritical crack growth in calcite. *J Geophys Res*. (2011) **116**:B04204. doi: 10.1029/2010JB008033
26. Hjuler ML, Fabricius I. Engineering properties of chalk related to diagenetic variations in the Upper Cretaceous onshore and offshore chalk in the North Sea Area. *J Petrol Sci Engin*. (2009) **68:**151–70. doi: 10.1016/j.petrol.2009.06.005
27. Charlez PA. *Rock Mechanics: Theoretical Fundamentals.* Paris: Editions Technip (1991).
28. Fjær E, Holt RM, Horsrud P, Raaen AM, Risnes R. *Petroleum Related Rock Mechanics, 2nd Edn.* Amsterdam: Elsevier (2008). p. 491
29. Korsnes RI, Madland MV, Austad T, Haver S, Røsland G. The effects of temperature on the water weakening of chalk by seawater. *J Petrol Sci Engin.* (2008) **60:**183–93. doi: 10.1016/j.petrol.2007.06.001
30. Omdal E. *The Mechanical Behavior of Chalk Under Laboratory Conditions Simulating Reservoir Operations (Phd Thesis).* Stavanger: University of Stavanger (2010).
31. de Waal JA. *On the Rate Type Compaction Behavior on Sandstone Reservoir Rock.* Amsterdam (1986).
32. Andersen MA, Foged N, Pedersen HF. *The Rate-Type Compaction of Weak North Sea Chalk.* Alexandria, VI: American Rock Mechanics Association (1992). 253–61 pp.
33. Griggs D. Creep of rocks. *J Geol.* (1939) **47:**225–51.
34. Bak P. *How Nature Works.* New York, NY: Copernicus Springer - Verlag (1996).
35. Stumpf MPH, Porter MA. Critical truths about power laws. *Science* (2012) **335:**665–6. doi: 10.1126/science.1216142
36. Pedersen J, Vinningland JL, Jettestuen E, Madland, MV, Hiorth A. Pore scale modeling of brine dependent pore space evolution in carbonates. (2013) *SPE* **164849:**1–10. doi: 10.2118/164849-ms
37. Karoussi O, Hamouda AA. Imbibition of sulfate and magnesium ions into carbonate rocks at elevated temperatures and their influence on wettability alteration and oil recovery. *Energy Fuels* (2007) **21**:2138–46. doi: 10.1021/ef0605246
38. Hiorth A, Jettestuen E, Cathles LM, Madland MV. Precipitation, dissolution, and ion exchange processes coupled with a lattice Boltzmann advection diffusion solver. *Geochim Cosmochim Acta* (2013) **104**:99–110. doi: 10.106/j.gca.2012.11.019
39. Andersen PO, Evje S, Madland MV, Hiorth A. A geochemical model for interpretation of chalk core flooding experiments. *Chem Eng Sci.* (2012) **84:**218–41. doi: 10.1016/j.ces.2012.08.038
40. Nermoen A, Korsnes RI, Christensen HF, Trads N, Hiorth A, Madland MV. *Measuring the Biot Stress Coefficient and Its Implications on the Effective Stress Estimate, Vol. 13–282.* San Francisco: ARMA. (2013) 1–9 p.
41. Goren L, Toussaint R, Aharonov E, Sparks DW, Flekkøy E. A general criterion for liquefaction in granular layers with heterogeneous pore pressure. In: *Fifth Biot Conference on Poromechanics* Vienna (2013).
42. Niebling M, Flekkøy EG, Måløy KJ, Toussaint R. Mixing of a granular layer falling through a fluid. *Phys Rev E* (2010) **82:**011301. doi: 10.1103/PhysRevE.82.011301
43. Alam MM, Fabricius IL, Christensen HF. Static and dynamic effective stress coefficient of chalk. *Geophysics* (2012) **77:**2. doi: 10.1190/GEO2010-0414.1
44. Szymczak P, Ladd A. Wormhole formation in dissolving fractures. *J Geophys Res.* (2009) **114:**B06203. doi: 10.1029/2008JB006122
45. Baud P, Wong T-F. Compaction localization in porous sandstones: spatial evolution of damage and acoustic emission activity. *J Struct Geol.* (2004) **26:**603–24. doi: 10.1016/j.jsg.2003.09.002
46. Appelo CAJ, Postma D. *Geochemistry, Groundwater and Pollution. 2nd Edn.* Amsterdam: CRC Press, Taylor and Francis Group (2005).

Conflict of Interest Statement: The authors declare that the research was conducted in the absence of any commercial or financial relationships that could be construed as a potential conflict of interest.

frontiers in Physics

ORIGINAL RESEARCH
published: 12 January 2016
doi: 10.3389/fphy.2015.00092

Influence of Layering on the Formation and Growth of Solution Pipes

Karine Petrus and Piotr Szymczak *

Faculty of Physics, Institute of Theoretical Physics, University of Warsaw, Warsaw, Poland

In karst systems, hydraulic conduits called solution pipes (or wormholes) are formed as a result of the dissolution of limestone rocks by the water surcharged with CO_2. The solution pipes are the end result of a positive feedback between spatial variations in porosity in the rock matrix and the local dissolution rate. Here, we investigate numerically the effect of rock stratification on the solution pipe growth, using a simple model system with a number of horizontal layers, which are less porous than the rest of the matrix. Stratification is shown to affect the resulting piping patterns in a variety of ways. First of all, it enhances the competition between the pipes, impeding the growth of the shorter ones and enhancing the flow in the longer ones, which therefore grow longer. This is reflected in the change of the pipe length distribution, which becomes steeper as the porosity contrast between the layers is increased. Additionally, stratification affects the shapes of individual solution pipes, with characteristic widening of the profiles in between the layers and narrowing within the layers. These results are in qualitative agreement with the piping morphologies observed in nature.

Keywords: karst, solution pipes, reactive flow, porous medium, dissolution

OPEN ACCESS

Edited by:
Bjornar Sandnes, Swansea University, UK

Reviewed by:
Yves Méheust, Université de Rennes 1, France
Espen Jettestuen, International Research Institute of Stavanger, Norway

***Correspondence:**
Piotr Szymczak
piotrek@fuw.edu.pl

Specialty section:
This article was submitted to Interdisciplinary Physics, a section of the journal Frontiers in Physics

Received: *01 July 2015*
Accepted: *03 December 2015*
Published: *12 January 2016*

Citation:
Petrus K and Szymczak P (2016) Influence of Layering on the Formation and Growth of Solution Pipes. Front. Phys. 3:92. doi: 10.3389/fphy.2015.00092

1. INTRODUCTION

The processes leading to the dissolution of a porous or fractured rock by a reactive fluid depend on a subtle interplay between the chemical reactions at mineral surfaces and fluid motion in the pores [1–3]. Strong, non-linear couplings between flow and dissolution may lead to the appearance of instabilities resulting in the formation of a variety of different geological patterns. Particularly relevant for the present study is the so-called *reactive-infiltration instability* [4, 5]: a relatively small change in pore geometry due to the dissolution may result in a variation of permeability, focusing the flow and leading to further changes in erosion. As a result, small inhomogeneities have a tendency to grow and get transformed into highly permeable, finger-like flow channels, which go by several different names depending on the field. In the petroleum industry, they are called "wormholes" [6] due to the resemblance with the tunnels dug by worms. Geologists call them "solution pipes," "karst funnels," or "geological organs" [1, 7, 8], whereas pedologists call them "soil tongues" [9].

Once formed, the channels continue to grow, focusing an ever-increasing portion of the flow, but also competing with each other: since the larger flow in the channel leads to increased dissolution—this again generates the positive feedback loop resulting in fast growth of the longer pipes and starvation of the shorter ones.

The flow-focusing instability has been known for a long time in the petroleum industry [10], where it was used to increase the effectiveness of reservoir stimulation techniques. In that context, it has also been studied experimentally [6, 11] and numerically [12–15]. In the physics community, the interest toward these systems has been sparked by classical papers of Daccord and Lenormand, which analyzed the patterns formed in a dissolving plaster and related them to other pattern-forming systems, such as diffusion-limited aggregation [16, 17]. In earth sciences, the understanding of the profound role that flow-focusing plays in karst development came with the pioneering works of Ewers [18], who has analyzed a number of analog models of karst formation made of sand or plaster of Paris. This has provided him with a number of important insights on the process of cave formation, and the role played in these processes by the competition between evolving flowpaths. Further insight into these effects has been provided by the numerical modeling of early stages of karst development [19–25].

Recent years have seen a growing number of experimental studies of dissolution-induced morphology evolution [26–29], many of them in the context of CO_2 sequestration [30–38]. Since many of the potential reservoirs for CO_2 storage are in carbonate strata, it is crucial to understand how the flow of CO_2-acidified brine impacts the long-term changes in porosity and permeability of the reservoirs and how it affects the caprock properties. Most of the systems analyzed in these studies are relatively small (1 − 10 cm scale), however even at that scale a strongly non-uniform character of the dissolution manifests itself in a profound way, with the appearance of wormholing patterns. Due to the self-similar character of the flow-focusing process [24, 39], one expects to find the dissolution channels at all scales, up to the system size. And this is indeed the case, with the karst solution pipes appearing in many places throughout the world [1, 7, 8, 40, 41], most of them on 1–10 m scale, although much longer structures, up to kilometer length, have also been reported [42].

In this paper, we focus on solution pipes in karst systems, analogous to the ones depicted in **Figure 1**. In particular, we investigate the influence of rock stratification on the solution pipe growth. As it turns out, the presence of low-porosity layers impacts the shapes of the solution pipes, which tend to narrow as they cut through the layers and then widen up to form bulbous caverns. These features are visible in the pipes in **Figure 1** and their detailed investigation is the goal of this study.

So far, the shapes of wormholes have been analyzed mainly in the context of acidization [11–13, 43, 44], where it has been established that they strongly depend on the flow rate and reaction rate. At low injection rates the growth of the dissolution channels is significantly influenced by diffusion and the resulting wormholes are conical-shaped. At higher flow rates the channels become more elongated—this regime is called in the acidization literature a "dominant wormhole" regime. In the geomorphological context, a systematic analysis of the lengths of solution pipes has been carried out by De Waele et al. [8], who have measured a collection of more than 200 solution pipes in the coastal areas of the Mediterranean and analyzed their length distribution, suggesting that it follows an exponential law. This data has been subsequently re-analyzed in Ref. [45], which led to the conclusion that—if one discards the partially buried pipes the full length of which remain unknown—the length distribution is found to be consistent with a power-law. Such scale-invariant distributions are a characteristic feature of a large number of hierarchical growth processes [46], observed experimentally e.g., in some of the viscous fingering systems [47, 48], dendritic side-branches growth in crystallization [49] or crack propagation in brittle solids [50].

To the best of our knowledge, the shapes of the solution pipes in the layered porous medium have not been analyzed in the literature. However, some of the insight into these questions can be gained from studying of the related problem of the growth of karst cutters [51, 52], i.e., solutionaly enlarged joints. The dissolution of cutters is somewhat different from that of solution pipes. In the former case the flow is focused from the very beginning within the joints, whereas in the latter the dominant flow pathways are created spontaneously due to the reactive-infiltration instability and the subsequent competition between the emerging wormholes. Nevertheless, some of the morphological features of the cutters and pipes seem to be similar. In particular, Howard [51] observes undulations on the sides of the cutters, which correlate with the strata and notes that cavernous widenings have the tendency to form predominantly beneath the layers. Analogous morphological characteristics are observed in the case of solution pipes (cf. **Figure 1** and the numerical results of Section 3). Understanding of the mechanism underlying the formation of these features is one of the goals of this study. Additionally, we will also go beyond the scale of a single pipe and analyze the impact of the layering on the competition between different pipes for the available flow.

The paper is organized as follows. In Section 2 the Darcy-scale mathematical model of a dissolving porous rock is briefly recalled. In Section 3 we introduce the model of a stratified medium and analyze numerically its impact on the dissolution patterns. Finally, the conclusions are drawn in Section 4.

2. GOVERNING EQUATIONS

Let us briefly recall the equations for the dissolution of a porous matrix [53]. The rate of groundwater flow through the porous medium is taken to be proportional to the pressure gradient (Darcy's law)

$$\mathbf{u} = -\frac{K(\phi)}{\mu}\nabla p \tag{1}$$

where $\mathbf{u}$ is the Darcy velocity, K-the permeability, μ-the viscosity of the fluid, ϕ-the porosity, and p-the fluid pressure. Here we will adopt the Carman-Kozeny relation for the permeability dependence on the porosity, $K(\phi) \sim \phi^3$. We also assume that the Darcy velocity field is incompressible,

$$\nabla \cdot \mathbf{u} = 0, \tag{2}$$

neglecting contributions to the fluid volume from reactants or dissolved products. Under typical geophysical conditions,

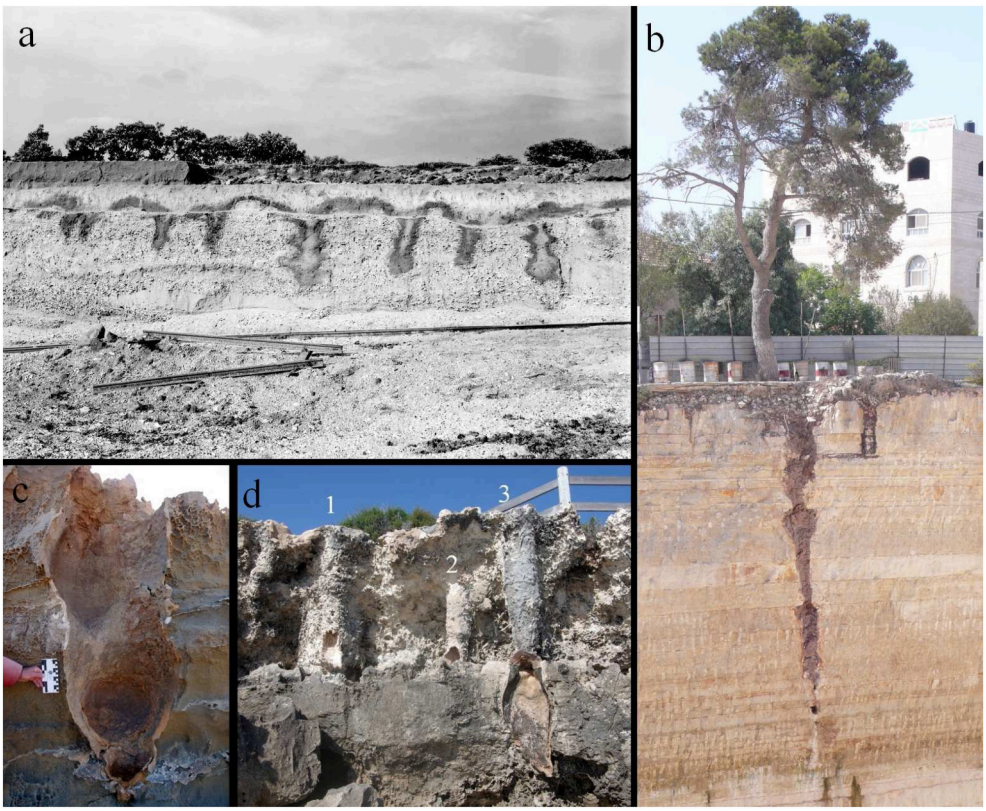

FIGURE 1 | Examples of the solution pipe morphologies in stratified systems. (A) Solution pipes in gravel with limestone clasts: gravel-pit, west of Rauceby Station, UK. Photo by J. Rhodes courtesy British Geological Survey (catalog no. P206264). **(B)** Solution pipe in Ramallah, Israel, cutting through stratified dolomites with marl beds. The photograph is courtesy of Sebastian Schmidt of University of Göttingen. **(C)** Solution pipe cutting through layered limestone rock at Cape Bridgewater, Victoria, Australia **(D)** three pipes with cemented rims in limestone formations at Burns Beach, Perth, Australia. Pipe no. 3 cuts through the more resistant bed in the lower portion of the photo.

dissolution is slow in comparison to flow and transport processes; we can therefore assume a steady state in both the flow and transport equations.

The concentration of the solute, c is calculated through the convection-diffusion-reaction equation

$$\nabla \cdot (\mathbf{u}c) - \nabla \cdot (D\phi \cdot \nabla c) = R(c), \tag{3}$$

where D is the diffusion coefficient and $R(c)$ is the reactive flux into the matrix. Finally, the erosion equation, which gives the increase of the porosity as a result of the dissolution, is

$$c_{sol}\partial_t \phi = R(c) \tag{4}$$

where c_{sol} is the mineral concentration of the solid species and $R(c)$ is the reaction rate. Here, we assume a linear kinetic equation for the reaction rate

$$R(c) = ks(c_{sat} - c)\,\theta(\phi_{max} - \phi) \tag{5}$$

where k is the kinetic rate and s is the specific reactive surface area per unit volume that we assume to be constant, $s = s_0$. Next, c_{sat} is the saturation concentration at which adding further solute results in precipitation. In the context of karst formation, c corresponds to the concentration of calcium ions, which controls the dissolution at moderate to large pH [54]. The Heaviside step function, $\theta(\phi_{max} - \phi)$ guarantees that the reaction term vanishes in the region where all of the soluble material has dissolved (which corresponds to the porosity $\phi = \phi_{max}$). In this region Equation (3) reduces to a convection-diffusion equation.

The above equations are supplemented by boundary conditions on the velocity and concentration field. Along the x direction (parallel to the flow):

$$p(x = 0, y) = p_0 \qquad c(x = 0, y) = 0, \tag{6}$$

and

$$p(x = L_x, y) = 0 \qquad c(x = L_x, y) = c_{sat}, \tag{7}$$

which accounts for the applied pressure drop p_0 and the inflow of unsaturated solution imposed at the inlet. In the case of solution pipes, the flow is mostly due to gravity. In the simulations, we keep the total volumetric flow rate through the system constant, and p_0 is changed dynamically as the permeability of the system evolves. Along the y direction periodic boundary conditions are

imposed. The above equations are solved numerically using a finite difference method, described in more detail in Ref. [23]. The initial porosity field is sampled from a lognormal distribution characterized by the standard deviation σ and the correlation length λ. In most of the simulations presented here, we choose a relatively small standard deviation of the initial porosity field, $\sigma = 10^{-3}$.

The inverse of the specific surface area, s_0^{-1} is a characteristic length in our system, which will be chosen as a unit of length in all the reported data, with the dimensionless coordinates $\hat{x}$ and $\hat{y}$ defined as

$$\hat{x} = xs_0 \qquad \hat{y} = ys_0 \tag{8}$$

On the other hand, the time is scaled by a characteristic dissolution time:

$$\hat{t} = t/\tau \tag{9}$$

$$\tau = \frac{c_{sol}}{ks_0 c_{sat}}. \tag{10}$$

Finally, the dimensionless concentration is defined as

$$\hat{c} = \frac{c_{sat} - c}{c_{sat}} \tag{11}$$

which is constrained to be in the interval (0,1). We also scale porosity by its maximum value, ϕ_{max},

$$\hat{\phi} = \frac{\phi}{\phi_{max}}. \tag{12}$$

The relative importance of convective, diffusive and reaction processes in the system are measured by the Péclet number and Damkölher number. The former is defined as [23]

$$\mathrm{Pe} = \frac{u_0}{Ds_0\phi_0} \tag{13}$$

and measures the ratio of the convective fluxes to the diffusive fluxes. Here u_0 is the average Darcy flux in the initial system whereas ϕ_0 is an initial porosity of the system. On the other hand, the Damkölher number

$$\mathrm{Da} = \frac{k}{u_0} \tag{14}$$

relates the surface reaction rate to the fluid flux.

As shown in a number of studies [11–13, 43, 55] the wormhole patterns depend strongly on the values of these two numbers. In particular, it has been shown that the Péclet number needs to be large enough for the instability to occur. This is why piping is often observed in unconsolidated rock and gravel, where the permeabilities (and thus flows) are large [56].

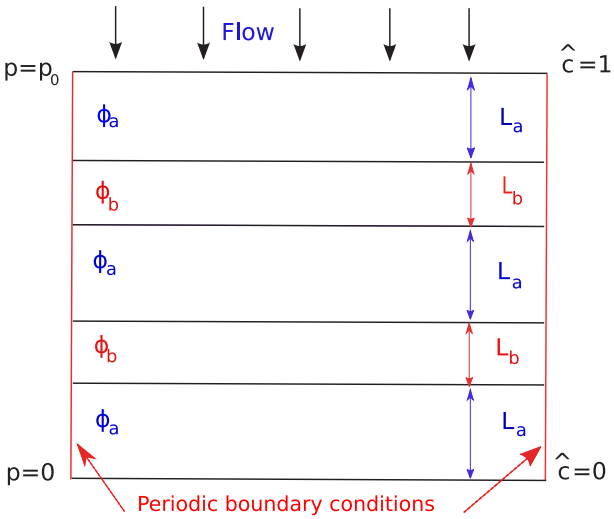

FIGURE 2 | Schematic of a model of stratified medium: alternating layers of porosities ϕ_a and ϕ_b.

3. DISSOLUTION OF A STRATIFIED MEDIUM

To study the influence of stratification on pipe shapes and dynamics, we have adopted a simple conceptual model of a stratified medium (see **Figure 2**). The porous medium is assumed to consist of alternate layers of higher and lower porosity, ϕ_a (of depth L_a) and ϕ_b (of depth L_b), respectively. The two parameters characterizing such a setup are the porosity ratio $C = \phi_a/\phi_b$ and the length ratio $\kappa = L_a/L_b$. In the following, we limit ourselves to two dimensions. However, the same methodology can be applied to the analysis of the 3D system, which will be the subject of a further study.

Figure 3 presents the results of the dissolution simulations for such a system for Pe = 100, Da = 0.5 with a porosity contrast of $C = 2$ and length ratio $\kappa = 5$. The characteristic undulations in the shape of the dissolution pipes are clearly visible here—the pipes become narrower in the less porous layers and widen up in between the layers. Another effect, clearly observed in **Figure 3** is that the less porous layer acts as a *dissolution barrier*, which stops the growth of shorter pipes, as there is not enough reactant transported through their bodies to be able to break through the layer. As a result, the tips of the shorter pipes often coincide with the layer boundary. This effect can also be observed in **Figure 1D**, where only the longest pipe (pipe no. 3) has succeeded in breaking through the packed layer.

3.1. Flow and Concentration Fields Near the Tips of the Pipes

Some insights into the mechanisms underlying this behavior can be obtained by the analysis of the flow and concentration fields in the vicinity of the tip of the pipe. These are shown in **Figures 4**, **5** for three different positions of the tip with respect to the layers: the pipe terminating in a porous region between the

layers (left panels), the pipe terminating within the packed layer (center panels), and the pipe emerging from the packed strata (right panels).

There are several things to be noted here. First of all, since the permeability of the pipe is much larger than that of the surrounding medium, the tip of the pipe is a local pressure maximum, distributing the flow to the porous matrix, both in the axial and in lateral direction (cf. **Figure 4**). However, due to the small permeability of the matrix in the packed layers, the lateral flows are diminished when the pipe enters a layer (center panel of **Figure 4**) with respect to the situation when the tip find itself in a more porous layer (left panel of this **Figure 4**). Smaller lateral flows give rise to a narrower region of elevated concentration (cf. **Figure 5**), which decreases the diameter of the pipe as it enters the packed strata.

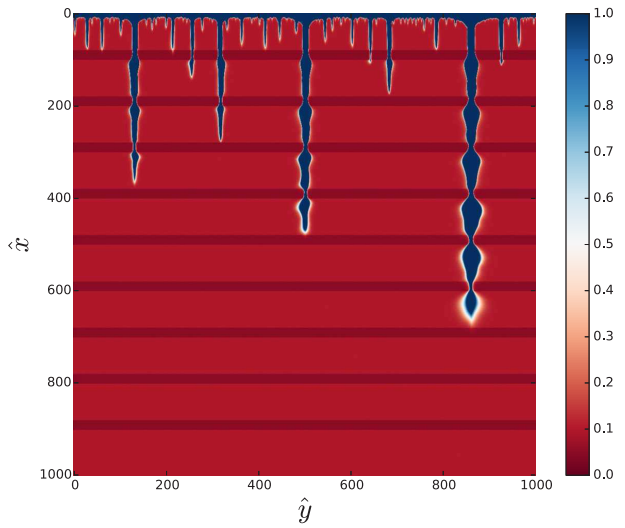

FIGURE 3 | Solution patterns at Pe = 100, Da = 0.5, the porosity contrast $C = 2$ and length ratio $\kappa = 5$ for a domain of the size $L_x = L_y = 1000 s_0^{-1}$. The colors represent rescaled porosity, $\hat{\phi}$, as indicated in the colorbar on the right.

Next, as the pipe emerges from the layer, the flow is distributed almost uniformly over a semi-circle in the downstream direction with the tip as its center, analogously to the flow created by the point source at the wall (right panel of **Figure 4**). The unsaturated solution is carried deeper into the matrix (right panel of **Figure 5**) which gives rise to a significant widening of the pipes as they emerge from the layer. However, as the pipe tip moves away from the layer, this effects weakens and the pipe comes back to its original width.

As observed in **Figure 5**, the undersaturated solution is concentrated along the length of the pipe with a halo around the tip. However, since the inside of the pipe is fully dissolved (with $\phi = \phi_{max}$), the reaction term vanishes there and the concentration is simply transported along the length of the pipe. The situation changes in the vicinity of the tip, where strong lateral currents push the undersaturated solution into the undissolved matrix. This is amply illustrated in **Figure 6**, where we plot the time derivative of the porosity field, $d\hat{\phi}/d\hat{t}$, which marks the regions of the active reaction. Comparing **Figure 6** with the corresponding concentration field (right panel of **Figure 5**), we see that the dissolution is mainly taking place around the tip and in a thin layer along the perimeter of the pipe.

3.2. Comparison with Natural Systems

The characteristic undulations of the solution pipes observed in the simulations are consistent with the features observed in natural systems. **Figure 1A** presents a number of spontaneously formed solution pipes in gravel with limestone clasts.

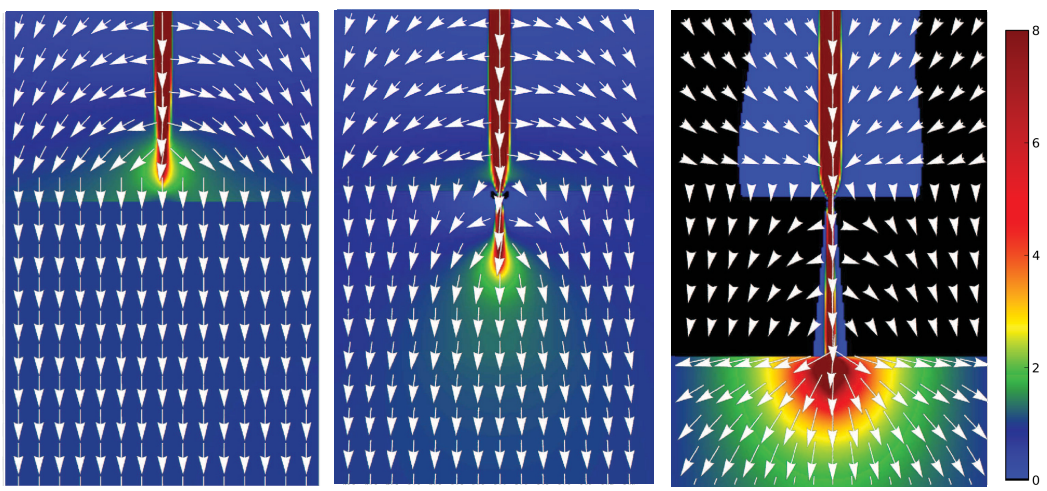

FIGURE 4 | The Darcy flow field around the tip of the pipe before hitting one of the layers (left), with the tip located within the layer (center), and after emerging from the layer (right). The colors represent the magnitude of the flow scaled by v_0. The lengths of the vectors in the overlaying vector plot has been scaled to $v(x, y)^{1/5}$ to aid visualization.

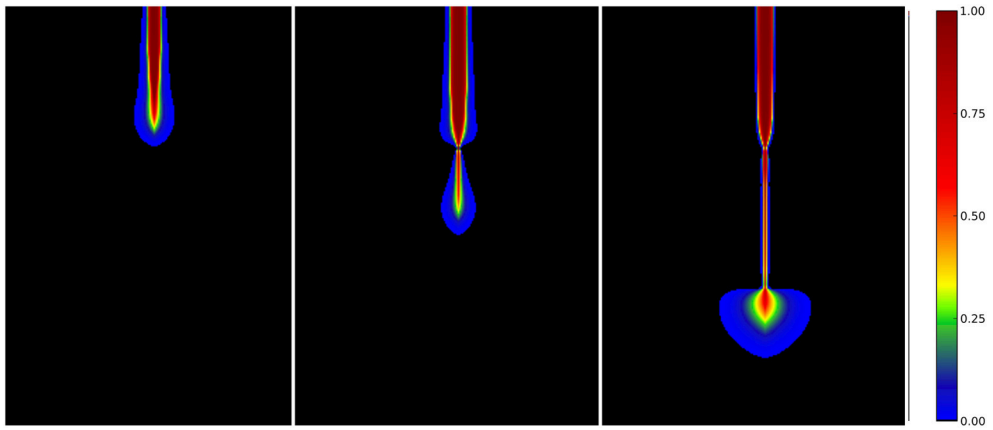

FIGURE 5 | The concentration field, $\hat{c}(x, y)$, around the tip of the pipe at the same times as in Figure 4.

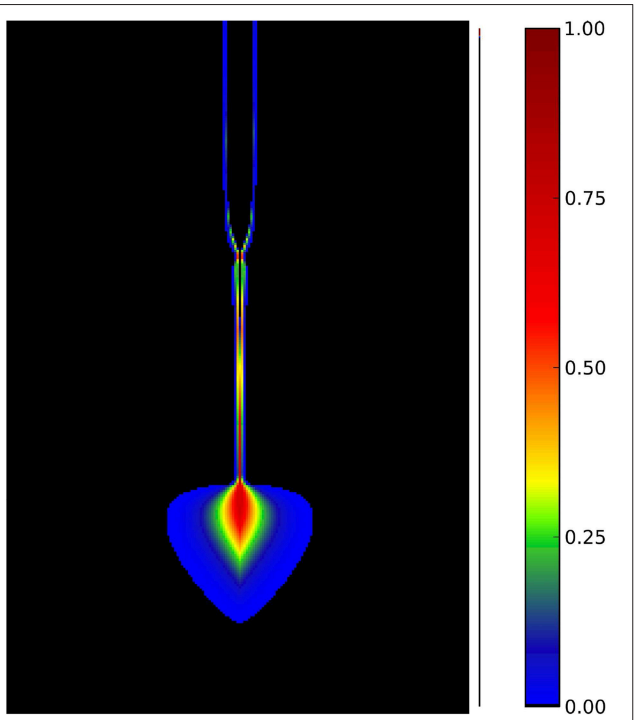

FIGURE 6 | The porosity change, $d\hat{\phi}/d\hat{t}$, corresponding to the concentration field in the right panel of Figure 5.

Undulations in different pipes are spatially correlated, which suggests the presence of at least three layers in this system. The dark rims along the perimeter of the pipes are most likely the result of clay and iron oxide accumulation due to the illuviation processes [57]. The clay particles are transferred by water from the upper parts of the soil and then flocculated at the clay-limestone boundary, where the pH changes from mildly acidic to alkaline. Such rims are commonly seen in solution pipes in which the infill is still present [7, 58].

In **Figure 1B** we see a solitary solution pipe, which might have been triggered by the presence of the tree. In fact, stemflow is usually significantly more acidic than incident precipitation [59] and thus it is often considered as one of the factors speeding up solution pipe formation [40, 41]. The pipe in **Figure 1B** cuts through several dolomite layers, with characteristic widenings, very similar to those observed in the numerical simulations. Finally, **Figures 1C,D** show the pipes formed in beach calcarenites in southern and western Australia. Again, the narrowings and widenings of the pipes as they cut through the layers are clearly visible here.

3.3. Hierarchical Growth of the Pipes and Their Length Distribution

The value of porosity contrast has a profound impact on the patterns, as it affects the intensity of the competition between the growing pipes. As observed in **Figure 7**, as C gets larger the number of long pipes in the system diminishes and the number of short ones increases. This means, however, that the longest pipes are getting significantly more flow in these systems (since the flow is then distributed between a smaller number of pipes). As a result, the longest pipe grows faster in the stratified systems with a large porosity contrast.

These observation can be quantified by the analysis of the distribution of the lengths of the pipes. As shown in a number of studies [24, 39, 45] a strong screening between the dissolution channels usually leads to the power-law distribution of their lengths,

$$N(L_p) \sim L_p^{-\alpha}, \tag{15}$$

where N denotes a number of pipes longer than L_p. In a homogeneous system, the exponent α is close to unity [24, 39, 45]. **Figure 8** shows the length distributions corresponding to the patterns presented in **Figure 7**. In the homogenous case ($C = 1$) the results are in full agreement with the earlier studies, indicating L_p^{-1} distribution over the entire length range. However, the situation is different for the layered system. The

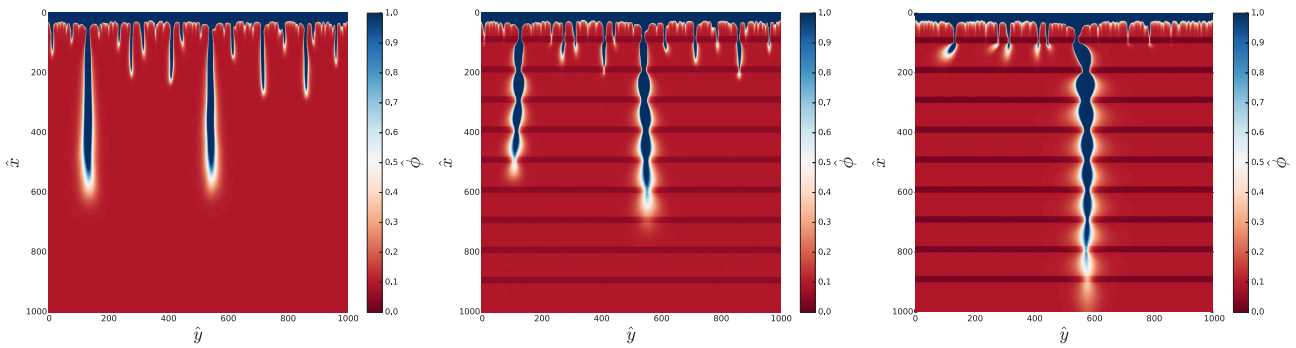

FIGURE 7 | Piping patterns for $C = 1$ (no layers, left), $C = 2$ (center), and $C = 4$ (right) for Pe = 100, Da = 0.1, and $\kappa = 5$.

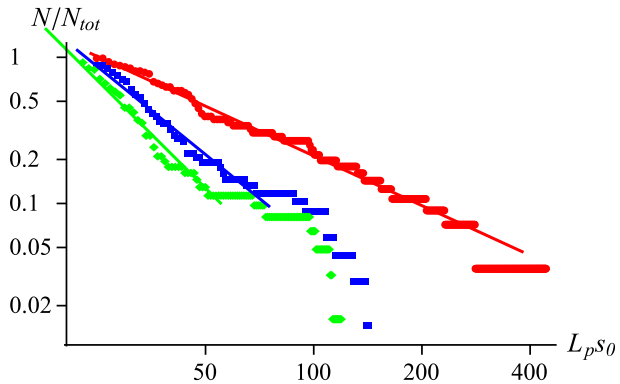

FIGURE 8 | The cumulative distribution $N(L)$ of solution pipe lengths for the patterns presented in Figure 7 with $C = 1$ (red points), $C = 2$ (blue), and $C = 4$ (green). The solid lines have slopes of 1.02 (red), 1.95 (blue), and 2.45 (green).

region characterized by the power-law distribution is now much narrower followed by a clearly visible shoulder in the distribution extending up to the location of the first layer (at $100 s_0^{-1}$), which corresponds to the surplus of pipes which have been stopped in their growth by the presence of the layer. Additionally, the power-law exponents for the layered case are significantly larger than 1, which confirms that the stratification indeed increases the screening between the pipes.

A quantity directly linked to the length distribution is the mean spacing between adjacent active pipes (i.e., pipes which continue to grow due to the presence of undersaturated solution). The initial spacing between the spontaneously formed pipes is determined by the spectral characteristics of the reactive-infiltration instability [4, 23, 60], which triggers the pipe formation process. Soon, however, the competition between the pipes for the available flow leads to the starvation of the shorter ones and the spacing between active pipes increases. Note that for the power-law length distribution (15) the characteristic separation between pipes of length L_p is equal to $L_y/N(L_p) \sim L_p^{\alpha}$, where L_y is the width of the domain. Hence, the increase of α exponent in the stratified case results in a larger spacing between the active pipes.

Before we move on, let us analyze the impact of the amplitude of the initial noise on the dissolution patterns. **Figure 9** presents the same systems as in **Figure 7** but with a much higher standard deviation, $\sigma = 0.15$. As observed, the pipes are now much more irregular and winding, but the overall patterns are very similar to those in **Figure 7**. This conclusion agrees with a more detailed analysis of Upadhyay et al. [45] which shows that the statistical properties of the dissolution patterns are only weakly sensitive to the parameters governing the randomness in the initial porosity field. In the remainder of the paper, we focus on the low-noise regime, since a more regular geometry of the pipes in this case allows us to better discern the effects of the stratification of the porous matrix.

3.4. Two-Pipe Case

To get more insight into the nature of the competition process, we have considered a case in which two pipes grow symmetrically at equal distances from the centerline of the system. To trigger the growth of the solution pipes at these places, small regions of increased porosity ("pipe seeds") have been placed in an initial porosity field. These seeds have a length of 3% of the system length and are placed at $L_y/4$ and $3L_y/4$, respectively. Although the seeds are equal at the beginning, small noise in the initial porosity field triggers the instability which eventually leads to one of them outcompeting the other, as shown in **Figure 10**.

An intriguing observation inferred from **Figure 10** is that in the low porosity layers the speed of the pipe growth increases. This is connected with the narrowing of the pipe in the packed layers and the related increase of the axial fluid velocities. This is a strong effect, which allows the pipe tip to advance faster, even though locally, at each specific point of the packed strata, the total amount of rock to dissolve is larger than at a corresponding point in the less porous layers.

Another observation is that—in the stratified case—just after the growth of the shorter pipe is stopped, the longer pipe starts to grow faster, since it is getting a larger fluid flux. Its speed is higher than that in the case of non-stratified medium (for example, at $\hat{t} = 200$ it reaches $\hat{x} = 540$ whereas the tip of pipe in a non-stratified medium is located at $\hat{x} = 480$ at the same time).

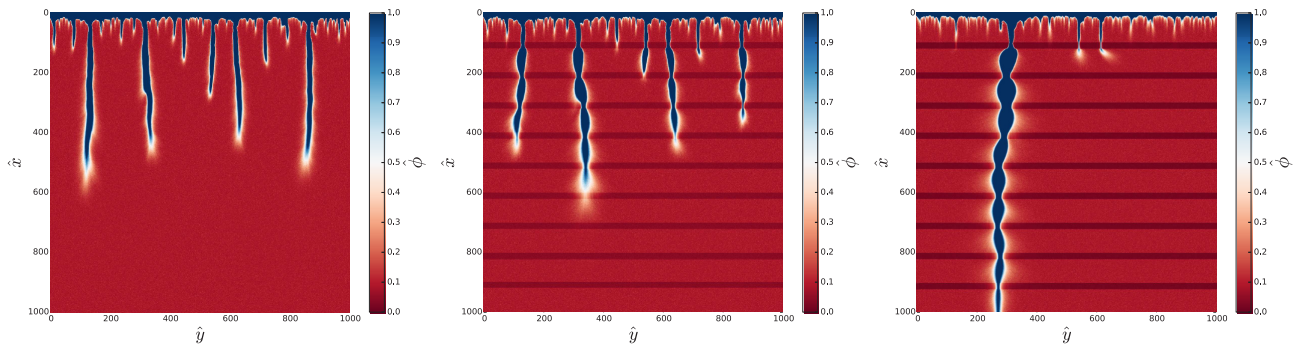

FIGURE 9 | Same as in Figure 7 but for a larger value of the initial noise.

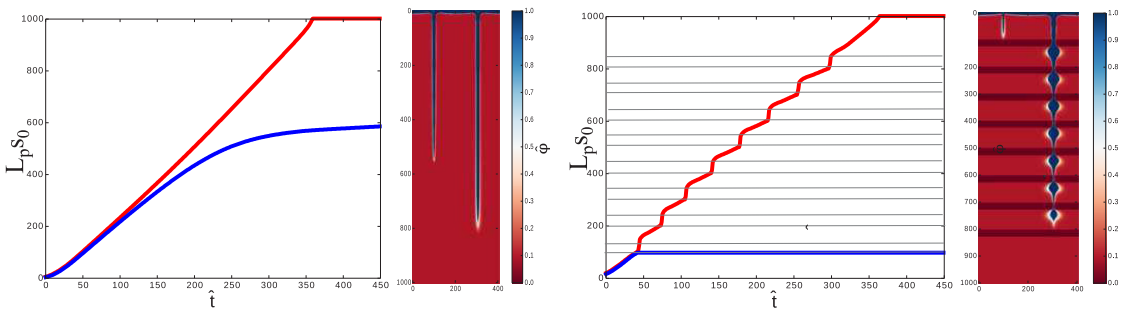

FIGURE 10 | The positions of the pipe tip vs. time in a two-pipe system in non-stratified (left) and stratified case. Red color marks the faster, winning pipe, and blue - the slower one. The 2d contour-plots show the corresponding dissolution patterns.

With time, however, the growth of the longer pipe in a stratified medium becomes impeded.

To understand the origin of such a slowdown of the dissolution in the stratified case, we have analysed the concentration profiles along the centreline of the winning solution pipe. **Figure 11** presents such profiles for non-stratified medium at Pe $=$ 8 and Pe $=$ 100 and for stratified medium ($C = 10$, $\kappa = 5$) at Pe $=$ 100. As observed, the undersaturation gradually decreases along the centreline. Since there is no reaction inside the pipe (the material there is fully dissolved), such a decrease must be connected with the diffusion of the calcium ions from the sides of the wormhole (where the reaction takes place) toward its center. This is further confirmed by the fact that the centreline concentration profile is strongly dependent on the Péclet number, with a characteristic lengthscale which is a function of the flow rate and diffusion within the pipe (cf. the left and center panel of **Figure 11**). In fact, the influence of Péclet number on the flow within the pipe is twofold. First, the total fluid flux through the cross-section of the pipe is smaller as Pe decreases. Second, the characteristic value of the local Darcy velocity within the pipe is further diminished, since the pipe diameter gets larger with the decreasing Pe.

Interestingly, in the stratified case, such a "diffusive" effect within the solution pipes is significantly stronger, and the profile at Pe $=$ 100 (right panel of **Figure 11**) has now a decay rate similar to than in the Pe $=$ 8 case in non-stratified medium. Although the quantitative model of this behavior still needs to be developed, the most plausible explanation is connected to the presence of widening in the pipe shape due to the stratification. The undulated shape has a much larger perimeter than its smooth counterpart, which increases the total diffusive flux of the calcium ions from the pipe walls.

3.5. Effects of the Layer Thickness, Porosity Contrast, Péclet, and Damkölher Number on the Dissolution Patterns

Let us now analyze the influence of the thickness of the packed layer on the wormhole shape. **Figure 12** compares the shapes of the pipes which emerge in the system with a single packed layer of two different widths. There are several things to be noted here. First, the shape of a bulbous widening carved by the pipe as it emerges from the layer is independent of the layer thickness. Similarly, the width of the pipe at the end of the packed layer, just before the emergence, again seems to be thickness-independent. The main differences between the shapes are visible in the upstream region: whereas in the thick-layer case the pipe is seen to have a necking at the entrance of the packed strata, its counterpart in the thin-layer case bulges out slightly, first widening and then gently narrowing as it approaches the layer.

Next, let us investigate how the shapes of the pipes are affected by the values of porosity contrast C and the Damkölher number,

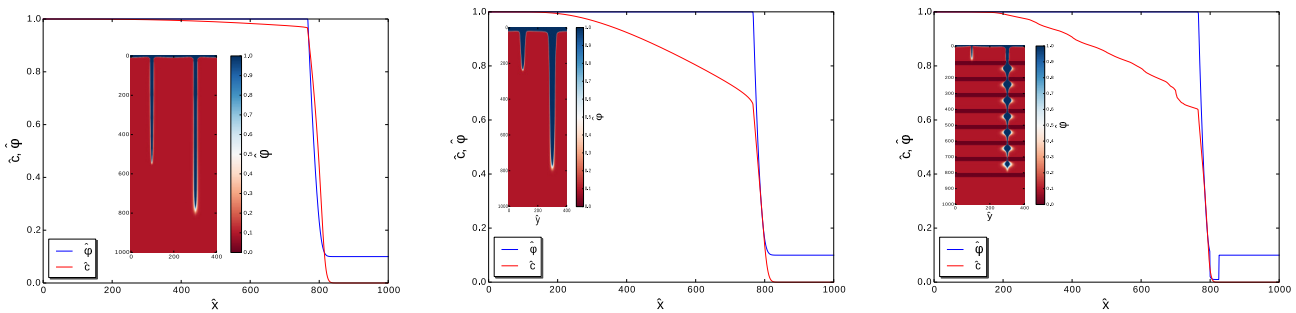

FIGURE 11 | Concentration (red) and porosity (blue) profiles along the line $y = 3/4L_y$, corresponding to the centreline of the winning pipe. Left: non-stratified case at Pe = 8, **center:** non-stratified case at Pe = 100, **right:** stratified case at Pe = 100.

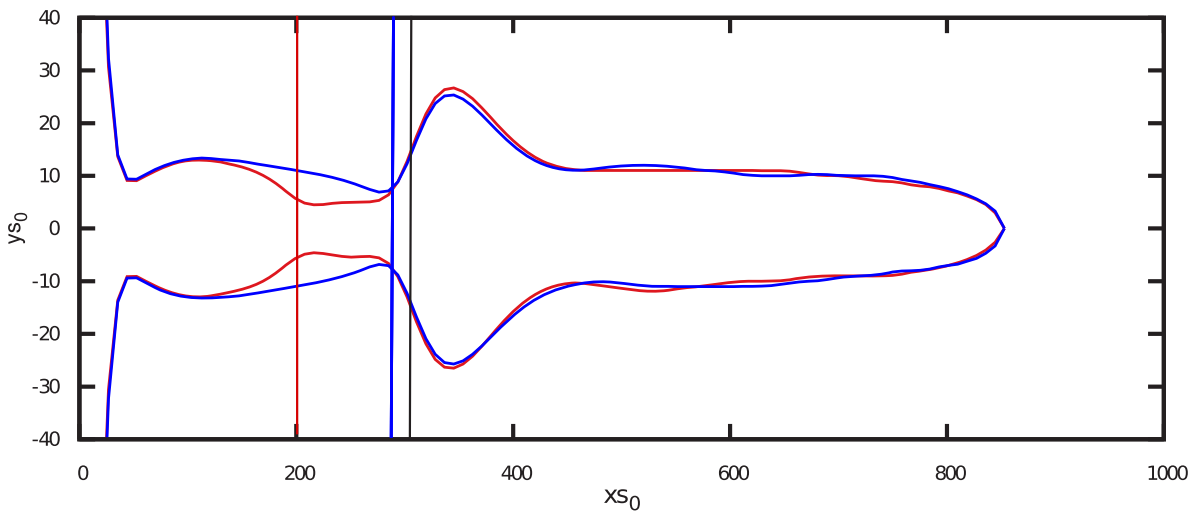

FIGURE 12 | Influence of thickness of the layer on the wormhole shape (Pe = 100, Da = 0.1, C = 10). The solution pipe in red corresponds to the case where the layer extends from the red vertical line to the black vertical line. The solution pipe in blue corresponds to the case where the layer extends from the blue line to the black line. Note that the aspect ratio of the plot has been altered to better visualize details.

Da. To this end we have carried out a number of simulations on the 1000 × 400 system with Pe = 100 and Da = 0.1 with different porosity contrasts ($1 < C < 4$) followed by a series of simulations with fixed $C = 10$ and different Da. The resulting wormhole shapes are presented in **Figures 13**, **14**, respectively.

A porosity contrast is seen to affect the patterns in a significant way. Whereas, in the non-stratified case the pipe has a very regular, cigar-like shape, introduction of even a small porosity contrast ($C = 1.25$) results in the appearance of pronounced undulations. Their amplitude increases with C-the pipes narrow down progressively in the packed layers and then widen up in the next porous zone, following the rule that the greater the narrowing, the more pronounced the subsequent widening. This can be rationalized by noting that—due to mass conservation—a small diameter of a pipe entails large flow velocities, which then get diverted in the lateral direction as the pipe emerges from a packed layer, resulting in larger cavities. Interestingly, after the bulge, the pipes quickly come back to their original widths, which do not seem to depend on the porosity contrast.

Furthermore, a close inspection of **Figure 13** reveals that the pipe begins narrowing already at some distance upstream from the low porosity layer and the higher the contrast is, the earlier the narrowing is taking place. It is particularly pronounced in the space between the first and the second layer—e.g., the $C = 10$ pipe (marked by an orange curve) begins to narrow down just after it has emerged from the bulge, whereas $C = 2$ and $C = 1.25$ pipes continue to grow for a while with a constant width, before eventually narrowing.

Let us now analyze **Figure 14**, which shows the influence of the Damkölher number on the pipe shapes. Strikingly, in this case the wormholes seem to have the same basic shape and the effect of Da comes down to the appropriate rescaling: the smaller the Da number, the larger the widenings of the pipe. In order to quantify these effects, we have measured the width and length of the bulbous widening (W and L in **Figure 14**) starting from the point where all of the pipe outlines overlap. Both W and L are plotted as a function of the Damkölher number in **Figure 15**. Interestingly, both seem to scale like $1/\sqrt{\mathrm{Da}}$, which can be understood in

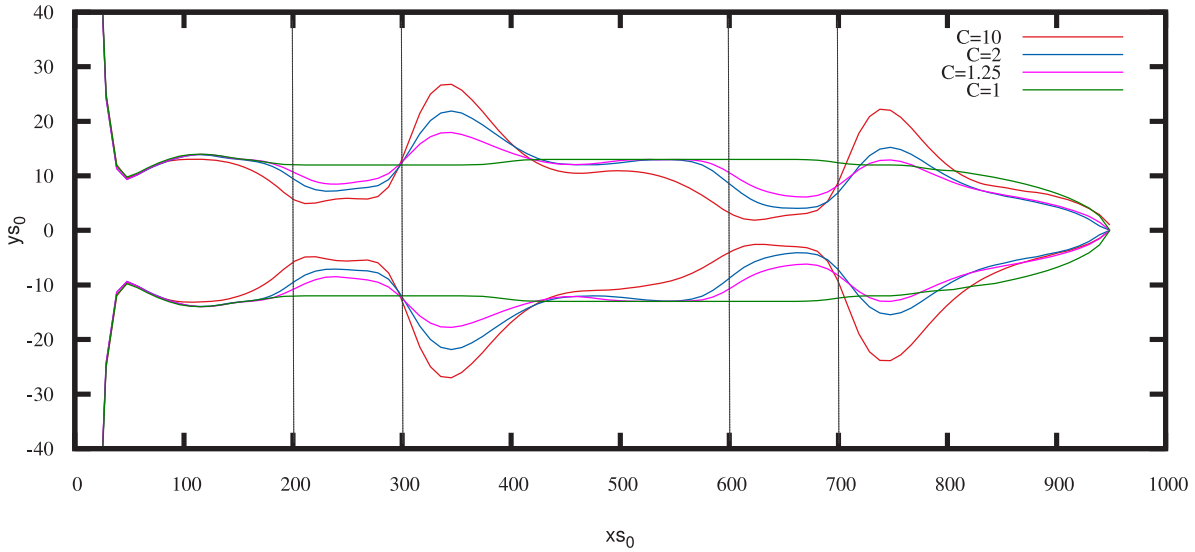

FIGURE 13 | Piping patterns for different contrasts of porosity (as marked) for Pe = 100, Da = 0.1. The aspect ratio of the plot has been altered to better visualize details.

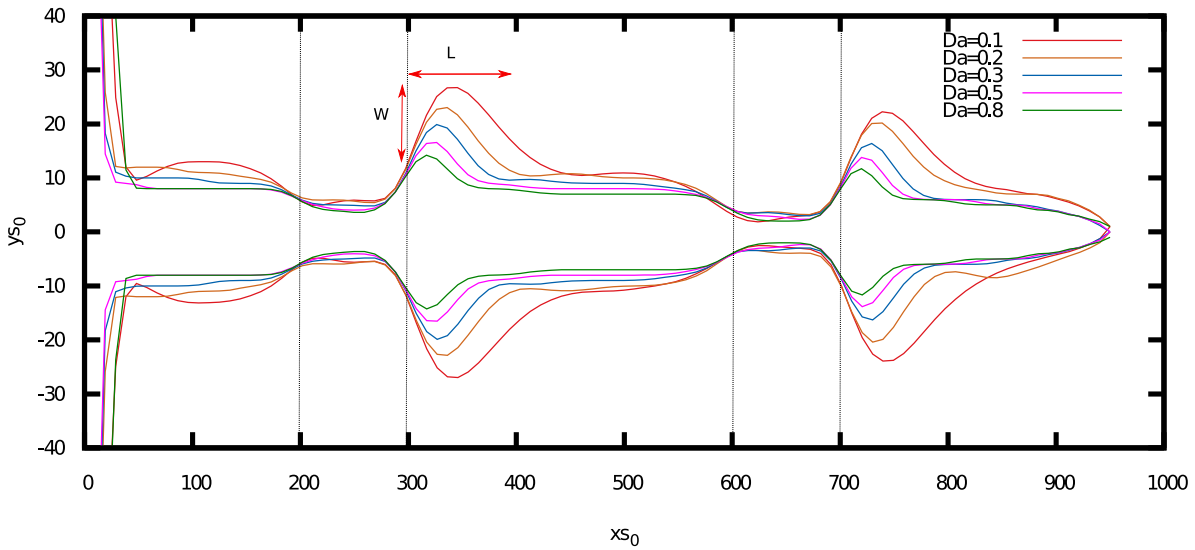

FIGURE 14 | Piping patterns for different Damkölher numbers for a stratification with a porosity contrast of *C* = 10. The aspect ratio of the plot has been altered to better visualize details.

terms of a simple model in which we assume the tip of the pipe emerging from the packed layer distributes the flow uniformly in the semi-circle ($-\pi/2 < \theta < \pi/2$). The Darcy flux near the tip is then

$$u = \frac{Q}{\pi r}\mathbf{e}_r \tag{16}$$

where r is the position vector in the polar coordinate system centered at the tip and $Q = v_0 L_y$ is the total fluid flux in the system (which we assume to be focused in the pipe). Since the flows within the pipe are high, we can neglect diffusion and obtain from the transport equation (near the tip).

$$\frac{Q}{\pi r}\frac{dc}{dr} = k(c_{sat} - c), \tag{17}$$

the solution of which reads simply

$$c(r) = c_{sat}\left(1 - e^{-\frac{\pi k r^2}{2Q}}\right) \tag{18}$$

with a characteristic decay length given by

$$l = \sqrt{\frac{Q}{\pi k}} = \sqrt{\frac{L_y}{\pi \mathrm{Da}}} \tag{19}$$

which indeed gives the $\mathrm{Da}^{-1/2}$ scaling, as observed in the simulations. Using $L_y = 400$ (which corresponds to the width of the system in **Figure 13**), we get the coefficient of 11.3 in this power-law. The difference between this value and the values reported in the fits in **Figure 15** (i.e., 6.5 and 41.5 respectively) is connected with the highly simplified character of the model. In reality, the outflow from the tip is expected to be anisotropic, with a larger flux directed along the axial direction [which is in fact reflected in a larger value of the coefficient of the L scaling (41.5) with respect to that of the W scaling (6.5)]. Next, the scaling Equation (19) has been derived for the concentration field. Porosity increase, however, is proportional to a time integral of the concentration [cf. Equation (4)]. Hence, in principle, one would need to know the entire time evolution of the c field to be able to estimate the respective porosity growth. However, as illustrated in **Figure 6**, the dissolution is active almost exclusively in a small region at the tip of the pipe. Hence, the cavern grows over a relatively short time only, $T = L/V$, where V is the growth velocity of the pipe. Our approximation then corresponds to neglecting the flow and concentration changes over that time.

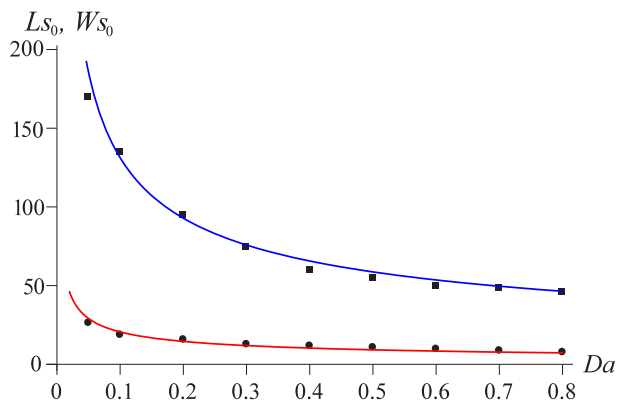

FIGURE 15 | The width (*W*) and length (*L*) of the widenings, as marked in Figure 13, as a function of the Damkölher number. The points represent the simulation data, whereas the curves are fit to $1/\sqrt{\mathrm{Da}}$ dependencies: $L(\mathrm{Da}) = 41.5/\sqrt{\mathrm{Da}}$ (blue curve) and $W(\mathrm{Da}) = 6.5/\sqrt{\mathrm{Da}}$ (red curve).

Moreover, the assumption that the flow from a pipe breaking through the layer corresponds to a point source at the wall is expected to hold only at large values of the porosity contrast, C. There are two reasons for this. The first is that at large C the narrowing of the pipes in the packed layers is more pronounced. Second, the smaller C ratios mean that a larger portion of the flow is transported through the porous matrix in the layer. By performing the simulations at different porosity contrast we have checked that the scaling (19) indeed deteriorates progressively as C is decreased, with both L and W decreasing less pronouncedly with Da.

It is worth noting that in three dimensions, an analysis analogous to Equations (16–19) would yield $\mathrm{Da}^{-1/3}$ scaling, thus the dependence on the dissolution rate is weaker in 3D.

Finally, let us discuss the influence of the Péclet number on the patterns. **Figure 16** presents the counterpart of **Figure 7** for a relatively small value of the Péclet number ($\mathrm{Pe} = 1$). Arguably the most pronounced effect that the decrease of the flow rate has on a dissolution patterns is the change of the overall shape of the pipes. Instead of the linear structures, the pipes are now more conical, with the diameter tapering toward the tip. However, the effects of the stratification remain qualitatively similar to those at higher Pe, with characteristic undulations superimposed on the conical shapes of the pipes. Getting back to the natural examples of **Figure 1** we can infer that the pipe in **Figure 1C** has been formed at a relatively small value of Pe, since the tapering is clearly visible here, whereas more linear forms of **Figures 1A,B,D** are probably associated with higher Péclet numbers.

4. CONCLUSIONS

In this paper, we have been analyzing the formation of solution pipes in stratified soluble rocks. We have shown that stratification influences the dissolution patterns in a significant way. By serving as a flow and dissolution barrier, the packed layers impede the growth of the shorter pipes and direct the entire fluid flux into the winning pipes. This affects the distribution of pipe lengths, which becomes steeper as the porosity contrast between the layers is increased.

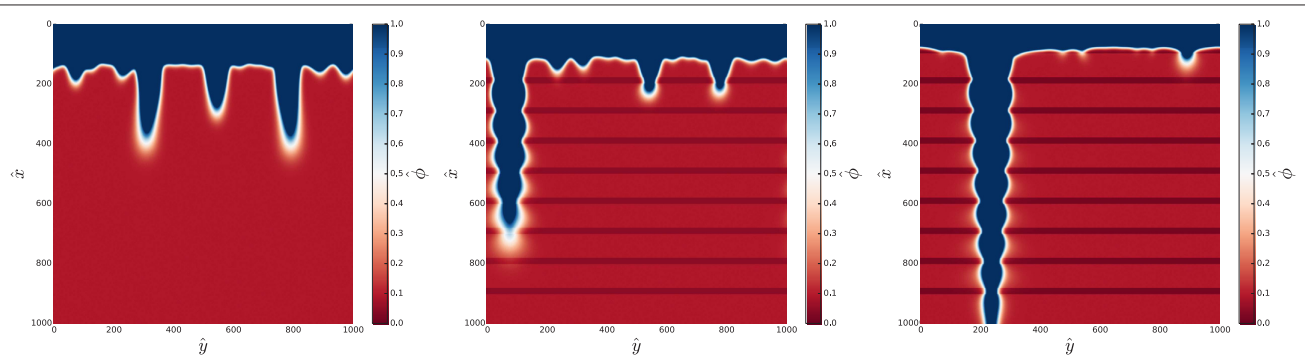

FIGURE 16 | Piping patterns for $C = 1$ (no layers, left), $C = 2$ (center), and $C = 4$ (right) for $\mathrm{Pe} = 1$, $\mathrm{Da} = 0.1$ and $\kappa = 5$.

Interestingly, the shapes of the pipes itself are also affected by the stratification, with characteristic narrowings within the packed layers and large bulbous widenings, carved by the pipes as they emerge from the layers. We have connected the appearance of these forms to the interplay of flow and dissolution in the pipes. In particular, we have argued that as the pipe emerges from a packed layer, the flow rate around its tip resembles that produced by a point source near a wall. Large lateral currents result then in a dramatic widening of the pipe. In two dimensions, the radius of a cavity thus formed is, to a first approximation, inversely proportional to the square root of the Damkölher number.

The results presented here can help in the interpretation of the natural patterns, such as those in **Figure 1**. For example, if one can measure the porosity and permeability contrast between the layers, as well as estimate the reaction rate based on the petrography of the rock, then the diameters of the pipes in the widest point can be used to estimate the flow conditions under which these structures were formed. Conversely, if the flow conditions can be guessed then these data can be used to calculate the permeability contrast in the layers.

ACKNOWLEDGMENTS

The authors benefited from discussions with Tony Ladd, Andrew Farrant, Sebastian Schmidt, Elena Abarca, Agnieszka Budek, Paweł Kondratiuk and Michał Pecelerowicz. Tony Ladd is also acknowledged for his finite-difference code *dissol*, which has been used in the simulations. Sebastian Schmidt is gratefully acknowledged for the photo and helpful discussion. We also thank Ken Grimes and Matej Lipar for their invaluable help with the exploration of solution pipes in southern and western Australia. KP acknowledges funding from the European Union Seventh Framework Programme for research, technological development and demonstration under grant agreement no 316889. PS acknowledges the support from National Science Centre (Poland) under research Grant No. 2012/07/E/ST3/01734.

REFERENCES

1. Jennings JN. *Karst Geomorphology.* Oxford: Blackwell (1985).
2. Palmer, Arthur, N. Origin and morphology of limestone caves. *Geol Soc Am Bull.* (1991) **103**:1–21.
3. Jamtveit B, Meakin P. *Growth, Dissolution and Pattern Formation in Geosystems.* Dordrecht: Springer (1999).
4. Chadam D, Hoff D, Merino E, Ortoleva P, Sen A. Reactive infiltration instabilities. *IMA J Appl Math.* (1986) **36**:207–21.
5. Ortoleva P, Chadam J, Merino E, Sen A. Geochemical self-organization II: the reactive-infiltration instability. *Am J Sci.* (1987) **287**:1008–40.
6. Hoefner ML, Fogler HS. Pore evolution and channel formation during flow and reaction in porous media. *AIChE J.* (1988) **34**:45–54.
7. Walsh P, Morawiecka-Zacharz I. A dissolution pipe palaeokarst of mid-Pleistocene age preserved in Miocene limestones near Staszów, Poland. *Palaeogeogr Palaeoclimatol Palaeoecol.* (2001) **174**:327–50. doi: 10.1016/S0031-0182(01)00317-0
8. De Waele J, Lauritzen SE, Parise M. On the formation of dissolution pipes in quaternary coastal calcareous arenites in mediterranean settings. *Earth Surf Proc Land.* (2011) **36**:143–57. doi: 10.1002/esp.2022
9. Yehle LA. Soil tongues and their confusion with certain indicators of periglacial climate [Wisconsin]. *Am J Sci.* (1954) **252**:532–46.
10. Rowan G. Theory of acid treatment of limestone formations. *J Inst Pet.* (1959) **45**:321.
11. Fredd CN, Fogler HS. Influence of transport and reaction on wormhole formation in porous media. *AIChE J.* (1998) **44**:1933–49.
12. Panga M, Ziauddin M, Balakotaiah V. Two-scale continuum model for simulation of wormhole formation in carbonate acidization. *AIChE J.* (2005) **51**:3231–48. doi: 10.1002/aic.10574
13. Cohen C, Ding D, Quintard M, Bazin B. From pore scale to wellbore scale: impact of geometry on wormhole growth in carbonate acidization. *Chem Eng Sci.* (2008) **63**:3088–99. doi: 10.1016/j.ces.2008.03.021
14. Maheshwari P, Ratnakar RR, Kalia N, Balakotaiah V. 3-D simulation and analysis of reactive dissolution and wormhole formation in carbonate rocks. *Chem Eng Sci.* (2013) **90**:258–74. doi: 10.1016/j.ces.2012.12.032
15. Ishibashi T, McGuire T, Watanabe N, Tsuchiya N, Elsworth D. Permeability evolution in carbonate fractures: competing roles of confining stress and fluid pH. *Water Resour Res.* (2013) **49**:2828–42. doi: 10.1002/wrcr.20253
16. Daccord G. Chemical dissolution of a porous medium by a reactive fluid. *Phys Rev Lett.* (1987) **58**:479–82.
17. Daccord G, Lenormand R. Fractal patterns from chemical dissolution. *Nature* (1987) **325**:41–3.
18. Ewers RO. *Cavern Development in the Dimensions of Length and Breadth.* Ph.D. thesis, McMaster University (1982).
19. Groves CG, Howard AD. Early development of karst systems. I. Preferential flow path enlargement under laminar flow. *Water Resour Res.* (1994) **30**:2837–46.
20. Hanna RB, Rajaram H. Influence of aperture variability on dissolutional growth of fissures in karst formations. *Water Resour Res.* (1998) **34**:2843–53.
21. Cheung W, Rajaram H. Dissolution finger growth in variable aperture fractures: role of the tip-region flow field. *Geophys Res Lett.* (2002) **29**:2075. doi: 10.1029/2002GL015196
22. Worthington S R., Ford D. C. Self-organized permeability in carbonate aquifers. *Groundwater* (2009) **47**:326–36. doi: 10.1111/j.1745-6584.2009.00551.x
23. Szymczak P, Ladd AJC. The initial stages of cave formation: beyond the one-dimensional paradigm. *Earth Planet Sci Lett.* (2011) **301**:424–32. doi: 10.1016/j.epsl.2010.10.026
24. Budek A, Szymczak P. Network models of dissolution of porous media. *Phys Rev E* (2012) **86**:056318. doi: 10.1103/PhysRevE.86.056318
25. Chaudhuri A, Rajaram H, Viswanathan H. Early-stage hypogene karstification in a mountain hydrologic system: a coupled thermohydrochemical model incorporating buoyant convection. *Water Resour Res.* (2013) **49**:5880–99. doi: 10.1002/wrcr.20427
26. Polak A, Elsworth D, Liu J, Grader AS. Spontaneous switching of permeability changes in a limestone fracture with net dissolution. *Water Resour Res.* (2004) **40**:W03502. doi: 10.1029/2003WR002717
27. Noiriel C, Gouze P, Made B. 3D analysis of geometry and flow changes in a limestone fracture during dissolution. *J Hydrol.* (2013) **486**:211–23. doi: 10.1016/j.jhydrol.2013.01.035
28. Luquot L, Rodriguez O, Gouze P. Experimental characterization of porosity structure and transport property changes in limestone undergoing different dissolution regimes. *Transport Porous Med.* (2014) **101**:507–32. doi: 10.1007/s11242-013-0257-4
29. Garcia-Rios M, Luquot L, Soler JM, Cama J. Influence of the flow rate on dissolution and precipitation features during percolation of CO_2-rich sulfate solutions through fractured limestone samples. *Chem Geol.* (2015) **414**:95–108. doi: 10.1016/j.chemgeo.2015.09.005
30. Luquot L, Gouze P. Experimental determination of porosity and permeability changes induced by injection of CO_2 into carbonate rocks. *Chem Geol.* (2009) **265**:148–59. doi: 10.1016/j.chemgeo.2009.03.028
31. Ellis BR, Peters CA, Fitts JP, Bromhal GS, McIntyre D, Warzinski R, et al. Deterioration of a fractured carbonate caprock exposed to CO_2-acidified brine flow. *Greenh Gases Sci Technol.* (2011) **1**:248–60. doi: 10.1002/ghg.25

32. Elkhoury JE, Ameli P, Detwiler RL. Dissolution and deformation in fractured carbonates caused by flow of co_2-rich brine under reservoir conditions. *Int J Greenh Gas Control* (2013) **16**:S203–15. doi: 10.1016/j.ijggc.2013.02.023
33. Hao Y, Smith M, Sholokhova Y, Carroll S. CO_2 -induced dissolution of low permeability carbonates . Part II : numerical modeling of experiments. *Adv Water Res.* (2013) **62**:388–408. doi: 10.1016/j.advwatres.2013.09.009
34. Deng H, Ellis BR, Peters CA, Fitts JP, Crandall D, Bromhal GS. Modifications of carbonate fracture hydrodynamic properties by CO_2-acidified brine flow. *Energy Fuels* (2013) **27**:4221–31. doi: 10.1021/ef302041s
35. Carroll S, Hao Y, Smith M, Sholokhova Y. Development of scaling parameters to describe CO_2-rock interactions within Weyburn-Midale carbonate flow units. *Int J Greenh Gas Control* (2013) **16**:S185–93. doi: 10.1016/j.ijggc.2012.12.026
36. Smith M, Sholokhova Y, Hao Y, Carroll S. CO_2-induced dissolution of low permeability carbonates. Part I: characterization and experiments. *Adv Water Resour.* (2013) **62**:370–87. doi: 10.1016/j.advwatres.2013.09.008
37. Elkhoury J, Detwiler R, Ameli P. Can a fractured caprock self-heal? *Earth Planet Sci Lett.* (2015) **417**:99–106. doi: 10.1016/j.epsl.2015.02.010
38. Ott H, Oedai S. Wormhole formation and compact dissolution in single- and two-phase CO_2-brine injections. *Geophys Res Lett.* (2015) **42**:2270–6. doi: 10.1002/2015GL063582
39. Szymczak P, Ladd AJC. A network model of channel competition in fracture dissolution. *Geophys Res Lett.* (2006) **33**:L05401. doi: 10.1029/2005GL025334
40. Herwitz SR. Stemflow influences on the formation of solution pipes in Bermuda eolianite. *Geomorphology* (1993) **6**:253–71.
41. Lipar M, Webb JA, White SQ, Grimes KG. The genesis of solution pipes: evidence from the middle–late pleistocene bridgewater formation calcarenite, Southeastern Australia. *Geomorphology* (2015) **246**:90–103. doi: 10.1016/j.geomorph.2015.06.013
42. Sun Q, Cartwright J, Wu S, Chen D. 3D seismic interpretation of dissolution pipes in the South China Sea: genesis by subsurface, fluid induced collapse. *Mar Geol.* (2013) **337**:171–81. doi: 10.1016/j.margeo.2013.03.002
43. Golfier F, Zarcone C, Bazin B, Lenormand R, Lasseux D, Quintard M. On the ability of a Darcy-scale model to capture wormhole formation during the dissolution of a porous medium. *J Fluid Mech.* (2002) **457**:213–54. doi: 10.1017/S0022112002007735
44. Golfier F, Bazin B, Lenormand R, Quintard M. Core-scale description of porous media dissolution during acid injection - Part I: theoretical development. *Comput Appl Math* (2004) **23**:21. doi: 10.1590/S0101-82052004000200005
45. Upadhyay VK, Szymczak P, Ladd AJC. Initial conditions or emergence: what determines dissolution patterns in rough fractures? *J Geophys Res Solid Earth* (2015) **120**:6102–21. doi: 10.1002/2015jb012233
46. Krug J. Origin of scale invariance in growth processes. *Adv Phys.* (1997) **46**:139–282.
47. Budek A, Garstecki P, Samborski A, Szymczak P. Thin-finger growth and droplet pinch-off in miscible and immiscible displacements in a periodic network of microfluidic channels. *Phys Fluids* (2015) **27**:112109. doi: 10.1063/1.4935225
48. Roy A, Roy S, Bhattacharyya AJ, Banerjee S, Tarafdar S. Discrete scale invariance in viscous fingering patterns. *Eur Phys J B* (1999) **12**:1–3. doi: 10.1007/s100510050966
49. Couder Y, Maurer J, González-Cinca R, Hernández-Machado A. Side-branch growth in two-dimensional dendrites. I. experiments. *Phys Rev E* (2005) **71**:31602. doi: 10.1103/PhysRevE.71.031602
50. Huang Y, Ouillon G, Saleur H, Sornette D. Spontaneous generation of discrete scale invariance. *Phys Rev E* (1997) **55**:6433–47.
51. Howard AD. The development of karst features. *Bull Natl Spel Soc.* (1963) **25**:45–65.
52. Palmer AN. Cutters and pinnacles in the Salem limestone of Indiana. In: Ginés A, Knez M, Slabe T, Dreybrodt W, editors. *Karst Rock Features: Karren Sculpturing.* Ljubljana: ZRC Publishing (2009). pp. 349–58.
53. Steefel CI. Geochemical kinetics and transport. In: Brantley SL, Kubicki JD, White AF, editors. *Kinetics of Water-Rock Interaction.* New York, NY: Springer (2008). pp. 545–89.
54. Dreybrodt W. The role of dissolution kinetics in the development of karst aquifers in limestone: a model simulation of karst evolution. *J Geol.* (1990) **98**:639–55.
55. Kalia N, Balakotaiah V. Modeling and analysis of wormhole formation in reactive dissolution of carbonate rocks. *Chem Eng Sci.* (2007) **62**:919–28. doi: 10.1016/j.ces.2006.10.021
56. Grimes KG. Solution pipes and pinnacles in syngenetic karst. In: Ginés A, Knez M, Slabe T, Dreybrodt W, editors. *Karst Rock Features. Karren Sculpturing.* Ljubljana: ZRC Publishing (2009). pp. 513–26.
57. Schaetzl R, Anderson S. *Soils: Genesis and Geomorphology.* New York, NY: Cambridge University Press (2005).
58. Kondratiuk P, Szymczak P. Steadily translating parabolic dissolution fingers. *SIAM J Appl Math.* (2015) **75**:2193–213. doi: 10.1137/151003751
59. Adriano DC, Havas M, editors. *Acidic Precipitation.* New York, NY: Springer (1989).
60. Szymczak P, Ladd AJC. Reactive infiltration instabilities in rocks. Part 2. Dissolution of a porous matrix. *J Fluid Mech.* (2014) **738**:591–630. doi: 10.1017/jfm.2013.586

Conflict of Interest Statement: The authors declare that the research was conducted in the absence of any commercial or financial relationships that could be construed as a potential conflict of interest.

This manuscript was edited by Bjornar Sandnes; a Topic Editor of the Research Topic Flow and Transformations in porous media, in the absence of bias and to the high standards of ethical conduct expected by Frontiers.

frontiers in Physics

ORIGINAL RESEARCH
published: 06 October 2015
doi: 10.3389/fphy.2015.00080

Long runout landslides: a solution from granular mechanics

Stanislav Parez and Einat Aharonov*

Faculty of Mathematics and Sciences, Institute of Earth Sciences, Hebrew University of Jerusalem, Jerusalem, Israel

Large landslides exhibit surprisingly long runout distances compared to a rigid body sliding from the same slope, and the mechanism of this phenomena has been studied for decades. This paper shows that the observed long runouts can be explained quite simply via a granular pile flowing downhill, while collapsing and spreading, without the need for frictional weakening that has traditionally been suggested to cause long runouts. Kinematics of the granular flow is divided into center of mass motion and spreading due to flattening of the flowing mass. We solve the center of mass motion analytically based on a frictional law valid for granular flow, and find that center of mass runout is similar to that of a rigid body. Based on the shape of deposits observed in experiments with collapsing granular columns and numerical simulations of landslides, we derive a spreading length $R_f \sim V^{1/3}$. Spreading of a granular pile, leading to a deposit angle much lower than the angle of repose or the dynamic friction angle, is shown to be an important, often dominating, contribution to the total runout distance. The combination of the predicted center of mass runout and the spreading length gives the runout distance in a very good match to natural landslides.

Keywords: long runout landslides, Heim's ratio, granular flows, granular materials, spreading, frictional weakening, apparent friction

OPEN ACCESS

Edited by:
Antonio F. Miguel, University of Evora, Portugal

Reviewed by:
Eric Josef Ribeiro Parteli, University of Cologne, Germany
Benjy Marks, University of Oslo, Norway

****Correspondence:***
Stanislav Parez, Faculty of Mathematics and Sciences, Institute of Earth Sciences, Hebrew University of Jerusalem, Edmond J. Safra Campus, Givat Ram, Jerusalem 91904, Israel
stanislav.parez@mail.huji.ac.il

Specialty section:
This article was submitted to Interdisciplinary Physics, a section of the journal Frontiers in Physics

Received: *29 June 2015*
Accepted: *09 September 2015*
Published: *06 October 2015*

Citation:
Parez S and Aharonov E (2015) Long runout landslides: a solution from granular mechanics. Front. Phys. 3:80. doi: 10.3389/fphy.2015.00080

1. Introduction

Landslides are natural hazards responsible for serious damage to life and property. Understanding their flow would allow us to predict their runout (horizontal travel distance), estimate their energy and reduce the associated risk. From the mechanical point of view, landslides are granular mass flowing down a hill slope and on a flat plane while spreading due to internal shear. However, the mechanical problem of evolution of a granular flow in the configuration depicted in **Figure 1** have not been fully solved yet. In this paper, we give an analytical solution for the case when the slide can be modeled as a granular flow driven by gravity and mechanical interaction between grains. We predict the runout distance L and compare the prediction to natural landslides.

Runout of landslides has attracted a lot of scientific interest. The most debated puzzle has been the "long runout landslides" problem: large landslides exhibit a surprisingly long runout that seems to violate common frictional behavior. For a rigid block of rock to travel the same distance as large landslides would require friction coefficient as low as 0.1, i.e., a small value compared to common friction coefficient of rocks $\simeq$ 0.4–0.7 observed in laboratory scale experiments if no plastic processes operate.

The energy conservation for a rigid body sliding with constant friction coefficient μ_C yields [1] $\rho g H_{COM} = \mu_C \rho g L_{COM}$, or

$$\frac{H_{COM}}{L_{COM}} = \mu_C \quad (1)$$

where H_{COM} and L_{COM} are drop height and runout of the center of mass (COM), as shown in **Figure 1**. For the same reason, Heim's ratio H/L (*a.k.a* apparent friction) is used as a proxy for friction coefficient of landslides. For ease of field measurements, H and L are the maximum drop height and runout (see **Figure 1**). **Figure 2A** shows Heim's ratio as a function of landslide volume, V, taken from Lucas et al. [2]. The data includes field data from literature and digital topography models using photogrammetry. Two surprising observations emerge: (a) Heim's ratio is not a constant like for the rigid block with constant friction coefficient, but decreases with landslide volume, and (b) the minimum value observed for largest landslides is as low as $H/L \approx 0.1$, i.e., considerably lower than friction coefficient of common rocks or soils. In other words, larger landslides achieve longer runouts on falling from a hill slope with given height. While field data is usually plotted in terms of Heim's ratio, the best collapse of data is achieved when plotting simply L as a function of V, as shown in **Figure 2B**. Legros [3] concludes that landslide spreading is essentially controlled by their volume, and not by H.

Several processes have been suggested to solve the long runout puzzle, *e.g.* frictional heating of pore fluids [4, 5], fluidization [8–11], or plastic deformation due to melting of grains [6, 7] and flash weakening [2, 4]. Here, we study a purely mechanical problem of granular flow under a gravitational field. In that case, two processes might account for the long runout of landslides relative to rigid block sliding: (a) the friction decreases considerably with volume, e.g., due to changes in shear rate, and/or (b) spreading of grains relative to COM is larger for larger landslides.

Our knowledge about granular flows mostly comes from laboratory scale experiments and computer simulations. As a result, three flow regimes were classified [12]: "solid" in which grains interact via long-lasting frictional contacts and deform slowly, "gaseous" in which grains interact through short collisions compared to deformation time scale, and "liquid" which is a transition between the two previous. For flow down a slope, the three regimes can be attained by changing the slope angle θ [13, 14]. If θ is small, no flow is observed, only an elastic deformation. Once θ exceeds the angle of repose, the flow accelerates. Yet, the increasing rate of collisions eventually leads to a steady flow. If, however, the slope is steep enough the flow keeps accelerating because the energy that grains receive during free fall between collisions exceeds the dissipation. We can expect that most of landslides flow in the liquid regime, in which flow is possible yet not too vigorous, because they occur when a slope becomes unstable, i.e., close to the angle of repose.

Evolution of granular flows in the liquid regime has been solved only approximately using "shallow water models" or by means of computer simulations. Neither of the approaches has established scaling laws for runout distance with volume. "Shallow water models" arise from depth-averaged mass and momentum conservation equations, originally derived by Savage and Hutter [15]. The resulting equation for mean velocity neglects spatial variation of velocity inside the moving body. Hence, the shallow water model is less accurate if shear rate is large. Flow down a slope was studied by Savage and Hutter [15], Pouliquen and Forterre [16], Mangeney et al. [17], Faccanoni and Mangeney [18] and Capart and Hung [19], including analytical

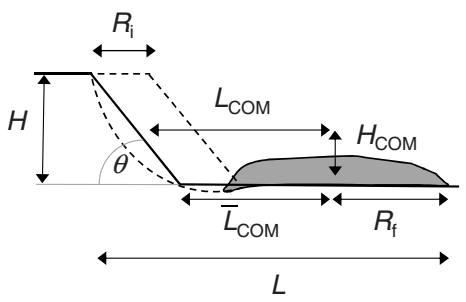

FIGURE 1 | Geometry of the landslide model. The dashed line identifies the region of the original slope that was removed by the landslide. The shaded area is the final deposit of the landslide. Calculation of the total runout L is divided in two sub-problems: (a) the center-of-mass runout L_{COM} and (b) the initial and final spreads R_i and R_f. L_{COM} is derived from an analytical solution for granular flow of constant thickness on an inclined plane. Spreading of the landslide due to its flattening is included in the calculation of R_f.

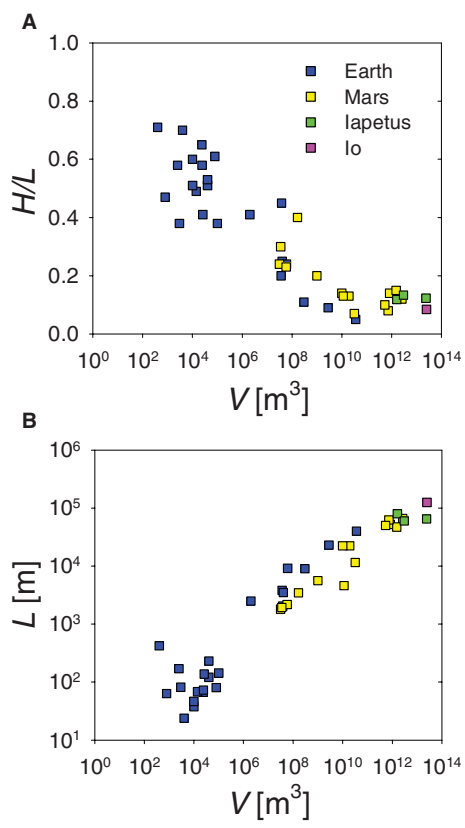

FIGURE 2 | (A) Heim's ratio H/L for a collection of landslides from the Earth ($g = 9.81\,\mathrm{ms}^{-2}$), Mars ($g = 3.73\,\mathrm{ms}^{-2}$), Iapetus ($g = 0.223\,\mathrm{ms}^{-2}$), and Io ($g = 1.796\,\mathrm{ms}^{-2}$), taken from Lucas et al. [2]. Note that Heim's ratio decreases with landslide volume to a value as low as ≈ 0.1, i.e., considerably lower than friction coefficient of common rocks or soils. **(B)** Runout as a function of landslide volume for the same collection of landslides.

solutions for evolution of velocity, front position and thickness. Those studies do not address cessation of the flow, or prediction of runout or Heim's ratio. The later was done by Lucas et al. [2] within a semi-empirical model. They showed that Heim's ratio based on the analytical solution of Mangeney et al. [17] and Faccanoni and Mangeney [18] is compatible with field data if the value of basal friction coefficient is adjusted appropriately. However, the optimal value is significantly lower than that obtained from laboratory experiments.

An alternative to analytical models is granular dynamics simulations. Campbell et al. [20] carried out large scale discrete simulations, which showed Heim's ratio as a function of volume similar to field data. Staron and Lajeunesse [21] suggest that the volumetric effect is dominated by spreading of the granular mass relative to COM, while Heim's ratio for COM, $H_{\mathrm{COM}}/L_{\mathrm{COM}}$ is volume independent. Yet, no quantitative estimation of the two contributions (COM runout and spreading length) has been given.

Experiments and simulations regarding flow on an inclined plane revealed scaling of steady flow velocity with flow thickness h as $\sim h^{3/2}$ [13, 14, 22, 23]. Later, this scaling was explained by dimensional analysis for friction coefficient [12, 23]. This opens a possibility that larger (thicker) slides achieve larger kinetic energy, which would result in longer runouts. However, unsteady flows, i.e., acceleration and deceleration and flow with varying thickness, have not been studied enough yet. In particular, the time scale over which landslide accelerate has not been derived. Consequently, it is not clear whether or how kinetic energy depends on landslide volume.

Another class of experiments is collapse of granular columns on a flat surface. A granular column that is initially supported by walls is suddenly released and spreads. Lajeunesse et al. [24] showed that the spread of the deposit is controlled by aspect ratio of the initial column, and that the slope angle at the foot of the deposit saturates at 5° (much lower than the angle of repose) for columns with large aspect ratios. Similar results were obtained in experiments by Lube et al. [25] and simulations by Utili et al. [26]. Granular column collapse experiments shed light on the role of spreading of landslide mass relative to COM. During their flow, landslides change their shape. They become thinner and spread along fronts and flanks as surface grains fall down or are squeezed out. As a consequence, total runout might be considerably larger than that due to COM.

In this work, we study kinematics of granular materials flowing down an inclined plane and decelerating on a flat plane thereafter. We solve the runout distance in two steps. First, we derive COM runout based on an analytical solution for velocity profile in granular flow of constant thickness. The prediction is compared to numerical simulations. Second, we account for the longitudinal spreading of the collapsing body. Finally, we compare the resulting runout to field data for natural landslides.

2. Methods

2.1. Simulations

The numerical simulations were used as a benchmark for analytical calculation of COM evolution. They employ the discrete element method (DEM) [27], in which the Newtonian equations of motion for a set of grains are solved in discrete steps.

Grains are modeled as disks with rotational and translational degrees of freedom. They interact via visco-elastic contact forces according to Hertz-Mindlin contact model [28, 29]

$$F_{ij}^n = \frac{\sqrt{2}E}{3(1-\eta^2)}\sqrt{R_{ij}\xi_{ij}}\xi_{ij} - \gamma\sqrt{R_{ij}\xi_{ij}}\dot{\xi}_{ij}\,,$$
$$F_{ij}^t = \min\left[\frac{2\sqrt{2}E}{(2-\eta)(1+\eta)}\sqrt{R_{ij}\xi_{ij}}\Delta s,\ \mu_{gg}F_{ij}^n\right], \qquad (2)$$

where F_{ij}^n and F_{ij}^t are normal and shear components of the contact force between grains i and j. R_{ij} is the harmonic mean of the grains radii and ξ_{ij} is the overlap between the two grains. Elastic moduli $E = 1.31 \times 10^{10}$ Pa and Poisson's ratio $\eta = 0.235$ were chosen to simulate quartz grains with density $\rho_{\mathrm{p}} = 2.5 \times 10^3\,\mathrm{kg\,m^{-3}}$. Energy dissipation is governed by a normal damping (the second term in F_{ij}^n) with damping coefficient $\gamma = 0.8$ and by the tangential friction F_{ij}^t. Restitution coefficient is not constant, but depends on velocities of colliding grains [28]. The tangential force is initially elastic, calculated from shear displacement Δs on contacts of the grains from the instant the contact was formed. Once the spring force exceeds the Coulomb friction criterion, the contact starts sliding with a constant shear force, $F_{ij}^t = \mu_{gg}F_{ij}^n$, where the grain-grain friction coefficient is $\mu_{gg} = 0.5$. Note that the grain-grain friction coefficient is not the same as the macroscopic dynamic friction coefficient, which is investigated below and found shear rate dependent.

Grain diameters were randomly drawn from a Gaussian distribution with both mean value and standard deviation equal to d. The distribution is however cut, so that all diameters fall within 0.8–1.2 d.

Periodic boundary conditions were applied in the direction of the flow, which is equivalent to constant thickness flow boundary condition used in the theory described below. The width of the simulation box along the flow direction was $96\,d$ (no size effects due to this scale were observed), while thickness of the flow varied among different simulations between $h = 12 - 96\,d$ to test the volumetric scaling.

Equations of motion were integrated using the velocity Verlet algorithm [30] with a time step $0.1d\sqrt{\rho_{\mathrm{p}}/E}$ small enough to resolve elastic waves due to grain-grain collisions.

Granular systems are initiated as layers with random loose packing, standing on a flat horizontal surface made of grains with the same properties that are glued together and whose positions are fixed. Subject to vertical gravitational acceleration the grains sediment. Then we turn the slope at an inclination angle $\theta = 17 - 25\,^\circ$. The selected range can accommodate steady flows, see Silbert et al. [13] and Pouliquen [14] for a phase diagram of flow regimes. For lower inclination angles no flow is initiated, while larger inclination angles lead to unstable acceleration and breakdown of the "liquid" flow regime.

Velocity and density profiles were monitored during the run of simulations. The distance traveled by a landslide was calculated as a running integral of COM velocity. Once the traveled distance reached the length of the slope available for

COM sliding, $H_{\mathrm{COM}}/\sin\theta$, for given H_{COM} and θ, the simulation was continued for $\theta = 0$, i.e., on the flat plane, until the COM velocity decayed to zero.

2.2. Theory

In this section, we solve kinematics of granular flow in the geometry depicted in **Figure 1** in order to obtain flow profiles and predict COM motion. For the derivation to be analytically tractable, we impose that thickness of the flow is constant and uniform. Driven by gravity, landslides preferentially spread along the slope direction rather than laterally. As a consequence, the flow is essentially two-dimensional with an elongated central homogeneous region. Assuming that this homogeneous region dominates the overall landslide momentum, its velocity average represents the COM velocity.

The longitudinal spreading reduces landslide's thickness, which is therefore not constant in time. It will be shown below that the COM runout does not vary significantly with thickness. Therefore, the prediction derived for the flow of constant thickness provides a good estimate for a general flow with an extensive homogeneous region.

The equation of motion for a two-dimensional flow of constant thickness is

$$\rho\frac{\partial v}{\partial t} = \rho g\sin\theta - \frac{\partial \tau}{\partial y} \tag{3}$$

where y is depth inside the flow measured from the top surface, t is time, $v(y,t)$ is velocity along the flow direction, $\tau(y,t)$ is shear stress, g is gravitational acceleration and ρ is flow mass density (of a representative volume). The first term on the right hand side is the gravitational force, the second term is friction force that resists acceleration. ρ is considered uniform [13] and constant (a very week dependence on flow velocity has been found [12, 23, 31]).

To form a closed set of equations we need another relation between τ and v, i.e., a rheological law. Friction is known from physics and geophysics to depend on sliding velocity. The only local dimensionless quantity for dry granular flow that dissipates energy through visco-elastic collisions is the so-called inertial number I

$$I(y,t) = \frac{\dot\gamma d}{\sqrt{N/\rho_{\mathrm{p}}}}, \tag{4}$$

where $\dot\gamma(y,t) = -\frac{\partial v}{\partial y}$ is shear rate (the negative sign is because y axis is pointing downwards), $N(y,t)$ is normal stress, d is grain size and ρ_{p} is mass density of the grain material ($2.5\times10^3\,\mathrm{kg\,m^{-3}}$ for sand). The friction coefficient μ (also dimensionless) can then be expressed as an expansion in I. The linearized version of the friction law is

$$\mu(y,t) \equiv \frac{\tau}{N} = \mu_0 + \beta I, \tag{5}$$

where μ_0 and β are material parameters ($\mu_0 \approx 0.55$ and $\beta \approx 0.5$ for sand [23]). This type of rheology, in which μ is a function of I, has been suggested and verified in laboratory experiments and simulations [12, 16, 23, 31] for variety of systems and boundary conditions. Since β has been found positive, friction increases with shear rate under constant normal stress, provided plastic processes are negligible.

The observed uniform and constant density ρ implies constant and linear normal stress $N = \rho g\cos\theta y$. This gives shear stress

$$\tau = \mu_0\rho g\cos\theta y + \rho\beta d\sqrt{\frac{1}{\nu}g\cos\theta y}\,\dot\gamma, \tag{6}$$

where $\nu \equiv \rho/\rho_{\mathrm{p}} \approx 0.55$ is solid fraction [13]. The first term in Equation (6) is rate independent, and controls the flow under low shear rate. Neglecting the other term would, according to Equation (3), lead to uniform acceleration $g(\sin\theta - \mu_0\cos\theta)$. The second term accounts for increase of friction with shear rate. As a result, flow becomes steady once the friction force balances the driving force.

We seek a solution of Equations (3) and (6) along with boundary conditions

$$\begin{aligned} &(a)\quad \tau = 0 \text{ for } y = 0,\\ &(b)\quad v = 0 \text{ for } y = h,\\ &(c)\quad v = v_0(y) \text{ at } t = 0, \end{aligned} \tag{7}$$

where h is flow thickness. The boundary conditions say that: (a) the top surface of the slide is free of stresses, (b) the velocity at the bottom of the sliding mass is zero (the ground surface is rough), and (c) the initial velocity is v_0.

The solution for velocity satisfying boundary conditions Equations (7a,b) is [Parez et al., under review]

$$\begin{aligned} v(y,t) &= v_{\mathrm{p}} + \frac{16}{9}h^2\sum_{n>0}\frac{b_n}{\kappa_n^2}\frac{\mathrm{d}}{\mathrm{d}y}\left[\sqrt{y}J_{2/3}\left(\kappa_n\left(\frac{y}{h}\right)^{3/4}\right)\right]e^{-t/T_n},\\ \text{where}\quad v_{\mathrm{p}} &= \begin{cases}\frac{2}{3}B(\theta)\frac{\sqrt{g}h^{3/2}}{d}\left[1-\left(\frac{y}{h}\right)^{3/2}\right] & \text{for } \theta > \theta_{\mathrm{r}}\\ -g(\mu_0\cos\theta - \sin\theta)t & \text{for } \theta < \theta_{\mathrm{r}}\end{cases}\\ T_n &= C(\theta)\frac{h^{3/2}}{\kappa_n^2\sqrt{g}d}, \end{aligned} \tag{8}$$

in which $J_{2/3}(z)$ is a Bessel function of the first kind [32], constants κ_n are given in **Table 1** for a few n and

$$\begin{aligned} B(\theta) &= \frac{\sqrt{\nu}(\sin\theta - \mu_0\cos\theta)}{\beta\sqrt{\cos\theta}},\\ C(\theta) &= \frac{16\sqrt{\nu}}{9\beta\sqrt{\cos\theta}}. \end{aligned} \tag{9}$$

The coefficients b_n in the expansion are determined from the initial condition Equation (7c) using the orthogonality relation [32] $\int_0^h \sqrt{y}J_{2/3}\left(\kappa_i\left(\frac{y}{h}\right)^{3/4}\right)J_{2/3}\left(\kappa_j\left(\frac{y}{h}\right)^{3/4}\right)\mathrm{d}y \sim \delta_{ij}$.

Note that the solution Equation (8) is different depending whether θ is greater or lower than angle of repose θ_{r} ($\approx 30^\circ$ for sand). The first applies for acceleration down a slope while the latter for deceleration on the flat plane.

TABLE 1 | Constants κ_n and T_n/T_1 used in the expansion in Equation (8).

n	κ_n	T_n/T_1
1	1.87	1
2	4.99	0.14
3	8.12	0.053

2.2.1. Acceleration down a slope

The down-slope flow starts when $\theta > \theta_r$. In that case, Equation (8) predicts acceleration toward a steady velocity given by the v_p term, which is consistent with the Bagnold flow profile [13, 22]. The second term is the transient toward the steady velocity. Because T_1 is sufficiently larger than the other T_n's (see **Table 1**), it dominates the time evolution after the very initial period. Keeping only the $T_1 \equiv T$ term (we drop the subscript in the following) and imposing $v_0 = 0$, velocity can be approximated as

$$v(y,t) = \frac{2}{3}B(\theta)\frac{\sqrt{g}h^{3/2}}{d}\left[1-\left(\frac{y}{h}\right)^{3/2}\right]\left(1-e^{-t/T}\right). \quad (10)$$

Note that T has the meaning of the acceleration duration scale.

The COM velocity is calculated as the depth averaged velocity

$$v_{\mathrm{COM}}(t) = \frac{1}{h}\int_0^h v(y,t)\mathrm{d}y = \frac{2}{5}B(\theta)\frac{\sqrt{g}h^{3/2}}{d}\left(1-e^{-t/T}\right). \quad (11)$$

The time t_s the landslide's COM takes to reach the bottom of the slope is set by the length of the slope $H_{\mathrm{COM}}/\sin\theta$ available to COM sliding

$$\frac{H_{\mathrm{COM}}}{\sin\theta} = \int_0^{t_s} v_{\mathrm{COM}}(t)\mathrm{d}t = \frac{2}{5}B(\theta)\frac{\sqrt{g}h^{3/2}}{d}\left[t_s - T\left(1-e^{-t_s/T}\right)\right]. \quad (12)$$

This time determines the velocity $v_s(y) = v(y,t_s)$ and kinetic energy per unit mass $\epsilon_s^k = \frac{1}{2h}\int_0^h v^2(y,t_s)\,\mathrm{d}y$ reached at the bottom of the slope. We can calculate their values analytically for the following two limiting cases. If $t_s >> T$, i.e., if the slide reaches a steady flow on the slope,

$$v_s = v_p = \frac{2}{3}B(\theta)\frac{\sqrt{g}h^{3/2}}{d}\left[1-\left(\frac{y}{h}\right)^{3/2}\right],$$
$$\epsilon_s^k = \frac{1}{10}B^2(\theta)\frac{gh^3}{d^2} \qquad (t_s >> T). \quad (13)$$

On the other hand, if $t_s << T$, i.e., the time to reach a steady flow is much larger than the time actually spent on the slope, then Equation (12) can be simplified as $\frac{H_{\mathrm{COM}}}{\sin\theta} \approx \frac{1}{5}B(\theta)\frac{\sqrt{g}h^{3/2}}{d}\frac{t_s^2}{T} = \frac{\kappa_1^2}{5}g\frac{B(\theta)}{C(\theta)}t_s^2$ and we get

$$v_s = \frac{2\sqrt{5}\kappa_1}{3}\sqrt{\frac{B(\theta)}{C(\theta)}\frac{gH_{\mathrm{COM}}}{\sin\theta}}\left[1-\left(\frac{y}{h}\right)^{3/2}\right],$$
$$\epsilon_s^k = \frac{\kappa_1^2}{2}\frac{B(\theta)}{C(\theta)}\frac{gH_{\mathrm{COM}}}{\sin\theta} \qquad (t_s << t). \quad (14)$$

Note that kinetic energy per unit mass (and the same can be shown for COM velocity and other kinematic properties) reached at the bottom of the slope does not depend on thickness h (or volume) of the slide if $t_s << T$. This is in agreement with Campbell's et al. large scale simulations, see Figure 9 in Campbell et al. [20].

The origin of the independence of flow properties on slide thickness for $t_s << T$ can be seen from the Taylor expansion of flow velocity Equation (11). Since both steady flow velocity and transient time T (see Equation 8) grow proportionally to $\sim h^{3/2}$, the average flow acceleration $v_{\mathrm{COM}}(t\to\infty)/T$ is independent of thickness. Therefore, all slides satisfying $t_s << T$ have the same evolution and reach the same depth-averaged properties (v_{COM}, ϵ_s^k) at the slope end.

We have seen that acceleration of the landslide's COM is determined by relative magnitudes of t_s and T. Since T is controlled by h, we can redefine this relation in terms of thickness. Using Equations (8) and (12) we can define a threshold thickness h_{thr} for which $t_s = T$

$$h_{\mathrm{thr}}^3 = \frac{45\kappa_1^2\beta^2}{16\nu(\sin\theta-\mu_0\cos\theta)\tan\theta}H_{\mathrm{COM}}d^2. \quad (15)$$

Hence, flow down a slope of length $H/\sin\theta$ is thickness-independent for slides with $h > h_{\mathrm{thr}}$, corresponding to the case $t_s < T$.

2.2.2. Deceleration on a Flat Plane

Once a slide reaches the flat plane it decelerates, because no driving force acts in the direction of motion. The evolution of velocity during deceleration is predicted by Equation (8) with $\theta = 0$ and $v_p = \mu_0 g\bar{t}$, where $\bar{t} = t - t_s$. The initial velocity is chosen to match the final velocity on the slope, $v_0 \equiv v(\bar{t}=0) = v_s$. Neglecting higher order terms than $T_1 \equiv \bar{T}$, velocity becomes

$$v(y,t) = v_s(y)e^{-(t-t_s)/\bar{T}} - \mu_0 g(t-t_s), \quad (t > t_s), \quad (16)$$

where the transient time $\bar{T}$ is related to T derived for the acceleration on the slope inclined at θ as $\bar{T} = T\sqrt{\cos\theta}$.

Once the velocity at given depth decays to zero, the layer becomes locked due to static friction and $v = 0$ thereafter. This happens at time $t_f(y)$, given by

$$v_s(y)e^{-(t_f(y)-t_s)/\bar{T}} - \mu_0 g(t_f(y)-t_s) = 0. \quad (17)$$

The distance $\bar{L}_{\mathrm{COM}}$ that COM of the slide travels on the flat plane is

$$\bar{L}_{\mathrm{COM}} = \frac{1}{h}\int_0^h\int_{t_s}^{t_f} v(y,t)\mathrm{d}t\mathrm{d}y. \quad (18)$$

While we can solve Equations (17) and (18) numerically, we can easily evaluate the maximum possible runout distance by assuming that friction has its minimum value μ_0. In that case, velocity decreases with a constant and uniform rate, $v(y,t) = v_s(y) - \mu_0 g(t-t_s)$, resulting in the breaking distance

$$\bar{L}_{\mathrm{COM}} = \frac{1}{2\mu_0 gh}\int_0^h v_s^2(y)\mathrm{d}y = \frac{\epsilon_s^k}{\mu_0 g}. \quad (19)$$

Hence, $\bar{L}_{\rm COM}$ is proportional to kinetic energy per unit mass $\epsilon_{\rm s}^{\rm k}$ reached at the bottom of the slope, which ranges between the limiting values given by Equations (13) and (14).

2.2.3. COM Runout and Heim's Ratio

The COM runout is the total horizontal distance traveled by COM of a slide $L_{\rm COM} = H_{\rm COM}/\tan\theta + \bar{L}_{\rm COM}$. Depending on relative magnitudes of h and $h_{\rm thr}$, the runout varies between the following two values

$$L_{\rm COM} = \begin{cases} \frac{H_{\rm COM}}{\tan\theta}\left[1 + 0.98\left(\frac{\tan\theta}{\mu_0} - 1\right)\frac{h^3}{h_{\rm thr}^3}\right] \approx \frac{H_{\rm COM}}{\tan\theta} \\ \qquad\qquad \text{if } h << h_{\rm thr}\,, \\ \frac{H_{\rm COM}}{\tan\theta}\left[1 + 0.98\left(\frac{\tan\theta}{\mu_0} - 1\right)\right] \approx \frac{H_{\rm COM}}{\mu_0} \\ \qquad\qquad \text{if } h >> h_{\rm thr}\,, \end{cases} \tag{20}$$

where we used Equations (19), (13), (14), and (15). Corresponding limiting values of Heim's ratio are

$$\frac{H_{\rm COM}}{L_{\rm COM}} = \begin{cases} \tan\theta & \text{if } h << h_{\rm thr}\,, \\ \mu_0 & \text{if } h >> h_{\rm thr}\,. \end{cases} \tag{21}$$

Note that $\tan\theta > \mu_0$ because the mass starts moving on a slope exceeding the effective friction angle $\arctan(\mu_0)$. Assuming $\theta = 30^\circ - 40^\circ$, Heim's ratio decreases from $\tan\theta = 0.58 - 0.84$ for small slides to $\mu_0 = 0.55$ for large slides. This range of values cannot explain the span observed for field data (see **Figure 2**), particularly the limiting value ≈ 0.1.

2.2.4. Spreading

Landslides change their shape during their flow. They become thinner while they spread along their perimeter, as grains on the surface fall down or are squeezed outwards. As a result, the horizontal extent of landslides, denoted as spread, changes. In this section, we estimate the spread of the final deposit based on the experiment by Lajeunesse et al. [24] and full landslide computer simulations by Campbell et al. [20].

Lajeunesse et al. performed experiments with granular columns that were suddenly released onto a flat plane and allowed to spread. The shape of the final deposit was conical with foot angle α depending on the aspect ratio a of the initial column. α decreased from angle of repose for $a \to 0$ to a saturated value of $\alpha_{\rm thr} = 5^\circ$ for $a > 3$. The core of the conical deposit with base area identical to the original column was almost undisturbed. Grain size and ground surface had a little effect on the spread.

Similar results were found by Campbell et al. for slides flowing down a slope in the same geometry as here (see **Figure 1**). The shape of final deposits was conical with foot angle $\alpha_{\rm thr} \approx 1.5^\circ$ independent of slide volume for large slides. The order of strata inside the slide was preserved as in the initial state.

Note that in both experiments the angle of the deposited pile is much lower than the angle of repose ($\approx 30^\circ$) if enough energy is provided for spreading.

Based on these results we might assume that natural landslides spread conically from their surface while the central region flows undisturbed, i.e., approximately described by Equation (11). We suggest that the foot angle is not a function of the initial aspect ratio, but more generally of energy per unit mass since it directly controls spreading even when the aspect ratio is low.

Assuming that deposits of large, long runout landslides studied here attain the threshold value $\alpha_{\rm thr}$, volume V of their deposit is $V = \pi R_{\rm f}^3 \tan\alpha_{\rm thr}/3$, where $R_{\rm f}$ is the spread of the deposit, i.e., radius of the cone base. Inversely, the spread depends on the landslide volume as

$$R_{\rm f} = \left(\frac{3}{\pi \tan\alpha_{\rm thr}} V\right)^{1/3}. \tag{22}$$

Deposits of natural landslides are not always conical. Sometimes, they are piled against the foot of the hill, or they are constrained by the landscape morphology. Yet, it is reasonable to expect that these constraints only change the pre-factor in Equation (22) while the $V^{1/3}$ scaling is still valid.

3. Results

3.1. COM Evolution

Figure 3 shows COM velocity evolution for landslides of different thickness. The quality of analytical prediction, Equation (11) (dashed lines), is tested against DEM simulations (solid lines) for $\theta = 17^\circ$, $d = 0.1$ m and $g = 9.81\,{\rm ms}^{-2}$. The slight difference between the two sets of curves is due to non-zero slip velocity observed in simulations. Note that larger landslides reach larger final steady flow velocity, but in progressively longer time.

On reaching the flat plane, landslides decelerate. In **Figure 4**, the decay of velocity profile is shown. The two sets of lines are simulation (solid lines) and analytical (Equation 16, dashed lines) results for $h = 9.6$ m, $\theta = 17^\circ$, $d = 0.1$ m, and $g = 9.81\,{\rm ms}^{-2}$. Since deep layers have lower velocity compared to the top of the landslide, they stop first. Consequently, the flow is confined to a gradually thinner layer near the top surface. The simulation profiles show a formation of a creeping layer at the depth where the flow stops. This is a non-local effect described in Kamrin et al. [33].

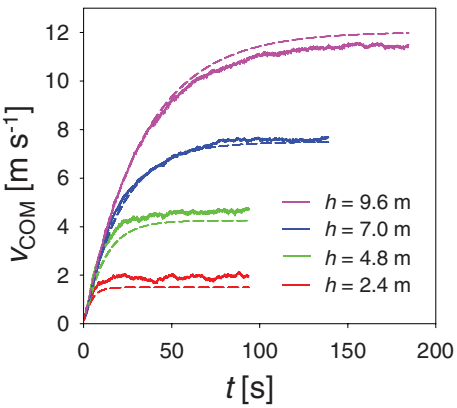

FIGURE 3 | Center of mass velocity during acceleration down a slope for landslides of thickness h = 2.4 – 9.6 m. Simulation results (solid lines) are compared to analytical prediction (dashed lines) after Equation (11). Note that larger landslides reach larger steady flow velocity. However, it takes them correspondingly longer time.

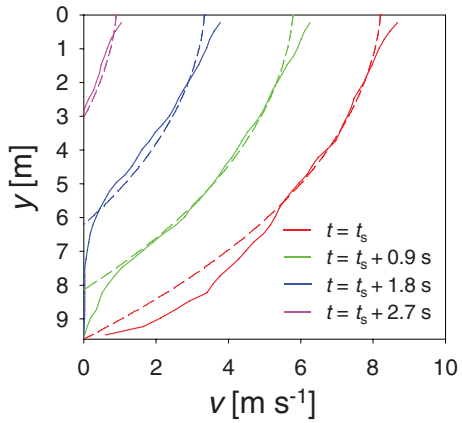

FIGURE 4 | Velocity profiles at various time instants during deceleration of the $h = 9.6$ m thick slide on a flat plane. Simulation results (solid lines) are compared to the analytical prediction (dashed lines) after Equation (16). The flow depth is gradually reduced.

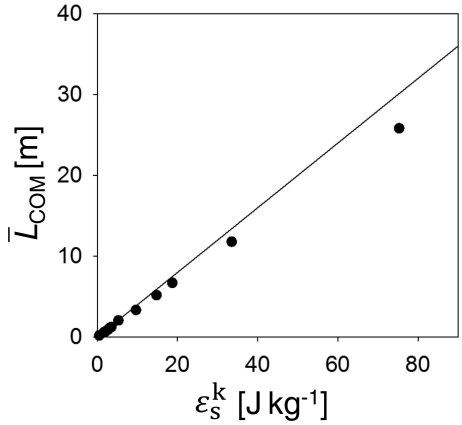

FIGURE 5 | Center of mass runout on the flat plane as a function of the kinetic energy achieved on the slope. Simulation results (points) were obtained for various slope lengths $H/\sin\theta = 10 - 100$ m and landslide thicknesses $h = 1.2 - 9.6$ m. The line denotes Equation (19), i.e., a deceleration distance derived for rate independent friction coefficient μ_0.

During the flow on the flat plane, landslides dissipate the kinetic energy achieved on the slope. **Figure 5** shows how the kinetic energy is transformed into the distance reached on the flat plane, $\bar{L}_{\rm COM}$. Points denote simulation results, in which the kinetic energy was varied by changing $H_{\rm COM}$, θ, h, d, or g. The line denotes the analytical prediction, Equation (19), derived for constant friction coefficient μ_0. For low kinetic energies, the simulation data follow the analytic solution. With increasing kinetic energy, shear rate increases, and, according to Equation (5), friction also increases. As a consequence, the resulting runout $\bar{L}_{\rm COM}$ is lower than predicted by Equation (19).

3.2. Runout and Heim's Ratio

To calculate total runout we have to sum up the horizontal extent of the initial mass, COM runout and the spread of the final deposit (see **Figure 1**)

$$L = R_{\rm i} + L_{\rm COM} + R_{\rm f}. \tag{23}$$

The initial extent can be estimated as $R_{\rm i} = (H - H_{\rm COM})/\tan\theta$. As shown in Equation (20), $L_{\rm COM}$ attains values between $H_{\rm COM}/\tan\theta$ (thin slides relative to $h_{\rm thr}$) and $H_{\rm COM}/\mu_0$ (thick slides relative to $h_{\rm thr}$). Since for typical slopes ($\theta = 30^\circ - 40^\circ$) $\tan\theta = 0.58 - 0.84$ is comparable to $\mu_0 = 0.55$, we can approximate $R_{\rm i} + L_{\rm COM} \approx (H - H_{\rm COM})/\mu_0 + H_{\rm COM}/\mu_0 = H/\mu_0$. Adding $R_{\rm f}$ from Equation (22) we arrive at

$$L = \frac{H}{\mu_0} + \left(\frac{3}{\pi \tan\alpha_{\rm thr}} V\right)^{1/3}. \tag{24}$$

Note that the first term is identical to runout that would be achieved by COM of a rigid block sliding from height H with friction μ_0. Runout of landslides is predicted to be longer by the spread length given by the second term.

In **Figure 6**, runout predicted from Equation (24) is compared to field observations. The field data (squares) is taken from Lucas et al. [2], and include values of H, L, and V for largest landslides observed in different planetary bodies. Circles denote the prediction of Equation (24) using the measured values of H and V for each landslide. The prediction matches the field observations over the whole range spanning 11 orders of magnitude.

The solid line in **Figure 6** is $2R_{\rm f}(V)$, i.e., as if L was equal to spread of a deposit resulting from a granular column collapse onto a horizontal surface. In the calculation of $R_{\rm f}$ from Equation (22), $\alpha_{\rm thr} = 1.5^\circ$ was used, based on the shape of deposits reported in Campbell et al. [20]. Since the $2R_{\rm f}$ line fits the circles, calculated as $H/\mu_0 + R_{\rm f}$, the two terms in Equation (24) are comparable. Thus, spreading of grains makes the toe of a landslide separated from the COM by a same-order distance as COM is separated from the head of the scarp left from the landslide on the hill. In other words, the runout is a few times longer than that of a rigid block sliding from the same height, i.e., $\simeq H/\mu_0$.

The fact that both terms of Equation (24) are of the same order of magnitude can be viewed as a relation between H and $V^{1/3}$. A closer examination of field data reveals that $H = 1.5V^{1/3}$ for landslides with $V < 10^5$ (for larger landslides the power is lower than 1/3). In other words, landslide linear dimension $V^{1/3}$ is comparable to the fall height H. This allows the following interpretation: Long runout landslides are likely to remove mass along an entire slope from the top at elevation H down to the valley at elevation 0, as sketched in **Figure 1**, i.e., not only the top of the slope as often assumed in simulation works. Furthermore, the relation $H \sim V^{1/3}$ implies, using Equation (24), $L \sim V^{1/3}$, which was found empirically in previous works [2, 3, 21].

Finally, **Figure 7** shows Heim's ratio H/L. The field observations (squares) are compared to the prediction based on Equation (24) (circles) for the values of H and V observed for the same collection of landslides. Despite the general agreement,

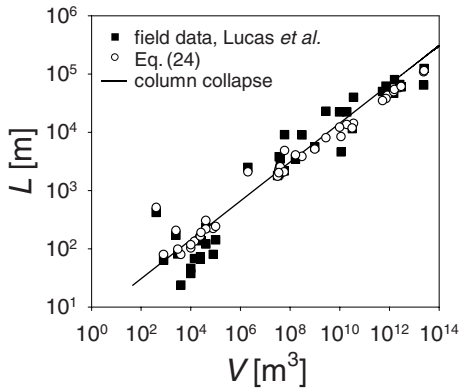

FIGURE 6 | Runout as a function of landslide volume. Full squares are field observations taken from [2]. Open circles denote Equation (24), in which H and V are taken from the same field observations and $\alpha_{\text{thr}} = 1.5^\circ$. Solid line is $2R_{\text{f}}(V)$ (see Equation 22), i.e., a total spread of a deposit resulting from a granular column collapse.

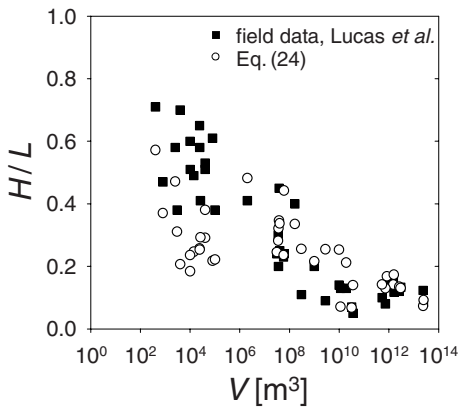

FIGURE 7 | Heim's ratio as a function of landslide volume. Full squares are field observations taken from Lucas et al. [2]. Open circles are prediction based on Equation (24), in which H and V are taken from the same field observations and $\alpha_{\text{thr}} = 1.5^\circ$.

predicted values are systematically lower for landslide with $V < 10^6\,\text{m}^3$. This might be because (a) relatively small landslides did not spread enough to achieve the minimum foot angle α_{thr} of their deposits and thus their spread is overestimated, or (b) the approximations leading to the term H/μ_0, i.e., exchanging μ_0 and $\tan\theta$, are too crude.

4. Discussion

Large landslides ($V > 10^8$) exhibit low Heim's ratio and corresponding long runout distance compared to sliding of a rigid body. This has traditionally been ascribed to processes that decrease friction coefficient (friction weakening), such as shear heating, flash weakening or fluidization [4–11]. These concepts require plastic processes or presence of pressurized pore fluids to reduce the frictional resistance, and achieve higher velocity and longer runout.

Natural landslides are likely subject to various processes that contribute to their runout distance. In this work, we study kinematics of granular flow, considering only granular mechanics. Yet, this simplest model, which does not require presence of fluids or rapid shearing, is consistent with field observations. In addition, many landslides are dry, and do not show evidence for rapid shearing or large scale melting of grains [34]. Deposits of many large landslides consist of sharp edged boulders of a similar size as in the original deposit, indicating granular flow rather than melting and plastic deformation.

Kinematics of landslides can be divided into COM motion and spreading relative to COM as the granular mass collapses. Analytical derivation, compared against DEM simulation, showed that the COM runout is nearly volume independent, and equal to H/μ_0 for large slides. Therefore, (a) increase of steady state velocity with landslide thickness, $v_{\text{p}} \sim h^{3/2}$ (see Equation 8), cannot explain increase of COM runout, and (b) a common friction coefficient $\mu_0 \approx 0.55$ is too large to achieve Heim's ratio of 0.1. In previous works [2, 5–11, 20], long runout landslides have been explained by reduction in friction coefficient μ_0, so that COM runout H/μ_0 is longer (and Heim's ratio is lower).

In contrast, the spreading length has not been quantified yet. Based on experiments with collapsing granular columns and computer simulations of landslides, we suggest that the spread of a landslide deposit is given by Equation (22), i.e., the radius of a shallow angle cone with volume identical to that of the landslide. Using the field observations of H and V for long runout landslides, the spreading length turns out to be the same order of magnitude as the COM runout, often being the dominant contribution. As a results, the calculated Heim's ratio drops to values as low as ≈ 0.1, in line with field observation, without the need for a reduced friction coefficient. In addition, the volumetric dependence of the spreading length accounts for the empirical scaling of landslide runout with volume $L \sim V^{1/3}$ [2, 3, 21].

While the long runout of large landslides can result from both friction weakening and spreading of granular mass, we can distinguish between the two mechanisms based on landslide velocity. The drop in friction coefficient leads to enhanced COM velocity, which is eventually transformed into long runout distance. On the other hand, spreading of grains takes place roughly evenly in all directions and does not affect the COM velocity. Therefore, we can compare maximum COM velocity of an actual landslide to the prediction assuming no friction reduction, i.e., Equation (11) at $t = t_{\text{s}}$ taken from Equation (12). Within the approximation $t_{\text{s}} << T$ (large landslides typically do not reach steady flow) the predicted velocity is

$$v^{\text{s}}_{\text{COM}} = 1.25\sqrt{\left(1 - \frac{\mu_0}{\tan\theta}\right) g H_{\text{COM}}}\,. \tag{25}$$

If the observed maximum velocity of a landslide is larger than Equation (25), friction weakening operates. For example, for a slope with $H = 100\,\text{m}$ and $\theta = 35^\circ$ frictional weakening processes would lead to velocity exceeding $18\,\text{ms}^{-1}$.

The prediction of landslide spread is derived for conical deposits with a shallow, volume independent, foot angle α_{thr}. Existence of such angle was observed in column collapse experiments, where deposits have self-similar shapes regardless of their volume for large enough aspect ratios of the original column. Why this angle saturates or what physical parameters control it if granular mass is collapsed on an inclined plane has not been investigated yet.

The present analytical solution might facilitate development of natural hazard assessment, and may be extended in the future to explore granular flows in different configurations and different rheologies. The model might be applied to study shaking of ground during earthquakes, liquefaction [29] or granular avalanches, e.g., those found to shape dunes on different planetary bodies [35].

5. Conclusions

Large landslides exhibit long runouts, exceeding several times the distance that would be achieved by a rigid block sliding from the same height. This has been traditionally explained by processes leading to frictional weakening, i.e., reduction of frictional resistance resulting in high velocity and long runout. We show that correct runout distance can be achieved by accounting for spreading of landslide mass without assuming any frictional weakening processes. Kinematics of a landslide can be divided into center of mass motion and spreading of the collapsing mass. We derive the center of mass motion analytically based on a frictional law valid for flow of dry granular materials, without frictional weakening. The resulting center of mass runout approaches H/μ_0, where H is the fall height and μ_0 is friction coefficient, similarly to rigid block sliding. Maximum center of mass velocity is $1.25\sqrt{gH(1-\mu_0/\tan\theta)}$, where θ is the slope angle. If a landslide reach higher velocity, friction weakening processes are likely to operate. The distance between the toe of a landslide and its COM is due to spreading associated with flattening of the flowing mass. The spreading distance grows with landslide volume as $(3V/\pi\tan\alpha_{\text{thr}})^{1/3}$, where α_{thr} is the foot angle of the deposit. The spreading distance might exceed the center of mass runout several times, and thus allows for the long runouts observed for large natural landslides.

Acknowledgments

We acknowledge fruitful discussions with R. Toussaint. The research leading to these results has received funding from the People Programme (Marie Curie Actions) of the European Union's Seventh Framework Programme FP7/2007-2013/ under REA grant agreement No. 316889.

Supplementary Material

The Supplementary Material for this article can be found online at: http://journal.frontiersin.org/article/10.3389/fphy.2015.00080

References

1. Dade WB, Huppert HE. Long-runout rockfalls. *Geology* (1998) **26**:803–6. doi: 10.1130/0091-7613(1998)026<0803:LRR>2.3.CO;2
2. Lucas A, Mangeney A, Ampuero JP. Frictional velocity-weakening in landslides on earth and on other planetary bodies. *Nat Commun.* (2014) **5**:3417. doi: 10.1038/ncomms4417
3. Legros F. The mobility of long-runout landslides. *Eng Geol.* (2002) **63**:301–31. doi: 10.1016/S0013-7952(01)00090-4
4. Rice JR. Heating and weakening of faults during earthquake slip. *J Geophys Res.* (2006) **111**:B05311. doi: 10.1029/2005JB004006
5. Goren L, Aharonov E. Long runout landslides: the role of frictional heating and hydraulic diffusivity. *Geophys Res Lett.* (2007) **34**:L07301. doi: 10.1029/2006GL028895
6. Erismann TH. Mechanisms of large landslides. *Rock Mech.* (1979) **12**:5–46. doi: 10.1007/BF01241087
7. Erismann TH. Flowing, rolling, bouncing, sliding: synopsis of basic mechanisms. *Acta Mech.* (1986) **64**:101–10. doi: 10.1007/BF01180101
8. Wang FW, Sassa K, Wang G. Mechanism of a long-runout landslide triggered by the august 1998 heavy rainfall in fukushima prefecture, japan. *Eng Geol.* (2002) **63**:169–85. doi: 10.1016/S0013-7952(01)00080-1
9. Wang G, Sassa K. Pore-pressure generation and movement of rainfall-induced landslides: effects of grain size and fine-particle content. *Eng Geol.* (2003) **69**:109–25. doi: 10.1016/S0013-7952(02)00268-5
10. Okura Y, Kitahara H, Ochiai H, Sammori T, Kawanami A. Landslide fluidization process by flume experiments. *Eng Geol.* (2002) **65**:65–78. doi: 10.1016/S0013-7952(02)00032-7
11. Melosh HJ. The physics of very large landslides. *Acta Mech.* (1986) **64**:89–99. doi: 10.1007/BF01180100
12. Forterre Y, Pouliquen O. Flows of dense granular media. *Annu Rev Fluid Mech.* (2008) **40**:1–24. doi: 10.1146/annurev.fluid.40.111406.102142
13. Silbert LE, Ertas D, Grest GS, Halsey TC, Levine D, Plimpton SJ. Granular flow down an inclined plane: bagnold scaling and rheology. *Phys Rev E* (2001) **64**:051302. doi: 10.1103/PhysRevE.64.051302
14. Pouliquen O. Scaling laws in granular flows down rough inclined planes. *Phys Fluids* (1999) **11**:542. doi: 10.1063/1.869928
15. Savage SB, Hutter K. The motion of finite mass of granular material down a rough incline. *J Fluid Mech.* (1989) **199**:177–215. doi: 10.1017/S0022112089000340
16. Pouliquen O, Forterre Y. Friction law for dense granular flows: application to the motion of mass down a rough inclined plane. *J Fluid Mech.* (2002) **453**:133–151. doi: 10.1017/S0022112001006796
17. Mangeney A, Heinrich P, Roche R. Analytical solution for testing debris avalanche numerical models. *Pure Appl Geophys.* (2000) **157**:1081–96. doi: 10.1007/s000240050018
18. Faccanoni G, Mangeney A. Exact solution for granular flows. *Int J Num Anal Meth Goemech.* (2013) **37**:1408–33. doi: 10.1002/nag.2124
19. Capart H, Hung CY, Stark CP. Depth-integrated equations for entraining granular flows in narrow channels. *J Fluid Mech.* (2015) **765**:R4. doi: 10.1017/jfm.2014.713
20. Campbell CS, Cleary PW, Hopkins M. Large-scale landslide simulations: global deformation, velocities and basal friction. *J Geophys Res.* (1995) **100**:8267–83. doi: 10.1029/94JB00937
21. Staron L, Lajeunesse E. Understanding how volume affects the mobility of dry debris flows. *Geophys Res Lett.* (2009) **36**:L12402. doi: 10.1029/2009GL038229
22. Bagnold RA. Experiments on a gravity-free dispersion of large solid spheres in a newtonian fluid under shear. *Proc R Soc Lond Ser A* (1954) **225**:49. Doi: 10.1098/rspa.1954.0186
23. MiDi GDR. On dense granular flows. *Eur Phys J E* (2004) **14**:341. doi: 10.1140/epje/i2003-10153-0

24. Lajeunesse E, Mangeney-Castelnau A, Vilotte JP. Spreading of a granular mass on a horizontal plane. *Phys Fluids* (2004) **16**:2371–81. doi: 10.1063/1.1736611
25. Lube G, Huppert H, Sparks SJ, Hallworth MA. Axisymmetric collapse of granular columns. *J Fluid Mech.* (2004) **508**:175–99. doi: 10.1017/S0022112004009036
26. Utili S, Zhao T, Houlsby GT. 3d dem investigation of granular column collapse: evaluation of debris motion and its destructive power. *Eng. Geol.* (2015) **186**:3–16. doi: 10.1016/j.enggeo.2014.08.018
27. Cundall PA, Strack OD. A discrete numerical model for granular assemblies. *Geotechnique* (1979) **29**:47. doi: 10.1680/geot.1979.29.1.47
28. Schafer J, Dippel S, Wolf DE. Force schemes in simulations of granular materials. *J Phys* (1996) **6**:5–20.
29. Goren L, Aharonov E, Sparks D, Toussaint R. The mechanical coupling of fluid-filled granular material under shear. *Pure Appl Geophys.* (2011) **168**:2289–323. doi: 10.1007/s00024-011-0320-4
30. Frenkel D, Smit B. *Understanding Molecular Simulations.* San Diego, CA: Academic Press (2002).
31. da Cruz F, Emam S, Prochnow M, Roux JN, Chevoir F. Rheophysics of dense granular materials: discrete simulation of plane shear flows. *Phys Rev E* (2005) **72**:021309. doi: 10.1103/PhysRevE.72.021309
32. Abramowitz M, Stegun IA. *Handbook of Mathematical Functions with Formulas, Graphs, and Mathematical Tables*. New York, NY: Dover Publications (1972).
33. Kamrin K, Koval G. Nonlocal constitutive relation for steady granular flow. *Phys. Rev. Lett.* (2012) **108**:178301. doi: 10.1103/PhysRevLett.108.178301
34. Shreve RL. The blackhawk landslide. *Spec Pap Geol Soc Am.* (1968) **108**:47. doi: 10.1130/spe108-p1
35. Bourke MC, Lancaster N, Fenton LK, Parteli EJR, Zimbelman JR, Radebaugh J. Extraterrestrial dunes: an introduction to the special issue on planetary dune systems. *Geomorphology* (2010) **121**:1–14. doi: 10.1016/j.geomorph.2010.04.007

Conflict of Interest Statement: The authors declare that the research was conducted in the absence of any commercial or financial relationships that could be construed as a potential conflict of interest.

frontiers in Physics

ORIGINAL RESEARCH
published: 01 September 2015
doi: 10.3389/fphy.2015.00067

Dynamics of hydrofracturing and permeability evolution in layered reservoirs

Irfan Ghani[1], *Daniel Koehn*[2]*, *Renaud Toussaint*[3] *and Cees W. Passchier*[1]

[1] Tectonophysics, University of Mainz, Mainz, Germany, [2] School of Geographical and Earth Sciences, University of Glasgow, Glasgow, UK, [3] Institut de Physique du Globe de Strasbourg, UMR 7516, Université de Strasbourg/EOST, Centre National de la Recherche Scientifique, Strasbourg, France

A coupled hydro-mechanical model is presented to model fluid driven fracturing in layered porous rocks. In the model the solid elastic continuum is described by a discrete element approach coupled with a fluid continuum grid that is used to solve Darcy based pressure diffusion. The model assumes poro-elasto-plastic effects and yields real time dynamic aspects of the fracturing and effective stress evolution under the influence of excess fluid pressure gradients. We show that the formation and propagation of hydrofractures are sensitive to mechanical and tectonic conditions of the system. In cases where elevated fluid pressure is the sole driving agent in a stable tectonic system, sealing layers induce permutations between the principal directions of the local stress tensor, which regulate the growth of vertical fractures and may result in irregular pattern formation or sub-horizontal failure below the seal. Stiffer layers tend to concentrate differential stresses and lead to vertical fracture growth, whereas the layer-contact tends to fracture if the strength of the neighboring rock is comparably high. If the system has remained under extension for a longer time period, the developed hydrofractures propagate by linking up confined tensile fractures in competent layers. This leads to the growth of large-scale normal faults in the layered systems, so that subsequently the effective permeability is highly variable over time and the faults drain the system. The simulation results are shown to be consistent with some of the field observations carried out in the Oman Mountains, where abnormal fluid pressure is reported to be a significant factor in the development of several generations of local and regional fracture and fault sets.

Keywords: hydrofractures, reservoirs, simulation, fluid pressure, stress

Edited by:
Lev Shchur, Landau Institute for Theoretical Physics, Russia

Reviewed by:
Haroldo Valentin Ribeiro, Universidade Estadual de Maringa, Brazil
Punyabrata Pradhan, S. N. Bose National Centre For Basic Sciences, India

***Correspondence:**
Daniel Koehn, School of Geographical and Earth Sciences, University of Glasgow, Gregory Building, Lillybank Gardens, Glasgow G12 8QQ, UK
daniel.koehn@glasgow.ac.uk

Specialty section:
This article was submitted to Interdisciplinary Physics, a section of the journal Frontiers in Physics

Received: *03 June 2015*
Accepted: *12 August 2015*
Published: *01 September 2015*

Citation:
Ghani I, Koehn D, Toussaint R and Passchier CW (2015) Dynamics of hydrofracturing and permeability evolution in layered reservoirs. Front. Phys. 3:67. doi: 10.3389/fphy.2015.00067

Introduction

Fluid overpressure in the Earth's crust is a major controlling factor for the mechanics of fracturing and faulting in a variety of geological settings [1]. Overpressure yields a feedback on the background stress regime at depths in the crust and enhances the potential brittle deformation of rocks [2, 3], so that existing fractures and joints open and the frictional resistance along fault planes is reduced.

In general stress fields within the Earth's crust can change as a function of fluid pressure, tectonic stresses or material heterogeneities. In confined sedimentary basins (impermeable fault zones and cap rocks) as well as regions of low-grade metamorphism, high fluid pressure develops and often becomes near-lithostatic to eventually trigger fluid assisted fracturing or hydrofracturing

(**Figure 1**). This phenomenon may also result in the permutation of the local stress tensor so that induced fractures become horizontal, a process that is sensitive to tectonic diagenesis and may trigger small scale seismic events or fault reactivation [4–8]. In addition, [9] indicated that heterogeneity and contrasting mechanical properties in rocks can also induce changes in the principal stress magnitude and intrusive bodies e.g., horizontal dykes and sills may render the process of stress permutation at least at the local scale [10, 11].

The mechanism of hydrofracturing is a highly dynamic process and consists of at least a two-way feedback between the hydraulic and mechanical domains of a geological system. In porous rocks the mechanical behavior of the solid material is related to its intrinsic porosity, which due to poroelastic effects is one of the governing factors for the permeability evolution. Effective stress perturbations due to pressure variations and fracturing influence the primary porosity and increase the bulk permeability of the host rock [12]. Hydrofracture propagation facilitates the development of permeable pathways, which significantly enhance flow rates. This behavior impacts on fluid migration in geological systems in a number of ways for instance reservoir quality [13–15], episodic expulsion and entrapment of ore-forming fluids [16] as well as the activation of geothermal circulation/venting with the induction of pressure and temperature anomalies [11, 17]. Miller and Nur [18] describe the "toggle switch" behavior of hydrofractures leading to sudden permeability enhancement or reduction associated with a switch from high to low pressure and backwards. Vass et al. [19] study the impact of chemical fracture sealing over the evolution of joint and faults created by overpressures due to fluid flow. Aochi et al. [20] model the seismicity induced along a fault by hydrofracture or fluid flow. Kobchenko et al. [21] image how fractures get activated and transport fluid during heating of low permeability rocks.

Most of the previous numerical tools used to study fracturing do not take the real time effects of material properties (e.g., stress-effective porosity evolution and vice versa due to poroelasticity) on the developing fracture patterns into account. Neither do they account for the seepage forces due to fluid circulation. This process is complex and depends also on the fracture geometry, fluid pressure diffusion and the strain field conditions. In the presented paper, we show how these factors influence the formation of different fracture patterns that develop under high fluid pressure gradients. The present work is a continuation of [22], in which a 2D coupled model with Darcy based fluid pressure diffusion is introduced and implemented to study hydrofracturing in homogeneous porous rocks. The model permits the quantitative and qualitative study of the evolution of the effective stress field in accordance with porosity-effective pressure elevation, the dynamic interaction with the initiation and growth of fractures in terms of deformation-induced permeability variations and the respective pattern formation. In the current work, we consider layered heterogeneous rock configurations to discuss the corresponding effects of material properties (e.g., stiffness, breaking strength) and initial noise in the system on the developing structures. In addition, we give an example of how layer-confined vertical fractures develop into normal faults, and how this transition changes the permeability (fluid flow) in a multi-layer sedimentary sequence [23]. The assigned numerical scheme [22] conceded a similar approach of

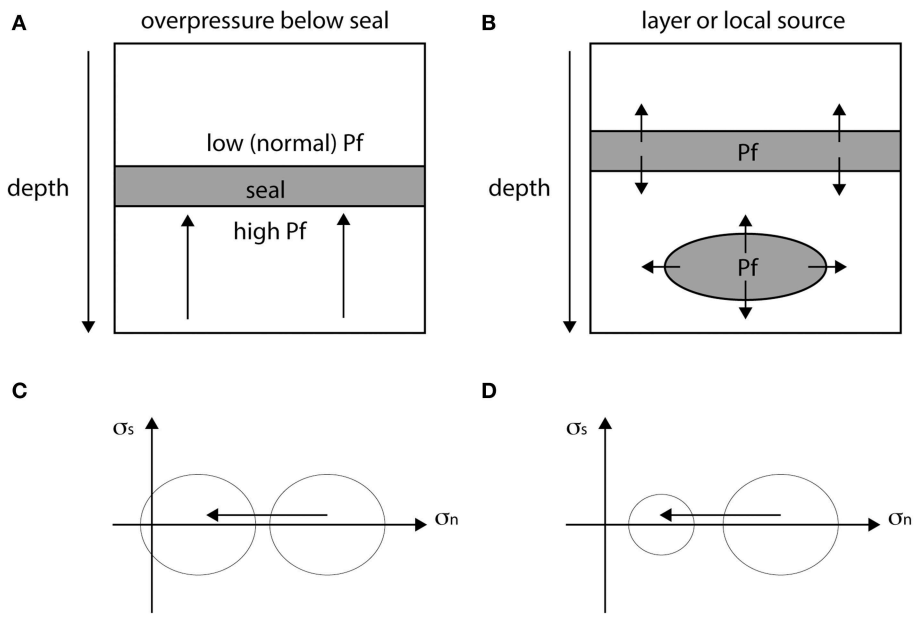

FIGURE 1 | (A) Fluid overpressure below a seal in a sedimentary basin. **(B)** Fluid overpressure developing in a source region that is either a layer or an elliptical area. **(C)** Mohr circle diagram showing how an increase in fluid pressure shifts the Mohr circle from its initial compressive stress state at the right side to the left into the tensile regime leading to failure. **(D)** Mohr diagram of effective stress state where fluid overpressure reduces the differential stress and fluidizes the system. The reduction of differential effective stress is found in sedimentary basins below seals [51].

poroelasticity and fluid flow in granular media [24–26], during hydrofracture or aerofracture [27–31], shearing of gouge layers in faults [32, 33] or instabilities during sedimentation [34–37].

Fracturing in the brittle crust mainly takes place in extensional and shear modes depending on the balance between the differential stress ($\sigma_1 - \sigma_3$) and rock tensile strength T. Theoretically, the predominant state of triaxial compressive stress due to gravity loading [38] favors only shear failure in rocks at depth, therefore for extensional fractures to open under these conditions, an additional force is needed to produce tensile stresses. This additional force is thought to come from the fluid pressure that builds up in pores and existing cracks [39–41].

For a fluid saturated rock mass in the crust, stresses that act on fluid and solid should be separated from stresses that act on the solid alone. Solid stresses can be defined by Terzaghi's law where normal effective stress σ'_{ij} is given by

$$\sigma'_{ij} = \sigma_{ij} - P_f \delta_{ij} \tag{1}$$

with σ_{ij} being the total normal stress, P_f the pore fluid pressure and δ_{ij} the Kronecker delta with the sign convention of positive compressive stress. A Mohr diagram is often used to illustrate the respective failure mode in Rock Mechanics. In **Figure 1** the Mohr circle represents a 2D stress state in the Earth's crust with σ_1 and σ_3 being compressive on the right hand side. Excess in fluid pressure P_f reduces the value of the effective stresses, driving Mohr's circle toward the left along the σ_n-axis from its initial compressive stress state. When the least effective stress transects the composite Mohr-Coulomb failure envelop in the tensile regime the rock fails.

In order to understand the effects of fluid pressure on fracturing and vice versa in heterogeneous systems one has to look at the evolution of fluid pressure gradients and the respective poroelastic response as a result of stress perturbations in the porous matrix [3, 24, 42–45]. For tensile fracturing in overpressured rocks the order of magnitude of the effect of pore pressure pertaining to Biot's poroelastic response on Terzaghi's effective stress state can be approximated by the pore-fluid factor λ_v [5, 40].

$$\lambda_v = \frac{P_f}{\sigma_v} = \frac{v}{1 - v - (1 - 2v)\alpha_p} \tag{2}$$

which is the ratio of pore fluid pressure to vertical stress. Depending on the poroelastic factor α_p (0–1 for most rocks) and the Poisson ratio v of the rock, the pore pressure required for hydraulic extensional fracturing is hydrostatic if ($\lambda_v < 0.4$) in near surface extensional regimes, superhydrostatic ($0.4 < \lambda_v < 1.0$) in low permeable and well cemented rocks and superlithostatic when ($\lambda_v \geq 1.0$) in compressional regimes at depth.

However, using Terzaghi's law in three dimensions assuming that all principal stresses are affected by fluid pressure in the same way is a simplification [46–49]. First of all the term fluid pressure has to be well defined. For example Cobbold and Rodrigues [50] argue that the fluid overpressure should be used in Terzaghi's law. Second of all the behavior of the rock depends on the mechanical and hydraulic boundary conditions, so that the fluid overpressure term in Equation (1) is not a scalar and the differential stress may change as well. These effects are observed by Hillis [51] for several sedimentary basins where overpressure leads to a reduction of the differential stress and the least principal stress is linked to the fluid pressure. In a simplified version the horizontal effective stress below a seal in an over pressurized zone in a sedimentary basin can be expressed by

$$\sigma'_3 = \kappa_e \left(\sigma_1 - P\right), \tag{3}$$

where P is the local overpressure and κ an elastic proportionality [50]. In this case the fluid overpressure affects the vertical and horizontal stress differently and as a consequence the differential stress is reduced (**Figure 1**). Rocks are porous so that fluid can percolate through the rock, therefore the actual force that acts on the walls of pores or cracks and leads to rock failure (hydrofracturing) is the fluid pressure gradient (leading to seapage forces, [50]). The fluid pressure in a simplified system can be expressed by the following equation [50]

$$P = \rho g z - \left(\frac{q\mu}{k}\right) z + \left(\frac{Q\mu}{2k}\right) z^2, \tag{4}$$

with the first term representing the hydrostatic fluid pressure (as a function of density ρ, gravity g and depth z), the second term representing fluid overpressure build up below a seal as a function of influx of fluid (with q = darcy velocity, μ = fluid viscosity and k = permeability) and the last term representing a source term, which could be fluid generation in a layer (with Q the fluid production, **Figure 1**). The last two terms in equation 4 lead to fluid assisted fracturing [50].

Materials and Methods

In order to numerically simulate the development of fluid assisted fractures and hydrofractures, we employ a coupled two-dimensional hydro-mechanical approach to model a 2D pressurized sedimentary section in the Earth's crust (**Figure 2**). The model is explained in detail in Ghani et al. [22]. The approach combines the continuum description of fluid pressure with a discrete description of deformable elastic solid where the later is represented by a hybrid triangular lattice-particle model and is blanketed over a stationary square grid (larger grid constant) of fluid pressure such that the boundaries of the two lattices coincide with each other. Accommodating local mass to momentum conservation a pressure gradient evolves for a given solid-fluid configuration according to local strain conditions through a poro-elasto-plastic relationship. The model is grounded on the same hypothesis as Flekkøy et al. [24], which emphasizes the growth of hydro-driven fractures in the light of instantaneous and synergistic evolution of rock permeability and interstitial pressure diffusion in the porous elastic medium. In the following subsections we outline the constitutive elements of the coupled scheme [23].

It is assumed that the seepage force at local scale as a function of the evolution of fluid pressure gradients induces localized

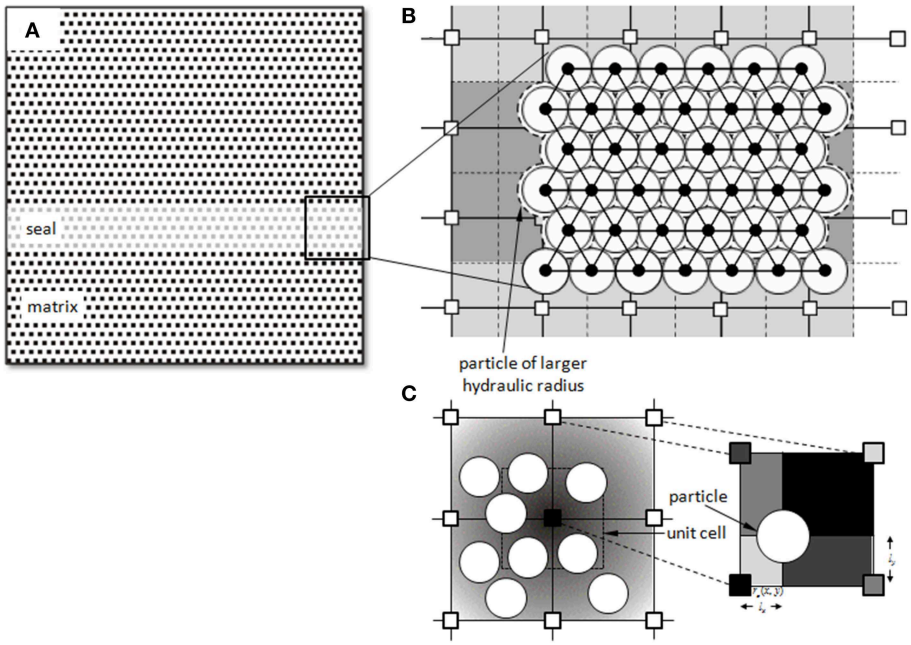

FIGURE 2 | The figure shows the initial model configuration and the fluid-solid interaction criteria [23]. (A) Sketch shows a single layered cap-rock geometry, where a sub-horizontal low permeable layer is sandwiched between a permeable matrix. **(B)** Sketch illustrating how the coupled particle-lattice model overlays the pressure grid field in physical space. The linear dark gray background depicts transactions of hydrostatic to lithostatic fluid pressures due to a low permeable seal. **(C)** Sketch showing the fluid-solid interaction according to the smoothing function, with the gray background depicting the pressure gradient toward the central fluid node.

perturbations in the effective stress field which may lead to rock deformation. Therefore, the continuum fluid phase is determined exclusively in terms of the pressure field $P(x, y)$, where (x, y) are the coordinates of the two-dimensional grid space. The inertia of the fluid is not considered in the model, which is justified for a fluid flow with low Reynolds number as in the concerned case where the fracture aperture or the particle movement is comparable to the diameter of the particles.

Using Darcy law in order to express the seepage velocity through the porous media, a time dependent governing Equation (5) of pressure diffusion is established from the mass conservation of fluid and solid [27, 33, 35].

$$\phi\beta\left[\frac{\partial P}{\partial t}+u\nabla\cdot P\right]=\nabla\cdot\left[(1+\beta P)\,\frac{K}{\mu}\nabla \mathrm{P}\right]-(1+\beta P)\,\nabla u, \quad (5)$$

where $\phi = 1 - \rho$ is the porosity, β is the fluid compressibility, P is the fluid pressure and u is the solid velocity field. K and μ stand for permeability and fluid viscosity respectively. The implementation of the diffusion equation is obtained by an Alternate Direction Implicit (ADI) method [52]. In the model, the pressure gradient over a given volume develops according to the permeability K, which is an explicit output of the discrete elastic model as a function of variation in local porosity $\emptyset(x, y)$. The local permeability $K(\emptyset)$ is determined through a Kozeny-Carman relation given by Carman [53]

$$K(\emptyset)=\frac{r^2}{45}\frac{\emptyset^3}{(1-\emptyset)^2}, \quad (6)$$

where r is a fixed grain size (1 μm) and 45 is an empirical constant valid for a packing of spherical grains.

The DEM elasto-plastic module "Latte" of the software package "Elle" [54, 55] is used to simulate brittle deformation in porous rocks. The setup is a 2D hybrid lattice-particle model in which the discrete elements are connected with linear elastic springs. The DEM model determines the discrete description of isotropic elastic continua of a real system with an elastic spring constant k as a function of the macro-scale elastic material property E. This setup can thus be used to simulate plain strain deformation problems according to linear elasticity theory [24] with

$$k=\frac{\sqrt{3}}{2}El, \quad (7)$$

where l stands for the two dimensional model thickness of a given configuration. In order to model heterogeneous material i.e., layered sedimentary rocks, local changes in spring constant k describe the corresponding variation in the mechanical properties (stiffness) of the material. A standard over-relaxation algorithm [56] is used to obtain the equilibrium configuration of the elastic system after each simulation time step (based on the net forces applied on each node). In the plastic part of the model, springs break and imitate local failure of the material if the force acting on them exceeds a prescribed threshold (σ_c) corresponding to the local tensile strength. The average threshold of the tensile strength is related to the stress intensity factor $K_I = \sigma_I \sqrt{c}$, where σ_I is the critical stress for the relevant

displacement of fracture walls and c is the characteristic length of micro-cracks in the material [24]. Broken springs get removed from the network and the associated particles lose cohesion but are still subject to repulsive forces when they meet.

Deformation mechanics of the coupled continuum-elastic model is governed by a mutual momentum exchange between the solid and fluid phase at the scale of a unit volume cell of the continuum system. The net force F_i^n acting on a particle i is composed of three components, interaction force f_e from neighboring particles (either connected with a spring or repulsive forces), seepage force f_p resulting from interstitial fluid pressure and external forces, which are gravity f_g and tectonic forces determined by imposed large scale strains (via forces implemented on the lateral boundaries of the model). The net force is given as

$$F_i^n = f_e + f_p + f_g. \tag{8}$$

In the elastic part of the model, each spring inherits a spring constant k and an equilibrium length a, which is identical to the sum of the initial radii of two connected particles. The inter-particle force f_e, which acts along the connected elastic springs is proportional to the given spring constant

$$f_e = \sum_j k_{ij} \left(\left| \overrightarrow{a}_{ij} \right| - \left| \overrightarrow{x}_{i-} \overrightarrow{x}_j \right| \right) \cdot \hat{n}_{ij}, \tag{9}$$

where the sum is over all connected neighbor nodes j, $\overrightarrow{x}_i$ and $\overrightarrow{x}_j$ are the positions of the connected nodes, and $\hat{n}_{ij}$ is the unit vector pointing from the centroid of node i to node j.

The seepage force is generated due to the gradient of the non-hydrostatic part of the pressure field and is a result of the momentum exchange between the elastic material and the viscous fluid flowing in the reservoir. Assuming negligible fluid-solid friction at the interface surface, the only coupling force is the pore pressure gradient ΔP induced by a fluid source in the reservoir. The pressure force f_p on the surface normal of a given particle configuration in the unit grid cell (**Figure 2**) of surface area dA is calculated by an area-weight smoothing function.

$$f_p = -\int P dA, \tag{10}$$

where $P = P_0 - \rho_f g z$, with P_0 the local fluid pressure in the reservoir at some reference depth z, ρ_f the fluid density, and g the gravity constant.

In the coupled model the term gravitational force incorporates the gravity effects of both the fluid and solid where the later together with the hydrostatic part of pore pressure determines the effective stress field $\sigma_{eff} = \left(\rho_s - \rho_f\right) g z$ in the system. The gravity force on each particle in the elastic module is inferred using the formulation

$$f_i^g = \rho_s \pi R_i^2 g C, \tag{11}$$

where ρ_s is the solid mass density, $R_i^2 = r_i^2 S$ with S the dimension of the real system (1000 m), g is the acceleration of gravity and $C = 2/3$ is a scale factor derived in Ghani et al. [22] to acquire a compatible one dimensional lithostatic stress for an isotropic 2D linear elastic solid.

The two way interaction between the porous solid and the hydrodynamic phase is achieved through the use of a projection operator from the discrete space to the fluid grid space, using a smoothing function $s\left(r_i - r_0\right)$, which distributes the weight of a particle over the four neighboring fluid grid nodes as shown in **Figure 2C**.

$$s\left(r_i - r_0\right) = \begin{cases} \left(1 - \frac{l_x}{\Delta x}\right)\left(1 - \frac{l_y}{\Delta y}\right) & \text{if } l_x < \Delta x,\ l_y < \Delta y \\ 0 & \text{otherwise} \end{cases} \tag{12}$$

where $r_i\left(x, y\right)$, $r_0\left(x, y\right)$ are the positions of the particle and grid node respectively, $l_x = \left|x_i - x_0\right|$ and $l_y = \left|y_i - y_0\right|$ are the relative distances and Δx, Δy are the lattice constant along the x and y coordinates. This setup is also called "cloud in cell" method which renders the translation of mass m and velocity v of individual particles into continuous local particle density $\rho\left(r_0\right) = \sum_i s\left(r_i - r_0\right)$ and velocity fields $u\left(r_0\right) = \sum_i u_i s\left(r_i - r_0\right)$, where subscript i runs over the number of particles present in a unit area associated with a particular grid node at position r_0. The same smoothing function is also used to obtain the drag force $f_p = -\sum_k s\left(r_i - r_0\right)\left(\nabla P / \rho_n\right)_k$ on a single particle due to fluid pressure, index k runs over four nearest grid nodes. The basic approximations to this approach are the multiplication of the calculated 2D solid fraction with 2/3, as well as setting of a lower cutoff of the 2D solid fraction e.g., $\rho_{min} = 0.25$, detailed descriptions are given in Ghani et al. [22]. This type of model for the fluid-solid coupling and mapping from 2D to 3D has been validated by successful comparison with experiments on mixed fluid/dense granular flows, in aerofracture [27, 30, 31] or instabilities during sedimentation [25, 26, 34, 35].

Two different approaches have been used in order to account for anisotropies in the model, we insert single layers and multi-layers of dissimilar material and sedimentary properties. A single horizontal layer is defined in the lower half section of the model in order to depict a sealed reservoir which inherits different stiffness values and low permeability relative to the underlying reservoir and overburden rock (**Figures 2A,B**). In the multi-layered model, four layers of low permeability and high stiffness are considered at regular intervals along the vertical coordinate. According to the boundary conditions considered, loading includes an increase of fluid pressure in the fluid lattice (corresponding to phase transition, fluid source or fluid injection in this zone), a vertical loading due to gravity, or a horizontal loading due to tectonic strains by moving the lateral boundary walls. In all models, the elastic system is constrained by elastic walls at the two lateral and the bottom boundaries, whereas the upper boundary is set free in order to attain an equilibrium under gravity loading. The elastic walls are described as linear elastic springs so that the force on any interacting particle from a wall is proportional to the distance that the particle is pushed into the wall. For instance, the force by a lateral wall on the particle

i contacted at location $x = x_w$ is

$$f_i = \begin{cases} -k_w\,(x_i + r_i - x_w)\,n_x, & if\ x_i + r_i - x_w > 0 \\ 0 & else \end{cases} \quad (13)$$

where k_w is a spring constant for wall interaction r_i is the particle radius, n_x is a unit vector along the x-axis. In the elastic domain, relaxation and plastic deformation (i.e., sliding and rearrangement of the relative grain positions) is assumed to be instantaneous relative to the diffusion of the fluid pressure. This amounts to neglect the inertial terms and the propagation of seismic waves and equilibrate elastic stresses with seepage forces and gravity. After each time dependent diffusion step of fluid pressure, the elastic equilibrium is acquired on account of the elasto-plastic deformation in the material by the subjected seepage forces and other loadings.

At layer interfaces, the elastic constant of springs is taken as an average of the constants of the respective boundary particles. This presents a gradual change of mechanical properties corresponding to models of layered sedimentary rocks. The Young's modulus, the breaking strength of springs and the layer thicknesses are predefined in the models. The respective constituents of the elastic system are assumed to be homogeneous corresponding to their material properties on large scale, however, in order to grasp the effect of the inherited disorder of a real material, we set a pseudo-random distribution of the breaking strength (**Figure 3**). Natural disorder in geological media corresponds to the ubiquitous presence of Griffith's micro-cracks, variation in their densities and lengths and other defects, which are present at the grain scale. It has been demonstrated that fracture patterns that are observed both in the field and laboratory can be numerically reproduced by implying realistic normal distributions of breaking strength in DEM models [57–60]. The overall breaking strength of the model material, and its failure mode, is sensitive to the lower values of the quenched distribution [61–63].

The subsequent model setup is thus analogous to confined reservoirs with seal layers of very low permeability. In each simulation the coupled model starts from a fully relaxed state and is progressively loaded in small steps. The model is subject to a random pressure source that complies a probability distribution function ($0 \leq P \leq 1$) with a maximum pressure in the middle of the lower permeable layer (below the seal)—this represents a possible phase transition in this lower layer associated with a pressure rise, or the arrival of fluid from the bottom. An increase in pore pressure in the source layer creates a linear pressure gradient across the impermeable seal, which ultimately develops high buoyancy forces in the surrounding matrix. This causes high concentration of stresses in the seal layer and depending on material properties of the model constituents it triggers different patterns of successive fracture propagation at relatively weak rock elements (intrinsic flaws). The induction of the fractures accommodates the strain and eventually the stress relief in the elastic system following a rearrangement of particle positions. This concurrently promotes a local change in the background porosity, which by influencing the permeability results in diffusion of pore overpressure in the fractured zone. The evolution of the pore fluid pressure provides a feedback to the stress field in the system and leads to fracture growth along the pressure gradient and results in a regular fracture network. The cycle is echoed successively following the two-way temporal and spatial feedback between hydraulic pressure and strain evolution and associated fracturing in the porous matrix until both the continuity equation and the discrete grains are relaxed, a dynamic stationary equilibrium is found and fracturing ceases.

A varying range of mechanical and hydraulic properties are used in the simulation setup in order to realistically represent the mechanism of quasi-static hydro-driven brittle deformation in heterogeneous rocks in the shallow crust. This involves a switch from sub-vertical to horizontal tensile fracturing as a function of the direction of the principal stress tensor due to high pressure gradients in high pressurized systems [5, 64] as well as in low permeability fault zones [7].

Results

We present 5 different simulations where the first four have a geometry with one horizontally aligned low-permeable

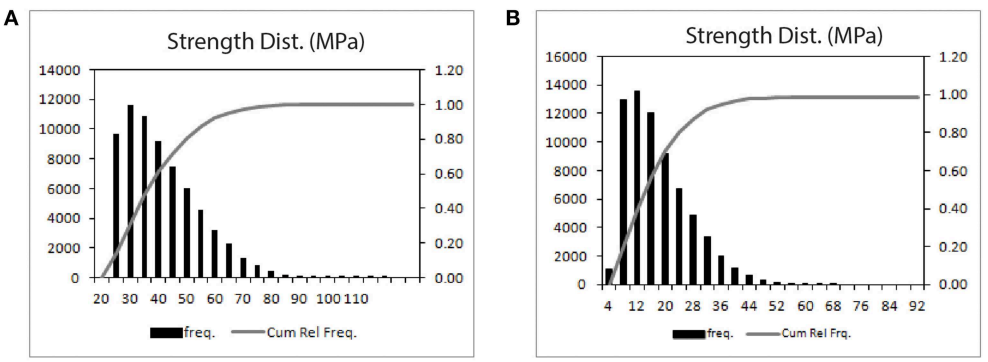

FIGURE 3 | Strength distribution of springs for the different simulations showing dimensionless (left hand side) and scaled values (right hand side). **(A)** Represents the distribution used in experiments 1–4 whereas **(B)** represents the layer properties used for experiment 5.

layer—similar to a cap-rock, whereas the fifth simulation contains multiple layers. **Figure 4A** illustrates the initial configuration of the single layered models where a horizontal layer with a thickness of 10% of the model height is emplaced in the lower half of the simulation. Tectonic loading is not included in these models. The fifth example shows fracture formation under an extensional stress regime in addition to abnormal fluid pressure and the developing patterns in a multilayer system.

In all the simulations the solid skeleton (elastic lattice) of the reference model has a resolution of 100 × 150 disc-shaped particles which define an area of 1:1 km, the model thus bears a linear gravitational loading of a 1 km long sedimentary column in the uppermost crust with a Poisson ratio of 1/3. The mechanical parameters and other characteristics for the respective simulation examples are given in **Table 1**, a low average porosity of 7% is taken for seal layers compared to 35% of the surrounding matrix. As boundary conditions the coupled system is confined mechanically at the lateral and lower boundaries until otherwise described whereas hydraulically it is restrained at the side boundaries. The distribution of breaking strengths for the different simulations are shown in **Figures 5A,B**. The overall breaking strength of the model material will be at the lower end of the distribution.

In the first simulation we attempt to model bedding parallel and bedding normal fractures in a heterogeneous medium, structures that can be found in limestone sequences of the Oman Mountains. **Figure 4A** shows the model evolution where red is the matrix, darker red the stiff seal layer and blue fractures. In the simulation the Young's modulus of the seal layer is taken to be 10 times higher than the surrounding matrix. In addition the breaking strength of springs in the horizontal seal layer are set to be 10 times lower than the strength of the matrix. The material has a background Young's modulus of 35 GPa and a breaking strength in the range of 21–115 MPa. The breaking strength of the whole aggregate will be controlled mainly by the lower values and thus be around 21–25 MPa. The fluid has a compressibility of 4.5×10^{-10} Pa^{-1}, a viscosity of 0.001 Pas and one time step in the model is equivalent to 0.1 days. Fluid pressure input is fast enough for fluid pressure gradients to build up.

The development of the fracture pattern in **Figure 4A** shows that the layer first develops layer perpendicular fractures. These are initiated by the fluid pressure gradient, however their orientation is given by the heterogeneous gravity-induced stress field so that the lowest stress is horizontal. During successive increase in fluid pressure the initial fractures cannot drain the system and a horizontal fracture develops at the lower boundary of the seal. In the closed and confined system, seepage forces generated by the accumulated pore pressure counter the lithostatic stress component σ_v. The vertical compressive stress reduces in a non-linear fashion and gradually turns into the tensile regime (**Figure 4C**). In the absence of any tectonic loading a subsequent increase in fluid pressure results in the directional

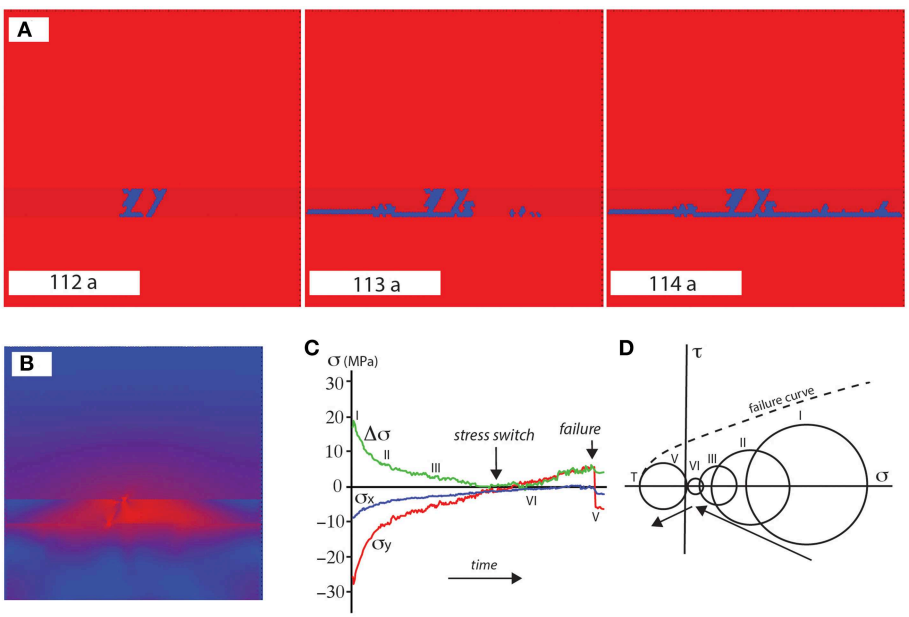

FIGURE 4 | (A) Shows a simulation of the development of initial layer perpendicular fractures in a stiffer impermeable seal (dark red layer) followed by layer parallel fractures. Time proceeds from left to right and fractures are represented by blue color. Fluid is injected randomly in the lowest soft and permeable layer. This creates a high pressure drop across the seal and results in permeability changes through fracturing. **(B)** The figure shows the differential stress state on the onset of fracturing in the system, where the blue color represents low and the red high differential stress. The less permeable seal shows high stress concentrations whereas the layer below the seal shows low stresses due to high fluid pressures. The high differential stress that is accumulated in the stiffer seal layer is relieved with time following fracturing in the seal. **(C)** Graph showing the evolution of the magnitude of the stress in the × (horizontal) and y (vertical) direction and the differential stress in the seal. A switch from compressive to a tensile state of vertical stress is seen in the seal and at the interface. The low permeability of the seal results in conditions for layer parallel fracturing. **(D)** Mohr circle description of the stress states graphed in c illustrating the complexity of stress changes as a function of an increase in fluid pressure.

TABLE 1 | Showing parameters for different experiments.

	Simulation 1	Simulation 2	Simulation 3	Simulation 4	Simulation 5
Young's modulus (GPa)	35	80	80	80	80
Seal-Young's modulus (GPa)	35 × 5	–	–	–	80 × 5
Model–Strength range (T_d)	21–115 MPa	4.8–74 MPa	4.8–74 MPa	4.8–74 MPa	4.8–74 MPa
Model–Av. strength (T_{dav})	35 MPa	15 MPa	15 MPa	15 MPa	15 MPa
Seal–strength range (MPa)	–	–	$T_d \times 0.5$	$T_d \times 0.1$	–
Seal–av. strength (MPa)	–	–	$T_{dav} \times 0.5$	$T_{dav} \times 0.1$	–
Model–av. Porosity (%)	35	35	35	35	35
Seal–av. porosity (%)	7	7	7	7	7
Pressure input (distribution)	Local 50 MPa/0.1 days	Local 50 MPa/0.1 days	Local 50 MPa/0.1 days	Local 50 MPa/0.1 days	Lower boundary 25 MPa
Lateral strain	–	–	–	–	0.0000001

switch of the compressive stress components, upon which the system is subjected to overburden uplift at the layer interface as well as the concentration of stresses in the low permeable seal layer (**Figure 4B**). The simulation exhibits two patterns of hydrofracture growth due to a high Young's modulus of the seal layer. Fluid pressure gradients and a high stress concentration in the seal lead to layer perpendicular fractures. In addition as shown in graph (**Figure 4C**), the vertical stress component reduces faster than the horizontal component which leads to a second set of successive layer parallel fractures at the seal and source layer interface. This results in tensile/hybrid tensile shear fracturing along the layer interface and eventually leads to seal failure. A graph showing the evolution of the stresses in the vertical (y) and the horizontal (x) directions and the corresponding trend of a Mohr diagram during the simulation are illustrated respectively in (**Figures 4C,D**). The Mohr diagram can be explained as follows: first both stresses, the vertical and the horizontal decrease due to the high fluid pressure gradients. The horizontal stress meets the simulation walls on the left and right hand side, which is mimicking an endless system. The vertical stress can act against the free upper surface that is only confined by gravity. Therefore, extension in this direction is easier so that the originally highest vertical stress becomes the smallest principal stress and eventually is tensile leading to layer parallel fracturing. This effect is enhanced by the sealing layer that leads to higher fluid pressure gradients in the vertical direction. In this scenario an increase in fluid pressure does not simply lead to a movement of the Mohr circle toward the left hand side of the Mohr diagram, but to an initial decrease of mean and differential stress, a flip of the stress direction and finally a small increase in differential stress leading to the final failure.

The presumed setup is analogous to confined reservoirs with seal rocks of low permeability. Seals in fluid filled layered reservoirs are commonly soft rocks i.e., shales, however, during the evolution of sedimentary basin the mechanical compaction and other diagenetic processes may increase the stiffness of the soft seal up to a significant order of magnitude, which may change the conditions for hydrofracturing, their arrest and propagation over time [65, 66]. If an increase in internal fluid pressure is the main forcing, it seems that a soft layer on top of the seal behaves as stress obstruction for fracture propagation. In this case the heterogeneous system may fail in the form of layer parallel shearing at the macro scale and thus facilitate fluid migration along layer contacts. This is in agreement with field studies [67, 68], which indicate that vertically growing fractures preferentially propagate through stiff rocks rather than through soft layers. On this basis one may predict that bedding parallel veins are a sign of abnormal fluid pressure.

Figure 5 illustrates three simulation runs in which the sandwiched seal layer has different properties than the one shown in **Figure 4**. The three layers in the model contain the same default value of Young's modulus, however the breaking strength of springs in the enclosed seal layer of the simulation shown in **Figures 5B,C** is 0.5 and 0.1 times weaker than that of the simulation shown in **Figure 5A** (**Table 1**). The material has a Young's modulus of 80 GPa and a breaking strength range of 5–74 MPa with a large-scale overall breaking strength of 15 MPa (**Figure 3**). The layered heterogeneities have a great influence on the fracture propagation and variable fracture pattern development. In addition, because the breaking strength of the matrix is low compared to the model shown in **Figure 4**, the fluid pressure gradient at the source is high enough to fracture the weaker matrix around the source where fluid pressure gradients are highest.

In the simulation shown in **Figure 5A** vertical tension fractures nucleate at the source zone in the lower layer and propagate upward (**Figure 5A**, timestep: 400, 40 days) under the influence of gravity and pressure gradients. Once the fractures reach the seal they are obstructed and stop to propagate vertically (**Figure 5A**, timestep: 700, 70 days). Because the mechanical properties of matrix and source layer are the same, the stress concentration in the seal is not high enough to promote fracture propagation across the seal. Since the seal is impermeable, the continuous buildup of fluid pressure does re-orient the principal stresses in the source layer so that the fractures below the seal propagate sideways and the seal does not fracture (**Figure 5A**, timestep: 750, 75 days).

The second and third simulation in **Figures 5B,C** show a different scenario. In this case the weak impermeable seal (strength 1/5th and 1/10th of matrix) tends to fail concurrently with the upward propagation of hydrofractures along the

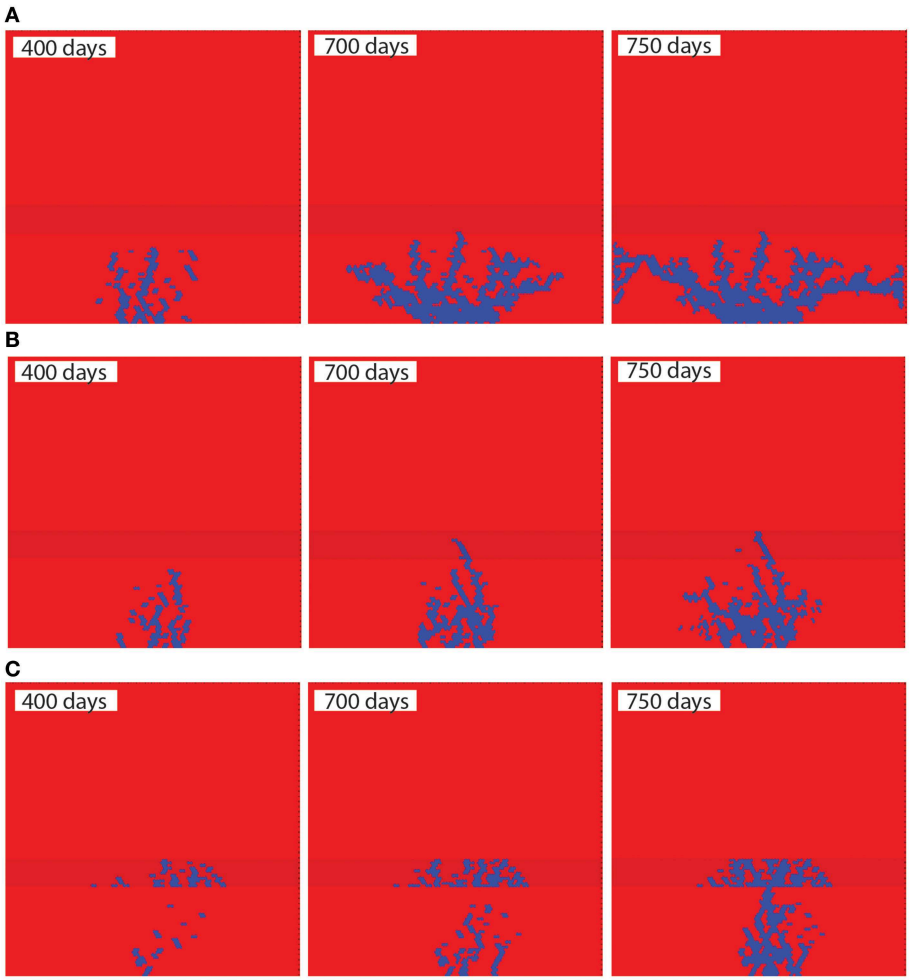

FIGURE 5 | Figure illustrating the progressive fracture development (from left to right) in three different simulations where the matrix is shown in red and the fractures shown in blue color [23]. (A) Figures show the development of irregular hydrofractures around an elliptical source in a weak rock unit. Because the seal has a comparatively high strength the growing fractures cannot propagate into the seal layer and change from a vertical to a sub-horizontal direction below the seal. This deflection indicates that the impermeable seal influences fluid pressure diffusion and the stress fields because high fluid pressure gradients build up. **(B,C)** illustrate the developing fracture patterns correspond to a seal layer that is 0.5 and 0.1 times weaker than the seal shown in simulation **(A)**. The simulations illustrate that the seal with a lower strength has a higher probability of seal failure and as a consequence vertical fractures propagate through the seal. With time the vertically growing fractures from the source zone link up with the fragmented parts of the much weaker seal layer.

pressure gradient. **Figure 5B** shows an intermediate case of fracture patterns between the extremes shown in **Figures 5A,C**. Even though the impermeability of the seal layer is a prerequisite for the generation of fluid pressure gradients below the seal, the actual failure of a seal is highly dependent on the presence of vertical discontinuities within the seal layer. Reduction in strength of the seal layer leads to vertical hydrofractures that gradually form from horizontal fractures.

The patterns of simulation 5a are similar to field examples of hydrofractures where large veins develop in the basement of the Oman Mountains in relatively weak schist. The veins are thick and show orientations that are very similar to the hydrofractures in the simulated examples, they look like sheets and steep conjugate shear like fractures.

In the following, we illustrate how tectonic deformation, fluid pressure gradients and gravity can influence the development of fracture networks in multilayer systems (**Figure 6**). The model setup consists of four hard layers of low permeability that are interbedded in a regular sequence with soft permeable layers. The model contains the same default values of the material parameters that are used in the last three simulations, however the Young's modulus of the impermeable layers is considered to be five times higher than that of the permeable layers (**Table 1**). For the first 250 days the model was subjected to gravity and fluid pressure input in order to build up a realistic hydraulic gradient in the system. Fluid pressure at the top of the box is set to 0 MPa whereas the bottom boundary is set to 10 MPa (assuming hydrostatic pressures). After 250 days a lateral tensile strain was

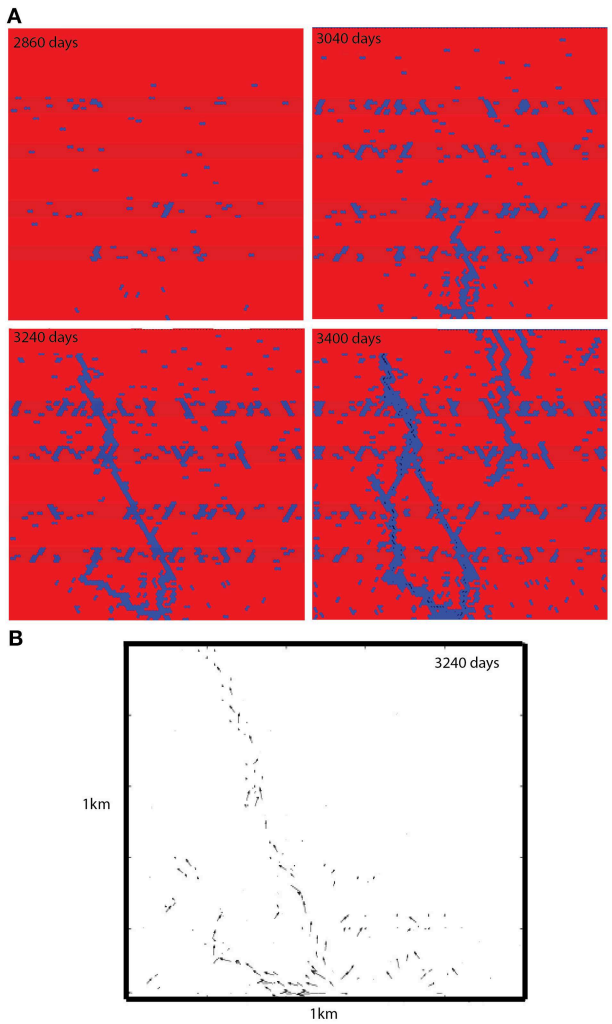

FIGURE 6 | (A) Figure shows a simulation with several stiff layers, a fluid source at the bottom of the model and a horizontal component of extension. Fractures are shown in blue. During the first time step fracturing is mainly taking place in the stiffer layers. From the second figure onwards a fault develops that nucleates at the fluid source and propagates upwards connecting all layers and draining the system. In the stiff layers vertical fractures develop with a defined spacing. One time-step in the model corresponds to 0.1 days. The observed pattern is very similar to the field example (**Figure 7B**). **(B)** Shows the resultant directional fluid field, where fluid drains through the system along the connected pathway. The fluid pathway is shown for the third time slice in the simulations shown in **(A)**.

introduced in the system, with a horizontal constant extension rate in order to model tectonic forcing and fluid pressure rise up to lithostatic levels (27 MPa).

Once tectonic strain builds up, the hard layers fracture and develop a characteristic spacing, whereas the soft permeable matrix does not fracture. After 3040 days and an extension of 0.54 m the fluid pressure gradients are high enough to fracture the soft matrix and a larger scale fracture develops that propagates through the first layers. The hard layers show a clear spacing of fractures and the larger scale fracture is running through the whole system linking the bottom of the simulation with the top and producing a fluid pathway. With progressive deformation the upward growing fractures interact with the local fractures in the hard layers and eventually turn into large-scale normal faults that run through the whole layer pack. This observation is consistent with field example in the Oman Mountains where faults are often associated with vein sets and affirms that the same deformation sequence is responsible for some of the veins and fault sets. The draining of the system by the permeable large-scale fault can also be observed in **Figure 6B** illustrating the development of fluid pathways through the model. Note that the local layer perpendicular fractures are not part of this large-scale fluid cell. Our model shows a behavior that is often observed in real system and can also be found in the Oman mountains. Layer perpendicular veins develop first but they are mainly associated with local fluid flow and develop because of the mechanical properties of specific layers. If the spacing is uniform this implies that tectonic forces are the main driver for these structures. Once strain becomes larger and fluid pressures are involved, the vein network develops into mature large-scale faults that localize fluid flow and can drain a high pressure system. This scenario may be present in the Oman mountains where layer perpendicular veins develop in hard carbonate beds and large-scale normal faults cut through the whole sequence and seem to drain deeper fluids [64].

In this section we present outcrop analogs of fluid filled fractures or veins observed in the Oman Mountains in Oman [69–71] and discuss the contrasting driving forces, fluid pressure, gravity and tectonic stresses that may be active during the formation of these structures. The Oman Mountains are thought to have experienced significantly high fluid pressures [64, 68, 72] and are composed of a Permian to Cretaceous well-bedded dolomite and limestone sequence that overlies pre-Permian basement rocks. The geological history includes southwards directed overthrusting of the Oman ophiolite sequence, a large-scale extensional event, the development of several strike slip systems and the final uplift of the mountains [64, 69–71, 73]. Especially extension and strike slip deformation were accompanied by several generations of regional fractures and faults, which are cemented with calcite and minor quartz. Bedding perpendicular vein sets often follow stress oriented anastomosing patterns with regular spacing showing single extensional or conjugate extensional shear patterns [59]. These regularly spaced patterns seem to be overprinted by chaotic and very closely spaced veins that indicate the existence of high fluid pressure gradients. Fracture/vein localization seems to be influenced by the layer succession, where deformation is commonly linked to competent carbonate beds or along the layer interfaces (**Figure 7A**). **Figure 7** shows both, layer perpendicular veining across a competent bed and layer parallel veining along the lower and upper boundaries of the competent bed. The bedding parallel veins are thought to be partly associated with the permutation of the effective stress field due to high fluid pressures. Moreover, most of the faults that are associated with vein sets appear to act as fluid flow contributors showing increased veining along the fault plane (**Figure 7B**) [64].

In **Figure 8** we show three outcrop examples of vein sets that we think show different driving forces, where outcrop photographs are shown in **Figures 8A,C,E** and fracture patterns

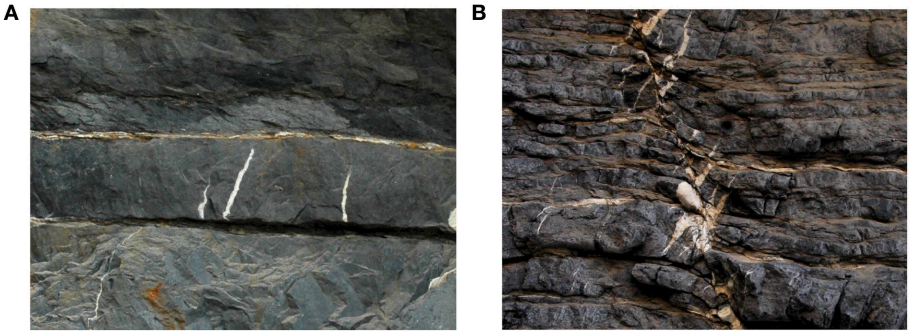

FIGURE 7 | (A) Bedding normal and parallel calcite veins in a limestone layer from the Oman Mountains. The layer is about 10 cm thick. **(B)** Example of a normal fault in the Oman Mountains (width of view is 2 m). In this case one can observe that a set of extension veins develops first which are later on cut by a normal fault. Veins and faults both seem to form in the same stress field.

are redrawn in **Figures 8B,D,F**. **Figures 8A,B** shows linear vein sets of well-defined spacing in a bedding plane on the very top of the sedimentary sequence in the Oman Mountains. The outcrop is situated just below a large-scale thrust where the Oman ophiolite with some exotic sedimentary units was thrust over the Permian to Cretaceous sequence. Though the veins in the layer follow several orientations they overall show a clear direction and spacing. We interpret the regularity of the pattern to reflect a heterogeneous stress field as a function of tectonic stresses indicating that fluid pressure was not the dominant pattern forming force. These structures should be termed tectonic fractures/veins, they may be fluid assisted but clear indicators are missing. The second example in **Figures 8C,D** shows veins in another locality of the same sequence as those shown in **Figure 8A.** In this case the veins still show a systematic orientation. However, the intensity of the veins is spatially highly variable, so that some of the veins form patches where the host-rock cannot be seen anymore. We argue that such a feature indicates that fluid pressure gradients start to become more important in the production of the veins. Especially the patches of vein material may be formed by local cells of high fluid pressure. Therefore, in contrast to **Figure 8A**, the veins shown in **Figure 8C** may be termed fluid assisted tectonic fractures/veins since fluid pressure is important but some orientation symmetry is still present indicating an influence of tectonic stresses. Finally, the veins exposed in the basement rocks (pre-Permian) of the Oman Mountains are shown in **Figures 8E,F**. These veins are found to be very thick, jagged, and highly chaotic. Some of the veins are sub-horizontal while others follow a vertical zig-zag pattern. Neither spacing nor any preferred orientation are visible that may indicate the influence of tectonic stresses. In this case it is clear that high fluid pressure gradients and gravity did play the main role in pattern formation, which promotes the hypothesis that the developed veins are real hydrofractures.

Discussion

The proposed two-dimensional hybrid hydro-elastic model successfully reproduces realistic patterns of fractures and faults that are associated with fluid pressure gradients as well as gravity and tectonic loading. The coupled model inherits a two-way feedback between the continuum and elastic domains and imitates the evolution of field scale veins and fracture networks in a layered sedimentary system. The presence of large pressure gradients due to permeability contrasts between the seal and the surrounding layers, and the dynamic link between fluid pressure and fracture growth causes oscillations of the stress field in the adjacent rock units immediately after a fracture forms.

In the first example we compare the numerical results with bedding parallel and irregular vein sets in layered limestone as shown in **Figures 7A**, **8E**. It is observed that heterogeneity in the lithology and mechanical properties e.g., Young's modulus and breaking strength distribution influence the evolution of buoyancy, fracture patterns and localization in seal and host rock layers. It is well established that hydrofractures in layered sedimentary rock sequences are more likely to develop in and propagate through stiff rather than soft layers due to concentration of stresses in the stiffer layers.

The layer contact is also considered to be an important parameter that represents a discontinuity in the matrix. Layer contacts in the solid continua tend to break easier and are case sensitive to the elevated effective stress gradient and tend to open up and thus influence the pattern formation of growing fractures [74, 75]. In our simulation, a high contrast in mechanical and material properties between the layers causes a weak bedding contact that fails once it is subject to high fluid pressure gradients. Most cap rocks in fluid filled layered reservoirs are shales that are composed of parallel-aligned clay minerals. Compaction and other diagenetic processes during the evolution of basins may result in further reduction of the clay's permeability, an increase in stiffness or the development of mechanical weak pockets in intrinsic strength [66], which may further alter the conditions of fracturing in layered reservoirs over time.

In this contribution we are simulating uniaxial strain models (gravity loading in undrained or tectonically relaxed basins), in which the minor horizontal stress σ_h increases with increasing P_f as consequence of poroelastic effects and eventually favors the propagation of fractures in the horizontal direction, a scenario that is usually associated with accretionary wedges [39, 76]. In the presence of a free upper surface the derived stress field

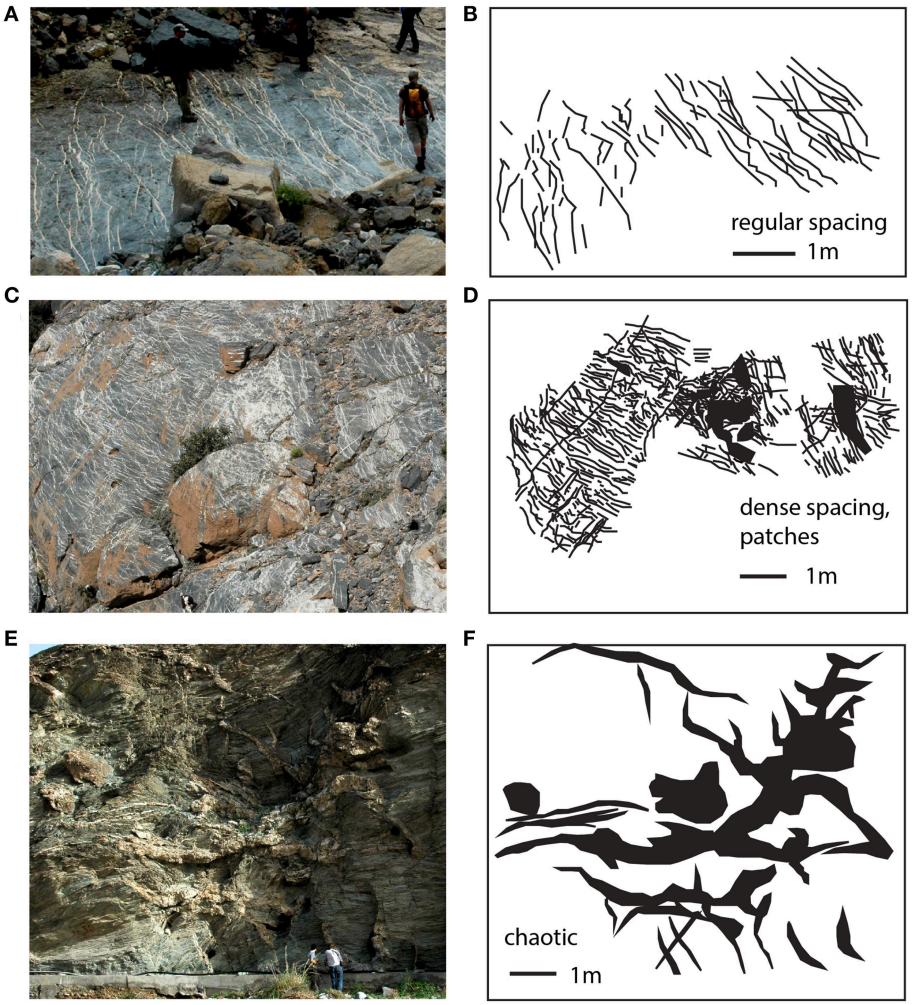

FIGURE 8 | Different vein patterns in the uppermost Cretaceous carbonate units (A–D) and pre-Permian rocks (E,F) of the Oman Mountains. (A) Photograph of well-oriented and regularly spaced linear vein geometries exhibiting a dominant influence of tectonic stresses, **(B)** sketch of the vein pattern showing clear spacing and orientation. **(C)** Photograph of a layer surface showing calcite patches surrounded by regularly spaced veins indicating that fluid pressure and tectonic stresses interacted, with local high fluid pressure gradients producing the patches. **(D)** Sketch of **(C)** illustrating a narrow spacing of veins and patches with 100% mineralization. **(E)** Thick basement veins that have zigzag geometries indicating a dominant role of fluid pressure gradients and gravity. **(F)** Sketch of e illustrating the chaotic geometry of the veins in the basement.

faces relatively less resistance in the vertical direction so that the system may expand vertically. If stresses are confined in the horizontal direction σ_h may become larger in magnitude than σ_v so that conditions for horizontal fracture propagation are approached [50]. Bedding parallel veins have generally been attributed to represent local principal stress permutations as a function of basinal supra-hydrostatic fluid pressure [64]. One should however note that seal thickness is also pivotal for pattern formation and fracture spacing. The strength distribution of the matrix is another crucial material property that can regulate the dynamics of induced fractures and is commonly simplified in numerical studies. A weaker seal layer will likely fail in a vertical direction during the ascending growth of fractures and will thus contribute to channeling of pressurized fluid flow across the seal to more permeable layers. Conversely a seal with a comparably high strength turns up to be a stress barrier to the vertically propagating fractures. Restriction in fracture propagation results in an increase in fluid pressure, which may cause a switch in the direction of principal effective stresses in the permeable host layer and subsequently divert the growth of the initially vertically induced fractures to near horizontal fracture sets. This situation is reached during the emplacement of sills where fluid pressure is at or above the lithostatic [77]. This observation is consistent with Flekkøy et al. [24], who state that in a geological context a vertical permeability variation is not enough to induce cap rock fracturing if the fluid pressure is the only driving force but that the background heterogeneity in the material properties is also important.

The developing fracture patterns in the simulations depend strongly on the fluid pressure gradient. This is inconsistent with

the idea that fluid pressure in rocks only moves the Mohr circle toward the tensile regime to induce extensional fractures [50]. This simplification leads to the wrong prediction of patterns and does not separate a fracture that is produced by fluid pressure gradients from a fracture that is produced by tectonic stresses. Our model shows that fluid pressure gradients can be extremely important in pattern formation (**Figure 9**). In the presence of fluid pressure gradients, gravity and tectonic stresses, it is observed that a whole set of fracture patterns can develop depending on the dominant driving force in the system. Fractures that are produced by fluid pressure gradients only can look fundamentally different from tectonically induced fractures.

It is also evident that permeability as such is a dynamic property that changes simultaneously with the deformation of an overpressure system. Fracture networks in **Figure 6** show that there is a strong correlation between layer perpendicular fracturing and faulting. Layered systems that are subjected to non-hydrostatic tectonic stresses in the presence of high fluid pressure gradients along anisotropies undergo a transition from layer fracturing to large scale shearing [78]. Fracturing in the model takes place on the local scale whereas faulting seems to drain the whole system and forms a large-scale connectivity [19]. Vertical fractures in stiff layers accommodate the additional strain locally with only a minor increase in stress, however under the prevailing conditions of fluid overpressure the differential stress can increase up to a critical limit leading to the development of large-scale faults. The stress drops significantly when the whole system fails along large-scale normal faults and high fluid pressure gradients along the fault may weaken the fault plane [79]. This has strong correlation with fluid drain where the growing fractures and the fluid pressure in the system influence each other depending on the effective permeability of the interconnected fracture network. This behavior is similar to what is observed in the Oman Mountains, where veins and faults correlate and stable isotopes seems to indicate that faults drain the system [64]. After their formation the faults usually behave as plastic systems and deter any further stress accumulation unless they are fully healed by the mineralization of the fracturing fluid. This phenomenon has strong influences on the strength of the fault planes and the subsequent earthquake events which may sometime turn into catastrophic failure [54].

The process of hydrofracturing has direct applications in many fields e.g., Geothermal reservoirs [80–82], normal oil and gas reservoirs, or CO_2 sequestration [83], where formation fluid pressure gradients play a role in cap-rock failure or permeability creation for the transport of pressurized fluid. We believe that

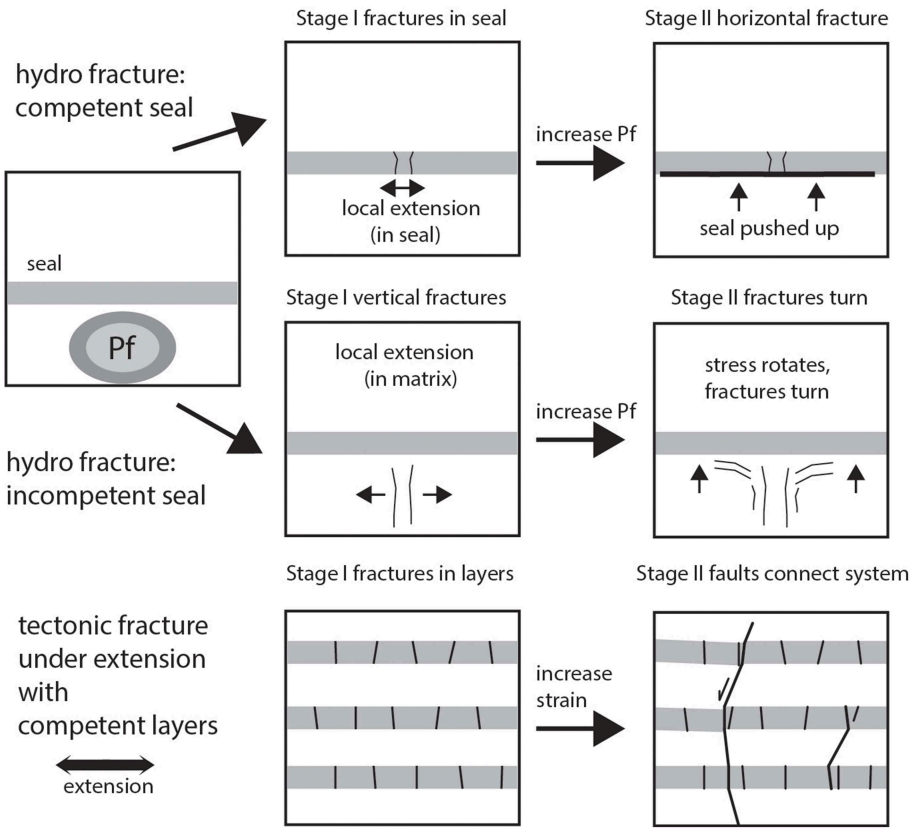

FIGURE 9 | Summary figure illustrating different fracture patterns that develop below and in a competent vs. an incompetent seal and fracture and fault patterns that develop in a layered sequence that is extended. Hydrofractures tend to develop around sources of high fluid pressures where fluid pressure gradients fracture the matrix or bend competent layers leading to fractures. During extension fractures are well spaced along the beds and at higher strain faults connect different layers and drain systems of high fluid pressure.

our model can form a basis for better understanding of the influence of fluid pressure gradients and tectonic stresses on the development of natural fractures in reservoirs. In subsequent work we will expand the model to look more closely at seismic patterns that develop under variable boundary conditions.

In conclusion, our coupled numerical model can simulate the dynamic evolution of hydrofracturing. The model can reproduce realistic geometries of the field scale fracture and vein networks and demonstrates how the pattern changes depending on the material properties (i.e., stiffness and breaking strength distribution) and the applied external forces e.g., high fluid pressure gradient, gravity and lateral tectonic forces. Results of the model indicate that layers of low permeability may result in local perturbation of the effective stress field in host rocks and subsequently causes diversion of the direction of growing hydrofractures. Hydrofracturing in the model produces a non-static permeability in an over-pressured system, where the permeability does adjust to the local fluid pressures and accordingly the evolved stresses. We tested the model for a number of different combinations of high fluid pressure gradients, gravity and tectonic stresses to produce complex patterns. We are able to define the first proxies that can be used to determine whether natural fracture, vein and fault networks are mainly due to tectonic stresses or high fluid pressure gradients.

Acknowledgments

Sections of this manuscript are presented in the Thesis of Dr. IG, which is available here: http://ubm.opus.hbz-nrw.de/volltexte/2013/3543/. This study was carried out within the framework of Deutsche Wissenschaftliche Gesellschaft für Erdöl, Erdgas und Kohle (German Society for Petroleum and Coal Science and Technology) research project 718 "Mineral Vein Dynamics Modelling," which is funded by the companies ExxonMobil Production Deutschland GmbH, GDF SUEZ E&P Deutschland GmbH, DEA Deutsche Erdoel AG and Wintershall Holding GmbH, within the basic research program of the WEG Wirtschaftsverband Erdoel- und Erdgasgewinnung e.V. We thank the companies for their financial support and their permission to publish these results. This work has received funding from the European Union's Seventh Framework Programme for research, technological development and demonstration under grant agreement no 316889 and support from the Alsace region within the REALISE program.

References

1. Fyfe WS, Price NJ, Thompson AB. *Fluids in the Earth's Crust: Their Significance in Metamorphic, Tectonic, and Chemical Transport Processes*. New York, NY: Elsevier Scientific Pub. Co. (1978).
2. Hubbert MK, Rubey WW. Role of fluid pressure in mechanics of overthrust faulting: I. mechanics of fluid-filled porous solids and Its application to overthrust faulting. *Geol Soc Am Bull.* (1959) **70**:115–66. doi: 10.1130/0016-7606(1959)70[115:ROFPIM]2.0.CO;2
3. Secor DT. Role of fluid pressure in jointing. *Am J Sci.* (1965) **263**:633–46. doi: 10.2475/ajs.263.8.633
4. Segall P, Fitzgerald SD. A note on induced stress changes in hydrocarbon and geothermal reservoirs. *Tectonophysics* (1998) **289**:117–28. doi: 10.1016/S0040-1951(97)00311-9
5. Sibson RH, Scott J. Stress/fault controls on the containment and release of overpressured fluids: examples from gold-quartz vein systems in Juneau, Alaska; Victoria, Australia and Otago, New Zealand. *Ore Geol Rev.* (1998) **13**:293–306. doi: 10.1016/S0169-1368(97)00023-1
6. Sibson RH. Fluid involvement in normal faulting. *J Geodyn.* (2000) **29**:469–99. doi: 10.1016/S0264-3707(99)00042-3
7. Collettini C, De Paola N, Goulty NR. Switches in the minimum compressive stress direction induced by overpressure beneath a low-permeability fault zone. *Terra N.* (2006) **18**:224–31. doi: 10.1111/j.1365-3121.2006.00683.x
8. Leclère H, Fabbri O, Daniel G, Cappa F. Reactivation of a strike-slip fault by fluid overpressuring in the southwestern French–Italian Alps. *Geophys J Int.* (2012) **189**:29–37. doi: 10.1111/j.1365-246X.2011.05345.x
9. Hu J-C, Angelier J. Stress permutations: three-dimensional distinct element analysis accounts for a common phenomenon in brittle tectonics. *J Geophys Res.* (2004) **109**:B09403. doi: 10.1029/2003JB002616
10. Bonafede M, Danesi S. Near-field modifications of stress induced by dyke injection at shallow depth. *Geophys J Int.* (1997) **130**:435–48. doi: 10.1111/j.1365-246X.1997.tb05659.x
11. Jamtveit B, Svensen H, Podladchikov YY, Planke S. Hydrothermal vent complexes associated with sill intrusions in sedimentary basins. *Geol Soc Lond Spec Publ.* (2004) **234**:233–41. doi: 10.1144/GSL.SP.2004.234.01.15
12. Wangen M. Effective permeability of hydrofractured sedimentary rocks. In: Andreas GK, Robert H, editors. *Norwegian Petroleum Society Special Publications*. Oxford, UK: Elsevier (2002). pp. 61–74. doi: 10.1016/s0928-8937(02)80007-8
13. Hunt JM. Generation and migration of petroleum from abnormally pressured fluid compartments. *AAPG Bull.* (1990) **74**:1–12.
14. Roberts SJ, Nunn JA. Episodic fluid expulsion from geopressured sediments. *Mar Petrol Geol.* (1995) **12**:195–204. doi: 10.1016/0264-8172(95)92839-O
15. Nunn JA, Meulbroek P. Kilometer-scale upward migration of hydrocarbons in geopressured sediments by buoyancy-driven propagation of methane-filled fractures. *AAPG Bull.* (2002) **86**:907–18. doi: 10.1306/61EEDBD4-173E-11D7-8645000102C1865D
16. Cathles LM, SmithAT. Thermal constraints on the formation of mississippi valley-type lead-zinc deposits and their implications for episodic basin dewatering and deposit genesis. *Econ Geol.* (1983) **78**:983–1002. doi: 10.2113/gsecongeo.78.5.983
17. Krynauw JR, Hunter DR, Wilson AH. Emplacement of sills into wet sediments at Grunehogna, western Dronning Maud Land, Antarctica. *J Geol Soc.* (1988) **145**:1019–32. doi: 10.1144/gsjgs.145.6.1019
18. Miller SA, Nur A. Permeability as a toggle switch in fluid-controlled crustal processes. *Earth Planet Sci Lett.* (2000) **183**:133–46. doi: 10.1016/S0012-821X(00)00263-6
19. Vass A, Koehn D, Toussaint R, Ghani I, Piazolo S. The importance of fracture-healing on the deformation of fluid-filled layered systems. *J Struct Geol.* (2014) **67**:94–106. doi: 10.1016/j.jsg.2014.07.007
20. Aochi H, Poisson B, Toussaint R, Rachez X, Schmittbuhl J. Self-induced seismicity due to fluid circulation along faults. *Geophys J Int.* (2013) **196**:1544–63. doi: 10.1093/gji/ggt356
21. Kobchenko M, Panahi H, Renard F, Dysthe DK, Malthe-Sørenssen A, Mazzini A, et al. 4D imaging of fracturing in organic-rich shales during heating. *J Geophys Res.* (2011) **116**:B12201. doi: 10.1029/2011JB008565
22. Ghani I, Koehn D, Toussaint R, Passchier CW. Dynamic development of hydrofracture. *Pure Appl Geophys.* (2013) **170**:1685–703. doi: 10.1007/s00024-012-0637-7
23. Ghani I. *Dynamic Development of Hydrofractures*. PhD thesis, University of Mainz, Germany (2013). pp.1–90. Available online at: http://ubm.opus.hbz-nrw.de/volltexte/2013/3543/
24. Flekkøy EG, Malthe-Sorenssen A, Jamtveit B. Modeling hydrofracture. *J Geophys Res Solid Earth* (2002) **107**:1–11. doi: 10.1029/2000JB000132

25. Vinningland JL, Johnsen O, Flekkøy EG, Toussaint R, Måløy KJ. Experiments and simulations of a gravitational granular flow instability. *Phys Rev E*. (2007a) **76**:051306. doi: 10.1103/PhysRevE.76.051306
26. Vinningland JL, Johnsen Ø, Flekkøy EG, Toussaint R, Måløy KJ. Granular Rayleigh-Taylor instability: experiments and simulations. *PhysRevLett* (2007b) **99**:048001. doi: 10.1103/PhysRevLett.99.048001
27. Johnsen Ø, Toussaint R, Måløy KJ, Flekkøy EG. Pattern formation during central air injection into granular materials confined in a circular Hele-Shaw cell. *Physical Rev E*. (2006) **74**:011301. doi: 10.1103/PhysRevE.74.011301
28. Johnsen Ø, Toussaint R, Måløy KJ, Flekkøy EG, Schmittbuhl, J. Coupled air/granular flow in a linear Hele-Shaw cell. *Phys Rev E*. (2008a) **77**:011301. doi: 10.1103/PhysRevE.77.011301
29. Johnsen Ø, Chevalier C, Lindner A, Toussaint R, Clément E, Måløy KJ, et al. Decompaction and fluidization of a saturated and confined granular medium by injection of a viscous liquid or a gas. *Phys Rev E*. (2008b) **78**:051302. doi: 10.1103/PhysRevE.78.051302
30. Niebling M, Toussaint R, Flekkøy EG, Måløy KJ. Estudios numéricos de Aerofractures en medios poros/Numerical Studies of Aerofractures in Porous Media. *Rev Cubana Fis*. (2012a) **29**:1E, 1E66.
31. Niebling MJ, Toussaint R, Flekkøy EG, Måløy KJ. Dynamic aerofracture of dense granular packings. *Phys Rev E*. (2012b) **86**:061315. doi: 10.1103/PhysRevE.86.061315
32. Goren L, Aharonov E, Sparks D, Toussaint R. Pore pressure evolution in deforming granular material: a general formulation and the infinitely stiff approximation. *J Geophys Res*. (2010) **115**:B09216. doi: 10.1029/2009JB007191
33. Goren L, Aharonov E, Sparks D, Toussaint R. The mechanical coupling of fluid-filled granular material under shear. *Pure Appl Geophys*. (2011) **168**:2289–323. doi: 10.1007/s00024-011-0320-4
34. Niebling MJ, Flekkøy EG, Måløy KJ, Toussaint, R. Mixing of a granular layer falling through a fluid. *Phys Rev E*. (2010a) **82**:011301. doi: 10.1103/PhysRevE.82.011301
35. Niebling MJ, Flekkøy EG, Måløy KJ, Toussaint, R. Sedimentation instabilities: impact of the fluid compressibility and viscosity. *Phys Rev E*. (2010b) **82**:051302. doi: 10.1103/PhysRevE.82.051302
36. Vinningland JL, Johnsen Ø, Flekkøy EG, Toussaint R, Måløy KJ. Influence of particle size in Rayleigh Taylor granular flow instability. *Phys Rev E*. (2010) **81**:041308. doi: 10.1103/PhysRevE.81.041308
37. Vinningland JL, Toussaint R, Niebling M, Flekkøy EG, Måløy, KJ. Family-Vicsek scaling of detachment fronts in Granular Rayleigh Taylor Instabilities during sedimenting granular/fluid flows. *Eur Phys J Spec Top*. (2012) **204**:27–40. doi: 10.1140/epjst/e2012-01550-2
38. Zoback MD. *Reservoir Geomechanics*. Cambridge, UK: Cambridge University Press (2007). doi: 10.1017/CBO9780511586477
39. Engelder T, Lacazette A. Natural hydraulic fracturing. In: Stephansson NBAO, editor. *Rock Joints: Proceedings of the International Symposium on Rock Joints*. Rotterdam; Loen: A.A. Balkema (1990). pp. 35–44.
40. Olson JE, Laubach SE, Lander RH. Natural fracture characterization in tight gas sandstones: integrating mechanics and diagenesis. *AAPG Bull*. (2009) **93**:1535–49. doi: 10.1306/08110909100
41. Segall P. Formation and growth of extensional fracture sets. *Geol Soc Am Bull*. (1984) **95**:454–62.
42. Biot MA. General theory of three-dimensional consolidation. *J Appl Phys*. (1941) **12**:155–64. doi: 10.1063/1.1712886
43. Secor DT. *Mechanics of Natural Extension Fracturing at Depth in the Earth's Crust*. Report 68–52, Geological Survey of Canada (1969). pp. 3–48.
44. Rice JR, Cleary MP. Some basic stress diffusion solutions for fluid-saturated elastic porous media with compressible constituents. *Rev Geophys*. (1976) **14**:227–41. doi: 10.1029/RG014i002p00227
45. Adachi J, Siebrits E, Peirce A, Desroches J. Computer simulation of hydraulic fractures. *Int J Rock Mech Min Sci*. (2007) **44**:739–57. doi: 10.1016/j.ijrmms.2006.11.006
46. Cleary MP, Wong SK. Numerical simulation of unsteady fluid flow and propagation of a circular hydraulic fracture. *Int J Numer Anal Methods Geomech* (1985) **9**:1–14. doi: 10.1002/nag.1610090102
47. Meyer BR. Design formulae for 2-D and 3-D vertical hydraulic fractures: model comparison and parametric studies. In: *SPE Unconventional Gas Technology Symposium*. Louisville, KY: Society of Petroleum Engineers, Inc. (1986).
48. Gordeyev YN, Zazovsky AF. Self-similar solution for deep-penetrating hydraulic fracture propagation. *Transp Porous Media*. (1992) **7**:283–304. doi: 10.1007/BF01063964
49. Tzschichholz F, Herrmann HJ, Roman HE, Pfuff M. Beam model for hydraulic fracturing. *Phys Rev B*. (1994) **49**:7056–9. doi: 10.1103/PhysRevB.49.7056
50. Cobbold PR, Rodrigues N. Seepage forces, important factors in the formation of horizontal hydraulic fractures and bedding-parallel fibrous veins ('beef' and 'cone-in-cone'). *Geofluids* (2007) **7**:313–22. doi: 10.1111/j.1468-8123.2007.00183.x
51. Hillis RR. Pore pressure/stress coupling and its implications for rock failure. In: Van Rensbergen P, Hillis RR, Maltman AJ, Morley CK, editors. *Subsurface Sediment Mobilization,* Vol. 216. London, UK: Geological Society of London Special Publication (2003). pp. 359–368. doi: 10.1144/gsl.sp.2003.216.01.23
52. Press WH. *Numerical Recipes in C: The Art of Scientific Computing*. Cambridge, UK: Cambridge University Press (1992).
53. Carman PC. Fluid flow through granular beds. *Trans Inst Chem Eng*. (1937) **15**:150.
54. Koehn D, Arnold J, Malthe-Sørrenssen A, Jamtveit B. Instabilities in stress corrosion and the transition to brittle failure. *Am J Sci*. (2003) **303**:956–71. doi: 10.2475/ajs.303.10.956
55. Bons PD, Koehn D, Jessell MW. Microdynamics simulation. In: *Springer Lecture Series in Earth Sciences*. Berlin; Heidelberg: Springer (2008). p. 406. doi: 10.1007/978-3-540-44793-1
56. Allen DNG. *Relaxation Methods*. New York, NY: McGraw-Hill (1954).
57. Malthe-Sørenssen A, Walmann T, Jamtveit B, Feder J, Jøssang T. Modeling and characterization of fracture patterns in the Vatnajökull Glacier. *Geology* (1998a) **26**:931–4.
58. Malthe-Sørenssen A, Walmann T, Feder J, Jøssang T, Meakin P, Hardy HH. Simulation of extensional clay fractures. *Phys Rev E* (1998b) **58**:5548–64. doi: 10.1103/PhysRevE.58.5548
59. Koehn D, Arnold J, Passchier CW. Fracture and vein patterns as indicators of deformation history: a numerical study. *Geol Soc Lond Spec Publ*. (2005) **243**:11–24. doi: 10.1144/GSL.SP.2005.243.01.03
60. Virgo, S, Abe, S, Urai, JL. The evolution of crack seal vein and fracture networks in an evolving stress field: insights from discrete element models of fracture sealing. *J Geophys Res Solid Earth*. (2014) **119**:8708–27. doi: 10.1002/2014jb011520
61. Hansen A, Hinrichsen EL, Roux, S. Scale-invariant disorder in fracture and related breakdown phenomena. *Phys Rev B*. (1991) **43**:665. doi: 10.1103/PhysRevB.43.665
62. Toussaint R, Pride SR. Interacting damage models mapped onto Ising and percolation models. *Phys Rev E*. (2005) **71**:046127. doi: 10.1103/PhysRevE.71.046127
63. Toussaint R, Hansen A. Mean-field theory of localization in a fuse model. *Phys Rev E*. (2006) **73**:046103. doi: 10.1103/PhysRevE.73.046103
64. Hilgers C, Kirschner DL, Breton JP, Urai JL. Fracture sealing and fluid overpressures in limestones of the Jabal Akhdar dome, Oman mountains. *Geofluids* (2006) **6**:168–84. doi: 10.1111/j.1468-8123.2006.00141.x
65. Valkø P, Econimedes MJ. *Hydraulic Fracture Mechanics*. New York, NY: John Wiley (1995).
66. Brenner SL, Gudmundsson A. Arrest and aperture variation of hydrofractures in layered reservoirs. *Geol Soc Lond Spec Publ*. (2004) **231**:117–28. doi: 10.1144/GSL.SP.2004.231.01.08
67. Gudmundsson A, Brenner SL. How hydrofractures become arrested. *Terra Nova* (2001) **13**:456–62. doi: 10.1046/j.1365-3121.2001.00380.x
68. Holland M, Saxena N, Urai JL. Evolution of fractures in a highly dynamic thermal, hydraulic, and mechanical system - (II) Remote sensing fracture analysis, Jabal Shams, Oman Mountains. *Geoarabia* (2009a) **14**:163–94.
69. Boudier F, Bouchez JL, Nicolas A, Cannat M, Ceuleneer G, Misseri M, et al. Kinematics of oceanic thrusting in the Oman ophiolite: model of plate convergence. *Earth Planet Sci Lett*. (1985) **75**:215–22. doi: 10.1016/0012-821X(85)90103-7
70. Breton JP, Bechennec F, Le Metour J, Moen-Maurel L, Razin P. Eoalpine (Cretaceous) evolution of the Oman Tethyan continental margin: insights from a structural field study in Jabal Akhdar (Oman Mountains). *Geoarabia* (2004) **9**:41–58.

71. Searle MP. Structural geometry, style and timing of deformation in the Hawasina window, Al Jabal al Akhdar and Saih Hatat culminations, Oman mountains. *Geoarabia* (2007) **12**:99–130.
72. Holland M, Urai JL, Muchez P, Willemse EJM. Evolution of fractures in a highly dynamic thermal, hydraulic, and mechanical system - (I) Field observations in Mesozoic Carbonates, Jabal Shams, Oman Mountains. *Geoarabia* (2009b) **14**:57–110.
73. Gomez-Rivas E, Bons PD, Koehn D, Urai JL, Arndt M, Virgo S, et al. The Jabal Akhdar Dome in the Oman Mountains: evolution of a dynamic fracture system. *Am J Sci.* (2014) **314**:1104–39. doi: 10.2475/07.2014.02
74. Cooke ML, Underwood CA. Fracture termination and step-over at bedding interfaces due to frictional slip and interface opening. *J Struct Geol.* (2001) **23**:223–38. doi: 10.1016/S0191-8141(00)00092-4
75. Gudmundsson A. Emplacement and arrest of sheets and dykes in central volcanoes. *J Volcanol Geothermal Res*. (2002) **116**:279–98. doi: 10.1016/S0377-0273(02)00226-3
76. Fischer MP, Engelder T, Brown KM, Bekins B, Clennell B, Dewhurst D, et al. Heterogeneous hydrofracture development and accretionary fault dynamics: comment and reply. *Geology* (1994) **22**:1052–4.
77. Gudmundsson A. Fluid overpressure and stress drop in fault zones. *Geophys Res Lett.* (1999) **26**:115–8. doi: 10.1029/1998GL900228
78. Bercovici D, Ricard Y, Schubert G. A two-phase model for compaction and damage: 1. General theory. *J Geophys Res Solid Earth*. (2001) **106**:8887–906. doi: 10.1029/2000JB900430
79. Zoback MD, Harjes H-P. Injection-induced earthquakes and crustal stress at 9 km depth at the KTB deep drilling site, Germany. *J Geophys Res.* (1997) **102**:18477–91. doi: 10.1029/96JB02814
80. Gentier S, Rachez X, Peter-Borie M, Blaisonneau A. Hydraulic stimulation of geothermal wells: modeling of the hydro-mechanical behavior of a stimulated fractured rock mass. In: *The Proceedings of the XII International Congress of Rock Mechanics.* Beijing (2011).
81. Neuville A, Toussaint R, Schmittbuhl J. Fracture roughness and thermal exchange: a case study at Soultz-sous-Forets, C.R.A.S. *Geoscience* (2009) **342**:616. doi: 10.1016/j.crte.2009.03.006
82. Neuville A, Toussaint R, Schmittbuhl J. Hydro-thermal flows in a self-affine rough fracture. *Phys Rev E*. (2010) **82**:036317. doi: 10.1103/PhysRevE.82.036317
83. Cappa F, Rutqvist J, Yamamoto K. Modeling crustal deformation and rupture processes related to upwelling of deep CO2 rich fluids during the 1965-1967 Matsushiro Earthquake Swarm in Japan. *J Geophys Res*. (2009) **114**:B10304. doi: 10.1029/2009JB006398

Conflict of Interest Statement: The authors declare that the research was conducted in the absence of any commercial or financial relationships that could be construed as a potential conflict of interest.

frontiers in Physics

ORIGINAL RESEARCH
published: 21 August 2015
doi: 10.3389/fphy.2015.00063

Transport efficiency and dynamics of hydraulic fracture networks

Till Sachau[1]*, *Paul D. Bons*[1] and *Enrique Gomez-Rivas*[2]

[1] Department of Geosciences, Universität Tübingen, Tübingen, Germany, [2] Department of Geology and Petroleum Geology, University of Aberdeen, Aberdeen, Scotland

Intermittent fluid pulses in the Earth's crust can explain a variety of geological phenomena, for instance the occurrence of hydraulic breccia. Fluid transport in the crust is usually modeled as continuous Darcian flow, ignoring that sufficient fluid overpressure can cause hydraulic fractures as fluid pathways with very dynamic behavior. Resulting hydraulic fracture networks are largely self-organized: opening and healing of hydraulic fractures depends on local fluid pressure, which is, in turn, largely controlled by the fracture network. We develop a crustal-scale 2D computer model designed to simulate this process. To focus on the dynamics of the process we chose a setup as simple as possible. Control factors are constant overpressure at a basal fluid source and a constant "viscous" parameter controlling fracture-healing. Our results indicate that at large healing rates hydraulic fractures are mobile, transporting fluid in intermittent pulses to the surface and displaying a $1/f^{\alpha}$ behavior. Low healing rates result in stable networks and constant flow. The efficiency of the fluid transport is independent from the closure dynamics of veins or fractures. More important than preexisting fracture networks is the distribution of fluid pressure. A key requirement for dynamic fracture networks is the presence of a fluid pressure gradient.

Keywords: hydraulic fracturing, fracture network, fluid flow, intermittent fluid flow, Earth's crust, dynamics fracture network, hydraulic breccia

OPEN ACCESS

Edited by:
Renaud Toussaint, University of Strasbourg, France

Reviewed by:
Marcus Ebner, OMV, Austria
Irfan Ghani, Centre National de la Recherche Scientifique, France
Ramon Planet, Université de Lyon 1, France

***Correspondence:**
Till Sachau, Department of Geosciences, Universität Tübingen, Wilhelmstr. 56, 72076 Tübingen, Germany
tsa@posteo.de

Specialty section:
This article was submitted to Interdisciplinary Physics, a section of the journal Frontiers in Physics

Received: *30 April 2015*
Accepted: *05 August 2015*
Published: *21 August 2015*

Citation:
Sachau T, Bons PD and Gomez-Rivas E (2015) Transport efficiency and dynamics of hydraulic fracture networks. Front. Phys. 3:63. doi: 10.3389/fphy.2015.00063

Introduction

Fluid flow in the Earth's crust is evidenced by a variety of geological phenomena, including veins and hydraulic breccias. Veins are dilatant structures, typically fractures, filled with minerals that precipitated from fluid (see review of [1], and references therein). Hydraulic breccias are fragmented rocks where the fragmentation is mainly caused by chaotic fracturing due to fluid overpressure [2–5], as opposed to tectonic breccias where the diminution is due to tectonic stresses, typically along faults [6–8].

Both veins and breccias usually show evidence for repeated fracturing. Veins commonly exhibit microstructures that are indicative of the "crack-seal mechanism" [9], where a crack repeatedly opens and is subsequently sealed again by mineral growth (**Figure 1**). This crack-sealing, which can be repeated thousands of times in a single vein, indicates that fluid flow is not continuous, but intermittent: fluid pressure builds up to exceed the tensional strength of the rock and cause failure, after which flow can occur until the fracture permeability is sealed off again [9–13]. Hydraulic breccias also typically show indications of repeated fracturing in the form of clasts in clasts and brecciated cement [4, 14].

Although evidence for intermittent fluid flow is abundant, relatively little is known on the duration of and time spans between fracturing events. An indirect indication can be achieved by considering fluid flow velocities and total fluxes. Theoretical considerations of fracture propagation velocity, and hence velocity of contained fluid, range from m/yr to m/s [15, 16]. The large range is mostly due to uncertainty in the fracture toughness of rocks. Field observations suggest that flow velocities can reach the upper end of the range. For example, [17] and [18] estimated flow velocities of 0.01–0.1 m/s from the size of grains that were carried up by the fluid. Using similar arguments, [24] derived flow velocities in excess of 5 m/s in a fluidized breccia with m-sized clasts from the Cloncurry District, Australia.

Weisheit et al. [4] describe a hydraulic breccia, the Hidden Valley Breccia, Australia, that is 10 km^2 in outcrop and contains clasts that range from <0.1 mm to >100 m in size. It formed over a period of more than 150 million years, as basement gneisses were exhumed in this area by over 12 km [19]. The estimated amount of fluid to have produced this breccia is about 20 km^3. Assuming a porosity of 10% and a flow rate of 1 m/s, at the upper end of the aforementioned range, the estimated duration of flow (Δt) would only be about 2100 s, or a mere few hours. This is a minute fraction of the >100 million years it took to form the breccia. Even if the flow rate was 1 m/yr, the total duration would only be about 2100 years. Fluid flow must therefore have been highly intermittent with only very occasionally short bursts of flow, and extremely long periods of pressure buildup. This mechanism can result in dense networks of veins composed of many crack-seal events that formed over long periods of time [e.g., 20].

Intermittent flow is predicted to occur when the matrix permeability of a rock is insufficient to accommodate fluid flow [21, 22]. This leads to an increase in fluid pressure and opening of hydrofractures. When exceeding a critical length, these can become mobile by propagation on one end and closure at the other. Such "mobile hydrofractures" thus propagate together with their contained fluid and can reach velocities in the order of m/s [16, 22, 23]. Possible fluid sources which may generate the necessary fluid pressure for hydraulic brecciation and hydraulic fracturing are fluid released by igneous intrusions [24], fluid release due to decompression [25, 26] or mineral dehydration reactions [27]. Dehydration of the mineral biotite appears to be the main fluid source in case of Hidden Valley [4].

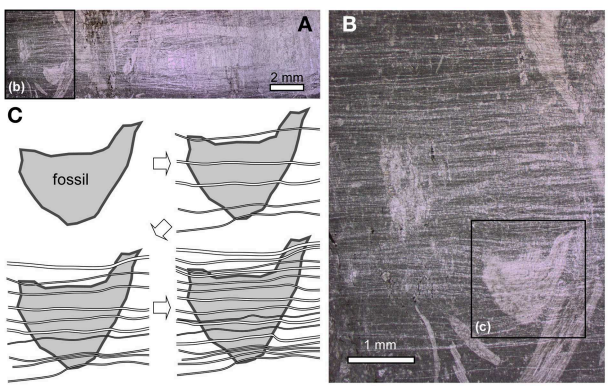

FIGURE 1 | Microphotograph and sketch of a crack seal vein from fossiliferous Cretaceous limestone in the Jabal Akhdar Dome, Oman [20]. (A) Overview of one half of the vein, composed of hundreds of individual crack-seal veinlets. **(B)** Distributed crack-seal veinlets, each tens of μm in width are visible in a close up. **(C)** Schematic development stages of the vertcially stretched fossil fragment in **(B)**. The actual order of fracture events cannot be determined from the thin section image. Plane-polarized light.

In contrast, classically large-scale fluid flow is assumed to take place by slow, convective fluid percolation, typically driven by topography or thermal instabilities, for example due to igneous intrusions [28, 29]. Such convective flow requires a fluid pressure that is close to hydrostatic, which is incompatible with the high, supra-lithostatic fluid pressures required to fracture rocks to produce veins and breccias [1].

A number of numerical models for hydrofracture formation exist already [30, 31] while new models are continuously developed [e.g., 32–36]. The current interest in these models is mainly triggered by the enormous economic importance of artificial hydraulic (aka "fracking") as a means of oil and gas extraction. However, these models are focused on the micro- to meso-scale, where single cracks and fractures can be numerically resolved. Existing numerical models for crustal scale flow, on the other hand, do not consider the interplay between fluid flow and hydraulic fracturing, but assume that the intrinsic matrix permeability of rocks is the only relevant parameter [e.g., 37–39]. Miller and Nur [21] developed a crustal scale cellular automaton model which was able to capture the general dynamics of large scale hydraulic fracture networks, but wasn't based on realistic concepts for fluid propagation and closing of fractures.

To our knowledge, the numerical model developed and applied in this study is the first discrete crustal scale 2D model which integrates fluid flow dynamics and hydrofracture formation. This setup permits modeling of dynamic hydraulic fracture networks and the derivation of the key control factors. The setup is intentionally simple compared to the "real" crust, since we are interested in the general characteristics of the fracture patterns and the efficiency of the transport mechanism.

Below we first show that the transport mechanism of crustal fluid must include hydraulic fracturing in order to explain the hydraulic rocks at Mount Painter. In a second step we investigate the hydraulic fracture patterns which develop in a simplified crust in a 2D model. We exclude the consideration of finer geological intricacies in the model, e.g., geological layering. Of more importance in this context are the influence of a crustal scale pressure gradient and the rate of closure of hydraulic fractures.

Fluid Flow and Hydraulic Fracturing in the Earth's Crust

The basic law governing laminar fluid flow q over a distance L through porous media is Darcy's law:

$$q = K\frac{\Delta\left(P_f - \rho_{H_2O}gz\right)}{L}, \quad (1)$$

where ρ_{H_2O} is the density of water, P_f the fluid pressure, g earth's acceleration, K the hydraulic conductivity, L the distance and z the height difference between start point and end point of the fluid flow. In case of vertical fluid flow, and with reference to the surface, $L = z$ and $P_{f,surface} = 0$.

It is commonly assumed that fluid overpressure causes tensile fracturing [e.g., 33, 40, 41, 43]. Therefore, fluid pressure is non-destructive as long as one of the following relation holds, which are commonly applied fracture conditions [compare for instance [33, 44, 47]:

$$P_f < \sigma_3 + P_{cr} \quad (2)$$

or

$$\sigma_1 - \sigma_3 \geq 4P_{cr} \quad (3)$$

where σ_1 and σ_3 are the maximum and minimum principal normal stress in the solid and P_{cr} is the tensile strength of the material. Here, tensile stress is negative.

The state of stress in the crust is probably among the most controversial issues in geology/geophysics. While it is generally safe to assume hydrostatic conditions for the fluid pressure, the conditions for solid stress in the crust are a topic of continuous debate. Elastic theory links uniaxial vertical loading stress to the horizontal stress via a function of the Poisson ratio μ, which is typically about 0.2–0.3 for geological materials. However, new data [48] suggests that solid stress in the crust is approximately isotropic if external tectonic stress is absent and below c. 1000 m depth., i.e., $\sigma_3 \approx \sigma_1$. The reason is that the loading stress is mainly compensated by brittle plastic deformation at this depth.

We apply this criterion in the numerical model, which means that we effectively adapt the so-called lithostatic stress model [e.g., 49], which assumes isotropic solid stress conditions. This choice has been partly made because one of the specific aims of this study was to use a simplified model, and to focus on the driving forces. The driving force for hydraulic fracturing is mainly the fluid pressure, independent of a specific crustal stress model, due to the nature of the fluid pressure gradient.

This means that the modeled solid stress field is probably not exactly correct very close to the surface. However, the range of possible horizontal stress values that has been reported is large and includes the isotropic stress case ($\sigma_v/\sigma_h = 1$) till approximately 250 m depth [48]. Since we are concerned with the fluid flow at a larger depth rather than in surface vicinity, this was considered an acceptable compromise. This compromise deems even more acceptable as we have to assume a permanent open fracture network close to the surface, whose non-dynamic behavior is not within the scope of interest for this study.

Under these conditions the criterion for failure is simply:

$$-P_{eff} > P_{cr}, \quad (4)$$

where $P_{eff} = \sigma_3 - P_f$ is the effective pressure. The *overpressure* P_o is defined as $P_o = -P_{eff}$, if $P_{eff} < 0$. Obviously, hydraulic fracturing occurs if $P_o > P_{cr}$.

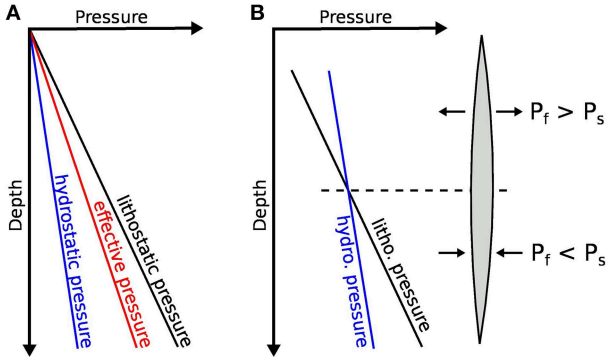

FIGURE 2 | (A) Idealized pressure gradients in the Earth's crust. Due to its higher density, the lithostatic (solid) pressure increases with depth faster than the hydrostatic (fluid) pressure. The effective pressure ($P_{eff} = P_S - P_f$) is in-between. **(B)** Formation of mobile hydrofractures [after 1]. The different pressure gradients of fluid and solid lead to fluid overpressure in the upper part of a fracture and to fluid underpressure at the lower part of the fracture. The fracture moves upward. Please note that the average fluid pressure in a hydraulic fracture is identical to the pressure in the solid.

Figure 2A shows the idealized increase of fluid and solid stress with depth. Due to different gradients of fluid pressure and solid pressure (P_s) the difference between P_{eff} and P_s increases with depth. Therefore, at large depth a required fluid pressure in order to initialize hydraulic fracturing is larger than at a shallower depth. This has the additional effect that the fluid pressure gradient in the vicinity of a fluid source is often higher at large depth than it is at shallower crustal levels, resulting in larger flow velocities on fractures at depth (Equation 1). Another effect of the different fluid and solid pressure gradients is the potential formation of mobile hydraulic fractures (**Figure 2B**, [1]).

Equation (1) in combination with the criterion for hydraulic fracturing (Equations 2–4) permits the calculation of the necessary minimum conductivity that crustal rocks must have in order to conduct fluid flow with a given flow rate. A potential fluid source in the Earth's crust are metamorphic dehydration reactions, which are caused by changing pressure and temperature conditions.

For simplicity we consider the mineral reaction biotite → feldspar + Fe/Mg-oxide + water as the single fluid source, which has been suggested for the Mount Painter breccias [4]. We further assume that the reaction occurs at a depth of 16 km depth [e.g., 4, 50]. With a tensile strength of 1 MPa [44] the fluid pressure is very close to the lithostatic pressure if hydraulic fracturing is initiated. If we assume a volumetric flux of 1 m/s, which has been suggested for Mount Painter, a necessary minimum conductivity of approximately 6×10^{-5} m/s for the conducting material follows from Equation (1). The conductivity of non-fractured crustal material is approximately in the range of 10^{-9}–10^{-12} ms/s [43], several orders of magnitude too small to allow the necessary fluid flow from the source zone to the surface.

It must be concluded that fluid transport on the scale as observed at Mount Painter can occur only along fractures. These fractures may be either stationary or dynamic and mobile,

TABLE 1 | Material parameters used in the simulations.

	Matrix porosity	Matrix conductivity	Fracture conductivity	Tensile strength	Solid density	Water density	Water bulk modulus	Water viscosity
Value	0.01	10^{-9} m/s	10^{-2} m/s	10^{6} Pa	2700 kg/m^3	1000 kg/m^3	2.5^{9} Pa	1.05^{-3} Pa s
Source	[42]	[43]	[43]	[44]	[1]	[45]	[45]	[46]

depending on the evolution of the fluid stress field and the rate of fracture closure/healing once the fluid pressure decreases. If fractures heal slowly enough, fractures remain open between intermittent fluid pulses, and the fracture network is therefore stationary. The most dominant contributions to the closure of fractures are *healing* (plastic deformation; [49], see also **Figure 4**) and *sealing* (e.g., due to mineral precipitation or cataclasis; [40]).

Numerical Model

The computer model consists of a 2D section of crustal dimensions through a material with constant porosity and conductivity of the undamaged rock matrix, which represents a simplified Earth's crust. Fluid flow through porous rocks and through fractures can be modeled as Darcian flow, using Equation (1). We solve the Darcy equation with a Monte Carlo approach applied to an explicit finite difference solution on a regular square grid, which allows the computation of fluid flow in highly anisotropic and heterogeneous media. The nodes in this grid represent fractured or undamaged material with two different predefined hydraulic conductivities (**Table 1**). Fractures can be either horizontally or vertically oriented, therefore the fracture conductivity is anisotropic.

Fracture nucleation and fracture propagation are distinctly different steps in the simulations. Nucleation takes place once fluid pressure at a node is sufficiently high to cause fracturing in either the horizontal or vertical direction, according to the fracture criterion outlined in Equations (2–4). In order to model the inherent disorder of the material, Gaussian noise is applied to the tensile strength of the nodes and to the conductivity of fractures. The solid stress is considered to be isotropic (see cp the discussion in Section Fluid Flow and Hydraulic Fracturing in the Earth's Crust), meaning that fracture nuclei increase conductivity in both directions, horizontal and vertical.

In the numerical model a layer of constant overpressure at the lower model boundary serves as the fluid source. This allows us an assessment of the efficiency of the fluid transport in the system as the effective conductivity of the system once the system reaches a state of dynamic equilibrium. We coined the term "effective conductivity" for this study, which describes the averaged conductivity from the source at the lower boundary to the sink at the surface. Other fluid sources, for instance a constant production of fluid mass instead of constant pressure, wouldn't allow a similarly simple description of the system.

The overpressure at the lower system boundary is freely selectable in each simulation. The rate of fluid production is therefore a direct function of the efficiency of the fluid transport from the source to the surface. Geologically, this might represent a pressure controlled fluid-producing mineral reaction.

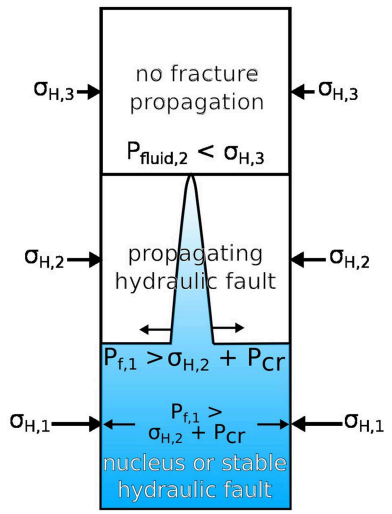

FIGURE 3 | Fractures propagate if the fluid pressure at a neighboring, already fractured node is larger than the local fracture criterion. Here, a vertical fracture propagates from layer 1 to layer 2, where it is arrested. σ_H, horizontal solid stress; P_f, fluid pressure; P_{cr}, critical stress.

Nodes are assumed to be mechanically coupled, which is a typical assumption for the formation and propagation of hydraulic fractures [e.g., 40, 51]. Thus, fractures propagate if the fluid stress at an already fractured node is sufficiently high to fulfill the fracture condition at a *neighboring* node too:

$$P_s^n - P_f < P_{cr}^n,$$

where the superscript n refers to the neighbor node (**Figure 3**).

Time stepping is often a non-trivial issue in the modeling of geological processes, where long-term processes cause and interact with dynamic processes on far shorter time scales. The computer simulations use adaptive time steps with a fixed maximum Δt_{max}. Time steps Δt are determined by an estimate of the minimum time it takes to build up sufficient pressure at the existing fracture tips to cause further fracture propagation. If this time estimate is larger than Δt_{max}, Δt is set to Δt_{max}.

Closing and healing of fractures is a complex process, which involves elastic and viscous closure of the fracture and dissolution and precipitation of minerals within the fracture former fracture aperture. Here we assume that a fracture is closed by viscous flow of the solid matrix into irregularities of the fault surface once $P_{eff} > 0$ only, an assumption which is suitable for the

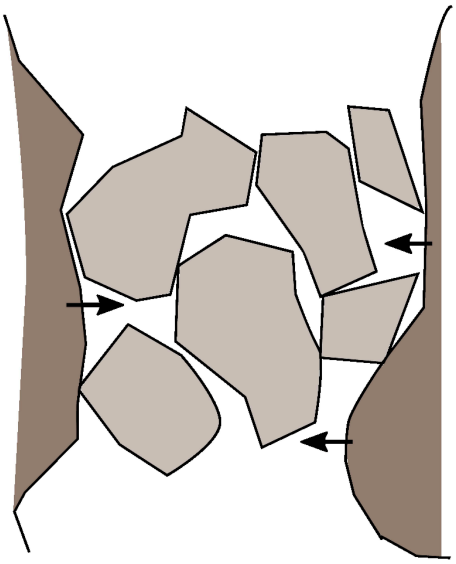

FIGURE 4 | Model for the closure of a fractured area by viscous flow of the solid into the fractured rock. The fracture is assumed to be formed by fractured clasts rather than by clear cut fracture walls. These clasts act as barriers against a simple elastic closure of the fracture once fluid pressure within the fracture zone is smaller than the solid pressure. Therefore, the fracture closes by viscous flow of the surrounding rock into the cavities made up by the clasts.

given fundamental assumption of damage zones or tectonic breccias rather than discrete faults with clear cut parallel walls (cp **Figure 4**). Because the impact of the fracture closure rate on the dynamics of the fracture network is one of the major interests in this study, the solid viscosity is considered homogeneous throughout the entire system. The fracture aperture is a function of the former fluid overpressure in the fracture and is calculated by a solution adapted from Maugis [51].

Setup of Numerical Simulations and Results

General Setup

Material parameters are compiled in **Table 1**. The following parameters are identical in all conducted simulations: the system size is 8000 (horizontal) by 16,000 m (vertical), with a distance Δl between fluid source and fluid sink of 15,750 m. A resolution of 100 × 200 grid points is commonly used, but has been occasionally compared to results with a solution of 150 × 300 in order to test the resolution dependency of the model. Gaussian normal distribution on the tensile strength of nodes assumes a mean strength of 1 MPa and a standard deviation of 0.1 MPa. The basal source layer with constant fluid overpressure $P_o = const$ and the fluid sink with $P_f = 0$ Pa are located at opposed system boundaries.

Modeling of individual fractures and fracture planes in a crustal scale model requires a resolution which is not achievable with today's computational equipment. The model therefore assumes that fractures form as fracture networks and affect the entire area defined by a gridpoint. Comparing the results from simulations with different resolutions did not show a change of the system behavior regarding fracture mobility and fluid transport efficiency.

In order to test the influence on the dynamics of the fracture network, P_o of the fluid source is varied between 0.5 and 2.0 MPa during the simulations and the solid viscosity ν between 10^{17} and 10^{23} Pa s, which can be assumed to be close to the geologically realistic lower and upper limit [52, 53]. We assume here that fractured nodes have the same conductivity as a typical sedimentary breccia [54–56], since fracturing in the crust typically results in the formation of a damage zone rather than an isolated fracture plane [34, 57].

The choice of a crustal stress model is a rather difficult one since the topic is still under intense debate. The model assumes a isotropic lithostatic solid stress, which is probably a good approximation in case of a vertical crustal section, given that the depth is considerably larger than ∼1 km and external tectonic forces are absent (compare discussion in Section Fluid Flow and Hydraulic Fracturing in the Earth's Crust). This assumption ignores natural variations in the horizontal stress field, which are frequently observed drill-holes, but are difficult to quantify in a model [58, 59].

Experiments in a System without Pressure Gradient ("Horizontal" Profile)

In order to test the influence of the pressure gradient on the dynamics of fracture formation and propagation, we compare the time evolution of hydraulic fractures through a vertical 2D section through the crust ($\Delta z = 16.000$ m) with a horizontal section ($\Delta z = 0$ m). Fluid stress is constant in the case of a horizontal section, i.e., $dP_f/dL = 0$.

Figure 5 displays the resulting hydraulic fracture pattern, the fluid mass change with time ($\Delta m_f/t$) and the fractured area in the horizontal system. The fluid source is located at the left system boundary with a constant overpressure $P_o = 1.2$ MPa while the sink is at the right of the system. Thus, the hydraulic head over the entire system length is $\Delta H = \Delta P = 1.2$ MPa, identical to simulations set in a vertical profile.

The final fracture network that develops in these experiments is stationary. Close to the source a fracture front develops, which is replaced by individual fractures once the front reaches a certain distance from the sink (**Figure 5**). Fractures do not close once formed but maintain sufficient fluid overpressure to keep existing fractures open.

If fractures penetrate the sink, a large amount of fluid is quickly drained into a fluid burst, creating the large negative peaks in **Figure 5B**. Once a sufficient number of fractures reach the sink, an equilibrium between fluid production and fluid drainage is reached and the fluid mass remains approximately constant (**Figure 5**, constant conditions are reached from 3000 years onward). From this point on the fracture pattern is stationary. Due to the constant fluid overpressure in fractures, the fracture viscosity is irrelevant to the development of the fracture network and the fault patterns are identical whether $\nu = 10^{17}$ or 10^{23} Pa s. Negative spikes in the fluid mass change between

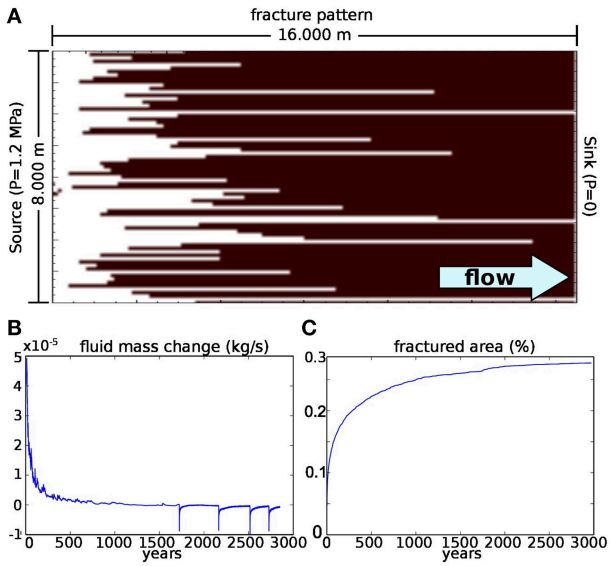

FIGURE 5 | Final fracture pattern (A), fluid mass change with time ($\Delta m_f/t$) (B) and total fractured area in % (C) in an simulation where the hydraulic fracture propagation is calculated for a *horizontal* 2D section through the crust, i.e., in the absence of an initial pressure gradient. The situation is somewhat similar to flow to a well. Low viscosity conditions ($\nu = 10^{17}$ *Pa s*), i.e., fractures close quickly. **(A)** Fractured nodes are *white*. Fluid source is a constant layer with constant fluid pressure $P_f = 1.2$ *MPa* at the left boundary of the model, the sink is at the right boundary with constant $P_f = 0$ *Pa*, similar to experiments with vertical fracture propagation. Fractures propagate until the source is sufficiently connected to the sink, at which point flow becomes stable. The fracture network is stationary, even though the viscosity is low. The fluid mass in the system remains constant from this point on **(B)**. *Negative peaks* are created by rapid drainage of the system fluid mass when a fracture reaches the other side and fluid pressure is rapidly released. From 3000 a onwards no further fracturing occurs. **(C)** Propagation of the fracture front is fast at the beginning, then slows down and converges against zero, which is indicated by a constant percentage of fractured material in the system.

1500 and 2700 years (**Figure 5B**) correlate with the permanent opening of single fractures, which cause sudden and very efficient drainage resulting in a short dewatering event. Once the fracture network is efficient enough to provide continuous pathways from the source to the sink, both the fracture distribution and the fluid mass in the system remain constant.

Unlike the vertical experiments described below, we were unable to establish a permanent pulsating regime in these experiments. If the fluid pressure at the source is to small, flow occurs within the rock matrix. If pressure is high, a stable fracture pattern develops, where the total number of fractures increases with the pressure at the source. Dynamic flow and fracture formation, however, seem to rely on the presence of a fluid pressure gradient, as in the numerical simulations discussed below.

Experiments with Fluid Pressure Gradient (Vertical Profile)

If basal fluid overpressure is sufficiently large (starting already at $P_o \approx 0.8$ MPa, due to the noise on the tensile strength), hydraulic fractures form and drain the fluid produced at the basal fluid source toward the surface. In all experiments the fractured area increases until the fracture network is efficient enough to create equilibrium between fluid production at the basal fluid source and fluid drainage at the surface.

Two sets of simulations have been computed: one set with $\nu = 10^{17}$ and 10^{23} Pa s (**Figures 6–10**). A detailed description follows in the sections below. The fluid overpressure of the fluid source was varied between 0.5 and 2.0 MPa. The characteristic values in **Figures 6**, **9**—the fractured area and the balance between fluid production and fluid drainage $\Delta m_f/t$—reach near-stable plateaus with recurring patterns, indicating that the system is in a dynamic or stable equilibrium (discussed in Section Intermittency of Fluid Flow).

Low Viscosity Simulations (Quick Fracture Healing)

Results for a viscosity mode ($\nu = 10^{17}$ Pa s) are displayed in **Figure 6**. At 0.85 MPa basal overpressure stationary hydraulic fractures form at locations with low tensile strength and propagate upwards from there. Although these fractures are spatially stationary, they are in a dynamic equilibrium as their tips open and close periodically.

Increasing the basal overpressure to 0.9 MPa leads to the formation of vertical *mobile* fracture clusters, which transport fluid pulses to the surface. The horizontal location of these vertical pathways is stationary and depends on the distribution of the tensile strength at the boundary layers between fluid source and non-fluid producing rock matrix. With increasing overpressure the horizontal width and the vertical extend of the fractured areas increase, and accordingly the total amount of fractured rock material. At a basal overpressure of approx. 1.8 MPa the system is completely fractured and fracture are stationary.

At the beginning of each low viscosity simulation fluid is transported by small mobile hydraulic fractures along distinct vertical pathways. These pathways are defined by the tensile strength at the interface between fluid source and rock matrix. These mobile fractures precede the fracture front and lead to permanent elevated fluid pressure along these vertical lines (**Figure 7**, right). Fractures propagate from both the surface, where effective stress is close to zero, and from the sink. With the onset of fracture formation at the surface in the more dynamic system with $\nu = 10^{17}$ Pa s, fluid is more efficiently drained and an intermediate plateau in the development of the fluid mass change with time $\Delta m_f/t$ is reached.

It is not intuitively clear why fractures form far from the fluid source and close to the surface (**Figure 7**, left panel). The reason is the increase of the fluid pressure along the fluid pathways (**Figure 7**, right panel). This permanent increase, coupled with flow enabled by the background permeability of the material, leads occasionally to fracturing even if the fluid source is in a distance. This phenomenon affects primarily rocks at a shallow depth, because the necessary increase in fluid pressure is comparatively low.

The interplay of the fracture network with the stress field is visible in **Figure 8**, where the effective stress is displayed at a random time after the system reached the state of

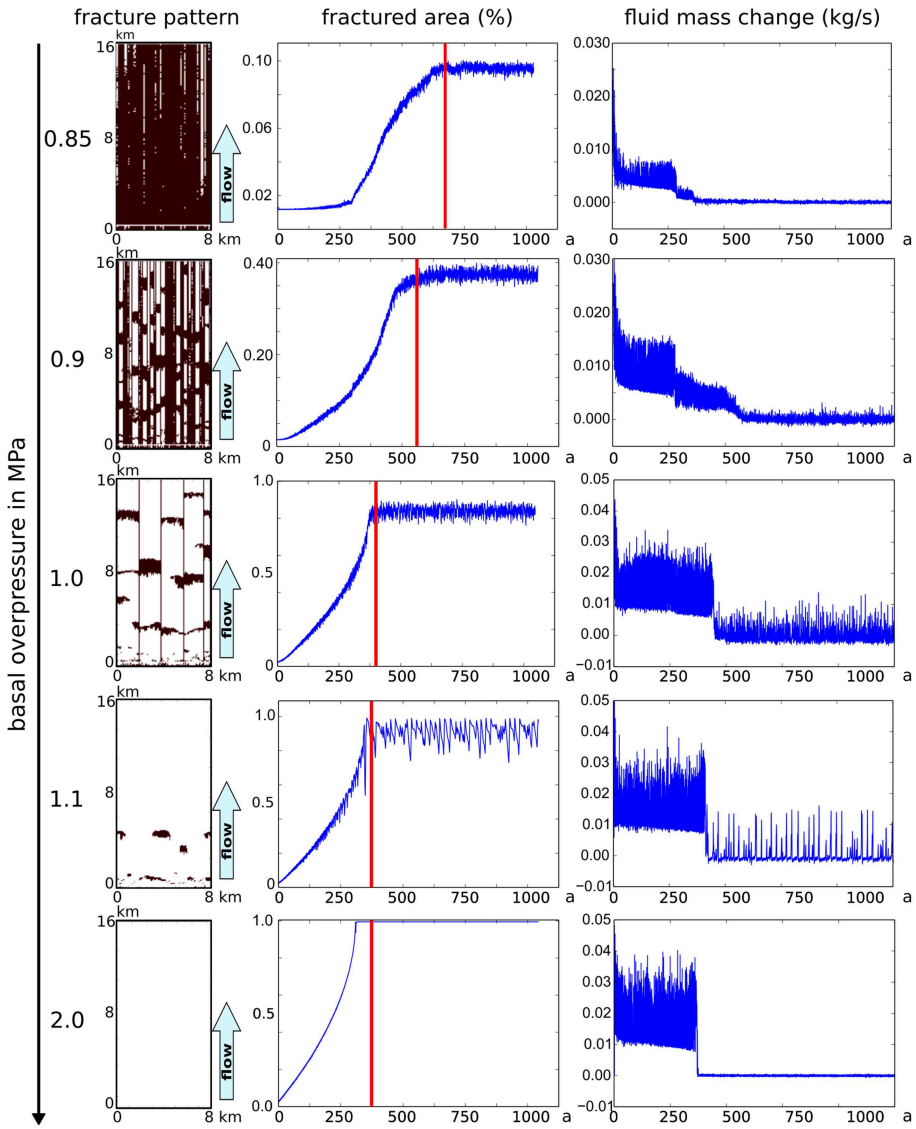

FIGURE 6 | Final fracture pattern, fluid mass change ($\Delta m_f/t$) and total fractured area in % in experiments with *vertical* hydraulic fracture propagation at low viscosity $\nu = 10^{17}$ Pa s. Fractured nodes are *white*. Fluid source is a constant layer with constant fluid overpressure at the bottom boundary of the model. The sink is at the top boundary with constant fluid pressure $P_f = 0$ Pa, representing a free surface. With increasing overpressure, the total fractured area increases until the entire system is damaged. Fracture clusters are dynamic and are mobile in the vertical direction, moving upwards. The horizontal position is fixed and determined by the Gaussian noise. Stable fracture patterns occur at fixed basal overpressures of 0.5 and 2.0 MPa. Periodic changes of the fractured area and of the fluid mass, even after fluid production and fluid drainage are in equilibrium, illustrate the dynamic nature of the fracture pattern and the fluid flow. Red line: From the marked time step onward the system is considered to be in a stable state. Power spectral density in **Figure 11** is calculated for the stable state.

dynamic equilibrium. If hydraulic fractures form only along distinct vertical pathways (at a basal overpressure of 0.9 MPa), the effective stress along these pathways increases, potentially boosting formation of future fractures along these lines. Fractures close at locations where the effective stress is high (cp. **Figure 8** at basal overpressure of 1.1 MPa).

High Viscosity Simulations (Slow Fracture Healing)

If the viscosity of the solid phase is increased to $\nu = 10^{23}$ Pa s fracture patterns are near-stationary, regardless of the overpressure at the source. The stability of the fracture network results from relatively large time interval which is necessary to close these fractures in between fluid pulses (**Figure 9**). The effective stress field (**Figure 10**) is a function of the fracture pattern.

An intermediate plateau of $\Delta m_f/t$ (approximately about 0.005–0.01 kg/s) is reached shortly before the fluid network is completed. This is similar to low viscosity simulations, but has a different reason: the plateau is reached once a first front of distinct hydraulic fractures reaches the surface. The interstitial

spaces between these fractures function as propagation path for a secondary fracture front. Once this secondary fracture front reaches the surface, fluid production and fluid drainage reach a balanced state and $\Delta m_f/t \rightarrow 0$.

Intermittency of Fluid Flow

If a signal is random can be distinguished by the power spectral distribution ("psd"). **Figure 11** displays the psd calculated for the normalized fractured area of various simulations. The signal is typical of the forma $f^{-\alpha}$, with α in the range 1.27–1.95, a clear sign that the signal is not random white noise, but shows a correlation in time.

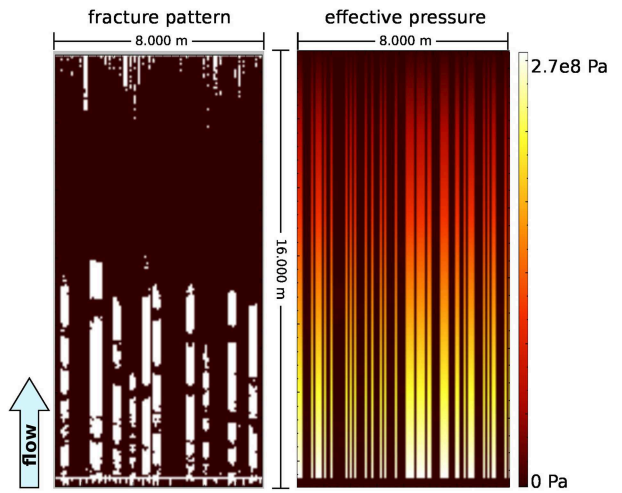

FIGURE 7 | Fracture pattern and effective stress at an intermediate state of the development of the fracture network with $\nu = 10^{17}$ Pa s. Vertical experiment with fixed basal overpressure of 0.9 MPa (cp. **Figure 6**). An initial front of mobile fractures develops early on in the development, generating columns of increased fluid pressure. This leads to the formation of vertical hydraulic fractures nucleating at and propagation downward from the surface, where the difference between hydrostatic fluid pressure and lithostatic pressure is small (cp. **Figure 2**).

In two cases the psd in the upper frequency band is non-linear. This affects simulations with a basal overpressures of 1.1/0.85 MPa and a viscosity $\nu = 10^{17}$. This result is most probably related to issues with relatively small spatial resolution or time intervals of the simulations. In these cases the α has been calculated for the linear part only. A value of $\alpha = 4.0$ results for the linear region in the lower frequency band in case of the simulation with overpressure 1.1 MPa/$\nu = 10^{17}$, but this value can be attributed to the error.

Numerical simulations with near-stationary fracture networks develop $\alpha = 0$, indicating constant values with some numerical random noise. This is the case in simulations where basal overpressure is relatively large (compare **Figures 6**, **9**). Psd plots whith $\alpha = 0$ were omitted from **Figure 11**.

The evolution of the fracture pattern for a particular simulation (with 0.9 MPa overpressure/$\nu = 10^{17}$) is shown in **Figure 12**. **Figure 12A** shows the vertical movement of fracture clusters in system snapshots from three consecutive years. When a cluster arrives at the surface fluid drainage occurs. The alternation with of fracture clusters with healed material causes the intermittency of the fluid flow. **Figure 12B** displays the time evolution of the fracture state of a horizontal section at 4000 m depth through a simulation. After c. 400 years the onset of a fracture pattern can be seen. From then on intermittent fracturing and healing occurs in almost regular intervals.

Transport Efficiency of Fracture Networks

The efficiency of the fracture network to transport fluid can be characterized by the hydraulic conductivity over the total system length from source to sink, which will be termed the effective conductivity K_{eff} in the following. K_{eff} is calculated from Equation (1):

$$K_{eff} = \frac{qL}{P_f^{source} - \rho_{H_2O} g L}.$$

The resulting conductivity of the system in the stable state is plotted against the overpressure of the fluid source in **Figure 13**. Conductivity increases linearly with the fluid overpressure at the

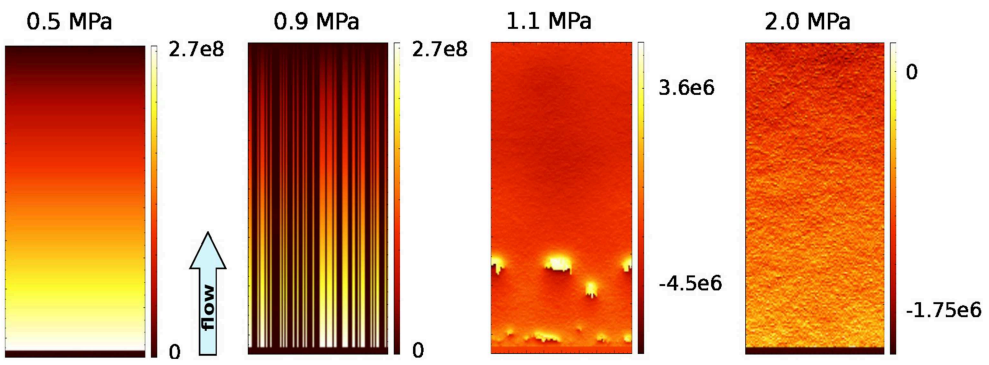

FIGURE 8 | Effective stress fields after equilibrium between fluid production and drainage is reached in vertical experiments with viscosity $\nu = 10^{17}$ Pa s. Preferred fluid pathways show heightened fluid pressure (very good visible at basal overpressure of 0.9 MPa). At a basal overpressure of 1.1 MPa, the heightened effective stress in areas of temporary non-fractured areas is obvious.

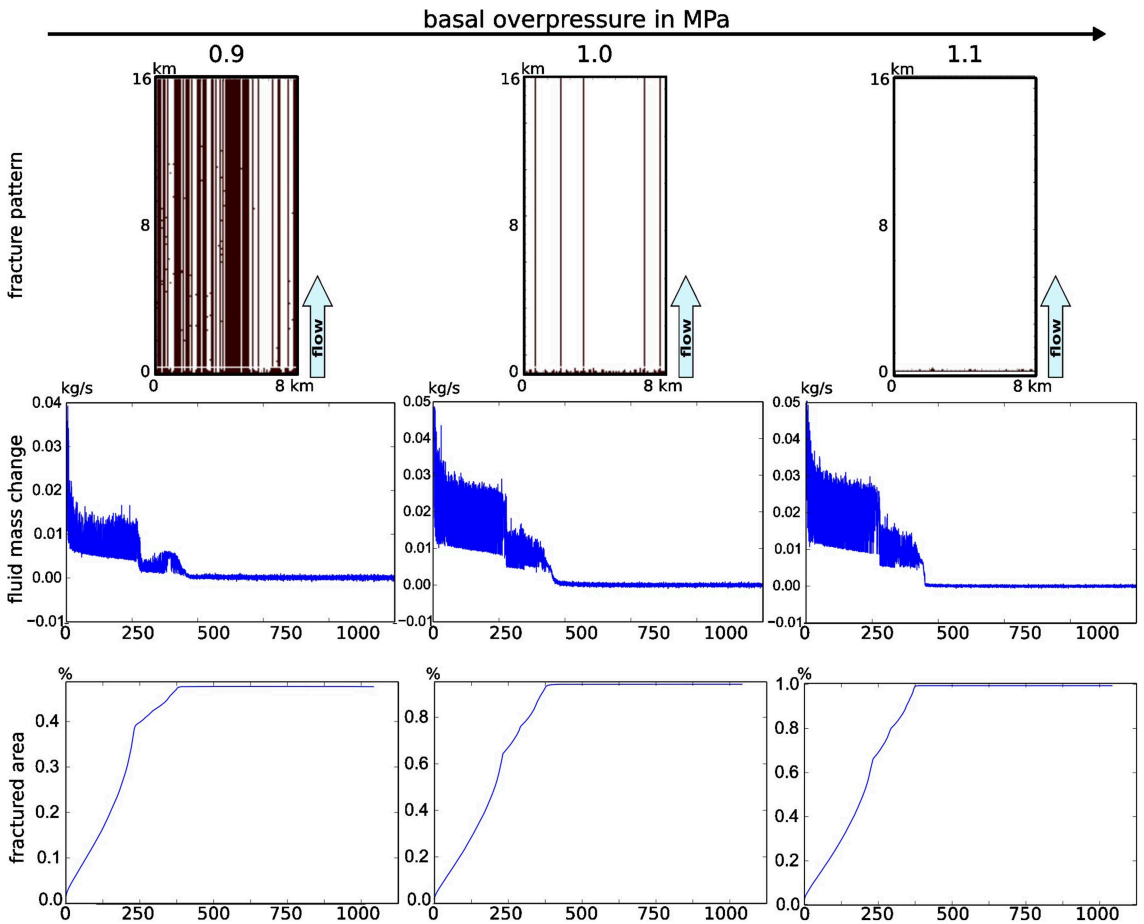

FIGURE 9 | Final fracture pattern, fluid mass change ($\Delta m_f/t$) and total fractured area in % in experiments with vertical hydraulic fracture propagation at high solid viscosity $\nu = 10^{23}$ Pa s. Fractured nodes are displayed in white. Most hydraulic fractures remain permanently open after their formation, and dynamic. Vertical clusters of hydraulic fractures, as under low viscosity conditions, do not occur, but continuous fractures develop connect between fluid source and surface. The vertical distribution of these fractures is determined by the Gaussian noise. Red line: From the marked time step onward the system is considered to be in a stable state. The power spectral density in **Figure 11** is calculated for the stable region.

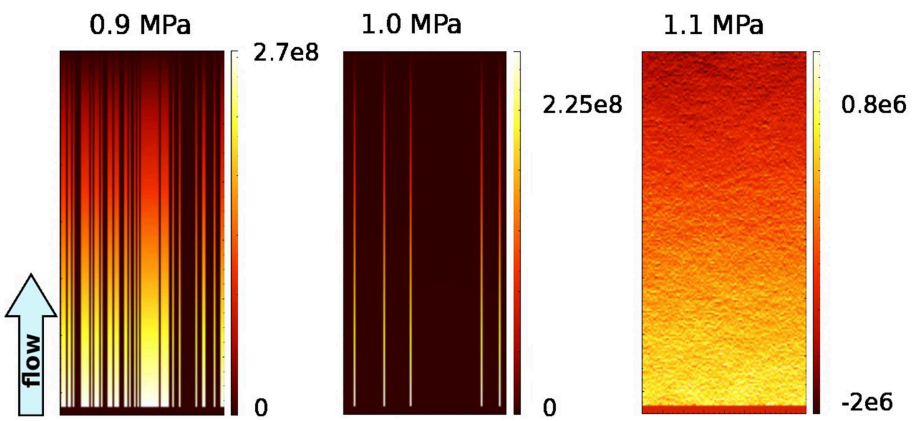

FIGURE 10 | Effective stress field after equilibrium between fluid production and drainage is reached in vertical experiments with high viscosity $\nu = 10^{23}$ Pa s. Fluid pathways are signified by lowered effective pressures.

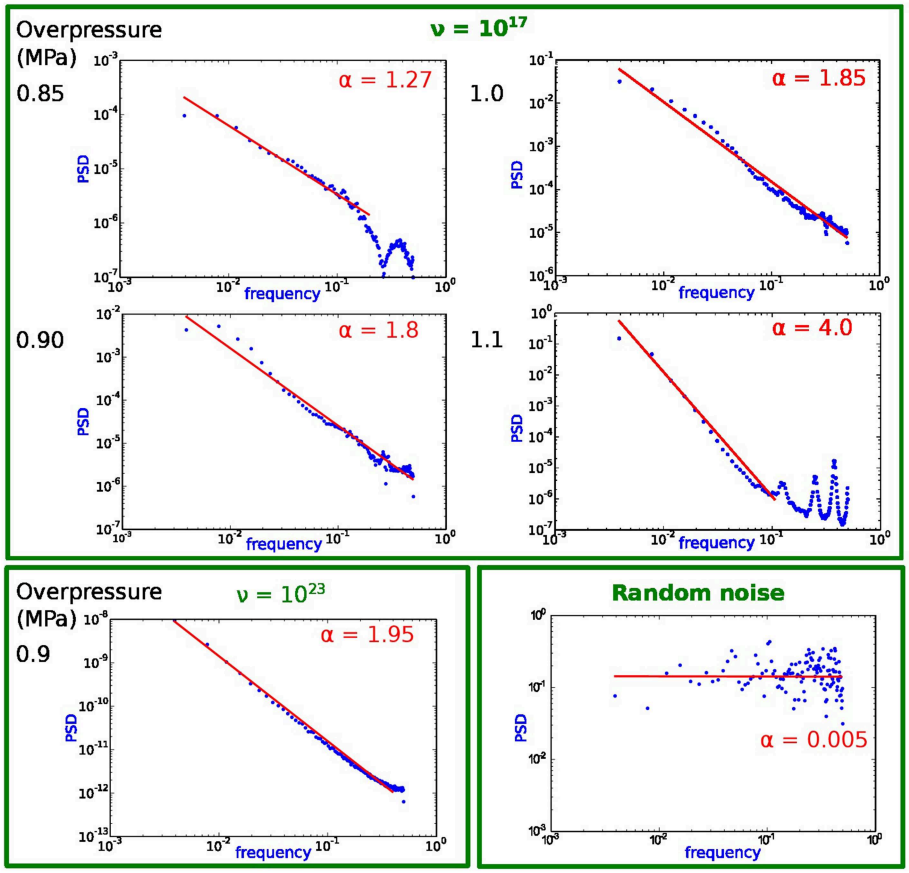

FIGURE 11 | 1/f$^{\alpha}$ power spectral density (psd), calculated from the normalized fractured area in the simulations shown in Figures 6, 9 with Welch's method. α is calculated by linear regression for the near-linear intervals in the lower frequency band (red line). Not shown is the psd for systems where $\alpha = 0$ (white noise), which was the case for $\nu = 10^{17}$/overpressure = 2.0 MPa, $\nu = 10^{17}$/1.0 MPa and $\nu = 10^{17}$/1.1 MPa (cp **Figures 6**, **9**). For comparison the psd for a random time series ($\alpha = 0$). The psd is close to 1/f if overpressure is small, α increases with increasing overpressure. The non-linearity at high frequencies of some simulations is probably related to the resolution and the simulation time.

source layer until it reaches a constant maximum, starting at an overpressure of approx. 1 MPa (**Figure 13**), which is also the mean tensile strength of the material.

This means that the mean efficiency of the fluid transport is independent of the fracture dynamics and the mobility of fractures. Even before equilibrium is reached, the efficiency of the different types of fracture networks in terms of fluid extraction from source to sink is similar (cp. the fluid mass change per time in **Figures 6**, **9**). The main difference between static and dynamic fracture networks is the occurrence of fluid pulses in case of a dynamic fracture network, in difference to near-continuous flow in case of a stationary network.

Discussion

Dynamics of the Fracture Pattern

The development of dynamic fracture patterns in the computer simulations—in difference to a stable stationary fracture network—depends on the following three preconditions:

- The fluid overpressure is close to the mean tensile strength of the material, otherwise either no fractures form or the entire system fractures homogeneously,
- A fluid pressure gradient is present, as is the case in vertical profiles through the Earth's crust, and
- Fractures close quickly (i.e., the matrix viscosity is low), once the fluid pressure dropped below the solid pressure of the rock matrix.

The interface layer between the fluid source and the rock matrix is particularly important for the dynamics of the process. It works similar to a valve: once sufficient fluid migrated from the source into the adjacent rock mass, vertical hydraulic fractures nucleate and propagate toward the surface, thus transporting large amounts of fluid in a short period of time. Once the interface layer is sufficiently drained and the fluid pressure is lower than the matrix solid pressure, fractures close and the process starts again. This process leads to a non-random 1/f$^{\alpha}$ type signal once the system reaches a state of dynamic equilibrium, with $1 < \alpha < 2$.

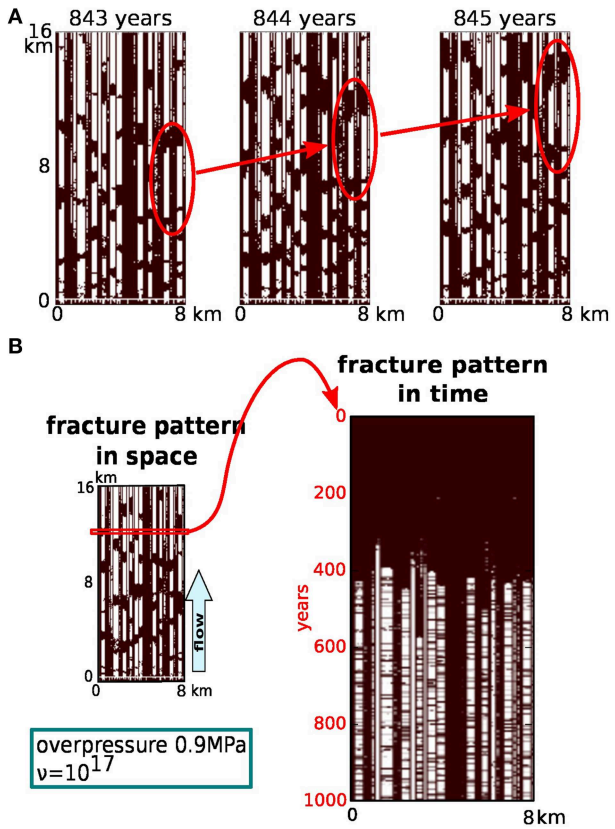

FIGURE 12 | Time evolution of fracture clusters, demonstrated with the simulation using $\nu = 10^{17}$ and a basal overpressure of 0.9 MPa (see Figure 6). (A) Three subsequent snapshots of the fracture pattern. A single cluster is highlighted for clarity. Note the vertical movement at ~2000 m per year. **(B)** Time evolution of fractures in a 1D section through the simulation. Section line is marked by the red rectangle, located at 4000 m depth. Onset of the fracture/healing process after c. 300. The figure illustrates the intermittency of the fracture opening/healing process, which is induced by intermittent fluid flow.

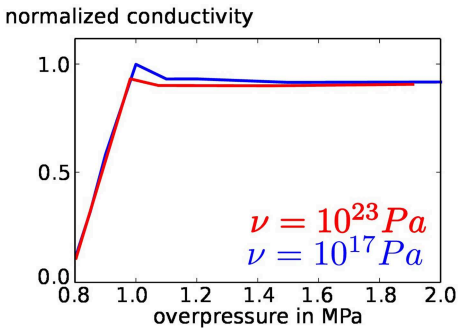

FIGURE 13 | Effective conductivity of the total system between source and sink after equilibrium between fluid production and fluid drainage exists, drawn against various overpressure values for the basal layer. Red: slow fracture closure ($\nu = 10^{17}$ Pa s). Blue: fast fracture closure ($\nu = 10^{17}$ Pa s). To avoid scaling problems the conductivity has been normalized by the highest value of both plots. The development of the conductivity is almost identical, regardless of the viscosity and the dynamics of the fracture network.

Preferred vertical fluid pathways develop according to the Gauss distribution at the interface. If a fracture closes, the fluid it transported is trapped and increases the local fluid pressure due to the very low matrix conductivity. The amount of additional fluid which is required to reactivate these nodes as fractures again is significantly smaller than in the adjacent material. These areas of heightened fluid pressure from potential future pathways for hydraulic fractures and quick fluid transport. Coupled with the non-destructive background diffusion of the fluid this can even lead to fracture initiation in a distance to the fluid source (**Figure 6**, left).

If the viscosity of the surrounding solid matrix is at 10^{23} Pa s fracture closure is typically slower than pressure build up and hydraulic fracture patterns are stationary. Fluid mass balance is reached once the fracture network is capable of draining the entire fluid mass produced at the basal source. At this point the fractured area and the drained fluid mass converge to constant values, regardless of specific parameters. Periodic deviations from the equilibrium occur if ν is small, and are most significant at a slight overpressure of approx. 1.1–1.3 MPa.

Of particular interest to the dynamics of intermittent fluid flow are the amplitude and the frequency of fluid pulses. Pulses occur in simulations with a more dynamic low viscosity setting, visible in the rate of change of the fluid mass in the system (**Figures 5**, **8**). The amplitude of fluid burst grows from low overpressure values till the overpressure is identical with the mean tensile stress is reached. A further increase of the fluid overpressure leads to the elimination of fluid bursts with small amplitudes, but still allows large fluid pulses in regular intervals.

Comparing the horizontal setup (without a fluid pressure gradient) to the results derived from vertical setups, it becomes clear that the fluid pressure gradient is essential for the development of dynamic fracture networks and fluid pulses.

The presented numerical method and simulations illustrate how a dynamic fluid flow system works, and the conditions under which they can efficiently transport large volumes of fluid to upper levels in the crust. These models are critical to understand highly complex transport systems, such as the ones responsible for the formation of large hydraulic breccias or dense networks of crack-seal veins.

The dynamics observed in the simulations—in particular the periodic changes of the fluid mass in the system, which was observed in most setups—might help to explain phenomena as the initially discussed hydraulic breccia, which depends on intermittent large scale fluid pulses.

It is of great interest to note that the efficiency of the fluid transport is virtually independent of the closing rate of the fractures. This means that velocity and dynamics of the fluid transport do not depend on the existence and reactivation of preexisting fracture networks, at least under model conditions. Potential fluid pathways are characterized by heightened local fluid pressure, which is a byproduct of previous fluid flow transport on fractures.

Summary and Conclusion

Fluid transport in the crust involves the formation of hydraulic fractures if the fluid overpressure at the source is sufficient. Geological evidence for this process exists, for instance in form of crack-seal veins or hydraulic breccias.

We simulated the dynamics of the vertical fluid flow from a fluid source with a constant overpressure to the surface, including the evolution of hydraulic fracture patterns. The ability to close fractures, once fluid pressure is lower than the solid pressure, is controlled by the matrix viscosity, which is taken to be at its uppermost and lowermost geologically realistic limits. The solid stress field is probably approximately accurate below 250 m depth, please note the discussion in Sections Fluid Flow and Hydraulic Fracturing in the Earth's Crust and General Setup.

Hydraulic fracture patterns may be either dynamic or stable, depending on the ability of fractures to close quickly, once the fluid pressure is released. In the dynamic case hydraulic fractures form mobile clusters and fluid transport occurs in periodic pulses. The reason is a valve function of the interface between fluid source and matrix rocks, where fluid pressure builds up by Darcian flow until it is sufficient to initiate fracture formation and quick removal of fluid mass toward the surface. The fracture dynamics follows a $1/f^{\alpha}$ pattern, with $1 < \alpha < 2$. If fractures heal slowly, the fracture network is stable and fluid flow is nearly constant.

The efficiency of the fluid transport is identical in both cases, regardless of the dynamics of the fracture network. While the dynamics of fluid flow and fracture formation differs considerably between the two settings, the efficiency of the fluid transport is not affected. Both systems have the same effective hydraulic conductivity. This is even more remarkable since the overpressure at the fluid source is constant, which means that the fluid production is entirely controlled by the efficiency of the transport mechanism. This means, in turn, that the existence of a stable fracture network is not as important as often assumed, as long as fluid overpressure is sufficient to initiate fracturing. More important than a fracture network are areas of heightened fluid pressure, where a relatively small amount of additional fluid is sufficient to initiate further fracturing. These areas are generally created by previous generations of hydraulic fracture swarms.

A key parameter for the dynamic fracture evolution is the presence of a fluid pressure gradient. In absence of a gradient fracture, as is the case of the "horizontal" setup, stable networks are being formed.

Acknowledgments

This study is carried out within the framework of DGMK (German Society for Petroleum and Coal Science and Technology) research project 718 "Mineral Vein Dynamics Modeling," which is funded by the companies ExxonMobil Production Deutschland GmbH, GDF SUEZ E&P Deutschland GmbH, RWE Dea AG and Wintershall Holding GmbH, within the basic research programme of the WEG Wirtschaftsverband Erdöl- und Erdgasgewinnung e.V. We thank the companies for their financial support and their permission to publish our results.

We further acknowledge support by Deutsche Forschungsgemeinschaft and Open Access Publishing Fund of University of Tübingen.

References

1. Bons PD, Elburg MA, Gomez-Rivas E. A review of the formation of tectonic veins and their microstructures. *J Struct Geol.* (2012) **43**:33–62. doi: 10.1016/j.jsg.2012.07.005
2. Lazincka P. Breccias and ores. Part 1: history, organization and petrography of breccias. *Ore Geol Rev*. (1989) **4**:315–44. doi: 10.1016/0169-1368(89)90009-7
3. Lorilleux G, Jébrak M, Cuney M, Baudemont D. Polyphase hydrothermal breccias associated with unconformity-related uranium mineralization (Canada): from fractal analysis to structural significance. *J Struct Geol.* (2002) **24**:323–38. doi: 10.1016/S0191-8141(01)00068-2
4. Weisheit A, Bons PD, Elburg MA. Long-lived crustal-scale fluid flow: the hydrothermal mega-breccia of Hidden Valley, Mt. Painter Inlier, South Australia. *Int J Earth Sci.* (2013) **102**:1219–36. doi: 10.1007/s00531-013-0875-7
5. Jébrak M. Hydrothermal breccias in vein-type ore deposits: a review of mechanisms, morphology and size distribution. *Ore Geol Rev*. (1997) **12**:111–34. doi: 10.1016/S0169-1368(97)00009-7
6. Sibson R. Brecciation processes in fault zones—inferences from earthquake rupturing. *Pure Appl Geophys*. (1986) **124**:159–75. doi: 10.1007/bf00875724
7. Keulen N, Heilbronner R, Stunitz H, Boullier A-M, Ito H. Grain size distribution of fault rocks: a comparison between experimentally and naturally deformed granitoids. *J Struct Geol*. (2007) **29**:1282–300. doi: 10.1016/j.jsg.2007.04.003
8. Mort K, Woodcock NH. Quantifying fault breccia geometry: Dent Fault, NW England. *J Struct Geol.* (2008) **30**:701–9. doi: 10.1016/j.jsg.2008.02.005
9. Ramsay J. The crack-seal mechanism of rock deformation. *Nature* (1980) **284**:135–9. doi: 10.1038/284135a0
10. Koehn D, Passchier CW. Shear sense indicators in striped bedding-veins. *J StructGeol.* (2000) **22**:1141–51. doi: 10.1016/S0191-8141(00)00028-6
11. Lee YJ, Wiltschko DV. Fault controlled sequential vein dilation: competition between slip and precipitation rates in the Austin Chalk, Texas. *J Struct Geol* (2000) **22**:1247–60. doi: 10.1016/S0191-8141(00)00045-6
12. Laubach SE, Reed RM, Olson JE, Lander RH, Bonnell RM. Coevolution of crack-seal texture and fracture porosity in sedimentary rocks: cathodoluminescence observations of regional fractures. *J Struct Geol.* (2004) **26**:967–82. doi: 10.1016/j.jsg.2003.08.019
13. Renard F, Andréani M, Boullier AM, Labaume P. Crack-seal patterns: records of uncorrelated stress release variations in crustal rocks. *Geol Soc Lond Spec Publ*. (2005) **243**:67–79. doi: 10.1144/GSL.SP.2005.243.01.07
14. Yilmaz TI, Prosser G, Liotta D, Kruhl JH, Gilg HA. Repeated hydrothermal quartz crystallization and cataclasis in the Bavarian Pfahl shear zone (Germany). *J Struct Geol* (2014) **68**:158–74. doi: 10.1016/j.jsg.2014.09.004
15. Nunn JA. Buoyancy-driven propagation of isolated fluid-filled fractures: implication for fluid transport in Gulf of Mexico geopressured sediments. *J Geophys Res.* (1996) **101**:2963–70. doi: 10.1029/95JB03210
16. Dahm T. On the shape and velocity of fluid-filled fractures in the Earth. *Geophys J Int.* (2000) **142**:181–92. doi: 10.1046/j.1365-246x.2000.00148.x
17. Eichhubl P, Boles JR. Rates of fluid flow in fault systems-evidence for episodic rapid fluid flow in the Miocene Monterey Formation, coastal California. *Am J Sci.* (2000) **300**:571–600. doi: 10.2475/ajs.300.7.571
18. Okamoto A, Tsuchiya N. Velocity of vertical fluid ascent within vein-forming fractures. *Geology* (2009) **37**:563–6. doi: 10.1130/G25680A.1

19. Weisheit A, Bons PD, Danisik, M, Elburg MA. Crustal-scale folding: Palaeozoic deformation of the Mt Painter Inlier, South Australia. *Geol Soc Lond Spec Publ.* (2014) **394**:53–77. doi: 10.1144/SP394.9
20. Gomez-Rivas E, Bons PD, Koehn D, Urai JL, Arndt M, Virgo S, et al. The Jabal Akhdar Dome in the Oman Mountains: evolution of a dynamic fracture system. *Am J Sci.* (2014) **314**:1104–39. doi: 10.2475/07.2014.02
21. Miller SA, Nur A. Permeability as a toggle switch in fluid-controlled crustal processes. *Earth Planet Sci Lett.* (2000) **183**:133–46. doi: 10.1016/S0012-821X(00)00263-6
22. Bons PD, van Milligen BP. New experiment to model self-organized critical transport and accumulation of melt and hydrocarbons from their source rocks. *Geology* (2001) **29**:919–22. doi: 10.1130/0091-7613(2001)029<0919:NETMSO>2.0.CO;2
23. Weertmann J. Theory of water-filled crevasses in glaciers applied to vertical magma transport beneath ocean ridges. *J Geophys Res.* (1971). **76**:1171–83. doi: 10.1029/JB076i005p01171
24. Oliver N, Rubenach M, Fu B, Baker J, Blenkinsop T, Cleverley J, et al. Granite-related overpressure and volatile release in the mid crust: fluidized breccias from the Cloncurry District, Australia. *Geofluids* (2006) **6**:346–58. doi: 10.1111/j.1468-8123.2006.00155.x
25. Staude S, Bons PD, Markl G. Hydrothermal vein formation by extension-driven dewatering of the middle crust: an example from SW Germany. *Earth Planet Sci Lett* (2009) **286**:387–95. doi: 10.1016/j.epsl.2009.07.012
26. Bons PD, Fusswinkel T, Gomez-rivas E, Markl G, Wagner T, Walter B. Fluid mixing from below in unconformity-related hydrothermal ore deposits. *Geology* (2014) **42**:1035–8. doi: 10.1130/G35708.1
27. Vry J, Powell R, Golden KM, Petersen K. The role of exhumation in metamorphic dehydration and fluid production. *Nat Geosci.* (2010) **3**:31–5. doi: 10.1038/ngeo699
28. Matthäi SK, Heinrich CA., Driesner T. Is the Mount Isa copper deposit the product of forced brine convection in the footwall of a major reverse fault? *Geology* (2005) **32**:357–360. doi: 10.1130/G20108.1
29. Person M, Mulch A, Teyssler C, Gao Y. Isotope transport and exchange within metamorphic core complexes. *Am J Sci.* (2007) **307**:555–89. doi: 10.2475/03.2007.01
30. Papanastasiou PC. A coupled elastoplastic hydraulic fracturing model. *Int J Rock Mech Min Sci.* (1997) **34**:240.e1–e15. doi: 10.1016/S1365-1609(97)00132-9
31. Vychytil J, Horii H. Micromechanics-based continuum model for hydraulic fracturing of jointed rock masses during HDR stimulation. *Mech Mater.* (1998) **28**:123–35. doi: 10.1016/S0167-6636(97)00061-6
32. Hossain M, Rahman M. Numerical simulation of complex fracture growth during tight reservoir stimulation by hydraulic fracturing. *J Petrol Sci Eng.* (2008) **60**:86–104. doi: 10.1016/j.petrol.2007.05.007
33. Ghani I, Koehn D, Toussaint R, Passchier CW. Dynamic development of hydrofracture. *Pure Appl Geophys.* (2013) **170**:1685–703. doi: 10.1007/s00024-012-0637-7
34. Ren L, Zhao J, Hu Y. Hydraulic fracture extending into network in shale: reviewing influence factors and their mechanism. *Sci World J.* (2014) **2014**:1–9. doi: 10.1155/2014/847107
35. Hu Y, Chen G, Cheng W, Yang Z. Simulation of hydraulic fracturing in rock mass using a smeared crack model. *Comput Struct.* (2014) **137**:72–77. doi: 10.1016/j.compstruc.2013.04.011
36. Wang T, Zhou W, Chen J, Xiao X, Li Y, Zhao X. Simulation of hydraulic fracturing using particle flow method and application in a coal mine. *Int J Coal Geol.* (2014) **121**:1–13. doi: 10.1016/j.coal.2013.10.012
37. Connolly J, Podlachikov Y. Compaction-driven fluid flow in viscoelastic rock. *Geodinamica Acta* (1998) **11**:55–84. doi: 10.1080/09853111.1998.11105311
38. Connolly J, Podlachikov Y. A hydromechanical model for lower crustal fluid flow. In: Harlov DE, Austrheim, H. editors. Metasomatism and the Chemical Transformation of Rock. Berlin; Heidelberg: Springer Berlin Heidelberg (2013), pp. 599–658.
39. Hasenclever J, Theissen-Krah S, Rüpke H, Morgan J, Iyer K, Petersen S, et al. Hybrid shallow on-axis and deep off-axis hydrothermal circulation at fast-spreading ridges. *Nature* (2014) **508**:508–12. doi: 10.1038/nature13174
40. Gudmundsson A, Fjeldskaar I, Brenner SL. Propagation pathways and fluid transport of hydrofractures in jointed and layered rocks in geothermal fields. *J Volcanol Geotherm Res.* (2002) **116**:257–78. doi: 10.1016/S0377-0273(02)00225-1
41. Majer EL, Doe TW. Studying hydrofractures by high frequency seismic monitoring. *Int J Rock Mech Min Sci Geomech Abstr.* (1986) **23**:185–199. doi: 10.1016/0148-9062(86)90965-4
42. Manger EG. *Porosity and Bulk Density of Sedimentary Rocks*. Washington, DC: United States Government Printing Office (1963).
43. Singhal BBS, Gupta RP. *Applied Hydrogeology of fractured Rocks*. Dordrecht; Heidelberg; London; New York: Springer (2010). doi: 10.1007/978-90-481-8799-7
44. Gudmundsson A. *Rock Fractures in Geological Processes*. Cambridge: Cambridge University Press (2011).
45. Hering E, Martin R, Stohrer M. *Physik für Ingenieure*. Düsseldorf: VDI Verlag (1992).
46. Fowler CMR. *The Solid Earth: An Introduction to Global Geophysics*. Cambridge: Cambridge University Press (2005). doi: 10.1029/90EO00309
47. Sun C, Jin Z. *Fracture Mechanics*. Amsterdam: Elsevier (2012).
48. Zhu Z. Evaluation of the range of horizontal stresses in the earth's upper crust by using a collinear crack model. *J Appl Geophys.* (2013) **88**:114–21. doi: 10.1016/j.jappgeo.2012.10.007
49. Fossen H. *Structural Geology*. Cambridge: Cambridge University Press (2010).
50. Matthes S. *Mineralogie*. Berlin; Heidelberg: Springer (1996).
51. Maugis D. *Contact, Adhesion, and Rupture of Elastic Solids*. Berlin; Heidelberg: Springer (2000).
52. Gölke M, Mechie J. Finite-element modelling of the structure and evolution of the South Kenya Rift, East Africa. *Tectonophysics* (1994) **236**:439–452. doi: 10.1016/0040-1951(94)90188-0
53. Wallner H, Schmeling H. Rift induced delamination of mantle lithosphere and crustal uplift: a new mechanism for explaining Rwenzori Mountains' extreme elevation? *Int J Earth Sci.* (2010) **99**:1511–24. doi: 10.1007/s00531-010-0521-6
54. Brace WF. Permeability of crystalline and argillaceous rocks. *Int J Rock Mech Min Sci Geomech Abstr* (1980) **17**:241–51. doi: 10.1016/0148-9062(80)90807-4
55. Owen P. *Geological Fluid Dynamics Sub-surface Flow and Reactions*. Cambridge: Cambridge University Press (2009).
56. Stober I. Researchers study conductivity of crystalline rock in proposed radioactive waste site. *Eos Trans Am Geophys Union* (1996) **77**:93. doi: 10.1029/96EO00062
57. Preisig G, Eberhardt E, Gischig V, Roche V, van der Baan M, Valley B, et al. Development of connected permeability in massive crystalline rocks through hydraulic fracture propagation and shearing accompanying fluid injection. *Geofluids* (2015) **15**: 321–37. doi: 10.1111/gfl.12097
58. Huffman A, Bowers G. *Pressure Regimes in Sedimentary Basins and Their Prediction*. Tulsa: The American Association of Petroleum and The Houston Chapter of The American Association of Drilling Engineers Geologists (2002).
59. Zang A, Stephansson O. *Stress Field of the Earth's Crust*. Dordrecht: Springer (2010).

Conflict of Interest Statement: The authors declare that the research was conducted in the absence of any commercial or financial relationships that could be construed as a potential conflict of interest.

Advantages of publishing in Frontiers

OPEN ACCESS
Articles are free to read, for greatest visibility

COLLABORATIVE PEER-REVIEW
Designed to be rigorous – yet also collaborative, fair and constructive

FAST PUBLICATION
Average 85 days from submission to publication (across all journals)

COPYRIGHT TO AUTHORS
No limit to article distribution and re-use

TRANSPARENT
Editors and reviewers acknowledged by name on published articles

SUPPORT
By our Swiss-based editorial team

IMPACT METRICS
Advanced metrics track your article's impact

GLOBAL SPREAD
5'100'000+ monthly article views and downloads

LOOP RESEARCH NETWORK
Our network increases readership for your article

Frontiers
EPFL Innovation Park, Building I • 1015 Lausanne • Switzerland
Tel +41 21 510 17 00 • Fax +41 21 510 17 01 • info@frontiersin.org
www.frontiersin.org

Find us on